

Volume 66 • Number 6 • December 2018

# Acta Geophysica

PAN  
POLISH ACADEMY OF SCIENCES



Institute of Geophysics  
Polish Academy of Sciences



Springer



# Stress studies in the Central Alborz by inversion of earthquake focal mechanism data

Shahrokh Pournbeyranvand<sup>1</sup>

Received: 23 October 2017 / Accepted: 24 September 2018 / Published online: 29 September 2018  
© Institute of Geophysics, Polish Academy of Sciences & Polish Academy of Sciences 2018

## Abstract

The Alborz is one of the most important seismotectonic provinces in Iran. Furthermore, emplacement of Tehran as a mega city in southern part of the Alborz intensifies the seismic vulnerability in this area. In this study, the focal mechanism data from teleseismic and local seismic networks are used for stress tensor inversion. The earthquake focal mechanisms in the Central Alborz are divided into several groups with respect to their location. Two different stress tensor inversions, linear and nonlinear, are used for obtaining the principal stress orientations. The results show spatial variations in tectonic stress field, consistent with fault orientations and faulting mechanisms. The maximum compressional stress directions obtained in this study are confirmed by fast S-wave polarization axes reported by a previous shear wave splitting study. The maximum horizontal stress directions are also compared with GPS strain rates. The results indicate a partitioning of deformation in the area due to regional stresses along preexisting faults.

**Keywords** Deformation partitioning · Earthquake · Focal mechanism · Inversion · Stress · Shear wave splitting

## Introduction

The Alborz Mountains places south of the Caspian Basin and separates Central Iran from Eurasia (Stocklin 1974). Talesh and Kopeh Dagh bound the Alborz as major thrust belts to the West and East, respectively (Fig. 1a, b). Significant differences exist in the eastern and western parts of the Central Alborz. The V-shaped pattern of faulting as it is appeared on the map, NW–SE trend in the eastern and NE–SW trend in the western parts, the differences in earthquake faulting mechanisms, and the variation in shortening rates perpendicular to the trend of the mountain range, are characteristics of the Alborz area. In the eastern part, mainly the left-lateral strike-slip movement (about 2 mm per year in the South and about 5 mm per year in the North) with a very low perpendicular shortening on the Khazar thrust (about 2 mm per year) is dominant (Djamour et al. 2010). In the western part, there is a small amount of left-lateral motion (about 2 mm/year in the north and 1 mm/year in the south),

in the presence of a major component (about 6 mm/year) of shortening motion (Djamour et al. 2010).

The tectonic processes in this important region, and the origin of the Alborz Mountains, are still unclear and a matter of debate (Berberian and King 1981; Berberian 1983; Allen et al. 2003). Acquiring the current state of the stress can help in better understanding the geodynamics of the region. Combining with the extensive paleostress studies already performed in the region, this information can provide a comprehensive insight into the tectonic evolution of the Alborz range. Furthermore, there are several applications for stress measurements in the Earth's crust in many fields such as oil and gas industries, civil, mining and geotechnical engineering. Importance of this kind of studies is highlighted due to major oil and gas potential and recent financial investments in the South Caspian Basin (SCB).

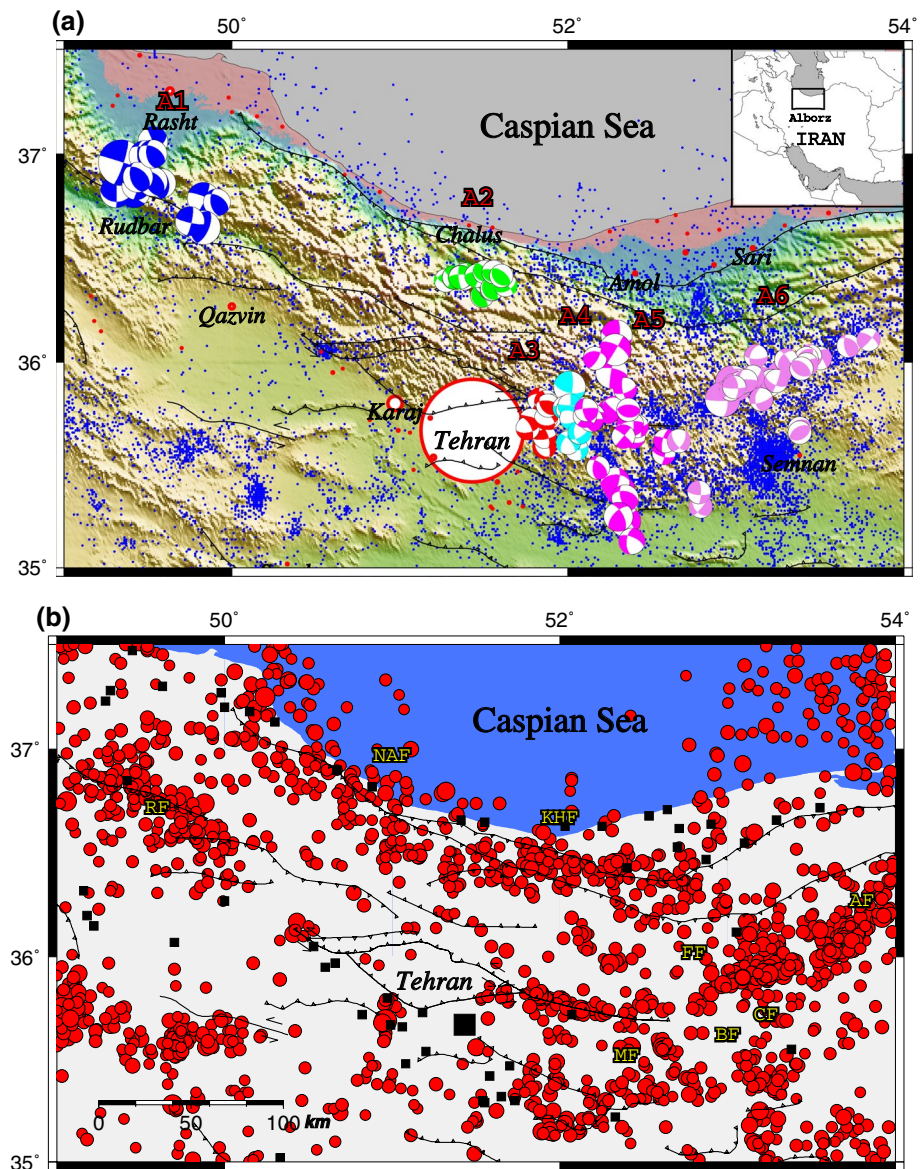
The stress orientation can also be inferred from seismic anisotropy caused by the preferred orientation of vertical fluid-filled micro-cracks present in the Earth's crust. Using shear wave splitting analysis, the polarization of the fast S wave and the time delay between the fast and slow S waves are measured. The S-fast polarization is usually parallel to the cracks, and the time delay is proportional to the crack density. The micro-cracks in the crust are aligned in a direction which is controlled by the local stress regime.

✉ Shahrokh Pournbeyranvand  
beyranvand@iiees.ac.ir

<sup>1</sup> Seismology Department, International Institute of Earthquake Engineering and Seismology, Tehran, Iran



**Fig. 1** **a** The Alborz range including its major faults overlaid on the topography (SRTM 90 m Digital Elevation Database) is shown in the figure. The earthquakes are from Iranian Seismological Center (IRSC) (2006 to 2018) catalogs, with magnitudes between 2.5 and 7.7. Focal mechanisms are clustered in six groups. The locations of the cities are indicated by red circles, filling with white color. The diameter of the circles is proportional to the population, as an example over 8 million for Tehran. The names of some important cities are printed. **b** The Alborz range (without topography) and its major faults in addition to major cities are shown by small black rectangles, while Tehran is printed near the big black rectangle. The seismicity is from the same catalog, described in Fig. 1a. The magnitude of the earthquakes is indicated by the diameter of the red circles. Faults name abbreviations: *RF* Rudbar Fault, *NAF* North Alborz Fault, *KHF* Khazar Fault, *MF* Moshfa Fault, *FF* Firouzkouh fault, *Bf* Bashm Fault, *CF* Chashm Fault, *AF* Astaneh Fault



Hence, the polarization of S-fast is usually parallel to the direction of the maximum compressional stress as it has been observed in many studies (e.g., Musumeci et al. 2005; Vavrycuk and Bouskova 2008).

In this study, the main stress field of the Central Alborz is determined by focal mechanisms inversion of the locally and teleseismically recorded earthquakes occurred in the study region. The spatial variation in the stress field is studied and compared with the polarization direction of the fast split S wave. By the interpretation of the stress directions with respect to the active faults, a better understanding of the faulting mechanism is achieved. The GPS strain rate studies in the region are also compared with the results of the study, while the P axes of the focal mechanisms and some paleostress directions are demonstrated and discussed.

In Fig. 1a, the location and population of the major cities in the study area are shown. The biggest seismic risk is apparently related to Tehran, with over 8 million populations. A simpler view is shown in Fig. 1b, where the cities, faults, and earthquakes are shown in order to correlate seismic hazard resulting from principal tectonic features, with the near population centers.

## Tectonic setting

The Alborz Mountains formed successively during the collision of Central Iran with Eurasia in the Late Triassic (Cimmerian Orogeny) and the collision of Arabia with Eurasia (Berberian and King 1981; Alavi 1996; Zanchi et al. 2006). Including Paleozoic sediments, the Alborz basement is

covered by Mesozoic and Cenozoic sediments. The volcanic activity has been observed during the Cenozoic, from Late Cretaceous to the quaternary (Alavi 1996).

Tectonic activity in this belt is currently understood to be controlled by two motions with different velocities, the 5 mm/year northward convergence of central Iran toward Eurasia causing a compression from 7 Ma and the 4 mm/year left-lateral shear north-westward motion of the SCB resulting in a left-lateral transpressive tectonic environment in the Alborz (Ritz et al. 2006; Vernant et al. 2004). Since middle Pleistocene transtensional motion is dominating the region because of acceleration of SCB motion toward North West (Ritz et al. 2006; Masson et al. 2006). Some studies indicate the presence of a transpressive tectonic environment in the borders of the Alborz range, while transtension is evidenced within the range (Ritz et al. 2006).

The seismicity rate of the area is high both from historical (Ambraseys and Melville 1982) and instrumental earthquakes catalogs (e.g., Engdahl et al. 1998). The focal mechanism solutions of the earthquakes from the GCMT (Ekström et al. 2012), teleseismic waveform modeling (Jackson et al. 2002) and local seismic networks (Tatar et al. 2007, 2012) indicate a left-lateral strike-slip motion and thrust faulting in the Alborz mountains. The study area contains many active faults, mainly parallel to the Alborz belt, form V shape like pattern with WNW–ESE, and NE–WSW strikes in western and eastern parts of the Central Alborz, respectively. North Alborz and Khazar south-dipping thrust faults are the main active thrust structures bounding the belt to the North. North Tehran, Garmsar and Parchin north-dipping thrust faults are the structures limiting the range to the South. The Taleghan, Moshā, and Firouzkouh faults localize the left-lateral strike-slip motion within the mountain range. (Berberian 1983; Ritz et al. 2006; Berberian and Yeats 2001).

## Focal mechanism data

The focal mechanism data are collected from published papers using local seismic networks, body waveform modeling (Jackson et al. 2002), and CMT solutions from the Global Centroid Moment Tensor Project (GCMT). The local focal mechanisms were derived based on polarity readings of the first P-wave motion of local earthquakes (Snoko et al. 1984). The locations of the events with computed focal mechanisms, the main active faults of the Central Alborz and the instrumental seismicity are shown in Fig. 1a.

The database available in the study area was subdivided into six clusters A1–A6 according to the spatial distribution of the events in order to determine the spatial variations of the stress field in the region. Each subdivided area should contain 20 to 30 earthquakes to ensure the reliability of the

stress inversion as it will be discussed later. The grouping in this step is based on the location of the events.

In most of the areas, the majority of the events occur in depth range between 5 and 15 km. The only exceptions are events of cluster A2, with depth ranging from 15 to 25 km. In addition, a few events in clusters A4, A5, and A6 have depth reaching 30 to 45 km. These events are related to underthrusting in the Central Alborz. However, the number of the events that occur out of the usual depth range is not sufficient for a reliable stress tensor inversion. Thus, the depth of events cannot be used as another factor in subdividing the data.

The focal mechanisms of the analyzed events are plotted on the Kagan's triangle diagram in Fig. 2 generated using the computer code presented by Kagan (1991). The diagram uses the plunge of the P, T and B axes of the focal mechanisms to indicate their type: the reverse, normal or strike-slip mechanism.

It is evident from Fig. 2a that most of the earthquakes in the region have a strike-slip or reverse mechanism which is reasonable due to the transpression tectonic environment. Some normal events in groups A4, A5 and A6 (see Fig. 2b) that exist according to local extensional environments will be discussed later.

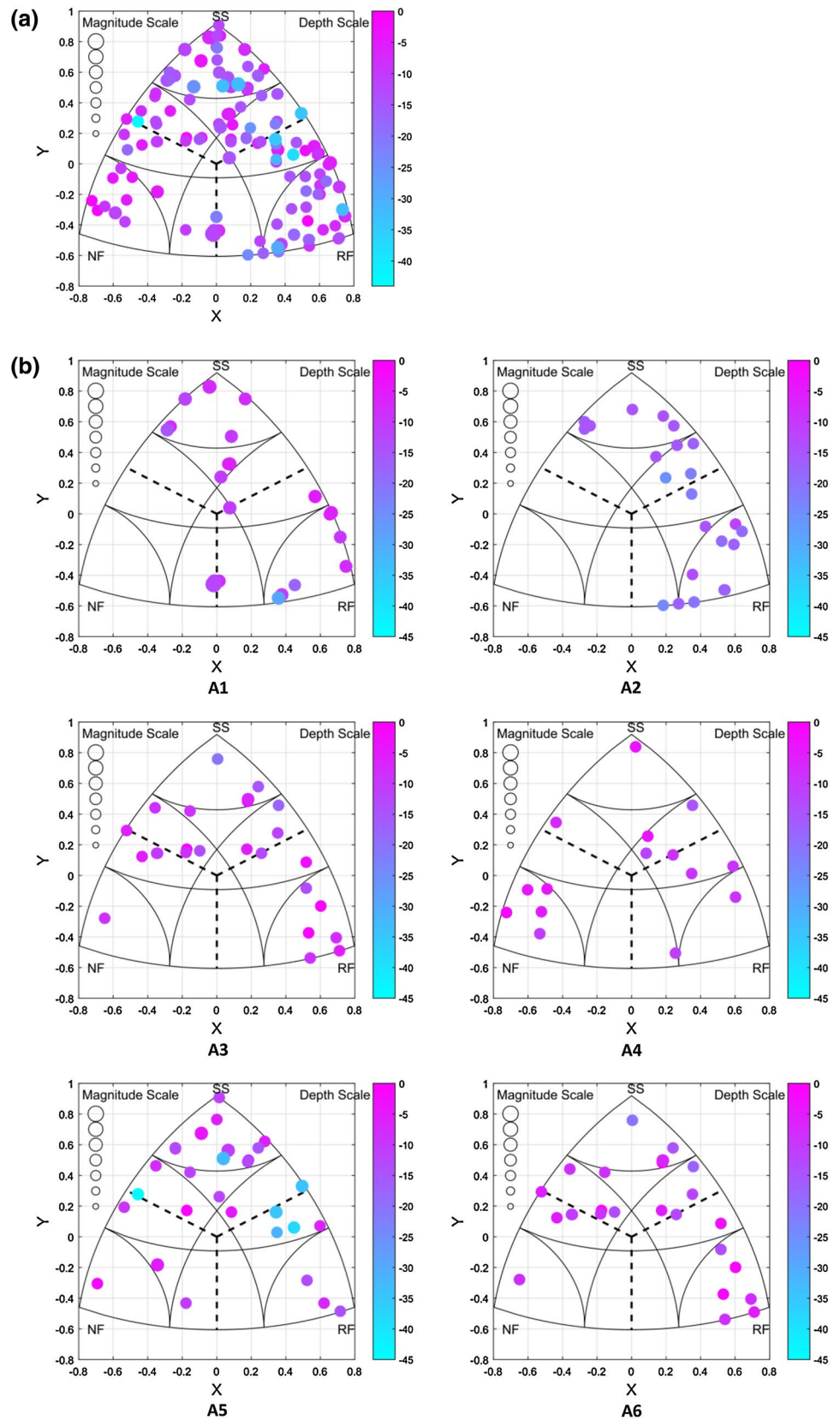
The input for the stress tensor inversion is strike, dip and rake of the focal mechanisms. In Fig. 3a, only the strike and dip of the fault planes are shown as a usual way to illustrate the data. If all of the focal mechanism parameters (strike, dip and rake) are plotted in the stereonet, they will be overlapped and the plots will be complex. It is also mandatory to solve the problem of distinguishing the fault plane from the other auxiliary plane, which is addressed in various stress inversion methods in different ways. As it will be discussed later, two different linear (Michael 1984) and nonlinear (Lund and Slunga 1999) approaches have been used for stress tensor inversion.

The P and T axes of the focal mechanisms in each group are shown in Fig. 3b on stereonets. All of the focal mechanisms used in this study are listed in "Appendix 1" including their relevant group.

Regarding the spatial distribution and clustering of the focal mechanisms, it should be noted that both geographical locations and number of the events in each cluster should be taken into account when subdividing the data. The limitation in the availability of the focal mechanisms in the region of interest caused that we had to include also some relatively far earthquakes in some of the clusters. The main cluster A1, for example, consists of less than 20 earthquakes, so it is necessary to include a few events, occurring east of the main cluster. The A2 group consists of a concentrated cluster of the events occupying a small area. The A3, A4, and A5 groups are close to each other and could be considered as one cluster, but the



**Fig. 2** Kagan triangular plot of the earthquake focal mechanisms, with the size of the circles as their magnitude (from 1 to 7) and the depth shown by the color scale; **a** all of the available earthquake focal mechanisms in the Alborz; **b** different groups of the data according to Fig. 1



initial trials showed the stress field to be extremely heterogeneous when inverting all focal mechanisms together. Thus, the dataset was subdivided into several clusters; in order to get the better results based on the quality control parameters. Groups A3 and A4 contain enough number of events, concentrating in a small area, so they should be inverted for the stress field reliably. But the A5 cluster contains events relatively far apart from each other and the number of the events did not permit further clustering. Thus, all of the events were inverted as one cluster and attributed the resulting  $SH_{\max}$  direction to the center of the earthquakes cluster. The A6 group consists of

where  $\vec{\tau}(\hat{n}, \sigma)$  is the tangential traction on the fault plane with unit normal  $\hat{n}$  due to the deviatoric stress tensor  $\sigma$ ; and  $\hat{\tau}$  is the unit vector associated with  $\vec{\tau}$ .  $\vec{\tau}$  is derived by subtracting the normal traction from the total traction through the equation:

$$\vec{\tau} = \sigma \hat{n} - [(\sigma \hat{n}) \cdot \hat{n}] \hat{n} \quad (2)$$

Then we remove  $|\vec{\tau}|$  by setting its value equal to 1 by assuming that it is constant on all of the fault planes considered.

Considering above equation and taking  $|\vec{\tau}| = 1$ , we have  $\vec{\tau} = \hat{s}$  which in combination with the constraint that the isotropic stress is zero or  $\sigma_{33} = -(\sigma_{11} + \sigma_{22})$  will lead to the following normal equation:

$$\begin{pmatrix} n_1 - n_1^3 + n_1 n_3^2 & n_2 - 2n_1^2 n_2 & n_3 + 2n_1^2 n_3 & n_1 n_3^2 - n_1 n_2^2 & -2n_1 n_2 n_3 \\ -n_2 n_1^2 + n_2 n_3^2 & n_1 - 2n_1 n_2^2 & -2n_1 n_2 n_3 & n_2 - n_2^3 + n_2 n_3^2 & n_3 - 2n_3 n_2^2 \\ -n_3 n_1^2 - n_3 + n_3^3 & -2n_1 n_2 n_3 & n_1 - 2n_3^2 n_1 & -n_3 n_2^2 - n_3 + n_3^3 & n_2 - 2n_2 n_3^2 \end{pmatrix} \begin{pmatrix} \sigma_{11} \\ \sigma_{12} \\ \sigma_{13} \\ \sigma_{22} \\ \sigma_{23} \end{pmatrix} = \begin{pmatrix} s_1 \\ s_2 \\ s_3 \end{pmatrix} \quad (3)$$

several events, distributed along an active fault system. The choice of the clusters looks satisfactory considering the severe limitations in the required data, and the spatial variation of the stress field.

## Methods

Since the uncertainties associated with the derived stress fields are difficult to estimate (e.g., Hardebeck and Hauksson 2001), two different stress tensor inversion algorithms were employed, a linear algorithm: SLICK (Michael 1984) and a nonlinear algorithm: STI (Lund and Slunga 1999) in order to ensure the reliability of the results. Each method has its own fault plane identification approach which will be discussed shortly.

### Slick (Michael 1984)

The popular linearized direct inversion scheme by Michael (1984) was used for focal mechanism stress tensor inversion. We go through the mathematics of the method to show its non-linear nature and to demonstrate how the problem is linearized.

This method employs a bootstrap resampling procedure to estimate the confidence limits of the resulting stress state. Assuming the direction of the tangential traction on the plane tends to be parallel to the slip direction, we have

$$\hat{\tau} = \frac{\vec{\tau}(\hat{n}, \sigma)}{|\vec{\tau}(\hat{n}, \sigma)|} = \hat{s} \quad (1)$$

By rewriting the equation into a simpler form, we get:

$$A^i \vec{\Sigma} = \hat{s}^i \quad (4)$$

here  $A^i$  is the matrix from the equation,  $\vec{\Sigma}$  is the vector of stress tensor elements and  $\hat{s}^i$  are the elements of the slip direction vector. Superscript  $i$  refers to the  $i$ th fault out of a group of  $n$  total measurements.  $3 \times m$  equations formed by stacking the equations for each observation are required for the inversion:

$$\begin{pmatrix} A^1 \\ A^2 \\ A^3 \\ \vdots \\ A^m \end{pmatrix} \vec{\Sigma} = \begin{pmatrix} \hat{s}^1 \\ \hat{s}^2 \\ \hat{s}^3 \\ \vdots \\ \hat{s}^m \end{pmatrix} \quad (5)$$

This equation can be solved for  $\vec{\Sigma}$  (the stress tensor elements) with the standard linear least squares technique. Then, the principal stresses and directions are known.

Quantity  $R$  is called the shape ratio and it is a measure of the relative sizes of the principal stresses:

$$R = (\sigma_1 - \sigma_2) / (\sigma_1 - \sigma_3) \quad (6)$$

Here,  $\sigma_1$ ,  $\sigma_2$  and  $\sigma_3$  are the principal stresses from most compressional to most dilatational, respectively.

Knowing the orientations of the faults in stress inversion procedures is necessary since using the incorrect orientations of the fault planes may produce inaccurate results (Michael 1984; Vavryuk 2014). This mostly applies to the



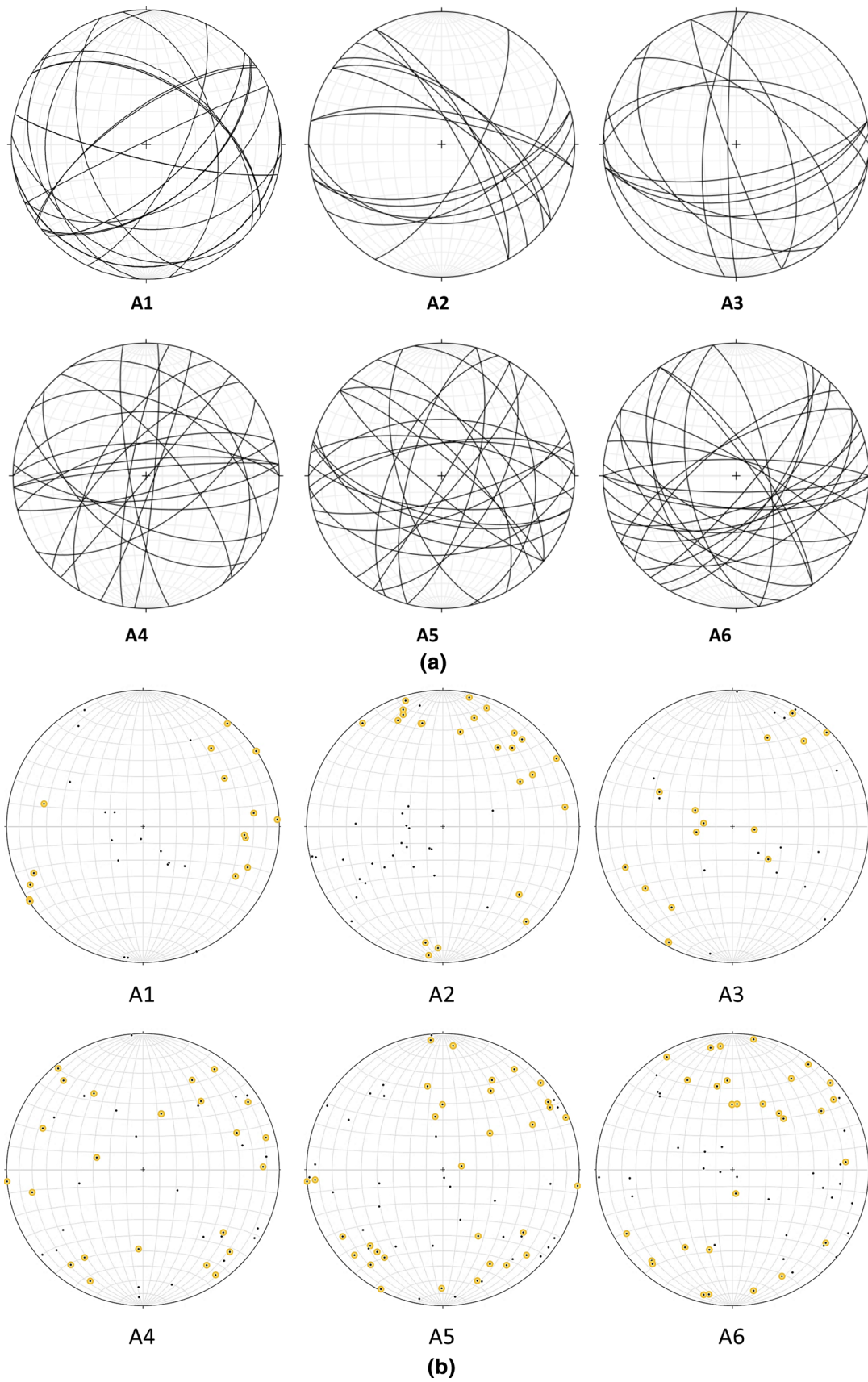


**Fig. 3** **a** Strike and dip of the fault planes obtained from earthquake focal mechanisms in each group of data. **b** P (highlighted) and T axis of the focal mechanisms for each group

shape ratio  $R$ ; the stress axes directions are less sensitive to the choice of the fault. The linear method (SLICK) is very fast, and this advantage is employed in order to statistically solve the problem by running the inversion repeatedly to determine the confidence regions using bootstrap resampling of the fault plane data.

### STI (Lund and Slunga 1999)

This algorithm searches through all directions of the principal stresses in a grid search and a range from zero to one of the shape ratio  $R$  (Eq. 6). The inversion minimizes the angle in the fault plane between the modeled maximum shear stress direction and the observed slip direction. The fault plane is chosen from the two nodal planes by the inversion, either as the most unstable plane in the tested stress field (instability method) or as the best fitting plane (slip angle method) in the tested stress field (Lund and Slunga 1999). The fault instability is calculated with a Mohr–Coulomb criterion and has been shown to provide fault plane information in agreement with geological structures (e.g., Keiding et al. 2009).

The STI method accounts for uncertainties in the focal mechanism determinations by including a number of well-fitting mechanisms for each event. All mechanisms are tested for each event, and each tested stress state, and the mechanism showing the best fit is chosen to represent the event. In this study, where only the best fitting mechanism for each event is available, mostly without uncertainties, the STI algorithm is extended by precomputing a range of focal mechanisms for each event by perturbing the original mechanisms slightly. The entire moment tensor (Kagan 1991) is rotated within a spherical cap centered on the P-axis, and additionally allows the B and T axes to rotate within certain range for each direction of the P-axis. The angular sizes of the spherical cap and rotation range, together with an angular increment, are set prior to the inversion. During the inversion, all these perturbed mechanisms are tested for each event. The procedure is similar to the “Exact” method of Gephart and Forsyth (1984). Maximum horizontal stress directions are properly calculated from the principal stress directions and ratio  $R$  (Lund and Townend 2007). Taking into account the formulation of a formal stress tensor inversion scheme, provided in the previous section, we neglect the mathematical details of the method seeking the conciseness of this section and refer to the original publication in this regard (Lund and Slunga 1999).

### Stress tensor inversion results

Stress tensor inversion shows noticeable variations in terms of rotations in the  $SH_{\max}$  directions in the Central Alborz. This confirms the complexity of the tectonic environment and heterogeneity of the stress field in the region. The results of stress inversions (Figs. 4 and 5 for SLICK and STI methods, respectively) indicate that the STI is accurate for the small groups, while the results of SLICK are more heterogeneous, based on the range of area covered on the stereonet, as an indication of confidence limits of the inversion results. On the other side, SLICK provides more realistic results which are more consistent with the geology of the study area, when inverting large groups of noisy focal mechanisms, containing more heterogeneous stress field samples. For all earthquake clusters including enough number and good quality of the focal mechanisms, the stress tensor orientations deduced from both methods are in a good agreement. The minimum angular difference was related to A6 group which is due to the availability of adequate focal mechanisms. The maximum difference occurred in group A5 which is over 14 degrees, according to the low quality of the focal mechanisms and the large extent of the clusters. In all cases, the difference between the linear and nonlinear approaches used for the stress inversions are less than 15 degrees, which seems reasonable regarding the uncertainties in the focal mechanism data.

As discussed before, the depth variations are not considered in the grouping of events, because of the limitation in the available focal mechanisms. Based on reliable focal depths of the Central Alborz deduced from well-located earthquakes recorded by local seismic networks (Tatar et al. 2012), it seems that most of our stress estimates are for the basement or lower parts of the sedimentary cover. It is known empirically (e.g., Lund and Bödvarsson 2002; Keiding et al. 2009) that at least 20 to 30 events per group is required for a good inversion result. Trial inversions with the Alborz data confirm that good constraints on the stress tensor are obtained with the chosen group sizes.

The results of the stress tensor inversions were selected based on their quality (Figs. 4 and 5). The stereonets, showing the axes of the principal stresses, in addition to their confidence regions, demonstrate significant changes in the maximum horizontal stress directions and confirm the inhomogeneity of the stress field and the complexity of the structural geology of the Central Alborz area. Based on the obtained results, in the western part of the study area, in A1 group, the  $SH_{\max}$  is oriented in the NE–SW direction. The small area of confidence limit in obtained stress tensor of both methods indicates the high quality of the inversion and homogeneity of the stress field in this region. In the second group of data, A2, the stress



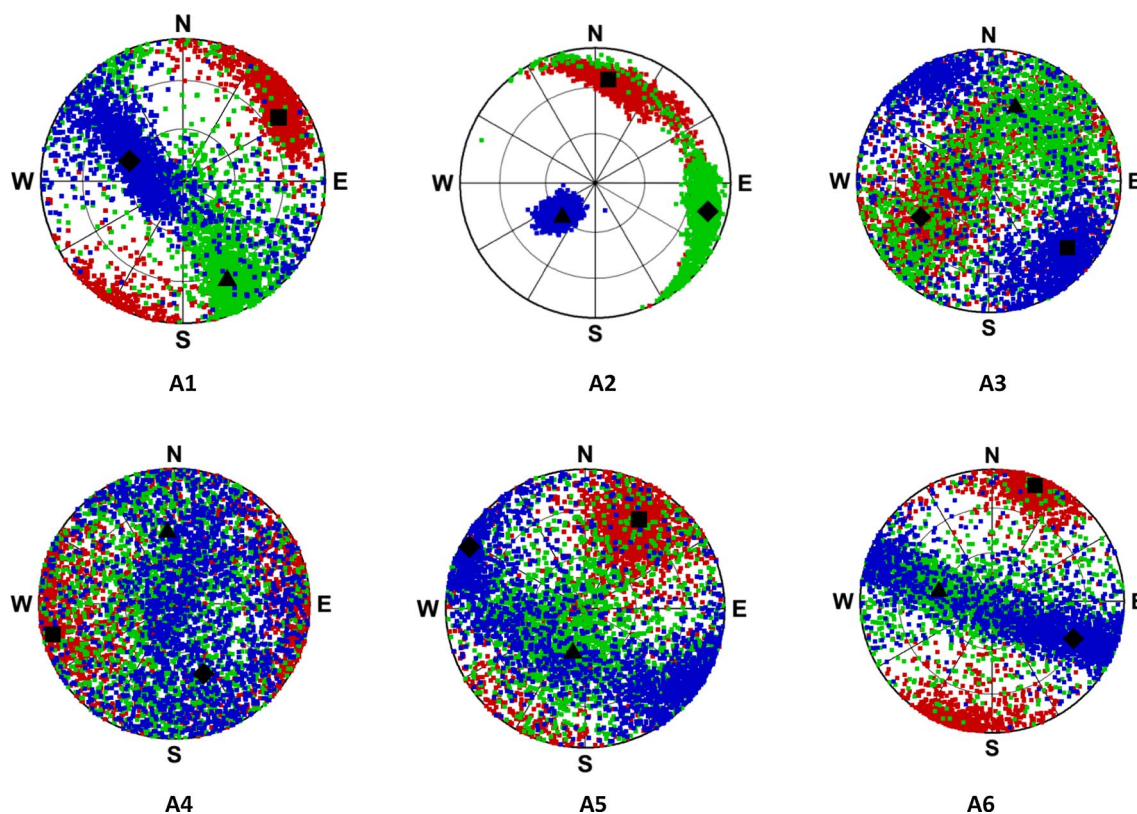


**Fig. 4** Stress tensor inversion results for six groups in Fig. 1 are shown on the stereonets. The red, green and blue dots show points representing  $\sigma_1$ ,  $\sigma_2$  and  $\sigma_3$  during bootstrap resampling, from the SLICK method. The black square, diamond, and triangle represent the optimum stress axes

field is also evaluated as homogenous based on the small confidence regions for principal stress axes on the stereonet. In this area, the  $SH_{\max}$  rotates counterclockwise and turns N–S with a slight deviation toward the NE–SW direction. In groups, A3, A4, and A5, the results of the stress tensor inversion are almost the same. The  $SH_{\max}$  shows the NE–SW direction with a tendency toward the East. In group A6, the maximum horizontal stress direction is NE–SW. The only exception is the A4 group, where the confidence regions on the stereonets are large in both methods. The reason for this observation will be described in the discussion section. Thus, the stress field is proved to be heterogeneous and  $SH_{\max}$  varies significantly as much as  $10^\circ$  in region A2 to  $69^\circ$  in region A4.

The main trends of the stresses obtained in previous studies in Iran (Gillard and Wyss 1995; Zarifi et al. 2014) are in good agreement with the results of this study. In Fig. 6, the average  $SH_{\max}$  obtained from both methods is shown by bars with different colors at the center of the focal mechanism clusters. The  $S_{\text{fast}}$  polarization direction is shown by yellow bars. Because of using a relatively more complete database and using two different approaches, the  $SH_{\max}$  variations obtained in this study have higher resolution and show more realistic variation in the study area compared to the previous

ones. The stress regime changes, determined in the inversion process by the STI method, are also indicated in Fig. 7 by different color of bars.

Thus, variation of the stress directions estimated from earthquake focal mechanisms is significant and shows the stress field to be heterogeneous and indicates structural complexities in the Alborz region.

### Anisotropy from shear wave splitting directions

The polarization of fast S waves is reported to be coherently aligned with the  $SH_{\max}$  orientation in many studies as mentioned before. The results from the shear wave splitting study in the Central Alborz (Sadikhoy et al. 2008) are used here for a comparison and interpretation purposes. It is observed, in Fig. 7, that the fast anisotropy directions are correlated well with the  $SH_{\max}$  in all cases where the available data permits comparison between the maximum horizontal stress directions deduced from earthquake focal mechanisms and the anisotropy fast polarization axes resulted from the Ps Moho phase method, with respect to the geographical distribution of the data.

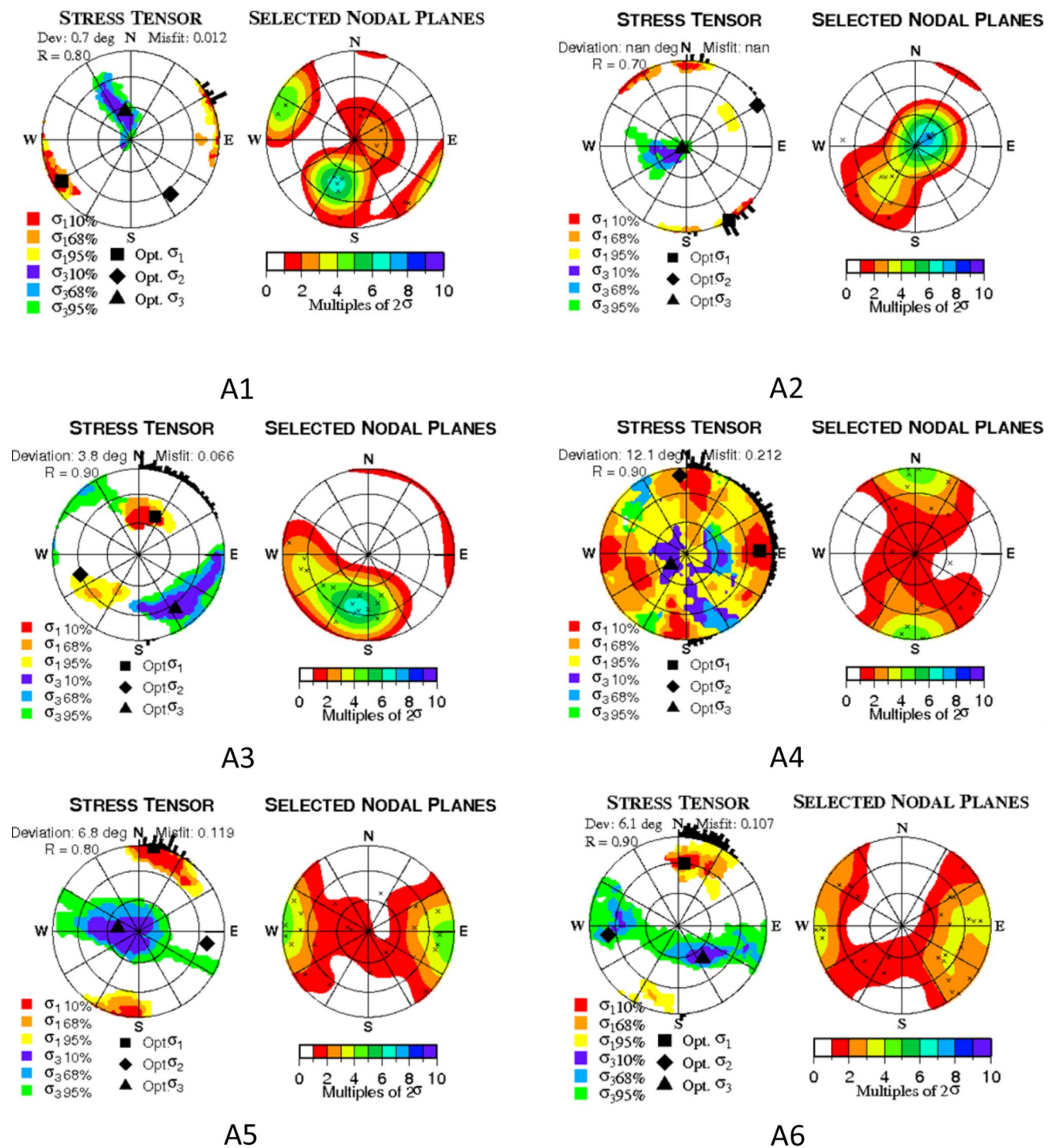


**Fig. 5** The results of stress tensor inversions from STI method for 6 groups shown in Fig. 1. Principal stress directions on lower hemisphere plots, with confidence regions of  $\sigma_1$  (warm colors) and  $\sigma_3$  (cold colors), and the optimal solution (symbols) are in left. The directions of greatest compressive horizontal stress,  $SH_{max}$ , are shown

with the histograms on the periphery of the stereonet. The fault planes that were selected during the inversions, on lower hemisphere plots of the fault plane normal (Kamb contours) can be seen on the right side for each set of plots

The Ps Moho phase method refers to anisotropy in the Earth’s crust, while the SKS phase method focuses on the anisotropy in the upper mantle (Sadidkhouy et al.2008).

Since our stress tensor inversion results are related to seismogenic depth, limited to the crust, the anisotropy directions from the Ps method are used for the comparison with the



**Fig. 6** The maximum horizontal stress directions from focal mechanism stress tensor inversions shown by in red, blue and green for reverse, normal and strike-slip stress regimes, respectively. The earthquakes are shown by various colors for different subdivisions of the data plus anisotropy directions by the Ps Moho phase method (yellow bars)

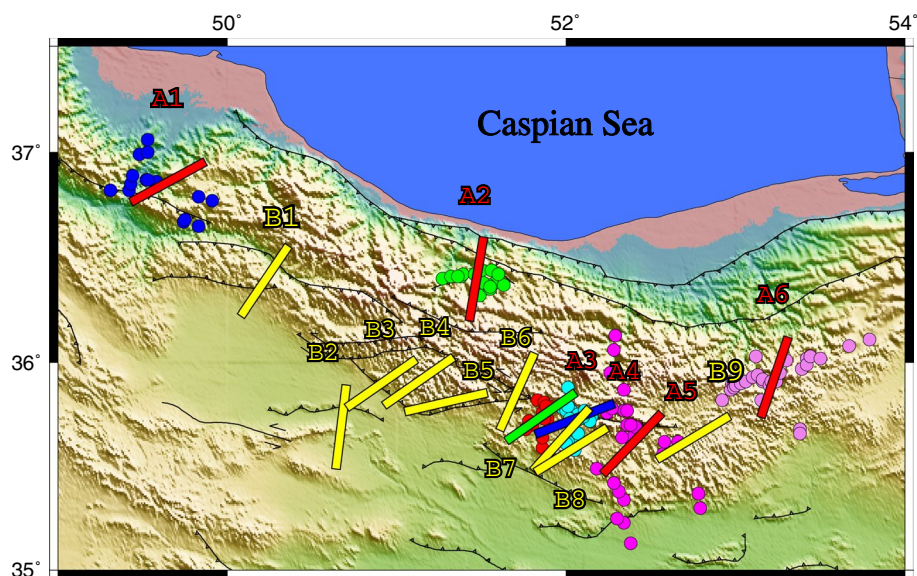
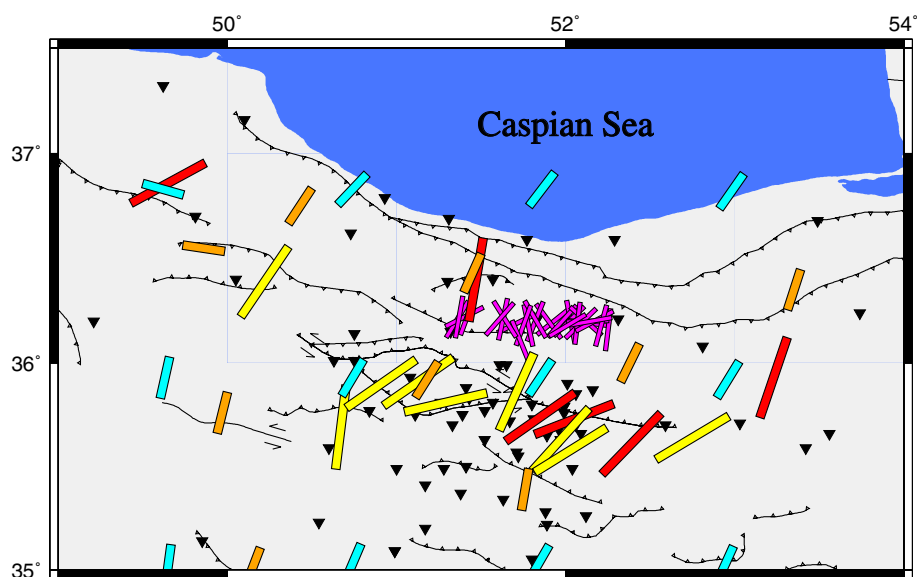


**Fig. 7** Comparison of the maximum horizontal stress directions (red) with crustal shear wave splitting fast direction axes using the Ps Moho phase (long yellow bars) from Sadidkhouy et al. (2008). Other information: short cyan bars: GPS strain rate study from Khorrami et al. (2012), Short orange bars: GPS strain rate study from Raeesi et al. (2016), Short magenta bars: paleostress directions from Mirzayi Suzani et al. (2016). The GPS stations used in strain rate studies are shown in black reverse triangles



stress directions. The stress inversion results are well correlated with the polarization of the fast split S wave neglecting some small deviations.

### GPS strain rates and paleostress data

Figure 7 shows a possible relation between various observations. In this figure, the average stress directions obtained using the above procedure are compared with the shear wave splitting fast direction axes (Sadidkhouy et al. 2008).

In Fig. 7, two different recent GPS strain rate studies are shown (by short orange and cyan bars, respectively) and compared (Khorrami et al. 2012; Raeesi et al. 2016). The

figure shows a good agreement between the mentioned studies, since the resulting strain rate axes are parallel throughout the range. In addition, Fig. 7 shows paleostress directions resulted from Mirzayi Suzani et al. (2016). The comparison of paleostress data with stress inversion results is an important issue that needs separate investigations, but the relationship between these axes,  $SH_{max}$  and fast anisotropy directions will be explained in the discussion part.

### Discussion

The fault planes in the Central Alborz area are often accompanied by numerous crossing directions since the considered earthquakes are located around the junction of

the V-shaped pattern of the faults in the Central Alborz. This is the reason for large confidence regions on the stereonet, representing the stress field heterogeneity in the inversion results, and indicating a complicated nature of the faulting mechanisms in the area.

Most of the events are reverse and strike-slips, with compound nature of faulting, some normal events also occur possibly due to the local extensional tectonic environment between strike-slip fault systems (Fig. 2a). Transpressive nature of the studied area indicates the existence of local tectonic regimes, created between different blocks. Thus, it seems that these normal mechanisms are caused by strike-slip motions on the Masha and Firouzkouh faults. The strike-slip components in faulting mechanisms can be seen all over the Alborz, but its extents vary in different locations.

Moho depth of the Central Alborz from different reliable studies varies from 52 km in southern part to 46 km in the northern part, south of the Caspian basin. However, deeper Moho interface up to 58 km has been reported for the region located beneath the Damavand volcano (e.g., Radjaee et al. 2010; Abbassi et al. 2010, Motavalli-Anbaran et al. 2011). All the well-located events in the Central Alborz (Tatar et al. 2012) are located at depths ranging mainly from 5 to 20 km. However, earthquakes with focal depths of ~30 km are reported in some areas, related to the underthrusting of the South Caspian basin beneath the Alborz crust. So, it is believed that most of the seismicity in the Central Alborz occurs in the upper crystalline crust, mainly on basement faults, extending toward shallow depth into sedimentary cover. It is evident that the pre-mentioned underthrusting starts at the higher latitudes, probably parallel to the Caspian Sea shoreline, approximately at Khazar thrust or North Alborz Fault and continues toward the Central Alborz, where comparatively deep earthquakes are observed in the middle parts of the Central Alborz.

The directions of the maximum horizontal stresses in the study area are in agreement with the existing geological facts. In the northern parts, the reverse faulting dominates the seismic events, because of the approximately perpendicular direction of  $SH_{max}$  with respect to the Khazar thrust and North Alborz fault. In the middle of the Central Alborz, the stress direction produces a greater EW component of the tectonic force resulting in strike-slip motion with regard to the orientation of the active faults in the area including Mosha, Firuzkuh, and Astaneh faults.

The angular differences between the  $SH_{max}$  and strain rate axes directions also generally decrease toward north. In most cases, these directions show major disagreements in the middle parts of the mountain range, i.e., A3, A4 and A5, while more correlation can be seen at higher latitudes in

the A1, A2 and A6 group (Fig. 7). In the framework of the tectonic transpressional environment in the area, the angular difference between the stress and strain rate directions implies the partitioning of the deformation on preexisting weak planes on strike-slip faults in the middle parts of the Central Alborz, while thrust faulting on northern parts represents shortening more dominantly.

## Conclusions

We show that the variation of the stress directions estimated from earthquake focal mechanisms is significant ranging as much as  $10^\circ$  in region A2 to  $69^\circ$  in region A4. It might be caused by a heterogeneous stress field to be heterogeneous indicating structural complexities in the Alborz region. Two linear and nonlinear methods, SLICK and STI, were used for determining stress for different groups of the focal mechanisms in the Alborz. The STI provided more accurate results in the small groups and the stress directions resulted from the SLICK were more consistent with the geology when implementing on large groups of noisy data. For most of the groups with a sufficient number of focal mechanisms, the stress tensor orientations deduced from both methods are in a good agreement. The study resulted in a successful determination of expected faulting mechanisms with respect to the stress directions and fault trends in the region while being confirmed by correlation with the shear wave splitting direction. The comparison of the maximum compressional stress directions with the GPS strain rate in the region supported the deformation partitioning, resulting from movements on preexisting weak planes due to strike-slip fault systems in the middle parts of the Central Alborz like Mosha and Firouzkouh faults, while shortening occurs on the northern flank of the mountain range more dominantly on the North Alborz fault and Khazar thrust.

**Acknowledgements** The author acknowledges International Institute of Earthquake Engineering and Seismology (IIEES), Tehran, Iran, for supporting this project (activity code: 9804) and deeply appreciate B. Lund from Uppsala University, M. Tatar from IIEES, H. Shomali from University of Tehran, and Th. Arnadóttir from Iceland University for providing the necessary codes, helpful comments, and their kind collaborations. And last but not least, I thank the anonymous reviewers of the journal, who I owe the improvements in all aspects and every single word of this paper, to their many careful and precise corrections.

## Appendix

See Table 1.

**Table 1** Earthquake focal mechanism database used in this study

No.	Long. (°)	Lat. (°)	M	Azimuth (°)	Dip (°)	Rake (°)	Depth (km)	Refs.	Group
1	49.83	36.79	5.4	291	80	510	12	Berberian and Walker (2010)	A1
2	49.91	36.77	4.6	302	50	54	6	Berberian and Walker (2010)	A1
3	49.52	36.87	4.9	103	81	10	8	Berberian and Walker (2010)	A1
4	49.83	36.65	5.3	26	69	87	15	Berberian and Walker (2010)	A1
5	49.48	36.99	5.3	302	51	54	6	Berberian and Walker (2010)	A1
6	49.75	36.68	4.9	103	81	10	8	Berberian and Walker (2010)	A1
7	49.43	36.85	4.8	103	81	10	8	Berberian and Walker (2010)	A1
8	49.53	36.87	4.9	309	47	65	10	Berberian and Walker (2010)	A1
9	49.44	36.89	4.8	235	70	−164	8	Berberian and Walker (2010)	A1
10	49.53	37	4.8	302	51	54	6	Berberian and Walker (2010)	A1
11	49.58	36.86	5	350	47	80	8	Berberian and Walker (2010)	A1
12	49.74	36.67	4.6	183	26	103	18	Berberian and Walker (2010)	A1
13	50.2	37.19	5.5	135	20	95	29	Jackson et al. (2002)	A1
14	50.38	37.08	5.3	160	52	136	5	Jackson et al. (2002)	A1
15	49.42	36.82	5.3	234	69	−163	15	Jackson et al. (2002)	A1
16	49.31	36.82	5.3	94	37	6	15	Jackson et al. (2002)	A1
17	49.53	37.06	5.1	65	49	178	15	Jackson et al. (2002)	A1
18	49.83	36.79	–	80	−10	5.4	12	Gillard and Wyss (1995)	A1
19	49.91	36.77	–	50	54	4.6	6	Gillard and Wyss (1995)	A1
20	49.52	36.87	–	81	10	4.9	8	Gillard and Wyss (1995)	A1
21	49.83	36.65	–	64	92	5.8	8	Gillard and Wyss (1995)	A1
22	49.48	36.99	–	51	54	5.3	6	Gillard and Wyss (1995)	A1
23	49.75	36.68	–	81	10	4.9	8	Gillard and Wyss (1995)	A1
24	49.43	36.85	–	81	10	4.8	8	Gillard and Wyss (1995)	A1
25	49.53	36.87	–	47	65	4.9	10	Gillard and Wyss (1995)	A1
26	49.44	36.89	–	47	65	5.1	10	Gillard and Wyss (1995)	A1
27	51.371	36.41	–	290	70	27	17	Tatar et al. (2007)	A1
28	51.273	36.395	–	120	65	120	15	Tatar et al. (2007)	A2
29	51.384	36.406	–	285	70	141	22	Tatar et al. (2007)	A2
30	51.471	36.42	–	280	70	133	22	Tatar et al. (2007)	A2
31	51.577	36.384	–	75	55	59	12	Tatar et al. (2007)	A2
32	51.387	36.423	–	−85	80	163	15	Tatar et al. (2007)	A2
33	51.603	36.417	–	305	60	87	18	Tatar et al. (2007)	A2
34	51.481	36.423	–	305	75	90	18	Tatar et al. (2007)	A2
35	51.513	36.347	–	75	60	66	19	Tatar et al. (2007)	A2
36	51.364	36.412	–	−75	82	147	15	Tatar et al. (2007)	A2
37	51.32	36.409	–	125	75	−161	16	Tatar et al. (2007)	A2
38	51.323	36.41	–	125	75	0	15	Tatar et al. (2007)	A2
39	51.489	36.321	–	330	80	90	24	Tatar et al. (2007)	A2
40	51.468	36.424	–	30	70	14	16	Tatar et al. (2007)	A2
41	51.539	36.366	–	90	40	61	17	Tatar et al. (2007)	A2
42	51.539	36.356	–	330	70	90	21	Tatar et al. (2007)	A2
43	51.355	36.411	–	30	70	−14	15	Tatar et al. (2007)	A2
44	51.512	36.384	–	80	45	59	19	Tatar et al. (2007)	A2
45	51.361	36.41	–	175	75	−22	16	Tatar et al. (2007)	A2
46	51.546	36.352	–	330	70	90	21	Tatar et al. (2007)	A2
47	51.456	36.417	–	10	75	28	16	Tatar et al. (2007)	A2
48	51.503	36.436	–	320	70	101	14	Tatar et al. (2007)	A2
49	51.548	36.355	–	330	70	90	21	Tatar et al. (2007)	A2
50	51.562	36.44	–	305	75	90	19	Tatar et al. (2007)	A2



**Table 1** (continued)

No.	Long. (°)	Lat. (°)	M	Azimuth (°)	Dip (°)	Rake (°)	Depth (km)	Refs.	Group
51	51.557	36.436	–	280	75	90	17	Tatar et al. (2007)	A2
52	51.629	36.372	–	60	50	15	26	Tatar et al. (2007)	A2
53	51.604	36.417	–	310	60	87	17	Tatar et al. (2007)	A2
54	51.83	35.82	4	275	50	7	3.9	Tatar et al. (2012)	A3
55	51.86	35.59	4	340	60	– 79	11.2	Tatar et al. (2012)	A3
56	51.86	35.76	4	180	85	179	4.2	Tatar et al. (2012)	A3
57	51.86	35.64	4	80	70	27	15	Tatar et al. (2012)	A3
58	51.89	35.73	4	140	40	– 47	4.6	Tatar et al. (2012)	A3
59	51.87	35.81	4	85	45	20	8.6	Tatar et al. (2012)	A3
60	51.79	35.7	4	80	55	– 119	4.8	Tatar et al. (2012)	A3
61	51.9	35.79	4	160	85	134	12.6	Tatar et al. (2012)	A3
62	51.8	35.7	4	105	45	– 71	2	Tatar et al. (2012)	A3
63	51.78	35.72	4	95	15	70	11.6	Tatar et al. (2012)	A3
64	51.76	35.68	4	80	60	– 151	7.2	Tatar et al. (2012)	A3
65	51.87	35.73	4	310	60	– 70	5.4	Tatar et al. (2012)	A3
66	51.88	35.79	4	270	50	47	9.5	Tatar et al. (2012)	A3
67	51.88	35.79	4	185	70	126	9.5	Tatar et al. (2012)	A3
68	51.88	35.79	4	280	55	64	9.6	Tatar et al. (2012)	A3
69	52.01	35.88	5.4	104	61	17	10	Javidfakhr et al. (2011)	A4
70	52.01	35.78	4	210	60	– 170	12.9	Tatar et al. (2012)	A4
71	52.03	35.77	4	270	70	179	11.3	Tatar et al. (2012)	A4
72	52.15	35.74	4	255	70	– 14	4.4	Tatar et al. (2012)	A4
73	52.14	35.72	4	265	85	45	4.4	Tatar et al. (2012)	A4
74	51.98	35.78	4	190	80	0	10.2	Tatar et al. (2012)	A4
75	52.07	35.63	4	130	50	36	15	Tatar et al. (2012)	A4
76	52.04	35.74	4	325	30	58	15	Tatar et al. (2012)	A4
77	52.08	35.73	4	225	70	179	7.4	Tatar et al. (2012)	A4
78	52.01	35.79	4	95	70	179	15	Tatar et al. (2012)	A4
79	52.16	36.02	4	30	70	53	31.2	Tatar et al. (2012)	A4
80	52	35.77	4	170	80	45	17.4	Tatar et al. (2012)	A4
81	52.1	35.74	4	40	89	179	11.7	Tatar et al. (2012)	A4
82	52.07	35.75	4	85	75	– 34	5.2	Tatar et al. (2012)	A4
83	52.11	35.77	4	115	60	73	13.6	Tatar et al. (2012)	A4
84	52.11	35.77	4	270	50	179	12	Tatar et al. (2012)	A4
85	52.11	35.77	4	265	80	26	12.9	Tatar et al. (2012)	A4
86	52.01	35.79	4	5	85	0	12.6	Tatar et al. (2012)	A4
87	52.02	35.73	4	300	45	– 49	10	Tatar et al. (2012)	A4
88	52.05	35.58	4	75	80	26	10.4	Tatar et al. (2012)	A4
89	52.01	35.62	4	20	85	– 45	6.8	Tatar et al. (2012)	A4
90	52	35.61	4	320	70	– 141	12.7	Tatar et al. (2012)	A4
91	52.07	35.66	4	55	60	– 49	18.5	Tatar et al. (2012)	A4
92	52.26	35.95	5.4	280	68	4	4	Jackson et al. (2002)	A5
93	52.29	36.13	5.3	104	61	17	10	Jackson et al. (2002)	A5
94	52.34	35.23	5.3	317	75	– 175	4	Jackson et al. (2002)	A5
95	52.31	35.38	5.1	348	31	– 41	5	Jackson et al. (2002)	A5
96	52.28	35.42	5	15	70	45	35	Javidfakhr et al. (2011)	A5
97	52.34	35.34	4.6	163	64	129	38	Javidfakhr et al. (2011)	A5
98	52.3	35.25	4.9	331	62	34	34	Javidfakhr et al. (2011)	A5
99	52.28	36.06	5.4	31	88	25	33	Javidfakhr et al. (2011)	A5
100	52.38	35.13	4.5	185	57	– 32	44	Javidfakhr et al. (2011)	A5

**Table 1** (continued)

No.	Long. (°)	Lat. (°)	M	Azimuth (°)	Dip (°)	Rake (°)	Depth (km)	Refs.	Group
101	52.57	35.56	4	105	65	11	8	Nemati et al. (2011)	A5
102	52.79	35.3	4	40	80	−45	0	Nemati et al. (2011)	A5
103	52.78	35.37	4	95	70	14	15	Nemati et al. (2011)	A5
104	52.34	35.77	4	85	40	90	14.4	Tatar et al. (2012)	A5
105	52.24	35.76	4	205	60	−170	11.3	Tatar et al. (2012)	A5
106	52.58	35.62	4	195	70	−14	7.7	Tatar et al. (2012)	A5
107	52.27	35.78	4	130	80	−80	10.7	Tatar et al. (2012)	A5
108	52.39	35.64	4	110	50	−76	2	Tatar et al. (2012)	A5
109	52.15	35.74	4	255	70	−14	4.4	Tatar et al. (2012)	A5
110	52.14	35.72	4	265	85	45	4.4	Tatar et al. (2012)	A5
111	52.36	35.7	4	260	70	−14	9.9	Tatar et al. (2012)	A5
112	52.16	36.02	4	30	70	53	31.2	Tatar et al. (2012)	A5
113	52.41	35.69	4	75	75	18	5.9	Tatar et al. (2012)	A5
114	52.18	35.49	4	310	55	50	6.4	Tatar et al. (2012)	A5
115	52.38	35.7	4	265	70	−14	13.5	Tatar et al. (2012)	A5
116	52.1	35.74	4	40	89	179	11.7	Tatar et al. (2012)	A5
117	52.11	35.77	4	115	60	73	13.6	Tatar et al. (2012)	A5
118	52.11	35.77	4	270	50	179	12	Tatar et al. (2012)	A5
119	52.11	35.77	4	265	80	26	12.9	Tatar et al. (2012)	A5
120	52.34	35.87	4	70	65	−22	8.1	Tatar et al. (2012)	A5
121	52.66	35.62	4	30	55	−39	9.3	Tatar et al. (2012)	A5
122	52.33	35.64	4	310	80	0	5.9	Tatar et al. (2012)	A5
123	52.36	35.77	4	270	55	84	7.1	Tatar et al. (2012)	A5
124	52.98	35.9	5.9	357	66	172	25	Hollingsworth et al. (2010)	A6
125	52.92	35.82	5.9	357	66	172	33	Jackson et al. (2002)	A6
126	57.07	35.65	5.4	82	77	10	4	Jackson et al. (2002)	A6
127	57.05	35.65	5.3	257	79	5	5	Jackson et al. (2002)	A6
128	58.22	35.51	5.4	57	42	23	26	Javidfakhr et al. (2011)	A6
129	57.92	35.45	5.4	156	65	−176	8	Javidfakhr et al. (2011)	A6
130	57.75	35.54	5	23	8	176	29	Javidfakhr et al. (2011)	A6
131	56.87	35.15	5.6	325	36	99	9	Javidfakhr et al. (2011)	A6
132	55.94	35.33	4.7	219	87	4	53	Javidfakhr et al. (2011)	A6
133	58.66	35.56	5.1	319	32	144	33	Javidfakhr et al. (2011)	A6
134	57.35	35.65	4.8	82	77	10	33	Javidfakhr et al. (2011)	A6
135	57.22	35.85	4.8	257	79	5	33	Javidfakhr et al. (2011)	A6
136	58.19	35.46	5.1	83	43	79	27	Javidfakhr et al. (2011)	A6
137	53	35.89	5.5	97	65	−8	25	Javidfakhr et al. (2011)	A6
138	55.94	35.33	4.7	219	87	4	53	Javidfakhr et al. (2011)	A6
139	54.11	35.57	4.5	96	66	48	13	Javidfakhr et al. (2011)	A6
140	59.02	34.07	7.1	254	84	5	17	Naimi-Ghassabian et al. (2015)	A6
141	59.02	34.07	6.4	320	70	90	10	Naimi-Ghassabian et al. (2015)	A6
142	58.16	34.1	6.3	115	54	85	9	Nemati et al. (2011); Naimi-Ghassabian et al. (2015)	A6
143	58.24	34.04	5.5	148	56	81	9	Naimi-Ghassabian et al. (2015)	A6
144	59.47	34.03	5.6	78	90	16	6	Naimi-Ghassabian et al. (2015)	A6
145	58.14	35.53	5.4	88	26	31	26	Naimi-Ghassabian et al. (2015)	A6
146	58.14	35.53	5.4	329	76	112	26	Naimi-Ghassabian et al. (2015)	A6
147	57.92	35.43	5.4	156	65	176	33	Naimi-Ghassabian et al. (2015)	A6
148	57.92	35.43	5.4	64	87	25	33	Naimi-Ghassabian et al. (2015)	A6
149	57.75	35.54	5.5	23	8	176	29	Naimi-Ghassabian et al. (2015)	A6

**Table 1** (continued)

No.	Long. (°)	Lat. (°)	M	Azimuth (°)	Dip (°)	Rake (°)	Depth (km)	Refs.	Group
150	57.75	35.54	5.5	117	89	82	29	Naimi-Ghassabian et al. (2015)	A6
151	59.15	34.07	6	260	78	6	15	Naimi-Ghassabian et al. (2015)	A6
152	59.15	34.07	6	169	84	168	15	Naimi-Ghassabian et al. (2015)	A6
153	59.17	33.84	6	84	79	12	8	Naimi-Ghassabian et al. (2015)	A6
154	59.17	33.84	6	67	52	7	10	Naimi-Ghassabian et al. (2015)	A6
155	59.41	34.19	6.5	267	49	5	15	Naimi-Ghassabian et al. (2015)	A6
156	59.41	34.19	6.5	174	86	139	15	Naimi-Ghassabian et al. (2015)	A6
157	59.5	33.96	6.5	293	34	46	11	Naimi-Ghassabian et al. (2015)	A6
158	59.5	33.96	6.5	257	88	5	13	Naimi-Ghassabian et al. (2015)	A6
159	59.78	34.37	6.5	256	53	1	12	Naimi-Ghassabian et al. (2015)	A6
160	59.78	34.37	6.5	347	89	143	12	Naimi-Ghassabian et al. (2015)	A6
161	59.78	34.02	6.6	160	89	177	10	Naimi-Ghassabian et al. (2015)	A6
162	59.78	34.02	6.6	85	85	1	6	Naimi-Ghassabian et al. (2015)	A6
163	59.58	34.45	7	261	67	19	25	Naimi-Ghassabian et al. (2015)	A6
164	59.58	34.45	7	358	73	156	25	Naimi-Ghassabian et al. (2015)	A6
165	59.77	34.06	7.1	261	82	8	8	Naimi-Ghassabian et al. (2015)	A6
166	59.89	34.13	5.9	113	84	21	10	Naimi-Ghassabian et al. (2015)	A6
167	56.83	35.11	5.6	350	44	121	15	Naimi-Ghassabian et al. (2015)	A6
168	56.83	35.11	5.6	129	53	63	15	Naimi-Ghassabian et al. (2015)	A6
169	55.94	35.33	5.3	219	87	4	53	Naimi-Ghassabian et al. (2015)	A6
170	55.94	35.33	5.3	129	86	177	53	Naimi-Ghassabian et al. (2015)	A6
171	58.6	35.09	5.2	319	32	144	33	Naimi-Ghassabian et al. (2015)	A6
172	58.6	35.09	5.2	80	72	63	33	Naimi-Ghassabian et al. (2015)	A6
173	56.95	35.72	5.4	82	77	10	33	Naimi-Ghassabian et al. (2015)	A6
174	56.95	35.72	5.4	350	80	166	33	Naimi-Ghassabian et al. (2015)	A6
175	57.22	35.85	5.3	257	79	5	33	Naimi-Ghassabian et al. (2015)	A6
176	57.22	35.85	5.3	166	85	169	33	Naimi-Ghassabian et al. (2015)	A6
177	59.82	33.88	7.2	156	89	169	13	Naimi-Ghassabian et al. (2015)	A6
178	59.43	34.04	5.8	180	71	169	15	Naimi-Ghassabian et al. (2015)	A6
179	59.43	34.04	5.8	273	79	19	15	Naimi-Ghassabian et al. (2015)	A6
180	59.46	33.97	5.7	181	87	170	8	Naimi-Ghassabian et al. (2015)	A6
181	61.29	35.78	5.3	160	5	89	25	Naimi-Ghassabian et al. (2015)	A6
182	61.29	35.78	5.3	342	85	90	25	Naimi-Ghassabian et al. (2015)	A6
183	61.19	35.9	4.9	162	43	67	23	Naimi-Ghassabian et al. (2015)	A6
184	61.19	35.9	4.9	13	51	110	23	Naimi-Ghassabian et al. (2015)	A6
185	61.5	35.91	4.9	107	41	112	20	Naimi-Ghassabian et al. (2015)	A6
186	61.5	35.91	4.9	259	53	72	20	Naimi-Ghassabian et al. (2015)	A6
187	58.21	35.23	5.3	83	43	79	27	Naimi-Ghassabian et al. (2015)	A6
188	58.21	35.23	5.3	278	48	100	27	Naimi-Ghassabian et al. (2015)	A6
189	60.34	35.66	5.1	316	30	109	30	Naimi-Ghassabian et al. (2015)	A6
190	60.34	35.66	5.1	114	62	79	30	Naimi-Ghassabian et al. (2015)	A6
191	57.63	34.31	4.7	305	84	1	25	Naimi-Ghassabian et al. (2015)	A6
192	57.63	34.31	4.7	39	89	174	25	Naimi-Ghassabian et al. (2015)	A6
193	58.6	34.5	5.1	310	42	101	13	Naimi-Ghassabian et al. (2015)	A6
194	58.6	34.5	5.1	116	49	81	13	Naimi-Ghassabian et al. (2015)	A6
195	59.36	35.17	5.5	188	57	155	28	Naimi-Ghassabian et al. (2015)	A6
196	59.36	35.17	5.5	292	70	36	28	Naimi-Ghassabian et al. (2015)	A6
197	59.94	34.51	5.2	168	30	114	21	Naimi-Ghassabian et al. (2015)	A6
198	59.94	34.51	5.2	321	62	77	21	Naimi-Ghassabian et al. (2015)	A6
199	53.5	36.02	–	–35	80	–134	9	Nemati et al. (2011)	A6



**Table 1** (continued)

No.	Long. (°)	Lat. (°)	M	Azimuth (°)	Dip (°)	Rake (°)	Depth (km)	Refs.	Group
200	53.67	36.08	–	170	60	120	14	Nemati et al. (2011)	A6
201	53.16	35.91	–	230	70	38	12	Nemati et al. (2011)	A6
202	52.97	35.87	–	40	80	26	1	Nemati et al. (2011)	A6
203	53.44	36.03	–	–75	80	26	2	Nemati et al. (2011)	A6
204	53.42	36.02	–	30	60	79	1	Nemati et al. (2011)	A6
205	53.42	35.99	–	240	70	27	18	Nemati et al. (2011)	A6
206	53.13	35.94	–	85	55	68	0	Nemati et al. (2011)	A6
207	53.16	35.92	–	160	40	–70	9	Nemati et al. (2011)	A6
208	53.12	36.03	–	90	70	–46	11	Nemati et al. (2011)	A6
209	53.26	35.95	–	–10	70	–152	9	Nemati et al. (2011)	A6
210	53.79	36.11	–	40	80	26	2	Nemati et al. (2011)	A6
211	53.3	36.01	–	–35	75	46	13	Nemati et al. (2011)	A6
212	52.99	35.89	–	75	60	–36	6	Nemati et al. (2011)	A6
213	53.2	35.89	–	75	60	49	3	Nemati et al. (2011)	A6
214	53.21	35.91	–	35	65	11	2	Nemati et al. (2011)	A6
215	53.1	35.93	–	45	65	–47	5	Nemati et al. (2011)	A6
216	53.03	35.9	–	145	45	–172	14	Nemati et al. (2011)	A6
217	53.39	35.97	–	120	40	82	8	Nemati et al. (2011)	A6
218	53.24	35.91	–	115	60	–170	9	Nemati et al. (2011)	A6
219	53.38	35.68	–	65	60	90	9	Nemati et al. (2011)	A6
220	53.38	35.66	–	60	40	90	5	Nemati et al. (2011)	A6
221	53.15	35.82	–	70	70	–46	8	Nemati et al. (2011)	A6
222	53.06	35.91	–	–90	80	45	5	Nemati et al. (2011)	A6
223	52.99	35.88	–	90	80	26	7	Nemati et al. (2011)	A6
224	53.5	36.02	–	–35	80	–134	9	Nemati et al. (2013)	A6
225	53.67	36.08	–	170	60	120	14	Nemati et al. (2013)	A6
226	53.16	35.91	–	230	70	38	12	Nemati et al. (2013)	A6
227	52.97	35.87	–	40	80	26	1	Nemati et al. (2013)	A6
228	53.44	36.03	–	–75	80	26	2	Nemati et al. (2013)	A6
229	53.42	36.02	–	30	60	79	1	Nemati et al. (2013)	A6
230	53.42	35.99	–	240	70	27	18	Nemati et al. (2013)	A6
231	53.13	35.94	–	85	55	68	0	Nemati et al. (2013)	A6
232	53.16	35.92	–	160	40	–70	9	Nemati et al. (2013)	A6
233	53.26	35.95	–	–10	70	–152	9	Nemati et al. (2013)	A6
234	52.99	35.89	–	75	60	–36	6	Nemati et al. (2013)	A6
235	53.2	35.89	–	75	60	49	3	Nemati et al. (2013)	A6
236	53.21	35.91	–	35	65	11	2	Nemati et al. (2013)	A6
237	53.1	35.93	–	45	65	–47	5	Nemati et al. (2013)	A6
238	53.03	35.9	–	145	45	–172	14	Nemati et al. (2013)	A6
239	53.39	35.97	–	120	40	82	8	Nemati et al. (2013)	A6
240	53.24	35.91	–	115	60	–170	9	Nemati et al. (2013)	A6
241	53.15	35.82	–	70	70	–46	8	Nemati et al. (2013)	A6
242	53.06	35.91	–	–90	80	45	5	Nemati et al. (2013)	A6
243	52.99	35.88	–	90	80	26	7	Nemati et al. (2013)	A6
244	58.22	35.51	5.4	57	42	23	26	Shabaniyan et al. (2010)	A6
245	57.92	35.45	5.4	156	65	–176	8	Shabaniyan et al. (2010)	A6
246	57.75	35.54	5	23	8	176	29	Shabaniyan et al. (2010)	A6
247	56.87	35.15	5.6	325	36	99	9	Shabaniyan et al. (2010)	A6
248	55.94	35.33	4.7	219	87	4	53	Shabaniyan et al. (2010)	A6
249	58.66	35.56	5.1	319	32	144	33	Shabaniyan et al. (2010)	A6

**Table 1** (continued)

No.	Long. (°)	Lat. (°)	M	Azimuth (°)	Dip (°)	Rake (°)	Depth (km)	Refs.	Group
250	57.35	35.65	4.8	82	77	10	33	Shabaniyan et al. (2010)	A6
251	57.22	35.85	4.8	257	79	5	33	Shabaniyan et al. (2010)	A6
252	58.19	35.46	5.1	83	43	79	27	Shabaniyan et al. (2010)	A6
253	60.84	35.66	5.2	316	30	109	30	Shabaniyan et al. (2010)	A6

## References

- Abbassi A, Nasrabadi A, Tatar M, Yaminifard F, Abbassi M, Hatzfeld D, Priestley K (2010) Crustal velocity structure in the southern edge of the Central Alborz (Iran). *J Geodyn* 49(2):68–78. <https://doi.org/10.1016/j.jog.2009.09.044>
- Alavi M (1996) Tectonostratigraphic synthesis and structural style of the Alborz mountain system in northern Iran. *J Geodyn* 21(1):1–33
- Allen M, Ghassemi MR, Sharabi M, Qorashi M (2003) Accommodation of late Cenozoic oblique shortening in the Alborz range, Iran. *J Struct Geol* 25:659–672
- Ambraseys NN, Melville CP (1982) A history of Persian earthquakes. Cambridge earth science series. Cambridge University Press, London, p 212
- Berberian M (1983) The southern Caspian: a compressional depression floored by a trapped, modified oceanic crust. *Can J Earth Sci* 20(2):163–183
- Berberian M, King GCP (1981) Towards a paleogeography and tectonic evolution of Iran. *Can J Earth Sci* 18:210–265
- Berberian M, Walker R (2010) The Rudbar Mw 7.3 earthquake of 1990 June 20; seismotectonics, coseismic and geomorphic displacements, and historic earthquakes of the western ‘High-Alborz’, Iran. *Geophys J Int* 182:1577–1602. <https://doi.org/10.1111/j.1365-246X.2010.04705.x>
- Berberian M, Yeats RS (2001) Contribution of archaeological data to studies of earthquake history in the Iranian Plateau. *J Struct Geol* 23:563–584
- Djamour Y, Vernant P, Bayer R, Nankali HR, Ritz JF, Hinderer J, Hatam Y, Luck B, Moigne N, Sedighi M, Khorrami F (2010) GPS and gravity constraints on continental deformation in the Alborz mountain range, Iran. *Geophys J Int* 183:1287–1301
- Ekström G, Nettles M, Dziewonski AM (2012) The global CMT project 2004–2010: Centroid-moment tensors for 13,017 earthquakes. *Phys Earth Planet Inter* 200–201:1–9. <https://doi.org/10.1016/j.pepi.2012.04.002>
- Engdahl ER, Van der Hilst R, Buland R (1998) Global teleseismic earthquake relocation with improved travel times and procedures for depth determination. *Bull Seismol Soc Am* 88:722–743
- Gephart JW, Forsyth DW (1984) An improved method for determining the regional stress tensor using earthquake focal mechanism data: application to the San Fernando earthquake sequence. *J Geophys Res* 89:9305–9320
- Gillard D, Wyss M (1995) Comparison of strain and stress tensor orientation: application to Iran and Southern California. *J Geophys Res Solid Earth* 100(B11):22197–22213
- Hardebeck J, Hauksson E (2001) Stress orientations obtained from earthquake focal mechanisms: what are appropriate uncertainty estimates? *Bull Seismol Soc Am* 91(2):250–262
- Hollingsworth J, Nazari H, Ritz JF, Salamati R, Talebian M, Bahroudi A, Walker R, Rizza M, Jackson J (2010) Active tectonics of the east Alborz mountains, NE Iran: Rupture of the left-lateral Astaneh fault system during the great 856 A.D. Qumis earthquake. *J Geophys Res*. <https://doi.org/10.1029/2009jb007185>
- Jackson J, Priestley K, Allen M, Berberian M (2002) Active tectonics of the South Caspian Basin. *Geophys J Int* 148:214–245
- Javidfakhr B, Bellier O, Shabaniyan E, Siame L, Léanni L, D Bourlès, Ahmadian S (2011) Fault kinematics and active tectonics at the southeastern boundary of the eastern Alborz (Abr and Khij fault zones): geodynamic implications for NNE Iran. *J Geodyn* 52:290–303
- Kagan YY (1991) 3-D rotation of double-couple earthquake sources. *Geophys J Int* 106:709–716
- Keiding M, Lund B, Arnadóttir Th (2009) Earthquakes, stress, and strain along an obliquely divergent plate boundary: Reykjanes Peninsula, Southwest Iceland. *J Geophys Res*. <https://doi.org/10.1029/2008jb006253>
- Khorrami F, Hesami Kh, Nankali HR, Tavakoli F (2012) Geosciences. *Geol Surv Iran* 82:223–230
- Lund B, Bödvarsson R (2002) Correlation of microearthquake body-wave spectral amplitudes. *Bull Seismol Soc Am* 92(6):2419–2433
- Lund B, Slunga R (1999) Stress tensor inversion using detailed microearthquake information and stability constraints: application to Olfus in southwest Iceland. *J Geophys Res* 104(B7):14947–14964
- Lund B, Townend J (2007) Calculating horizontal stress orientations with full or partial knowledge of the tectonic stress tensor. *Geophys J Int* 170:1328–1335. <https://doi.org/10.1111/j.1365-246X.2007.03468.x>
- Masson F, Djamour Y, Van Gorp S, Chéry J, Tatar M, Tavakoli F, Nankali H, Vernant P (2006) Extension in NW Iran driven by the motion of the South Caspian Basin. *Earth Planet Sci Lett* 252(1–2):180–188. <https://doi.org/10.1016/j.epsl.2006.09.038>
- Michael AJ (1984) Determination of stress from slip data: faults and folds. *J Geophys Res* 89(B13):11517–11526
- Mirzayi Suzani M, Shahidi A, Ramezani Omali R, Alizadeh Suri F (2016) Geosciences. *Geol Surv Iran* 95:39–48
- Motavalli-Anbaran S, Zeyen H, Brunet M, Ardestani VE (2011) Crustal and lithospheric structure of the Alborz Mountains, Iran and surrounding areas from integrated geophysical modeling. *Tectonics*. <https://doi.org/10.1029/2011tc002934>
- Musumeci C, Patanè D, Scarfì L, Gresta S (2005) Stress directions and shear-wave anisotropy: observations from local earthquakes in Southeastern Sicily, Italy. *Bull Seismol Soc Am* 95(4):1359–1374. <https://doi.org/10.1785/0120040108>
- Naimi-Ghassabian N, Khatib M, Nazari H, Heyhat M (2015) Present-day tectonic regime and stress patterns from the formal inversion of focal mechanism data, in the North of Central–East Iran Blocks. *J Afr Earth Sci* 111:113–126. <https://doi.org/10.1016/j.jafrearsci.2015.07.018>
- Nemati M, Hatzfeld D, Gheitanchi MR, Sadidkhouy A, Mirzaei N (2011) Microseismicity and seismotectonics of the Firuzkuh and Astaneh faults (East Alborz, Iran). *Tectonophysics* 506(1–4):11–21. <https://doi.org/10.1016/j.tecto.2011.04.007>
- Nemati M, Hollingsworth J, Zhan Z, Bolourchi MJ, Talebian M (2013) Microseismicity and seismotectonics of the South Caspian

- Lowlands, NE Iran. *Geophys J Int* 193(3):1053–1070. <https://doi.org/10.1093/gji/ggs114>
- Radjaee A, Rham D, Mokhtari M, Tatar M, Priestley K, Hatzfeld D (2010) Variation of Moho depth in the central part of the Alborz. *Geophys J Int* 181:173–184. <https://doi.org/10.1111/j.1365-246X.2010.04518.x>
- Raeesi M, Zarifi Z, Nilfouroushan F, Boroujeni SA, Tiampo K (2016) Quantitative analysis of seismicity in Iran. *Pure Appl Geophys* 174(3):793–833. <https://doi.org/10.1007/s00024-016-1435-4>
- Ritz J-F, Nazari H, Ghassemi A, Salamati R, Shafei A, Solaymani S, Vernant P (2006) Active transtension inside central Alborz: a new insight into northern Iran-southern Caspian geodynamics. *Geology* 34(6):477–480
- Sadidkhoy A, Javan-Doloei G, Siahkoobi HR (2008) Seismic anisotropy in the crust and upper mantle of the Central Alborz Region, Iran. *Tectonophysics* 456(3–4):194–205
- Shabanian E, Bellier O, Abbassi MR, Siame L, Farbod Y (2010) Plio-Quaternary stress states in NE Iran: Kopeh Dagh and Allah Dagh-Binalud mountain ranges. *Tectonophysics* 480(1–4):280–304
- Snoke JA, Munsey JW, Teague AC, Bollinger GA (1984) A program for focal mechanism determination by combined use of polarity and SV -P amplitude ratio data, *Earthquake Notes*, 55, #3, 15
- Stocklin J (1974) Possible ancient continental margin in Iran. In: Burke C, Drake C (eds) *Geology of continental margins*. Springer, New York, pp 873–877
- Tatar M, Jackson J, Hatzfeld D, Bergman E (2007) The 28 May 2004 Baladeh earthquake (Mw 6.2) in the Alborz, Iran: implications for Tehran and the geology of the South Caspian Basin margin. *Geophys J Int* 170:249–261
- Tatar M, Hatzfeld D, Abbassi A, Yamini Fard F (2012) Microseismicity and seismotectonics around the Mosha fault (Central Alborz, Iran). *Tectonophysics* 544–545:50–59
- Vavryčuk V (2014) Iterative joint inversion for stress and fault orientations from focal mechanisms. *Geophys J Int* 199(1):69–77. <https://doi.org/10.1093/gji/ggu224>
- Vavrycuk V, Bouskova A (2008) S-wave splitting from records of local micro-earthquakes in West Bohemia/Vogtland: an indicator of complex crustal anisotropy. *Stud Geophys Geod* 52:631–650. <https://doi.org/10.1007/s11200-008-0041-z>
- Vernant Ph, Nilfouroushan F, Chéry J, Bayer Y, Djamour R, Massona F, Nankali H, Ritz JF, Sedighi M, Tavakoli F (2004) Deciphering oblique shortening of central Alborz in Iran using geodetic data, *Earth planet. Sci Lett* 223:177–185
- Zanchi A, Berra F, Mattei M, Ghassemi M, Sabouri J (2006) Inversion tectonics in central Alborz, Iran. *J Struct Geol* 28:2023–2037
- Zarifi Z, Nilfouroushan F, Raeesi M (2014) Crustal stress map of Iran: insight from seismic and geodetic computations. *Pure Appl Geophys* 171(7):1219–1236





# On estimating time offsets in the ambient noise correlation function caused by instrument response errors

Fang Ye<sup>1,2</sup> · Jun Lin<sup>1,2</sup> · Xiaopu Zhang<sup>1,2</sup> · Xiaoxue Jiang<sup>1,2</sup>

Received: 20 September 2017 / Accepted: 25 October 2018 / Published online: 31 October 2018  
© Institute of Geophysics, Polish Academy of Sciences & Polish Academy of Sciences 2018

## Abstract

Broadband seismic networks are becoming more intensive, generating a large amount of data in the long-term collection process. When processing the data, the researchers rely almost on instrument response files to understand the information related to the instrument. Aiming at the process of instrument response recording and instrument response correction, we identify several sources of the instrument response phase error, including pole–zero change, the causality difference in instrument correction method, and the problem of filter coefficient recording. The data time offset range from the instrument response phase error is calculated from one sample point to several seconds using the ambient noise data recorded by multiple seismic stations. With different data delays, the time offset of the noise correlation function is estimated to be 74% to 99% of the data delay time. In addition, the influence of instrument response phase error on the measurement of seismic velocity change is analyzed by using ambient noise data with pole–zero change, and the results show that the abnormal wave velocity with exceeding the standard value is exactly in the time period of the instrument response error, which indicates that the instrument response error affects the study of seismology.

**Keywords** Time offset · Instrument response · Seismic ambient noise · Seismic velocity change

## Introduction

Over the past decade, a wide range of broadband seismic networks with multiple scales and perfect seismic data centers have been established worldwide. The observation data provided by them have driven great progress in both theory and practice in seismic ambient noise research (Weaver and Lobkis 2001; Derode et al. 2003; Snieder 2004; Paul et al. 2005; Sato 2013), and this has achieved fruitful results (Campillo and Paul 2003; Shapiro and Campillo 2004; Shapiro et al. 2005; Brenguier et al. 2008a, b). The method of ambient noise cross-correlation is free from the seismological limitations of the temporal and spatial distribution of earthquakes. With the extensive development of research on the internal structure of the earth, more intensive broadband seismic networks are continuously established. More

comprehensive broadband seismic networks are being established, and many new broadband seismic instruments are gradually emerging.

Most major seismic data centers, such as IRIS DMC (the Incorporated Research Institutions for Seismology Data Management Center), distribute seismic data in SEED (Standard for the Exchange of Earthquake Data) format. The SEED format provides the possibility to distribute comprehensive metadata on instrument response and seismic records. Seismologists obtain data from the data centers and then follow the instrument response correction to obtain ground motion from these original records through extensive application of standardized and simplified software for end users. In fact, they can only rely on the instrument response file and do not know the actual working status of seismic instrument, and incorrect data processing results will occur when the actual situation of the instrument is inconsistent with the record file. This is also the important reason that affects the data quality of the early broadband seismic network.

The previous studies have shown that clock synchronization errors between two stations can lead to a time offset in the noise cross-correlation function (Sens-Schönfelder 2008;

✉ Jun Lin  
lin\_jun@jlu.edu.cn

<sup>1</sup> College of Instrumentation & Electrical Engineering, Jilin University, Changchun 130026, China

<sup>2</sup> National Geophysical Exploration Instrument Engineering Technology Research Center, Changchun 130026, China

Xia et al. 2015; Gouédard et al. 2014). From another point of view, we analyze the causes of the phase error of the instrument response after understanding the instrument response of the broadband seismic station. The ambient noise data of the regional broadband seismic network are then used to calculate the data delays that the phase errors may cause, and further estimate the time offset range of these data delays to noise cross-correlation function which is further calculated. Finally, we discuss the influence of the time offset generated by the instrument response error on monitoring temporal variations in crustal properties.

## Theory

The cross-correlation of ambient noise data recorded by A and B at two stations is given by

$$C_{AB}(t) = \int_0^T f_A(r_1, \tau) f_B(r_2, \tau + t) d\tau, \quad (1)$$

where  $v_A(r_1, \tau)$  and  $v_B(r_2, \tau)$  are the observed fields at spatial locations  $r_1$  and  $r_2$ , respectively,  $T$  is the observation time,  $\tau$  is time, and  $t$  is the delay time. For a spatially uniform broadband noise distribution in a uniform medium with sound speed  $c$ , it can be considered (Sabra et al. 2005) that the derivative of the noise cross-correlation  $C_{AB}$  is

$$\frac{dC_{AB}}{dt} \approx -\frac{\delta(t + L/c)}{L} + \frac{\delta(t - L/c)}{L}, \quad (2)$$

where the interstation distance is  $L = |r_2 - r_1|$ , and  $C_{AB}$  is zero for  $|t| > L/c$ , noncontinuous at  $t = \pm L/c$ , and continuous for  $|t| < L/c$ . The noise events that propagate from station A to B yield a positive correlation time delay  $t$ , and noise events that propagate from station B to A yield a negative correlation time delay  $-t$ .

It is assumed (Hannemann et al. 2014) that a delta impulse excited at time  $\tau_\delta$  and location  $r_\delta$  in a homogeneous half-space with velocity  $c$ , which is received by station  $n$  at location  $r_n$ ,

$$f_n(\tau) = \delta\left(\tau - \tau_\delta - \frac{r_n - r_\delta}{c}\right). \quad (3)$$

Similarly, when considering stations A and B and assuming that there is time delay  $\tau_c$  in station B, the nonzero of the cross-correlation function of the two stations is

$$t = -\frac{L}{c} - \tau_c. \quad (4)$$

Therefore, compared with Eq. 2, the lag time of the cross-correlation function is delayed by the time  $\tau_c$ , which also indicates a time delay in one of the two stations would make

a time shift of the whole cross-correlation waveform to lead to a larger travel time in the positive time and a smaller travel time in the negative, or vice versa.

In practice, in addition to instrumental errors, the travel time of the surface waves for both positive and negative cross-correlation times is also affected by a physical change in the medium and a change in the spatial distribution of the noise sources (Stehly et al. 2007). So the travel time variation  $\delta\tau(t)$  measured from a surface wave by cross-correlations can be written as:

$$\delta\tau(t) = D(t) + \varphi(t) + \varepsilon(t), \quad (5)$$

where  $\delta\tau(t)$  is the variation in surface wave travel time measured either on the positive or on the negative part,  $D(t)$  is the time delay caused by the instrumental errors,  $\varphi(t)$  is the time offset due to changes in the medium, and  $\varepsilon(t)$  is the time offset changes in the spatial distribution of the noise sources.  $D(t)$  is an even function, and  $\varphi(t)$  is an odd function.

Then, the time offset due to the station instrumental errors can be obtained from Eq 5:

$$D(t) = \frac{\delta\tau(t) + \delta\tau(-t)}{2} + \frac{\varepsilon(t) + \varepsilon(-t)}{2}, \quad (6)$$

under the assumption that  $D(t)$  is large compared to  $\varepsilon(t) + \varepsilon(-t)/2$ ,  $D(t)$  can be evaluated by

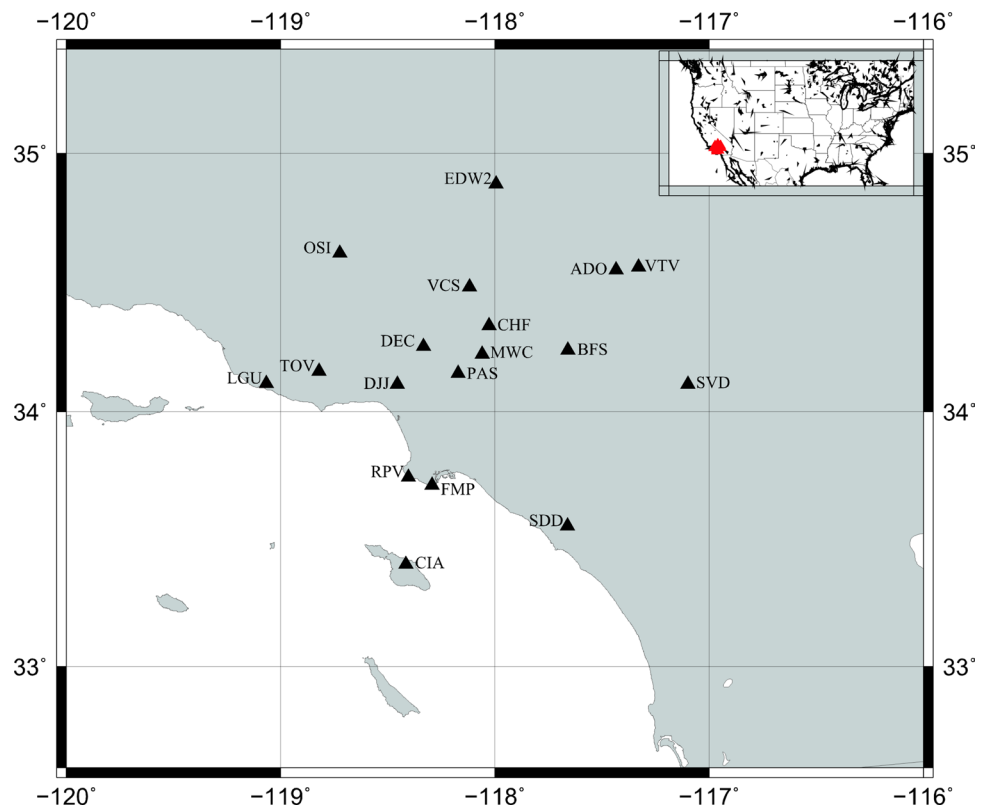
$$D(t) = \frac{\delta\tau(t) + \delta\tau(-t)}{2}. \quad (7)$$

by using cross-correlation of a larger time windows, the term  $\varepsilon(t)$  is expected to be smaller, and smaller long-term instrumental errors can be identified more easily.

## Data and processing

With the more intensive deployment of the broadband seismic network, the development of the regional seismological network which is conducive to the study of diversified seismology is more common. Therefore, we choose the regional seismic network as the research target and select the station of the Caltech (CI) regional seismic network in the Los Angeles basin in southern California. So far, the observation data of stations in this area have been widely used in the research of ambient noise (e.g., Sabra et al. 2005; Stehly et al. 2006; Moschetti et al. 2007; Meier et al. 2010). We choose continuous data recorded from 18 stations in CI network from January 2005 to December 2006. The two-year observation window is long enough to capture the effects of seasonal variations. The distribution of the selected stations is shown in Fig. 1. The interstation distance is the key factor that determines the period range: When the interstation distance becomes much larger than the dominant wavelength, correlation in the time domain is useful (Chávez-García

**Fig. 1** Map of the study area. Stations equipped with broadband seismic instrumentation are indicated by triangles with station names beside each symbol. The inset shows the locations of stations on the larger map



and Rodríguez, 2007). All of the interstation distances are approximately 10–200 km, so the period range selected is 5–25 s. These stations are equipped with STS2 or Trillium 240 seismometers and Quanterra Q330HR digitizers, which provide mostly complete information on the nature of ground motion.

We download the SEED volumes that contain data and instrument responses from IRIS DMC. The volumes are segmented into day-long time series and resampled to 20 Hz, with mean, trend, and instrument responses subsequently removed. Therefore, we use Welch's method (Seatz et al. 2012) and spectral normalization (Bensen et al. 2007) to mitigate the effects of temporal fluctuations of noise sources and to minimize the influence of high-amplitude events and instrument irregularities. After the Butterworth bandpass filtering between 5 and 25 s, the processed one-day-long traces are split into 3600 s with 50% overlap between adjacent windows. The corresponding time windows of two stations are calculated by cross-correlation, and the average of these cross-correlation results across all time windows in a single day is the 'one-day cross-correlation function.'

In order to improve the signal-to-noise ratio of the correlation trace, but also to maintain individual differences, 1-day cross-correlation functions are stacked to create daily cross-correlation functions in a moving 15-day window. Figure 2 shows daily correlation functions of the station pair DEC–TOV vary with day. High signal-to-noise

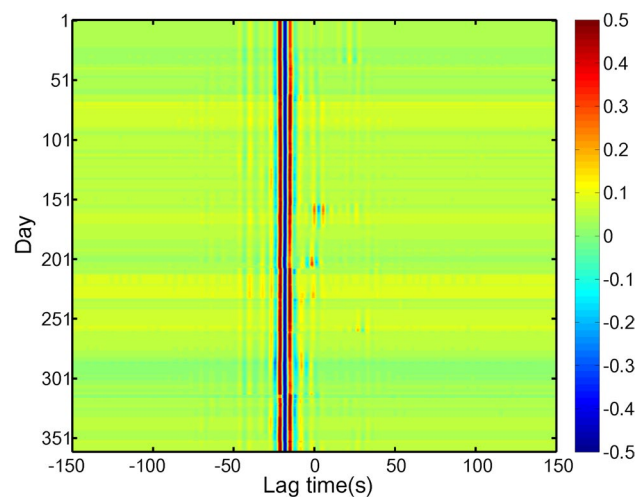


**Fig. 2** Example of daily cross-correlation functions stacked using a moving 15-day window over one year at station pair DEC–TOV. The amplitude is normalized to the maximum of each correlation trace

ratio and similar waveforms ensure reliable estimates of temporal variations. The normalized daily cross-correlation functions present stable surface waves throughout the one year. Asymmetry of the positive and negative parts of the correlation trace is related to the nonisotropic distribution of noise sources (Stehly et al. 2006).



## Instrument response and sources of phase errors

Broadband seismic stations can record the complete ground motion information in the 0.01-Hz to 50-Hz frequency band, which contributes to the study of key issues such as high-resolution images of the earth's interior, evolution of the continental structure, the nature of the seismic faults, and the origin of the earthquake. We use the typical broadband seismic station in USArray's Transportable Array as an example to illustrate the configuration and deployment of broadband seismic stations, as shown in Fig. 3.

In order to obtain good low-frequency performance, the seismic station deployment needs to comply with strict installation requirements. The installation site of a broadband seismograph requires a good control environment, and other noise disturbances, such as traffic and wind noise, must be considered. To reduce interference from surface vibrations and to protect the equipment, the seismometer would be buried 10 to 20 feet below the ground inside an augered hole. This hole will be cased in either PVC or steel, to keep the hole open, and then capped to protect the hole. Power is provided by solar panels mounted nearby on a pole or a hut and powered by a combination of battery and fuel cell systems. A fiberglass hut with solar panels on the roof is placed about 3.5 m (~10 ft) from the sensor to house the batteries, data collection computer, and communication electronics. Cables contained within a conduit connect the sensor to the equipment in the hut. Data are transmitted to

the data processing center via cellular, broadband, or satellite communication systems.

The complete broadband measurement system (sensors and data loggers) is considered as a linear time invariant (LTI) system that transfers analog input signals  $x(t)$  to discrete output signals  $r[t]$ . In Fig. 3, a typical measurement system is displayed via the broadband high-gain vertical channel of the station TOV.

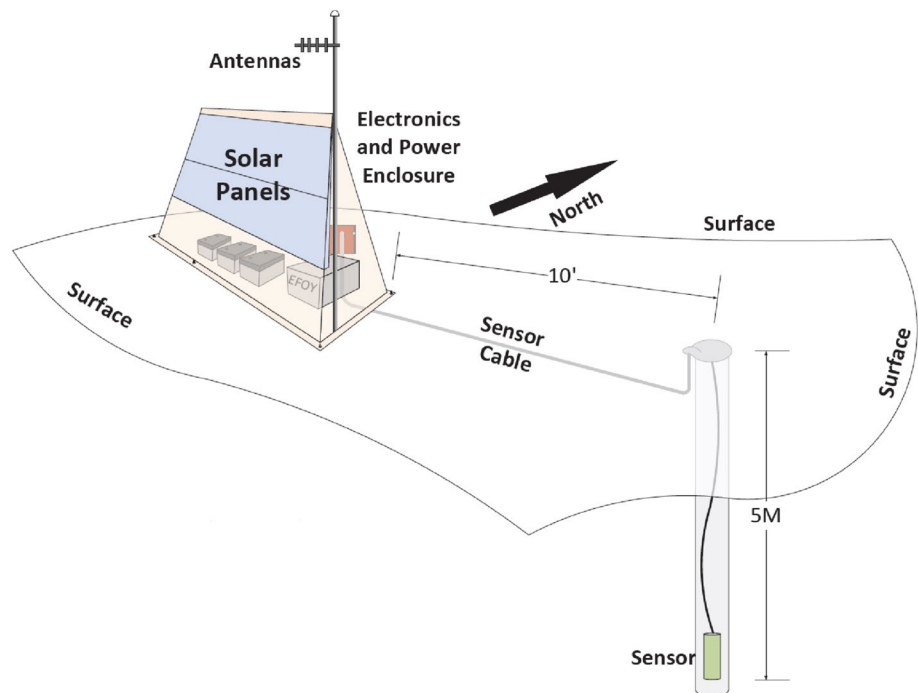
An LTI system can be described as the frequency response function of a measurement system in the frequency domain. It can be divided into three stages: analogue, analogue–digital (A/D) converter, and digital. In fact, by multiplying the discrete frequency response function at all stages, the complete frequency response function is finally obtained (Davis et al. 2005):

$$G(f) = S_d A_0 \frac{\prod_{n=1}^N (s - r_n)}{\prod_{m=1}^M (s - p_m)} = S_d A_0 H_p(s), \quad (8)$$

where the scalar  $S_d$  contains all information about the stage's sensitivity, the factor  $A_0$  is chosen to normalize the series at a canonical frequency  $f_0$ ,  $r_n$  and  $p_m$  are the zeros and poles. The variables in the Laplace transform are given by  $s$  which related to angular frequency via the  $s = i\omega$ .

In addition, oversampling is commonly used to reduce the quantization noise of A/D converter and improve amplitude resolution. Then, the original discrete data stream  $x[t]$  is low-pass filtered and resampled to obtain the expected sampling rate of the discrete time series  $r[t]$ . In general, the

**Fig. 3** Schematic diagram of the configuration of a typical broadband seismic station



sampling to the desired sampling rate is obtained by cascading a number of extractors with digital anti-alias (DAA) filters, as shown in Fig. 4.

The SEED format provides all the analog phase, digital stage instrument response information and also includes the transfer function of the DAA filter stage. The discrete transfer function  $T(z)$  of the DAA filter in the digital  $z$  plane is usually described by the numerator and denominator coefficients:

$$T(z) = \frac{\sum_{l=0}^M b_l z^{-l}}{\sum_{k=0}^N a_k z^{-k}} \tag{9}$$

In general, the data acquisition system can program the DAA filter with a minimum phase filter or a linear phase filter and also correct the delay generated by the linear phase filter.

Moreover, the broadband sensor needs special attention because it has a high sensitivity to low-frequency interference caused by temperature-induced tilt. In some cases, it may even be necessary to install it in the borehole to keep away from the noise near the surface. The vertical sensor is affected by variable buoyancy caused by pressure changes. In short, each instrument will provide response parameters accurately in layout, but with a long time of work, they may be aging or other deviations, so the actual response parameters of the instrument need to be regularly measured and modified.

In the process of seismic data processing, the instrument information is only involved in deconvolution operation with the form of instrumental response of Eq. 8. Therefore, the phase error of instrument response is mainly generated in the process of instrument response recording and instrument response correction. We analyze several sources of error in this process, including the change of the pole–zeros related to the phase of the instrument response in Eq. 8, the error in the record of the transfer function coefficient of the DAA filter in Eq. 9, and the causality difference in different instrument response correction methods.

### The change of pole–zeros

During a long period of data collection, the replacement or aging of the broadband sensor may cause the actual pole–zeros to deviate from the recorded pole–zeros. Besides, atmospheric pressure, humidity, and temperature may also cause the change of pole–zeros. If it is not timely to measure the new pole–zeros and update the instrument response file, but using the pole–zeros recorded in the original instrument response file for data processing, it is possible to cause the time offset of the noise cross-correlation function.

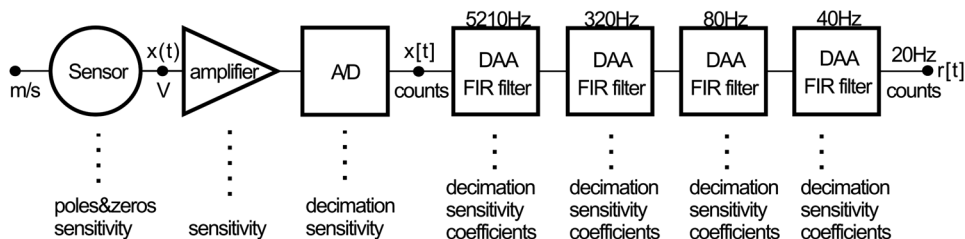
We take station TOV as an example, and its pole–zeros due to the replacement of the seismograph have changed as shown in Fig. 5. The two instrument responses before and after the pole–zero change are calculated according to Eq. 8, and they are used in the instrumental correction for one-day ambient noise data of the station TOV. The time difference between the two groups of noise data after instrumental correction is 0.025 s in period band 5–10 s and 0.063 s in period band 10–25 s, respectively.

### The problem of transfer function coefficients

The SEED format records the coefficients of the transfer function of the DAA filter stage according to Eq. 9 and the correction time of the linear phase filter. The delay time of the filter means that the data move backwards through the filter, and then the data logger corrects the time series by shifting the time series back to the earlier time after filtering. The usual instrumental correction is based on Eq. 8, so the time delay that has been corrected in the acquisition system is not considered. However, when the recorded filter coefficients differ from the actual corrected time delay, there will be a delay in the recording data.

We use a common mistake as an example to illustrate that the coefficients are recorded in reverse order; in fact, SEED format specifies that the coefficients should be recorded in the forward order. The filter with the inverse coefficient has the same amplitude response spectrum as the original filter, but has a distinct phase response spectrum, so there will be a different time delay. The filter coefficients recorded in the instrument response file of station CIA are calculated in two different orders, as shown in Table 1, which contains delay times calculated by filter coefficients in forward order,

**Fig. 4** Block diagram of the broadband high-gain vertical channel of a seismological measuring system sampling at 20 Hz. The description of the corresponding instrument response in the SEED is marked below each part



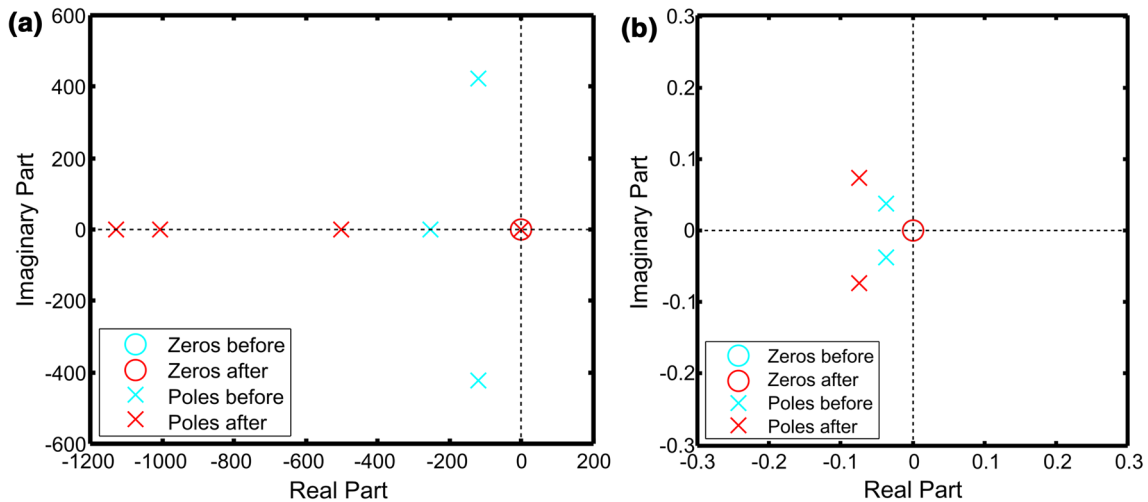


**Fig. 5** **a** Pole–zeros of station TOV are distributed before and after the change. **b** Zoom-in coordinates near 0 point in (a)

**Table 1** Delay times of filters in station CIA

Different conditions	Stage 4 (s)	Stage 5 (s)	Stage 6 (s)	Total delay time (s)
Filter in forward order	0.003	0.012	0.398	0.413
Correction time	0.003	0.012	0.398	0.413
Filter in reverse order	0.024	0.276	0.852	1.152
Difference	0.021	0.264	0.464	0.739

correction times in the data logger, delay times calculated by filter coefficients in reverse order, and the delay time differences between the two kinds of coefficients. With the decreasing sampling rate at each stage, the delay time difference caused by the coefficient order becomes larger. For low sampling data, such mistakes would lead to greater errors, and the time delay difference is significantly up to 0.464 s in the stage 6. The total delay time difference in all stages is 0.739 s, which is different from the correction time, resulting in the time offset of data.

### The causality of instrumental correction

Haney et al. (2012) described a general method for causal instrumental correction, with particular attention to maintaining causal properties after correction in order to observe the first action and maintain relative timing information between different frequencies. However, most of the instrumental response correction methods are noncausal. The causality of instrumental correction mainly lies in the choice of filter, so we compare the zero-phase filters commonly used in instrumental correction with IIR causal filters used in causal instrumental correction. Then, the two instrumental correction methods are, respectively, used for one day

of ambient noise raw data from station SDD, and the time difference between the two corrected data is 0.03 s.

### Time offset measurement results

We have made clear that the instrument itself, the data processing, and the management of the metadata are several sources that may cause the phase error of the instrument response in the process of long-time data acquisition. In order to understand the influence of these errors on the data, the time offset caused by the phase error of the instrument response is calculated by using the ambient noise data of the 18 seismic stations shown in Fig. 1.

During the 2-year observation period, only station TOV has pole–zero change. Therefore, in order to explain the time offset caused by different pole–zero changes, there is also a station CHF for selected longer observation (4 years). The instrumental response of two stations before and after the pole–zero changes is calculated, respectively, and the phase frequency characteristic curves of the two stations are obtained, as shown in Fig. 6.

The phase of the instrument response of the two stations increases gradually from short period to long period: one station reached 10 degrees and the other 20 degrees in the

**Fig. 6** Phases of the instrument response of (a) the station TOV and (b) the station CHF are calculated from the pole–zeros before and after the change. The frequency band we are working with is indicated by gray shading

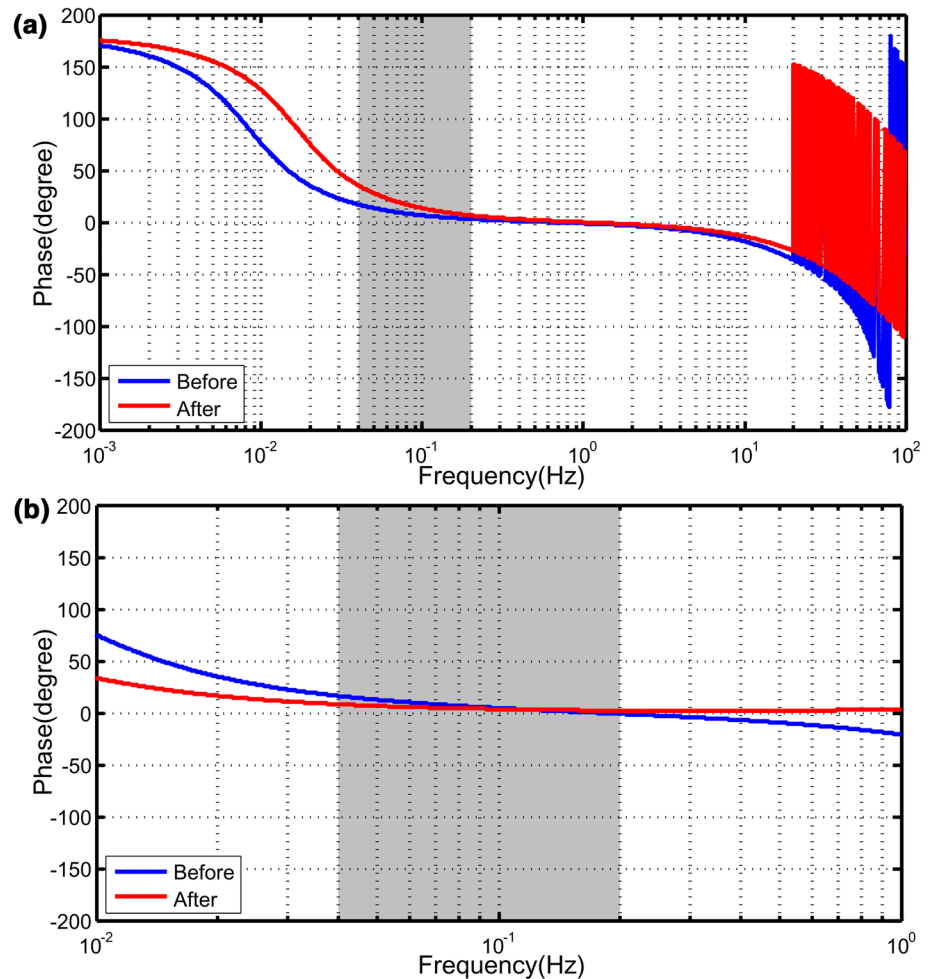


**Table 2** Average time offset caused by the change of pole–zeros

Station	Time offset in period 5–10 (s)	Time offset in period 10–20 (s)
CHF	−0.0313	−0.0375
TOV	−0.0500	−0.1375

frequency range we studied, suggesting that the time offset caused by the change of pole–zeros is frequency dependent. Therefore, we choose the two-band range of 5–10 s and 10–20 s, respectively, and the two instrument responses before and after the pole–zero change of each station are used to for instrumental correction of a day series. The time offset between the two datasets per day was repeated over the two-year observation, and the average time offset is shown in Table 2.

The result of time offset is related to the frequency dependence of the phase, in which the phase change of the CHF station is smaller than that of the station TOV, so its time offset difference is also smaller within two periods.

This verifies that the pole–zeros of the seismograph are changed if updates to the instrument response file are not made in time, which can introduce unnecessary data delay.

We have known that the time offset of a single day's time series of station SDD caused by causality differences in instrumental correction is 0.03 s. For each of the 18 stations, the time shift of each day in the observation is calculated and the average time offset caused by the causality differences in the instrumental correction is finally obtained as shown in Table 3. The time offset caused by this error is about 2 sampling points, but it is an error that cannot be ignored in the study of seismology, such as the clock synchronization of an underwater geophone, which requires accurate time values.

The transfer function coefficient record problem or the correction time error of data acquisition system will lead to the time offset of data time series. We consider calculating the time offset of data from all 18 stations caused by this error, in which the filters of the station ADO are the same as those of the stations BFS, CHF, FMP, RPV, SDD, SVC, the filters of the station CIA are the same as those of the stations DJJ, LGU, MWC, SDD, VCS, and the filters of the station OSI are the same as those of the stations PAS, SVD, TOV,



**Table 3** Average time offset caused by causality differences

Station	Time offset (s)
ADO	−0.0391
BFS	−0.0333
CHF	−0.0250
CIA	−0.0362
DEC	−0.0249
DJJ	−0.0348
EDW2	−0.0277
FMP	−0.0588
LGU	−0.0393
MWC	−0.0423
OSI	−0.0399
PAS	−0.0250
RPV	−0.0283
SDD	−0.0252
SVD	−0.0262
TOV	−0.0465
VCS	−0.0234
VTV	−0.0334

VTV. Therefore, the data time offset caused by the transfer function coefficients of two different orders is calculated by selecting the filter of ADO, CIA, and OSI, and the results are shown in Table 4. If an incorrect instrument response is used to recover ground motion from the data record, the time series is likely to exceed the time offset of 1 s in this error case.

In particular, the result of these errors is to delay or advance the time series of the ambient noise, so we analyze the effect of the time offset caused by the phase error of the instrument response on the time offset of the noise cross-correlation function. The data of the station ADO are selected as the target, and the data time offset of the station ADO is about 1 s due to the transfer function coefficient problem, so the one-day sequence after the background noise data preprocessing is delayed about 1 s. And from the previous results, it is known that the time offset of the data generated by the instrument response error ranges from a sampling point to a few seconds, so different data time offsets (0.05 s, 0.1 s, 0.5 s, 1 s) are set up to represent the results of different instrument response phase error sources.

**Table 4** Time offset caused by the problem of transfer function coefficients

Station	Stage 4 (s)	Stage 5 (s)	Stage 6 (s)	Sum (s)
ADO	0.026	0.243	0.496	0.765
CIA	0.021	0.264	0.454	0.739
OSI	0.067	0.418	0.641	1.126

The interstation distance between ADO and VTV is only 9.6 km and does not satisfy the condition of building a noise cross-correlation function. Therefore, data from ADO and the other 16 stations are used to calculate the travel time offset  $\delta\tau(t)$  between the daily cross-correlation functions obtained from the time offset data and the daily cross-correlation functions obtained from the original data and to obtain the time offset  $D(t)$  of noise cross-correlation function caused by phase errors in instrument response according to Eq. 7. Finally, we obtain the average time offset of the cross-correlation function of all station pairs during the observation, as shown in Table 5.

The effect of the noise source on the each of the two cross-correlation functions is the same, so the time offset obtained is only influenced by the time error of the instrument. From the results, with the increase in delay time, the time offset of noise cross-correlation function increases. The results measured in the period band of 10–20 s are less than 5–10 s. In spite of the minimum delay time, the time offset also reaches 74% of the delay time. Although we simulate the data delay caused by the instrument response error, it can be seen that the phase error of the instrument will cause an obvious time offset of noise cross-correlation function, which will affect the study of surface wave imaging (Shapiro et al. 2005; Sabra et al. 2005; Lin et al. 2007), wave velocity monitoring (Wegler and Sens-Schönfelder 2007; Brenguier et al. 2011; Durand et al. 2011), and ground motion prediction (Prieto and Beroza 2008; Denolle et al. 2013, 2014) using the noise cross-correlation function in seismology.

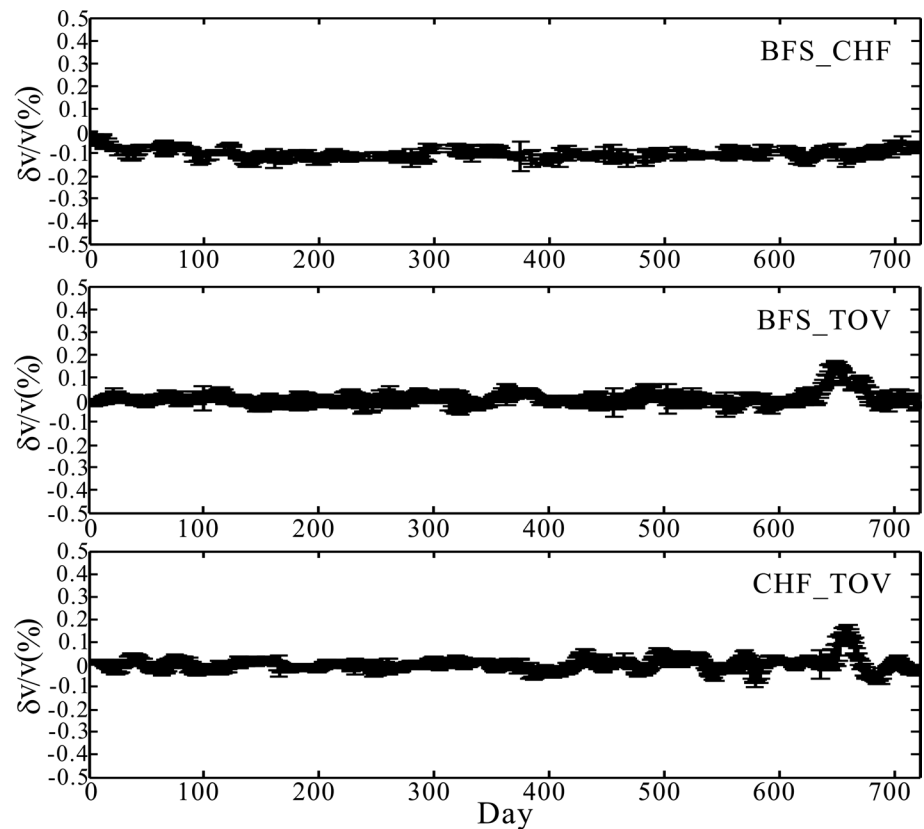
## Application of monitoring velocity variations

Ambient noise interferometry has widely been applied in monitoring temporal variations in crustal properties in recent years (Sens-schönfelder and Wegler 2006; Wegler and Sens-schönfelder 2007; Brenguier et al. 2008b). Because ambient noise is recorded at all times and places, the passive monitoring method is more repeatable and avoids the uncertainty in earthquake source locations and origin times and also more economical than controlled repeated sources.

**Table 5** Average time offset of noise cross-correlation functions of all station pairs

Data delay time (s)	D(t) in 5–10 (s)	$\Delta D(t)$ in 5–10 (s)	D(t) in 10–20 (s)	$\Delta D(t)$ in 10–20 (s) (%)
0.05	−0.0422	84%	−0.0368	74
0.1	−0.0906	90%	−0.0781	78
0.5	−0.4898	98%	−0.4758	95
1	−0.9898	99%	−0.9758	98

**Fig. 7** Temporal velocity perturbations and errors at three station pairs: **a** BFS–CHF, **b** BFS–TOV, and **c** CHF–TOV



Therefore, it enables continuous monitoring the temporal evolution of the seismic wave velocity of the medium by tracking the time shifts of noise cross-correlation function.

If the medium experiences a spatially homogeneous relative seismic velocity change  $\Delta v/v$ , the relative travel time shift  $\Delta\tau/\tau$  between a short-term current Green function and the long-term reference Green function is independent of the lapse time at which it is measured and  $\Delta v/v = -\Delta\tau/\tau$ . We followed the optimization method of Brenguier et al. (2008a, b) using the moving window cross-spectral analysis to monitor variations in seismic velocity. In a short window centered at time  $\tau$ , there are cross-spectrum between the reference correlation function and the current correlation function, and phase difference between the two traces in different frequency. If the two waveforms are similar, the time difference between the two traces  $\Delta\tau$  is estimated by the slope of phase differences  $\Delta\tau = \Delta f / (2\pi \times f)$ . Then, the linear fitting slope of the time offset calculated in a series of continuous narrow windows over a path between the two stations is the negative of the average fractional velocity perturbation, i.e.,  $\Delta\tau/\tau = -\Delta v/v$ .

We choose the noise cross-correlation function of the station pairs composed of three stations BFS, CHF, and TOV. Among them, the pole–zeros of the instrument response at station TOV were changed on day 644 as shown in Fig. 1. We have shown that failure to update the instrument response

file in time will result in data delay and time offset of the noise correlation function. Therefore, the original instrument response file is selected for the instrument response correction of the station TOV in data preprocessing to simulate this error. For each station pair, the noise cross-correlation functions stacked over the 2-year period of study define the long-term reference trace and the noise cross-correlation functions stacked in 15-day-long moving windows defines the short-term current Green function.

Figure 7 presents the relative velocity changes  $\Delta v/v$  measured over 2 years for the three station pairs, and the seismic velocity variations are small ( $< \pm 0.1\%$ ). The station pairs BFS–TOV and CHF–TOV yield similar temporal variations which reveal a prominent sudden increase in seismic velocity perturbation of  $\sim 0.2\%$  about on day 650, after this increase, the velocity gradually returns to its mean level. Because three stations are in the same area, the changes in the geological structure will result in all three station pairs to have seismic velocity perturbations at the same time. Therefore, only the stations connected with the TOV station have the speed disturbance, which is consistent with the expected station TOV, indicating the influence of the instrument response error on the geological structure study. Therefore, only the station pairs related to the station TOV have the velocity disturbance, which is consistent with the expected instrument response error of the station TOV, indicating the

influence of the instrument response error on analyses of changes in geologic structure.

## Conclusion

On the basis of understanding the configuration of the broadband seismograph, the calculation of the instrument response, and the parameters of the corresponding SEED format metadata, we analyze several sources of the instrument response phase error, including the change of the pole–zeros, the problem of the parameter recording of the filter transfer function, and the causality difference in different the instrument response correction methods. Using the ambient noise data of 18 broadband seismic stations, the time offset of the data caused by the three phase error sources is calculated from one sampling point to a few seconds. By setting the data time delay of the station ADO caused by instrument response error which is 0.05 s, 0.1 s, 0.5 s, and 1 s, we obtain time offset range of the noise cross-correlation function which is 74% to 99% of data delay time. Therefore, we demonstrate that the time offset of noise cross-correlation function is not only related to clock synchronization, but also closely related to instrument response. In addition, we use ambient noise data with instrument response phase error and the method of ambient noise seismic interferometry, to analyze the influence of the instrument's phase error data on the relative variation in wave velocity. The results show that when monitoring the relative changes in seismic wave velocity, disturbances significantly larger than standard wave velocity occur during instrument response errors that experience pole–zero changes. The stability of instrument response and the accuracy of processing are prerequisites for data analysis, especially for ambient noise data.

## References

- Bensen GD et al (2007) Processing seismic ambient noise data to obtain reliable broad-band surface wave dispersion measurements. *Geophys J Int* 169:1239–1260. <https://doi.org/10.1111/j.1365-246X.2007.03374.x>
- Brenguier F, Campillo M, Hadziioannou C, Shapiro NM, Nadeau RM, Larose E (2008a) Postseismic relaxation along the San Andreas Fault at Parkfield from continuous seismological observations. *Science* 321:1478–1481. <https://doi.org/10.1126/science.1160943>
- Brenguier F, Shapiro NM, Campillo M, Ferrazzini V, Duputel Z, Coustant O, Nercessian A (2008b) Towards forecasting volcanic eruptions using seismic noise. *Nat Geosci* 1:126–130
- Brenguier F, Clarke D, Aoki Y, Shapiro NM, Campillo M, Ferrazzini V (2011) Monitoring volcanoes using seismic noise correlations. *Comptes Rendus Geosci* 343:633–638
- Campillo M, Paul A (2003) Long-range correlations in the diffuse seismic coda. *Science* 299:547–549. <https://doi.org/10.1126/science.1078551>
- Chávez-García FJ, Rodríguez M (2007) The correlation of microtremors: empirical limits and relations between results in frequency and time domains. *Geophys J Int* 171:657–664. <https://doi.org/10.1111/j.1365-246X.2007.03529.x>
- Davis P, Ishii M, Masters G (2005) An assessment of the accuracy of GSN sensor response information. *Seismol Res Lett* 76:678–683. <https://doi.org/10.1785/gssrl.76.6.678>
- Denolle MA, Dunham EM, Prieto GA, Beroza GC (2013) Ground motion prediction of realistic earthquake sources using the ambient seismic field. *J Geophys Res Solid Earth* 118:2102–2118
- Denolle MA, Dunham EM, Prieto GA, Beroza GC (2014) Strong ground motion prediction using virtual earthquakes. *Science* 343:399–403
- Derode A, Larose E, Campillo M, Fink M (2003) How to estimate the Green's function of a heterogeneous medium between two passive sensors? application to acoustic waves. *Appl Phys Lett* 83:3054–3056. <https://doi.org/10.1063/1.1617373>
- Durand S, Montagner JP, Roux P, Brenguier F, Nadeau RM, Ricard Y (2011) Passive monitoring of anisotropy change associated with the Parkfield 2004 earthquake. *Geophys Res Lett* 38:142–154
- Gouédard P, Seher T, McGuire JJ, Collins JA, van der Hilst RD (2014) Correction of ocean-bottom seismometer instrumental clock errors using ambient seismic noise. *Bull Seismol Soc Am* 104:1276–1288. <https://doi.org/10.1785/0120130157>
- Haney MM, Power J, West M, Michaels P (2012) Causal instrument corrections for short-period and broadband seismometers. *Seismol Res Lett* 83:834–845. <https://doi.org/10.1785/0220120031>
- Hannemann K, Krüger F, Dahm T (2014) Measuring of clock drift rates and static time offsets of ocean bottom stations by means of ambient noise. *Geophys J Int* 196:1034–1042. <https://doi.org/10.1093/gji/ggt434>
- Lin FC, Ritzwoller MH, Townend J, Bannister S, Savage MK (2007) Ambient noise Rayleigh wave tomography of New Zealand. *Geophys J R Astron Soc* 170:649–666
- Meier U, Shapiro NM, Brenguier F (2010) Detecting seasonal variations in seismic velocities within Los Angeles basin from correlations of ambient seismic noise. *Geophys J Int* 181:985. <https://doi.org/10.1111/j.1365-246X.2010.04550.x>
- Moschetti MP, Ritzwoller MH, Shapiro NM (2007) Surface wave tomography of the western United States from ambient seismic noise: Rayleigh wave group velocity maps. *Geochem Geophys Geosyst* 8:Q08010. <https://doi.org/10.1029/2007GC001655>
- Paul A, Campillo M, Margerin L, Larose E, Derode A (2005) Empirical synthesis of time-asymmetrical Green functions from the correlation of coda waves. *J Geophys Res Solid Earth* 110:B08302. <https://doi.org/10.1029/2004JB003521>
- Prieto GA, Beroza GC (2008) Earthquake ground motion prediction using the ambient seismic field. *Geophys Res Lett* 35:137–149
- Sabra KG, Gerstoft P, Roux P, Kuperman WA, Fehler MC (2005) Extracting time-domain Green's function estimates from ambient seismic noise. *Geophys Res Lett* 32:L03310. <https://doi.org/10.1029/2004GL021862>
- Sato H (2013) Green's function retrieval from the CCF of random waves and energy conservation for an obstacle of arbitrary shape: noise source distribution on a large surrounding shell. *Geophys J Int* 193:997–1009. <https://doi.org/10.1093/gji/ggt032>
- Seats KJ, Lawrence JF, Prieto GA (2012) Improved ambient noise correlation functions using Welch's method. *Geophys J Int* 188:513–523. <https://doi.org/10.1111/j.1365-246X.2011.05263.x>
- Sens-Schönfelder C (2008) Synchronizing seismic networks with ambient noise. *Geophys J Int* 174:966–970. <https://doi.org/10.1111/j.1365-246X.2008.03842.x>
- Sens-Schönfelder C, Wegler U (2006) Passive image interferometry and seasonal variations of seismic velocities at Merapi Volcano, Indonesia. *Geophys Res Lett* 33:L21302. <https://doi.org/10.1029/2006GL027797>

- Shapiro NM, Campillo M (2004) Emergence of broadband Rayleigh waves from correlations of the ambient seismic noise. *Geophys Res Lett* 31:07614. <https://doi.org/10.1029/2004gl019491>
- Shapiro NM, Campillo M, Stehly L, Ritzwoller MH (2005) High-resolution surface-wave tomography from ambient seismic noise. *Science* 307:1615–1618. <https://doi.org/10.1126/science.1108339>
- Snieder R (2004) Extracting the Green's function from the correlation of coda waves: a derivation based on stationary phase. *Phys Rev E*. <https://doi.org/10.1103/physreve.69.046610>
- Stehly L, Campillo M, Shapiro NM (2006) A study of the seismic noise from its long-range correlation properties. *J Geophys Res Solid Earth* 111:B10306. <https://doi.org/10.1029/2005JB004237>
- Stehly L, Campillo M, Shapiro NM (2007) Traveltime measurements from noise correlation: stability and detection of instrumental time-shifts. *Geophys J Int* 171:223–230. <https://doi.org/10.1111/j.1365-246X.2007.03492.x>
- Weaver RL, Lobkis OI (2001) Ultrasonics without a source: thermal fluctuation correlations at MHz frequencies. *Phys Rev Lett* 87:134301. <https://doi.org/10.1103/PhysRevLett.87.134301>
- Wegler U, Sens-Schönfelder C (2007) Fault zone monitoring with passive image interferometry. *Geophys J Int* 168:1029–1033. <https://doi.org/10.1111/j.1365-246X.2006.03284.x>
- Xia Y, Ni S, Zeng X, Xie J, Wang B, Yuan S (2015) Synchronizing intercontinental seismic networks using the 26 s persistent localized microseismic source. *Bull Seismol Soc Am* 105:2101–2108. <https://doi.org/10.1785/0120140252>





# Seismic crust structure beneath the Aegean region in southwest Turkey from radial anisotropic inversion of Rayleigh and Love surface waves

Özcan Çakır<sup>1</sup>

Received: 2 April 2018 / Accepted: 7 November 2018 / Published online: 14 November 2018  
© Institute of Geophysics, Polish Academy of Sciences & Polish Academy of Sciences 2018

## Abstract

The Turkish plate is covered by hundreds of accelerometer and broadband seismic stations with less than 50 km inter-station distance providing high-quality earthquake recordings within the last decade. We utilize part of these stations to extract the fundamental mode Rayleigh and Love surface wave phase and group velocity data in the period range 5–20 s to determine the crust structure beneath the Aegean region in southwest Turkey. The observed surface wave signals are interpreted using both single-station and two-station techniques. A tomographic inversion technique is employed to obtain the two-dimensional group velocity maps from the single-station group velocities. One-dimensional velocity–depth profiles under each two-dimensional mesh point, which are jointly interpreted to acquire the three-dimensional image of the shear-wave velocities underneath the study area, are attained by utilizing the least-squares inversion technique, which is repeated for both Rayleigh and Love surface waves. The isotropic crust structure cannot jointly invert the observed Rayleigh and Love surface waves where the radial anisotropic crust better describes the observed surface wave data. The intrusive magmatic activity related to the northward subducting African plate under the Turkish plate results the crust structure deformations, which we think, causing the observed radial anisotropy throughout complex pattern of dykes and sills. The magma flow resulting in the mineral alignment within dykes and sills contributes to the observed anisotropy. Due to the existence of dykes, the radial anisotropy in the upper crust is generally negative, i.e., vertically polarized S-waves ( $V_{sv}$ ) are faster than horizontally polarized S-waves ( $V_{sh}$ ). Due to the existence of sills, the radial anisotropy in the middle-to-lower crust is generally positive, i.e., horizontally polarized S-waves ( $V_{sh}$ ) are faster than vertically polarized S-waves ( $V_{sv}$ ). Similar radial anisotropic results to those of the single-station analyses are obtained by the two-station analyses utilizing the cross-correlograms. The widespread volcanic and plutonic rocks in the region are consistent with the current seismic interpretations of the crustal deformations.

**Keywords** Aegean region · Group velocity · Phase velocity · Radial anisotropy · Surface waves · Tomography

## Introduction

The anisotropy found in many parts of the earth (i.e., crust, mantle, inner core) is that the transmission speed of a seismic wave depends on its direction of propagation and/or of polarization (e.g., Anderson 1961). There are several anisotropic minerals such as micas, amphiboles and olivines in the earth that when aligned by deformation strains they

produce constructively interfering pattern of seismic anisotropy along a preferred orientation in a polycrystalline aggregate (e.g., Mahan 2006; Karato et al. 2008; Ko and Jung 2015). The preferred orientation results in two kinds of anisotropy, i.e., lattice (or crystallographic) preferred orientation (LPO or CPO) and shape preferred orientation (SPO). Among many other researchers, Zhang and Karato (1995) upon laboratory experiments have reported that under simple shear deformation the olivine mineral in aggregates produced the lattice preferred orientation with its [100] axis aligned nearly parallel to the flow direction. The anisotropy due to the LPO is often used as seismic clue to study the flow and stress patterns in the upper mantle where the olivine is the dominant mineral (e.g., Long and Becker 2010; Faccenda and Capitanio 2013). Stack of thin layers, vertical

---

**Electronic supplementary material** The online version of this article (<https://doi.org/10.1007/s11600-018-0223-1>) contains supplementary material, which is available to authorized users.

---

✉ Özcan Çakır

<sup>1</sup> Çanakkale, Turkey

cracks in the brittle upper crust, dykes and sills, oriented melt pockets and sheet-like melts are some structural patterns to produce the seismic anisotropy due to the shape preferred orientation (e.g., see Backus 1962; Crampin 1984; Schoenberg and Douma 1988). Researchers have utilized evidence obtained from the observed seismic anisotropy to identify the shape characteristics of the respective earth structure (e.g., Bastow et al. 2010; Obrebski et al. 2010; Godfrey et al. 2017). We employ the shaped preferred orientation (SPO) more specifically dykes and sills along with the respective mineral alignment to interpret the observed radial anisotropy related to our Rayleigh and Love surface wave data.

The radial anisotropy is sufficient to model our observed surface wave data. In this system, the vertical axis is the symmetry axis and the phase velocity surface is ellipsoidal. Depending on the sign of anisotropy, this ellipsoidal surface could be defined as watermelon (i.e., negative—fast symmetry axis) or pumpkin (positive—slow symmetry axis). Therefore, the wave (P and S) speed is a function of angle of incidence measured from the vertical axis. In case of fast symmetry axis, horizontally propagating P-wave is slower and vertically propagating P-wave is faster. Horizontally propagating S-wave splits, i.e., vertically polarized S-wave (SV with  $V_{sv}$  velocity) is faster than horizontally polarized S-wave (SH with  $V_{sh}$  velocity). Vertically propagating S-wave does not split and is faster (i.e.,  $V_s \sim V_{sv}$ ). In case of slow symmetry axis, the above sense of plus or minus sign for both P and S-wave is reversed (e.g., see Anderson 1989). The Rayleigh surface waves are created by constructive interference of multiply reflected and refracted P- and SV-waves in a multilayered half-space. In a similar manner, the Love surface waves result from constructive interference of multiply reflected and refracted SH-waves in the same medium. The radial anisotropy properties of Rayleigh and Love surface waves are subsequently inherited from the radial anisotropy properties of P-, SV- and SH-waves. Herein, we primarily use the shear-wave splitting to identify the sign of the radial anisotropy. For instance, if the Rayleigh wave velocity for some depth range is greater than the Love wave velocity, then this corresponds to negative anisotropy characterized as  $V_{sv} > V_{sh}$ .

We try to explain the current anisotropy observations in terms of vertical dykes (negative anisotropy) and horizontal sills (positive anisotropy) in the crust. It should also be mentioned that the magma flow within the network of dykes and sills results in the alignment of anisotropic minerals to contribute to the SPO of mineral phases. In case of vertical dykes, the shape ellipsoid of anisotropic minerals is *confined* to be vertically aligned (i.e., vertically standing watermelon), while in case of horizontal sills, the shape ellipsoid is horizontally aligned (i.e., horizontally lying watermelon). The latter case results in azimuthal

anisotropy if the magma flow within the horizontal structure occurs preferentially in certain direction. We actually try to subdue the effect of azimuthal anisotropy, which is not currently modeled, by averaging over many events with different approach azimuths. However, if the horizontal flow is radially outward away from the magma source, then this component of anisotropy contributes positively to our measurement of anisotropy corresponding to the horizontal sill structures by emulating an overall radial anisotropy with vertical slow symmetry axis. The vertical magma flow within the channels of dykes should also contribute constructively to our measurement of radial anisotropy corresponding to the vertical dyke structures.

The surface wave recordings are effectively used to determine the earth velocity structure for which there exist several data analysis techniques (e.g., see Nolet 1990; Ritzwoller and Levshin 1998; Yoshizawa and Kennett 2002, 2004; Lin et al. 2008; Behr et al. 2011; Agius and Lebedev 2014). In these techniques, either the band-pass filtered waveforms or the dispersion curves (mostly fundamental mode) extracted from the waveforms are inverted for the velocity structure. The earthquake source mechanism, velocity structure and recording instrument are three factors to affect the amplitude and phase on a seismogram. The known instrument response is deconvolved from the recordings. A global catalog (e.g., Centroid Moment Tensor—Dziewonski et al. 1981; Ekström et al. 2012) is used to determine the source parameters (i.e., origin time, location, depth, moment tensor). The unknown velocity structure characterizing the earth structure is solved in the inversion process (e.g., Fichtner and Villaseñor 2015).

We employ both source-to-station (also called single station) and source-to-station-pair (also called inter-station or two stations) in our surface wave analysis. Either phase/group velocity curves or three-component waveforms are inverted to determine the shear-wave velocities corresponding to the source–station path. The single-station group velocities are attained by applying the multiple-filter technique—MFT (e.g., see Feng et al. 2004; Cho et al. 2011) in which the surface waves are isolated using multiple narrow-band Gaussian filters centered at certain frequencies and then the frequency-dependent group velocity curves are computed from the group arrival times (e.g., see Dziewonski et al. 1969; Herrmann 1973). The MFT has similar principles to frequency–time analysis—FTAN (Levshin et al. 1992). In the case of single-station phase velocities, one may prefer a roller-coaster-type algorithm (e.g., see Beuclet et al. 2003) where the observed fundamental and higher mode surface waveforms are jointly inverted to attain the path-averaged phase velocity curves. In another approach, for instance, Friederich (2003) has considered inversion of full shear and surface waveforms along with 3-D waveform sensitivity kernels taking into account off-path sensitivity

and Fresnel zones for tomographic image of underground S-velocity structure.

Inter-station approaches effectively removing the source (earthquake) phase effect are frequently applied to obtain phase velocities between two seismic stations located along the same great circle path with the source location (e.g., see Yoshizawa et al. 2010). The phase difference between the seismic stations directly proportional to the wave propagation effect is employed to extract the corresponding phase and group velocity curves. The phase differences may be computed from either the cross-correlogram of two stations (e.g., see Soomro et al. 2016), or an image analysis technique employing both cross-correlation and narrow-band filtering (e.g., see Yao et al. 2005) or slant stacking of multiple-station data in the phase slowness–time intercept ( $p$ – $\tau$ ) plain (e.g., see McMechan and Yedlin 1981). Because of lateral heterogeneity, the incoming wave field of teleseismic surface waves may deviate from the great circle path indicating non-plane waves. The two-plane-wave method (e.g., see Li et al. 2003; Yang and Forsyth 2006) approximates the incoming non-plane wave field of surface waves across an array of seismic stations by an interference of two plane waves each characterized by their own direction, amplitude and phase. The plane wave parameters and phase velocity values at each grid point of two-dimensional (2-D) mesh model are unknown parameters which are iteratively solved. Recently, another method is introduced by Jin and Gaherty (2015) for dense seismic arrays in which the phase differences between adjacent seismic stations are computed from cross-correlations. Frequency-dependent 2-D phase velocity maps follow after inverting the phase variations employing the Eikonal equation. Phase velocity corrections that may be needed due to multipathing are considered solving the surface wave amplitude measurements via the Helmholtz equation.

Herein, we consider both, single-station group velocities and two-station phase and group velocities, for the crust structure analysis. For the group velocities, the multiple-filter technique along with the phase-matched filter (Herrin and Goforth 1977) is employed to extract the corresponding fundamental mode group velocity curves. For the phase and group velocities, we employ a cross-correlation technique to extract the corresponding fundamental mode phase velocity curves between two stations on the same great circle path. The software package “Computer Programs in Seismology” by Herrmann (2002) is utilized for the data analysis of surface waves.

The Turkish plate and the surrounding area have been studied by many researchers using the seismic surface waves (e.g., Cambaz and Karabulut 2010; Karagianni et al. 2005; Karagianni and Papazachos 2007; Salaün et al. 2012; Tezel et al. 2007; Çınar and Alkan 2016), ambient noise (e.g., Warren et al. 2013), receiver function (e.g., Zor et al.

2003; Vanacore et al. 2013; Licciardia et al. 2018), local earthquake tomography (e.g., Polat et al. 2016), body wave tomography (e.g., Piromallo and Morelli 2003), joint inversion (e.g., Gök et al. 2011), magnetotelluric (e.g., Kaya 2010; Unsworth 2010; Tank et al. 2018) and gravity (e.g., Dogru et al. 2018). The widespread geothermal activity (e.g., Ozer et al. 2018) suggests that the crust (with high heat flow  $110 \text{ mW/m}^2$ —İlkışık 1995) is abnormally hot in the region.

We present our results for the radial anisotropic seismic crust structure beneath the Aegean region in southwest Turkey using the Rayleigh and Love fundamental mode surface waves regionally recorded at 142 accelerometer and 20 broadband seismic stations after 231 moderate-to-high-magnitude regional earthquakes ( $M_w > 3.6$ ) occurred within the last decade. The transverse isotropy with the vertical axis of symmetry defines the radial anisotropy (e.g., Visser et al. 2008). The Rayleigh and Love fundamental mode group velocity curves for the paths between the earthquakes and the recording stations are solved using a tomography program to obtain frequency-dependent 2-D group velocity maps. The group velocity curves for each geographic location acquired from the 2-D group velocity maps are inverted to construct the 3-D crust velocity structure beneath the Aegean region. The Rayleigh and Love phase and group velocity curves are jointly inverted for the crust structure corresponding to some paths between pair of stations. The Rayleigh–Love wave discrepancy under the study area is observed. We propose crustal radial anisotropic model structures to explain the observed anisotropy, which should shed some light on the crustal evolution of the Aegean region.

## Regional geology

The Turkish plate bounded by Eurasia to the north, Africa to the south and Arabia to the southeast belongs to the Alpine–Himalayan tectonic evolution. The Mesozoic–Cenozoic closure of Tethyan Ocean resulted various tectonic features (e.g., Izmir–Ankara–Erzincan suture, Kırşehir block, Sakarya continent—see small inset in Fig. 1). In fact, Ketin (1966) defined four major tectonic units in the Turkish plate, i.e., Pontides in northern Turkey, Anatolides to the south of Izmir–Ankara–Erzincan suture in southwest Turkey, Taurus platform and border folds associated with the Arabian collision in southeast Turkey. Following the extensional tectonic regimes, the rifts opened resulting Paleotethys in the Paleozoic–Early Mesozoic and Neotethys in the Mesozoic–Early Tertiary and closed as the megacontinents collided following subduction (e.g., see Şengör 1979a, 1987; Şengör and Yılmaz 1981; Okay and Tüysüz 1999; Stampfli 2000). Such plate movements set side by side many different tectonic blocks (also known as orogenic collage) belonging



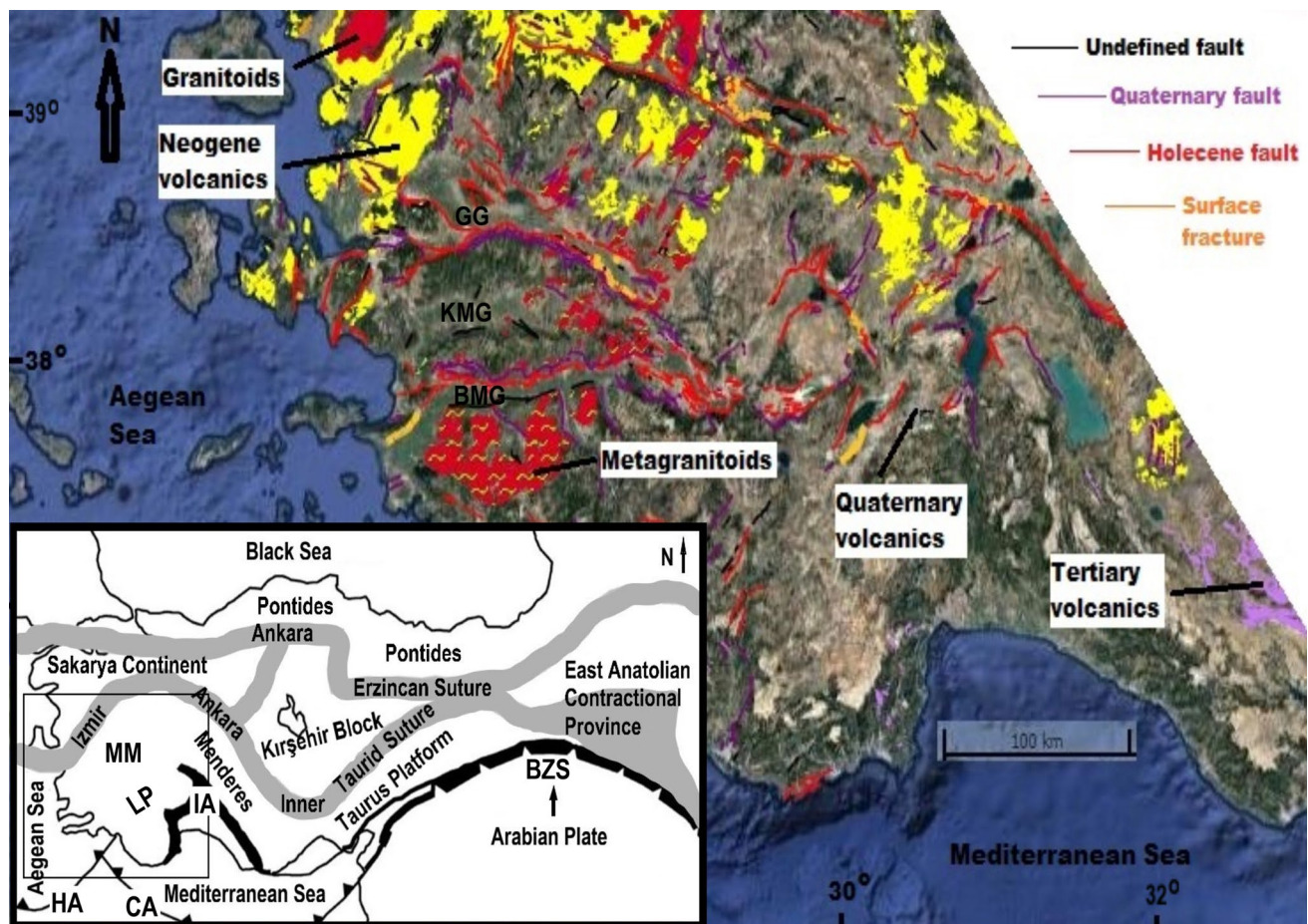


**Fig. 1** Simplified geologic map of the southwest Turkey (adapted from MTA 2002, also see Emre et al. 2013; Akbaş et al. 2017) is shown where GG stands for Gediz Graben, BMG for Büyük Menderes Graben and KMG for Küçük Menderes Graben. Paleotectonic structures in Turkey (adapted from Aydemir 2009 as modified from

Gursoy et al. 1998) are given in the small inset where the study area is marked by a rectangle and MM stands for Menderes Massif, LN for Lycian Nappes, IA for Isparta Angle, HA for Hellenic Arc, CA for Cyprus Arc and BZS for Bitlis–Zagros suture

to Gondwana and Laurasia joined together throughout the Turkish plate and the surrounding region. The suture zones characterized by accretionary wedges attaching to the subducting plates and ophiolites (on-land relics of oceanic crust in mountain belts) are widespread throughout the Turkish plate.

After the closing of the southern Neotethys along the Bitlis–Zagros suture (BZS—SE Turkey), the Paleotectonic period ended 11 Ma ago and then the Neotectonic period started for Turkey, which is governed by the collisional relation between the African and Eurasian plates (e.g., Şengör 1979b). The Arabian plate with plate movement of 18 mm/y (GPS measurements—McClusky et al. 2000) moving northward along the Dead Sea fault creates a compressional tectonic regime resulting crustal thickening and uplift in eastern Turkey. The compressional tectonic regime was replaced by a westward escape of the Turkish plate between Arabian and Eurasian plates along the North

Anatolian Fault (NAF—24 mm/y) and the East Anatolian Fault (EAF—9 mm/y) toward the north–south extending Aegean region characterized as back-arc extensional regime along with exhumation of metamorphic terranes due to trench rollback on the Hellenic arc associated with the African plate (specifically east Mediterranean slab) northward subducting beneath the Anatolian plate (e.g., Le Pichon and Angelier 1979). Mesozoic volcanic activities (calc-alkaline and alkaline) associated with the closure of oceans and the neotectonic events are vast in the Turkish plate. Sedimentary basins unconformably covering the Mesozoic–Lower Tertiary Neotethyan units are mainly filled by Miocene fluvial–lacustrine material (e.g., see Görür et al. 1998).

The geologically complex Aegean region in southwest Turkey takes place in the Aegean north–south extension regime and is limited by the Hellenic subduction zone extending under the Mediterranean Sea in the south, by the Izmir–Ankara Inner Taurid suture zone along with the



Sakarya continent in the north, by the Aegean Sea in the west and the Menderes–Taurus platform in the east (e.g., see Şengör and Yılmaz 1981; Okay et al. 1991; Bonev and Beccaletto 2007; Janssen et al. 2009). The Sakarya (continent) zone consists of Variscan basement of granitic and metamorphic rocks and of the Permo-Triassic Karakaya Complex (Bingöl et al. 1975), which is unconformably overlain by the Jurassic-to-Paleocene sedimentary and volcano-sedimentary units (e.g., Altıner et al. 1991). The intrusion of several granitoids of Late Oligocene–Miocene age attends Late Eocene–Miocene volcanic activity (e.g., Delaloye and Bingöl 2000; Okay and Satır 2000).

The Isparta Angle (IA) is a north-pointing cusp separating the tectonically overlying Lycian Nappes consisting of metasediments, a *mélange* unit and an ophiolitic sequence (e.g., see Rimmelé et al. 2003a) in the east from the Taurus platform in the west (see Fig. 1—small inset). The Fethiye–Burdur fault zone extending in the western side of the Isparta Angle (e.g., see Koçyiğit and Özacar 2003; Özbakır et al. 2017) is a left-lateral strike-slip fault linking subductions along the Hellenic and Cyprus arcs (e.g., Hall et al. 2014a). Waldron (1984) has reported that allochthonous deep-to-shallow-water sedimentary rocks (Mesozoic) and ophiolite pieces make the center of the Isparta Angle, which is surrounded by Mesozoic platform carbonate units. The Menderes Massif exposing exhumed metamorphic rocks with an approximate size of 200 × 100 km is inferred continental extensional detachments since the late Oligocene (e.g., van Hinsbergen 2010). Dilek and Altunkaynak (2010) have reported that the alkaline volcanic rocks in western Turkey get older from Quaternary in the south to Miocene in the north becoming progressively more potassic–ultrapotassic southward. They have also reported subduction-driven crustal-sediment recycling within the upper mantle consistent with the geochemical and isotopic data and decreasing amounts of subduction-derived crustal components in the mantle and an increasing role of asthenospheric input judged by isotopic differences from north to south.

Various seismically active normal fault segments striking in the E–W direction associated with the graben system filled with alluvium deposits tectonically deform the Aegean region in southwest Turkey where the GPS stations are moving at about 30 mm/y to the SW relative to the Eurasian plate (McClusky et al. 2000). The surface geology illustrated in Fig. 2 reveals the complex geology in the study area—many different geological units spanning a time period from Paleozoic to Cenozoic take place side by side. There are several geological units illustrated using a wide color scale, but only 11 of these major geological units are indicated in Fig. 2 (i.e., U1–U11). The core in the Menderes Massif, which is central to our study area, consists of granitic augen gneiss, high-grade schist and minor migmatitic and metavolcanic rocks (e.g., see Hetzel et al. 1995). The unroofing of the core

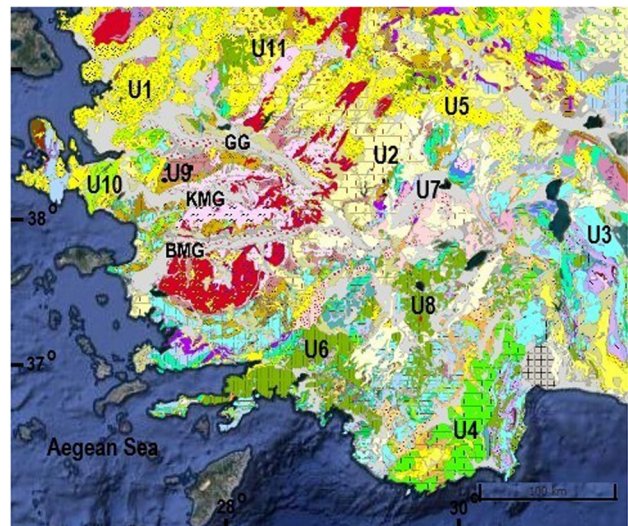


**Fig. 2** Main surface geological units in the study area (adapted from MTA 2002, also see Emre et al. 2013; Akbaş et al. 2017). U1: unallocated volcanics, pyroclastics (Lower–Middle Miocene), U2: lake carbonates (Upper Miocene), U3: neritic limestone (Jura–Cretaceous), U4: neritic limestone (Cretaceous), U5: lake limestone, marn, shale (Miocene), U6: peridotites (Mesozoic), U7: unallocated Quaternary unit, U8: peridotites (Mesozoic), pelagic limestone (Jura–Cretaceous), ophiolitic *mélange* (Upper Cretaceous), dunit (Mesozoic), U9: quartzite, schist (Paleozoic), U10: peridotites (Mesozoic), carbonates (Upper Senonian), neritic limestone (Middle Trias–Cretaceous), basalt, spilite (Upper Cretaceous), U11: dacite, rhyolite, rhyodacite (Middle Miocene), ophiolitic *mélange* (Upper Cretaceous). The magmatic rocks and the graben systems are indicated in Fig. 1

complex created an overlying cover series. The Lower–Middle Miocene unallocated volcanics and pyroclastics (U1) to the northeast change to the Middle Miocene extrusive volcanic rocks of dacite, rhyolite, rhyodacite and the Upper Cretaceous ophiolitic *mélange* (U11) to the east. The Cretaceous neritic limestone unit (U4) makes the southeastern boundary of the Lycian Nappes. The geological units 6 (Mesozoic peridotites) and 8 (Mesozoic peridotites, Jura–Cretaceous pelagic limestone, Upper Cretaceous ophiolitic *mélange* and Upper Senonian carbonates) characterize the border region between the southern Menderes Massif and the Lycian Nappes. The Upper Miocene lake carbonates depicted by U2 cover most of the northeastern end of the central Menderes Massif.

## Surface wave data

The Turkish strong ground motion database currently includes 658 accelerometer stations spread all over the Turkish plate. The stations spread more or less uniformly with 50 km or less distance between adjacent stations (see AFAD 2017). Starting from 2010, this strong ground motion network improved from a few stations to approximately ten

stations per square area of  $1^\circ \times 1^\circ$  and still improves. Three types of instruments are installed in those station locations, i.e., Guralp/CMG5TD:CMG-5T, Geosig/GMPLUS:AC-73 and Sara/ACEBOX:SA10. The Aegean region is now covered by 142 such accelerometer stations from which we acquire three-component accelerogram recordings. The study area also includes 20 broadband stations deployed by Kandilli Observatory and Earthquake Research Institute (KOERI) from which we acquire three-component broadband recordings. We have scanned the regional earthquakes occurred within close proximity of the study area from year 2007 to 2017 and have found 22,153 events with magnitude  $M_w \geq 3.5$  of which 231 events have satisfied our selection criteria based on visual inspection of waveforms. Overall, the selected events have the magnitude range  $3.6 \leq M_w \leq 6.5$  and the focal depth range  $1.5 \leq h \leq 48$  km.

For the broadband recordings, we use the pole–zero files provided by KOERI to remove the instrument responses. The acceleration recordings multiplied by the instrument constant but not corrected for the transfer function are provided by AFAD (Turkish Disaster and Emergency Management Presidency) in units of  $\text{cm/s}^2$ . The instruments Guralp/CMG5TD:CMG-5T (GURALP 2013) and Geosig/GMPLUS:AC-73 (GEOSIG 2012; also personal communication) have amplitude and phase frequency response flat from dc to at least 10 Hz. In this frequency range, these instruments have the frequency response with 0 dB amplitude gain and  $0^\circ$  phase shift. On the other hand, the Sara/ACEBOX:SA10 stations having different transfer functions before and after April 07, 2017, have needed the instrument corrections (SARA 2017; also personal communication) for which we have used the pole–zero files provided by the instrument distributor.

The earthquake parameters (i.e., date, origin time, epicenter location, depth, magnitude) are attained from the AFAD catalog. These parameters are also cross-checked with the European–Mediterranean Seismological Centre (EMSC) and the United States Geological Survey (USGS) catalogs. The source parameter differences between these three catalogs are negligible. We use the ray theoretical backazimuth to rotate the recordings originally in N–S, E–W, vertical system into radial, transverse, vertical system. The accelerograms are converted into velocity recordings by direct integration and are band-pass filtered in the period range 5–20 s before using them in the data analysis. The Love surface wave data are acquired from the transverse component, while the Rayleigh surface wave data are acquired from the vertical component. In order to avoid the effect of complex near-surface geology, the surface wave energy below 5-s period is suppressed. We restrict our surface wave analysis to periods shorter than 20 s since the accelerometers have low sensitivity to surface wave energy at relatively longer periods (e.g., see Cho et al. 2007).

## Dispersion analysis method

### Single-station group velocities

We measure the single-station group velocities by employing the multiple-filter technique (Dziewonski et al. 1969; Herrmann 1973). The observed waveforms are filtered in the frequency domain using the narrow-band Gaussian filter  $\exp[-\alpha(f - f_c)^2/f_c^2]$  where  $f_c$  represents the filter center frequency. Here,  $\alpha$  is the filter parameter trading off resolution between the time and frequency domains. Larger  $\alpha$  provides narrower frequency domain filter, while the corresponding time domain signal gets longer in duration. After some trial-and-error efforts, we set  $\alpha = 12.5$ . Often discontinuous and noisy group velocity curves have resulted with larger  $\alpha$  (e.g.,  $\alpha \geq 25$ ). Smaller  $\alpha$  values (e.g.,  $\alpha \leq 6.25$ ) have resulted group velocity curves continuous and smooth at the expense of suppressing the observational characteristics. We utilize the software developed by Herrmann (2002) for the multiple-filter technique where  $\alpha = 25$  is normally suggested for the source–station distances shorter than 1000 km. In fact, the optimal  $\alpha$  filter parameter depends on the source–station distance. For our single-station group velocities, the source–station distance range is  $\sim 50$ –500 km for which  $\alpha = 12.5$  is adequate. The higher modes, scattering and noise interfere with the observed data where the phase-matched filter (Herrin and Goforth 1977) embedded in the software by Herrmann (2002) helps extract the fundamental mode energy.

The multiple-filter technique is applied to all the earthquakes in our database, and Fig. 3 shows some examples. The resultant Rayleigh fundamental mode group velocities are shown in Fig. 3c, while the Love fundamental mode group velocities are shown in Fig. 3d. The vertical axis indicates the group velocity (km/s), and the horizontal axis is the surface wave period (s). We handpick the observed group velocity values as shown by the white dots on the color-coded group velocity–period profile surfaces where the reliability of the predicted group velocity increases from green-to-yellow-to-red color. The result of phase-matched filter applied to the observed Rayleigh surface waves is shown in Fig. 3a. The observed vertical wave train is given in the upper row, the matched fundamental mode waveform is shown in the middle row, and the residual signal representing the difference between the observed and the matched waveforms is shown in the lower row. The various group arrival times from 2 to 7 km/s are indicated by the vertical bars. The same procedure is applied to the observed Love surface waves in the transverse component as shown in Fig. 3b.

We visually inspect the observed waveforms and rely on the information provided by the procedure summarized in

2017/07/20 22:31:09 27.44 (E°) 36.92 (N°) Depth = 19.4 km Distance = 300 km  $M_w = 6.5$

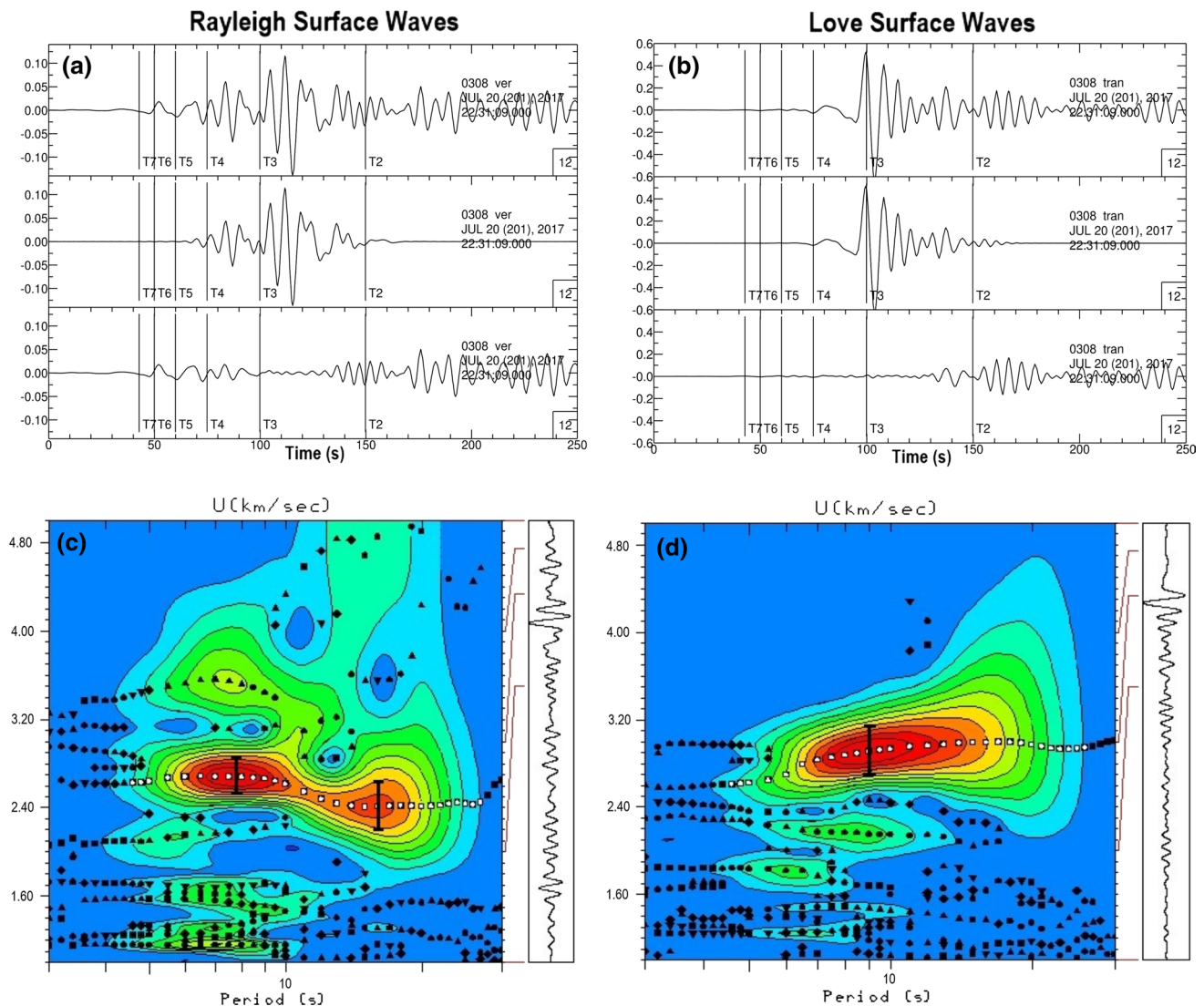


**Fig. 3** Examples of the multiple-filter technique applied to the observed Rayleigh (**a**, **c**) and Love (**b**, **d**) surface waves are shown. The group velocities given by the white spots in **c**, **d** are handpicked. **a**, **b** The results of the phase-matched filter

Fig. 3. As shown by the upper rows in Fig. 3a, b, we first require that the fundamental mode signal is clearly visible on the corresponding component (vertical or transverse). Second, as shown by the middle rows in Fig. 3a, b, the phase-matched signal is required to truly represent the fundamental mode. Third, as shown in Fig. 3c, d, the group velocity dispersion curve is required to be clearly visible on the color-coded group velocity–period profile surfaces. The observed signal is discarded from the database if all these three criteria are not simultaneously satisfied.

Two examples of discarded waveforms that do not satisfy our selection criteria are shown in Fig. 4a (Rayleigh surface waves) and 4b (Love surface waves). The corresponding

earthquake event recorded at 88 km distance at an accelerometer station is mid-size ( $M_w = 4.1$ ) having 10.9 km focal depth. The group velocity–period profile surface for periods under 30 s on the MFT spectrum shows no clear maximum. As shown in Fig. 3c, d, it is not possible to observe a clearly described, continuous group velocity curve.

We predict standard errors in the observed group velocity values from the multiple-filter analysis performed for each source–station path. For the Rayleigh surface waves, the average error is predicted as  $u_R \pm 0.20$  km/s, and for the Love surface waves, the average error is predicted as  $u_L \pm 0.25$  km/s. Here,  $u_R$  and  $u_L$  represent the period-dependent Rayleigh and Love wave group velocities, respectively.



2017/07/21 03:59:01 27.60 (E°) 36.90 (N°) Depth = 10.9 km Distance = 88 km  $M_w = 4.1$

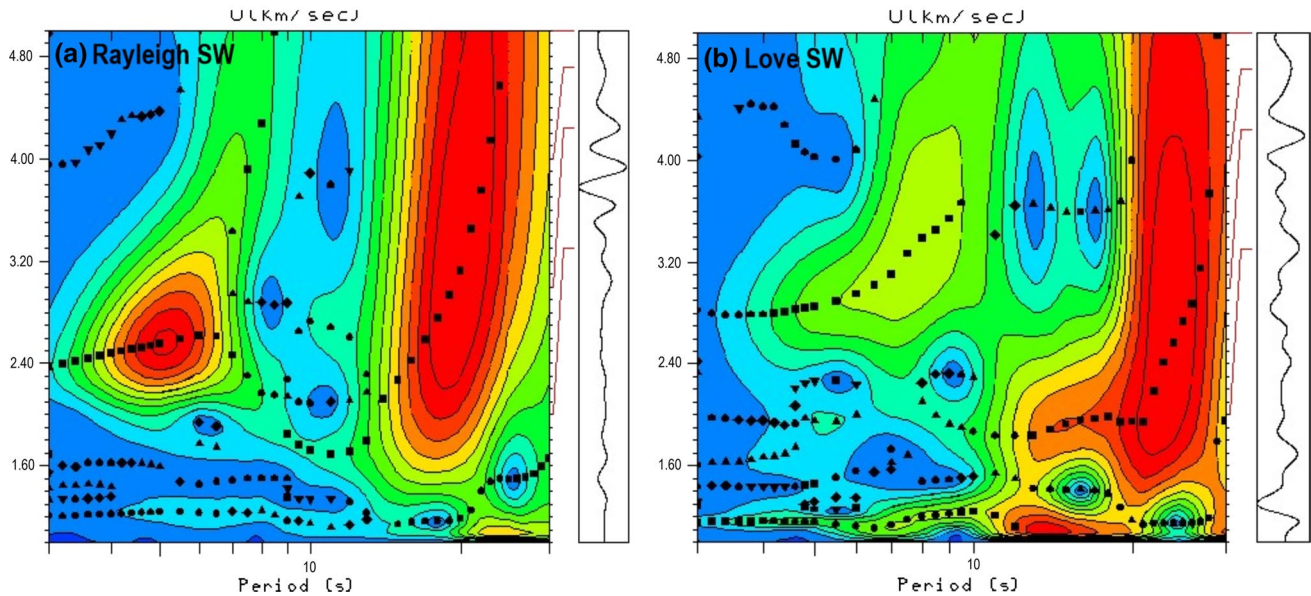


**Fig. 4** Two examples of the multiple-filter technique (MFT) applied to the observed Rayleigh (a) and Love (b) surface waves rejected from the database are shown

The vertical bars in Fig. 3c, d depict some examples of this procedure. The predicted error values for the Rayleigh surface waves are approximately  $\pm 0.16$  km/s at  $\sim 9$ -s period and  $\pm 0.22$  km/s at  $\sim 18$ -s period (Fig. 3c), and for the Love surface waves, it is predicted as  $\pm 0.23$  km/s at  $\sim 9$ -s period (Fig. 3d). Herein, the vertical bars represent the average width of the red color region (most trusted) on the MFT spectrum. The error predictions in travel time are obtained from the group velocity error predictions and are used as priori error information in the tomography program described below.

We continue with the 2-D group velocity tomography after the group velocity curves for each source–station path are determined. The surface wave tomography code provided by Rawlinson and Sambridge (2003) is utilized for this purpose. In this tomography code, 2-D spherical shell coordinates (constant radius, variable latitude and longitude) are used to compute the travel times from point sources to receivers. The models on the spherical shells are defined by a grid of nodes with bi-cubic B-spline interpolation. A grid-based Eikonal solver described as a fast marching method (FMM) is used to compute the source–receiver travel times. A subspace inversion method based on the nonlinear relationship between the velocity and travel time is iteratively used to solve the inverse problem. The source code allows both smoothing and damping regularizations in order to alleviate the effect of the non-uniqueness of the solution. The observed travel times are iteratively matched by the theoretical travel times by optimizing the following objective

function  $\phi(m)$  (e.g., Tarantola and Nercessian 1984; Tarantola 1987; Mottaghi et al. 2013; Dias et al. 2015).

$$\phi(m) = [g(m) - d]^T C_d^{-1} [g(m) - d] + \sigma [m - m_o]^T C_m^{-1} [m - m_o] + \gamma m^T D^T D m, \quad (1)$$

where  $g(m)$  describes the theoretical group travel times,  $d$  the observed group travel times,  $m$  the unknown vector of model parameters,  $m_o$  the initial or reference/background model,  $C_d^{-1}$  the data covariance matrix,  $C_m^{-1}$  the model covariance matrix,  $\sigma$  the damping factor,  $\gamma$  the smoothing factor and  $D$  the smoothness matrix. The fast marching method has found several applications in tomography studies (e.g., see Rawlinson and Sambridge 2004a, b, 2005).

The velocity grid is interpolated using the cubic B-spline velocity patches, which is called the grid dicing in latitude and longitude, to form the continuous velocity field. Therefore, there are the velocity grid with nodes adjusted by the inversion scheme to fit the observed data and the propagation grid with interpolated nodes used by the FMM to solve the Eikonal equation. The propagation grid is always less than the minimum wavelength of the structure defined by the velocity (inversion) grid. In our group velocity tomography, the 2-D spherical shell has the latitude range  $35.3^\circ$ – $39.9^\circ$  and the longitude range  $25.7^\circ$ – $31.6^\circ$  where we locally use 47 grid points on the latitude axis and 60 grid points on the longitude axis. This corresponds to a grid size given by  $0.1^\circ \times 0.1^\circ$  in latitude and longitude, respectively. There are  $47 \times 60 = 2820$  nodes defining the velocity grid. The grid dicing in latitude and longitude is set to  $5 \times 5$ . There are  $[(47 - 1) \times 5 + 1] \times [(60 -$



$1) \times 5 + 1] = 68,376$  nodes defining the propagation grid. The damping factor is set to 0.75, and the smoothing factor is set to 1.50. We set the damping and smoothing factors after some trial-and-error inversions primarily favoring smooth inverted models while still satisfying the data. Here, the damping and smoothing factors work in harmony to prevent the inverted model from diverge too far from the initial model while constraining the smoothness of the resultant model.

## Two-station phase and group velocities

We use the cross-correlation technique (e.g., see Meier et al. 2004; Erduran et al. 2008) for the two-station analysis of surface waves. The two-station method eliminates the source phase by selecting the two stations on the same great circle path with the source location. Some deviation from the great circle path is allowed since the selection condition is not always met exactly (e.g., see Yao et al. 2006). The deviation from the great circle path could be measured by the two angles, i.e., the azimuthal difference of the earthquake to the two stations ( $\theta_1$ ) and the azimuthal difference between the earthquake to the first station and the first station to the second station ( $\theta_2$ ). We set the two angles as  $\theta_1 \leq 1^\circ$  and  $\theta_2 \leq 5^\circ$ . Under these conditions, we compute the inter-station phase velocity as follows:

$$c(\omega) = \frac{\omega r}{\arctan \{ \text{Imag}[\psi(\omega)] / \text{Real}[\psi(\omega)] \} + 2n\pi}, \quad (2)$$

where  $\omega$  is the angular frequency,  $\psi(\omega)$  is the spectral cross-correlation function and  $r$  is the distance between the two stations. The frequency-dependent phase velocity  $c(\omega)$  has  $2n\pi$  uncertainty. In order to obtain the inter-station phase and group velocities, Herrmann (2002) has extended the use of the MFT to include the seismic ambient noise. The MFT is able to simultaneously compute the phase and group velocities using the cross-correlation between the two stations for which a new switch (IG) for the inter-station group velocity is introduced. The phase velocity uncertainty has extra phase term (i.e.,  $2n\pi + \pi/4$ ) since this procedure is originally intended to use the seismic ambient noise recordings. In order to apply this new switch to the earthquake recordings, we correct the observed phase velocities for the extra phase term  $\pi/4$ .

## Two-dimensional group velocity tomography from single-station measurements

For each source–station path, the period-dependent Rayleigh and Love surface wave group velocity dispersion curves are obtained using the MFT. These dispersion curves are rearranged into separate input files with three columns at periods in the range 5–20 s with 1-s interval.

The first column states if there exist data for the respective source–station path, the second column enters the travel time in seconds, and the third column describes the standard error in seconds for the corresponding observation. There are 142 accelerometers and 20 broadband stations recorded 231 earthquake events utilized in the current study. The geographic locations of the sources and receivers are also arranged into two separate input files.

In order to see the effectiveness of the ray-path coverage (source–receiver straight lines) for Rayleigh and Love surface waves propagating across the study area, we have performed synthetic checkerboard resolution tests. The propagating medium has constant velocity (i.e., 2.8 km/s), and a checkerboard pattern with  $\pm 0.8$  km/s perturbation is superimposed. The source–receiver geometry is obtained from the real data. In the checkerboard tests, we utilize the same damping and smoothing factors used in the real data (i.e.,  $\sigma = 0.75$  and  $\gamma = 1.50$ ). Figure 5 shows the result of this test at 10-s period. The input model alternates with a cell size of  $0.4^\circ \times 0.4^\circ$  in Fig. 5a, b, while the cell size is set to  $0.8^\circ \times 0.8^\circ$  in Fig. 5c, d. The ray-path coverage is superimposed on the propagating medium with stars (sources) and triangles (stations). The checkerboard tests for both Rayleigh (Fig. 5a, c) and Love (Fig. 5b, d) surface waves show that when the ray-path density is high, the anomalous structure is satisfactorily recovered. The input model resolution is reduced outside the ray-path distribution and the alternating velocity highs and lows are not well resolved at the edge of the study area. In the following sections, we study those features in the well-resolved region and discard the poorly resolved group velocity maps in the edge region. Similar checkerboard test results are obtained for the other surface wave periods in the range 5–20 s (not shown here).

We invert the observed travel times obtained from 10-s Rayleigh and Love surface wave field recorded by the seismic array in southwest Turkey and show the results in Fig. 6. The background (or initial) velocity structure is assumed constant at 2.6 km/s for Rayleigh surface waves (Fig. 6a) and 3.0 km/s for Love surface waves (Fig. 6b) as indicated by the white color. This constant velocity field is properly perturbed by the tomography source code (e.g., see Rawlinson and Sambridge 2003) to fit the observed travel times in ten iterations. The blue color variations indicate group velocities faster than the assumed background velocity, while those corresponding to the red color variations are slower. The 2-D distribution of group velocities for both Rayleigh and Love surface waves shows that the slow surface wave group velocities are separated from those fast velocities. The fast surface waves travel more inland, while the slow surface waves travel along the coastal range of the Aegean Sea and the eastern Mediterranean Sea. The surface waves crossing the graben

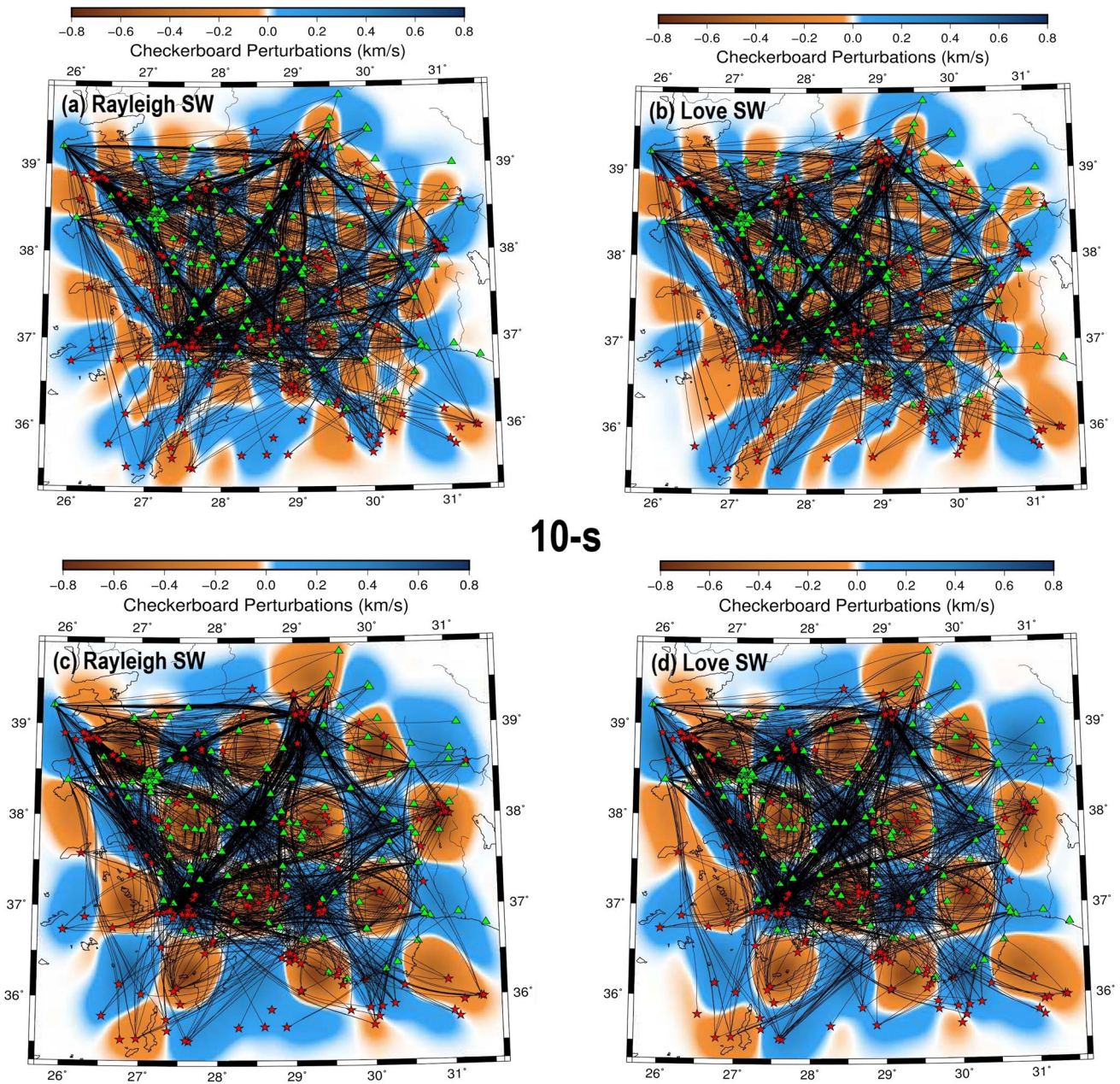


**Fig. 5** Checkerboard tests for the Rayleigh (**a, c**) and Love (**b, d**) surface waves. The perturbation cell size is  $0.4^{\circ} \times 0.4^{\circ}$  in **a, b** and  $0.8^{\circ} \times 0.8^{\circ}$  in **c, d**. The red stars are earthquakes, and the green triangles are recording seismic stations

system filled with alluvium deposits [i.e., Gediz Graben (GG), Büyük Menderes Graben (BMG) and Küçük Menderes Graben (KMG)—see Figs. 1, 2] to the northwest and Isparta Angle (IA) characterized by deep-to-shallow-water sedimentary rocks to the southeast are also slow. On the other hand, the surface waves crossing the Menderes Massif exposing exhumed metamorphic rocks are fast as indicated by the blue-to-dark-blue color.

The fit of the observed travel time data by the solution model is revealed by the frequency histograms in Fig. 6c,

d. The number of rays sampling the study area is 1876 in the case of 10-s Rayleigh surface waves (Fig. 6c), and the number of rays is 1792 in the case of 10-s Love surface waves (Fig. 6d). Figure 6c indicates that 68% of the Rayleigh surface wave travel times are fit with the travel time residuals in the range  $-2.5 \leq T_{\text{res}} \leq 2.5$  s. In the same panel, 15% of the travel times have the residuals in the range  $-7.5 \leq T_{\text{res}} < -2.5$  s and the other 14% have the residuals in the range  $2.5 < T_{\text{res}} \leq 7.5$  s. The remaining 3% are fit with greater travel time residuals (s). Similar percentage travel



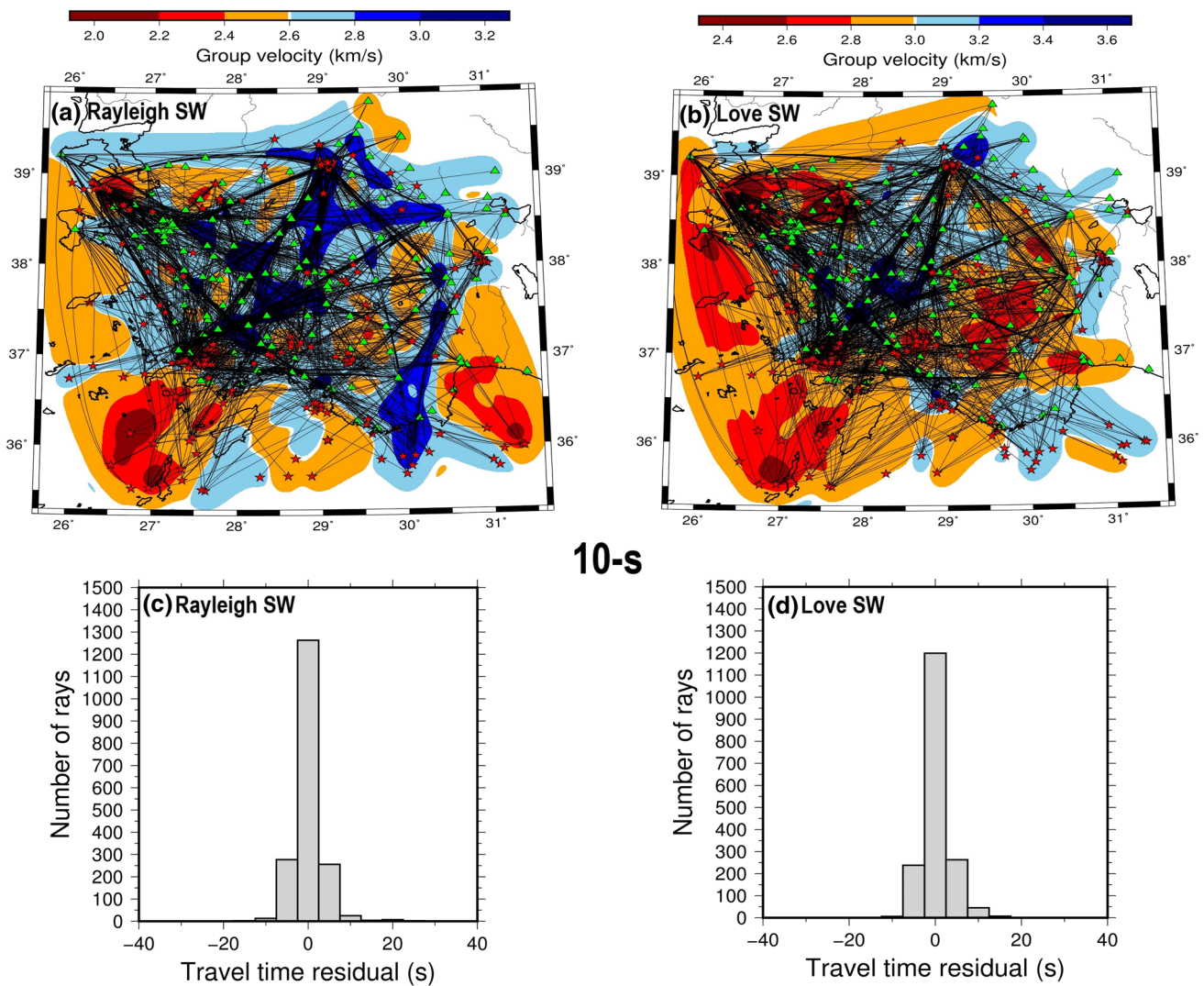


**Fig. 6** 2-D tomographic inversion of the measured Rayleigh (a) and Love (b) wave dispersion curves. The stars are earthquakes and the triangles are seismic stations. The frequency histograms show the travel time misfit of the solution model for the Rayleigh (c) and Love (d) surface waves

time residuals are obtained for the 10-s Love surface wave travel times as shown in Fig. 6d. Smaller travel time residuals are desired so that majority of the observational data are explained by the solution model. However, the observational data are mostly saturated by various kind noises that we try to overcome in the data analysis.

First, systematic errors in the group velocity measurements may result from mislocating the earthquake and error in the determination of earthquake origin time. In order to minimize the mislocation and origin time errors, we utilize three different earthquake catalogs (i.e., AFAD, EMSC and USGS). Second, the use of a single seismogram may not eliminate the effect of the source phase on the group velocity measurement, which is theoretically affected by the source radiation pattern. But this effect is mostly important for periods greater than 75 s (e.g., see Levshin et al. 1999). Third, a

spectra hole near a period due to the earthquake focal mechanism may cause skewness in the group velocity measurements (e.g., see Çakır and Erduran 2001). We restrict our group velocity measurement below the skewness period. Fourth, the ray paths currently cross different geological structures with somewhat sharp boundaries (e.g., Menderes Massif, Isparta Angle, graben systems, Izmir–Ankara suture) that may result off-great circle arrivals due to the multipathing, scattering and refraction (e.g., see Yao et al. 2006). Specifically these four mentioned noise sources have resulted in some poorly modeled travel time residuals.

We determine the averages of the observed Rayleigh and Love surface wave group velocities to utilize them as period-dependent background (or propagating medium) velocities in the 2-D tomographic inversions. The result of the corresponding procedure is shown in Fig. 7. These computed

average group velocities at each period along with the standard deviations (vertical bars) are depicted in turquoise color, while the individual observed group velocity curves are depicted in purple color. In the group velocity tomographic inversions, we utilize the period-dependent group velocity values depicted in green color, which closely follow the averages, as the background velocities. The latter procedure helps us choose the initial model close to the global minima avoiding the inversion procedure getting trapped in local minima.

As shown in Fig. 6, we perform similar group velocity tomographic inversions for the other surface wave periods in the range 5–20 (not shown here). The fast and slow regions in the 2-D distribution of group velocities persist across the range of other surface wave periods. The number of rays and the azimuthal coverage decrease as the surface wave period increases. For instance, the number of rays at 20-s period decreases to approximately one-half of 10-s surface waves. But it is still proper to tomographically solve the 2-D distribution of both Rayleigh and Love surface wave group velocities at longer periods. Location-dependent group velocities on a  $0.1^\circ \times 0.1^\circ$ -sized grid at periods from 5 to 20 s are eventually attained. The corresponding grid locations are shown as white dots in Fig. 8. The best-fitting shear velocity model for  $V_{sv}$  (vertically polarized) and  $V_{sh}$  (horizontally polarized) velocity structure of the crust is obtained by applying the damped least-squares inversion, which is employed point by point for the dispersion curves at all grid points. The crust is modeled as a multilayered structure above the half-space at 40 km depth. As the depth sensitivities of phase and group

velocities (e.g., see Moschetti et al. 2007; Lin et al. 2008) indicate, the current longest period (i.e., 20 s) surface waves resolve the target depth at 40 km. However, the Moho discontinuity and the associated velocity jump are not resolved well. The surface wave periods longer than 35 s are required

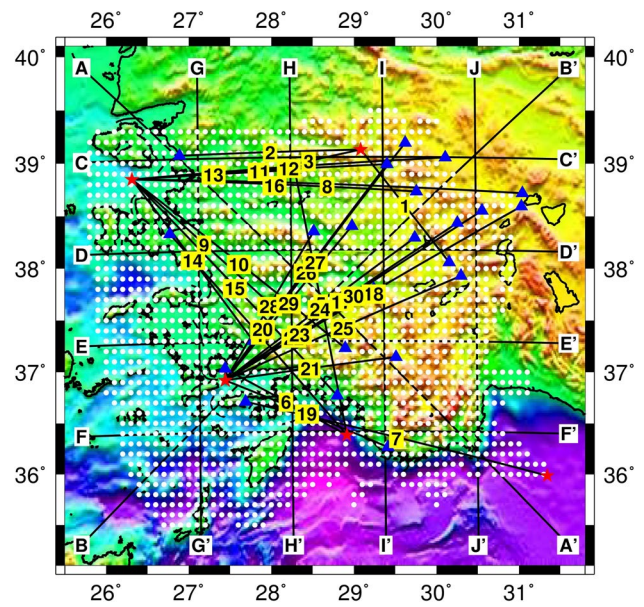
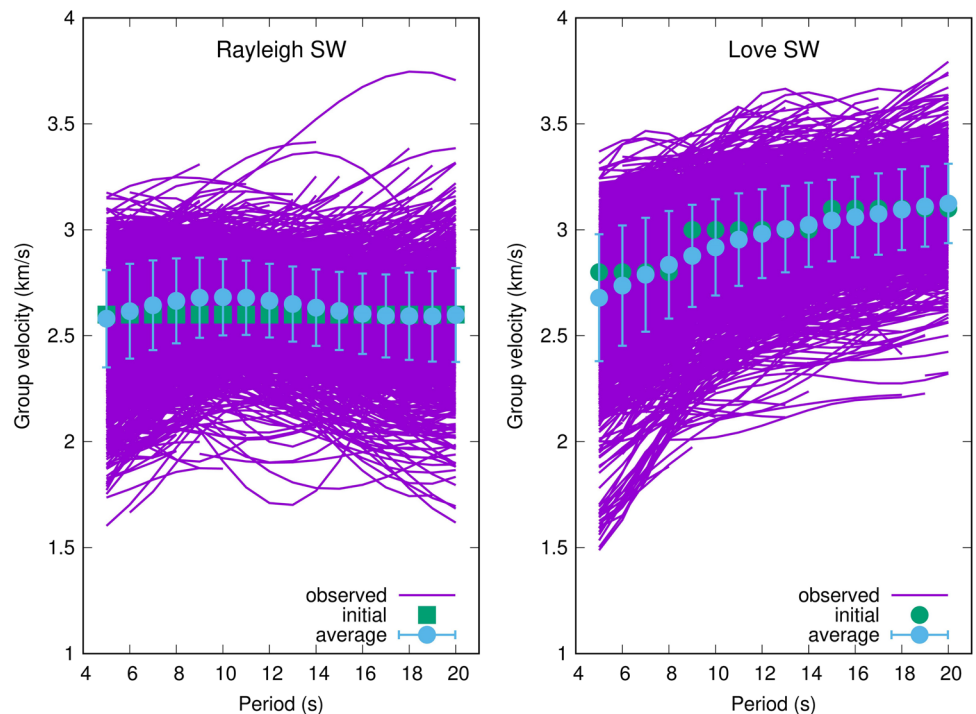


**Fig. 8** The locations of retrieved group velocity curves (white dots) and the ten selected profiles (A–A', B–B', C–C', D–D', E–E', F–F', G–G', H–H', I–I', J–J') are shown. Also shown are 30 source–station paths depicted by numbers on yellow background

**Fig. 7** The observed Rayleigh (left) and Love (right) group velocity curves are shown along with the period-dependent averages and standard deviations. The green color values are used as initial values in the tomographic inversions





to better model the S-velocity increases at the Moho (e.g., see Lebedev et al. 2013).

We serve some examples of group velocity fits between the observed and the inverted group velocity curves obtained for some selected source–station paths. These paths selected to show both Rayleigh and Love group velocity curves are indicated by the numbers in range 1–30 written on yellow background in Fig. 8. These examples aim to show the effect of the initial model (see Fig. 7) and the damping ( $\sigma = 0.75$ ) and smoothing ( $\gamma = 1.50$ ) parameters on the 2-D group velocity tomography results. Accounting for both latitude and longitude directions along with a second derivative, the smoothing factor controls how much deviations between 2-D mesh points are allowed. The damping factor manages how much the group velocity values at the 2-D mesh points diverge from the initial model. The MFT analysis described above is used to procure the observed Rayleigh (green color) and Love (purple color) group velocity curves illustrated along with the error bounds (vertical bars). The ray tracing on the 2-D group velocities (white dots in Fig. 8) associated with each source–station path is used to attain the inverted Rayleigh (orange color) and Love (cyan color) group velocity curves illustrated with thin solid lines. The observed group velocity curves are satisfactorily inverted by the 2-D tomographic group velocities as displayed by the group velocity fits in Fig. 9 where the majority of the group velocity fits occurs within the error bounds.

For both Rayleigh and Love surface waves, some group velocity fits (e.g., source–station paths 1, 3 and 13) show poor fits. The observed velocities are either slower or faster than the inverted ones. This might be due to the error in the determination of origin times and locations of the earthquake events. Most likely, due to the error in the MFT analysis of noise saturated spectral amplitudes at corresponding periods some group velocity fits (e.g., source–station paths 10, 14, 20, 21 and 25) show poor fits for part of the group velocity spectrum. For some source–station paths (e.g., 2, 20, 21, 22 and 23), especially the Rayleigh inverted group velocities show irregular spectrum characterized as jumps in the group velocity curves. This is most likely due to the change in ray-path density from one region to another across the range of surface wave periods. Both smaller and larger damping and smoothing parameters than the current ones (i.e.,  $\sigma = 0.75$  and  $\gamma = 1.50$ ) have been tried in the inversion, but the group velocity fits shown in Fig. 9 have not improved.

## Synthetic tests

There are some issues that we need to discuss before we continue with the inversion of the actual dispersion data. The noise issue mentioned above may lead us to incorrect identification of the radial anisotropy. The different resolution

power of SV- and SH-waves and model simplification may also lead us to somewhat incorrect solution of the shear-wave velocities. Some theoretical isotropic inversions summarized in the following are performed to help us develop inversion strategies for the actual data. The crust model shown in Fig. 10 (purple color in the middle row) is isotropic having seven layers over the half-space at 30 km depth. The uppermost crust is made of two low-velocity layers. The seismic velocities in the upper-to-middle crust depths have a modest gradient represented by three layers. The Moho discontinuity with 4.6 km/s S-velocity is represented by a two-layer gradual velocity increase. We have computed three-component synthetic seismograms at two receiver locations with the same azimuth utilizing the source code by Herrmann (2002). The first receiver is located at  $1^\circ$  distance and the second one at  $2^\circ$  distance. The point double-couple source parameters (i.e., depth, strike, rake, dip and station azimuth) are  $10 \text{ km}/90^\circ/45^\circ/60^\circ/45^\circ$ , respectively.

We extract the synthetic two-station MFT group and phase velocities by applying the same data processing techniques applied to the actual recordings. These dispersion data are then inverted separately for the Rayleigh and Love surface waves to retrieve the crust S-velocity structure. We first invert the Rayleigh surface waves for which the initial model is selected as a half-space with constant S-velocity at 4.5 km/s. In Fig. 10, the inverted SV-wave crust structure ( $V_{sv}$ ) is depicted using a blue color line. Secondly, we invert the Love surface waves for which the resulting SV-wave velocity–depth profile is employed as the initial model. In Fig. 10, the inverted SH-wave velocity–depth profile ( $V_{sh}$ ) is shown using a red color line. We emulate the noise conditions by using the noise-added group velocities ( $u$ ) in the inversion along with the relation  $u = \bar{u} + \sigma(r - 0.5)$  where  $\bar{u}$  stands for the unperturbed MFT Rayleigh and Love group velocity curves,  $r(0 \leq r < 1)$  is a random number and  $\sigma$  defines the error bound for the surface wave group velocities. Three different values (i.e.,  $\sigma = 0.1 \text{ km/s}$ ,  $\sigma = 0.2 \text{ km/s}$  and  $\sigma = 0.3 \text{ km/s}$ ) are employed to characterize the error bound.

The upper row in Fig. 10 shows randomly contaminated Rayleigh (green color squares) and Love (purple color circles) surface wave data representing the observed group velocities. The inverted Rayleigh (blue color line) and Love (red color line) surface wave dispersion curves are shown superimposed on the contaminated group velocity data. We invert for only the shear-wave velocities. The compressional-wave velocities are computed by setting Poisson's ratio to 0.25 in the  $V_p/V_s$  ratio. The Nafe–Drake relation (e.g., Brocher 2005) is utilized to compute the density from the compressional-wave velocity. The wave propagation medium is represented by 20 thin layers each with 2 km thickness. The same parametrization is used for the inversion of the observed dispersion curves.

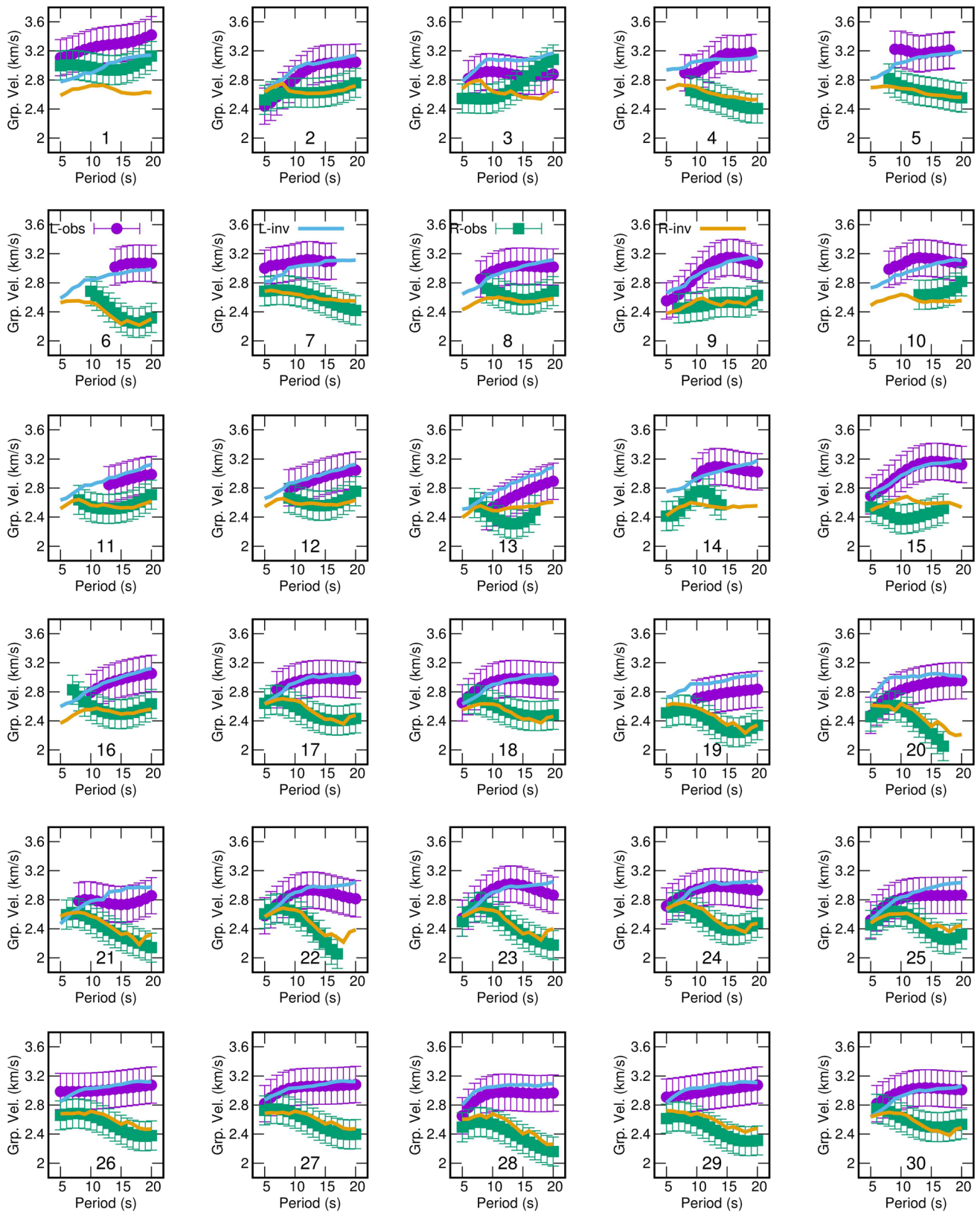


**Fig. 9** The group velocity fits obtained for thirty source-station paths selected to test the validity of the 2-D group velocity tomography results are shown. R(L)-obs and R(L)-inv stand for Rayleigh (Love) surface wave observed and inverted group velocity curves

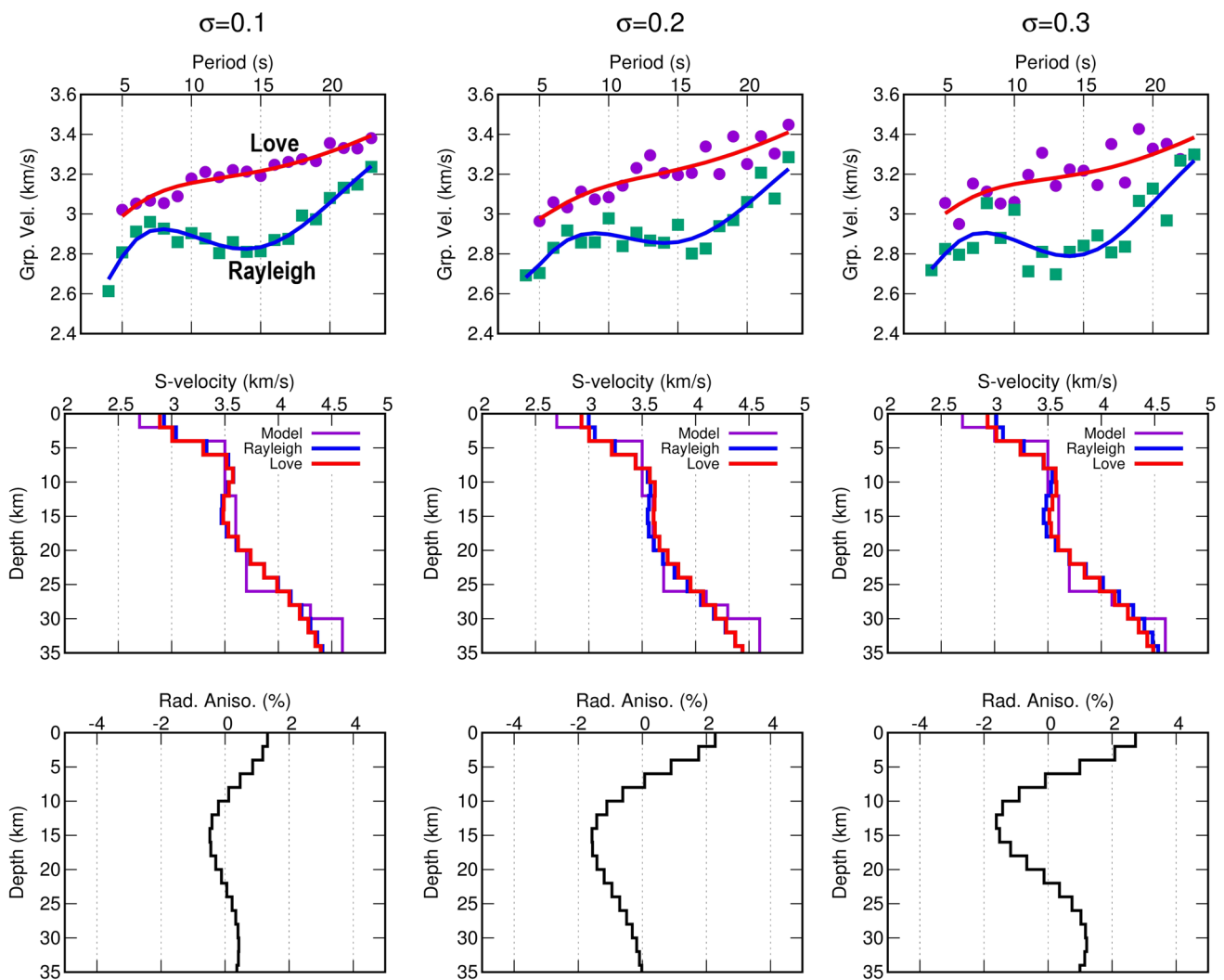


**Fig. 10** The observed (squares and circles) and the inverted group velocities (upper row), the model structure and the inverted structures (middle row) and the radial anisotropy (lower row) are shown

A nonlinear relationship (e.g., see Haskell 1953) is employed to compute the group and phase velocity of a model structure. Linearization procedure is used which leads to a linear system given by  $A\vec{x} = \vec{b}$  where  $A$  is the system matrix,  $\vec{b}$  the observed data vector and  $\vec{x}$  update for the unknown model structure vector. By introducing a new variable  $\vec{y} = W\vec{x}$ , the following equation is iteratively applied in a manner similar to steepest descent to solve the unknown model structure using the singular value decomposition of the system matrix, i.e.,  $A_{n \times m} W_{m \times m}^{-1} = U_{n \times k} S_{k \times k} V_{k \times m}^T$  where the columns of orthogonal matrix  $U$  are the left singular vectors, the diagonal matrix  $S$  has the singular values and the rows of orthogonal matrix  $V^T$  are the right singular vectors (e.g., see Herrmann 2002).

$$\vec{x} = W^{-1}V(S^2 + \lambda^2 I)^{-1} S U^T \vec{b}. \tag{3}$$

Herein,  $x_{i+1} = x_i + x$  is the updated model structure,  $\lambda$  the damping factor and  $W$  the first difference matrix used to minimize the difference between adjacent model values. The default value of  $\lambda^2$  is set to 1.0 in the source code, but we use a larger damping factor set to  $\lambda^2 = 3.0$  because of noise effect. The linearized inversion is solved in 24 iterations. Four different  $\lambda^2$  values changing as 10.0, 7.5, 5.0 and 3.0 each with six iterations are applied in a decreasing order. This strategy provides better convergence to the global minima.

The structural features in the theoretical model are satisfactorily resolved as shown by the isotropic inversions in Fig. 10 (middle row). The model simplification and the limited band width of the surface waves (i.e., 5–20-s period band) cause some unresolved features such as depth to and velocity jumps at the discontinuities. The change in radial anisotropy with depth is shown in the lower row. The



following parameter computed from the inverted  $V_{sv}$  and  $V_{sh}$  velocities (e.g., see Shapiro and Ritzwoller 2002) is utilized to quantify the strength of the radial anisotropy.

$$\eta = \frac{(V_{sh} - V_{sv})}{V_s} \dots V_s^2 = \frac{(2V_{sv}^2 + V_{sh}^2)}{3}, \quad (4)$$

where the Voigt isotropic average shear-wave velocity is the velocity  $V_s$ . The radial anisotropy ( $\eta$ ) is positive when  $V_{sh} > V_{sv}$  and is negative when  $V_{sv} > V_{sh}$ . The theoretical model is isotropic. The corresponding radial anisotropy should be ideally zero, but instead shows a change with depth in the range  $\pm 3\%$ , which is mainly due to the fact that the Rayleigh and Love surface waves have different resolving powers with depth (e.g., see Fu and Li 2015; Harmon and Rychert 2015). The Rayleigh and Love surface waves differently resolve those velocity jumps and discontinuity depths. Therefore, the radial anisotropy associated with the difference between  $V_{sh}$  and  $V_{sv}$  in Eq. (4) shows undesirable fluctuations with depth. Somewhat different radial anisotropy fluctuations with depth results when different initial models other than the current 4.5 km/s half-space model are used (not shown here). We first invert the Rayleigh surface waves and then use the result as initial model for the Love surface wave inversion to alleviate this unexpected fluctuation. Therefore, we favor an isotropic inversion around the Rayleigh surface wave solution, which significantly mitigates the mentioned fluctuation, but still leaves some fluctuation with depth around  $\pm 1\text{--}2\%$  radial anisotropy. This falsely comes into play due largely to different resolution powers of SH- and SV-waves and model simplification. We bear this point in mind to interpret the actual data inversions.

## Cross sections

The crust structure in the Aegean region overriding the subducting African plate is continuously deformed by active tectonic forces producing widespread seismicity as shown in Fig. 11 where the epicenters of earthquakes (AFAD catalog) are denoted by the red color stars. The black color circles bring out the epicenter locations taking place close to profiles A–A' and B–B'. The considered events with magnitude range  $3.5 \leq M_w \leq 6.5$  are crustal range events with focal depth  $\leq 40$  km. The timespan covers a 28-year period from 1990 to 2018. The region undergoing extensional tectonics mainly governed by the trench rollback on the Hellenic arc comprises a complex set of tectonic structures of differing geological age amalgamated side by side, e.g., graben system, metamorphic core complex, strike-slip fault, volcanism, thrust and suture zones. These prominent surface geological units (see Figs. 1, 2) are indicated in Fig. 11. By providing additional information regarding the seismicity related to the subduction process, the spatial distribution of earthquake

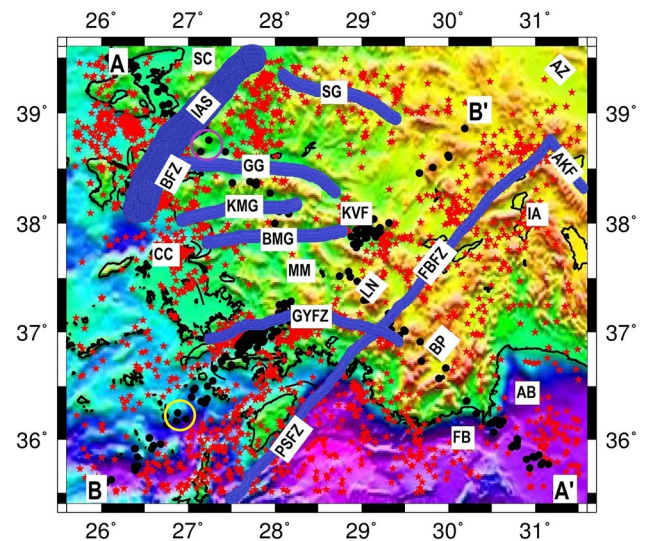


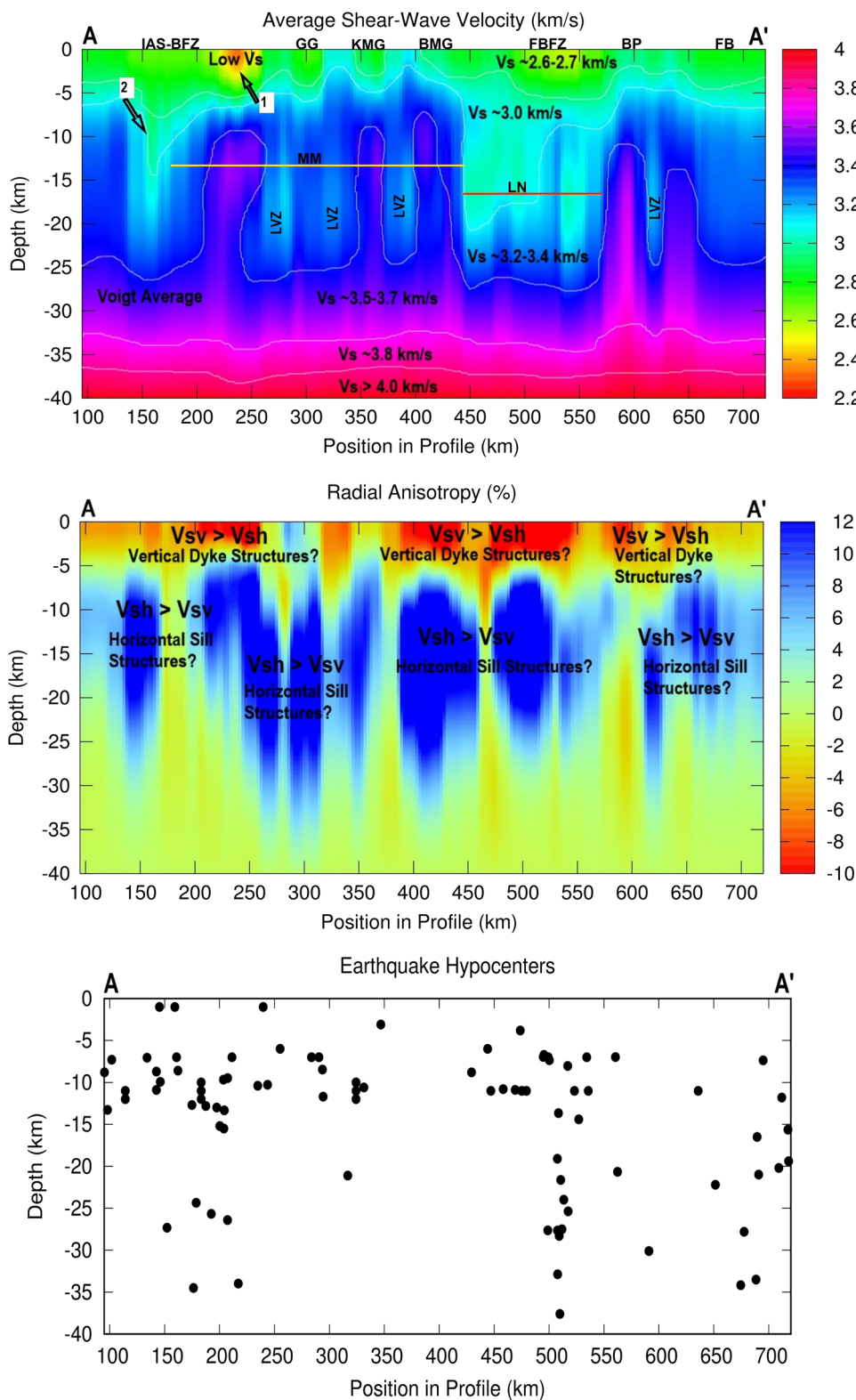
**Fig. 11** Seismicity in the study area is shown with red stars. Seismicity shown with black circles is those taking place along profiles A–A' and B–B' indicated in Fig. 8. Main tectonic units are also marked using abbreviations: AB: Antalya Basin, AKF: Aksu-Kyrenia Fault, AZ: Afyon Zone, BFZ: Bornova Flysch Zone, BMG: Büyük Menderes Graben, BP: Beydağları Platform, CC: Cycladic Complex, FB: Finike Basin, FBFZ: Fethiye–Burdur Fault Zone, GG: Gediz Graben, GYFZ: Gökova–Yeşilüzümlü Fault Zone, IA: Isparta Angle, IAS: Izmir–Ankara suture, KVF: Kula Volcanic Field, LN: Lycian Nappes, MM: Menderes Massif, PSFZ: Pliny-Strabo Fault Zone, SC: Sakarya Continent, SG: Simav Graben

hypocenters helps us make better interpretation of our crustal anisotropy patterns.

We select ten profiles (see Fig. 8) to study the inverted shear-wave velocities beneath the Aegean region in southwest Turkey as cross sections where the observed group velocity curves are inverted following the strategy described in Fig. 10. The crust structure in the NW–SE direction is displayed in the first cross section A–A' (see Fig. 12). The vertically polarized SV-wave velocities ( $V_{sv}$ ) are obtained from inverting the observed Rayleigh surface wave group velocities. The horizontally polarized SH-wave velocities ( $V_{sh}$ ) are attained from inverting the observed Love surface wave group velocities. The Voigt isotropic average shear-wave velocities ( $V_s$ ) computed from Eq. (4) are shown in Fig. 12 (upper panel). The crust structure beneath profile A–A' is represented by mainly five depth sections over the half-space using the color-coded velocity variations with depth. The third and fourth depth sections from the top are the most heterogeneous showing significant lateral variation where the higher-velocity lower crust material appears to intrude the upper-to-middle crust depths at several locations. The crust structure beneath profile A–A' is radially anisotropic as indicated by the pronounced differences between the inverted SV and SH velocities at some depth ranges, i.e., Rayleigh and Love surface wave discrepancy is evident.



**Fig. 12** The inverted Voigt average S-wave (upper panel) velocities beneath profile A–A' are shown. The corresponding radial anisotropy is given in the middle panel. The lower panel shows the regional earthquake hypocenters



Using a simple isotropic model, the Rayleigh and Love surface wave dispersion cannot be fit simultaneously.

The radial anisotropic structures with pronounced anisotropy rates beneath profile A–A' are illustrated in Fig. 12

(middle panel) where there are significant anomalies with positive ( $V_{sh} > V_{sv}$ ) and negative ( $V_{sv} > V_{sh}$ ) radial anisotropy. The positive anomalies ( $\eta \sim 12\%$ ) take place in the middle-to-lower crust, while these negative anomalies

( $\eta \sim -10\%$ ) exist in the upper crust. Due to the magmatic intrusions above the northward-dipping Hellenic subduction zone, the intrusion of several granitoids likely causes these radial anisotropic structures. In the middle-to-lower crust, consecutive thin layers with relatively high and low velocities (i.e., sill units) result in the positive anomaly. These negative anomalies in the upper crust above the sill units are likely result of vertically ascending dyke structures. The Rayleigh surface waves are made of constructive interference of P- and SV-waves, while the Love surface waves result from constructive interference of SH-waves. In the case of positive radial anisotropy, horizontally propagating P- and SH-waves are faster and SV-waves are slower, while vertically propagating P- and S-waves are slower. In the case of negative radial anisotropy, horizontally propagating P- and SH-waves are slower and SV-waves are faster, while vertically propagating P- and S-waves are faster. In Fig. 12 (middle panel), these positive anomalies characterized as  $V_{sh} > V_{sv}$  are capped by the negative anomalies (i.e.,  $V_{sv} > V_{sh}$ ). Both negative and positive anisotropic anomaly structures are horizontally variable where the continuity is interrupted by relatively weaker anisotropy values at some depth ranges. Contrary to the general trend, the negative anomaly in the upper crust is replaced by a positive anomaly around 280 km distance.

Four general steps of partial melting, melt separation, magma ascent and granite emplacement are involved in the granite generation (e.g., see Petford et al. 1997; Vigneresse et al. 1999). The trapped igneous rocks intruding into horizontal layers in the hosting crustal rock at shallower depths constitute the sill structures, which are important part of granite generation and are supplied with magma through the dyke structures. The principal stress tensor has the form  $\sigma_1 > \sigma_2 > \sigma_3$ . The arising magma is deposited into the plane of maximum ( $\sigma_1$ ) and intermediate ( $\sigma_2$ ) principal stress components perpendicular to the least principal stress component ( $\sigma_3$ ), which is initially a vertical plane. By pushing out on the walls of the host rock (i.e., lower crust), vertically intruding dike increases the horizontal least principal stress, which is dilation, thus causing reorganization of the local stress field by increasing  $\sigma_3$  and  $\sigma_2$ . The local least principal stress becomes vertical favoring horizontal intrusions after subsequent intrusions. The opening plane switches from vertical to horizontal constituting a change from vertically oriented, dike-shaped intrusions to sub-horizontal laccoliths when the lithostatic load is overcome. The vertical maximum principal stress in the overlying brittle layer (i.e., upper crust) that favors extension by either dyke intrusion or normal faulting is increased by the enlarging horizontal sill unit (e.g., Parsons et al. 1992; Burchardt 2008). The crustal radial anisotropic structures manifested by magmatic intrusions are effectively studied by using the surface wave

dispersion (e.g., see Jaxybulatov et al. 2014; Mordret et al. 2015; Spica et al. 2017).

In order to place our results into the geological context, we overlay the positions of the main surface geological units (see Fig. 11) onto the shear-wave cross section. The inverted average S-wave velocities beneath profile A–A' (upper panel in Fig. 12) show that the Menderes Massif—MM (e.g., Okay 2008), which is the horizontal range indicated by the yellow line, is characterized by faster crustal velocities ( $\sim 3.5$  km/s) reaching 25 km deep and extending on  $\sim 250$  km long, whereas in the Lycian Nappes—LN (e.g., Rimmelé et al. 2003a), which is the horizontal range indicated by the red line, the seismic waves are slower ( $\sim 3.0$  km/s). The uppermost crustal depth range highly deformed by the Fethiye–Burdur Fault Zone—FBFZ (e.g., Hall et al. 2014b) shows relatively slower shear waves around 2.5 km/s. The hypocentral distribution of the earthquakes occurring within the 40-km-wide zone underneath the FBFZ (lower panel) correlates with the crustal expression of the eastern limit of the asthenospheric window (Karaoğlu and Helvacı 2014; Gessner et al. 2017) above the Aegean and Cyprus slab fragments (Biryol et al. 2011; Gessner et al. 2013; Govers and Fichtner 2016; Portner et al. 2018). The FBFZ is connected to the left-lateral Rhodes Transform Fault farther to the southwest along which the Hellenic arc is offset ( $\sim 270$  km) southwestward from the Cyprus arc (e.g., see Yolsal-Çevikbilen et al. 2014). A similar transformation occurs along the right-lateral Cephalonia Transform Fault where a transition ( $\sim 80$  km) between the northern and southern segments of the Western Hellenic Subduction Zone takes place (e.g., Pearce et al. 2012).

In the uppermost crust of Menderes Massif, the Aegean graben system (e.g., Purvis and Robertson 2005) consisting of Gediz Graben (GG), Küçük Menderes Graben (KMG) and Büyük Menderes Graben (BMG) filled by Neogene–recent sediments is clearly visible where the uppermost crustal shear-wave velocity is slower around 2.7 km/s characterizing the sediment fill. Note that under each graben structure the deeper crustal velocities are relatively faster ( $\sim 3.5$  km/s) while there exists a low-velocity zone (vertically aligned LVZ signs) with  $\sim 3.1$  km/s in the middle crust ( $\sim 12$ – $24$  km) to the left of each graben structure (i.e., to northwest). Under the Beydağları Platform—BP (e.g., Arslan et al. 2013), the crustal velocities are abnormally high  $\sim 3.7$  km/s and there exists another middle crust range low-velocity zone (vertically aligned LVZ sign) to the right (i.e., to southeast). The Finike Basin—FB (e.g., Hall et al. 2014b) with  $\sim 5$  km thickness is characterized by slower seismic velocities  $\sim 2.7$  km/s.

The two arrows in Fig. 12 show two depth sections with low-velocity anomalies. The first arrow indicates a low-velocity pocket (LVP) with  $\sim 2.3$  km/s velocity of which the surface projection is displayed by the purple circle in Fig. 11. The second low-velocity anomaly with much less

pronounced contrast (i.e.,  $\sim 0.4$  km/s) is deeper ( $\sim 6$ – $8$  km depth) and is located  $\sim 70$  km away from the first one to the northwest lying underneath the Izmir–Ankara suture—IAS and Bornova Flysch zone—BFZ (e.g., Okay et al. 2012) (see Figs. 1, 11). The low-velocity material (i.e., submarine sliding or olistostromes) filling the BFZ around 190 km distance extends down to  $\sim 7$  km depth, and the radial anisotropy under the BFZ is rather weak. An accretionary prism is a wedge-shaped body of faulted and folded material added to a continental margin in a subaqueous thrust zone. The low-velocity material representing an accretionary prism around 160 km distance under the IAS, which marks a collisional front, extends deeper down to  $\sim 15$  km depth. Farther northwest under the IAS, the high-velocity material around 130 km distance correlates with the ophiolites (e.g., van Hinsbergen 2010), which formed during the collision of the Sakarya and Tauride–Anatolide continental blocks in the late Paleocene (e.g., Dilek and Altunkaynak 2010). The Sakarya continental rocks and the ophiolitic units of the IAS are intruded by a series of east–west trending Eocene and Oligo-Miocene granitoid plutons (e.g., Altunkaynak 2007). The radial anisotropy under the IAS around 160 km distance is positive, which we think that it corresponds to a horizontal sill structure related to the (suture zone) granitoid plutons with perhaps frozen-in horizontal flow. The suture representing the boundaries of former lithospheric plates is ideally displayed as a fault zone in the brittle upper crust and a ductile shear zone in the lower crust extending down to the lithospheric mantle (e.g., Okay and Tüysüz 1999). The hypocentral distribution of the earthquakes occurring within the 35-km-wide zone characterizes the latter fault zone under the IAS.

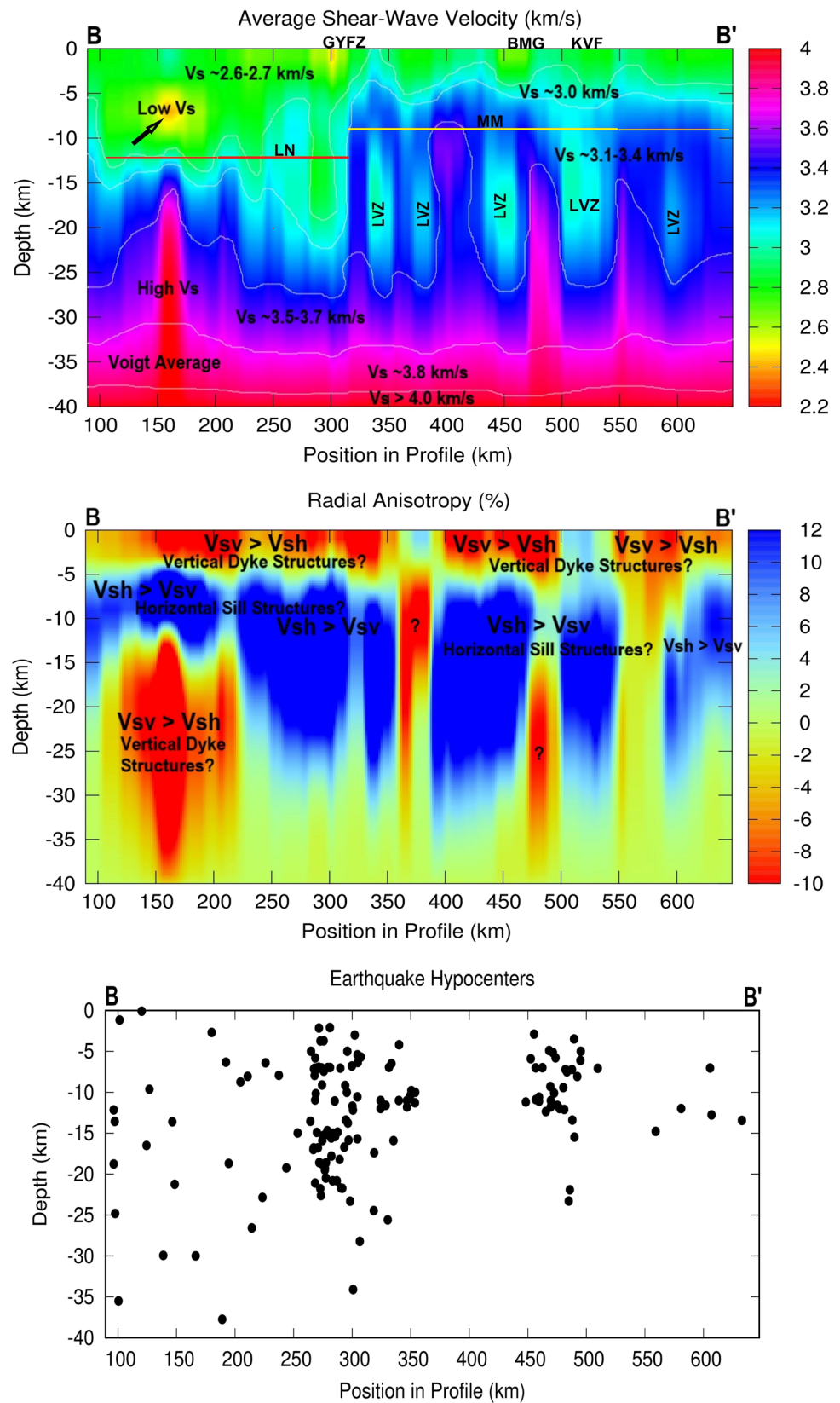
The high-temperature conditions due to the magmatism may lower the P- and S-wave velocities by reducing the rock strength and also may cause partial melting in the crust (e.g., see Lees 2007). Therefore, it is reasonable to suggest that, in our shear-wave velocity maps, the high-velocity anomalies correspond to magmatic intrusions already cooled, while those low-velocity anomalies show still cooling depth sections. The low-velocity pocket (LVP) in the first three kilometers indicated by the first arrow in Fig. 12 reveals the negative radial anisotropy (middle panel), which corresponds to still cooling vertical dyke structure with vertical flow. This LVP underlain by intrusive rocks with high velocity (i.e., already cooled) and positive radial anisotropy in the middle crust is close to the region densely populated by Neogene volcanic rocks (see Fig. 1). The three low-velocity zones marked by vertically oriented LVZ signs in the Menderes Massif may also indicate still cooling depth sections where the pattern of positive radial anisotropy in the middle crust is interrupted. As reported by Dilek and Altunkaynak (2009, Fig. 7 therein), the region of Menderes Massif (MM) is intruded by recent (i.e.,  $< 2$  Ma) alkaline volcanic rocks.

We think that plutonic rocks corresponding to this magmatic activity cause the latter LVZs in the MM. The extensional tectonics and the associated crustal movements resulting in plastically to brittlely deformations by extensional shear zones and normal faults (e.g., Dilek and Altunkaynak 2009) likely create azimuthal anisotropy dominant in these LVZs, but this azimuthal anisotropy is mostly suppressed in our data processing. On the contrary, the LVZ around 620 km distance is associated with clear positive radial anisotropy developed in the lower crust. Note that the middle-to-lower crust under the Beydağları Platform (BP) with magma intrusion around 590 km distance, which is already cooled, shows (weak) negative radial anisotropy around  $-3\%$  which means disturbed dyke structure and weak mineral alignment.

The seismicity cross section in the lower panel (Fig. 12) illustrates that the earthquake focal depths mostly take place in the brittle upper crust shallower than 15 km. There are some earthquakes deeper than 15 km accumulated beneath the Izmir–Ankara suture (IAS) zone and the Lycian Nappes (LN). These earthquakes indicate crustal-scale movements between micro-plates within the Aegean domain, but may also include effects of vertical magma flow ascending from a batholith. There are also some deep earthquakes underneath the Finike Basin (FB), but these earthquakes are more sporadic and may correspond to near-trench crustal deformations within the Turkish plate overriding the subducting African plate (e.g., Hall et al. 2014a).

The crust structure in the SW–NE direction is displayed in the second cross section B–B' (see Fig. 8). The observed Rayleigh surface wave group velocities are inverted to retrieve the vertically polarized SV-wave velocities ( $V_{sv}$ ). The observed Love surface wave group velocities are inverted to recover the horizontally polarized SH-wave velocities ( $V_{sh}$ ). In a similar fashion to Fig. 12, the Voigt isotropic average shear-wave velocities computed from Eq. (4) show the crust  $V_s$  velocities beneath profile B–B' (Fig. 13—upper panel). Using the color-coded velocity variations with depth, the crust structure is represented by five depth sections over a half-space. The third and fourth depth sections from the top show significant lateral variation. The upper-to-middle crust depths at several locations are intruded by the higher-velocity lower crust material. The crust structure beneath profile B–B' is radial anisotropic; i.e., a simple isotropic velocity structure cannot model Rayleigh and Love wave dispersions simultaneously. The pronounced differences between the inverted SV and SH velocities indicate the Rayleigh and Love surface wave discrepancy (Fig. 13—middle panel). These positive anomalies characterized as  $V_{sh} > V_{sv}$  are capped by the negative anomalies ( $V_{sv} > V_{sh}$ ) except that around 370 km and 520 km distances where the upper crust negative anomaly is replaced by the positive anomaly. Another exception occurs around 160 km distance where a negative anomaly in the lower

**Fig. 13** The inverted Voigt average S-wave (upper panel) velocities beneath profile B–B' are shown. The corresponding radial anisotropy is given in the middle panel. The regional earthquake hypocenters are shown in the lower panel





crust, which is interpreted as a dyke structure, underlies the middle crust positive anomaly. Here, the vertical structure can be seen as cooled through the correlation between the results of inverted S-wave velocities (upper panel) and radial anisotropy (middle panel). The sill units characterized as consecutive thin layers with relatively high and low velocities are interpreted to result in the positive anomalies in the middle-to-lower crust. The vertically arising dyke structures in the upper crust above the sill units are interpreted to cause these negative anomalies.

In Fig. 13 (upper panel), the positions of the main surface geological units attained from Fig. 11 are overlaid onto the shear-wave cross section. Similar to Fig. 12, the seismic waves are slower in the Lycian Nappes (LN—horizontal range indicated by red line), whereas the Menderes Massif (MM—horizontal range indicated by yellow line) is characterized by faster crustal velocities. The yellow and red lines in Fig. 13 are partly drawn thinner to indicate the horizontal extensions of these geological provinces. The thin yellow line shows the northeastern elongate of the Menderes Massif toward the Afyon Zone—AZ (e.g., Akay et al. 2011), while the thin red line indicates the southwestern extend of the Lycian Nappes under the Aegean Sea. Under the Gökova–Yeşilüzümlü Fault Zone—GYFZ (e.g., Hall et al. 2014a), the uppermost crustal depth range is highly deformed causing relatively slower shear waves around 2.5 km/s. The uppermost crust corresponding to the Büyük Menderes Graben (BMG) filled by Neogene–recent sediments is characterized by slower shear waves  $\sim 2.7$  km/s. Within the Menderes Massif (MM), there exists a horizontal sequence of high and low velocities in the middle crust depth range  $\sim 12$ – $24$  km. The high-velocity depths intruded by ascending magma represent the depth sections already cooled, while the low velocities exhibit still cooling crustal depths. The region corresponding to the Kula Volcanic Field—KVF (e.g., Heineke et al. 2016) is characterized by noticeable low-velocity zone (horizontally aligned LVZ sign in Fig. 13) in the middle crust, which is also reported by Çubuk-Sabuncu et al. (2017).

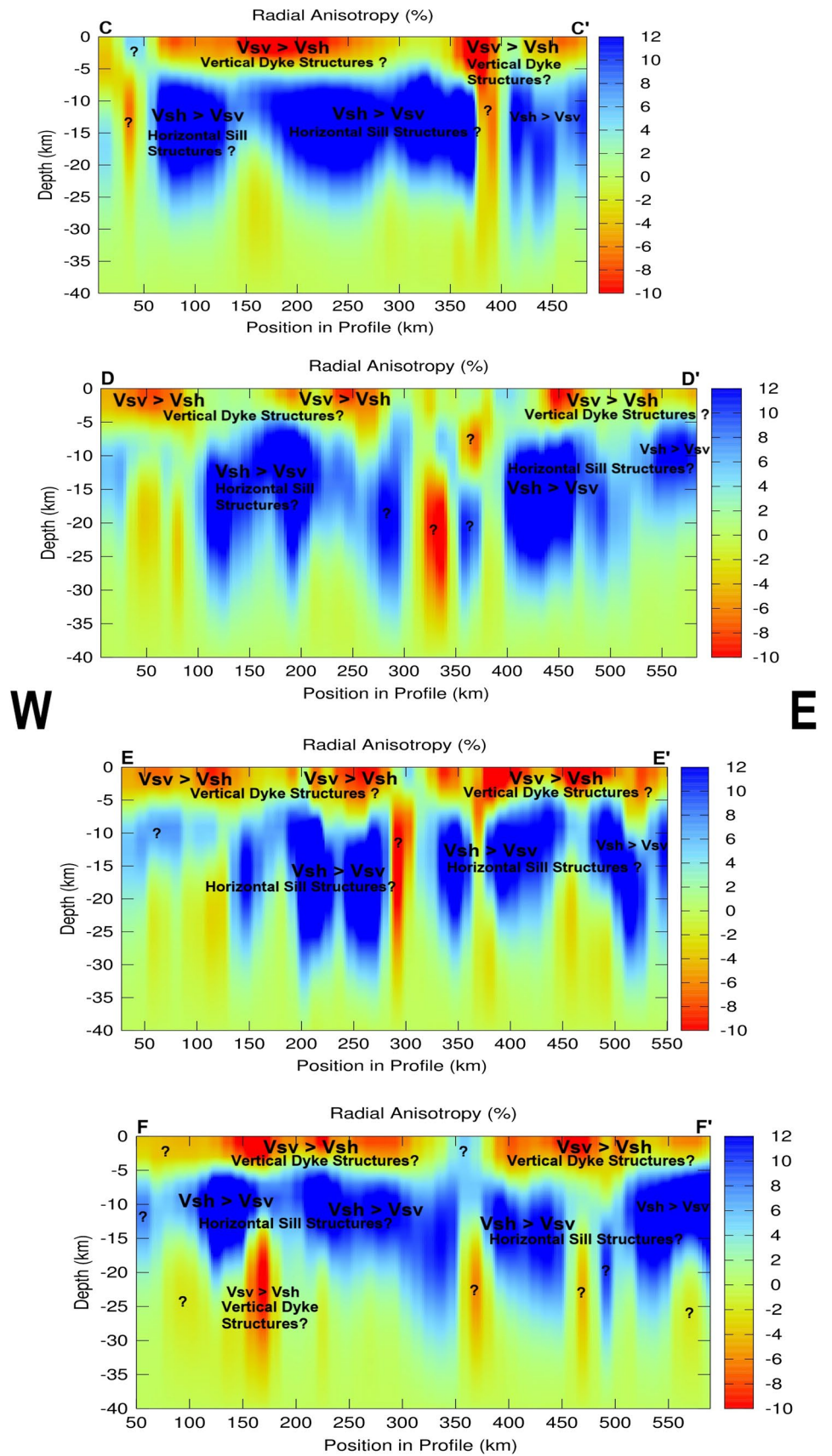
The arrow in Fig. 13 (upper panel  $\sim 160$  km distance) indicates a low-velocity pocket (LVP) around 7 km depth ( $\sim 2.5$  km/s) in the upper crust below which there exists a large vertical structure with high seismic velocity greater than 4.0 km/s in the lower crust. The yellow circle in Fig. 11 displays the surface projection of this anomalous region. The radial anisotropy corresponding to the shallower low-velocity anomaly is positive (middle panel in Fig. 13), which suggests a final cooling phase of horizontal sill structure with probably horizontal flow. The deeper high-velocity anomaly is associated with negative radial anisotropy, which seems to indicate a vertical dyke structure already cooled. The vertical mineral alignment due to a vertical flow that has existed at a certain geological period (i.e., frozen texture)

results the observed radial anisotropy. The corresponding earthquake hypocenters (to left in lower panel) also suggest that the latter dyke structure is cold since there does not exist any specific earthquake activity that may be attributed to this anomaly structure. In this region, the hypocenters are rather sporadic and are most likely related to the seismic activity in the Turkish crust interacting with the subducting African plate. There are two regions with noticeable earthquake activity, i.e., the first one around 300 km and the second one around 490 km distance. The first activity is related to the Gökova–Yeşilüzümlü Fault Zone (GYFZ), which identifies the transitional region from the Lycian Nappes (LN) to the Menderes Massif (MM). The second one takes place under the region corresponding to the eastern end of the Büyük Menderes Graben (BMG).

The Kula Volcanic Field (KVF) comprising  $\sim 80$  cinder cones and Quaternary basaltic lava flows (e.g., see Heineke et al. 2016) is characterized by positive radial anisotropy ( $\sim 12\%$ ) with horizontal flow in the middle-to-lower crustal depth range (lower panel). Çubuk-Sabuncu et al. (2017) have also reported a similar observation with anisotropy in the range 10–20%. Although somewhat weaker ( $\sim 5\%$ ), the upper crust also shows positive radial anisotropy, which might be specific to cinder cone volcanoes. Our interpretation is that the vertical magma flow beneath the KVF is actually deep seated and the root with possibly negative radial anisotropy is not detected well by our surface waves because of limited period range 5–20 s. The dyke structure (i.e.,  $V_{sv} > V_{sh}$ ) close to the KVF around 480 km distance with a question mark has provided a vertical magma flow at a certain geological time, but the high seismic velocities (i.e., already cooled) corresponding to this dyke suggest that the flow has stopped.

The remaining ten profiles are interpreted as shown in Figs. 14 and 15. The first four cross sections (i.e., C–C' through F–F') in Fig. 14 trend in the east–west direction, while the other four cross sections (i.e., G–G' through J–J') in Fig. 15 trend in the north–south direction. The radial anisotropic crust structure beneath the Aegean region in southwest Turkey has three different types of dyke and sill formations (I, II and III). The first formation (I) is made of horizontal sill units ( $V_{sh} > V_{sv}$ ) emplaced close to surface. Some examples of this formation are seen in the cross section G–G' around 210 km distance (Fig. 15) and the cross section H–H' around 240 km distance (Fig. 15). The second formation (II) has a sequence of dyke and sill units in which the upper crust is made of vertical dyke structures ( $V_{sv} > V_{sh}$ ) below which horizontal sill structures ( $V_{sh} > V_{sv}$ ) constitute the middle-to-lower crustal depths. Formation II is seen most frequently under the study area. Some examples are seen in the cross section A–A' around 420 km distance (Fig. 12), the cross section B–B' around 270 km distance (Fig. 13) and the cross section C–C' around 220 and 425 km

**Fig. 14** The east–west trending four radial anisotropy cross sections are shown. The locations of these profiles are illustrated in Fig. 8



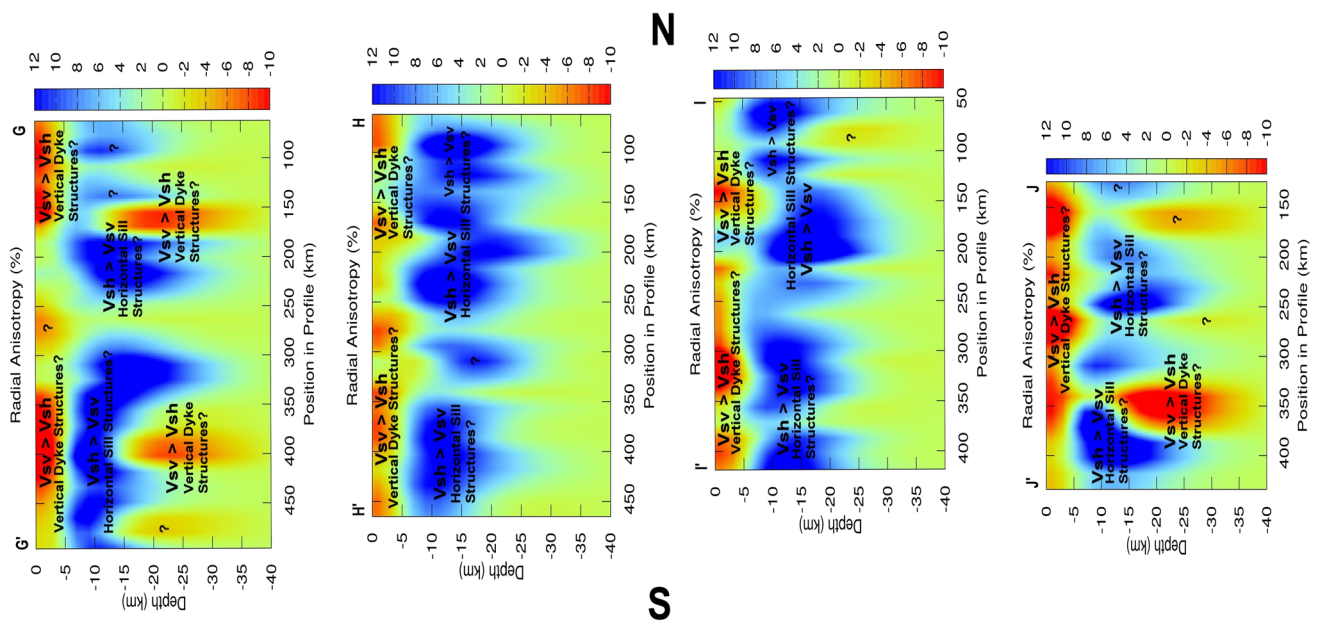


**Fig. 15** The north–south trending four radial anisotropy cross sections are shown. The locations of these profiles are illustrated in Fig. 8

distances (Fig. 14). The third formation (III) has more complex sequence of dyke and sill units in which the upper crust is made of vertical dyke structures ( $V_{sv} > V_{sh}$ ) below which horizontal sill structures ( $V_{sh} > V_{sv}$ ) occupy the middle crust depths. The latter sequence continues with vertical dyke structures ( $V_{sv} > V_{sh}$ ) in the lower crust. Some examples of this formation are seen in the cross section B–B' around 150 km distance (Fig. 13), the cross section F–F' around 160 km distance (Fig. 14) and the cross section J–J' around 360 km distance (Fig. 15). Perhaps there is a fourth formation, which is made of vertical dyke structures in the middle-to-lower crust depths. Possible such structures are marked with question marks, e.g., one in the cross section B–B' around 370 km distance (Fig. 13) and another one in the cross section E–E' around 290 km distance (Fig. 14).

The study area which takes place in the back-arc region of the northward-dipping Hellenic subduction zone is mostly populated by plutonic and volcanic rocks (see Figs. 1, 2). Researchers have suggested that the magmatism in the Aegean, which began in the Eocene following the closure of the Neotethyan oceanic basin, was first provided by asthenospheric flow generated by slab break-off, which was then followed by another phase of asthenospheric flow related to lithospheric delamination. In the final stage, upward asthenospheric flow was driven by tectonic extension. Variable magma types showing a wide range of chemistry and petrology from calc-alkaline to alkaline or shoshonitic constitute the Aegean volcanic rock types suggesting a range of geodynamic environments within the back-arc region accompanied by heating

of subcontinental mantle and lower crust (e.g., see Dilek and Sandvol 2009; Dilek and Altunkaynak 2009; Jolivet and Brun 2010). The trench-retreat and progressively slab tearing of the subducting African plate perturbs the sublithospheric mantle flow pattern under the Aegean region. The alkaline basalt volcanism at the KVF is perhaps the result of hot asthenosphere material rising thru the tearing window (e.g., see Biryol et al. 2011; Jolivet et al. 2013; Çubuk-Sabuncu et al. 2017). There should be a batholith (or stock) which is a large body of igneous rock formed beneath the Aegean region by the intrusion and solidification of buoyant magma. Our surface wave data are not able to resolve the depth extent of the latter structure because of the limited band width (i.e., 5–20 s). This batholith structure should underlie the three formations described in Figs. 14 and 15 and should be connected with the sill and dyke units above in the middle-to-lower crust. The magma body most likely discharges throughout multiple dykes aggregating the case of  $V_{sv} > V_{sh}$  at lower crustal depths for which case the radial anisotropy is either very weak or not observed (isotropic).

### Phase and group velocity inversions using two-station data

For the structural inversion, we simultaneously utilize the group and phase velocity measurements in this section. The earthquake is recorded by two stations located with little deviation from the great circle path and minimum inter-station distance of  $0.5^\circ$ . The two angles  $\theta_1 \leq 1^\circ$  and



$\theta_2 \leq 5^\circ$  described above are used to measure the amount of allowed azimuthal deviation. A cross-correlation between the seismic recordings at these two stations is considered. This process removes the common source phase and squares the effect of amplitude spectrum. The cross-correlogram is treated as a recording at the second (distant) station due to a source located at the first (near) station. The relation given in Eq. (2) is used to compute the corresponding frequency-dependent phase velocity curve. The MFT already described above (Dziewonski et al. 1969; Herrmann 1973) is employed to compute the frequency-dependent group velocity curve. Because the group velocities are measured using the amplitude spectrum and the phase velocities are measured using the phase spectrum, the error processes in the measurements of phase and group velocities are mostly independent (e.g., see Dziewonski and Hales 1972).

Two earthquakes and four broadband stations are selected to study the inter-station surface waves as shown in Fig. 16. The first earthquake is moderate size with magnitude  $M_w = 4.3$ . The two broadband stations (BODT and CHOS) with 184 km inter-station distance measure the study area in approximately SE–NW direction. The corresponding inter-station ray path crosses the coastal range of the Aegean Sea. The second earthquake is also moderate size with magnitude  $M_w = 4.9$ . The two broadband stations (AYDB and ELL) with 223 km inter-station distance measure a different part of the study area similarly in SE–NW direction. The two inter-station ray paths cross a mix of two different anisotropic regions (formations I and II) described in Figs. 14 and 15.

The group (U) and phase (C) velocity dispersion curves acquired for the first event with magnitude  $M_w = 4.3$  in Fig. 16 are shown in Fig. 17. The dispersion curves of the Rayleigh surface waves (period range 4–25 s) are shown in Fig. 17a, and the dispersion curves of the Love surface waves (period range 4–28 s) are shown in Fig. 17b. For the second event with magnitude  $M_w = 4.9$ , the corresponding dispersion curves are shown in Fig. 18. The Rayleigh surface wave group velocities have the period range 4–19 s (Fig. 18a), while the Love surface wave group velocities have the period range 4–29 s (Fig. 18b). Both phase and group velocities are handpicked in each panel. The white dotted lines on the color-coded diagrams of the multiple-filter technique (MFT) applied on the cross-correlogram depict the group velocities. The red dotted lines on the diagrams computed using the phase of the cross-correlograms depict the phase velocities. Because of the  $2n\pi$  uncertainty in the phase velocity, the dotted lines above and below the red line multiply develop. The correct fundamental mode phase velocity curve is chosen using the separation between the dotted lines increasing with increasing period.

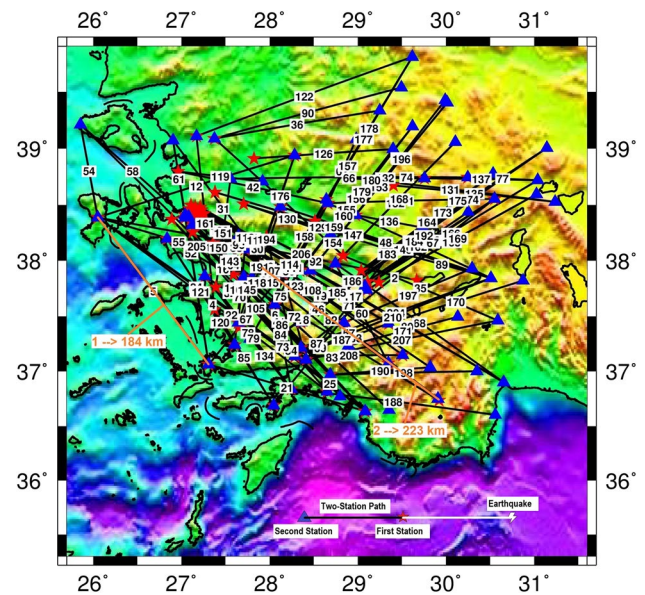


**Fig. 16** All the two-station paths are shown. These paths 5 and 44 (number obscured) individually highlighted by orange color lines are used in the inter-station analysis. The earthquake locations all within the display frame (see Fig. 6) are not shown. The first station (red star) is close to the earthquake, while the second station (blue triangle) is further away

The crust shear-wave velocity structure beneath the first inter-station ray path (5) is retrieved inverting the Rayleigh and Love dispersion curves shown in Fig. 17. The strategy described in Fig. 10 is followed to invert the observed group and phase velocity dispersion curves. Figure 19 shows the result of the three types of inversions performed, i.e., (a) inversion of only Rayleigh dispersion, (b) inversion of only Love dispersion and (c) simultaneous inversion of Rayleigh and Love dispersions. The fits obtained for the Rayleigh phase and group velocity curves are illustrated in Fig. 19a, and the fits obtained for the Love phase and group velocity curves are shown in Fig. 19b. The simultaneous dispersion fits obtained for the Rayleigh and Love phase (C) and group (U) velocity curves are depicted in Fig. 19c. Using different colors, in Fig. 19d, we illustrate the inverted velocity–depth profiles corresponding to the three inversions. For the second inter-station ray path (44), the corresponding inversion results using the dispersion curves in Fig. 18 are shown in Fig. 20. Although still reasonable and smooth, the fits to the observed curves for both Rayleigh and Love surface waves show some unmodeled (particularly group velocity) dispersion data because the observed dispersion curves for both cases (i.e., inter-station paths 5 and 44) are disturbed by the ambient noise. The earth structure between the recording stations is not isotropic as indicated by the simultaneous fits to the observed Rayleigh and Love dispersions, which are poor (Figs. 19c, 20c). The Rayleigh and Love dispersions are jointly better explained by the radial anisotropic model. In Fig. 19d, the differences between the



2010–08–08 00:24:12 27.31 (E°) 37.06 (N°)  $h = 22.93$  km  $M_w = 4.3$

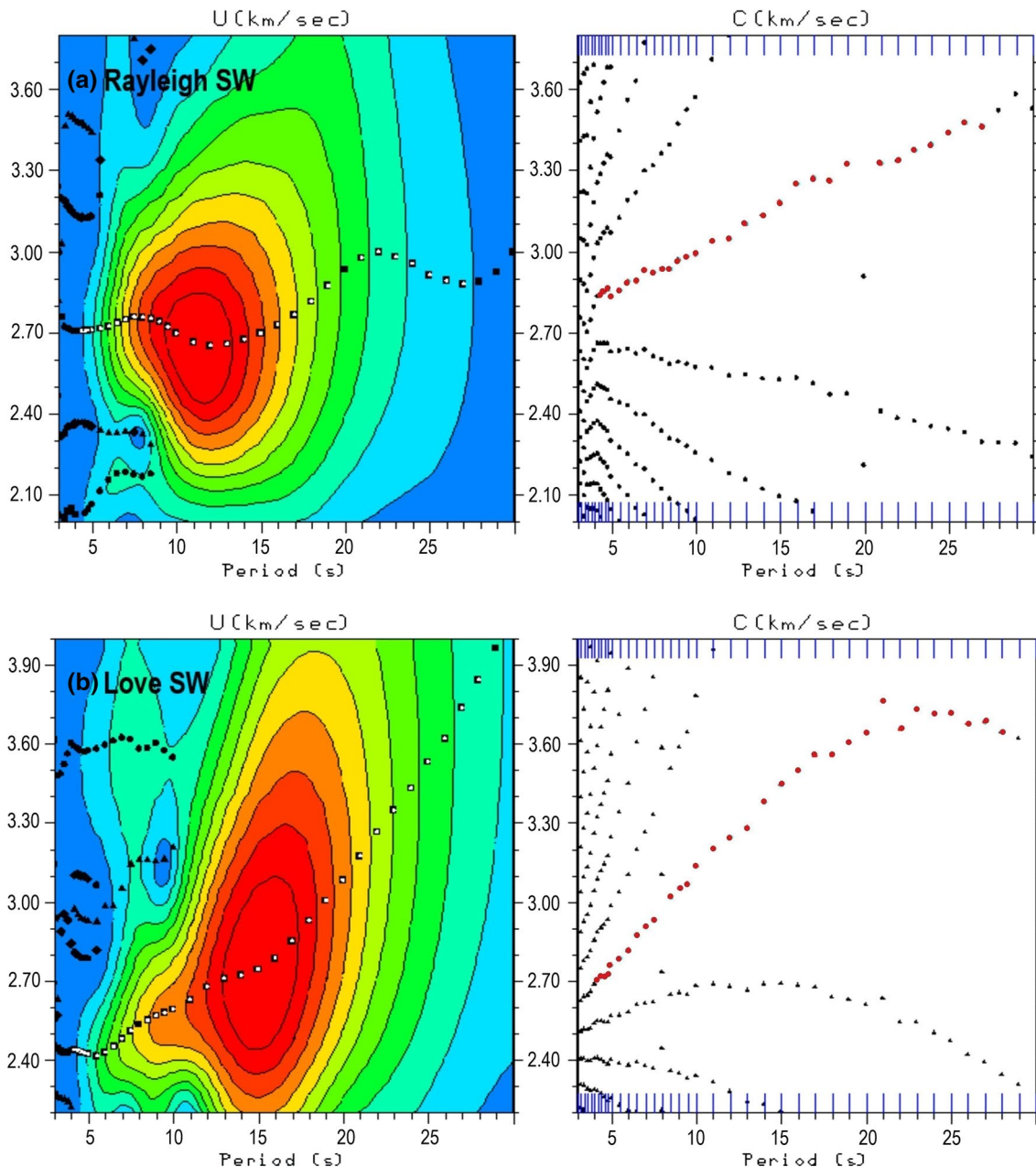


**Fig. 17** The group velocity (U) and phase velocity (C) dispersion curves are shown for the inter-station Rayleigh (a) and Love (b) surface waves. The event parameters are listed in the upper row. The

white and red dotted lines show the observed group and phase velocity curves, respectively. The black dotted lines arise due to the uncertainty in the phase velocity

blue (L—Love) and red (R—Rayleigh) color velocity–depth profiles show that the observed radial anisotropy ( $\eta$ ) is negative (i.e.,  $V_{sv} > V_{sh}$ ) for the upper crust and positive (i.e.,  $V_{sh} > V_{sv}$ ) for the middle and lower crust. In the upper crust,  $\eta$  is approximately  $-15\%$  and changes to approximately  $15\%$  in the middle-to-lower crust. Similar anisotropy–depth profile occurs for the second inter-station ray path (44), but the anisotropy values change, i.e., ( $\eta \sim -5\%$ ) in the upper crust and

( $\eta \sim 13\%$ ) in the middle-to-lower crust. The two inter-station ray paths (5 and 44) traverse a structure made of a mix of formations I and II defined in Figs. 14 and 15.

The final two-station ray paths recovered from quality checked cross-correlograms total to 210 (see Fig. 16), which does not provide enough ray-path coverage to perform the 2-D phase and group velocity tomography similar to those shown in Fig. 6. Instead, we compute the average

2014–12–06 06:20:54 27.90 (E°) 37.95 (N°)  $h = 14.15$  km  $M_w = 4.9$

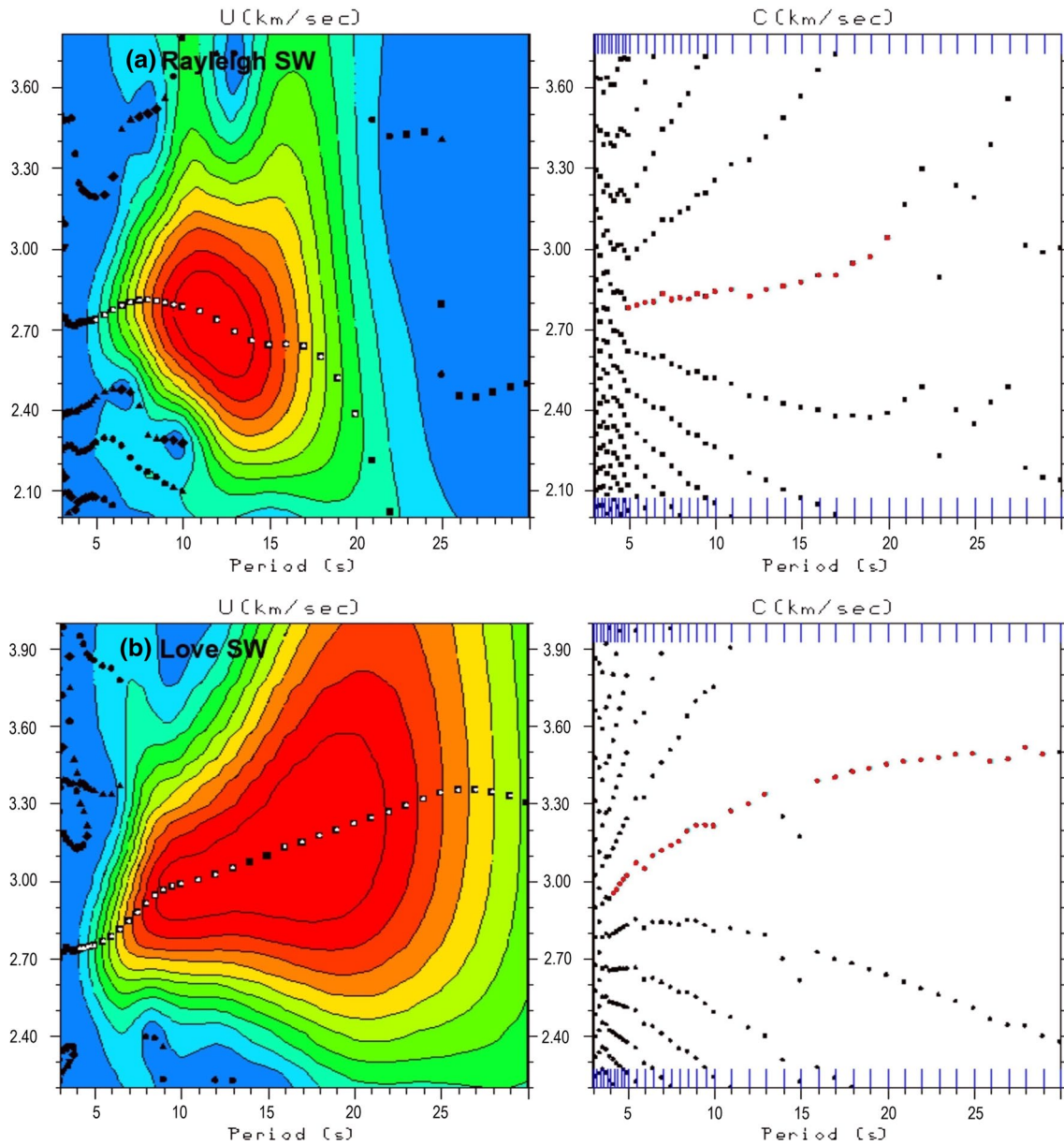


**Fig. 18** The group velocity ( $U$ ) and phase velocity ( $C$ ) dispersion curves are shown for the inter-station Rayleigh (a) and Love (b) surface waves. The event parameters are listed in the upper row. The

observed group and phase velocity curves are indicated by the white and red dotted lines, respectively. The black dotted lines are due to the uncertainty in the phase velocity

Rayleigh and Love surface wave group and phase velocity curves using the two-station dispersion curves in Fig. 16 to represent the average of the study area. The result corresponding to this procedure is summarized in Fig. 21. The average Rayleigh group (orange color) and phase (cyan color) velocity dispersion curves along with the standard deviations (vertical bars) are shown in Fig. 21a superimposed on the observed group (purple color) and phase (green color) velocities. The same set of dispersion

curves for the Love surface waves is shown in Fig. 21b. The computed average dispersion curves are inverted using the same strategy followed in the above surface wave data. The inverted velocity–depth profiles are illustrated in Fig. 21c where the red color velocity structure corresponds to the Rayleigh (R) surface waves and the blue color velocity structure represents the Love (L) surface waves. The radial anisotropy in the upper crust is measured negative ( $V_{sv} > V_{sh}$ ) showing approximately  $-4\%$ , and the radial

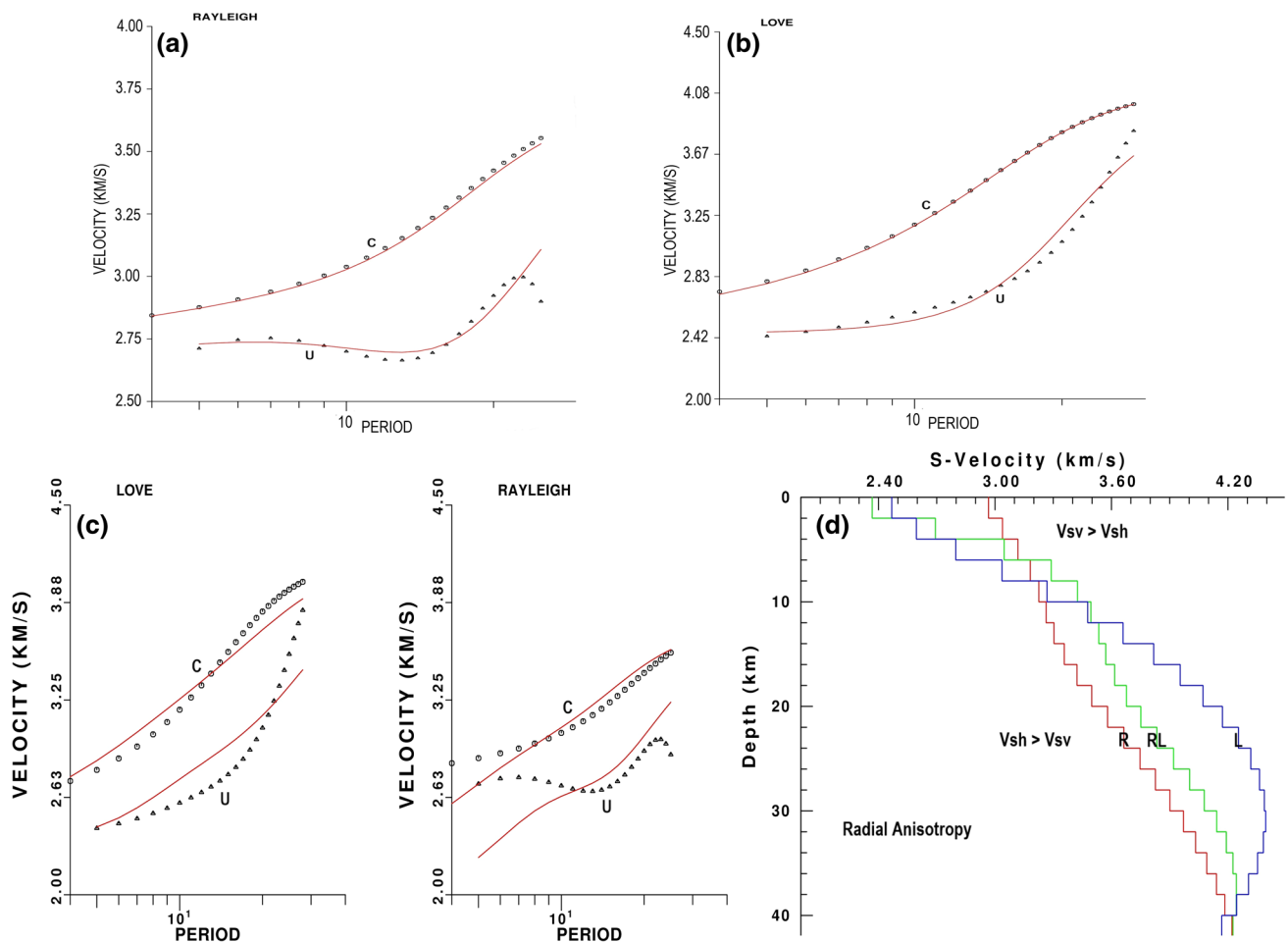


**Fig. 19** The dispersion curve fits for the Rayleigh (R) surface waves (a), the dispersion curve fits for the Love (L) surface waves (b), simultaneous dispersion curve fits for the Rayleigh and Love (RL)

surface waves (a), the inverted S-velocity–depth profiles (d). The first inter-station ray path (5 in Fig. 16) is considered

anisotropy in the middle-to-lower crust is measured positive ( $V_{sh} > V_{sv}$ ) showing approximately 9%. Especially in the upper crust, the latter case anisotropy is weaker than those measured in Figs. 14 and 15. This happens because the two-station ray paths traverse the vertical dyke structures resulting in the measured negative radial anisotropy, but underneath some parts of the study area these structures are absent causing a weaker average radial anisotropy. The same is also true for the two-station ray paths sampling the middle-to-upper crust depths, i.e., the horizontal sill structures resulting in the measured positive radial anisotropy are absent underneath some parts of the study area. Provided as online supplementary material (Figure 22), the inversions of the average Rayleigh and Love group velocity curves given in Fig. 7 have resulted very similar velocity–depth profiles to these depicted in Fig. 21c.

## Discussion and conclusions

The geology of the Aegean region in southwest Turkey (see Figs. 1, 2) is complex mostly populated by plutonic and volcanic rocks formed above the northward-dipping Hellenic subduction zone. This geologically complex region is presently studied using the seismic surface wave dispersion acquired from 231 regional events of magnitude  $3.6 \leq M_w \leq 6.5$  and of shallow focal depth  $1.5 \leq h \leq 48$  km occurring between 2007 and 2017. The earthquakes are recorded by 142 accelerometer and 20 broadband digital stations and are analyzed by the multiple-filter technique to obtain the Rayleigh ( $\sim 1876$  ray paths) and Love ( $\sim 1792$  ray paths) group velocity curves in the period range 5–20 s. The 2-D tomographic inversions are performed to obtain the period-dependent group velocities, which are individually least squares inverted, at  $0.1^\circ \times 0.1^\circ$ -sized grid cells of a mesh covering the study area. Horizontally and vertically varying shear-wave velocities are observed. Due to

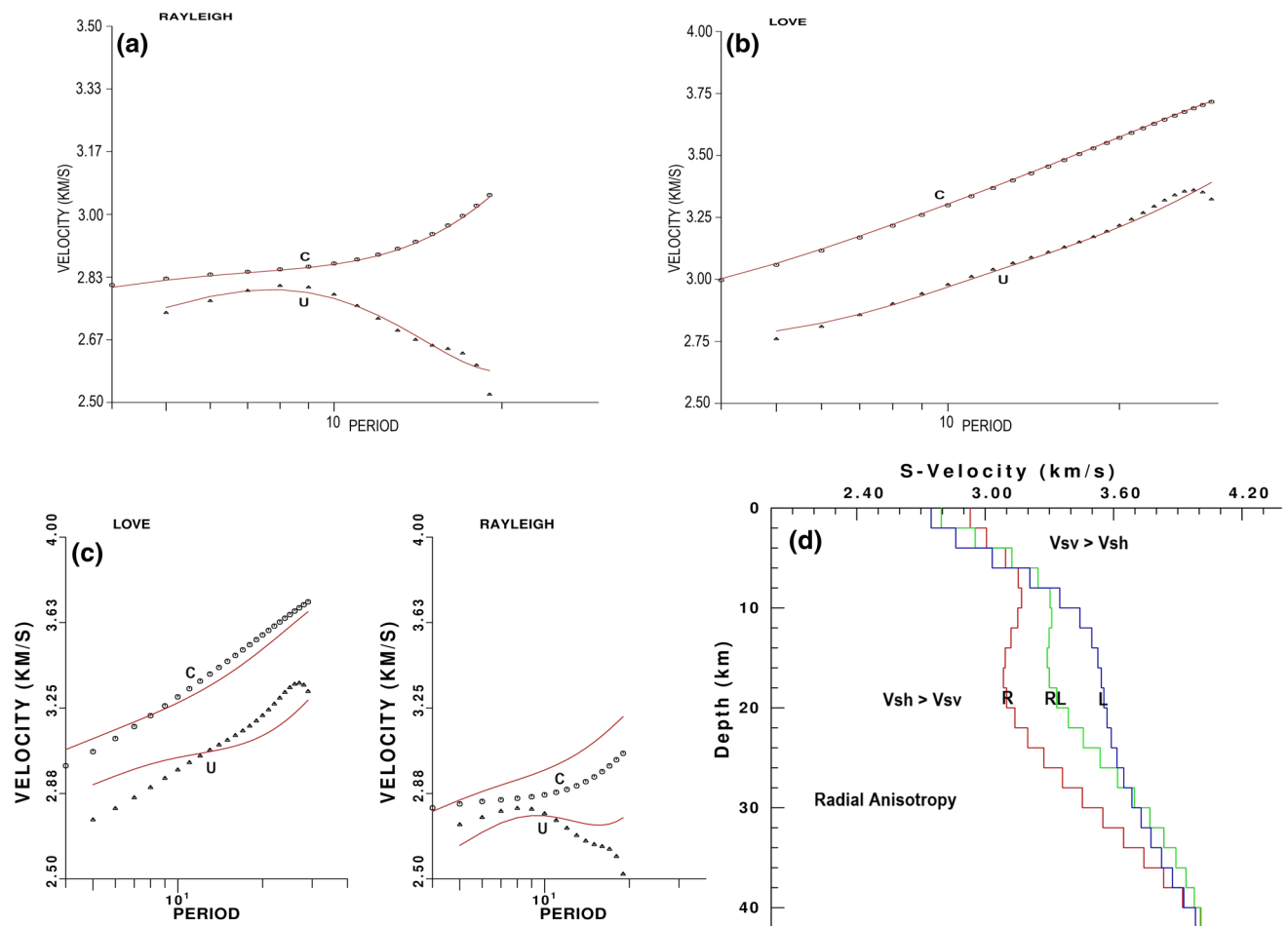


**Fig. 20** The dispersion curve fits for the Rayleigh (R) surface waves (a), the dispersion curve fits for the Love (L) surface waves (b), simultaneous dispersion curve fits for the Rayleigh and Love (RL) surface waves (c), the inverted S-velocity–depth profiles (d). The second inter-station ray path (44 in Fig. 16) is considered

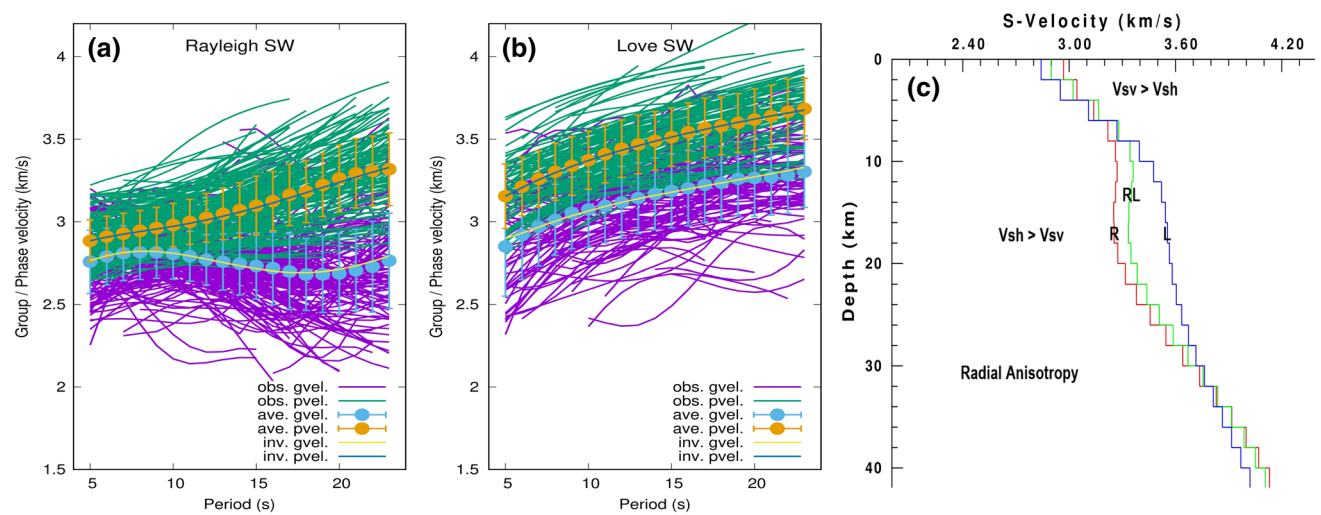


**Fig. 21** The two-station observed phase (pvel.) and group (gvel.) velocity dispersion curves and the corresponding averages are shown in a, b. The average dispersion curves are inverted as shown in c. The dispersion fits obtained after the inversions are shown by the blue (phase velocity) and yellow (group velocity) color lines superimposed in a, b



the discrepancy in the transmission velocities of Rayleigh and Love waves, the models of isotropic seismic velocity in the crust cannot fit simultaneously the observed dispersion curves indicating the existence of radial anisotropy. The spatial extent of the radial anisotropy beneath the study area is studied as cross sections with a depth range down to 40 km along ten selected profiles. The vertical dyke structures and horizontal sill structures associated with the regional plutonic and volcanic rocks and the related magmatic flow along with the mineral alignment are believed to be the main cause for the observed depth-dependent radial anisotropy—the indicator of crust deformation styles.

The various fault segments related to the back-arc N–S extensional regime actively deform the crust structure of the Aegean region in southwest Turkey. Figure 1 shows the major active faults, but in fact the region is populated by hundreds of small faults dominantly located in and around the graben systems and within the Isparta Angle, which are not shown in the figure to prevent the illustration from becoming cluttered. Such a fracture system likely creates azimuthal anisotropy primarily in the upper crust, which could be represented by hexagonal symmetry with horizontal symmetry axis oriented in different directions aligned with the regional tectonic units. The general anisotropic surface waves include azimuth-independent and azimuth-dependent terms where the azimuth-independent term, which we utilize, corresponds to the averaging across all azimuths describing hexagonal symmetry with vertical symmetry axis (Montagner and Nataf 1986; Montagner and Anderson 1989; Montagner 2007). By averaging over multiple events with varying approach azimuths, we try to remove all the azimuthal effects for which the ray paths approaching from all events show good enough azimuthal coverage (see Fig. 6).

The number of two-station paths is unfortunately limited to only 210, which does not allow tomographic inversions to hold up the 2-D group velocity maps. Instead, using two earthquakes and four recording stations we invert the two-station surface waves. The inverted shear velocity–depth profiles are consistent with the single-station group velocity analyses. However, most likely due to the ambient noise effect on the observed dispersion curves the radial anisotropy is somewhat over-estimated, i.e.,  $\sim -15\%$  in the upper crust and  $\sim 15\%$  in the middle-to-lower crust (e.g., see Fig. 19). We also invert the average two-station phase and group velocity curves. The averaging process helps suppress the ambient noise effect, but then the radial anisotropy is underestimated (i.e.,  $\sim -4\%$  in the upper crust and  $\sim 9\%$  in the middle-to-lower crust, see Figs. 16, 21) since the averaging process does not differentiate between the isotropic and anisotropic regions. With additions of new earthquake data and recording stations, the two-station surface waves can be better inspected.

The deformations in the crust can be mapped using the seismic anisotropy particularly radial anisotropy. For instance, Hacker et al. (2014) have utilized surface wave tomography to show S-wave radial anisotropy of at least 4% beneath the Central Tibet, concluding that this was due to the partially melted mica-bearing crust. Harmon and Rychert (2015) have used the surface waves derived from the ambient noise tomography reporting 6% radial anisotropy beneath Costa Rica corresponding to the melt sills in the deep crust. Godfrey et al. (2017) have used Rayleigh and Love wave ambient noise measurements to create the S-wave models beneath the Tongariro Volcanic Centre in New Zealand, reporting that the upper crust structures such as dykes or cracks in the vertical plane resulted in the Love–Rayleigh discrepancy.

The number of various geophysical studies dealing with the crust structure beneath the Aegean region in southwest Turkey is unfortunately limited. For instance, Çubuk-Sabuncu et al. (2017) have performed the full-waveform tomography of the western Turkey using the three-component complete waveforms of the regional earthquakes and have concluded the radial anisotropy in the range  $\pm (10\text{--}20)\%$  throughout the crust structure. Endrun et al. (2008) have studied the Rayleigh and Love surface wave discrepancy beneath the Aegean Sea region using two-station phase velocities between broadband stations and have concluded the positive radial anisotropy to exist in the lower crust beneath the northern Aegean due to the ductile flow in the lower crust that accommodated lithospheric stretching. Ozer et al. (2018) have used local earthquake tomography method to understand the crustal structure and geothermal potential of the Aegean region of Turkey interpreting the 3-D  $V_p$  and  $V_p/V_s$  models. The velocity highs and lows under the Aegean Graben system (GG, KMG, BMG—profile 2 therein) correlate well with the current results presented in Fig. 12. Erduran (2009) has employed joint inversion of receiver functions and dispersion curves to determine the crust S-wave velocity structure beneath station ISP in the Isparta Angle (IA). In the depth range 0–5 km, the S-wave velocity increases from 2.5 to 3.0 km/s and then increases to 3.2 km/s in the depth range 5–10 km. The third depth range 10–20 km has constant velocity 3.62 km/s with a velocity jump from 3.20 km/s at 10 km depth. The S-wave velocity drops to 3.4 km/s at 20 km depth persistent down to 27.5 km. These S-wave velocities considerably slower (e.g., see Delph et al. 2015) than those of the Preliminary Reference Earth Model—PREM (Dziewonski and Anderson 1981) are generally consistent with the current results (e.g., see Figs. 12, 13).

Bakırcı et al. (2012) have investigated the 3-D upper-mantle structure beneath Turkey using the phase velocities of fundamental mode Rayleigh surface waves employing the two-station method. They have observed low velocities

beneath the Isparta Angle and Antalya Basin, which they have interpreted as hot materials of asthenosphere rising from a slab tear between the Cyprus and the Hellenic subductions. Our inverted S-wave velocities in the crustal depth range are slower especially around the Fethiye–Burdur Fault Zone (FBFZ). The current surface wave ray-path coverage for the Isparta Angle (IA) and Antalya Basin (AB) is relatively poor (see Figs. 6, 11), but the available ray paths in Fig. 6 suggest some low-velocity material. Gessner et al. (2016) have used the joint inversion of gravity and magnetic data to study the crustal structure of the northern Menderes Massif, concluding that granites and volcanic complexes are interspersed across their study area, being much more numerous in the west. Their observation is consistent with the current findings that the crust structure under southwest Turkey is heterogeneous as being site of widespread magmatism producing plutonic rocks (e.g., Yılmaz 1997). Gessner et al. (2017) have reported that the largest geothermal areas in the Menderes Massif in western Anatolia are located in the widest graben and at fault intersections where secondary porosity caused by brittle faulting of metamorphic basement rocks has provided the key pathways for fluids and melts. The inverted S-wave velocities in Fig. 12 (upper panel) show three well-developed, middle crust low-velocity zones—LVZs (still cooling) most likely providing the heat source for the observed geothermal activity in the Menderes Massif.

The ray-path coverage of our surface wave data is able to resolve the crust structures with size  $0.4^\circ \times 0.4^\circ$  or  $\sim 45$  km horizontal resolution length as the checkerboard tests in Fig. 5 indicate. The radial anisotropic anomaly structures shown in Figs. 12, 13, 14 and 15 correspond to this resolution length. Embedded in those radial anisotropic anomaly structures ensemble of small-scale structures (i.e., sills and dykes) constructively interfere with each other to create the observed radial anisotropy described herein. With the given resolution length, we assert the resolution of the embedding (ensemble) large-scale structure, but not the resolution of the embedded small-scale structures in the ensemble. As a result, beneath the Aegean region the Rayleigh surface waves travel faster than the Love surface waves in the upper crust generally populated by dykes (i.e.,  $V_{sv} > V_{sh}$ ), while the Love surface waves travel faster than the Rayleigh surface waves in the middle-to-lower crust generally populated by sills (i.e.,  $V_{sh} > V_{sv}$ ).

There exist strong trade-offs between the seismic velocities above and below an interface and depth to this interface with the surface wave data. More data with different sensitivities (particularly surface waves and receiver functions) are employed together in the joint inversions (e.g., Julià et al. 2000; Shen et al. 2013) in order to alleviate the trade-off problem. Regarding the estimation of the Moho depth by the surface waves, Lebedev et al. (2013) have suggested the inversion of the crustal and upper-mantle structure first in

broad period range and then this inversion be used as reference to determine the Moho depth in a narrow period range most sensitive to the Moho structure. Different geophysical data such as receiver functions, topography, gravity and prior information on crustal and mantle structure, which can be used in the joint analysis, are also important to reduce the trade-offs and uncertainties.

Three different dyke–sill structures placed side by side from north to south constitute the general radial anisotropy (see Figs. 14, 15). The negative radial anisotropy ( $V_{sv} > V_{sh}$ ) reaching  $-10\%$  and the positive radial anisotropy ( $V_{sh} > V_{sv}$ ) around  $12\%$  are estimated for the crustal range rocks. Within the overriding Turkish plate induced by slab rollback in the frame of the Hellenic subduction zone, the strength and spatial distribution of the radial anisotropic structures support the existence of N–S extensional forces (e.g., see Agostini et al. 2010). The lateral variation of the lithospheric rheology and the differential movement underneath the study area with approximately  $5^\circ \times 4^\circ$  size are also indicated by the strong heterogeneities in the middle-to-lower crust depths (e.g., see Figs. 12, 13). Within the horizontal sill structures, the observed positive radial anisotropy is relatively strong sometimes reaching  $16\%$  (e.g., see Fig. 13—cross section B–B' around 440 km distance). Our prediction is that the presence of molten fractions under pure shear deformation produces  $\sim 3\%$  extra anisotropy added to the anisotropy in horizontally oriented sills (e.g., see Jaxybulatov et al. 2014; Hier-Majumder and Drombosky 2015).

Following the continental collision between the Sakarya and Anatolide–Tauride blocks in the pre-middle Eocene, the Aegean region in SW Turkey has experienced widespread magmatism (e.g., Yılmaz 2008) where voluminous granitic magmas were generated and emplaced into the crystalline basement rocks (e.g., Altunkaynak et al. 2012). We interpret the radial anisotropic crust structure beneath the study area in terms of three different types of dyke and sill formations (I, II and III), which is the first time reported herein. The plutonic rocks (as batholiths) sometimes appear as horizontal sill structures in the middle crust (formation I) and a sequence of vertical dyke structures in the upper crust and horizontal sill structures in the middle crust (formation II). The sequence in formation II is sometimes underlain by vertical dyke structures in the lower crust (formation III). The mineral alignment due to the magma flow within the system of dyke and sill units contributes to the observed radial anisotropy. In addition, the metamorphic rocks frequently observed in the study area contribute to the observed anisotropy as outlined in the following.

The Menderes Massif surrounded by ophiolite belts and nappes exposes metamorphic rocks of high-pressure (HP) and low-temperature (LT) as well as low-pressure (LP) and high-temperature (HT) metamorphism (Oberhänsli et al. 1997; Candan et al. 2001; Rimmelé et al. 2003a; Whitney

et al. 2008) and was derived from the Anatolide–Tauride block that underwent Eocene underthrusting below and collision with the Sakarya continent (Şengör and Yılmaz 1981; Kaymakci et al. 2009; Torsvik and Cocks 2009). Neogene exhumation of these rocks to the surface has been attributed to the activity of extensional detachments with preserved NE–SW to N–S stretching lineations (Şengör et al. 1984; Hetzel et al. 1995; Bozkurt and Oberhänsli 2001; Işık and Tekeli 2001; Ring et al. 2003; Seyitoğlu et al. 2004). The Massif is surrounded by metamorphosed and non-metamorphosed older, structurally higher thrust slices (e.g., van Hinsbergen 2010). The seismic surface waves are generally faster in the Menderes Massif (MM) as clearly shown by the inverted S-wave velocities in Figs. 12 and 13. There exist three low-velocity zones (LVZs) with  $\sim 3.1$  km/s velocity characterizing the middle crust depth range in the massif. The LVZs, considered as still cooling plutonic rocks, are accompanied by high-velocity zones, considered as already cooled plutonic rocks, with  $\sim 3.5$  km/s velocity in the same depth range. In the uppermost crust, the Aegean Graben system (GG, KMG and BMG; e.g., Yılmaz et al. 2000) filled by Neogene–recent sediments is clearly visible on the inverted S-wave velocities where the Horst structures are evident with high velocity ( $\sim 3.0$  km/s) and within the Graben structures the seismic surface waves are slower with  $\sim 2.7$  km/s velocity (see Figs. 12, 13—upper panel). The radial anisotropy in the MM is generally observed as formations I and II (see Figs. 12, 13—middle panel). The Precambrian metamorphic basement in the MM is reported to comprise primarily medium-to-high-grade schists, paragneisses, migmatites, orthogneisses, metagranites, charnockites and metagabbros (e.g., Candan et al. 2001). The cover metasedimentary sequence of the Menderes Massif ranges from garnet micaschists at the base to slightly recrystallized Paleocene wildflysch at the top, which is overlain by thrust contact by the Triassic to Jurassic metasedimentary rocks of the Lycian nappes (e.g., Okay 2001).

The Lycian nappes, commonly regarded as stack of sedimentary thrust slices and an overlying ophiolite and ophiolitic mélangé, structurally overlie Precambrian–Ordovician to Lower Cretaceous carbonate rocks intercalated with volcano-sedimentary and epiclastic rocks (Demirtasli et al. 1984; Özgül 1984; Gürsu et al. 2004) of the Tauride block farther south (Collins and Robertson 1997; Ring and Layer 2003) and represent the tectonic outliers of the Cretaceous oceanic crust derived from the IASZ with correlation to the Bornova Flysch zone (Okay 1989; Collins and Robertson 1997; Rimmelé et al. 2003a; Candan et al. 2005). These Lycian nappes have once covered the Menderes metamorphic massif and then have been removed due to the tectonic uplift and erosion associated with the exhumation of the Menderes core complex during the late Cenozoic (Ring and Layer 2003; Thomson and Ring 2006). The seismic surface

waves in the Lycian nappes (LN) travel slower as clearly shown by the inverted S-wave velocities in Figs. 12 and 13. The middle crust S-wave velocity in the LN is  $\sim 3.1$  km/s, whereas the corresponding velocity in the Menderes Massif (MM) to the northwest is  $\sim 3.5$  km/s and  $\sim 3.7$  km/s under the Beydağları Platform (BP) to the southeast (see Fig. 12—upper panel). The radial anisotropy in the LN is generally observed as formations II and III (see Figs. 12, 13—middle panel). Oberhänsli et al. (2001) have reported low-grade, high-pressure (HP) metamorphism where the Fe–Mg–carpholite and its breakdown products such as chloritoid and pyrophyllite trace an extensive area in the LN (as also reported by Rimmelé et al. 2003a).

The Aegean region in SW Turkey as part of Alpine orogeny has complex tectonic history (e.g., van Hinsbergen et al. 2010) where various tectonic components (e.g., subductions, collisions, core complexes, sutures, ophiolites, magmatism, compressions, extensions, rotations, nappes, fault zones) have played key roles to shape the regional geology (e.g., Şengör and Yılmaz 1981; Şengör 1987; Yılmaz 1997; Okay 2008). Accompanying these tectonic movements, high-pressure (HP) and high-temperature (HT) conditions were also dominant in the region to transform the rock formations, i.e., high-grade metamorphism (e.g., Dilek et al. 2009). Depending on the heat, pressure and chemical processes buried deep below Earth's surface, the metamorphic rocks could be foliated (e.g., gneiss, phyllite, schist and slate) or non-foliated (e.g., hornfels, marble, quartzite and novaculite). The foliated metamorphic rocks having layered or banded appearance show anisotropic behavior usually defined with hexagonal symmetry (e.g., Ji et al. 2015). If the metamorphic rocks include some lineation along with the foliation, then the orthorhombic system replaces the hexagonal symmetry.

There exist several studies documenting the anisotropic properties of metamorphic rocks. For instance, Johnson and Wenk (1974) have measured the physical properties of 110 metamorphic rocks from the Central Alps using the ultrasonic pulse transmission technique and have observed strong anisotropy in the thermal and elastic properties of the samples. Vernik et al. (1992) have studied the anisotropic strength of some metamorphic rocks from Germany where they have reported varying anisotropy in lineated amphibolites in the range 9–12% and for the mica-rich foliated gneisses in the range 42–60%. Ji and Salisbury (1993) have measured seismic velocities for ten high-grade, granulite and upper amphibolite-facies mylonites from Canada. They have reported S-wave anisotropy ranging from 11% in amphibolitic mylonites to 2% in granulite-facies pyroxene-bearing and tonalitic mylonites, whereas hornblende-bearing granitic mylonites were found to display intermediate S-wave anisotropy (6–7%). Saroglou et al. (2004) have tested to establish the anisotropic behavior of two types of gneissic rocks from Greece, i.e., banded gneiss A with fine-sized grains and

light-colored minerals having petrographic composition of actinolitic gneiss and typical Gneiss B with medium-sized grains and dark-colored minerals characterized as epidotitic, actinolitic schistous gneiss. They have reported that the wave velocity perpendicular to the foliation planes was approximately 40% lower than that parallel to them and also the longitudinal and transverse wave velocity was minimal when the foliation planes had an orientation of 75°. Chan and Schmitt (2015) have examined foliated granite composed mainly of quartz and feldspars a metamorphic rock from the Canadian shield in northeastern Alberta and have reported seismic anisotropy (~ 10%) explained by the preferential alignment of minerals and microcracks. Özbek et al. (2018) have studied the effect of anisotropy on strengths of several metamorphic rocks (foliated phyllite, schist, gneiss and marble–calcschist) of Menderes Massif in SW Turkey where L- and N-type Schmidt hammers were applied in the directions perpendicular and parallel to the foliation. They have observed rebound values in the direction perpendicular to the foliation slightly higher than that in the direction parallel to foliation.

Ji et al. (2015) have measured seismic anisotropy for 132 mica- or amphibole-bearing metamorphic rocks to constrain their departures from transverse isotropy. They have reported the average bulk P-wave anisotropy for the chlorite schists (12%), mica schists (12.8%), phyllites (12.8%), sillimanite mica schists (17%) and amphibole schists (12.9%). In the foliation plane, the average P-wave anisotropies were 2.4% for phyllites, 3.3% for mica schists, 4.1% for chlorite schists, 6.8% for sillimanite mica schists and 5.2% for amphibole schists. This departure from transverse isotropy was due to the presence of amphibole, sillimanite and quartz where amphibole and sillimanite developed strong crystallographic preferred orientations (CPO) with the fast *c* axes parallel to the lineation.

The metamorphic rocks are widespread in the Aegean region (e.g., Okay 1986) where the Menderes metamorphic core complex making the center piece of the study area is one of the largest core complexes of the world (e.g., van Hinsbergen 2010; Baran et al. 2010), which consists essentially of a Pan-African basement association made up of granites and gneisses and its cover sequence made up of schists, phyllites and marbles (e.g., Yılmaz 2008). In fact, there are numerous studies dealing with metamorphic rock associations in southwest Turkey (e.g., Bozkurt 2004; Rimmelé et al. 2003b, 2005; Ersoy et al. 2010). For instance, Çelik and Delaloye (2003) have reported that the metamorphic rocks (amphibolite) in the Lycian ophiolites have affinities of mid-ocean ridge basalt, island-arc tholeiite and within-plate basalt and are cut by doleritic dykes having greenschist facies mineral collection. Some well-developed lineation and foliation are observed in the metamorphic sole rocks while those dykes are deficient of such structures.

Candan et al. (2005) have informed that the Pan-African basement in the Afyon Zone comprising garnet–mica schists intruded by sodic amphibole-bearing metagabbros and leucocratic metagranites shows Barrovian-type amphibolite-facies metamorphism. The Pan-African basement is unconformably overlain by a continuous metasedimentary sequence extending from Triassic to early Paleocene.

There are issues regarding the kinematics of deformation history in the Aegean domain. For instance, Roche et al. (2016) have stated that the main structures and associated kinematics in the Cycladic Complex—CC (Fig. 11) extending under the Aegean Sea are well constrained, but the kinematics of deformation before 35 Ma, coeval with the exhumation of blueschists and eclogites of the CC, are poorly established. The seismic surface waves capable of delineating the near-surface as well as deeply buried anisotropic structures such as presented herein should greatly help resolve the poorly understood deformation history of a region under consideration. In the Aegean region, the seismic studies dealing with metamorphic rock formations unfortunately suffer from a setback. The azimuthal anisotropy besides the radial anisotropy should be highly beneficial to better decide the issues (e.g., metamorphic rocks) directly related to the tectonics of a region.

## Concluding remarks

1. The Menderes metamorphic core complex is evident by faster S-wave velocity (~ 3.5 km/s) in the middle crust (see also Çubuk-Sabuncu et al. 2017).
2. In the Aegean graben system, the horst structures are faster (~ 3.0 km/s) than the graben structures (~ 2.7 km/s).
3. In the Menderes Massif, there exist low-velocity zones (~ 3.1 km/s) in the middle crust characterized as still cooling depth sections.
4. There exist low-velocity pockets (~ 2.3 km/s) in the upper crust interpreted as still cooling depth sections.
5. The vertical structures in the middle-to-lower crust are interpreted as cooled through the correlation between the results of faster inverted S-wave velocities and negative radial anisotropy.
6. The fault zones in the region are characterized by slower S-wave velocity (~ 2.5 km/s) in the uppermost crust (see also Çubuk-Sabuncu et al. 2017).
7. The Lycian Nappes are evident by slower S-wave velocity (3.0 km/s) in the middle crust.
8. The overall seismic velocities beneath the Aegean region are abnormally slow compared with, for instance, the PREM model of Dziewonski and Anderson (1981) (see also Erduran 2009; Delph et al. 2015).
9. The Rayleigh–Love discrepancy is evident in the observed surface wave dispersion data, which is mod-



eled using the radial anisotropy having positive and negative signs where the azimuthal effects are suppressed by averaging across all azimuths.

10. The positive radial anisotropy is associated with the horizontal sill structures, while the negative radial anisotropy is considered to involve with the vertical dyke structures.
11. The dyke and sill structures are found to exist in the crust in three different formations.
12. The mineral alignments due to the magma flow in the three different formations contribute to the observed radial anisotropy.
13. If the foliation plane of metamorphic rock is horizontal, then the foliation anisotropy is added to the observed positive radial anisotropy of horizontal sill structures.
14. If the foliation plane of metamorphic rock is vertical, then the lineation anisotropy due to the crystallographic preferred orientation is added to the observed negative radial anisotropy of vertical dyke structures.
15. Large-scale structures embedded by small-scale structures (i.e., dykes and sills), mineral alignment due to the magma flow and orthorhombic system of metamorphic rocks appear to contribute to the observed radial anisotropy.
16. Aligned melt pockets due to the extensional regime and frozen fabrics of mica- and amphibole-bearing rocks formed by past ductile deformation in the crust should also contribute to the observed radial anisotropy.
17. The above structures are also associated with azimuthal anisotropy, which could be studied with more data providing efficient ray-path coverage to better determine the effect of individual anisotropic structures.

The Turkish plate and the surrounding area in general and the Aegean domain in particular as part of the Alpine orogeny are truly fascinating regions to serve as natural laboratory full of almost all the tectonic features that one would not expect to witness in such a small area (e.g., see Taymaz et al. 2007; van Hinsbergen 2010; Jolivet et al. 2013; Pourteau et al. 2015). An integrated study designed in an interdisciplinary fashion (i.e., seismology, gravity, magnetism, magnetotellurics, geothermal, geochemistry, volcanology, structural geology, geodetic data) should certainly prove beneficial to better understand the geodynamic history of this interesting region.

**Acknowledgements** We would like to thank the anonymous reviewers for critically reviewing the manuscript. KOERI (Kandilli Observatory and Earthquake Research Institute) is gratefully acknowledged for the broadband seismograms. AFAD (Disaster and Emergency Management Presidency) is thanked for providing the accelerogram recordings. We gratefully acknowledge the use of Generic Mapping Tool (GMT) in

several figure illustrations. Accelerogram instrument distributors kindly provided the pole-zero files.

## Compliance with ethical standards

**Conflict of interest** On behalf of all authors, the corresponding author states that there is no conflict of interest.

## References

- AFAD (2017) Strong ground motion database of Türkiye (TR-NSMN). Disaster and Emergency Management Presidency, Ankara
- Agius MR, Lebedev S (2014) Shear-velocity structure, radial anisotropy and dynamics of the Tibetan crust. *Geophys J Int* 199:1395–1415
- Agostini S, Doglioni C, Innocenti F, Manetti P, Tonarini S (2010) On the geodynamics of the Aegean rift. *Tectonophysics* 488:7–21
- Akay E, İşintek I, Erdoğan B, Hasözbeke A (2011) Stratigraphy of the Afyon Zone around Emet (Kütahya, NW Anatolia) and geochemical characteristics of the Triassic volcanism along the northern Menderes Massif. *Neues Jahrbuch Für Mineralogie—Abhandlungen* 188:297–316
- Akbaş B, Akdeniz N, Aksay A, Altun İ, Balcı V, Bilginer E, Bilgiç T, Duru M, Ercan T, Gedik İ, Günay Y, Güven İH, Hakyemez HY, Konak N, Papak İ, Pehlivan Ş, Sevin M, Şenel M, Tarhan N, Turhan N, Türkecan A, Ulu Ü, Uğuz MF, Yurtsever A et al (2017) Geological map of Turkey. MTA (General Directorate of Mineral Research and Exploration of Turkey) Publications, Ankara
- Altner D, Koçyiğit A, Farinacci A, Nicosia U, Conti MA (1991) Jurassic, Lower Cretaceous stratigraphy and paleogeographic evolution of the southern part of the northwestern Anatolia. *Geol Rom* 18:13–80
- Altunkaynak S (2007) Collision-driven slab breakoff magmatism in northwestern Anatolia, Turkey. *J Geol* 115:63–82
- Altunkaynak Ş, Dilek Y, Genç CŞ, Sunal G, Gertisser R, Furnes H, Foland KA, Yang J (2012) Spatial, temporal and geochemical evolution of Oligo–Miocene granitoid magmatism in western Anatolia, Turkey. *Gondwana Res* 21:961–986
- Anderson DL (1961) Elastic wave propagation in layered anisotropic media. *J Geophys Res* 66:2953–2963
- Anderson DL (1989) *Theory of the Earth*. Blackwell Scientific Publications, Oxford
- Arslan A, Güngör T, Erdoğan B, Passchier CW (2013) Tectonic transport directions of the Lycian nappes in southwest Turkey constrained by kinematic indicators. *J Asian Earth Sci* 64:198–209
- Aydemir A (2009) Tectonic investigation of Central Anatolia, Turkey, using geophysical data. *J Appl Geophys* 68:321–334
- Backus GE (1962) Long-wave anisotropy produced by horizontal layering. *J Geophys Res* 66:4427–4440
- Bakırcı T, Yoshizawa K, Özer MF (2012) Three-dimensional S-wave structure of the upper mantle beneath Turkey from surface wave tomography. *Geophys J Int* 190:1058–1076
- Baran Z, Dilek Y, Kadioglu YK (2010) Geology and geochemistry of the synextensional Salihli granitoid in the Menderes core complex, western Anatolia, Turkey. *Int Geol Rev* 52:336–368
- Bastow ID, Pilidou S, Kendall J-M, Stuart GW (2010) Melt-induced seismic anisotropy and magma assisted rifting in Ethiopia: evidence from surface waves. *Geochem Geophys Geosyst* 11:Q0AB05. <https://doi.org/10.1029/2010GC003036>
- Behr Y, Townend J, Bannister S, Savage MK (2011) Crustal shear wave tomography of the Taupo Volcanic Zone, New Zealand,

- via ambient noise correlation between multiple three-component networks. *Geochem Geophys Geosyst* 12:Q03015. <https://doi.org/10.1029/2010GC003385>
- Beucler É, Stutzmann É, Montagner JP (2003) Surface wave higher-mode phase velocity measurements using a roller-coaster-type algorithm. *Geophys J Int* 155:289–307
- Bingöl E, Akyürek B, Korkmaz B (1975) Geology of the Biga peninsula and some characteristics of the Karakaya blocky series. In: Proceedings of the Congress of Earth Sciences on the Occasion of the 50th Anniversary of the Turkish Republic. General Directorate of Mineral Research and Exploration of Turkey (MTA), Ankara, pp 71–77
- Biryol CB, Beck SL, Zandt G, Özacar AA (2011) Segmented African lithosphere beneath the Anatolian region inferred from teleseismic P-wave tomography. *Geophys J Int* 184:1037–1057
- Bonev N, Beccaletto L (2007) From syn- to post-orogenic Tertiary extension in the north Aegean region: constraints on the kinematics in the eastern Rhodope–Thrace, Bulgaria–Greece and the Biga Peninsula, NW Turkey. *Geol Soc Lond Spec Publ* 291:113–142. <https://doi.org/10.1144/SP291.6>
- Bozkurt E (2004) Granitoid rocks of the southern Menderes Massif (Southwest Turkey): field evidence for Tertiary magmatism in an extensional shear zone. *Int J Earth Sci* 93:52–71
- Bozkurt E, Oberhänsli R (2001) Menderes Massif (Western Turkey): structural, metamorphic and magmatic evolution—a synthesis. *Int J Earth Sci* 89:679–708
- Brocher TM (2005) Empirical relations between elastic wavespeeds and density in the Earth's crust. *Bull Seismol Soc Am* 95:2081–2092
- Burchardt S (2008) New insights into the mechanics of sill emplacement provided by field observations of the Njardvik Sill, Northeast Iceland. *J Volcanol Geotherm Res* 173:280–288
- Çakır Ö, Erduran M (2001) Effect of earth structure and source time function on inversion of single station regional surface waves for rupture mechanism and focal depth. *J Balk Geophys Soc* 4:69–90
- Cambaz MD, Karabulut H (2010) Love-wave group velocity maps of Turkey and surrounding regions. *Geophys J Int* 181:502–520
- Candan O, Dora OÖ, Oberhänsli R, Çetinkaplan M, Partzsch JH, Warkus FC, Dürr S (2001) Pan-African high-pressure metamorphism in the Precambrian basement of the Menderes Massif, western Anatolia, Turkey. *Int J Earth Sci* 89:793–811
- Candan O, Çetinkaplan M, Oberhänsli R, Rimmelé G, Akal C (2005) Alpine high-P/low-T metamorphism of the Afyon Zone and implications for the metamorphic evolution of Western Anatolia, Turkey. *Lithos* 84:102–124
- Çelik ÖF, Delaloye M (2003) Origin of metamorphic sole rocks and their post kinematic mafic dyke swarms in the Antalya and Lycian ophiolites, SW Turkey. *Geol J* 38:235–256
- Chan J, Schmitt DR (2015) Elastic anisotropy of a metamorphic rock sample of the Canadian Shield in Northeastern Alberta. *Rock Mech Rock Eng* 48:1369–1385
- Cho K-H, Herrmann RB, Ammon CJ, Lee K (2007) Imaging the upper crust of the Korean Peninsula by surface-wave tomography. *Bull Seism Soc Am* 97:198–207
- Cho K-H, Chen H-W, Kang I-B, Lee S-H (2011) Crust and upper mantle structures of the region between Korea and Taiwan by surface wave dispersion study. *Geosci J* 15:71–81. <https://doi.org/10.1007/s12303-011-0009-9>
- Çınar H, Alkan H (2016) Crustal S-wave structure beneath Eastern Black Sea Region revealed by Rayleigh-wave group velocities. *J Asian Earth Sci* 115:273–284
- Collins AS, Robertson AHF (1997) Lycian mélange, southwest Turkey: an emplaced Cretaceous accretionary complex. *Geology* 25:255–258
- Crampin S (1984) Effective anisotropic elastic constants for wave propagation through cracked solids. *Geophys J R Astron Soc* 76:135–145
- Çubuk-Sabuncu Y, Taymaz T, Fichtner A (2017) 3-D crustal velocity structure of western Turkey: constraints from full-waveform tomography. *Phys Earth Planet Inter* 270:90–112
- Delaloye M, Bingöl E (2000) Granitoids from western and northwestern Anatolia: geochemistry and modeling of geodynamic evolution. *Int Geol Rev* 42:241–268
- Delph JR, Biryol CB, Beck SL, Zandt G, Ward KM (2015) Shear wave velocity structure of the Anatolian Plate: anomalously slow crust in southwestern Turkey. *Geophys J Int* 202:261–276
- Demirtaslı E, Turhan N, Bilgin AZ, Selim M (1984) Geology of the Bolkar Mountains. In: Tekeli O, Göncüoğlu MC (eds) *Geology of the Taurus Belt, Proceedings of the International Symposium, Ankara-Turkey*, pp 125–141
- Dias RC, Julià J, Schimmel M (2015) Rayleigh-wave, group-velocity tomography of the Borborema Province, NE Brazil, from ambient seismic noise. *Pure appl Geophys* 172:1429–1449
- Dilek Y, Altunkaynak Ş (2009) Geochemical and temporal evolution of Cenozoic magmatism in western Turkey: mantle response to collision, slab break-off, and lithospheric tearing in an orogenic belt. *Geol Soc Lond Spec Publ* 311:213–233
- Dilek Y, Altunkaynak Ş (2010) Geochemistry of Neogene—quaternary alkaline volcanism in western Anatolia, Turkey, and implications for the Aegean mantle. *Int Geol Rev* 52:631–655
- Dilek Y, Sandvol E (2009) Seismic structure, crustal architecture and tectonic evolution of the Anatolian-African plate boundary and the Cenozoic Orogenic Belts in the Eastern Mediterranean Region. *Geol Soc Lond Spec Publ* 327:127–160
- Dilek Y, Altunkaynak Ş, Öner Z (2009) Syn-extensional granitoids in the Menderes core complex, and the late Cenozoic extensional tectonics of the Aegean Province. In: Ring U, Wernicke B (eds) *Extending a continent: architecture, rheology and heat budget, vol 321*. Geological Society of London (Special Publications), London, pp 197–223
- Dogru F, Pamukcu O, Gonenc T, Yildiz H (2018) Lithospheric structure of western Anatolia and the Aegean Sea using GOCE-based gravity field models. *Bollettino di Geofisica Teorica ed Applicata* 59:135–160
- Dziewonski AM, Anderson DL (1981) Preliminary reference Earth model. *Phys Earth Planet Inter* 25:297–356
- Dziewonski AM, Hales AL (1972) Numerical analysis of dispersed seismic waves. In: *Methods in computational physics: advances in research and applications, vol 11*, pp 39–85
- Dziewonski A, Bloch S, Landisman M (1969) A technique for the analysis of transient seismic signals. *Bull Seismol Soc Am* 59:427–444
- Dziewonski AM, Chou T-A, Woodhouse JH (1981) Determination of earthquake source parameters from waveform data for studies of global and regional seismicity. *J Geophys Res* 86:2825–2852. <https://doi.org/10.1029/JB086iB04p02825>
- Ekström G, Nettles M, Dziewonski AM (2012) The global CMT project 2004–2010: centroid-moment tensors for 13,017 earthquakes. *Phys Earth Planet Inter* 200–201:1–9. <https://doi.org/10.1016/j.pepi.2012.04.002>
- Emre Ö, Duman TY, Özalp S, Elmacı H, Olgun Ş, Şaroğlu F (2013) Active faults map of Turkey (scale: 1/1.125.000). MTA (General Directorate of Mineral Research and Exploration of Turkey) Publications, Ankara
- Endrun B, Meier T, Lebedev S, Bohnhoff M, Stavrakakis G, Harjes H-P (2008) S velocity structure and radial anisotropy in the Aegean region from surface wave dispersion. *Geophys J Int* 174:593–616
- Erduran M (2009) Teleseismic inversion of crustal S-wave velocities beneath the Isparta Station. *J Geodyn* 47:225–236
- Erduran M, Endrun B, Meier T (2008) Continental versus oceanic lithosphere beneath the eastern Mediterranean Sea—implications from Rayleigh wave dispersion measurements. *Tectonophysics* 457:42–52

- Ersoy YE, Helvacı C, Sözbilir H (2010) Tectono-stratigraphic evolution of the NE–SW-trending superimposed Selendi basin: implications for late Cenozoic crustal extension in Western Anatolia, Turkey. *Tectonophysics* 488:210–232
- Faccenda M, Capitanio FA (2013) Seismic anisotropy around subduction zones: insights from three dimensional modeling of upper mantle deformation and SKS splitting calculations. *Geochem Geophys Geosyst* 14:1–20. <https://doi.org/10.1029/2012GC004451>
- Feng M, Assumpção M, Van der Lee S (2004) Group-velocity tomography and lithospheric S-velocity structure of the South American continent. *Phys Earth Planet Inter* 147:315–331
- Fichtner A, Villaseñor A (2015) Crust and upper mantle of the western Mediterranean—constraints from full-waveform inversion. *Earth Planet Sci Lett* 428:52–62
- Friederich W (2003) The S-velocity structure of the East Asian mantle from inversion of shear and surface waveforms. *Geophys J Int* 153:88–102
- Fu YV, Li A (2015) Crustal shear wave velocity and radial anisotropy beneath the Rio Grande rift from ambient noise tomography. *J Geophys Res* 120:1005–1019. <https://doi.org/10.1002/2014JB011602>
- GEOSIG (2012) Geosig, AC-73 triaxial force balance accelerometer. [http://www.seismicsystems.net/images/pdfs/GS\\_AC-73\\_Leaflet\\_V12.pdf](http://www.seismicsystems.net/images/pdfs/GS_AC-73_Leaflet_V12.pdf). Accessed 24 July 2017
- Gessner K, Gallardo LA, Markwitz V, Ring U, Thomson SN (2013) What caused the denudation of the Menderes Massif: review of crustal evolution, lithosphere structure, and dynamic topography in southwest Turkey. *Gondwana Res* 24:243–274
- Gessner K, Gallardo LA, Wedin F, Sener K (2016) Crustal structure of the northern Menderes Massif, western Turkey, imaged by joint gravity and magnetic inversion. *Int J Earth Sci* 105:2133–2148
- Gessner K, Markwitz V, Güngör T (2017) Crustal fluid flow in hot continental extension: tectonic framework of geothermal areas and mineral deposits in western Anatolia. *Geol Soc Lond Spec Publ* 453:289–311
- Godfrey HJ, Fry B, Savage MK (2017) Shear-wave velocity structure of the Tongariro Volcanic Centre, New Zealand: fast Rayleigh and slow Love waves indicate strong shallow anisotropy. *J Volcanol Geotherm Res* 336:33–50
- Gök R, Mellors RJ, Sandvol E, Pasyanos M, Hauk T, Takedatsu R, Yetirmishli G, Teoman U, Turkelli N, Godoladze T, Javakishviri Z (2011) Lithospheric velocity structure of the Anatolian plateau-Caucasus-Caspian region. *J Geophys Res* 116:B05303. <https://doi.org/10.1029/2009JB000837>
- Görür N, Tüysüz O, Şengör AMC (1998) Tectonic evolution of the Central Anatolian basins. *Int Geol Rev* 40:832–850
- Govers R, Fichtner A (2016) Signature of slab fragmentation beneath Anatolia from full-waveform tomography. *Earth Planet Sci Lett* 450:10–19
- GURALP (2013) Guralp systems, CMG-5TD digital accelerometer, operator's guide. <https://www.guralp.com/documents/MAN-050-0005.pdf>. Accessed 20 July 2017
- Gursoy H, Piper JDA, Tatar O, Mesci L (1998) Paleomagnetic study of the Karaman and Karapınar volcanic complexes, Central Turkey: neotectonic rotation in the south-central sector of the Anatolian Block. *Tectonophysics* 299:191–211
- Gürsu S, Göncüoğlu MC, Bayhan H (2004) Geology and geochemistry of the pre-early Cambrian rocks in the Sandıklı area: implications for the Pan-African evolution of NW Gondwanaland. *Gondwana Res* 7:923–935
- Hacker BR, Ritzwoller MH, Xie J (2014) Partially melted, micabearing crust in Central Tibet. *Tectonics* 33:1408–1424. <https://doi.org/10.1002/2014TC003545>
- Hall J, Aksu AE, Elitez I, Yalıtırak C, Çiğçi G (2014a) The Fethiye–Burdur Fault Zone: a component of upper plate extension of the subduction transform edge propagator fault linking Hellenic and Cyprus Arcs, Eastern Mediterranean. *Tectonophysics* 635:80–99
- Hall J, Aksu AE, King H, Gogacz A, Yalıtırak C, Çiğçi G (2014b) Miocene—recent evolution of the western Antalya Basin and its linkage with the Isparta Angle, eastern Mediterranean. *Mar Geol* 349:1–23
- Harmon N, Rychert CA (2015) Seismic imaging of deep crustal melt sills beneath Costa Rica suggests a method for the formation of the Archean continental crust. *Earth Planet Sci Lett* 430:140–148
- Haskell NA (1953) The dispersion of surface waves on multilayered media. *Bull. Seism. Soc. Am.* 43:17–34
- Heineke C, Niedermann S, Hetzel R, Akal C (2016) Surface exposure dating of Holocene basalt flows and cinder cones in the Kula volcanic field (Western Turkey) using cosmogenic  $^3\text{He}$  and  $^{10}\text{Be}$ . *Quat Geochronol* 34:81–91
- Herrin E, Goforth T (1977) Phase-matched filters: application to the study of Rayleigh waves. *Bull Seismol Soc Am* 67:1259–1275
- Herrmann RB (1973) Some aspects of band-pass filtering of surface waves. *Bull Seismol Soc Am* 63:663–671
- Herrmann RB (2002) Computer programs in seismology, version 3.30. St. Louis University, Missouri
- Hetzel R, Ring U, Akal C, Troesch M (1995) Miocene NNE-directed extensional unroofing in the Menderes Massif, southwestern Turkey. *J Geol Soc Lond* 152:639–654
- Hier-Majumder S, Drombosky T (2015) Development of anisotropic contiguity in deforming partially molten aggregates: 2. Implications for the lithosphere–asthenosphere boundary. *J Geophys Res Solid Earth* 120:764–777. <https://doi.org/10.1002/2014JB011454>
- İlkişik OM (1995) Regional heat flow in western Anatolia using silica temperature estimates from thermal springs. *Tectonophysics* 244:175–184
- İşık V, Tekeli O (2001) Late orogenic crustal extension in the northern Menderes massif (western Turkey): evidence for metamorphic core complex formation. *Int J Earth Sci* 89:757–765
- Janssen C, Bohnhoff M, Vapnik Y, Görgün E, Bulut F, Plessen B, Pohl D, Aktar M, Okay AI, Dresen G (2009) Tectonic evolution of the Ganos segment of the North Anatolian Fault (NW Turkey). *J Struct Geol* 31:11–28
- Jaxybulatov K, Shapiro NM, Koulakov I, Mordret A, Landès M, Sens-Schönfelder C (2014) A large magmatic sill complex beneath the Toba caldera. *Science* 346:617–619
- Ji S, Salisbury MH (1993) Shear-wave velocities, anisotropy and splitting in high-grade mylonites. *Tectonophysics* 221:453–473
- Ji S, Shao T, Michibayashi K, Oya S, Satsukawa T, Wang Q, Zhao W, Salisbury MH (2015) Magnitude and symmetry of seismic anisotropy in mica- and amphibole-bearing metamorphic rocks and implications for tectonic interpretation of seismic data from the southeast Tibetan Plateau. *J Geophys Res Solid Earth* 120:6404–6430. <https://doi.org/10.1002/2015JB012209>
- Jin G, Gaherty JB (2015) Surface wave phase-velocity tomography based on multichannel cross-correlation. *Geophys J Int* 201:1383–1398
- Johnson LR, Wenk HR (1974) Anisotropy of physical properties in metamorphic rocks. *Tectonophysics* 23:79–98
- Jolivet L, Brun J-P (2010) Cenozoic geodynamic evolution of the Aegean. *Int J Earth Sci* 99:109–138
- Jolivet L, Faccenna C, Huet B, Labrousse L, Le Pourhiet L, Lacombe O, Lecomte E, Burov E, Denèle Y, Brun J-P, Philippon M, Paul A, Salaün G, Karabulut H, Piromallo C, Monié P, Gueydan F, Okay AI, Oberhänsli R, Poureteau A, Augier R, Gadenne L, Driussi O (2013) Aegean tectonics: strain localisation, slab tearing and trench retreat. *Tectonophysics* 597–598:1–33
- Julià J, Ammon CJ, Herrmann RB, Correig AM (2000) Joint inversion of receiver function and surface wave dispersion observations. *Geophys J Int* 143:99–112



- Karagianni EE, Papazachos CB (2007) Shear velocity structure in the Aegean region obtained by joint inversion of Rayleigh and Love waves. *Geol Soc Lond Spec Publ* 291:159–181
- Karagianni EE, Papazachos CB, Panagiotopoulos DG, Suhadolc P, Vuan A, Panza GF (2005) Shear velocity structure in the Aegean area obtained by inversion of Rayleigh waves. *Geophys J Int* 160:127–143
- Karaoğlu Ö, Helvacı C (2014) Isotopic evidence for a transition from subduction to slab-tear related volcanism in western Anatolia, Turkey. *Lithos* 192:226–239
- Karato S, Jung H, Katayama I, Skemer P (2008) Geodynamic significance of seismic anisotropy of the upper mantle: new insights from laboratory studies. *Annu Rev Earth Planet Sci* 36:59–95
- Kaya C (2010) Deep crustal structure of northwestern part of Turkey. *Tectonophysics* 489:227–239
- Kaymakci N, Özçelik Y, White SH, van Dijk PM (2009) Tectono-stratigraphy of the Çankiri Basin: late Cretaceous to early Miocene evolution of the Neotethyan suture zone in Turkey. In: van Hinsbergen DJJ, Edwards MA, Govers R (eds) *Collision and collapse at the Africa–Arabia–Eurasia subduction zone*, vol 311. Geological Society of London (Special Publication), London, pp 67–106
- Ketin I (1966) Tectonic units of Anatolia (Asia Minor). *Miner Resour Explor Inst Turk (MTA) Bull* 66:22–34
- Ko B, Jung H (2015) Crystal preferred orientation of an amphibole experimentally deformed by simple shear. *Nat Commun* 6:6586. <https://doi.org/10.1038/ncomms7586>
- Koçyiğit A, Özacar AA (2003) Extensional neotectonic regime through the NE edge of the Outer Isparta Angle, SW Turkey: new field and seismic data. *Turk J Earth Sci* 12:67–90
- Le Pichon X, Angelier J (1979) The Hellenic arc and trench system: a key to the neotectonic evolution of the eastern Mediterranean area. *Tectonophysics* 60:1–42
- Lebedev S, Adam JM-C, Meier T (2013) Mapping the Moho with seismic surface waves: a review, resolution analysis, and recommended inversion strategies. *Tectonophysics* 609:377–394
- Lees JM (2007) Seismic tomography of magmatic systems. *J Volcanol Geotherm Res* 167:37–56
- Levshin A, Ratnikova L, Berger J (1992) Peculiarities of surface-wave propagation across central Eurasia. *Bull Seismol Soc Am* 82:2464–2493
- Levshin AL, Ritzwoller MH, Resovsky JS (1999) Source effects on surface wave group travel times and group velocity maps. *Phys Earth Planet Inter* 115:293–312
- Li A, Forsyth DW, Fischer KM (2003) Shear velocity structure and azimuthal anisotropy beneath eastern North America from Rayleigh wave inversion. *J Geophys Res* 108(B8):2362. <https://doi.org/10.1029/2002JB002259>
- Licciardia A, Eken T, Taymaz T, Agostinetti NP, Yolsal-Çevikbilen S (2018) Seismic anisotropy in central North Anatolian Fault Zone and its implications on crustal deformation. *Phys Earth Planet Inter* 277:99–112
- Lin FC, Moschetti MP, Ritzwoller MH (2008) Surface wave tomography of the western United States from ambient seismic noise: Rayleigh and Love wave phase velocity maps. *Geophys J Int* 173:281–298
- Long MD, Becker TW (2010) Mantle dynamics and seismic anisotropy. *Earth Planet Sci Lett* 297:341–354
- Mahan K (2006) Retrograde mica in deep crustal granulites: implications for crustal seismic anisotropy. *Geophys Res Lett* 33:L24301. <https://doi.org/10.1029/2006GL028130>
- McClusky S, Balassanian S, Barka A, Demir C, Ergintav S, Georgiev I, Gurkan O, Hamburger M, Hurst K, Kahle HG, Kastens K, Kekelidze G, King R, Kotzev V, Lenk O, Mahmoud S, Mishin A, Nadariya M, Ouzounis A, Veis G (2000) Global Positioning System constraints on plate kinematics and dynamics in the eastern Mediterranean and Caucasus. *J Geophys Res* 105:5695–5719
- McMechan GA, Yedlin MJ (1981) Analysis of dispersive waves by wave field transformation. *Geophysics* 46:869–874
- Meier T, Dietrich K, Stöckhert B, Harjes H-P (2004) One-dimensional models of shear wave velocity for the eastern Mediterranean obtained from the inversion of Rayleigh wave phase velocities and tectonic implications. *Geophys J Int* 156:45–58
- Montagner JP (2007) Deep Earth structure—upper mantle structure: global isotropic and anisotropic elastic tomography. In: Dziewon-ski AM, Romanowicz B (eds) *Treatise on geophysics*, volume 1: seismology and structure of the Earth. Elsevier, Amsterdam, pp 559–590
- Montagner J-P, Anderson DL (1989) Petrological constraints on seismic anisotropy. *Phys Earth Planet Inter* 54:82–105. [https://doi.org/10.1016/0031-9201\(89\)90189-1](https://doi.org/10.1016/0031-9201(89)90189-1)
- Montagner J-P, Nataf H-C (1986) A simple method for inverting the azimuthal anisotropy of surface waves. *J Geophys Res* 91:511–520. <https://doi.org/10.1029/JB091iB01p00511>
- Mordret A, Rivet D, Landès M, Shapiro NM (2015) Three-dimensional shear velocity anisotropic model of Piton de la Fournaise Volcano (La Réunion Island) from ambient seismic noise. *J Geophys Res Solid Earth* 120:406–427. <https://doi.org/10.1002/2014JB011654>
- Moschetti MP, Ritzwoller MH, Shapiro NM (2007) Surface wave tomography of the western United States from ambient seismic noise: Rayleigh wave group velocity maps. *Geochem Geophys Geosyst* 8:Q08010. <https://doi.org/10.1029/2007GC001655>
- Mottaghi AA, Rezapour M, Korn M (2013) Ambient noise surface wave tomography of the Iranian Plateau. *Geophys J Int* 193:452–462
- MTA (2002) Geological map of Turkey (scale:1/500000). MTA (General Directorate of Mineral Research and Exploration of Turkey) Publications, Ankara
- Nolet G (1990) Partitioned waveform inversion and two-dimensional structure under the network of autonomously recording seismographs. *J Geophys Res* 95(B6):8499–8512
- Oberhänsli R, Candan O, Dora ÖO, Dürr SH (1997) Eclogites within the Menderes Massif/Western Turkey. *Lithos* 41:135–150
- Oberhänsli R, Partzsch J, Candan O, Cetinkaplan M (2001) First occurrence of Fe–Mg–carpholite documenting a high-pressure metamorphism in metasediments of the Lycian Nappes, SW Turkey. *Int J Earth Sci* 89:867–873
- Obrebski M, Kiselev S, Vinnik L, Montagner J-P (2010) Anisotropic stratification beneath Africa from joint inversion of SKS and P receiver functions. *J Geophys Res* 115:1–15. <https://doi.org/10.1029/2009JB006923>
- Okay AI (1986) High-pressure/low-temperature metamorphic rocks of Turkey. *Geol Soc Am Mem* 164:333–347
- Okay AI (1989) Geology of the Menderes Massif and the Lycian Nappes south of Denizli, western Taurides. *Miner Resour Explor Bull* 109:37–51
- Okay AI (2001) Stratigraphic and metamorphic inversions in the central Menderes Massif: a new structural model. *Int J Earth Sci* 89:709–727
- Okay AI (2008) Geology of Turkey: a synopsis. *Anschmitt* 21:19–42
- Okay AI, Satır M (2000) Coeval plutonism and metamorphism in a latest Oligocene metamorphic core complex in northwest Turkey. *Geol Mag* 137:495–516
- Okay AI, Tüysüz O (1999) Tethyan sutures of northern Turkey. In: Durand B, Jolivet L, Horváth D, Séranne M (eds) *The Mediterranean basins: tertiary extension within the Alpine Orogen*, vol 156. Geological Society of London (Special Publication), London, pp 475–515
- Okay AI, Siyako M, Bürkan KA (1991) Geology and tectonic evolution of the Biga Peninsula, northwest Turkey. *Bull Tech Univ Istanbul* 44:191–256



- Okay AI, İşintek İ, Altınır D, Özkan-Altınır S, Okay N (2012) An olistostrome–mélange belt formed along a suture: Bornova Flysch zone, western Turkey. *Tectonophysics* 568–569:282–295
- Özbakır AD, Govers R, Wortel R (2017) Active faults in the Anatolian–Aegean plate boundary region with Nubia. *Turk J Earth Sci* 26:30–56
- Özbek A, Gül M, Karacan K, Alca Ö (2018) Anisotropy effect on strengths of metamorphic rocks. *J Rock Mech Geotech Eng* 10:164–175
- Ozer C, Gok E, Polat O (2018) Three-dimensional seismic velocity structure of the Aegean Region of Turkey from local earthquake tomography. *Ann Geophys* 61, 1:SE111. <https://doi.org/10.4401/ag-7543>
- Özgül N (1984) Stratigraphy and tectonic evolution of the Central Taurides. In: Tekeli O, Göncüoğlu MC (eds) *Geology of the Taurus Belt, Proceedings of the International Symposium on the Geology of the Taurus Belt, 1983, Ankara-Turkey*, Mineral Research and Exploration Institute of Turkey, Ankara, pp 77–90
- Parsons T, Sleep NH, Thompson GA (1992) Host rock rheology controls on the emplacement of tabular intrusions: implications for underplating of extending crust. *Tectonics* 11:1348–1356
- Pearce FD, Rondenay S, Sachpazi M, Charalampakis M, Royden LH (2012) Seismic investigation of the transition from continental to oceanic subduction along the western Hellenic Subduction Zone. *J Geophys Res* 117:B07306. <https://doi.org/10.1029/2011JB009023>
- Petford N, Clemens JC, Vigneresse JL (1997) Application of information theory to the formation of granitic rocks. In: Bouchez JL, Hutton DHW, Stephens WE (eds) *Granite: from segregation of melt to emplacement fabrics*. Kluwer, Dordrecht, pp 3–10
- Piomallo C, Morelli A (2003) P wave tomography of the mantle under the Alpine-Mediterranean area. *J Geophys Res* 108:2065. <https://doi.org/10.1029/2002JB001757>
- Polat G, Özel NM, Koulakov I (2016) Investigating P- and S-wave velocity structure beneath the Marmara region (Turkey) and the surrounding area from local earthquake tomography. *Earth Planets Space* 68:132. <https://doi.org/10.1186/s40623-016-0503-4>
- Portner DE, Delph JR, Biryol CB, Beck SL, Zandt G, Özacar AA, Sandvol E, Türkelli N (2018) Subduction termination through progressive slab deformation across Eastern Mediterranean subduction zones from updated P-wave tomography beneath Anatolia. *Geosphere* 14:907–925
- Pourteau A, Oberhänsli R, Candan O, Barrier E, Vrielynck B (2015) Neotethyan closure history of western Anatolia: a geodynamic discussion. *Int J Earth Sci* 105:203–224
- Purvis M, Robertson A (2005) Sedimentation of the Neogene–Recent Alaşehir (Gediz) continental graben system used to test alternative tectonic models for western (Aegean) Turkey. *Sediment Geol* 173:373–408
- Rawlinson N, Sambridge M (2003) Seismic traveltimes tomography of the crust and lithosphere. *Adv Geophys* 46:81–198
- Rawlinson N, Sambridge M (2004a) Multiple reflection and transmission phases in complex layered media using a multistage fast marching method. *Geophysics* 69:1338–1350
- Rawlinson N, Sambridge M (2004b) Wavefront evolution in strongly heterogeneous layered media using the fast marching method. *Geophys J Int* 156:631–647
- Rawlinson N, Sambridge M (2005) The fast marching method: an effective tool for tomographic imaging and tracking multiple phases in complex layered media. *Explor Geophys* 36:341–350
- Rimmelé G, Jolivet L, Oberhänsli R, Goffé B (2003a) Deformation history of the high-pressure Lycian Nappes and implications for tectonic evolution of SW Turkey. *Tectonics* 22:1007. <https://doi.org/10.1029/2001TC901041>
- Rimmelé G, Oberhänsli R, Goffé B, Jolivet L, Candan O, Çetinkaplan M (2003b) First evidence of high-pressure metamorphism in the “Cover Series” of the southern Menderes Massif. Tectonic and metamorphic implications for the evolution of SW Turkey. *Lithos* 71:19–46
- Rimmelé G, Parra T, Goffé B, Oberhänsli R, Jolivet L, Candan O (2005) Exhumation paths of high-pressure–low-temperature metamorphic rocks from the Lycian Nappes and the Menderes Massif (SW Turkey): a multi-equilibrium approach. *J Petrol* 46:641–669
- Ring U, Layer PW (2003) High-pressure metamorphism in the Aegean, eastern Mediterranean: underplating and exhumation from the Late Cretaceous until the Miocene to Recent above the retreating Hellenic subduction zone. *Tectonics* 22:1022. <https://doi.org/10.1029/2001TC001350>
- Ring U, Johnson C, Hetzel R, Gessner K (2003) Tectonic denudation of a Late Cretaceous–Tertiary collisional belt: regionally symmetric cooling patterns and their relation to extensional faults in the Anatolide belt of western Turkey. *Geol Mag* 140:421–441
- Ritzwoller MH, Levshin AL (1998) Eurasian surface wave tomography: group velocities. *J Geophys Res* 103(B3):4839–4878
- Roche V, Laurent V, Cardello GL, Jolivet L, Scaillet S (2016) Anatomy of the Cycladic Blueschist Unit on Sifnos Island (Cyclades, Greece). *J Geodyn* 97:62–87
- Salaün G, Pedersen H, Paul A, Farra V, Karabulut H, Hatzfeld D, Papazachos C, Childs DM, Pequegnat C, The SIMBAAD Team (2012) High-resolution surface wave tomography of the Aegean–Anatolia region: constraints on upper mantle structure. *Geophys J Int* 190:406–420
- SARA (2017) Sara electronics instruments, SA10 force balance accelerometer. [http://www.sara.pg.it/documents/commercial/SA10\\_DATASHEET\\_ENG.PDF](http://www.sara.pg.it/documents/commercial/SA10_DATASHEET_ENG.PDF). Accessed 26 July 2017
- Saroglou H, Marinos P, Tsiambaos G (2004) The anisotropic nature of selected metamorphic rocks from Greece. *S Afr Inst Min Metall* 104:217–222
- Schoenberg M, Douma J (1988) Elastic wave propagation in media with parallel fractures and aligned cracks. *Geophys Prospect* 36:571–590
- Şengör AMC (1979a) Mid-Mesozoic closure of Permo-Triassic Tethys and its implications. *Nature* 279:590–593
- Şengör AMC (1979b) The north Anatolian transform fault: its age, offset and tectonic significance. *J Geol Soc Lond* 136:269–282
- Şengör AMC (1987) Tectonics of the Tethysides: orogenic collage development in a collisional setting. *Annu Rev Earth Planet Sci* 15:213–244
- Şengör AMC, Yılmaz Y (1981) Tethyan evolution of Turkey: a plate tectonic approach. *Tectonophysics* 75:181–241
- Şengör AMC, Satır M, Akkök R (1984) Timing of tectonic events in the Menderes Massif, Western Turkey: implications for tectonic evolution and evidence for Pan-African basement in Turkey. *Tectonics* 3:697–707
- Seyitoğlu G, Işık V, Çemen I (2004) Complete Tertiary exhumation history of the Menderes massif, western Turkey: an alternative working hypothesis. *Terra Nova* 16:358–364
- Shapiro NM, Ritzwoller MH (2002) Monte-Carlo inversion for a global shear-velocity model of the crust and upper mantle. *Geophys J Int* 151:88–105
- Shen W, Ritzwoller MH, Schulte-Pelkum V (2013) A 3-D model of the crust and uppermost mantle beneath the Central and Western US by joint inversion of receiver functions and surface wave dispersion. *J Geophys Res Solid Earth* 118:262–276. <https://doi.org/10.1029/2012JB009602>
- Soomro RA, Weidle C, Cristiano L, Lebedev S, Meier T, PASSEQ Working Group (2016) Phase velocities of Rayleigh and Love waves in central and northern Europe from automated, broadband, interstation measurements. *Geophys J Int* 204:517–534

- Spica Z, Perton M, Legrand D (2017) Anatomy of the Colima volcano magmatic system, Mexico. *Earth Planet Sci Lett* 459:1–13
- Stampfli GM (2000) Tethyan oceans. In: Bozkurt E, Winchester JA, Piper JDA (eds) *Tectonics and magmatism in Turkey and the surrounding area*, vol 173. Geological Society of London (Special Publication), London, pp 1–23
- Tank SB, Özyayın S, Karas M (2018) Revealing the electrical properties of a gneiss dome using three-dimensional magnetotellurics: burial and exhumation cycles associated with faulting in Central Anatolia, Turkey. *Phys Earth Planet Inter* 283:26–37
- Tarantola A (1987) *Inverse problem theory*. Elsevier Science Company Inc., Amsterdam, pp 187–255
- Tarantola A, Nercessian A (1984) Three-dimensional inversion without blocks. *Geophys J R Astron Soc* 76:299–306
- Taymaz T, Yılmaz Y, Dilek Y (eds) (2007) *The geodynamics of the Aegean and Anatolia: introduction*, vol 291. Geological Society of London (Special Publications), London, pp 1–16
- Tezel T, Erduran M, Alptekin Ö (2007) Crustal shear wave velocity structure of Turkey by surface wave dispersion analysis. *Ann Geophys* 50:177–190
- Thomson SN, Ring U (2006) Thermochronologic evaluation of postcollision extension in the Anatolide orogen, western Turkey. *Tectonics* 25:TC3005. <https://doi.org/10.1029/2005TC001833>
- Torsvik TH, Cocks LRM (2009) The Lower Palaeozoic palaeogeographical evolution of the northeastern and eastern peri-Gondwanan margin from Turkey to New Zealand. *Geol Soc Lond Spec Publ* 325:3–21
- Unsworth M (2010) Magnetotelluric studies of active continent–continent collisions. *Surv Geophys* 31:137–161
- van Hinsbergen DJJ (2010) A key extensional metamorphic complex reviewed and restored: the Menderes Massif of western Turkey. *Earth Sci Rev* 102:60–76
- van Hinsbergen DJJ, Kaymakci N, Spakman W, Torsvik TH (2010) Reconciling the geological history of western Turkey with plate circuits and mantle tomography. *Earth Planet Sci Lett* 297:674–686
- Vanacore EA, Taymaz T, Saygin E (2013) Moho structure of the Anatolian Plate from receiver function analysis. *Geophys J Int* 193:329–337
- Vernik L, Lockner D, Zoback MD (1992) Anisotropic strength of some typical metamorphic rocks from the KTB pilot hole, Germany. *Sci Drill* 3:153–160
- Vigneresse J-L, Tikoff B, Améglio L (1999) Modification of the regional stress field by magma intrusion and formation of tabular granitic plutons. *Tectonophysics* 302:203–224
- Visser K, Trampert J, Lebedev S, Kennett BLN (2008) Probability of radial anisotropy in the deep mantle. *Earth Planet Sci Lett* 270:241–250
- Waldron JWF (1984) Structural history of the Antalya Complex in the ‘Isparta angle’, Southwest Turkey. *Geol Soc Lond Spec Publ* 17:273–286
- Warren LM, Beck SL, Biryol CB, Zandt G, Özacar AA, Yang Y (2013) Crustal velocity structure of Central and Eastern Turkey from ambient noise tomography. *Geophys J Int* 194:1941–1954
- Whitney DL, Teyssier C, Kruckenberg SC, Morgan VL, Iredale LJ (2008) High pressure–low-temperature metamorphism of meta-sedimentary rocks, southern Menderes Massif, western Turkey. *Lithos* 101:218–232
- Yang Y, Forsyth DW (2006) Regional tomographic inversion of the amplitude and phase of Rayleigh waves with 2-D sensitivity kernels. *Geophys J Int* 166:1148–1160
- Yao H, Xu G, Zhu L, Xiao X (2005) Mantle structure from interstation Rayleigh wave dispersion and its tectonic implication in western China and neighboring regions. *Phys Earth Planet Inter* 148:39–54
- Yao H, Van der Hilst RD, De Hoop MV (2006) Surface-wave array tomography in SE Tibet from ambient seismic noise and two-station analysis—I. Phase velocity maps. *Geophys J Int* 166:732–744
- Yılmaz Y (1997) *Geology of Western Anatolia*. E.T.H. Univ. Press, Zurich. In: Schindler C, Fister MP (eds) *Active tectonics of Northwestern Anatolia—the Marmara Poly-Project*. Vdf Hochschulverlag AG an der ETH, Zürich, pp 31–53
- Yılmaz Y (2008) Main geological problems of Western Anatolia and the significance of the Bodrum magmatic province. *IOP Conf Ser Earth Environ Sci*. <https://doi.org/10.1088/1755-1307/2/1/012007>
- Yılmaz Y, Genç ŞC, Güler F, Bozcu M, Yılmaz K, Karacik Z, Altunkaynak Ş, Elmas A (2000) When did the Western Anatolian grabens begin to develop? *Geol Soc Lond Spec Publ* 173:353–384
- Yolsal-Çevikbilen S, Taymaz T, Helvacı C (2014) Earthquake mechanisms in the Gulfs of Gökova, Sığacık, Kuşadası, and the Simav Region (western Turkey): neotectonics, seismotectonics and geodynamic implications. *Tectonophysics* 635:100–124
- Yoshizawa K, Kennett BLN (2002) Determination of the influence zone for surface wave paths. *Geophys J Int* 149:440–453
- Yoshizawa K, Kennett BLN (2004) Multimode surface wave tomography for the Australian region using a three-stage approach incorporating finite frequency effects. *J Geophys Res* 109:B02310. <https://doi.org/10.1029/2002JB002254>
- Yoshizawa K, Miyake K, Yomogida K (2010) 3D upper mantle structure beneath Japan and its surrounding region from inter-station dispersion measurements of surface waves. *Phys Earth Planet Inter* 183:4–19
- Zhang S, Karato S (1995) Lattice preferred orientation of olivine deformed in simple shear. *Nature* 375:774–777. <https://doi.org/10.1038/375774a0>
- Zor E, Sandvol E, Gürbüz C, Türkelli N, Seber D, Barazangi M (2003) The crustal structure of the East Anatolian plateau (Turkey) from receiver functions. *Geophys Res Lett* 30:8044. <https://doi.org/10.1029/2003GL018192>



# Mantle dynamics beneath Greece from SKS and PKS seismic anisotropy study

George Kaviris<sup>1</sup> · Ioannis Fountoulakis<sup>1</sup> · Ioannis Spingos<sup>1</sup> · Christos Millas<sup>1</sup> · Panayotis Papadimitriou<sup>1</sup> · George Drakatos<sup>2</sup>

Received: 27 July 2018 / Accepted: 13 November 2018 / Published online: 19 November 2018  
© Institute of Geophysics, Polish Academy of Sciences & Polish Academy of Sciences 2018

## Abstract

SKS and PKS splitting parameters were determined in the broader Greek region using data from 45 stations of the Hellenic Unified Seismological Network and the Kandilli Observatory and Earthquake Research Institute, utilizing teleseismic events that occurred between 2010 and 2017. Data were processed for shear-wave splitting with the Minimum Energy Method that was considered the optimal. The results generally confirm the existence of anisotropic zonation in the Hellenic subduction system, with alternating trench-normal and trench-parallel directions. The zonation is attributed to the upper and lower olivine fabric layers that can, potentially, be present in the subduction zone. At the edges of this zone, two possible toroidal flow cases have been identified, implying the existence of tears that allow the inflow of asthenospheric material in the mantle wedge. The high number of null measurements in the KZN and XOR stations indicates a possible anisotropic transition zone between the fore-arc and back-arc areas. SKS and PKS splitting results are jointly interpreted, given that they yield similar values in most cases.

**Keywords** Shear-wave splitting · Tear · Hellenic Subduction Zone · Mantle wedge

## Introduction

Upper mantle anisotropy has been studied worldwide by investigating the properties of both body (e.g., P-waves, as seen in Raitt et al. 1969; Bean and Jacob 1990) and surface waves (e.g., Kawasaki and Kon’no 1984). However, it is widely accepted that shear-wave splitting (SWS) is one of the most suitable methodologies for that purpose. The physical quantities to be determined are the fast shear-wave polarization direction ( $\varphi$ ) and the time-delay ( $\delta t$ ) between the two split shear-wave arrivals. Among the possible causes of anisotropy, only few have dominated the international bibliography. Concerning the upper mantle, crystalline anisotropy (Nicolas and Christensen 1987), also known as Lattice

Preferred Orientation (LPO), is the most common interpretation for observations of SWS. It refers to the minerals’ orientation when they are found under specific temperature and pressure conditions (e.g., Tommasi et al. 1999). There is a clear, but also complicated, correlation between LPO and mantle deformation (e.g., Savage 1999).

The upper mantle is mainly composed of highly anisotropic phases: olivine (which primarily contributes to the anisotropy due to its high volumetric density), enstatite (orthopyroxene) and diopside (clinopyroxene) (Christensen and Salisbury 1979). Experimental studies revealed that the olivine fast axis, i.e., the a-axis, tends to be aligned with the maximum shear direction for high strains (Zhang and Karato 1995). The latter implies that the fast shear-wave polarization reflects the maximum shear stress direction beneath the station.

Five olivine fabric types have been determined by experimental studies (Karato et al. 2008). Regarding the interpretation of SWS measurements, the A-type fabric seems to be the main factor of the relation between anisotropy and the various tectonic settings (e.g., Long and Silver 2009), whereas the B-type is considered to be limited in the subduction zones (Karato 2008).

✉ George Kaviris  
gkaviris@geol.uoa.gr

<sup>1</sup> Section of Geophysics and Geothermics, Department of Geology and Geoenvironment, National and Kapodistrian University of Athens, Panepistimiopolis, Zografou, 157 84 Athens, Greece

<sup>2</sup> Geodynamic Institute, National Observatory of Athens, Lofos Nymfon, Thission, 11810 Athens, Greece

The anisotropic behavior of the mantle is often examined by studying core phases, such as SKS and PKS. These phases demonstrate certain advantages in the investigation of SWS in the upper mantle. The conversion in the boundary between core and mantle (CMB) affects the polarization, considering that the anisotropy at the station is solely restricted on the receiver side (CMB surface). Seismic anisotropy constitutes a powerful tool regarding the analysis and the interpretation of mantle dynamics regarding both subduction zones and continental regions, due to the undoubted relation between the mantle flow–deformation and the splitting directions. Studies in subduction zones are mainly utilizing SKS phases, as they are very sensitive to the sub-slab, slab and wedge anisotropy (Abt et al. 2010; Baccheschi et al. 2011). SWS results in subduction zones, especially in mantle wedges, are quite complex. Polarization directions in such areas are generally oriented either parallel (e.g., Russo and Silver 1994) or perpendicular to the trench. According to Long and Wirth (2013), time-delays in mantle wedges present spatial variations, with their values ranging between 0.1 s and 1.5 s. An additional complication is the existence of transitions from trench-parallel to trench-perpendicular directions, and vice versa, close to the arc and in the back-arc (Long and van der Hilst 2006). Regarding continental regions, SWS results demonstrate anisotropy that is closely related with surficial geological structures (Behn et al. 2004).

Upper mantle SWS in the Greek region was first studied by Hatzfeld et al. (2001) who observed heterogeneous anisotropy over the Aegean region with the most consistent and large ( $> 1$  s) time-delays in the North Aegean. A correlation between the fast polarization parameters and the recent strain rates, supporting a vertical coherent deformation, was also observed. Schmid et al. (2004) characterized the SWS results in Crete as “badly defined” due to heterogeneous anisotropy caused by the proximity to the slab. Evangelidis et al. (2011) observed a NE-SW fast polarization trend in the Aegean back-arc region (trench-normal), accompanied by a gradual increase in the time-delays and a trench-parallel fast direction in the fore-arc area, as well as beneath Peloponnese and Rhodes, with a possible sub-slab source of anisotropy. Olive et al. (2014) separated the Greek region into three zones, i.e., the near trench (NT), fore-arc (FA) and back-arc (BA) areas. They interpreted the trench-normal fast polarization directions in the NT and BA as a result of sub-slab and supra-slab anisotropy sources, connected to the mantle flow. A thin serpentine layer was also proposed above the slab to explain the fast direction parallel to the subduction in the FA domain. Paul et al. (2014) favor an asthenospheric source of the observed anisotropy and suggest that the NW–SE orientations in Anatolia (results of a toroidal flow) are attributed to a tear (slab window). Confal et al. (2016) identified NE-SW polarizations in the Aegean subduction zone, interpreted by

the presence of olivine in the asthenospheric mantle due to slab rollback induced flow. Evangelidis (2017) enriched the existing database and applied the source-side splitting technique to estimate the depths of anisotropy. He observed a trench-normal sub-slab anisotropy in the western part of the Hellenic arc. In addition, he supported the geodynamical model of a young tear fault at the Kefalonia transform fault (KTF) and the existence of a connection between the ongoing tearing and the mantle flow.

In the present work, seismic anisotropy properties of the upper mantle beneath Greece are investigated, measuring the SWS parameters of the SKS and PKS phases. The main goal is to acquire the highest quality of SWS measurements by analyzing a significantly larger dataset compared to previous studies. It is the first time that results from PKS phases in the Greek region are presented, enhancing the available dataset. Stations from Turkey are also used to thoroughly investigate geodynamics. In general, the obtained measurements are in agreement with the observations from previous studies, but also reveal new aspects of the anisotropic behavior of the upper mantle in Greece.

## Study area

The area of Greece constitutes a remarkable physical and geological laboratory, with different and complex tectonic settings. The active kinematics of the Hellenic system are attributed to two phenomena the rollback of the Eastern Mediterranean oceanic slab and the westward movement of the Anatolian plate along the North Anatolian Fault (NAF) (e.g., Jolivet 2001). Essentially, the right-lateral NAF bounds the Anatolian and the prominent Aegean microplate (e.g., McKenzie 1972). A displacement transportation from the NAF to the western part of the Hellenic trench with the Center Hellenic Shear Zone (CHSZ) has been identified, i.e., a specific shear zone that extends from Turkey to the Ionian Sea (Papanikolaou and Royden 2007). In addition, the Aegean–Western Anatolia region is undergoing extensional deformation, given the existence of normal faults and the corresponding focal mechanisms (e.g., Papadimitriou and Sykes 2001; Kiratzi and Louvari 2003; Karakostas et al. 2003, 2014; Kassaras and Kapetanidis 2018; Papadimitriou et al. 2018).

The Hellenic subduction system can be considered segmented into two areas with different subduction rates. They are separated from each other close to the island of Kefalonia, in a region that is characterized by another important tectonic feature, the KTF. The basic features of the Greek modern tectonics are presented in Fig. 1. The KTF lies in the transition between the oceanic subduction and the continental collision, to the south and the north, respectively. Suckale et al. (2009) consider the KTF as a



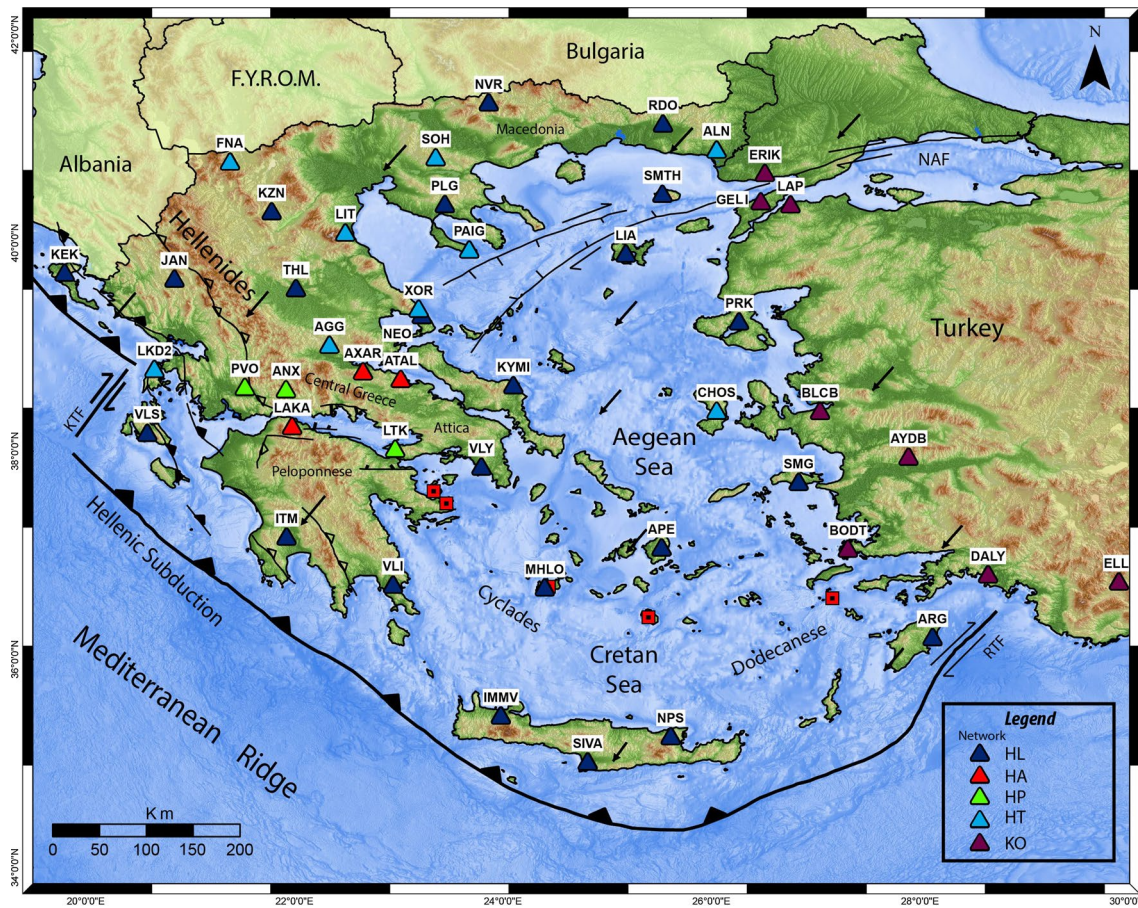


**Fig. 1** Geodynamic setting of the broader Greek region based on Royden and Papanikolaou (2011). Arrows indicate the overall direction of plate movement, in the frame system GSRM v2.1 (Kreemer

et al. 2014). Red squares indicate the most important centers in the volcanic arc. Stations utilized in the present study are presented. Each color represents a different network according to the legend

vertical tear along the oceanic and continental lithosphere. In addition, the KTF is characterized as a Subduction-Transform-Edge-Propagator (STEP) fault (Govers and Wortel 2005). The KTF has caused a significant number of earthquakes in the Central Ionian Islands (Kouskouna et al. 1993; Papadimitriou 2002; Papadimitriou et al. 2006; Kassaras et al. 2015; Ganas et al. 2016; Sokos et al. 2016).

The well-defined subduction south of Crete is highlighted by the existence of active seismic and volcanic zones that come as a direct consequence of the subduction mechanism. The main centers of the volcanic arc are presented in Fig. 1. The subducting plate is characterized by a Benioff zone with an angle of subduction of about  $16^\circ$  (Papazachos et al. 2005). This has led to the shallow and intermediate-depth seismicity that reaches a depth of approximately 200 km in the Central Aegean (Makropoulos et al. 2012). In general, Greece is characterized by very high seismicity (Papazachos and Papazachou 2003; Makropoulos et al. 2012; Kouskouna and Sakkas 2013; Stucchi et al. 2013).

Geodetic studies in the Aegean region provide valuable information regarding the plate kinematics and the existing extension in the back-arc. GPS data (e.g., Kahle et al. 1998; Reilinger et al. 2006) indicate the occurrence of a counterclockwise rotation in the Eastern Mediterranean relative to Eurasia. Values of the velocity field increase toward the Crete trench, implying extension in the Aegean, in an area where the slab is subducted with a velocity reaching  $\sim 35$  mm/yr.

In addition, slab tearing may also exist in the Hellenic trench (Royden and Papanikolaou 2011; Bocchini et al. 2018). Gaps are connected to STEP faults (or tear faults) that bound the Hellenic trench (Govers and Wortel 2005), to the west (Kefalonia area) and to the east (eastern Aegean region). These structures are strike-slip transform faults that produce tearing in the subducted plate lithosphere (Nijholt and Govers 2015). The existence of slab tearing in the eastern Aegean forms two segments, i.e., the Cyprus and Aegean trenches. Tearing in the broader area has also been identified by tomographic studies (e.g., Salaiu et al. 2012). Bocchini

et al. (2018) concluded, from a seismicity perspective, that there is a clear subducting slab, dipping to the NW, close to Rhodes and reject the NE-SW STEP fault model.

## Data and methodology

For the current study, seismic data recorded by 37 permanent stations of the Hellenic Unified Seismic Network (HUSN) and eight seismographs belonging to the Kandilli Observatory and Earthquake Research Institute (KOERI) have been analyzed (Fig. 1). Earthquake information for the time period 2010–2017 was acquired from the catalogue of the United States Seismological Survey (USGS), and specific criteria were applied to select eligible events for analysis. To ensure that the dataset comprises of events suitable for the SKS anisotropy study, a cutoff moment magnitude ( $M_w$ ) of 6.0 and an epicentral distance window ranging between  $90^\circ$  and  $130^\circ$  was defined. The magnitude threshold was chosen to ensure that the SKS phase amplitude is large enough to be safely identified. In addition, aiming to increase the available dataset, PKS phases were also employed, adjusting the epicentral distance window to  $120^\circ$ – $180^\circ$ , where according to widely used earth models, such as IASP91 (Kennett and Engdahl 1991) and AK135 (Montagner and Kennett 1996) this phase can be recorded and identified. The above selection resulted to 410 teleseismic events for SKS and 360 for PKS that fulfill the criteria (Fig. 2).

SKS and PKS phases experience similar receiver-side splitting, due to similar upgoing ray paths, and it is common practice to be considered jointly (e.g., Graw and Hansen 2017). Based on the catalogue's origin times and locations, arrival times of SKS and PKS phases have been calculated using IASP91 (Kennett et al. 1995), to extract the part of the waveforms that includes these phases from the continuous data. The start time of the traces was the event's origin time, whereas the end-time was equal to 200 s after the theoretical SKS or PKS arrival time.

The SWS results were obtained with the Splitlab software (Wüstefeld et al. 2008), allowing the simultaneous evaluation of SWS parameters ( $\varphi$ ,  $\delta t$ ) with three methods. Namely, the rotation–correlation (RC), introduced by Bowman and Ando (1987), the minimum energy (SC) and the eigenvalue (EV), both proposed by Silver and Chan (1991), methods are included. The EV method uses a grid search technique to identify the pair of SWS parameters that produces the smallest eigenvalue  $\lambda_2$ , whereas the SC method is a special case of the EV methodology and is valid when the isotropic polarization vector is known, as in the case of SKS and PKS phases. For SC, the optimal pair is selected also via a grid search, aiming to minimize the transverse component energy. On the other hand, the RC technique works with the corrected horizontal components and identifies the cross-correlation coefficient maximum.

The Splitlab software provides diagnostic plots for all of the above-mentioned methods, which were used for the evaluation of every measurement. Analysis is initiated with

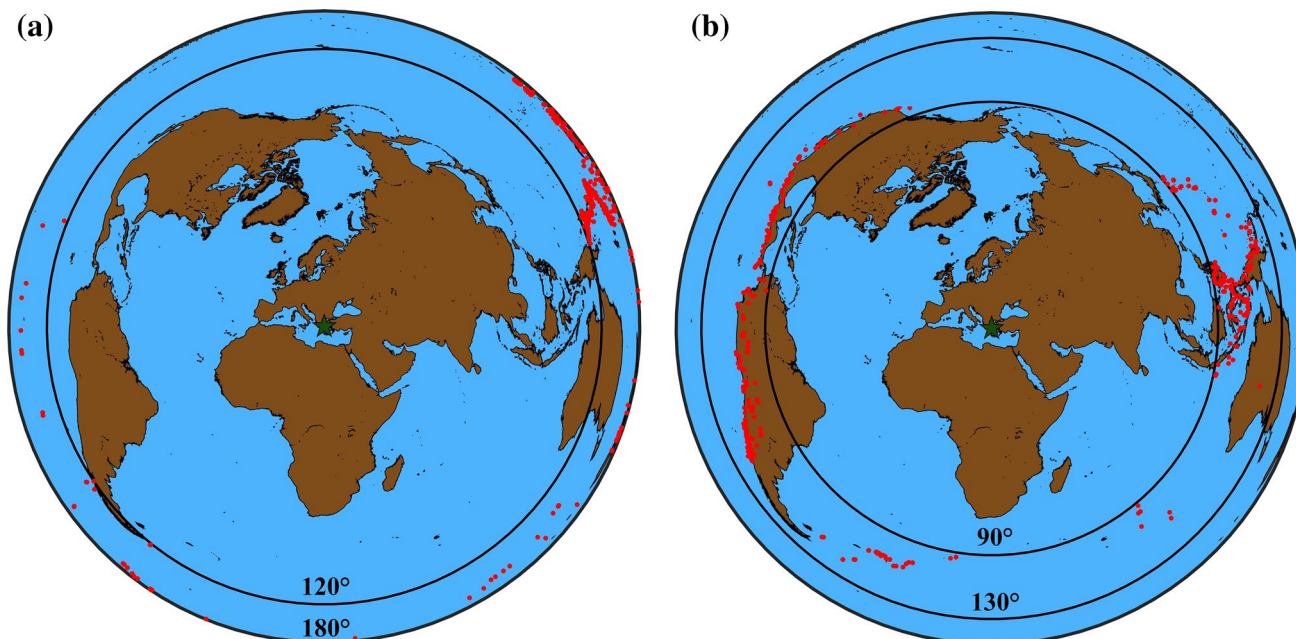


**Fig. 2** Spatial distribution of teleseismic events that have been used for the anisotropy analysis for: **a** PKS and **b** SKS phases. The map is centered on Greece. Minimum and maximum epicentral distances are also shown



the selection of an appropriate signal window that contains one or more full periods of the phase (SKS or PKS). To clearly identify the phase to be analyzed, a bandpass filter between 0.020 Hz and 0.250 Hz was utilized. Nevertheless, in cases of clear and impulsive arrivals of SKS or PKS phases, no filter was applied. The results are categorized as good, fair, poor and null, according to qualitative and quantitative characteristics (Wüstefeld et al. 2008; Liu and Gao 2013). Good measurements present clear and impulsive SKS or PKS arrival on the R-T components, full removal of the SKS or PKS energy on the corrected transverse component, linear corrected polarization and evident minimum regarding the contour energy map. Results ranked as fair exhibit lower-quality measures compared to good. Measurements categorized as poor do not provide reliable information. For that reason, poor results are not utilized in the present study. Figure 3 presents a typical example of a measurement that was categorized as good based on the above-mentioned criteria.

Vecsey et al. (2008) concluded that the RC and EV methods may provide unstable, and even false, results compared to the SC, which constitutes a reliable method for

core–mantle refracted waves. According to the above suggestion, the results that will be accepted for further examination are those acquired with the SC method. Nevertheless, the application of more than one method in order to evaluate the obtained SWS measurements is significant, given that it facilitates the improvement in the dataset quality (Vecsey et al. 2008). In addition, nulls from non-nulls observations can be distinguished by comparing the results determined by the RC and SC methods (Wüstefeld and Bokelmann 2007).

## Results

The SWS analysis procedure led to 898 high-quality (good and fair)  $\varphi$  and  $\delta t$  pairs, including null measurements, from more than 19,000 waveforms that were analyzed, with an overall 4.6% percentage of acceptable measurements, mainly due to operational problems of stations, noise contamination and large errors of SWS results. In more detail, the analysis resulted in 696 and 202 accepted pairs for the SKS and PKS phases, respectively. This difference in the number of accepted pairs can be explained by the dataset availability,

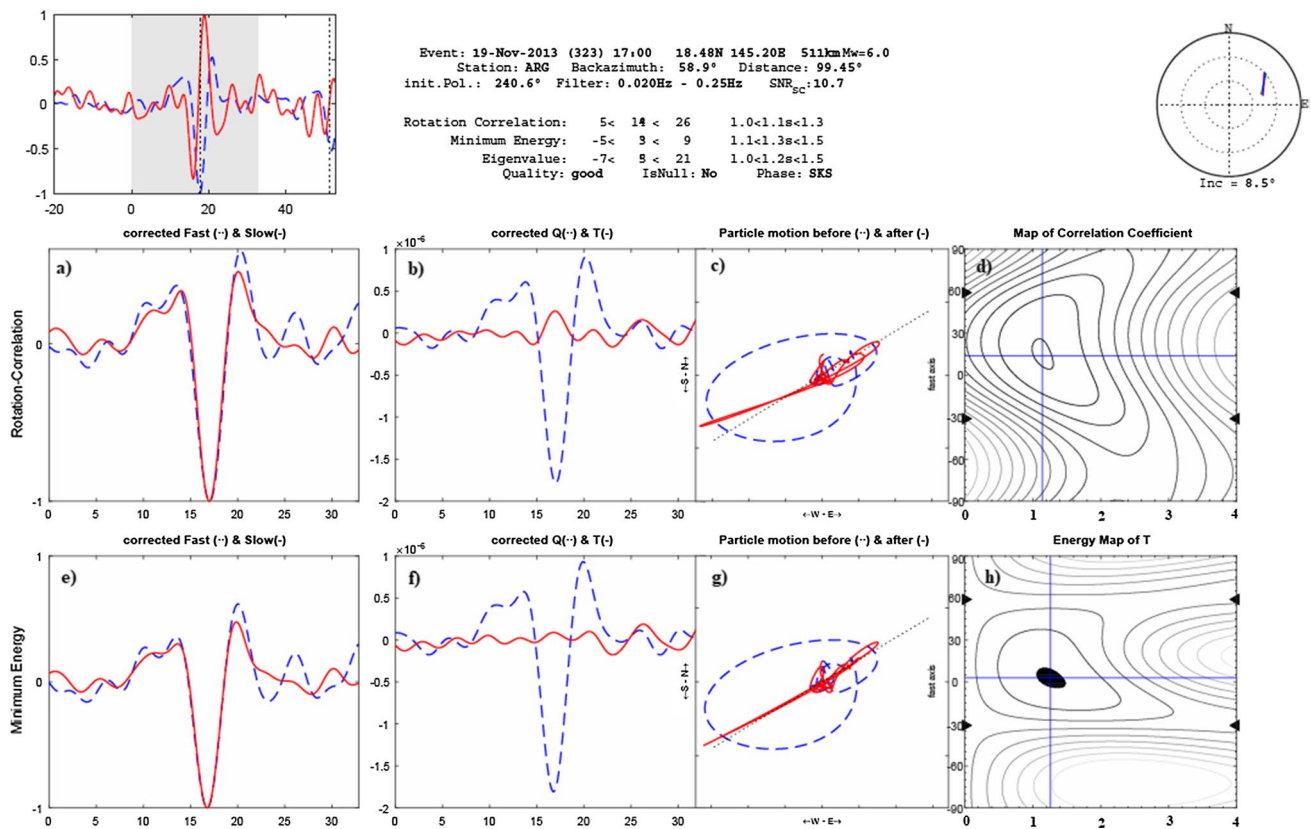


**Fig. 3** Diagnostic plot that displays the results of the SWS analysis, for an event (19/11/2013- $M_w$  6.0) recorded by ARG station. **a** and **e** represent the fast and slow components after the correction, **b**, **f** represent the corrected radial and transverse components, **c** and **g** show

the particle motion without and with correction and **d** and **h** present the correlation coefficient and the minimum energy map, for the RC and SC methods, respectively. Overall results are shown in the upper panel

given that the earthquakes within the PKS window were significantly less. Also, 118 null measurements were identified. For each station, the circular median values were calculated for  $\varphi$ , using the Circular Statistics Toolbox (Berens 2009). Circular statistics were employed for angular data, given that they are not affected by the wrapping that occurs at  $180^\circ$  for simple orientation-independent directions. Similar directions, which are arithmetically different (e.g.,  $0^\circ$  and  $180^\circ$ ), are considered identical. Mean values of the  $\delta t$  were calculated using common statistics. In addition, the standard deviation and the error of the results were calculated. The detailed outputs of this procedure are presented in Table 1 (SKS phases) and Table 2 (PKS phases). Furthermore, the average SKS and PKS splitting results are displayed at each station (Fig. 4), along with the major tectonic features.

Back-azimuthal coverage is not uniform and is concentrated between  $50^\circ$ – $100^\circ$  and  $200^\circ$ – $310^\circ$  for both SKS and PKS phases. The observed gaps prevent the identification of possible complex anisotropic behavior beneath the stations, considering that the variation patterns of anisotropy direction and time-delay values that are due to the presence of more than one anisotropic layers require full back-azimuth coverage (Savage 1999). Thus, adopting the simplest anisotropic model for the interpretation, the so-called single layer, is more appropriate. The single-layer hypothesis can be also justified by the quite homogenous behavior of the results within the available back-azimuthal windows. The single-layer assumption has also been made in previous research efforts in Greece (Evangelidis et al. 2011; Paul et al. 2014). To ensure that  $\varphi$  measurements were independent of the back-azimuth, we performed a Pearson's Chi-square test in the two ranges stated above. Results were initially categorized accordingly, and the frequencies of the distribution of  $\varphi$  for those back-azimuths were obtained (bins of  $10^\circ$ ). The test was then performed, between the respective frequencies of the two ranges. For  $p < 0.05$ , the measurements are considered independent. We observed the independence of  $\varphi$  against the back-azimuth for most stations. For example, station JAN with 35 measurements presented a  $p$  value of 0.007, while the test for PRK yielded a  $p$  value of 0.017 with 44 measurements. It is noted that for the above test, PKS and SKS measurements were considered as a single group.

Although fast polarizations directions, as well as time-delays are not uniform in the entire Greek region, specific patterns are identified. Regarding the North Aegean Sea, the splitting behavior is quite homogenous, with polarization directions generally oriented NE-SW and time-delays of approximately 2.0 s. A similar anisotropy direction has also been determined in both the South Aegean and Central Aegean. However, in these regions the mean  $\delta t$  is significantly lower, in the order of 0.8 s. Results are vastly different in the stations located near the Hellenic subduction, where anisotropy directions are trench-perpendicular in Crete and

parallel or sub-parallel close to the Rhodes and Kefalonia transform faults. In the broader area of Macedonia, there is an alteration in the mean anisotropy directions from the western to the southern part, changing from NW–SE to NE–SW and forming a characteristic V shape. In Central Greece, the directions follow the pattern (NE-SW) of the stations in the Aegean, with the exceptions of the AXAR and ATAL stations (Fig. 1). In the area of Peloponnese, there are no clear patterns, probably due to the lack of satisfactory station distribution. The cases of the KZN and XOR stations (Fig. 1) are worth noting, given that the high majority of the measurements are good and fair nulls. In addition, stations NEO and PLG (Fig. 1) exhibit a significant number of nulls.

Regarding most cases, SKS and the PKS phases provide similar SWS values. The latter is justified by their almost identical upward ray paths. The mean anisotropy directions (Fig. 4) obtained for the SKS and PKS phases differ significantly in the LTK and VLY stations. LTK and VLY polarization values versus back-azimuth plots are presented in Fig. 5, according to which similar time-delays have been obtained. However, given that the SKS and PKS results are similar in most cases, they are evaluated jointly in the interpretation.

## Discussion

### Depth evaluation

A major issue that needs to be resolved is the depth identification of the origin of seismic anisotropy, i.e., lithospheric, mantle lithospheric or asthenospheric. The latter will facilitate assessing the geodynamical interpretation of the determined SWS results. Generally, core phases (SKS/PKS) that are usually incorporated in SWS studies offer poor analysis of the anisotropy distribution in depth, given the path-integrated nature of SWS results. This means that measurements performed on surface stations contain an accumulation of splitting information, which is acquired due to shear waves propagating in the mantle and crust.

For the vast majority of cases, shallow anisotropic sources have been identified in the upper crust. In general, for the latter part of the Earth's interior, it is reported that the magnitude of anisotropy ranges between 2% and 4% (Barrool and Mainprice 1993). Endrun et al. (2011) determined magnitude of lower crustal azimuthal anisotropy of around 1.8% regarding the North and 3.5% the Central and South Aegean Sea. On the other hand, according to their results for the lithospheric mantle, the azimuthal anisotropy is approximately 2% in the North and quite smaller ( $< 1\%$ ) in the Central-South Aegean. Based on Wüstefeld et al. (2010) and using a maximum magnitude of anisotropy of 3.5% and crustal thickness of 50 km, a maximum theoretical delay time of  $\sim 0.4$  s is expected due to crust effects in the Greek region.



**Table 1** Obtained SKS splitting parameters and calculated standard deviation ( $\sigma$ ). The geographical coordinates of each station are also provided

Station	Network	Events analyzed	Latitude (°N)	Longitude (°E)	$\varphi$ (N°E)	$\sigma_{\varphi}$ (N°E)	$\delta t$ (s)	$\sigma_{\delta t}$ (s)	No of results
ATAL	HA	67	38.6926	23.0213	-15.09	36.91	1.17	0.76	7
AXAR	HA	143	38.7664	22.6590	-35.02	26.70	1.06	0.33	7
LAKA	HA	433	38.2401	21.9785	19.78	19.78	1.45	0.44	8
APE	HL	460	37.0727	25.5230	19.86	13.05	0.80	0.30	27
ARG	HL	382	36.2135	28.1212	19.84	19.63	0.91	0.28	26
IMMV	HL	437	35.4606	23.9811	12.74	12.48	0.78	0.29	17
ITM	HL	470	37.1787	21.9252	3.83	36.89	1.25	0.86	15
JAN	HL	371	39.6561	20.8487	16.54	18.55	0.90	0.34	22
KEK	HL	372	39.7127	19.7962	23.74	17.72	1.35	0.49	28
KYMI	HL	194	38.6331	24.1001	60.21	14.51	1.66	0.28	5
KZN	HL	458	40.3033	21.7820	-	-	-	-	29
LIA	HL	432	39.8972	25.1805	27.19	15.50	2.23	0.58	32
MHLO	HL	423	36.6898	24.4017	15.23	26.57	1.68	0.60	14
NEO	HL	385	39.3056	23.2218	-53.13	13.51	2.40	1.78	10
NPS	HL	419	35.2613	25.6103	-24.97	51.51	0.66	0.25	9
NVR	HL	369	41.3484	23.8651	20.71	20.71	1.21	0.36	33
PLG	HL	336	40.3714	23.4438	-30.58	46.69	1.78	1.69	12
PRK	HL	451	39.2456	26.2649	24.79	5.31	1.90	0.17	44
RDO	HL	373	41.1450	25.5355	20.73	8.61	1.45	0.40	29
SMG	HL	451	37.7042	26.8377	7.38	18.81	1.17	0.36	31
SMTH	HL	459	40.4709	25.5305	47.83	13.51	2.34	0.70	24
THL	HL	382	39.5646	22.0144	-9.93	19.91	2.21	1.23	13
VLI	HL	478	36.7180	22.9468	23.28	23.28	1.36	1.16	9
VLS	HL	335	38.1768	20.5886	50.63	11.83	1.39	0.28	15
VLY	HL	386	37.8524	23.7942	-25.14	15.70	1.08	0.25	22
ANX	HP	192	38.5933	21.9202	21.09	11.53	0.89	0.42	7
LTK	HP	370	38.0228	22.9673	-37.88	5.44	1.03	0.30	4
PVO	HP	284	38.6167	21.5259	13.76	38.39	1.09	0.26	8
AGG	HT	408	39.0211	22.3360	14.56	14.56	1.43	0.13	4
ALN	HT	409	40.8957	26.0497	10.75	10.75	1.49	0.33	32
CHOS	HT	414	38.3868	26.0506	5.15	5.15	1.97	0.42	19
FNA	HT	377	40.7818	21.3835	-49.43	23.67	0.84	0.20	8
LIT	HT	393	40.1003	22.4893	-44.41	22.12	1.39	0.64	10
LKD2	HT	393	38.7889	20.6578	21.03	21.03	2.03	0.28	17
PAIG	HT	410	39.9363	23.6768	13.28	13.28	0.69	0.11	9
SOH	HT	433	40.8206	23.3556	15.67	47.47	1.51	1.32	6
XOR	HT	428	39.3660	23.1920	-	-	-	-	15
AYDB	KO	316	37.9467	27.8908	7.74	7.75	1.45	0.80	5
BLCB	KO	179	38.3853	27.0420	20.06	32.98	1.17	0.42	11
BODT	KO	322	37.0622	27.3103	-9.76	21.65	1.62	0.19	4
DALY	KO	411	36.8162	28.6532	0.20	16.13	1.18	0.24	9
ELL	KO	350	36.7483	29.9085	-16.32	7.47	1.04	0.10	7
ERIK	KO	184	40.6708	26.5132	22.44	2.99	1.77	0.22	18
GELI	KO	204	40.3980	26.4742	30.62	3.30	1.91	0.28	8
LAP	KO	169	40.3703	26.7593	36.61	4.19	1.57	0.28	7

**Table 2** Obtained PKS splitting parameters and calculated standard deviation ( $\sigma$ ) for each station

Station	Network	Events analyzed	Latitude (°N)	Longitude (°E)	$\varphi$ (N°E)	$\sigma_{\varphi}$ (N°E)	$\delta t$ (s)	$\sigma_{\delta t}$ (s)	No of results
LAKA	HA	139	38.2401	21.9785	31.27	13.29	1.44	0.42	3
APE	HL	142	37.0727	25.5230	13.37	17.93	1.04	0.26	7
ARG	HL	126	36.2135	28.1212	19.11	12.96	1.16	0.21	14
IMMV	HL	134	35.4606	23.9811	26.80	20.28	0.81	0.23	6
JAN	HL	126	39.6561	20.8487	20.13	7.00	1.02	0.31	13
KEK	HL	123	39.7127	19.7962	22.72	6.08	1.84	0.17	9
KYMI	HL	56	38.6331	24.1001	48.56	2.76	1.77	0.10	2
LIA	HL	133	39.8972	25.1805	18.84	4.50	2.28	0.29	8
NEO	HL	135	39.3056	23.2218	37.10	39.96	1.22	0.45	3
NPS	HL	127	35.2613	25.6103	20.74	23.99	1.15	0.51	3
PRK	HL	141	39.2456	26.2649	29.98	4.54	2.21	0.18	10
RDO	HL	145	41.1450	25.5355	16.72	6.69	1.79	0.46	17
SIVA	HL	115	35.0178	24.8120	-1.56	0.06	1.25	0.07	2
SMG	HL	136	37.7042	26.8377	8.72	7.24	1.17	0.20	18
SMTH	HL	151	40.4709	25.5305	27.34	6.32	1.93	0.51	8
VLY	HL	130	37.8524	23.7942	1.76	15.84	1.19	0.25	13
ANX	HP	99	38.5933	21.9202	23.49	8.09	1.12	0.12	6
LTK	HP	126	38.0228	22.9673	-5.01	3.40	1.29	0.11	5
PVO	HP	89	38.6167	21.5259	20.35	19.40	1.34	0.03	2
AGG	HT	121	39.0211	22.3360	35.38	8.17	1.77	0.51	9
ALN	HT	144	40.8957	26.0497	6.06	6.62	1.94	0.36	9
CHOS	HT	127	38.3868	26.0506	8.86	6.19	1.93	0.21	4
FNA	HT	108	40.7818	21.3835	-17.29	4.28	1.86	0.48	7
LKD2	HT	122	38.7889	20.6578	-4.03	7.05	1.40	0.29	6
AYDB	KO	102	37.9467	27.8908	14.54	10.17	0.72	0.18	3
BLCB	KO	60	38.3853	27.0420	5.42	1.24	2.00	0.12	3
DALY	KO	111	36.8162	28.6532	6.37	10.06	1.61	0.38	4
ERIK	KO	69	40.6708	26.5132	19.35	2.52	2.10	0.34	5
GELI	KO	73	40.3980	26.4742	24.53	3.30	2.49	0.16	3

The geographical coordinates of each station are also provided

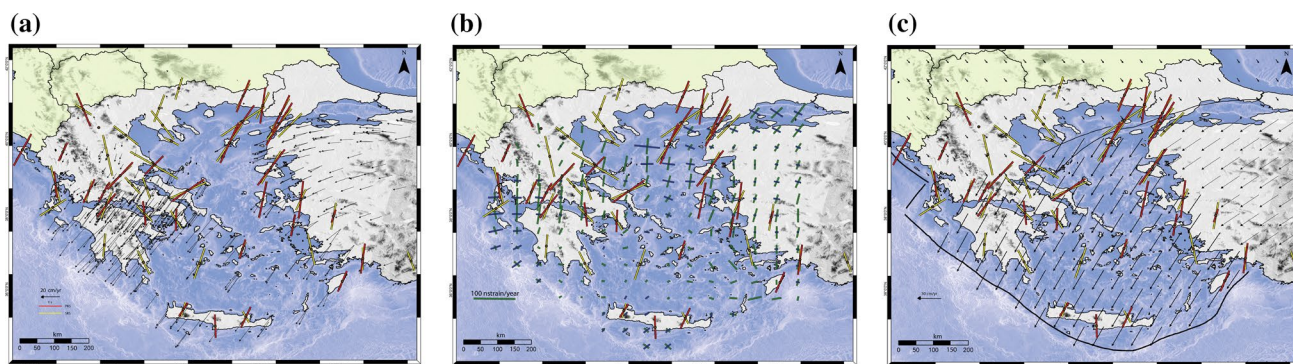


**Fig. 4** Station-averaged splitting results from the SWS analysis. The mean anisotropy directions ( $\varphi$ ) at each station are represented with yellow (SKS) and red (PKS) bars, whose length is proportional to the calculated average time-delay ( $\delta t$ ), along with: **a** GPS displacement

vectors (Nyst and Thatcher 2004; Reilinger et al. 2006; Floyd et al. 2010; Chousianitis et al. 2013), **b** strain rates from Floyd et al. (2010) and **c** absolute plate motion modeled in the frame system GSRM v2.1 (Kreemer et al. 2014)

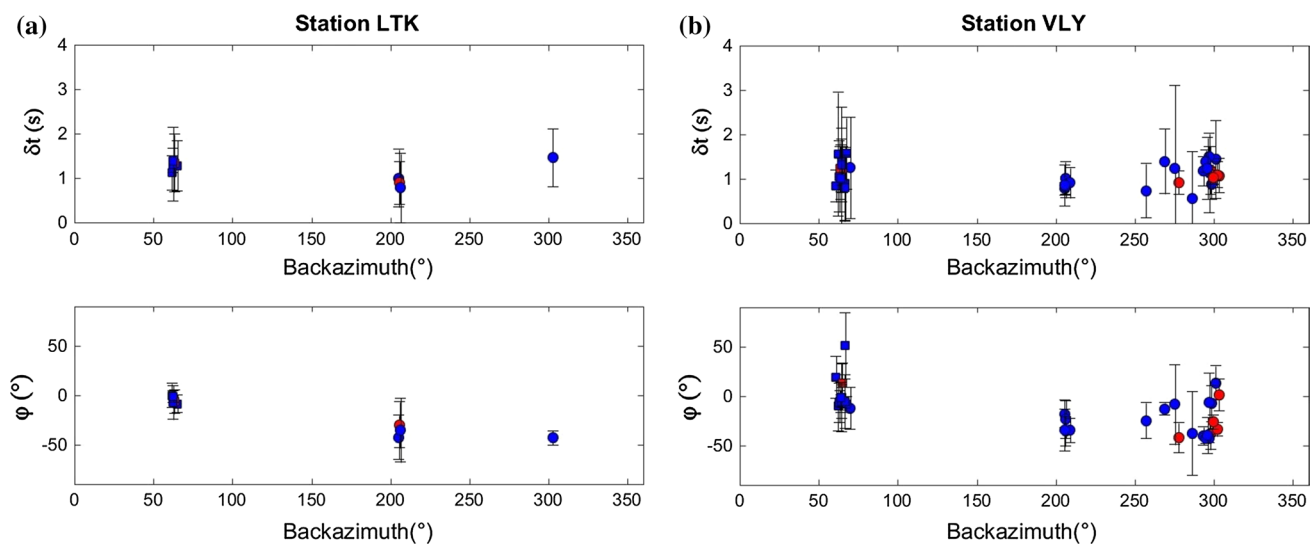


**Fig. 5** Plots of SWS parameters for the stations VLY and LTK, with the variations in delay times (a) and fast polarization directions (b) compared to the back-azimuth. The circles depict the SKS and the squares the PKS results. The red color represents good and the blue fair results

The delay time values of the present study are significantly higher, ranging between 0.7 s and 2.5 s (Tables 1 and 2).

Reliable results from local upper crust anisotropy studies for the Gulf of Corinth (Kapetanidis et al. 2015), Attica and Santorini (Papadimitriou et al. 2015) present  $\delta t$  values up to 0.19 s (Papadimitriou et al. 1999; Kaviris et al. 2015, 2017, 2018a, b). The presence of a low velocity zone in the Aegean (e.g., Karagianni et al. 2005; Salaün et al. 2012) is a sign of a thin lithosphere that cannot significantly contribute to the anisotropic observations, as also indicated by Paul et al. (2014). In either case, the lithosphere cannot offer the necessary conditions to be considered the anisotropy source, taking into account that the average delay times in some cases, especially in northern Greece, exceed 2.0 s. Savage (1999) suggests that time-delays that exceed 0.2–0.3 s are possibly related to upper mantle sources of anisotropy.

Anisotropy in the Aegean Sea is considered uniform. Regarding North Aegean and NW Turkey, SKS/PKS fast polarization directions are approximately NE-SW and trench-normal, with time-delays that exceed 2.0 s. This trend changes to more NNE-SSW in the Central and the South Aegean, with a smooth decrease that reaches 1.0 s, in the values of time-delays. The latter results are consistent with the ones by Paul et al. (2014) and Confal et al. (2016), who have densely covered the North and the Central/South Aegean, respectively. A uniform pattern in the North Aegean and NW Turkey is evident, based on these studies (Fig. 6).

Hatzfeld et al. (2001) first proposed the anisotropic nature of the lithosphere and possibly the asthenosphere in North Aegean. As it has already been mentioned, the high time-delay values ( $> 2.0$  s) support the hypothesis of an anisotropic asthenosphere source. The smooth decrease in the

time-delays from the area toward the trench seems to support the suggestion of Evangelidis et al. (2011) that the observed anisotropy is caused by the mantle wedge flow. This decrease in time-delay values can be attributed to the reduction in the anisotropic material thickness from the North to the South Aegean, fact also supported by tomographic results regarding the mantle wedge (Piomallo and Morelli 2003). The determined time-delay observations are similar to the ones previously obtained in the area (e.g., Paul et al. 2014; Confal et al. 2016), with the exception of the study by Evangelidis et al. (2011), where  $\delta t$  values are significantly smaller, as Confal et al. (2016) also noticed.

### Lithospheric and asthenospheric motion

The principal idea related to the investigation of anisotropy directions is that they reflect asthenospheric flow and can be considered as an approximation to deduce the orientation of deformation regarding the upper mantle. Adopting this assumption, the motion of the asthenosphere in the Aegean and NW Turkey exhibits almost constant NE-SW direction, turning to NNE-SSW in the Central Aegean.

The comparison between the SWS measurements and crustal deformation is a useful tool to evaluate the existence of a possible coupling/decoupling among the crust and the mantle. Figure 4 presents the obtained SKS/PKS results, superimposed by GPS velocity data, which reveal a counterclockwise rotational flow in the Middle East and Aegean regions, attributed to slab rollback (Le Pichon and Kreemer 2010). However, the fast polarization directions are not consistent with the GPS results for the major part of the Greek region, with a possible exception in the south Aegean



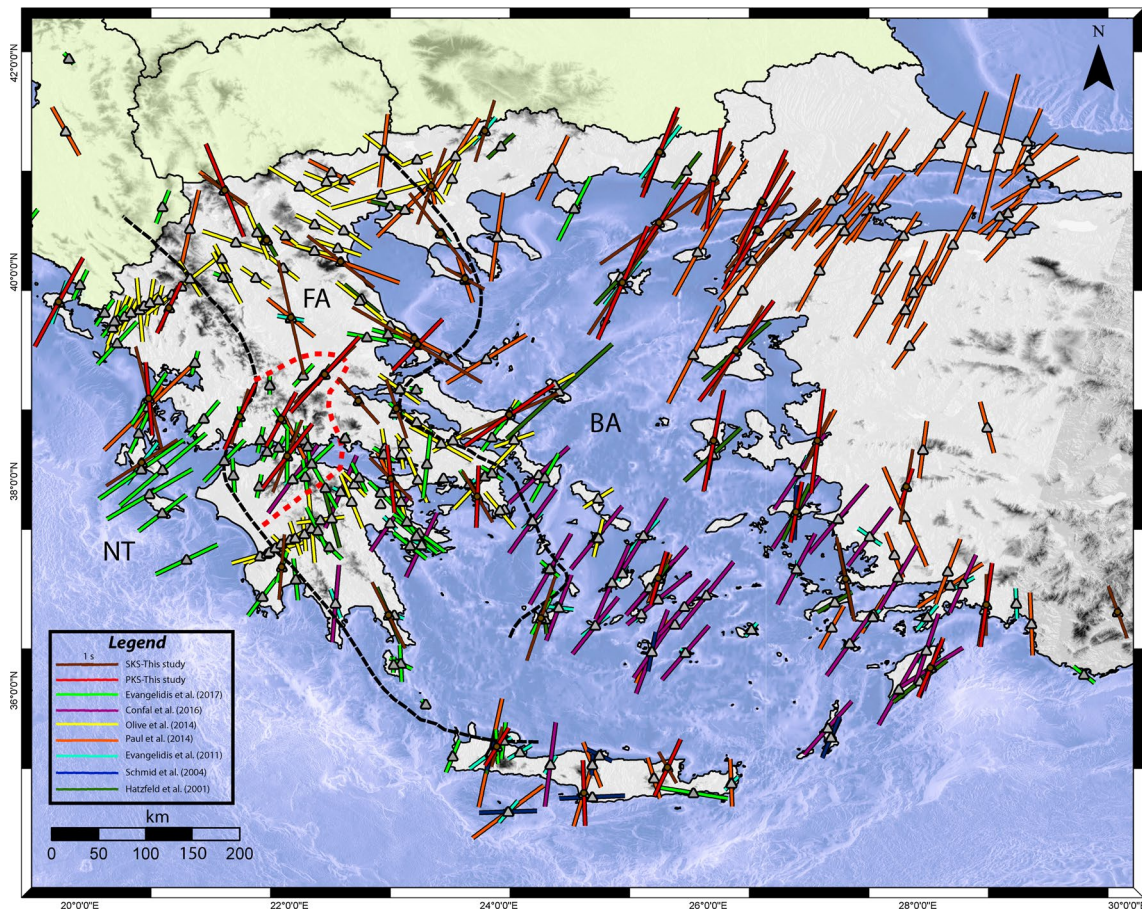


**Fig. 6** Station-averaged splitting results from the available SWS analysis studies in the Greek region by Hatzfeld et al. (2001), Schmid et al. (2004), Evangelidis et al. (2011), Olive et al. (2014), Paul et al. (2014), Confal et al. (2016), Evangelidis (2017) and the current study.

The mean values at each station are represented with a different color for each study (see legend) and indicate the fast direction ( $\varphi$ ) and the time-delay ( $\delta t$ ). The three anisotropic zones, according to Evangelidis (2017), are superimposed

(Cyclades), where GPS and SKS/PKS results provide similar directions (Fig. 4a). This phenomenon can be attributed to the thinner lithosphere in the central and southern Aegean (Karagianni et al. 2005; Salaün et al. 2012). Menant et al. (2016) investigated mantle flow in E. Mediterranean with 3D numerical modeling and suggested that the transmission is enabled by the lithosphere which is thinner in the extensional domain. In addition, the fast polarization directions do not follow the strain rate directions or the strike of the NAF, which is a major tectonic structure in the Aegean (Fig. 4b). An exception is observed in the north-central Aegean, where a possible correlation with the extension directions can be identified, but with significant deviations. Moreover, the comparison between the absolute plate motion and the SKS/PKS anisotropy directions reveals a consistency in the same area (Fig. 4c). For the rest of the Greek region, the above comparisons failed to reveal consistent patterns.

Jolivet et al. (2013) proposed a strong decoupling of the mantle and crust, resulting in movement of the crust parallel

to the CHSZ and to the NAF. This may explain the fact that anisotropy directions are not parallel to the NAF, as well as the differences between the SKS/PKS and GPS directions. Even if the lithospheric extent of the NAF is still debated (Berk Biryol et al. 2011; Salaün et al. 2012), it is almost certain that the NAF does not reach the depth of the anisotropic source. Mutlu and Karabulut (2011) performed an anisotropic Pn tomography study and traced a similar trend to the one obtained by SKS phases beneath the Aegean Sea, just below the Moho discontinuity. Pn anisotropy anomalies were determined mostly in Central Greece with the Pn velocity directions correlating very well with the obtained SKS/PKS directions in the major part of the study region. It is worth noting that the Pn directions are in good agreement with the SKS/PKS directions at the eastern tear of the Hellenic system, a region characterized by significant anisotropic variations. Endrun et al. (2011) obtained azimuthal anisotropy phase velocity maps through tomographic inversion, using Rayleigh waves. A partial consistency between



the present SKS/PKS directions and the determined from the latter study fast axes is observed in the Aegean for the lower crust, i.e., the N–S trend in the North Aegean. On the other hand, no correlation for the mantle lithosphere is identified with SKS fast directions, neither regarding the present nor the previous studies, as reported by Endrun et al. (2011) as well. Global anisotropic velocity maps also reveal a similar behavior with NE–SW fast axes for the broader Greek-Anatolian area (e.g., Visser et al. 2008), but the lack of local resolution does not permit a more detail examination.

All the above suggest that, apart from the one between the lithospheric mantle and the asthenospheric mantle, there is another differential contact zone among the lower crust and the uppermost part of the mantle, as Jolivet et al. (2013) claim. Therefore, the strict characterization of a specific decoupling zone is venturesome, due to the possible existence of more than one partly or strongly coupling/decoupling zones. Numerical modeling studies (Sternai et al. 2014; Menant et al. 2016) favor a lithosphere/asthenosphere coupling and that the strain in some extent is controlled by the asthenospheric flow. However, the shape of the asthenospheric flow does not seem to have a clear connection with the form of the crustal flow, implying a completely independent behavior.

### Anisotropic zonation

Three zones of anisotropic behavior in the Greek region, also adopted by Evangelidis (2017), were considered by Olive et al. (2014). The proposed specific zonation type (NT, FA and BA) in the Hellenic system is obvious, and it is even more distinguishable when all available data in the Greek region are utilized (Fig. 6). The greater part of mainland Greece belongs to the FA domain with a general trend of fast parallel directions.

It is worth noting that most subduction zones worldwide are characterized by trench-parallel anisotropy directions (Long and Silver 2008), except Cascadia (e.g., Currie et al. 2004) and the Hellenic subduction, with spatially stable trench-normal directions in the near trench area. The main question in this case is whether the anisotropic signature in the NT originates from slab or sub-slab sources. Long and Silver (2008), who studied subduction systems globally, found no relation between slab age and thickness, and time-delays. The latter is a sign that the contribution of the slab is not primary, and the authors suggest that the observed signal has sub-slab sources with an intrinsic A-type LPO that is appropriate for the subduction system physical conditions. This simple type of active mantle flow is also supported by the numerical models of Faccenda and Capitanio (2013) that proposed an upper and a lower fabric domain with trench-normal and trench-parallel directions, respectively.

This A-type assumption is also valid for the BA region that exhibits the same behavior.

Exceptions regarding the trench-normal behavior were identified in two parts, the eastern and the western, of the subduction zone. Regarding the eastern one, between E. Crete and the southwestern coasts of Turkey, close to Kos and Rhodes Islands, the fast polarization directions diverge from the trench-normal pattern and convert to trench-parallel. Similar behavior has also been identified by previous SKS studies for the same region (Olive et al. 2014; Evangelidis 2017), contradicting to a certain extent the previous A-type assumption for the NT area. The existence of slab tearing in the eastern Aegean is still debated, although an increasingly number of publications are in favor of the existence of a tear (Berk Biryol et al. 2011; Salaün et al. 2012). Superimposing the full dataset of SKS/PKS results for the area with the proposed slab tear geometry in E. Aegean, according to Bocchini et al. (2018), a specific pattern of asthenospheric flow can possibly be identified (Fig. 7). The trench-parallel directions appear to go across the possible slab tear, indicating an escape of the asthenospheric flow toward the mantle wedge, imaging a toroidal flow that initiates from the eastern edge of the slab. The 3D representation of Fig. 7 reveals in more detail the flow behavior, displaying the spatial correlation between the subducted Aegean slab, which could reach in depth the lower mantle, as proposed by Portner et al. (2018), and the tear geometry.

Faccenda and Capitanio (2013) concluded, through numerical modeling, that there is a possible trench-parallel core beneath the trench-normal fabric in the sub-slab area and that the lower fabric can be better expressed in the near edge areas. The proposed model satisfactory fits the results of the present study, especially in the East Aegean, and could justify the observed trench-parallel direction in the FA area. The nature and the behavior of this trench-parallel core are debated due to the trench-normal source-side directions (Evangelidis 2017). Nevertheless, source-side measurements, especially the ones with larger time-delays, could sample deeper regions compared to SKS. Thus, even an alteration of cores with different fabric behaviors is possible.

Trench-parallel anisotropy directions can be produced by petrological conditions. Classical models (Jung and Karato 2001; Kneller and Van Keken 2008; Long and Silver 2009), in contrast with the serpentinized layer suggested by Olive et al. (2014), could not explain the lack of correlation in the FA region between the mantle wedge thickness and time-delay values. In addition, Evangelidis (2017), studying the fore-arc area, suggests that the observed trench-parallel pattern has sub-slab origin (due to similar source-side splitting pattern) and that it is possibly created by a trench-parallel sub-slab mantle flow.

The fore-arc domain exhibits time-delay values of  $\sim 1.0$  s, and thus, it is quite difficult to approximate the depth of the

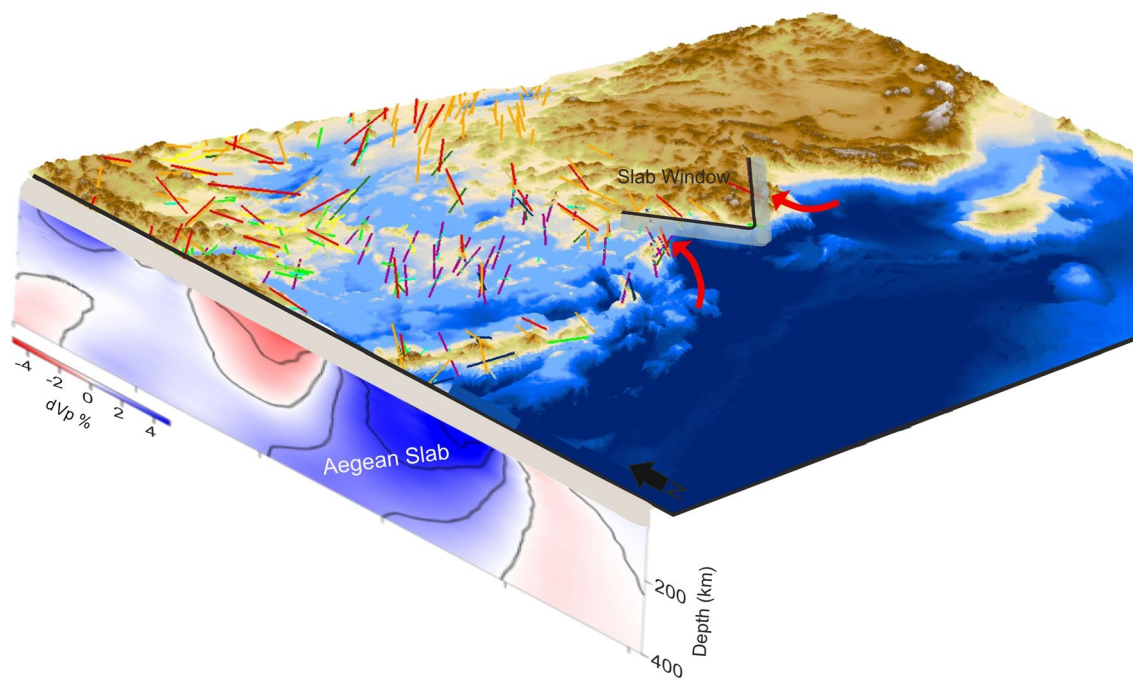


**Fig. 7** 3D representation of the broader Greek area with the proposed asthenospheric flow (red arrows), based on the SWS results. The tomographic image presents the Aegean slab in depth (Portner et al.

2018), with colors indicating  $V_p$  variations, and the proposed slab tear from Bocchini et al. (2018)

anisotropic source (on either side of the slab) based only on this characteristic. The thin layer of serpentine (Olive et al. 2014) could produce these values of time-delays, on the basis of its highly anisotropic nature (Jung 2011). It is certain, however, that a serpentine layer is not dominant beneath Greece. Regarding Peloponnese, the identification of a weak velocity contrast above the mantle wedge revealed subtle signs of serpentinization (Pearce et al. 2012). Halpaap et al. (2018) found small  $V_p/V_s$  values for the lower overriding crust–mantle wedge’s cold corner, results that cannot be related to serpentines that present high  $V_p/V_s$  values. Halpaap et al. (2018) also noticed that the determined  $P$  velocities (higher than 8 km/s) are typical for mantle peridotites, also indicating dry mantle wedge corner. Abers et al. (2017) also support the dry nature of the Hellenic mantle wedge. All the above indicate that the existence of a serpentine layer of sufficient thickness as a source of anisotropy is highly unlikely and are in favor of an anisotropic signature that is originated in the sub-slab area.

Interpreting SWS considering a petrological aspect, the B-type consists the sole olivine fabric that can immensely change the connection of the mantle flow and the SWS observations (Jung and Karato 2001). The latter type is connected with high water level contents, high stresses and low temperatures (Karato 2008). B-type olivine may explain, in mantle wedge terms, the shift from the trench-normal (BA) to trench-parallel (FA) and back to trench-normal (NT)

directions. However, the existence of an extensive B-type fabric in the Hellenic mantle wedge cannot be feasible, considering its dry nature. As a result, the hypothesis of an asthenospheric or petrological flow change above the slab is not highly possible.

### SWS in the Western Hellenic Subduction Zone

Regarding the western part of the subduction and specifically in the broader region near the KTF, there is another observable deviation from the directions that are perpendicular to the trench. The fast directions remain constantly trench oblique to the north, regarding the JAN and KEK stations that are installed in the continental part of the subduction system. Near the KTF, the stations LKD2, in Lefkada, and VLS, in Kefalonia, demonstrate a clockwise rotation that becomes sub-parallel to the KTF. In order to acquire a better picture of the variation in the SWS parameters, all measurements were projected to the ray piercing point in 200 km depth, considered as an average value of the expected anisotropic layer from the literature (Savage 1999) and our observations. This projection offers a comprehensive view of the SWS measurements in the area dominated by the KTF, revealing a rotation of anisotropy directions from the northern to the southern segment.

The geometry of the Western Hellenic Subduction Zone (WHSZ) and the transition between these two segments,

presented in Fig. 8, are still debated and have been a scientific topic of intense investigation. Suckale et al. (2009) propose a tear perpendicular to the subduction in the boundary of the oceanic and continental lithosphere that can cause an influx of the flow material in the mantle wedge. Royden and Papanikolaou (2011) are also in favor of the existence of segments in the WHSZ, in the KTF area, that results to dextral strike-slip movement. Pearce et al. (2012) suggest that a smooth ramp can be considered as the transition between the two segments, not fully rejecting though the tearing. However, Halpaap et al. (2018) propose the existence of a slab which is smoothly deformed. On the other hand, Guillaume et al. (2013) support the hypothesis of a tear fault, which is not fully subducted, with a newly formed tear window. According to our results, the SKS and PKS anisotropy directions indicate the possible existence of a toroidal cell (Fig. 8), initiating from the northern KTF segment. The existence of the toroidal cell presupposes the occurrence of a slab window, as initially proposed by Govers and Wortel (2005), but the age and the development condition of the tear cannot be approached by a SWS splitting study.

### Null measurements as a possible transition zone

There is no doubt that the upper mantle in the Greek region is in general highly anisotropic. However, SWS results obtained for certain stations indicate a completely different behavior with high number of null measurements. Specifically, stations KZN and XOR present exclusively null results, whereas the PLG and NEO stations also exhibit a significant number of nulls, compared to the total available results.

In general, nulls are identified if the shear wave (SKS/PKS) is not split. The lack of splitting can be attributed to various factors, such as fossil anisotropy, complex anisotropy and deformation in the lithospheric part of the mantle (Barruol et al. 1997). Regarding the KZN and XOR stations, the absence of seismic anisotropy is observed in all the available back-azimuths; thus, it is considered as relatively constrained. The latter leads to the rejection of the hypothesis that null measurements result from the parallelization of the initial polarization with the one caused by the anisotropic medium. Moreover, due to the back-azimuthal gaps, we are

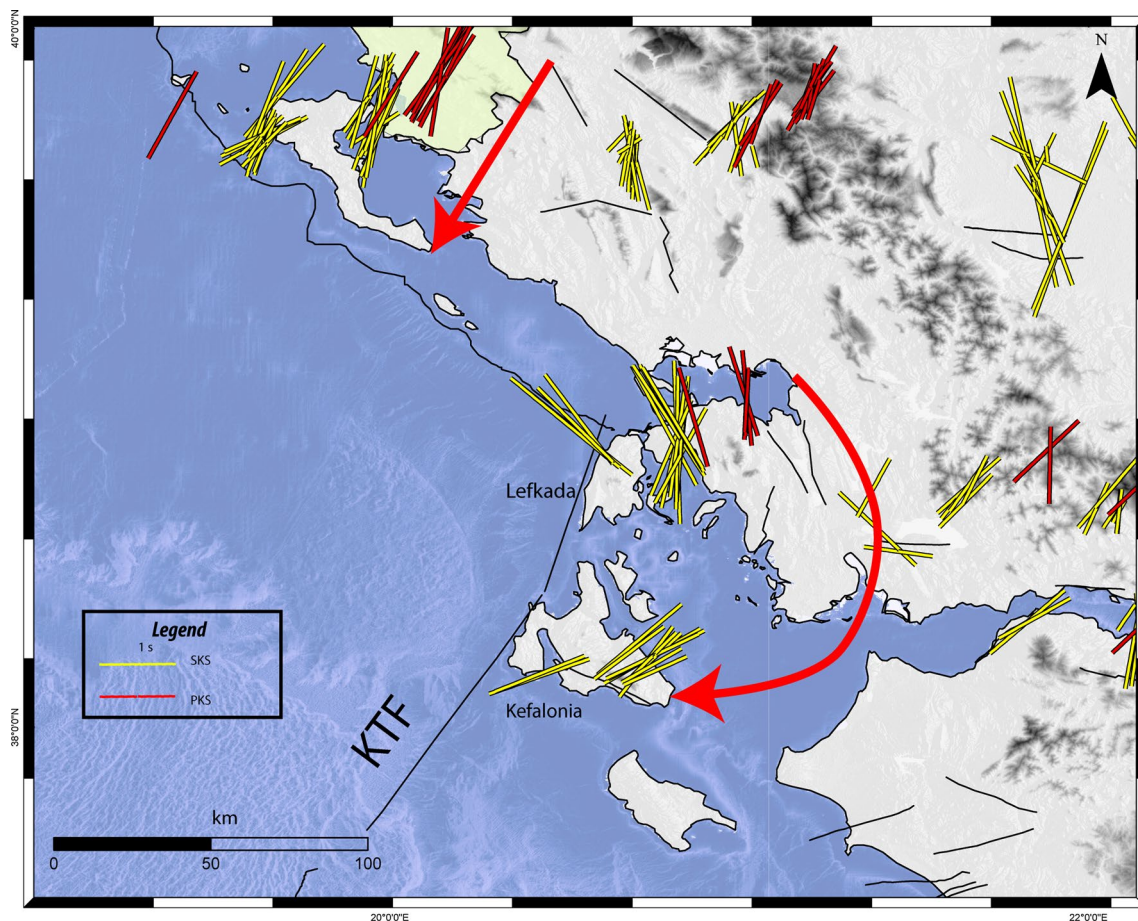


**Fig. 8** Map of SWS results at 200 km depth in the Western Hellenic Subduction Zone. Red arrows indicate the proposed asthenospheric flow. Faults from Ganas et al. (2013)



not able to identify variations in the anisotropic parameters, which would be interpreted with the presence of two or more anisotropic layers. Stations that yield high number of null measurements are very close to the boundaries of the FA and the BA zone. Thus, assuming a simple asthenospheric flow, the stations related to null measurements can possibly be located on a transition zone between the FA and BA zones. Nevertheless, this assumption cannot be verified, due to lack of back-azimuthal coverage.

Another exception regarding the proposed zonation by Evangelidis (2017) is Central Greece and northern Peloponnese, where the polarization directions are trench-parallel instead of trench-normal. This area constitutes the transition from the northern to the southern Hellenides, possibly influencing the anisotropic signature due to the transition from the NT to the FA, or due to the slab window that is responsible for the inflow of material originating from the asthenosphere.

## Conclusions

In the present study, more than 19,000 SKS and PKS event-station pairs have been analyzed at stations of the HUSN and KOERI networks to investigate the upper mantle flow beneath Greece, yielding 898 high-quality (good and fair) measurement pairs ( $\varphi$ ,  $\delta t$ ). Our results strongly support zonation in the Hellenic subduction system, as already proposed by previous studies (Olive et al. 2014; Evangelidis 2017), with an alteration of trench-normal, trench-parallel and again trench-normal directions moving toward the interior. This alteration can be attributed to different in-depth sources of the anisotropic signature. The observed anisotropic patterns can better be explained by the proposed model by Facenda and Capitanio (2013) with the existence of upper and lower fabric with trench-perpendicular and trench-parallel expressions of the directions, respectively. Important exceptions regarding anisotropic zonation have been identified in Central Greece and northern Peloponnese.

The anisotropic behavior reveals two cases of possible toroidal flow in the eastern and western parts of the subduction zone, implying the presence of slab windows that permit the intrusion of asthenospheric material into the mantle wedge. However, the geometry and condition of each tear cannot be identified. Moreover, PKS results seem to coincide with the SKS results, indicating similar ray paths and the same anisotropic source.

**Acknowledgements** We are grateful to the two anonymous reviewers for their constructive comments that helped to ameliorate the final version of the present study. We also thank Ms Varvara Tsironi for her assistance in the schematic 3D representation of Fig. 7. The tomographic image of Fig. 7 was obtained by the IRIS service <http://ds.iris.edu/dms/products/emc>. We thank all researchers who participated in the installation and maintenance of the of the HUSN and KOERI

stations. The Obspy framework was used for the processing of the seismological data (Beyreuther et al. 2010). This study was supported by the project HELPOS—Hellenic Plate Observing System (MIS 5002697).

## References

- Abers GA, Van Keken PE, Hacker BR (2017) The cold and relatively dry nature of mantle forearcs in subduction zones. *Nat Geosci* 10:333–337
- Abt DL, Fischer KM, Abers GA, Protti M, González V, Strauch W (2010) Constraints on upper mantle anisotropy surrounding the Cocos slab from SK(K)S splitting. *J Geophys Res Solid Earth* 115:1–16. <https://doi.org/10.1029/2009JB006710>
- Baccheschi P, Margheriti L, Steckler MS, Boschi E (2011) Anisotropy patterns in the subducting lithosphere and in the mantle wedge: a case study—The southern Italy subduction system. *J Geophys Res Solid Earth* 116:1–15. <https://doi.org/10.1029/2010JB007961>
- Barruol G, Mainprice D (1993) A quantitative evaluation of the contribution of crustal rocks to the shear-wave splitting of teleseismic SKS waves. *Phys Earth Planet Inter* 78:281–300. [https://doi.org/10.1016/0031-9201\(93\)90161-2](https://doi.org/10.1016/0031-9201(93)90161-2)
- Barruol G, Silver PG, Vauchez A (1997) Seismic anisotropy in the eastern United States: Deep structure of a complex continental plate. *J Geophys Res Earth* 102:8329–8348. <https://doi.org/10.1029/96jb03800>
- Bean CJ, Jacob AWD (1990) P-wave anisotropy in the lower lithosphere. *Earth Planet Sci Lett* 99(1–2):58–65. [https://doi.org/10.1016/0012-821X\(90\)90070-E](https://doi.org/10.1016/0012-821X(90)90070-E)
- Behn MD, Conrad CP, Silver PG (2004) Detection of upper mantle flow associated with the African Superplume. *Earth Planet Sci Lett* 224:259–274. <https://doi.org/10.1016/j.epsl.2004.05.026>
- Berens P (2009) Circular statistics matlab toolbox. *J Stat Softw* 31:1–21
- Berk Biryol C, Beck SL, Zandt G, Özacar AA (2011) Segmented African lithosphere beneath the Anatolian region inferred from teleseismic P-wave tomography. *Geophys J Int* 184:1037–1057. <https://doi.org/10.1111/j.1365-246X.2010.04910.x>
- Beyreuther M, Barsch R, Krischer L, Megies T, Behr Y, Wassermann J (2010) ObsPy: a python toolbox for seismology. *Seismol Res Lett* 81:530–533. <https://doi.org/10.1785/gssrl.81.3.530>
- Bocchini GM, Brüstle A, Becker D, Meier T, van Keken PE, Ruscic M, Papadopoulos GA, Rische M, Friederich W (2018) Tearing, segmentation, and backstepping of subduction in the Aegean: new insights from seismicity. *Tectonophysics* 734–735:96–118. <https://doi.org/10.1016/j.tecto.2018.04.002>
- Bowman JR, Ando MA (1987) Shear-wave splitting in the upper mantle wedge above the Tonga subduction zone. *Geophys J R A S* 88:24–41
- Chousianitis K, Ganas A, Gianniu M (2013) Kinematic interpretation of present-day crustal deformation in central Greece from continuous GPS measurements. *J Geodyn* 71:1–13. <https://doi.org/10.1016/j.jog.2013.06.004>
- Christensen NI, Salisbury MH (1979) Seismic anisotropy in the oceanic upper mantle: evidence from the Bay of Islands Ophiolite Complex. *J Geophys Res Sol Earth* 84(B9):4601–4610. <https://doi.org/10.1029/JB084iB09p04601>
- Confal JM, Eken T, Tilmann F, Yolsal-Çevikbilen S, Çubuk-Sabancı Y, Saygin E, Taymaz T (2016) Investigation of mantle kinematics beneath the Hellenic-subduction zone with teleseismic direct shear waves. *Phys Earth Planet Inter* 261:141–151. <https://doi.org/10.1016/j.pepi.2016.10.012>



- Currie CA, Cassidy JF, Hyndman RD, Bostock MG (2004) Shear wave anisotropy beneath the Cascadia subduction zone and western North American craton. *Geophys J Int* 157:341–353. <https://doi.org/10.1111/j.1365-246X.2004.02175.x>
- Endrun B, Lebedev S, Meier T, Tirel C, Friederich W (2011) Complex layered deformation within the Aegean crust and mantle revealed by seismic anisotropy. *Nat Geosci* 4:203–207. <https://doi.org/10.1038/ngeo1065>
- Evangelidis CP (2017) Seismic anisotropy in the Hellenic subduction zone: effects of slab segmentation and subslab mantle flow. *Earth Planet Sci Lett* 480:97–106. <https://doi.org/10.1016/j.epsl.2017.10.003>
- Evangelidis CP, Liang WT, Melis NS, Konstantinou KI (2011) Shear wave anisotropy beneath the Aegean inferred from SKS splitting observations. *J Geophys Res Solid Earth* 116:1–14. <https://doi.org/10.1029/2010JB007884>
- Faccenda M, Capitanio FA (2013) Seismic anisotropy around subduction zones: insights from three-dimensional modeling of upper mantle deformation and SKS splitting calculations. *Geochem Geophys Geosyst* 14:243–262. <https://doi.org/10.1002/ggge.20055>
- Floyd MA, Billiris H, Paradissis D, Veis G, Avallone A, Briole P, McClusky S, Nocquet JM, Palamartchouk K, Parsons B, England PC (2010) A new velocity field for Greece: implications for the kinematics and dynamics of the Aegean. *J Geophys Res Solid Earth* 115:1–25. <https://doi.org/10.1029/2009JB007040>
- Ganas A, Oikonomou IA, Tsimi C (2013) NOAfaults: a digital database for active faults in Greece. *Bull Geol Soc Greece* 47:518. <https://doi.org/10.12681/bgsg.11079>
- Ganas A, Elias P, Bozionelos G, Papathanassiou G, Avallone A, Papastergios A, Valkaniotis S, Parcharidis I, Briole P (2016) Coseismic deformation, field observations and seismic fault of the 17 November 2015  $M=6.5$ , Lefkada Island, Greece earthquake. *Tectonophysics* 687:210–222
- Govers R, Wortel MJR (2005) Lithosphere tearing at STEP faults: response to edges of subduction zones. *Earth Planet Sci Lett* 236:505–523. <https://doi.org/10.1016/j.epsl.2005.03.022>
- Graw JH, Hansen SE (2017) Upper mantle seismic anisotropy beneath the Northern Transantarctic Mountains, Antarctica from PKS, SKS, and SKKS splitting analysis. *Geochem Geophys Geosyst* 18:544–557. <https://doi.org/10.1002/2016GC006729>
- Guillaume B, Husson L, Funicello F, Faccenna C (2013) The dynamics of laterally variable subductions: Laboratory models applied to the Hellenides. *Solid Earth* 4:179–200. <https://doi.org/10.5194/se-4-179-2013>
- Halpaap F, Rondenay S, Ottemöller L (2018) Seismicity, deformation, and metamorphism in the Western Hellenic subduction zone: new constraints from tomography. *J Geophys Res Solid Earth* 123:3000–3026. <https://doi.org/10.1002/2017JB015154>
- Hatzfeld D, Karagianni E, Kassaras I, Kiratzi A, Louvari E, Lyon-Caen H, Makropoulos K, Papadimitriou P, Bock G, Priestley K (2001) Shear wave anisotropy in the upper mantle beneath the Aegean related to internal deformation. *J Geophys Res* 106:30737–30753. <https://doi.org/10.1029/2001JB000387>
- Jolivet L (2001) A comparison of geodetic and finite strain pattern in the Aegean, geodynamic implications. *Earth Planet Sci Lett* 187:95–104. [https://doi.org/10.1016/S0012-821X\(01\)00277-1](https://doi.org/10.1016/S0012-821X(01)00277-1)
- Jolivet L, Faccenna C, Huet B, Labrousse L, Le Pourhiet L, Lacombe O, Lecomte E, Burov E, Denèle Y, Brun JP, Philippon M, Paul A, Salaün G, Karabulut H, Piromallo C, Monié P, Gueydan F, Okay AI, Oberhänsli R, Pourteau A, Augier R, Gadenne L, Driussi O (2013) Aegean tectonics: Strain localisation, slab tearing and trench retreat. *Tectonophysics* 597–598:1–33. <https://doi.org/10.1016/j.tecto.2012.06.011>
- Jung H (2011) Seismic anisotropy produced by serpentine in mantle wedge. *Earth Planet Sci Lett* 307:535–543. <https://doi.org/10.1016/j.epsl.2011.05.041>
- Jung H, Karato SI (2001) Water-induced fabric transitions in olivine. *Science* 293:1460–1463. <https://doi.org/10.1126/science.1062235>
- Kahle HG, Straub C, Reilinger R, McClusky S, King R, Hurst K, Veis G, Kastens K, Cross P (1998) The strain rate field in the eastern Mediterranean region, estimated by repeated GPS measurements. *Tectonophysics* 294:237–252. [https://doi.org/10.1016/S0040-1951\(98\)00102-4](https://doi.org/10.1016/S0040-1951(98)00102-4)
- Kapetanidis V, Deschamps A, Papadimitriou P, Matrullo E, Karakonstantis A, Bozionelos G, Kaviris G, Serpetsidaki A, Lyon-caen H, Voulgaris N, Bernard P, Sokos E, Makropoulos K (2015) The 2013 earthquake swarm in Helike, Greece: seismic activity at the root of old normal faults. *Geophys J Int* 202:2044–2073. <https://doi.org/10.1093/gji/ggv249>
- Karagianni EE, Papazachos CB, Panagiotopoulos DG, Suhadolc P, Vuan A, Panza GF (2005) Shear velocity structure in the Aegean area obtained by inversion of Rayleigh waves. *Geophys J Int* 160:127–143. <https://doi.org/10.1111/j.1365-246X.2005.02354.x>
- Karakostas V, Papadimitriou E, Karakaisis G, Papazachos C, Scordilis E, Vargemezis G, Aidona E (2003) The 2001 Skyros, northern Aegean, Greece, earthquake sequence: off-fault aftershocks, tectonic implications, and seismicity triggering. *Geophys Res Lett* 30:1012. <https://doi.org/10.1029/2002/GL015814>
- Karakostas V, Papadimitriou E, Gospodinov D (2014) Modelling the 2013 North Aegean (Greece) seismic sequence: geometrical and frictional constraints, and aftershock probabilities. *Geophys J Int* 197:525–541. <https://doi.org/10.1093/gji/ggt523>
- Karato SI (2008) Deformation of earth materials: introduction to the rheology of solid earth. Cambridge University Press, Cambridge
- Karato SI, Jung H, Katayama I, Skemer P (2008) Geodynamic significance of seismic anisotropy of the upper mantle: new insights from laboratory studies. *Ann Rev Earth Planet Sci.* 36:59–95. <https://doi.org/10.1146/annurev.earth.36.031207.124120>
- Kassaras I, Kapetanidis V (2018) Resolving the tectonic stress by the inversion of earthquake focal mechanisms. Application in the region of Greece. In: Sebastiano DM (ed) Moment tensor solutions: a useful tool for seismotectonics, 1st edn. Springer, Berlin, pp 405–452
- Kassaras I, Kalantoni D, Benetatos Ch, Kaviris G, Michalaki K, Sakellariou N, Makropoulos K (2015) Seismic damage scenarios in Lefkas old town (W. Greece). *Bull Earth Eng* 13(12):3669–3711
- Kaviris G, Papadimitriou P, Kravvariti Ph, Kapetanidis V, Karakonstantis A, Voulgaris N, Makropoulos K (2015) A detailed seismic anisotropy study during the 2011–2012 unrest period in the Santorini Volcanic Complex. *Phys Earth Planet Int* 238:51–88. <https://dx.doi.org/10.1016/j.pepi.2014.11.002>
- Kaviris G, Spingos I, Kapetanidis V, Papadimitriou P, Voulgaris N, Makropoulos K (2017) Upper crust seismic anisotropy study and temporal variations of shear-wave splitting parameters in the western Gulf of Corinth (Greece) during 2013. *Phys Earth Planet Int* 269:148–164. <https://doi.org/10.1016/j.pepi.2017.06.006>
- Kaviris G, Millas C, Spingos I, Kapetanidis V, Fountoulakis I, Papadimitriou P, Voulgaris N, Makropoulos K (2018a) Observations of shear-wave splitting parameters in the Western Gulf of Corinth focusing on the 2014  $M_w=5.0$  earthquake. *Phys Earth Planet Inter* 282:60–76. <https://doi.org/10.1016/j.pepi.2018.07.005>
- Kaviris G, Spingos I, Millas C, Kapetanidis V, Fountoulakis I, Papadimitriou P, Voulgaris N, Drakatos G (2018b) Effects of the January 2018 seismic sequence on shear-wave splitting in the upper crust of Marathon (NE Attica, Greece). *Phys Earth Planet Inter* 285:45–58. <https://doi.org/10.1016/j.pepi.2018.10.007>

- Kawasaki I, Kon'no F (1984) Azimuthal anisotropy of surface waves and the possible type of the seismic anisotropy due to preferred orientation of olivine in the uppermost mantle beneath the Pacific Ocean. *J Phys Earth* 32:229–244. <https://doi.org/10.4294/jpe1952.32.229>
- Kennett BLN, Engdahl ER (1991) Traveltimes for global earthquake location and phase identification. *Geophys J Int* 105:429–465. <https://doi.org/10.1111/j.1365-246X.1991.tb06724.x>
- Kennett BLN, Engdahl ER, Buland R (1995) Constraints on seismic velocities in the Earth from traveltimes. *Geophys J Int* 122:104–108. <https://doi.org/10.1111/j.1365-246X.1995.tb03540.x>
- Kiratzis A, Louvari E (2003) Focal mechanisms of shallow earthquakes in the Aegean Sea and the surrounding lands determined by waveform modelling: a new database. *J Geodyn* 36:251–274. [https://doi.org/10.1016/S0264-3707\(03\)00050-4](https://doi.org/10.1016/S0264-3707(03)00050-4)
- Kneller EA, Van Keken PE (2008) Effect of three-dimensional slab geometry on deformation in the mantle wedge: implications for shear wave anisotropy. *Geochem Geophys Geosyst* 9:1–21. <https://doi.org/10.1029/2007GC001677>
- Kouskouna V, Sakkas G (2013) The University of Athens Hellenic Macroseismic Database (HMDB.UoA): historical earthquakes. *J Seismol* 17:1253–1280. <https://doi.org/10.1007/s10950-013-9390-3>
- Kouskouna V, Makropoulos K, Tsiknakis K (1993) Contribution of historical information to a realistic seismicity and hazard assessment of an area. The Ionian Islands earthquakes of 1767 and 1769: historical investigation. In: Stucchi, M (ed) Historical investigation of European earthquakes, materials of the CEC project review of historical seismicity in Europe, 1:195–206
- Kreemer C, Blewitt G, Klein EC (2014) A geodetic plate motion and Global Strain Rate Model. *Geochem Geophys Geosyst* 15:3849–3889. <https://doi.org/10.1002/2014GC005407>
- Le Pichon X, Kreemer C (2010) The miocene-to-present kinematic evolution of the Eastern Mediterranean and Middle East and its implications for dynamics. *Annu Rev Earth Planet Sci* 38:323–351. <https://doi.org/10.1146/annurev-earth-040809-152419>
- Liu KH, Gao SS (2013) Making reliable shear-wave splitting measurements. *Bull Seismol Soc Am* 103:2680–2693. <https://doi.org/10.1785/0120120355>
- Long MD, Silver PG (2008) The subduction zone flow field from seismic anisotropy: a global view. *Science* 319:315–318. <https://doi.org/10.1126/science.1150809>
- Long MD, Silver PG (2009) Shear wave splitting and mantle anisotropy: measurements, interpretations, and new directions. *Surv Geophys* 30:407–461
- Long MD, van der Hilst RD (2006) Shear wave splitting from local events beneath the Ryukyu arc: trench-parallel anisotropy in the mantle wedge. *Phys Earth Planet Int* 155:300–312. <https://doi.org/10.1016/j.pepi.2006.01.003>
- Long MD, Wirth EA (2013) Mantle flow in subduction systems: the mantle wedge flow field and implications for wedge processes. *J Geophys Res Solid Earth* 118:583–606. <https://doi.org/10.1002/jgrb.50063>
- Makropoulos K, Kaviris G, Kouskouna V (2012) An updated and extended earthquake catalogue for Greece and adjacent areas since 1900. *Nat Hazards Earth Syst Sci* 12:1425–1430. <https://doi.org/10.5194/nhess-12-1425-2012>
- McKenzie D (1972) Active tectonics of the Mediterranean Region. *Geophys J Int* 30:109–185. <https://doi.org/10.1111/j.1365-246X.1972.tb02351.x>
- Menant A, Sternai P, Jolivet L, Guillou-Frotter L, Gerya T (2016) 3D numerical modeling of mantle flow, crustal dynamics and magma genesis associated with slab roll-back and tearing: the eastern Mediterranean case. *Earth Planet Sci Lett* 442:93–107. <https://doi.org/10.1016/j.epsl.2016.03.002>
- Montagner JP, Kennett BLN (1996) How to reconcile body-wave and normal-mode reference earth models. *Geophys J Int* 125:229–248. <https://doi.org/10.1111/j.1365-246X.1996.tb06548.x>
- Mutlu AK, Karabulut H (2011) Anisotropic Pn tomography of Turkey and adjacent regions. *Geophys J Int* 187:1743–1758. <https://doi.org/10.1111/j.1365-246X.2011.05235.x>
- Nicolas A, Christensen NI (1987) Formation of anisotropy in upper-mantle peridotites: a review, in composition, structure and dynamics of the lithosphere-asthenosphere system. *Am Geophys Union Geo Dyn Monogr Ser* 16:111–123. <https://doi.org/10.1029/GD016>
- Nijholt N, Govers R (2015) The role of passive margins on the evolution of Subduction-Transform Edge Propagators (STEPs). *J Geophys Res Solid Earth* 120:7203–7230. <https://doi.org/10.1002/2015JB012202>
- Nyst M, Thatcher W (2004) New constraints on the active tectonic deformation of the Aegean. *J Geophys Res Solid Earth* 109:1–23. <https://doi.org/10.1029/2003JB002830>
- Olive JA, Pearce F, Rondenay S, Behn MD (2014) Pronounced zonation of seismic anisotropy in the Western Hellenic subduction zone and its geodynamic significance. *Earth Planet Sci Lett* 391:100–109. <https://doi.org/10.1016/j.epsl.2014.01.029>
- Papadimitriou EE (2002) Mode of strong earthquake recurrence in the central Ionian Islands (Greece): possible triggering due to Coulomb stress changes generated by the occurrence of previous strong shocks. *Bull Seismol Soc Am* 92:3293–3308
- Papadimitriou EE, Sykes LR (2001) Evolution of the stress field in the Northern Aegean Sea (Greece). *Geophys J Int* 146:747–759. <https://doi.org/10.1046/j.0956-540X.2001.01486.x>
- Papadimitriou P, Kaviris G, Makropoulos K (1999) Evidence of shear-wave splitting in the eastern Corinthian Gulf (Greece). *Phys Earth Planet Inter* 114:3–13. [https://doi.org/10.1016/S0031-9201\(99\)00041-2](https://doi.org/10.1016/S0031-9201(99)00041-2)
- Papadimitriou P, Kaviris G, Makropoulos K (2006) The Mw=6.3 2003 Lefkada Earthquake (Greece) and induced transfer changes. *Tectonophysics* 423:73–82
- Papadimitriou P, Kapetanidis V, Karakonstantis A, Kaviris G, Voulgaris N, Makropoulos K (2015) The Santorini Volcanic Complex: a detailed multi-parameter seismological approach with emphasis on the 2011–2012 unrest period. *J Geodyn* 85:32–57. <https://doi.org/10.1016/j.jog.2014.12.004>
- Papadimitriou P, Kassaras I, Kaviris G, Tselentis G-A, Voulgaris N, Lekkas E, Chouliaras G, Evangelidis C, Pavlou K, Kapetanidis V, Karakonstantis A, Kazantzidou-Firtinidou D, Fountoulakis I, Millas C, Spingos I, Aspiotis T, Moutoulidou A, Skourtsos E, Antoniou V, Andreadakis E, Mavroulis S, Kleanthi M (2018) The 12th June 2017 Mw=6.3 Lesbos earthquake from detailed seismological observations. *J Geodyn* 115:23–42. <https://doi.org/10.1016/j.jog.2018.01.009>
- Papanikolaou DJ, Royden LH (2007) Disruption of the Hellenic arc: late Miocene extensional detachment faults and steep Pliocene-Quaternary normal faults—Or what happened at Corinth? *Tectonics*. <https://doi.org/10.1029/2006TC002007>
- Papazachos B, Papazachou K (2003) Earthquakes in Greece (in Greek). Ziti Publications, Athens
- Papazachos BC, Dimitriadis ST, Panagiotopoulos DG, Papazachos CB, Papadimitriou EE (2005) Deep structure and active tectonics of the southern Aegean volcanic arc. *Dev Volcano* 7:47–64. [https://doi.org/10.1016/S1871-644X\(05\)80032-4](https://doi.org/10.1016/S1871-644X(05)80032-4)
- Paul A, Karabulut H, Mutlu AK, Salaün G (2014) A comprehensive and densely sampled map of shear-wave azimuthal anisotropy in the Aegean-Anatolia region. *Earth Planet Sci Lett* 389:14–22. <https://doi.org/10.1016/j.epsl.2013.12.019>
- Pearce D, Rondenay S, Sachpazi M, Charalampakis M, Royden LH (2012) Seismic investigation of the transition from continental to oceanic subduction along the western Hellenic subduction

- Zone. *J Geophys Res Solid Earth*. <https://doi.org/10.1029/2011JB009023>
- Piromallo C, Morelli A (2003) P wave tomography of the mantle under the Alpine-Mediterranean area. *J Geophys Res Solid Earth* 108:1–23. <https://doi.org/10.1029/2002JB001757>
- Portner D, Delph J, Biryol B, Beck S, Zandt G, Özacar A, Sandvol E, Türkelli N (2018) Subduction termination through progressive slab deformation across Eastern Mediterranean subduction zones from updated P-wave tomography beneath Anatolia. *Geosphere* 14(3):907–925. <https://doi.org/10.1130/GES01617.1>
- Raitt RW, Shor GG Jr, Francis TJG, Morris GB (1969) Anisotropy of the Pacific upper mantle. *J Geophys Res* 74(12):3095–3109. <https://doi.org/10.1029/JB074i012p03095>
- Reilinger R, McClusky S, Vernant P, Lawrence S, Ergintav S, Cakmak R, Ozener H, Kadirov F, Guliev I, Stepanyan R, Nadariya M, Hahubia G, Mahmoud S, Sakr K, ArRajehi A, Paradissis D, Al-Aydrus A, Prilepin M, Guseva T, Evren E, Dmitrotsa A, Filikov SV, Gomez F, Al-Ghazzi R, Karam G (2006) GPS constraints on continental deformation in the Africa–Arabia–Eurasia continental collision zone and implications for the dynamics of plate interactions. *J Geophys Res Solid Earth* 111:1–26. <https://doi.org/10.1029/2005JB004051>
- Royden LH, Papanikolaou DJ (2011) Slab segmentation and late Cenozoic disruption of the Hellenic arc. *Geochem Geophys Geosyst* 12:1–24. <https://doi.org/10.1029/2010GC003280>
- Russo RM, Silver PG (1994) Trench-parallel flow beneath the Nazca plate from seismic anisotropy. *Science* 263:1105–1111. <https://doi.org/10.1126/science.263.5150.1105>
- Salaün G, Pedersen HA, Paul A, Farra V, Karabulut H, Hatzfeld D, Papazachos C, Childs DM, Pequegnat C, Afacan T, Aktar M, Bourova-Flin E, Cambaz D, Hatzidimitriou P, Hubans F, Kementzetzidou D, Karagianni E, Karagianni I, Komec Mutlu A, Dimitrova L, Ozakin Y, Roussel S, Scordilis M, Vamvakaris D (2012) High-resolution surface wave tomography beneath the Aegean-Anatolia region: constraints on upper-mantle structure. *Geophys J Int* 190:406–420. <https://doi.org/10.1111/j.1365-246X.2012.05483.x>
- Savage MK (1999) Seismic anisotropy and mantle deformation: what have we learnt from shear wave splitting? *Rev Geophys* 37:65–106. <https://doi.org/10.1029/98RG02075>
- Schmid C, van der Lee S, Giardini D (2004) Delay times and shear wave splitting in the Mediterranean region. *Geophys J Int* 159:275–290. <https://doi.org/10.1111/j.1365-246X.2004.02381.x>
- Silver PG, Chan WW (1991) Shear wave splitting and sub continental mantle deformation. *J Geophys Res* 96:429–454. <https://doi.org/10.1029/91JB00899>
- Sokos E, Zahradník J, Gallovič F, Serpetsidaki A, Plicka V, Kiratzi A (2016) Asperity break after 12 years: the Mw6.4 2015 Lefkada (Greece) earthquake. *Geophys Res Lett* 43(12):6137–6145. <https://doi.org/10.11002/2016GL069427>
- Sternai P, Jolivet L, Menant A, Gerya T (2014) Driving the upper plate surface deformation by slab rollback and mantle flow. *Earth Planet Sci Lett* 405:110–118. <https://doi.org/10.1016/j.epsl.2014.08.023>
- Stucchi M, Rovida A, Gomez Capera AA, Alexandre P, Camelbeeck T, Demircioglu MB, Gasperini P, Kouskouna V, Musson RMW, Radulian M, Sesetyan K, Vilanova S, Baumont D, Bungum H, Fäh D, Lenhardt W, Makropoulos K, Martinez Solares JM, Scotti O, Živčić M, Albin P, Battlo J, Papaioannou C, Tavecossian R, Locati M, Meletti C, Viganò D, Giardini D (2013) The SHARE European Earthquake Catalogue (SHEEC) 1000–1899. *J Seismol* 17:523–544. <https://doi.org/10.1007/s10950-012-9335-2>
- Suckale J, Rondenay S, Sachpazi M, Charalampakis M, Hosa A, Royden LH (2009) High-resolution seismic imaging of the western Hellenic subduction zone using teleseismic scattered waves. *Geophys J Int* 178:775–791. <https://doi.org/10.1111/j.1365-246X.2009.04170.x>
- Tommasi A, Tikoff B, Vauchez A (1999) Upper mantle tectonics: three-dimensional deformation, olivine crystallographic fabrics and seismic properties. *Earth Planet Sci Lett* 168:173–186. [https://doi.org/10.1016/S0012-821X\(99\)00046-1](https://doi.org/10.1016/S0012-821X(99)00046-1)
- Vecsey L, Plomerová J, Babuška V (2008) Shear-wave splitting measurements—problems and solutions. *Tectonophysics* 462:178–196. <https://doi.org/10.1016/j.tecto.2008.01.021>
- Visser K, Trampert J, Kennett BLN (2008) Global anisotropic velocity maps for higher mode Love and Rayleigh waves. *Geophys J Int* 172:1016–1032. <https://doi.org/10.1111/j.1365-246X.2007.03685.x>
- Wüstefeld A, Bokelmann G (2007) Null detection in shear-wave splitting measurements. *Bull Seismol Soc Am* 97:1204–1211. <https://doi.org/10.1785/0120060190>
- Wüstefeld A, Bokelmann G, Zaroli C, Barruol G (2008) SplitLab: a shear-wave splitting environment in Matlab. *Comput Geosci* 34:515–528. <https://doi.org/10.1016/j.cageo.2007.08.002>
- Wüstefeld A, Al-Harrasi O, Verdon JP, Wookey J, Kendall JM (2010) A strategy for automated analysis of passive microseismic data to image seismic anisotropy and fracture characteristics. *Geophys Prospect* 58:755–773. <https://doi.org/10.1111/j.1365-2478.2010.00891.x>
- Zhang S, Karato S (1995) Lattice preferred orientation of olivine aggregates deformed in simple shear. *Nature* 375:774–777. <https://doi.org/10.1038/375774a0>





# Declustering of Iran earthquake catalog (1983–2017) using the epidemic-type aftershock sequence (ETAS) model

Nader Davoudi<sup>1</sup> · Hamid Reza Tavakoli<sup>1</sup> · Mehdi Zare<sup>2</sup> · Abdollah Jalilian<sup>3</sup>

Received: 10 July 2018 / Accepted: 11 October 2018 / Published online: 19 October 2018  
© Institute of Geophysics, Polish Academy of Sciences & Polish Academy of Sciences 2018

## Abstract

The main goal of this article is to decluster Iranian plateau seismic catalog by the epidemic-type aftershock sequence (ETAS) model and compare the results with some older methods. For this purpose, Iranian plateau bounded in 24°–42°N and 43°–66°E is subdivided into three major tectonic zones: (1) North of Iran (2) Zagros (3) East of Iran. The extracted earthquake catalog had a total of 6034 earthquakes ( $M_w > 4$ ) in the time span 1983–2017. The ETAS model is an accepted stochastic approach for seismic evaluation and declustering earthquake catalogs. However, this model has not yet been used to decluster the seismic catalog of Iran. Until now, traditional methods like the Gardner and Knopoff space–time window method and the Reasenber link-based method have been used in most studies for declustering Iran earthquake catalog. Finally, the results of declustering by the ETAS model are compared with result of Gardner and Knopoff (Bull Seismol Soc Am 64(5):1363–1367, 1974), Uhrhammer (Earthq Notes 57(1):21, 1986), Gruenthal (pers. comm.) and Reasenber (Geophys Res 90:5479–5495, 1985) declustering methods. The overall conclusion is difficult, but the results confirm the high ability of the ETAS model for declustering Iranian earthquake catalog. Use of the ETAS model is still in its early steps in Iranian seismological researches, and more parametric studies are needed.

**Keywords** Declustering · Earthquake catalog · Seismotectonic provinces of Iran · Windowing methods · ETAS model

## Abbreviations

Re	Reasenberg
Uh	Uhrhammer
G-K	Gardner and Knopoff
Gr	Gruenthal method
ETAS	Epidemic-type aftershock sequence model

## Introduction

Declustering an earthquake catalog or, similarly, separating it into independent earthquakes (mainshocks) and dependent earthquakes (foreshocks and aftershocks) is very important in seismological studies. There are several declustering approaches that have been proposed over the years (Van Stiphout et al. 2012) which include deterministic approaches such as window-based method (Gardner and Knopoff 1974; Uhrhammer 1986; Gruenthal pers. comm.), single-link cluster method (Frohlich and Davis 1990; Davis and Frohlich 1991), linking to spatial interaction zones (Reasenber 1985; Savage 1972) and probabilistic approaches such as stochastic model (Kagan and Jackson 1991; Zhuang et al. 2002, 2004, 2006), independent stochastic declustering model (Marsan and Longline 2010), model-based inter-event time distribution (Hainzel et al. 2006), coefficient of variant inter-event times (Bottiglieri et al. 2009). (See Van Stiphout et al. 2012 for more information about the Gruenthal method.)

The epidemic-type aftershock sequence (ETAS) model is a statistical approach based on a space–time branching process model that explains how each earthquake epidemically can generate its aftershocks (Van Stiphout et al. 2012).

✉ Hamid Reza Tavakoli  
tavakoli@nit.ac.ir  
Nader Davoudi  
naderdawoodi@gmail.com  
Mehdi Zare  
mzare@iiees.ac.ir  
Abdollah Jalilian  
jalilian@razi.ac.ir

<sup>1</sup> Department of Civil Engineering, Babol Noshirvani University of Technology, Babol, Iran  
<sup>2</sup> Department of Seismology, International Institute of Earthquake Engineering and Seismology, Tehran, Iran  
<sup>3</sup> Department of Statistics, Razi University, Kermanshah, Iran

Despite the great potential of the ETAS model, mainly due to the simplicity of traditional methods, generally, researchers have used traditional deterministic approaches to decluster Iran earthquake catalog. The Iranian plateau is part of the Alpine-Himalayan seismotectonic belt. The vast seismic zone in the earthquake-prone Iranian plateau has various seismotectonic provinces with different seismicity pattern. In this paper, based on the zoning proposed by Shahvar et al. (2013), a new zoning is presented. The Iranian plateau is divided into three major seismotectonic zones, and a central region without recorded seismic sequences is neglected. Researchers have proposed different major seismotectonic provinces for Iran. Mirzaei et al. (1997) provide a uniform seismic catalog of Iran (22°–42°N and 42°–66°E) in time span 4th century B.C.—1994. They subdivide Iranian plateau into five main seismotectonic areas: (1) Alborz-Azerbaijan, (2) Kopeh-Dagh, (3) Zagros, (4) Central-East of Iran, (5) Makran. Following this research, this zoning has been documented in many studies (Zafarani and Soghrat 2012; Karimiparidari et al. 2013; Zare et al. 2014; Mousavi-Bafrouei et al. 2015). Shahvar et al. (2013) present an integrated catalog for Iranian plateau (1900–2011,  $M_w > 4$ ). They subdivide Iran's plateau into two major areas: (1) Zagros and (2) Alborz-Central Iran and decluster the extracted catalog by Uhrhammer (1986) procedure. Karimiparidari et al. (2013) present a uniform catalog for the Iranian earthquakes (3rd century B.C.—2010). They use Gardner and Knopoff (1974) window method to decluster the compiled catalog. Mousavi-Bafrouei et al. (2015) prepared an integrated catalog for the Iranian plateau from the 4th century B.C. to 2012. They used Gardner and Knopoff (1974), Uhrhammer (1986) and Reasenber (1985) methods to decluster Iran earthquake catalog. Amini (2014) compared Reasenber (1985) and Gruenthal (pers. comm.) declustering methods for Alborz-Azerbaijan and Kopeh-Dagh seismotectonic regions in the north of Iranian plateau in time span 550 B.C.—2006. She concluded that Reasenber's (1985) declustering method estimates the number of mainshocks three times more than the Gruenthal's (pers. comm.) method. Ommi et al. (2016) have studied aftershock decay rate for 15 selected earthquakes occurred in Iranian plateau during the period 2002–2013. They used Gardner and Knopoff (1974), Wells and Copper-smith (1994) and Burkhard and Grünthal (2009) methods to decluster the earthquake catalog of Iran.

In this study, Iranian plateau is subdivided into three major seismotectonic zones: (1) North of Iran, (2) Zagros and (3) East of Iran. An earthquake catalog including 6034 earthquakes ( $M_w > 4$ ) in the time span 1983–2017 is extracted for these three zones. Finally, the extracted catalog has been declustered using the window-based method (Gardner and Knopoff 1974; Uhrhammer 1986; Gruenthal pers. comm.), single-link cluster method (Reasenber 1985) and ETAS model. The results are compared, and discussions and conclusions are made.

## Methods

### Window-based methods

So far, in most studies conducted to decluster earthquake catalogs, the Reasenber's (1985) linked-window method or the variant of Gardner and Knopoff (1974) windowing technique has been used. In Gardner and Knopoff's windowing method, a specified distance interval  $L(M)$  and a specified time interval  $T(M)$  have been defined for each earthquake with a magnitude of  $M$ . Subsequent earthquakes will be identified as an aftershock if they occur within this time-space window. Foreshocks will be identified the same as aftershocks. The largest shock in a sequence has the largest time-space window and is a mainshock (Van Stiphout et al. 2012). The size of time-space windows in Gardner and Knopoff (1974), Uhrhammer (1986) and Gruenthal (pers. comm.) methods is shown in Table 1.

In the linked-window method (Cluster Method) presented by Reasenber (1985), earthquakes are associated with clusters by defining spatial and temporal interaction zone around the earthquakes. The temporal property of the interaction zone is defined by Omori's law. The spatial extension of the interaction zone is chosen according to stress distribution near the mainshocks. (For more details, see Reasenber 1985; Molchan and Dmitrieva 1992; Van Stiphout et al. 2012.) The input parameters for the Cluster Method are presented in Table 2. In this study, the standard parameters of Reasenber (1985) method are used.

**Table 1** Windows sizes in Gardner and Knopoff (1974), Uhrhammer (1986) and Gruenthal (pers. comm.) declustering methods

Method	Distance (km)	Time (day)
Gardner and Knopoff (1974)	$10^{0.1238M + 0.983}$	$\begin{cases} 10^{0.032M + 2.7389} & \text{if } M \geq 6.5 \\ 10^{0.5409M - 0.547} & \text{else} \end{cases}$
Uhrhammer (1986)	$10^{1.77 + (0.037 + 1.02M)^2}$	$\begin{cases} e^{-3.95 + (0.62 + 17.32M)^2} & \text{if } M \geq 6.5 \\ 10^{2.8 + 0.024M} & \text{else} \end{cases}$
Gruenthal (pers. comm.)	$e^{-1.024 + 0.804M}$	$e^{-2.87 + 1.235M}$

**Table 2** Input parameters for the Cluster Method presented by Reasenber (1985)

Parameter	Standard	Min	Max
$\tau_{\min}$	1	0.5	2.5
$\tau_{\max}$	10	3	15
$p_1$	0.95	0.9	0.99
$x_{\text{meff}}$	4.0	0	1
$x_k$	0.5	1.6	1.8
$r_{\text{fact}}$	10	5	20

$\tau_{\min}$  and  $\tau_{\max}$  are the minimum and maximum look-ahead time of observing the next earthquake at a certain probability,  $p_1$ .  $x_k$  is the increase of the lower cutoff magnitude during clusters:  $x_{\text{meff}} = x_{\text{meff}} + x_k M$ , where  $M$  is the magnitude of the largest event in the cluster,  $x_{\text{meff}}$  is the effective lower magnitude cutoff for catalog,  $r_{\text{fact}}$  is the number of crack radii surrounding each earthquake within new events considered to be part of the cluster (Van Stiphout et al. 2012)

### ETAS model

An earthquake catalog typically includes date, time ( $t$ ), magnitude ( $m$ ) and epicenter coordination [longitude ( $x$ ), latitude ( $y$ )] of earthquakes. The earthquake catalog can be expressed by a point pattern in time-space (Vere-Jones 1970; Ogata 1998; Zhuang et al. 2002). As many scholars explained (Molchan and Dmitrieva 1992; Ogata 1998; Zhuang et al. 2002; Van Stiphout et al. 2012) that such point process can be described by conditional intensity function as follows:

$$\lambda(t, x, y | \mathcal{H}_t) = \mu(x, y) + \sum_{\{i: t_i < t\}} \kappa(m_i) g(t - t_i) f(x - x_i, y - y_i; m_i) \quad (1)$$

where  $\lambda(t, x, y | \mathcal{H}_t)$  is the space-time conditional intensity function.  $\mathcal{H}_t = \{(t_i, x_i, y_i, m_i); t_i < t\}$  is the history of earthquakes occurrence up to time  $t$  (Ogata 1998; Zhuang et al. 2002).  $\mu(x, y)$  is the background seismicity rate and  $\kappa(m_i) g(t - t_i) f(x - x_i, y - y_i; m_i)$  is the seismicity rate induced by the  $i_{\text{th}}$  event that has already occurred (Zhuang 2011).

$\kappa(m_i)$  is the expected number of triggered earthquakes from an earthquake of magnitude  $m_i$ .  $g(t - t_i)$  and  $f(x - x_i, y - y_i; m_i)$  respectively are the probability density function of the occurrence time and occurrence location of triggered earthquakes.

The background seismicity rate function is assumed to be stationary in time and is defined by a Poisson process.

Occurrence time function is based on modified Omori law and occurrence location function is a radially symmetric function dependent on the location and magnitude of earthquakes (Ogata 1998; Zhuang et al. 2002). The second part in Eq. 1 shows how a mainshock with the magnitude of  $m_i$  trigger its aftershocks. In the ETAS model, any triggered earthquake (aftershock) can also have its aftershocks. The aftershocks sequence can be continued epidemically. As proposed by Zhuang et al. (2002), the probability that the  $j_{\text{th}}$  earthquake is triggered by the  $i_{\text{th}}$  earthquake can be estimated by Eq. 2 (Van Stiphout et al. 2012):

$$p_{ij} = \frac{k(M_i) g(t_j - t_i) f(x_j - x_i, y_j - y_i | M_i)}{\lambda(t_j, x_j, y_j, M | \mathcal{H}_{ij})} \quad (2)$$

Consequently, the probability that the  $j_{\text{th}}$  earthquake is a triggered (dependent) earthquake is

$$p_j = \sum_{i=1}^{j-1} p_{ij} \quad (3)$$

The value of  $p_j$  can range from 0 to 1. An earthquake catalog can be declustered by calculating this probability for all events in the catalog and considering a threshold value of  $p_j$ .

### Results and discussion

In a statistical approach such as the ETAS model, the data quality and quantity have a great impact on the final results. The earthquake catalog that is used in this study is extracted from the data center of the International Institute of Engineering and Seismology (<http://www.iiees.ac.ir/fa/eqcatalog/>). The study area is bounded at 24°–42°N and 43°–66°E, and the study time period is 1983–2017. We subdivide the Iranian plateau into three major tectonic zones: (1) North of Iran, (2) Zagros and (3) East of Iran (Fig. 1). Our analysis showed that these three seismic zones have different seismicity regimes in stochastic approach and should not be combined together. Finally, our extracted catalog had a total of 6034 earthquakes ( $M_w > 4$ ) in the time span 1983–2017. As shown in Fig. 1, the number of earthquakes occurring in the center of Iranian plateau is very small. Modeling this region is not possible due to lack of required data. Adding this area to the eastern region will reduce the seismicity rate incorrectly. Thus, this region is neglected in this study.



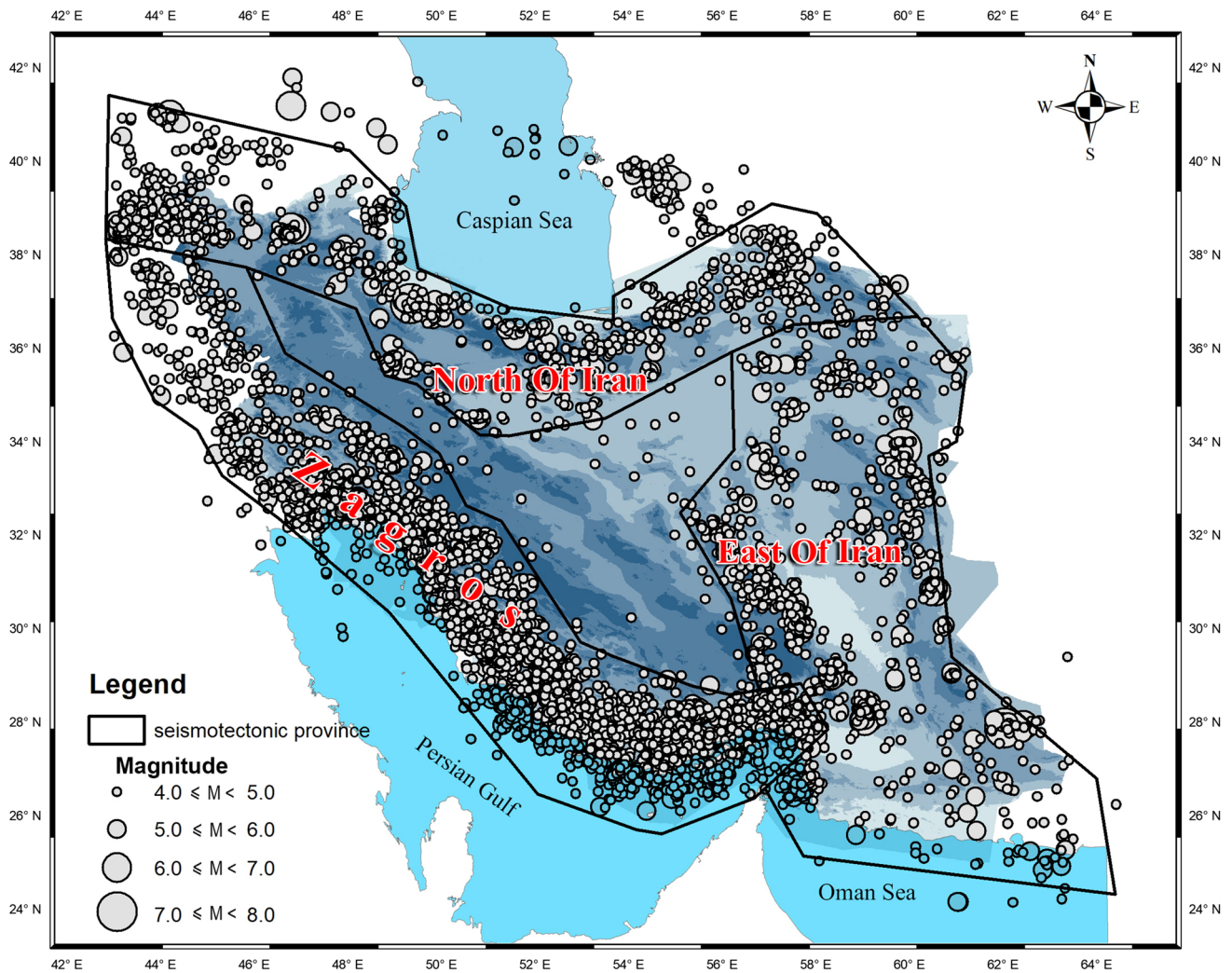


**Fig. 1** Major seismotectonic provinces of Iran. Zoning that is used in this study. Circles show epicenters of earthquakes ( $M_w > 4$ ) that occurred from 1983 to 2017

The moment magnitude scale ( $M_w$ ) is the most appropriate scale for earthquakes. This scale has not been saturated; it has physical meaning and is a more adequate magnitude scale for great earthquakes (Kanamori 1977). For preparing a unified catalog, all other magnitudes scales are converted to the moment magnitude scale using the regression method and statistical analysis proposed by Shahvar et al. (2013). As Huang and LiWX (1994) pointed out, “the completeness and reliability of data are the basis of earthquake research”. In particular, data reliability will be more important when using the stochastic ETAS model. Actually, we need a large

number of recorded earthquake sequences in the catalog to fit the ETAS model. The date January 1, 1983 is the starting point of analysis by investigating the Iranian instrumental earthquake catalog considering the Iranian seismic network development. The magnitude of completeness ( $M_c$ ) is variable in different seismotectonic zones. The study results (Zare et al. 2014; Mousavi-Bafrouei et al. 2015) show that the threshold of  $M_c$  optimistically is above 4 ( $M_w > 4$ ) for a recent modern instrumental catalog of the Iranian plateau.

According to Eq. 3, the probability that the  $j_{th}$  earthquake is a mainshock or a dependent earthquake (aftershock and

foreshock) can be estimated with the intensity function values and background seismicity rate. The catalog can be declustered with this specified probability for each event available in the catalog. In fact, a probability threshold must be chosen. If the value of  $1 - p_j$  from Eq. 3 be greater than the selected threshold of probability, the event will be considered as a mainshock. Selecting the threshold value is optional and based on engineering judgment. Obviously, assuming different thresholds will result in different catalogs. In fact, this user-defined optional property of the ETAS approach is one of the advantages of this probabilistic model compared to the traditional deterministic declustering methods. The three listed seismotectonic zones of Iran have different seismic parameters. By fitting a separated ETAS model on any of the three zones, the background seismicity rate and the declustered catalog are extracted. In this study, we use the R (Jalilian and Zhuang 2016) package ETAS from the Comprehensive R Archive Network (CRAN) available at <http://CRAN.R-project.org/package=ETAS> and GitHub at <https://github.com/jalilian/ETAS> (under GPL 2 license). Also in this study, the ZMAP software package (Weimer 2001) is used to decluster the Iran earthquake catalog, using the mentioned windowing methods. The results of declustering the earthquake catalog in the three major seismotectonic regions of Iran are presented in Table 3 by different methods in ZMAP software.

The final maximum likelihood estimates values of the ETAS model parameters for the three different major seismotectonic zones of Iran are presented in Table 4. In Fig. 2 are shown the background seismicity rate and the clustering coefficient for the three zones.

**Table 3** Results of declustering the earthquake catalog of Iran (1983–2017,  $M_w > 4$ ) using ZMAP software

Zone name	Total number of earthquakes	Method	Number of clusters	Number of mainshocks	Mainshock ratio to total events
North of Iran	1196	a	39	974	0.81
		b	83	764	0.63
		c	151	638	0.53
		d	184	521	0.43
Zagros	3741	a	149	3251	0.86
		b	332	2531	0.67
		c	509	1684	0.45
		d	547	1094	0.29
East of Iran	1097	a	48	905	0.82
		b	78	686	0.62
		c	124	544	0.49
		d	151	433	0.39

(a) Reasenberg (1985), (b) Uhrhammer (1986), (c) Gardner and Knopoff (1974) and (d) Gruenthal (pers. comm.)

**Table 4** Maximum likelihood estimates values of ETAS model in the three seismotectonic provinces of Iran

Parameter	North of Iran	Zagros	East of Iran
$\mu$	0.802126	0.767781	0.827309
$A$	0.280538	0.418631	0.396799
$c$	0.024071	0.012243	0.020602
$\alpha$	1.018709	1.278380	0.949921
$P$	1.10199	1.074867	1.120693
$D$	0.002009	0.009581	0.002298
$q$	1.832303	2.091095	1.532486
$\gamma$	0.887649	0.181203	0.558234

The frequency of each magnitude in the declustered earthquake catalogs is presented in Figs. 3, 4 and 5. The total number of earthquakes in the catalogs after declustering by different methods is shown and compared in Fig. 6. For a better comparison in Fig. 6, the ETAS model results are presented with respect to different threshold values. As expected, we have a catalog with a maximum number of independent earthquakes considering the least threshold (0.5). Uhrhammer and Reasenberg's methods compared to ETAS model estimate more mainshocks in the declustered catalog. This is the case in all seismotectonic zones in this study. There is a great difference that roughly we can say that the Uhrhammer and Reasenberg's methods overestimate the mainshocks number. The maximum number of clusters and therefore a maximum number of dependent earthquakes are estimated using the Gruenthal windowing

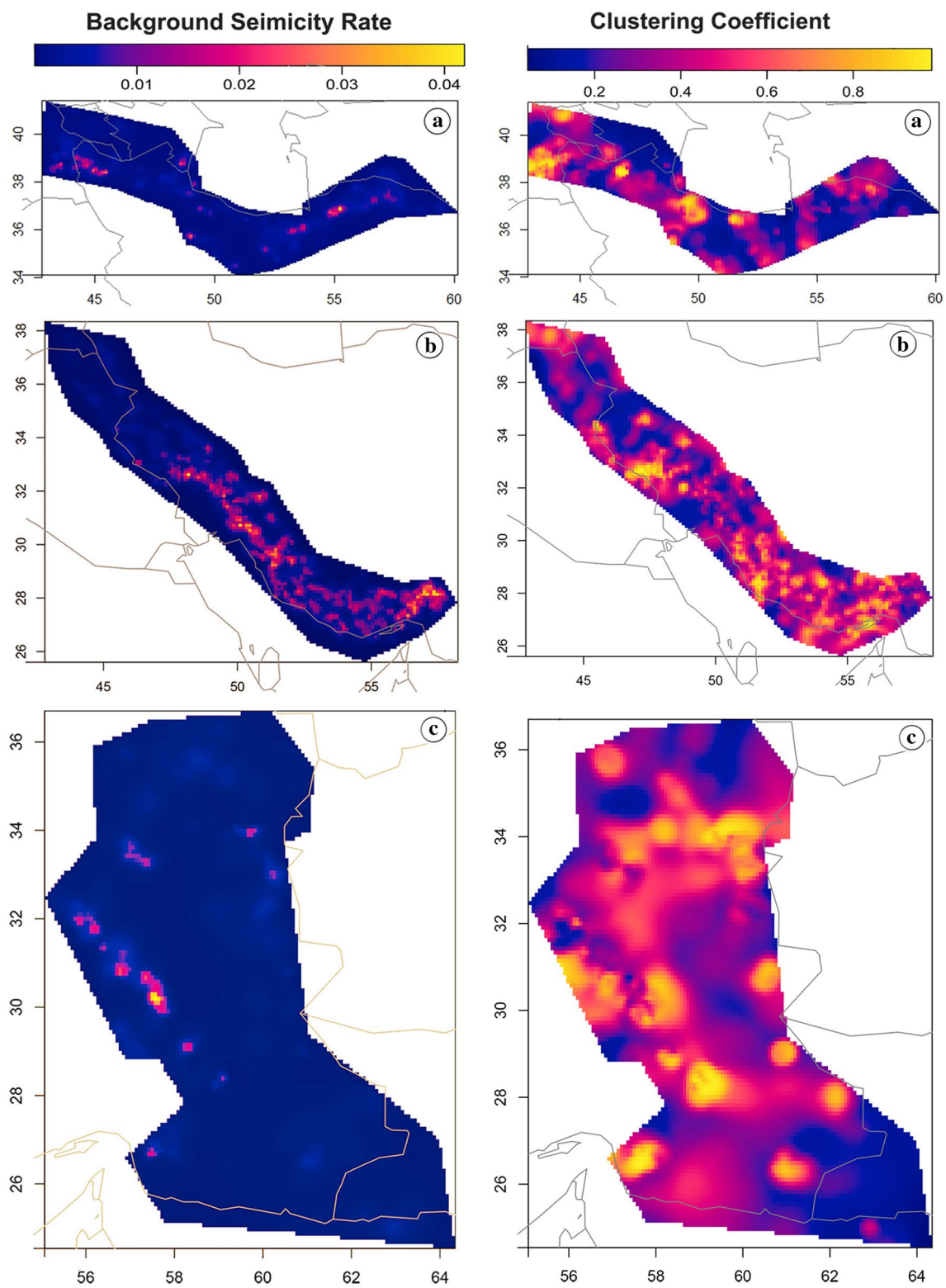


**Fig. 2** Background seismicity rate and clustering coefficient for the three major seismotectonic zones of Iran using ETAS model. **a** North of Iran. **b** Zagros region. **c** East of Iran

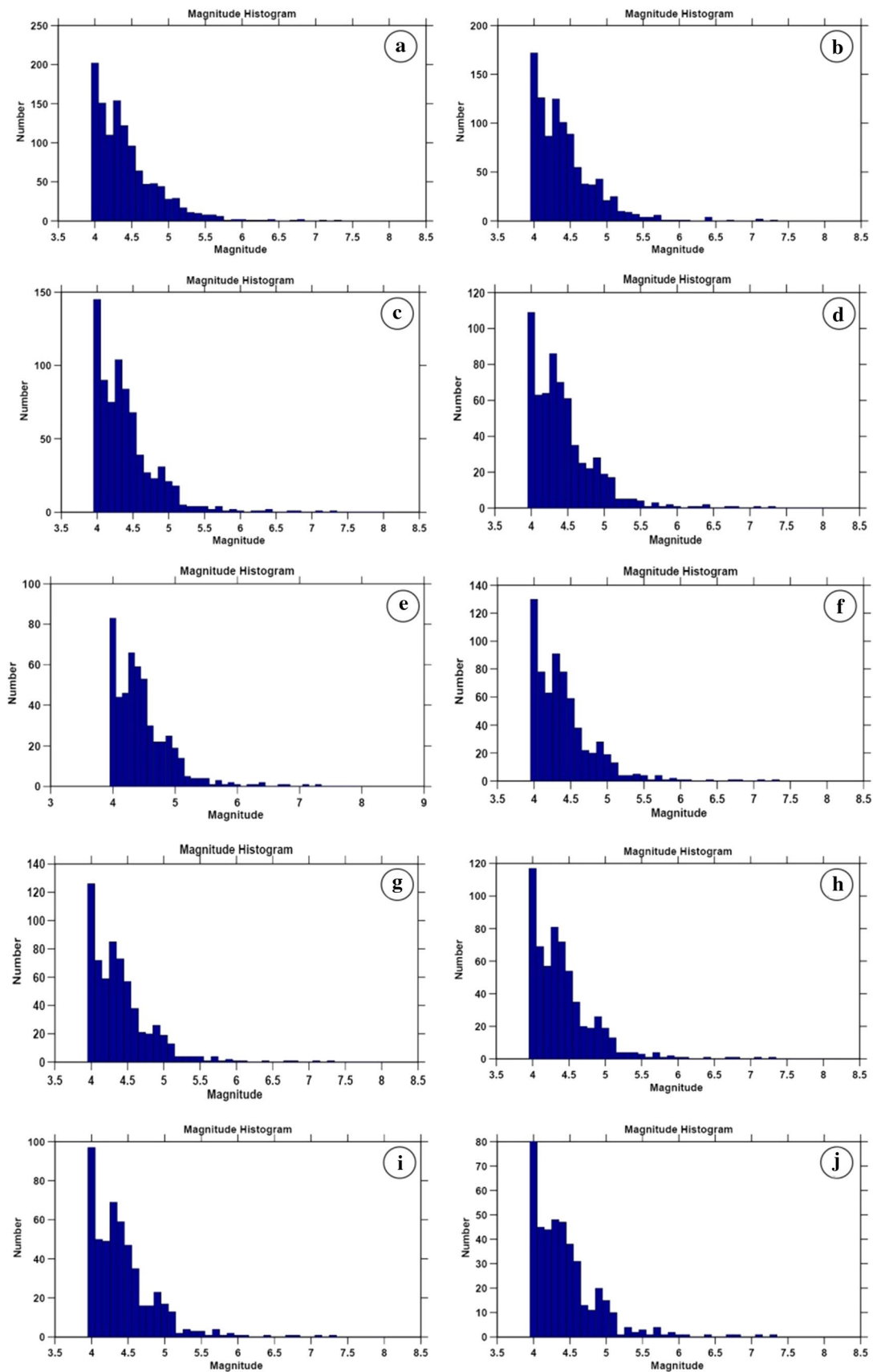


**Fig. 3** Frequency of each magnitude in earthquake catalog of North of Iran that is declustered using different methods. **a** not declustered. **b** Reasenberg. **c** Uhrhammer. **d** Gardner and Knopoff. **e** Gruenthal method. **f, g, h, i, j** ETAS model with probability thresholds 0.5, 0.6, 0.7, 0.8, 0.9, respectively



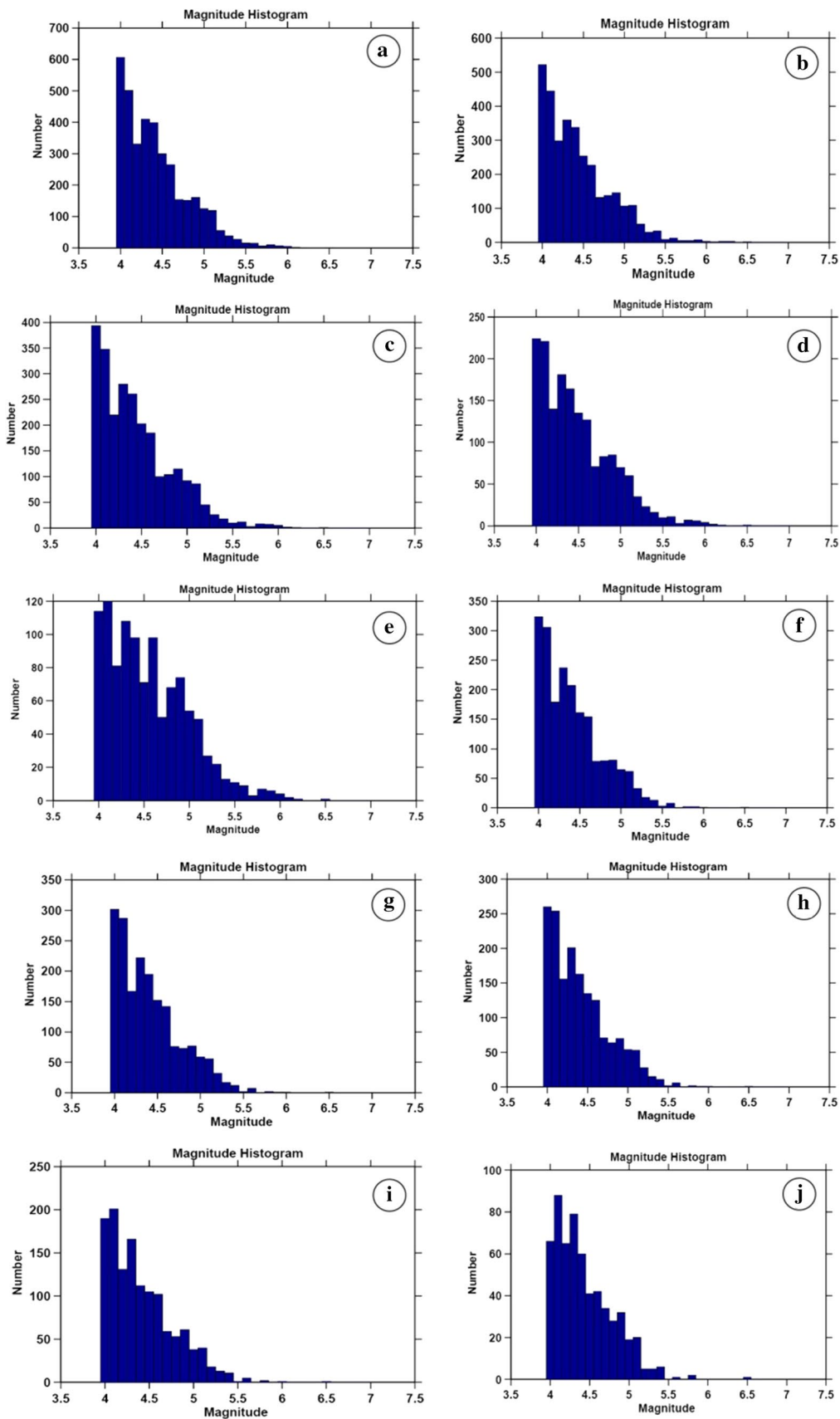


Fig. 4 As in Fig. 3 for Zagros region of Iran

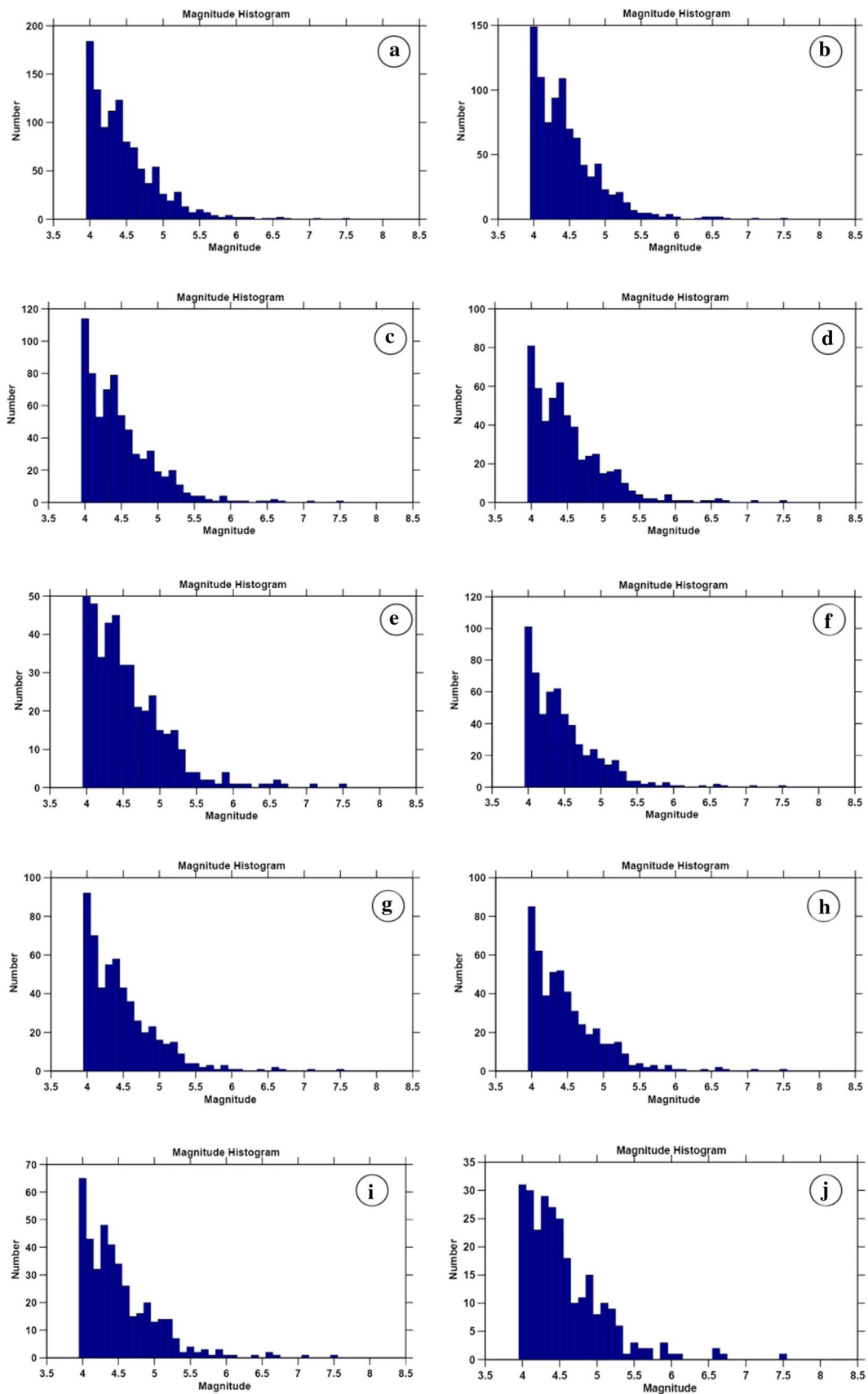
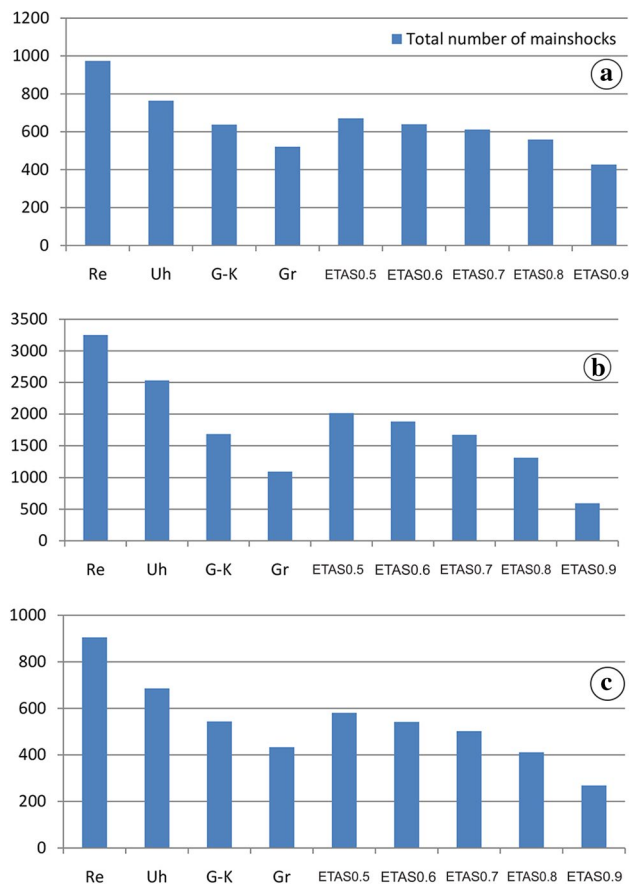


Fig. 5 As in Fig. 3 for East of Iran



**Fig. 6** A chart for comparing the results of different declustering methods. Re: Reasenberg method, Uh: Uhrhammer method, G-K: Gardner and Knopoff method, Gr: Gruenthal method, ETAS: ETAS model with different thresholds. **a** North of Iran. **b** Zagros. **c** East of Iran

method. On the other hand, the Reasenberg's method estimates a catalog with the least number of clusters.

As previously stated, according to different thresholds in the ETAS model, different catalogs will be obtained. In this study, for North and East of Iran, the number of mainshocks in the declustered catalog by the Gardner and Knopoff method was equal to that of the ETAS model with a threshold of 0.6. In the Zagros region, the threshold values in the ETAS model increased to 0.7 to match the results of the two methods. The number of mainshocks in the declustered catalog by the Gruenthal method and the ETAS model will be matched considering the threshold in the ETAS model equal to 0.79 in East and North of Iran and equal to 0.84 in Zagros region. In Table 5, the ratio of the number of dependent earthquakes to the total number of earthquakes is calculated for Iran seismotectonic zones using the discussed methods. The results presented in Table 5 confirm that there is the highest number of dependent earthquakes in the

**Table 5** Dependent earthquakes–total number of earthquakes ratio in the Iranian earthquake catalog

Seismotectonic province	Total number of earthquakes	Percent of dependent earthquakes (%)
North of Iran	1196	52
Zagros	3741	64
East of Iran	1097	57

Time interval 1983–2017,  $M_w > 4$ . This catalog is declustered using the ETAS model with a threshold of probability equal to 0.8

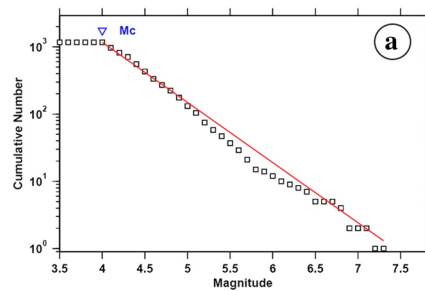
Zagros region. In other words (and neglecting foreshocks), the earthquakes in this region can trigger more aftershocks.

In Figs. 7, 8 and 9, the cumulative number–magnitude distribution plot in the three tectonic zones of Iran is calculated using ZMAP software (Weimer 2001). The summary of calculated plots in Figs. 7, 8 and 9 is presented in Table 6 including a value and b value in the Gutenberg and Richter (1944) relation. The Chi-square test is used to check the null hypothesis that the declustered catalogs follow the Poissonian distribution. The results of the Chi-square test showed that all the declustered catalogs in the three seismotectonic areas follow the Poisson process. It should be noted that in most of the commonly used techniques for Poisson test the declustered catalogs such as Chi-square test and Kolmogorov–Smirnov test, the spatial location of earthquakes has been ignored (Luen and Stark 2012). It can change the results, especially when the study area is large like the current study.

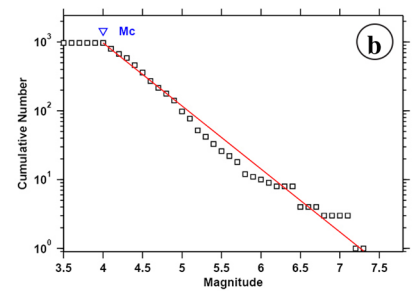
## Conclusions

In this article, the Iran earthquake catalog during the period 1983–2017 is declustered by different methods. Windowing methods include Gardner and Knopoff, Gruenthal, Uhrhammer, the linking Reasenberg's method and epidemic-type aftershock sequence (ETAS) model. We believe that due to the uncertainties and unknown nature of earthquake sequences, it is impossible to do a precise comparison between results of various declustering methods. This is the first article that uses the ETAS model for declustering the Iranian seismic catalog. This case and the other mentioned issues make comparisons difficult. However, the results show the good ability of the ETAS model for declustering of the earthquake catalog and evaluating aftershock probabilities. The authors emphasize that the use of the ETAS model is still in its early steps in Iranian seismological research and more parametric studies are needed. Some of the initial challenges in future studies are the use of Poisson test techniques that take into account the effect of the earthquake location,

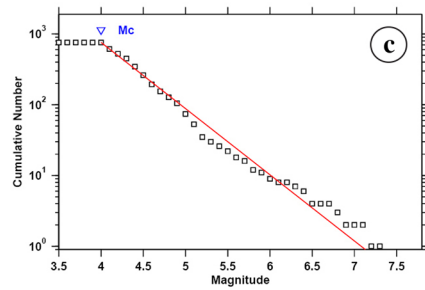
**Fig. 7** Cumulative number–magnitude plot in North of Iran. **a** not declustered. **b** Reasenberg. **c** Uhrhammer. **d** Gardner and Knopoff. **e** Gruenthal method. **f, g, h, i, j** ETAS model with probability thresholds 0.5, 0.6, 0.7, 0.8, 0.9, respectively. The magnitude of completeness ( $M_c$ ) considered equal to the minimum magnitude ( $M_w = 4.0$ )



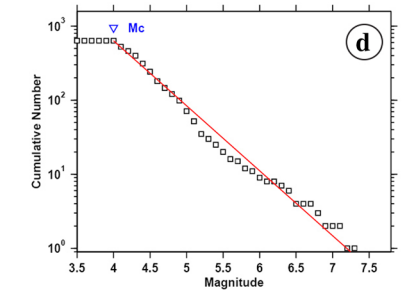
b-value = 0.89 +/- 0.02, a value = 6.65, a value (annual) = 5.13



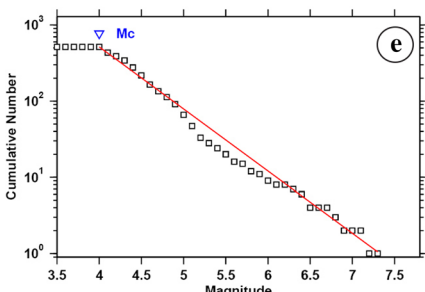
b-value = 0.92 +/- 0.03, a value = 6.65, a value (annual) = 5.13



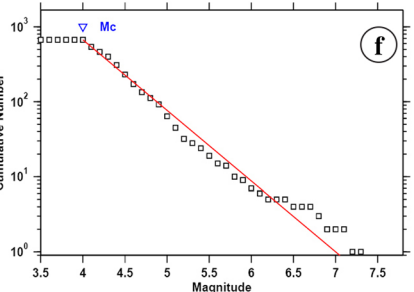
b-value = 0.94 +/- 0.03, a value = 6.62, a value (annual) = 5.1



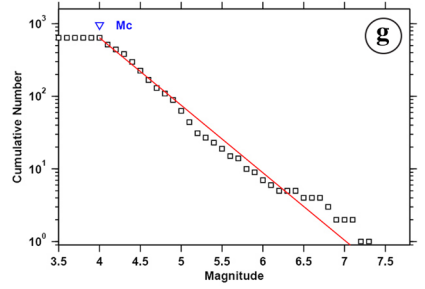
b-value = 0.88 +/- 0.03, a value = 6.31, a value (annual) = 4.79



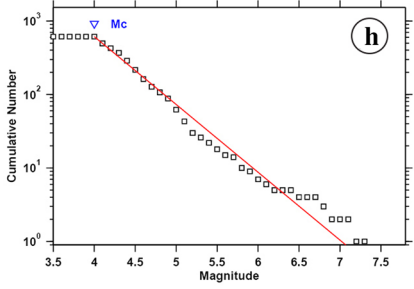
b-value = 0.82 +/- 0.03, a value = 5.97, a value (annual) = 4.46



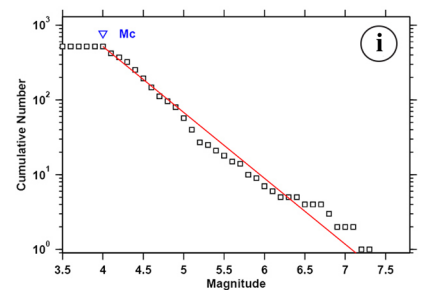
b-value = 0.94 +/- 0.04, a value = 6.6, a value (annual) = 5.08



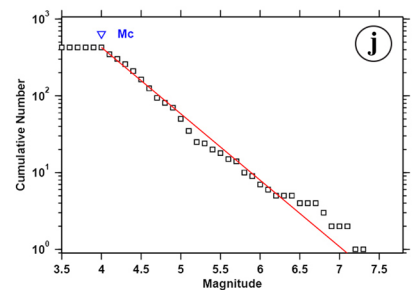
b-value = 0.93 +/- 0.03, a value = 6.52, a value (annual) = 5.01



b-value = 0.92 +/- 0.04, a value = 6.48, a value (annual) = 4.96



b-value = 0.88 +/- 0.04, a value = 6.24, a value (annual) = 4.72



b-value = 0.86 +/- 0.04, a value = 6.09, a value (annual) = 4.57



**Fig. 8** As in Fig. 7 for Zagros region of Iran

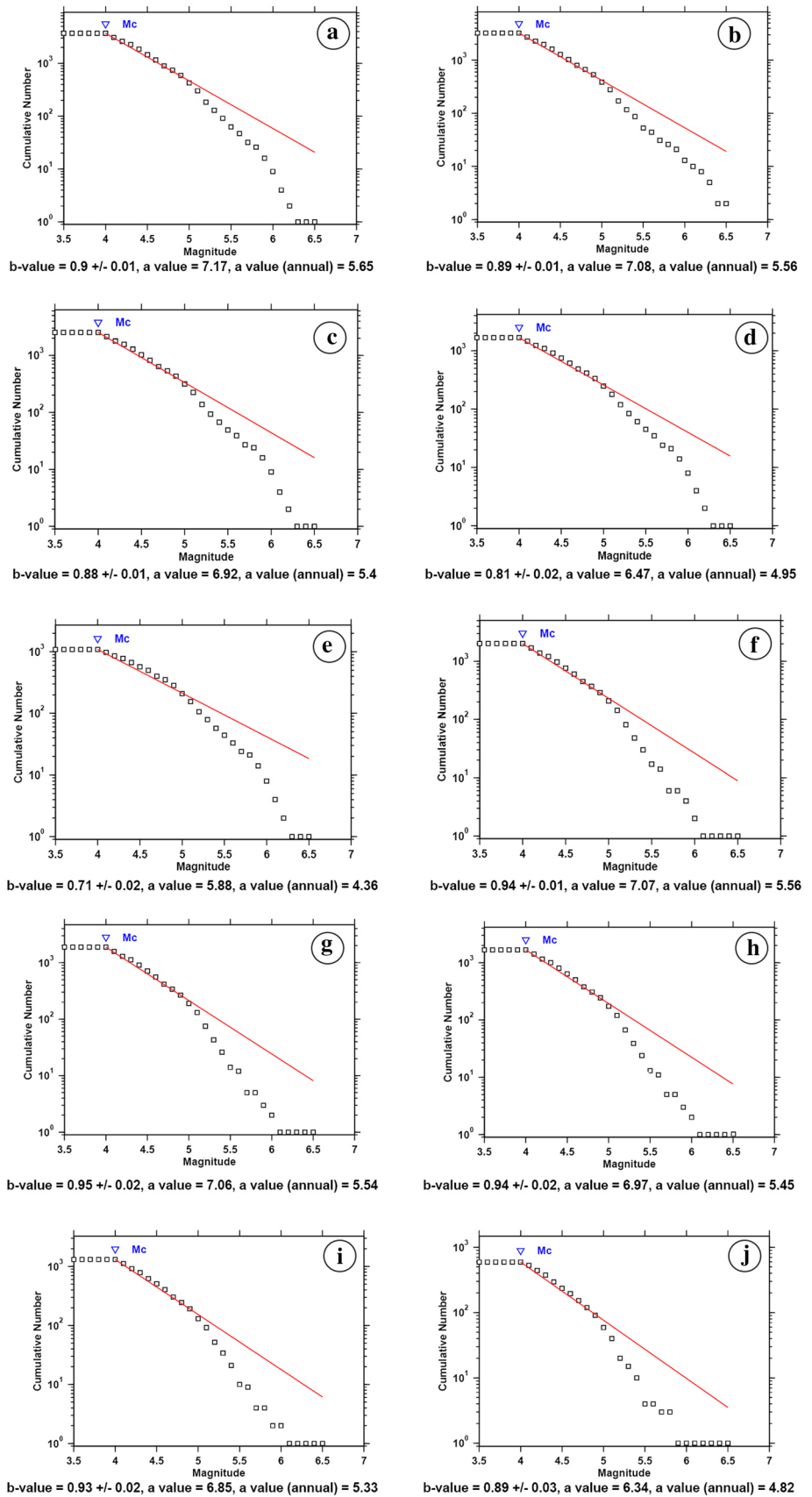
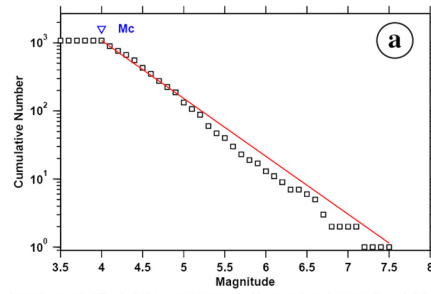
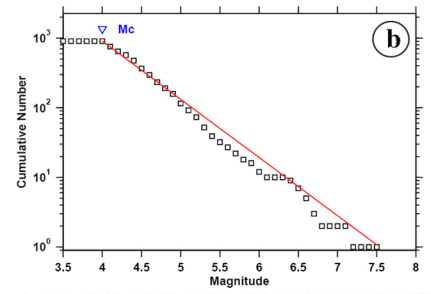


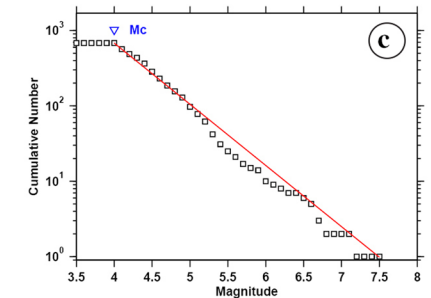
**Fig. 9** As in Fig. 7 for East of Iran



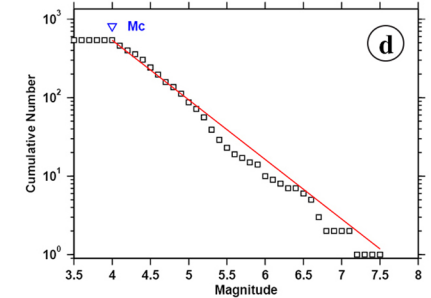
**b-value = 0.85 +/- 0.02, a value = 6.43, a value (annual) = 4.91**



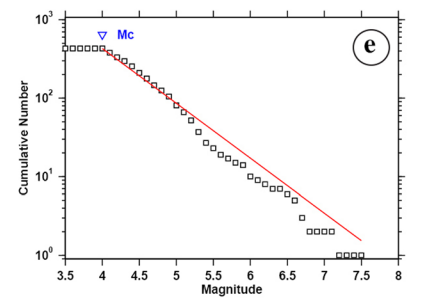
**b-value = 0.84 +/- 0.03, a value = 6.3, a value (annual) = 4.78**



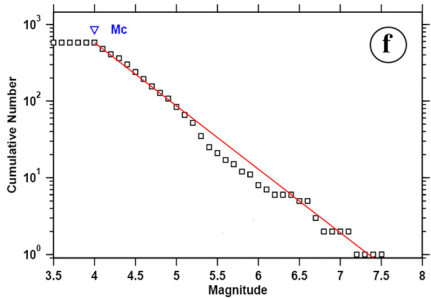
**b-value = 0.81 +/- 0.03, a value = 6.08, a value (annual) = 4.56**



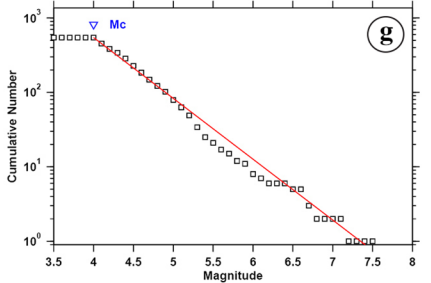
**b-value = 0.76 +/- 0.03, a value = 5.77, a value (annual) = 4.25**



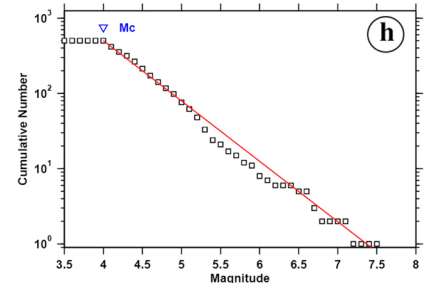
**b-value = 0.7 +/- 0.03, a value = 5.43, a value (annual) = 3.91**



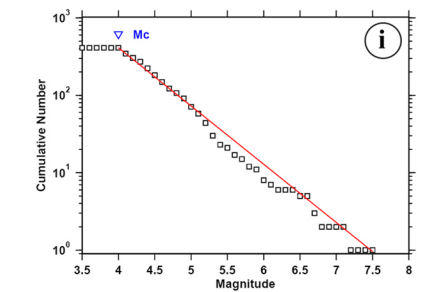
**b-value = 0.83 +/- 0.03, a value = 6.07, a value (annual) = 4.55**



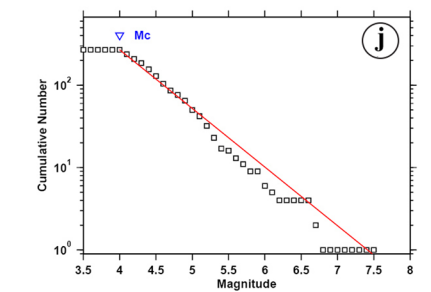
**b-value = 0.82 +/- 0.03, a value = 6, a value (annual) = 4.49**



**b-value = 0.8 +/- 0.03, a value = 5.91, a value (annual) = 4.39**



**b-value = 0.75 +/- 0.03, a value = 5.62, a value (annual) = 4.1**



**b-value = 0.71 +/- 0.03, a value = 5.28, a value (annual) = 3.76**

**Table 6** *a* value and *b* value in the declustered catalog of Iran's major tectonic zones using different methods

Zone	Declustering method																	
	Re		Uh		G-K		Gr		ETAS-0.5		ETAS-0.6		ETAS-0.7		ETAS-0.8		ETAS-0.9	
	<i>a</i>	<i>B</i>	<i>a</i>	<i>b</i>	<i>A</i>	<i>b</i>	<i>a</i>	<i>b</i>	<i>a</i>	<i>b</i>	<i>a</i>	<i>b</i>	<i>a</i>	<i>b</i>	<i>a</i>	<i>b</i>	<i>a</i>	<i>b</i>
North of Iran	5.13	0.92	5.10	0.94	4.79	0.88	4.46	0.82	5.08	0.94	5.01	0.93	4.96	0.92	4.72	0.88	4.57	0.86
East of Iran	4.78	0.84	4.56	0.81	4.25	0.76	3.91	0.70	4.55	0.83	4.49	0.82	4.39	0.80	4.10	0.75	3.76	0.71
Zagros	5.56	0.89	5.40	0.88	4.95	0.81	4.36	0.71	5.56	0.94	5.54	0.95	5.45	0.94	5.33	0.93	4.82	0.89

Time interval 1983–2017. (Re) Reasenberg, (Uh) Uhrhammer, (G-K) Gardner and Knopoff, (Gr) Gruenthal method. ETAS model with probability thresholds 0.5, 0.6, 0.7, 0.8 and 0.9, respectively

choosing different catalogs at different time intervals, evaluating the impact of the threshold magnitude and zoning of seismotectonic regions.

**Acknowledgements** The authors acknowledge the funding support of Babol Noshirvani University of Technology through Grant No. BUT/388011/97. We wish to appreciate Mohammad Shahvar for his help in providing the earthquake catalog and magnitude conversation relations used in this article.

**Authors' contributions** HRT proposed the initial idea and guided us in the analysis. ND analyzed the data completed all experiments and wrote the manuscript. MZ directed us to create a seismic catalog and seismic zoning. AJ developed the ETAS model code. All authors read and approved the final manuscript.

## Compliance with ethical standards

**Conflict of interest** The authors declare that they have no conflict of interest.

## References

- Amini H (2014) Comparing Reasenberg and Gruenthal declustering methods for north of Iran. In Second European conference on earthquake engineering and seismology
- Bottiglieri M, Lippiello E, Godano C, de Arcangelis L (2009) Identification and spatiotemporal organization of aftershocks. *J Geophys Res*. <https://doi.org/10.1029/2008JB005941>
- Burkhard M, Grünthal G (2009) Seismic source zone characterization for the seismic hazard assessment project PEGASOS by the Expert Group 2 (EG1b). *Swiss J Geosci* 102(1):149–188
- Davis SD, Frohlich C (1991) Single-link cluster analysis, synthetic earthquake catalogs, and aftershock identification. *Geophys J Int* 104:289–306
- Frohlich C, Davis SD (1990) Single-link cluster analysis as a method to evaluate spatial and temporal properties of earthquake catalogs. *Geophys J Int* 100:19–32
- Gardner JK, Knopoff L (1974) Is the sequence of earthquakes in Southern California, with aftershocks removed, Poissonian? *Bull Seismol Soc Am* 64(5):1363–1367
- Gutenberg B, Richter CF (1944) Measurement error models. *Bull Seismol Soc Am* 34:185–188
- Hainzl S, Scherbaum F, Beauval C (2006) Estimating background activity based on interevent-time distribution. *Bull Seismol Soc Am* 96(1):313–320
- Huang WQ, LiWX Cao XF (1994) Research on the completeness of earthquake data in the Chinese mainland (I)North China. *Acta Seismol Sin* 7(3):351–359
- Jalilian A, Zhuang J (2016) ETAS: modeling earthquake data using ETAS model. R package version 0.2. <https://CRAN.R-project.org/package=ETAS>
- Kagan Y, Jackson D (1991) Long-term earthquake clustering. *Geophys J Int* 104(1):117–134
- Kanamori H (1977) The energy release in great earthquakes. *J Geophys Res* 82(20):2981–2987
- Karimiparidari S, Zare M, Memarian H, Kijko A (2013) Iranian earthquakes, a uniform catalog with moment magnitudes. *J Seismol* 17(3):897–911
- Luen B, Stark PB (2012) Poisson tests of declustered catalogs. *Geophys J Int* 189(1):691–700
- Marsan D, Lengline O (2010) A new estimation of the decay of aftershock density with distance to the mainshock. *J Geophys Res [Solid Earth]*. <https://doi.org/10.1029/2009JB007119>
- Mirzaei N, Gao MT, Chen YT, Wang J (1997) A uniform catalog of earthquakes for seismic hazard assessment in Iran. *Acta Seismol Sin* 10(6):713–726. <https://doi.org/10.1007/s11589-997-0003-5>
- Molchan G, Dmitrieva O (1992) Aftershock identification: methods and new approaches. *Geophys J Int* 109:501–516
- Mousavi-Bafrouei SH, Mirzaei N, Shabani E (2015) A declustered earthquake catalog for the Iranian Plateau. *Ann Geophys*. <https://doi.org/10.4401/ag-6395>
- OGata Y (1998) Space-time point-process models for earthquake occurrences. *Ann Inst Stat Math* 50(2):379–402
- Omni S, Zafarani H, Zare M (2016) Aftershock decay rates in the Iranian plateau. *Pure Appl Geophys* 173(7):2305–2324 (**Springer Basel Switzerland**)
- Reasenberg P (1985) Second-order moment of central California seismicity. 1969–1982. *J Geophys Res* 90:5479–5495
- Savage WU (1972) Microearthquake clustering near fairview peak, Nevada, and in the Nevada seismic zone. *J Geophys Res* 77(35):7049–7056
- Shahvar MP, Zare M, Castellaro S (2013) A unified seismic catalog for the Iranian plateau (1900–2011). *Seismol Res Lett* 84(2):233–249
- Uhrhammer R (1986) Characteristics of northern and central California seismicity. *Earthq Notes* 57(1):21
- Van Stiphout T, Zhuang J, Marsan D (2012) Seismicity declustering, Community online resource for statistical seismicity analysis. <https://doi.org/10.5078/corssa-52382934>. Available at <http://www.corssa.org>
- Vere-Jones D (1970) Stochastic models for earthquake occurrence. *J Roy Stat Soc: Ser B (Methodol)* 32(1):1–62
- Wells DL, Coppersmith KJ (1994) New empirical relationships among magnitude, rupture length, rupture width, rupture area, and surface displacement. *Bull Seismol Soc Am* 84(4):974–1002

- Wiemer S (2001) A software package to analyze seismicity: ZMAP. *Seismol Res Lett* 72:373–382
- Zafarani H, Soghrat M (2012) Simulation of ground motion in the Zagros region of Iran using the specific barrier model and the stochastic method. *Bull Seismol Soc Am* 102(5):2031–2045
- Zare M, Amini H, Yazdi P, Sesetyan K, Demircioglu MB, Kalafat D, Erdik M, Giardini D, Asif Khan M, Tsereteli N (2014) Recent developments of the Middle East catalog. *J Seismol* 18(4):749–772 (**Springer**)
- Zhuang J (2011) Next-day earthquake forecasts for the Japan region generated by the ETAS model. *Earth Planets Space* 63(3):5 (**Springer Japan**)
- Zhuang J, Ogata Y, Vere-Jones D (2002) Stochastic declustering of space-time earthquake occurrences. *J Am Stat Assoc* 97(458):369–380
- Zhuang J, Ogata Y, Vere-Jones D (2004) Analyzing earthquake clustering features by using stochastic reconstruction. *J Geophys Res [Solid Earth]*. <https://doi.org/10.1029/2003JB002879>
- Zhuang J, Ogata Y, Vere-Jones D (2006) Diagnostic analysis of space-time branching processes for earthquakes. In: Baddeley A, Gregori P, Mateu J, Stoica R, Stoyan D (eds) *Case Studies in Spatial Point Process Modeling*. *Lecture Notes in Statistics*, vol 185. Springer, New York, NY, pp 275–292





# New magnitude scaling relations for earthquake early warning in the Alborz region, Iran

Mohammad Sasani<sup>1</sup> · Mohammad Reza Ghayamghamian<sup>1</sup> · Anooshiravan Ansari<sup>1</sup>

Received: 25 August 2018 / Accepted: 16 October 2018 / Published online: 26 October 2018  
© Institute of Geophysics, Polish Academy of Sciences & Polish Academy of Sciences 2018

## Abstract

Rapid magnitude estimation relations for earthquake early warning systems in the Alborz region have been developed based on the initial first seconds of the  $P$ -wave arrival. For this purpose, a total of 717 accelerograms recorded by the Building and Housing Research Center in the Alborz region with the magnitude ( $M_w$ ) range of 4.8–6.5 in the period between 1995 and 2013 were employed. Average ground motion period ( $\tau_c$ ) and peak displacement ( $P_d$ ) in different time windows from the  $P$ -wave arrival were calculated, and their relation with magnitude was examined. Four earthquakes that were excluded from the analysis process were used to validate the results, and the estimated magnitudes were found to be in good agreement with the observed ones. The results show that using the proposed relations for the Alborz region, earthquake magnitude could be estimated with acceptable accuracy even after 1 s of the  $P$ -wave arrival.

**Keywords** Earthquake early warning · Magnitude estimation · Alborz region · Average period · Peak displacement

## Introduction

Many big cities such as Tehran, the capital of Iran, have been developed in areas where seismic hazards impose serious treats to the lives and assets of the people. Earthquake forecast as a practical method to mitigate seismic risk seems to be far from realization due to the large complexity in earthquake source processes (e.g., Kanamori et al. 1997). Nevertheless, considering the advent of digital data logging and transmission, earthquake early warning system (EWS) is an effective strategy in earthquake risk reduction in high-seismic-risk countries like Iran, Japan, and the USA (Allen 1978; Nakamura 1988; Allen and Kanamori 2003; Heidari et al. 2013; Colombelli and Zollo 2016). This approach provides a few seconds to tens of seconds of warning time for impending ground motions, allowing for mitigation measures in the short term (Allen et al. 2009).

The use of the initial few seconds of  $P$ -wave arrivals to estimate the earthquake parameters was first introduced by Nakamura (1988). He suggested that the earthquake magnitude could be scaled with the frequency content of the initial few seconds of  $P$ -wave arrival. Based on this outcome, the dominant ground motion period ( $\tau_p^{\max}$ ) (Allen and Kanamori 2003; Olson and Allen 2005) and the average ground motion period ( $\tau_c$ ) (Kanamori 2005; Wu and Kanamori 2005a, b, 2008) were introduced by the researchers to develop magnitude scaling relationships. In addition to the above methods, different approaches such as artificial neural networks (Böse 2006), virtual seismologist (Cua and Heaton 2007; Yamada et al. 2007), and slip-weakening distance of near-fault records (Ghayamghamian et al. 2014) as well as the amplitude of the initial few seconds of  $P$ -wave arrivals ( $P_d$ ) have been also developed for such purposes.

Iran is one of the seismically active regions of the world where many active faults have caused many devastating earthquakes. These circumstances, along with the concentration of population in Tehran mega-city, emphasize the importance of an early warning system implementation to reduce losses caused by earthquakes. Tehran is located in the south part of Alborz seismotectonic province, which is recognized with the same seismogenic features and seismicity all over the region including the Tehran area (Mirzaei et al. 1999). Alborz seismotectonic province has

✉ Mohammad Sasani  
m.sasani@iiees.ac.ir

Mohammad Reza Ghayamghamian  
mrgh@iiees.ac.ir

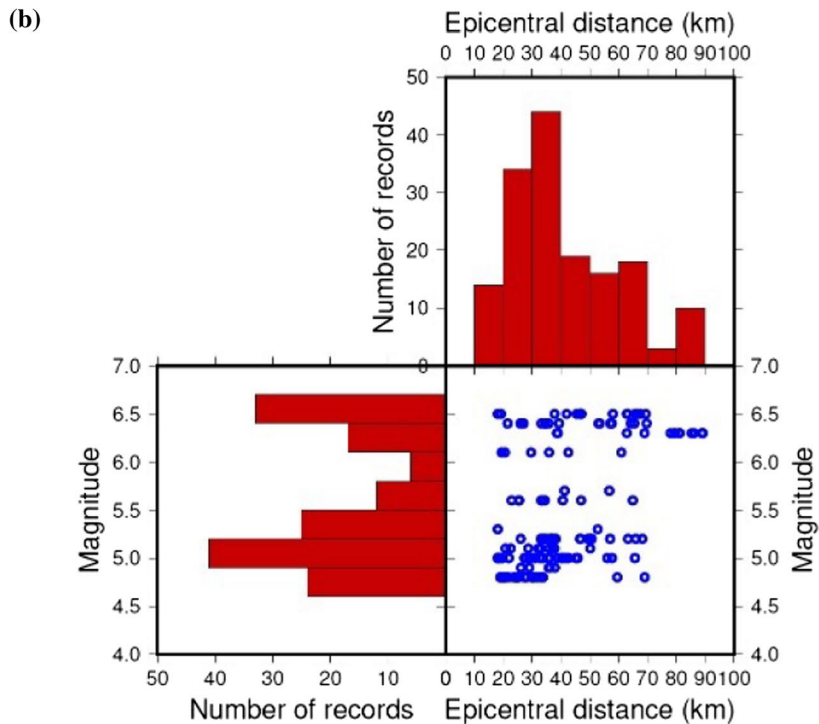
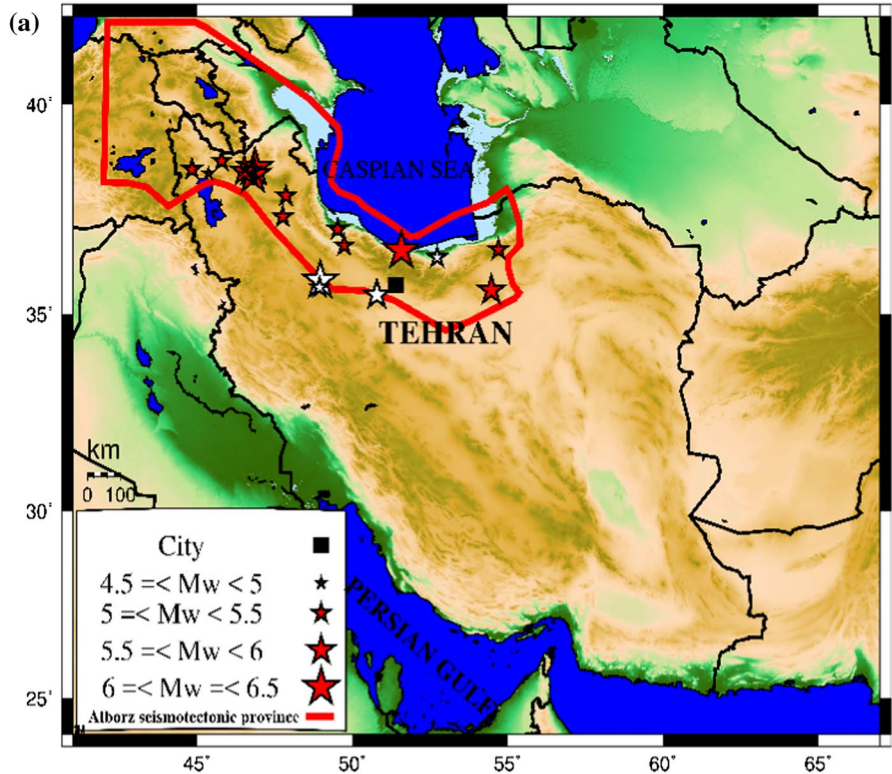
Anooshiravan Ansari  
a.ansari@iiees.ac.ir

<sup>1</sup> International Institute of Earthquake Engineering and Seismology, Tehran, Iran

experienced many major earthquakes with the magnitude of up to 7.4 (Fig. 1a). This may provide a unique opportunity to employ major earthquake data to examine the applicability and accuracy of the previously introduced

relations from the small earthquakes (Heidari et al. 2013). Heidari et al. (2013) made an effort to estimate magnitude scaling relation using  $\tau_c$  and  $\tau_p^{\max}$  methods for Tehran city. They used the seismic stations recently established

**Fig. 1** **a** Distribution of events in Alborz area (solid stars) and events that are used for verification analysis (white stars). **b** Distribution of earthquake magnitudes versus epicentral distances in the Alborz seismotectonic province



or developed in Tehran area by different institutions and organizations such as the Institute of Geophysics University of Tehran (IGUT), the Tehran Center Seismologic Network (TCSN), and the International Institute of Earthquake Engineering and Seismology (IIEES). By using the data from these stations, they provide some scaling relations for magnitude estimation in Tehran city. However, due to no major earthquake occurrence in Tehran area, their employed data were limited only to the earthquakes with magnitudes lower than 4.6. This may not be an ideal approach and needs to be further examined.

In this study, an attempt is made to introduce new scaling relations by employing the data not only in the Tehran area, but also in the whole Alborz region, which has experienced earthquakes with magnitudes of up to 7.4. To this end, the acceleration data recorded by Building and Housing Research Center (BHRC) in the Alborz region are used here. These data are collected among 81 stations with magnitudes in the range of 4.8–6.5 and distances in the range of 18–90 km (Fig. 1b) in the period between 1995 and 2013. The  $\tau_c$  and  $P_d$  parameters are estimated from the displacement records calculated using vertical accelerograms. Then their relations with the magnitude are examined.

The  $\tau_c$  method was first introduced by Kanamori (2005), which was originally developed by Nakamura (1988). In this method, the average period parameter ( $\tau_c$ ) is calculated from the initial seconds of  $P$ -wave data as:

$$r = \frac{\int_0^{t_0} \dot{u}^2(t) dt}{\int_0^{t_0} u^2(t) dt}, \quad (1)$$

where  $u(t)$  and  $\dot{u}(t)$  are displacement and velocity ground motions, respectively. The time interval of integration begins from the arrival time of  $P$ -wave, and  $t_0$  is set equal to the length of time window. Then  $\tau_c$  is:

$$\tau_c = \frac{2\pi}{\sqrt{r}}. \quad (2)$$

One possible approach toward issuing reliable warning is to combine two or more relations in parallel to increase reliability and avoid false alarms. Thus, the possible application of  $P_d$  in magnitude estimation from the few seconds of initial  $P$ -wave is also examined (Wu and Kanamori 2005b; Hsiao et al. 2009; Huang et al. 2015). The  $P_d$  is determined as the maximum amplitude of initial few seconds of  $P$ -wave using vertical displacement records. The estimated  $P_d$  values also show good correlation with the magnitudes and are found to be much less sensitive to the cutoff frequency in displacement estimation from vertical accelerograms as will be explained in detail in the next sections.

## Data processing

A total of 717 horizontal and vertical accelerograms, with sampling rate of 200 samples per second, from 23 events between 1995 and 2013 were selected for analysis. Table 1 shows the specifications of the selected events. Since the main goal of EEWS is to alarm the catastrophic earthquakes, the events with magnitudes larger than 4.7 are employed.

To determine  $\tau_c$  and  $P_d$  parameters, different time windows from  $P$ -wave arrival (1, 2, 3, and 4 s) of vertical accelerograms are selected and analyzed to find the optimum time window for early warning system. Vertical accelerograms were integrated two times to compute displacement waveforms. Although the  $P$ -wave arrival time should be picked automatically in the operational phase (e.g., Allen 1978), it is manually picked in this stage to increase the accuracy in derivation of scaling relations. Furthermore, it is necessary to remove undesired long-period trends and baseline drifts introduced by double integration during the calculation of displacement waveform. A common practice is to apply a causal high-pass filter (usually Butterworth type) with a 0.075 Hz cutoff frequency (e.g., Wu and Kanamori 2005a).

**Table 1** Specifications of the events used in this study

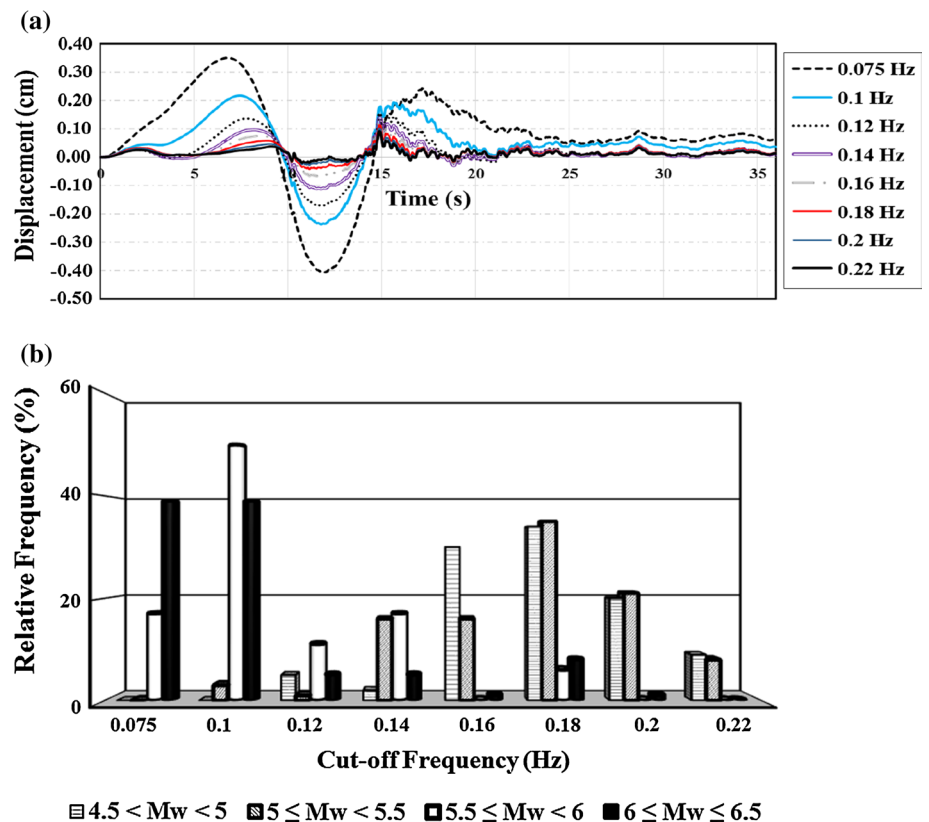
Origin time (yyyy/mm/dd)	Latitude (°N)	Longitude (°E)	$M_w$	Number of the stations
1995/10/15	37.06	49.53	5.1	1
1997/02/28	38.30	48.06	6.1	6
1997/03/02	37.86	47.87	5.3	3
2002/04/19	36.67	49.74	5.2	13
2002/06/22 <sup>a</sup>	35.8	48.97	6.5	8
2002/09/02 <sup>a</sup>	35.65	48.95	5.2	4
2004/05/28	36.55	51.58	6.3	21
2005/09/26	37.36	47.77	5.2	3
2007/06/18 <sup>a</sup>	34.47	50.79	5.5	9
2008/09/02	38.69	45.79	5	9
2010/08/27	35.58	54.48	5.7	3
2011/08/11	36.57	54.71	5	5
2012/01/11 <sup>a</sup>	36.38	52.74	5	13
2012/08/11	38.52	46.86	6.5	21
2012/08/11	38.36	46.80	6.4	28
2012/08/11	38.47	46.76	5.2	11
2012/08/15	38.35	46.61	5	13
2012/08/16	38.36	46.70	4.8	17
2012/11/07	38.45	46.52	5.6	15
2012/11/16	38.49	46.54	4.8	9
2012/12/23	38.49	44.84	5.1	9
2013/01/26	38.29	46.81	4.8	9
2013/04/18	38.39	45.37	4.9	9

<sup>a</sup>Events that were only used in the verification

The filter cutoff frequency needs to be appropriately selected since it not only removes the artificial distortion, but also affects the low-frequency content of the record and, thus, the magnitude estimation procedure. Therefore, it is important to check the applicability of conventional cutoff frequency (0.075 Hz) for the BHRC recording system, whose quality could be different from those recording systems employed in other countries. To select an appropriate cutoff frequency, high-pass filters with different cutoff frequencies (0.075, 0.1, 0.12, 0.14, 0.16, 0.18, 0.2, and 0.22 Hz) are applied, and the displacement waveforms of each filtered record are visually inspected one by one to select the best cutoff frequency. This procedure is shown in Fig. 2 for a record with  $M_w = 4.8$ . The results demonstrated that for the records with earthquake magnitudes of  $M_w \geq 5.5$  and  $M_w < 5.5$ , the cutoff frequency of less than 0.12 Hz and more than 0.16 Hz needs to be used, respectively (Fig. 2). This means that moderate earthquakes need larger cutoff frequencies than the strong ones.

In the next step, the records in short epicentral distance are excluded from the employed database to avoid possible contamination of  $P$ -wave by the  $S$ -wave motion. Furthermore, the records with a high signal-to-noise ratio are selected based on two criteria as peak acceleration ( $P_a$ )  $> 2.5$  cm/s<sup>2</sup> and peak velocity ( $P_v$ )  $> 0.05$  cm/s for initial few seconds of  $P$ -wave arrival (Wu et al. 2007; Zollo et al. 2010). Finally, 537 records out of 717 met the above constraints.

**Fig. 2** **a** Displacement record of an earthquake with  $M_w = 4.8$  with different cutoff frequencies. **b** Relative frequency of selected filter for different ranges of magnitudes



## Magnitude estimation

### Average period

The average period is calculated for all the records using Eq. 2 in the time windows of 1, 2, 3, and 4 s. To examine the sensitivity of estimated magnitudes to the filter cutoff frequencies, the scaling relation is developed for different combinations of selected cutoff frequencies for two magnitude ranges ( $M_w \geq 5.5$  and  $M_w < 5.5$ ). This leads to 48 regression analyses between  $\tau_c$  and magnitude for different cutoff frequencies and time windows. Then the correlation coefficient ( $R$ ) and standard error ( $\delta_{SE}$ ) for each derived relation were determined and evaluated to select the optimum cutoff frequencies in each time window. Based on the results, for all time windows, the cutoff frequencies of 0.1 Hz and 0.22 Hz are selected for the records with  $M_w \geq 5.5$  and  $M_w < 5.5$ , respectively. Finally, four scaling relations between averaged  $\tau_c$  and magnitude together with their estimated  $R$  and  $\delta_{SE}$  are calculated as shown in Fig. 3 and tabulated in Table 2.

As shown in Table 2, final scaling relations slightly differ for different time windows, which means that it may be possible to use even one relation for magnitude estimation for different time windows in early warning system. In other words, one can use only one relation for all time windows, and after every 1 s, the previous estimation could be



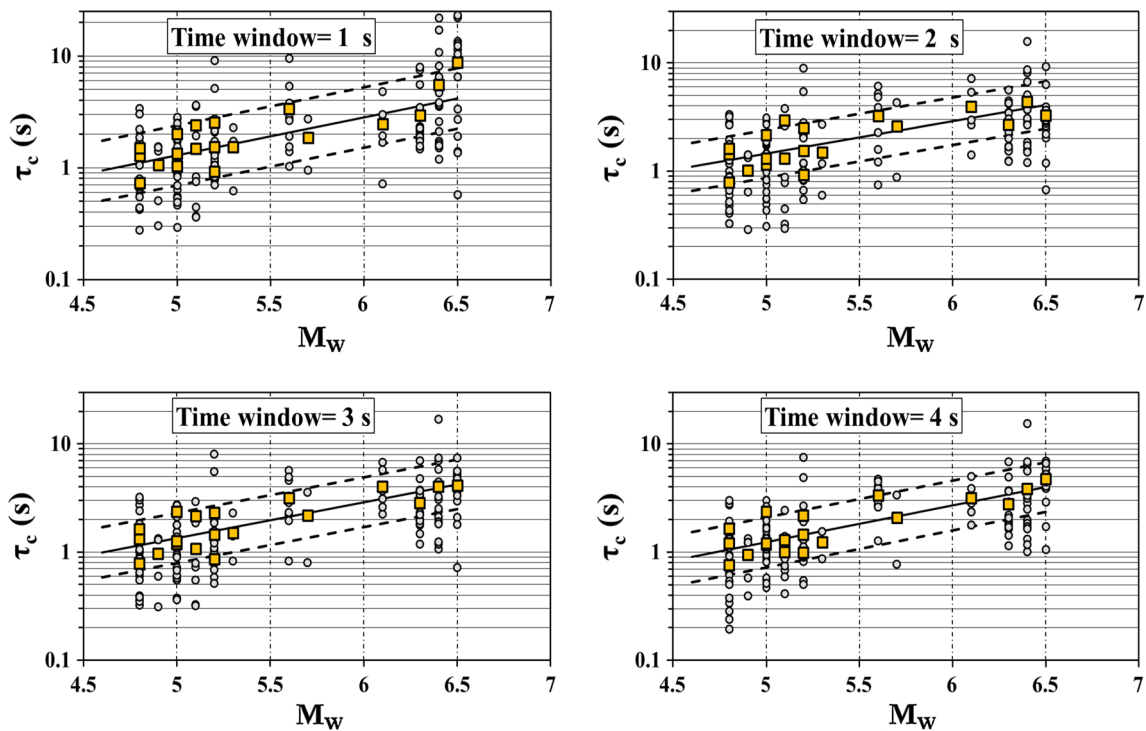


**Fig. 3** Distribution of  $\tau_c$  versus  $M_w$  and the proposed scaling relation (the solid black line) with the plus/minus one standard deviation from the fit line (dashed lines) in different time windows

**Table 2** Results of regression analysis for  $\tau_c$  parameters in each time window

Time window (s)	$M_w = a \log(\tau_c) + b \pm \delta_{SE}$				
	$a$	$b$	$R$	$\delta_{SE}$	
1	1.75	4.89	0.82	0.33	
2	1.94	4.83	0.77	0.37	
3	1.98	4.86	0.81	0.34	
4	2.02	4.90	0.83	0.32	

**Table 3** Results of regression analysis for  $P_d$  parameter in each time window

Time window (s)	$M_w = a \log(P_d) + b \log(R_{ep}) + c \pm \delta_{SE}$				
	$a$	$b$	$c$	$R$	$\delta_{SE}$
1	0.88	1.29	4.51	0.73	0.45
2	0.85	1.29	4.39	0.74	0.44
3	0.91	1.27	4.41	0.77	0.42
4	0.96	1.34	4.31	0.79	0.41

revised without need to use different relations for different time windows.

**Peak amplitude of displacement**

In spite of a good correlation for  $\tau_c$  relations, one big disadvantage remains: the decision on the filter cutoff frequencies before an earthquake occurrence. To overcome this deficiency, the relation between  $P_d$  parameter estimated from initial few seconds of  $P$ -wave arrival and magnitude is examined. Conventionally, the  $P_d$  parameter shows dependence on the magnitude and distance as the global form of Eq. 3 (e.g., Wu and Zhao 2006):

$$\log(P_d) = A + B \times M_w + C \times \log(R_{ep}), \tag{3}$$

where  $R_{ep}$  is epicentral distance. In this study the scaling relations between  $P_d$ ,  $M_w$ , and epicentral distance are developed in the same way as the  $\tau_c$  relations and are shown in Table 3. It is important to emphasize that the filter cutoff frequency of 0.1 Hz is found to be appropriate for all the time windows and magnitudes; thus, there is no need to select filter cutoff frequency in advance.

As shown in Table 3 and Fig. 4, the  $P_d$  values in the different time windows show slight differences as was the case of  $\tau_c$ , which may suggest that even by selecting one of the relations for different time windows, the earthquake magnitude can still be appropriately estimated. Thus, it is not necessary to spend additional time to select the corresponding equation for different time windows. Furthermore, in contrast to the  $\tau_c$  relations, this method does not require filter

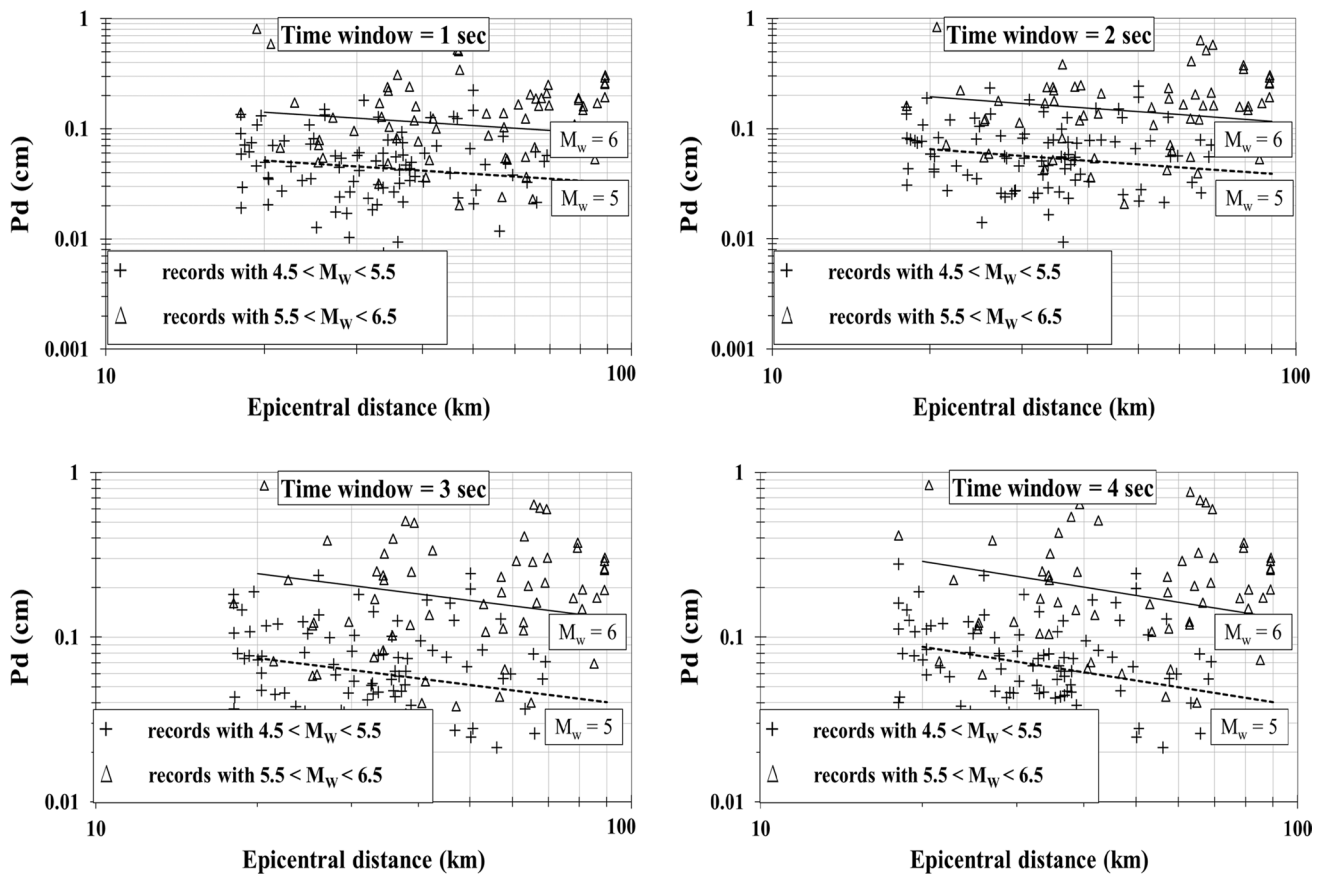


**Fig. 4** Distribution of the observed Pd measurements. Two lines are calculated from the linear  $\log(P_d) - \log(R_{ep})$  relationship: solid line for magnitude 6 and dashed line for magnitude 5

selection based on the magnitude of the earthquake, and for all the observed magnitudes, a certain cutoff frequency (0.22 Hz) can be used.

**Proposed relation for magnitude estimation**

Based on the above results for all the parameters and in attention to the small differences among the relations for different time windows of each parameter, the relations for a 4-s time window of the parameters are used to estimate the magnitude of the earthquake in the study area. However, the estimation process will start just after 1 s of P-wave arrival and as time passes, the estimated magnitude will be updated. To increase the reliability and accuracy in estimating earthquake magnitude, the combination of the mentioned relations is used in such a way that both methods contribute to the final relation according to their standard errors. In other words, any relationship with less error in earthquake magnitude estimation has a larger contribution in the final estimation. Therefore, the final relation to calculate earthquake magnitude is given as:

$$M_w = 0.56 M_{w_{\tau_c}} + 0.44 M_{w_{P_d}} \pm 0.36. \tag{4}$$

**Verification of the results**

To examine the validity of the developed relation for  $\tau_c$  parameter, the proposed relation is compared with those given for other countries, as shown in Fig. 5 (Wu and Kanamori 2005a, 2008; Alcik et al. 2011; Carranza et al. 2013; Heidari et al. 2013; Peng et al. 2017). As shown in this figure, the results of this study are generally consistent in trend with those observed in other countries. Meanwhile, there are some differences in values among the relations that make it unreasonable to directly use their relationships. This may prevent the direct use of developed relations from other countries in a specific region such as the Alborz in Iran.

Heidari et al. (2013) introduced scaling relation for Tehran (part of the Alborz region) as:

$$M_L = 8.6 \log(\tau_c) + 8.8. \tag{5}$$

This relation is derived based on 194 events around Tehran city with magnitudes in the range of 2.5–4.6. They claim that this relation is applicable to use in EEWs for damaging earthquakes in spite of the magnitude limitation in their employed data. When comparing relation 5 with the

**Fig. 5** Comparison between the results of the analysis for the average period with the results of other researchers. The solid black line is related to the analysis of this paper, and dashed lines represent the plus/minus one standard deviation from the fit line

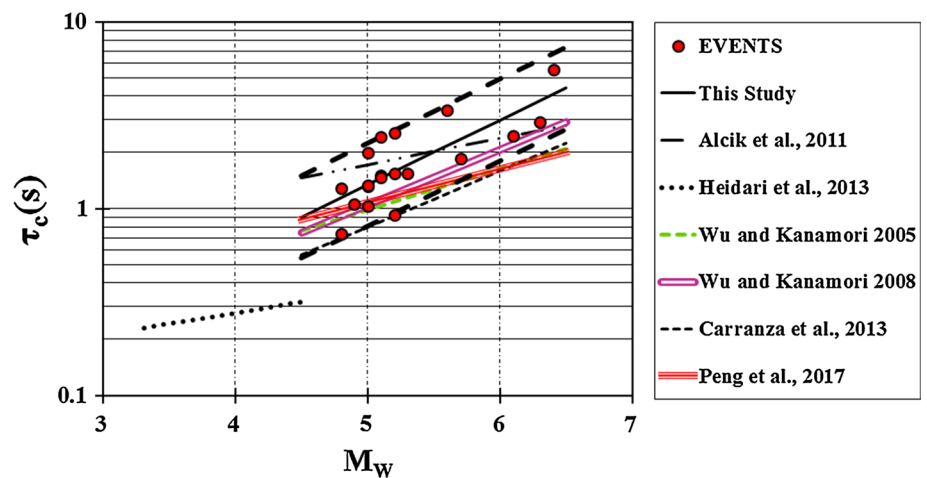


**Table 4** Estimated and observed magnitudes for earthquakes that were excluded from the analysis

Event date (yyyy/mm/dd)	Estimated magnitude			$M_{w_{reported}}$	Percentage error (%)
	$M_{w_{\tau_c}}$	$M_{w_{P_d}}$	$M_{w_{final}}$		
2002/06/22	6.2	6.2	6.2	6.5	4.6
2002/09/02	5.1	5.5	5.3	5.2	1.9
2007/06/18	6.1	5.3	5.7	5.5	3.6
2012/01/11	5	5.1	5	5	0.0

proposed one here as well as those given by other researchers in Fig. 5, the Heidari et al. (2013) relation shows large differences with the other relations. It is noteworthy that the application of their relation could largely overestimate the earthquake magnitude in Tehran city as a part of the Alborz region, which may lead to false alarms.

To validate the results, the four earthquakes that were excluded from the analyses (Table 1) were used here for verification. Then their magnitudes were estimated using the proposed relationships and were compared with those of the ones observed, as shown in Table 4. The results show that using the proposed relations, one can estimate the magnitude of the earthquake within 1 s after the  $P$ -wave arrival with good accuracy. This shows the accuracy and reliability of the proposed relations for EEWS in the Alborz region.

## Conclusions

In this paper, the possibility on the application of the earthquake early warning system in Tehran city as a part of the Alborz region was examined. In order to provide an efficient algorithm, the  $\tau_c$  and  $P_d$  parameters are used to estimate earthquake magnitude for the time windows of 1, 2, 3, and 4 s after  $P$ -wave arrival. The scaling relations among  $\tau_c$  and  $P_d$  parameters with the magnitude are developed for all the

time windows. It is shown that the introduced relation of the parameters for one-second time window provides reasonable (standard error of  $\pm 0.37$ ) earthquake magnitude estimation only after one second of  $P$ -wave arrival. The developed relations for different time windows showed a slight difference, suggesting that a single relation could be used for different time windows. The current studies in the field of EEWS generally estimate these parameters in the 3-s time window. A 2-s reduction in computing time leads to a decrease in earthquake losses in a wide range of target areas. In areas where cities are located near active faults (such as Tehran), this reduction in time can be considered as an important achievement in effective performance of the earthquake early warning system. This change in the time of calculations has a direct impact on the casualties caused by the earthquake.

In order to validate the results, the proposed relations are compared with those developed by other researchers in different countries. They showed a good agreement in trend, but revealed some differences in value. This may be used to emphasize the fact that the scaling relations in a specific region cannot be directly employed for the other regions and need to be further examined. Furthermore, the comparison of the results with those developed by Heidari et al. (2013) for Tehran city shows that the developed relation for data with earthquake magnitudes limited to 4.6 leads to large error and overestimates the magnitude. The proposed relations are also further examined by comparison between observed and estimated magnitudes for four different earthquakes, which are excluded from the employed data in derivation of the proposed relations. The good agreement between the observed and estimated magnitudes provides more confirmation to the results and is used to validate the accuracy of the proposed relations for earthquake early warning system in Tehran.

**Acknowledgements** We sincerely thank the anonymous reviewers whose comments lead to improvement of this article. The authors

would like to thank Building and Housing Research Center (BHRC) for providing original accelerograms. Figure 1 is made using Generic Mapping Tools (Wessel et al. 2013).

## References

- Alcik H, Ozel O, Wu Y-M, Ozel NM, Erdik M (2011) An alternative approach for the Istanbul earthquake early warning system. *Soil Dyn Earthq Eng* 31:181–187
- Allen RV (1978) Automatic earthquake recognition and timing from single traces. *Bull Seismol Soc Am* 68:1521–1532
- Allen RM, Kanamori H (2003) The potential for earthquake early warning in Southern California. *Science* 300:786–789
- Allen RM, Gasparini P, Kamigaichi O, Böse M (2009) The status of earthquake early warning around the world: an introductory overview. *Seismol Res Lett* 80(5):682–693
- Böse M (2006) Earthquake early warning for Istanbul using artificial neural networks. Ph.D. thesis, Karlsruhe University, Germany
- Carranza M, Buforn E, Colombelli S, Zollo A (2013) Earthquake early warning for southern Iberia: a P wave threshold-based approach. *Geophys Res Lett* 40:4588–4593
- Colombelli S, Zollo A (2016) Rapid and reliable seismic source characterization in earthquake early warning systems: current methodologies, results, and new perspectives. *J Seismol* 20:1171–1186
- Cua G, Heaton T (2007) The virtual seismologist (VS) method: a Bayesian approach to earthquake early warning. In: Gasparini P, Manfredi G, Zschau J (eds) *Earthquake early warning systems*. Springer, New York, pp 85–132
- Ghayamghamian MR, Sasani M, Ansari A (2014) Determination of the fault slip using near-fault records. In: 16th Iranian geophysical conference, Tehran, Iran (**in Persian**)
- Heidari R, Shomali ZH, Ghayamghamian MR (2013) Magnitude-scaling relations using period parameters  $\tau_c$  and  $\tau_{pmax}$  for Tehran region, Iran. *Geophys J Int* 192:275–284
- Hsiao N-C, Wu Y-M, Shin T-C, Zhao L, Teng T-L (2009) Development of earthquake early warning system in Taiwan. *Geophys Res Lett* 36(2):L00B02
- Huang P-L, Lin T-L, Wu Y-M (2015) Application of  $\tau_c * P_d$  in earthquake early warning. *Geophys Res Lett* 42:1403–1410
- Kanamori H (2005) Real-time seismology and earthquake damage mitigation. *Annu Rev Earth Planet Sci* 33:195–214
- Kanamori H, Hauksson E, Heaton T (1997) Real-time seismology and earthquake hazard mitigation. *Nature* 390:461–464
- Mirzaei N, Gao M, Chen Y (1999) Delineation of potential seismic sources for seismic zoning of Iran. *J Seismol* 3:17–30
- Nakamura Y (1988) On the urgent earthquake detection and alarm system (UrEDAS). In: *Proceedings of the 9th world conference on earthquake engineering*, Tokyo-Kyoto, Japan
- Olson EL, Allen RM (2005) The deterministic nature of earthquake rupture. *Nature* 438:212–215
- Peng CY, Yang JS, Zheng Y, Zhu XY, Xu ZQ, Chen Y (2017) New  $\tau_c$  regression relationship derived from all P wave time windows for rapid magnitude estimation. *Geophys Res Lett* 44:1724–1731
- Wessel P, Smith WHF, Scharroo R, Luis JF, Wobbe F (2013) Generic mapping tools: improved version released. *EOS Trans AGU* 94:409–410
- Wu Y-M, Kanamori H (2005a) Experiment on an onsite early warning method for the Taiwan early warning system. *Bull Seismol Soc Am* 95:347–353
- Wu Y-M, Kanamori H (2005b) Rapid assessment of damage potential of earthquakes in Taiwan from the beginning of P waves. *Bull Seismol Soc Am* 95:1181–1185
- Wu Y-M, Kanamori H (2008) Development of an earthquake early warning system using real-time strong motion signals. *Sensors* 8:1–9
- Wu Y-M, Zhao L (2006) Magnitude estimation using the first three seconds P-wave amplitude in earthquake early warning. *Geophys Res Lett* 33:L16312
- Wu Y-M, Kanamori H, Allen R, Hauksson E (2007) Determination of earthquake early warning parameters,  $\tau_c$  and  $P_d$ , for southern California. *Geophys J Int* 170:711–717
- Yamada M, Heaton T, Beck J (2007) Real-time estimation of fault rupture extent using near-source versus far-source classification. *Bull Seismol Soc Am* 97(6):1890–1910
- Zollo A, Amoroso O, Lancieri M, Wu Y-M, Kanamori H (2010) A threshold-based earthquake early warning using dense accelerometer networks. *Geophys J Int* 183:963–974





# Regularized inversion of amplitude-versus-incidence angle (AVA) based on a piecewise-smooth model

Zhiyong Li<sup>1,2</sup> · Mantao Wang<sup>1,2</sup> · Feng Xu<sup>3</sup>

Received: 18 May 2018 / Accepted: 18 September 2018 / Published online: 9 October 2018  
© Institute of Geophysics, Polish Academy of Sciences & Polish Academy of Sciences 2018

## Abstract

Different from the stacked seismic data, pre-stack data includes abundant information about shear wave and density. Through inverting the shear wave and density information from the pre-stack data, we can determine oil-bearing properties from different incident angles. The state-of-the-art inversion methods obtain either low vertical resolution or lateral discontinuities. However, the practical reservoir generally has sharp discontinuities between different layers in vertically direction and is horizontally smooth. Towards obtaining the practical model, we present an inversion method based on the regularized amplitude-versus-incidence angle (AVA) data to estimate the piecewise-smooth model from pre-stack seismic data. This method considers subsurface stratum as a combination of two parts: a piecewise smooth part and a constant part. To fix the ill-posedness in the inversion, we adopt four terms to define the AVA inversion misfit function: the data misfit itself, a total variation regularization term acting as a sparsing operator for the piecewise constant part, a Tikhonov regularization term acting as a smoothing operator for the smooth part, and the last term to smoothly incorporate a priori information for constraining the magnitude of the estimated model. The proposed method not only can incorporate structure information and a priori model constraint, but also is able to derive into a convex objective function that can be easily minimized using iterative approach. Compared with inversion results of TV and Tikhonov regularization methods, the inverted P-wave velocity, S-wave velocity and density of the proposed method can better delineate the piecewise-smooth characteristic of strata.

**Keywords** Pre-stack seismic inversion · Unsuitability · Multi-scale construction · Regularization

## Introduction

The inversion of pre-stack seismic data is of great importance in hydrocarbon exploration and exploitation. Seismic amplitude versus incidence angle (AVA) inversion is a common approach to estimate P-wave velocity, S-wave velocity and density of the subsurface stratum from pre-stack seismic data. AVA inverse problem requires the minimization of the misfit between observed and modeled data. The solutions are inherently non-unique, since there are several models that all fit the data equally well. AVA inversion is also an ill-posed

problem, because a small amount of noise can lead to large errors in the solution. Such problem is generally studied in geophysical inverse theory and regularization problems where a large number of possible candidate solutions are exposed to specific assumptions (Bosch et al. 2010; Theune et al. 2010; Asnaashari et al. 2013; Li et al. 2016a, b). It is apparent that by directly imposing different assumptions leads to different regularization approaches which produce different solutions. An appropriate regularization method should be developed to maintain stabilization while avoiding meaningless solutions.

The Tikhonov regularization usually gives a particular solution with appropriate properties using  $l_2$ -norm (Tikhonov and Arsenin 1977). This regularization technique produces a smoothed solution while blurring edges, a property called over-smoothing (Guitton and Symes 2003; Wang et al. 2011). Some other regularization method preserves edge information and reinforces boundaries between different strata, which creates distinctive features for geological structures and highlights relatively thin strata (Li et al. 2014; Zhang et al. 2014a, b; Zhang and Zhang 2017). Among

✉ Zhiyong Li  
359081137@qq.com

<sup>1</sup> College of Information Engineering, Sichuan Agricultural University, Ya'an 625014, China

<sup>2</sup> Key Laboratory of Agricultural Information Engineering of Sichuan Province, Sichuan Agricultural University, Ya'an 625014, China

<sup>3</sup> College of Geoscience and Technology, Southwest Petroleum University, Chengdu 610500, China

these edge-preserving approaches, the most popular technique is the total variation (TV) regularization that requires the model to have a sparse gradient which is enforced to be minimal with respect to  $l_1$ -norm (Acar and Vogel 1994). Therefore, TV method is able to reconstruct piecewise constant solutions of ill-posed problems, and preserves edges while roughening regions of steady change, a property called under-smoothing (Anagaw and Sacchi 2012).

Subsurface strata are usually distributed in layers, and the physical attribute of each stratum is different from one another. When there are significant differences in the physical attributes of two adjacent strata, the contact surface of two strata is deemed a reflective interface or a geological interface, otherwise, these two adjacent strata are regarded as continuous deposition. Subsurface strata can contain edge discontinuities that separate regions of steady change. For the inversion of piecewise-smooth model, the above-mentioned methods are limited by their inherent assumptions, and thus, combinations or modifications of these methods have been commonly used to address the problem caused by the assumption in the method (Gholami and Hosseini 2013; Zhang et al. 2014a, b; Lin and Huang 2015; Li et al. 2017a, b).

In this study, the Tikhonov and TV regularizations have been integrated and advanced to invert piecewise-smooth model, which could demonstrate more details in high frequency domain as much as that in low frequency domain. It was first assumed that subsurface physical property can be parameterized as a combination of a piecewise smooth part and a constant part. Then, more realistic assumptions of smoothness and sparseness were imposed on each part. A third regularization term was introduced to constrain the magnitude of estimated parameters determined by a priori information. An iterative approach was used as an efficient algorithm to minimize the cost functional. Synthetic model tests and applications to real data indicate significantly improved performance of the proposed method in comparison to TV or Tikhonov regularizations alone.

### Forward modeling

Different methods have been used to forward the seismic wave propagation, such as discrete wavenumber integration (Bouchon and Aki 1977; Wang and Tao 2011), finite difference (Wang and Fehler 2018a, b), and finite difference methods (Wang et al. 2013). Here we adopt an analytical method to speed the forward procedure. Assume the validity of the well-known three-term Fatti approximation to the Zoeppritz equations (Fatti et al. 1994) and consider the P-wave reflection coefficient as a function of incidence angle, a plane wave that arrives at an interface that separates two different media of homogeneous materials can be described as:

$$R_{pp}(\theta) = \frac{1}{2}c_1\mathbf{D}_1\mathbf{L}_p + \frac{1}{2}c_2\mathbf{D}_1\mathbf{L}_s + \frac{1}{2}c_3\mathbf{D}_1\mathbf{L}_d, \tag{1}$$

where  $L_p = \ln \rho V_p$ ,  $L_s = \ln \rho V_s$ ,  $L_d = \ln \rho$ ,  $c_1 = \sec^2 \theta$ ,  $c_2 = -8\gamma^2 \sin^2 \theta$ ,  $c_3 = 4\gamma^2 \sin^2 \theta - \tan^2 \theta$ ,  $\gamma = V_s/V_p$ ,  $\mathbf{D}_1$  is the first-order derivative operator

$$\mathbf{D}_1 = \begin{bmatrix} -1 & 1 & & & \\ & -1 & 1 & & \\ & & \ddots & \ddots & \\ & & & -1 & 1 \\ & & & & -1 & 1 \end{bmatrix}, \tag{2}$$

Hampson et al. (2005) assumed a linear correlation between the logarithm of P-impedance and both S-impedance and density, and then obtained a linearized approximation for reflectivity. If the seismic trace is expressed as the convolution of the wavelet  $\mathbf{W}$  with the reflectivity  $R_{pp}(\theta)$ , the angle trace becomes

$$d(\theta) = \left(\frac{1}{2}c_1 + \frac{1}{2}kc_2 + mc_3\right)\mathbf{W}\mathbf{D}_1\mathbf{L}_p + \frac{1}{2}c_2\mathbf{W}\mathbf{D}_1\Delta\mathbf{L}_s + c_3\mathbf{W}\mathbf{D}_1\Delta\mathbf{L}_d, \tag{3}$$

$$\mathbf{W} = \begin{bmatrix} w_1 & 0 & \cdots & 0 \\ w_2 & w_1 & \cdots & \vdots \\ \vdots & w_2 & \cdots & \vdots \\ w_n & \vdots & \cdots & w_1 \\ 0 & w_n & \cdots & w_2 \\ \vdots & 0 & \cdots & \vdots \\ 0 & 0 & \cdots & w_n \end{bmatrix}, \tag{4}$$

$$\Delta\mathbf{L}_s = k\mathbf{L}_p + k_c - \mathbf{L}_s, \tag{5}$$

$$\Delta\mathbf{L}_d = m\mathbf{L}_p + m_c - \mathbf{L}_d, \tag{6}$$

$$V_p = \exp(\mathbf{L}_p - \mathbf{L}_d), \tag{7}$$

$$V_s = \exp(\mathbf{L}_s - \mathbf{L}_d), \tag{8}$$

$$\rho = \exp(\mathbf{L}_d), \tag{9}$$

where  $w_i$  is the elements of wavelet sequence,  $k$  and  $m$  are gradients,  $k_c$  and  $m_c$  are intercepts, and formula (3) in matrix form is:

$$\begin{bmatrix} d(\theta_1) \\ d(\theta_2) \\ \vdots \\ d(\theta_m) \end{bmatrix} = \begin{bmatrix} \tilde{c}_1(\theta_1)\mathbf{W}\mathbf{D}_1 & \tilde{c}_2(\theta_1)\mathbf{W}\mathbf{D}_1 & \tilde{c}_3(\theta_1)\mathbf{W}\mathbf{D}_1 \\ \tilde{c}_1(\theta_2)\mathbf{W}\mathbf{D}_1 & \tilde{c}_2(\theta_2)\mathbf{W}\mathbf{D}_1 & \tilde{c}_3(\theta_2)\mathbf{W}\mathbf{D}_1 \\ \vdots & \vdots & \vdots \\ \tilde{c}_1(\theta_m)\mathbf{W}\mathbf{D}_1 & \tilde{c}_2(\theta_m)\mathbf{W}\mathbf{D}_1 & \tilde{c}_3(\theta_m)\mathbf{W}\mathbf{D}_1 \end{bmatrix} \begin{bmatrix} \mathbf{L}_p \\ \Delta\mathbf{L}_s \\ \Delta\mathbf{L}_d \\ \vdots \end{bmatrix}, \tag{10}$$

where  $\tilde{c}_1 = \left(\frac{1}{2}c_1 + \frac{1}{2}kc_2\right) + mc_3$ ,  $\tilde{c}_2 = \frac{1}{2}c_2$ ,  $\tilde{c}_3 = c_3$ .

The goal of this study is to invert a model from noisy seismic measurements, which has been widely studied in mathematical sciences. Generally, such problems can be formulated by a linear discrete problem:

$$\mathbf{d} = \mathbf{G}\mathbf{m} + \mathbf{e}, \quad (11)$$

where  $\mathbf{d}$  is the vector of seismic observed data,  $\mathbf{G}$  is the prestack seismic forward operator,  $\mathbf{m}$  is a vector of unknown physical property,  $\mathbf{e}$  is an error vector.

## Inversion method

AVA inversion relies on an iterative local optimization that is usually considered as a linearized least-squares problem. The optimization attempts to minimize residuals between observed and modeled data. The linearized inverse problem remains ill-posed, and hence multiple model-driven solutions can provide a satisfactory fit for the observed data. The general definition of the misfit function for solving ill-posed inverse problems can be recast as the following cost function:

$$J(\mathbf{m}) = C_d(\mathbf{m}) + \lambda C_m(\mathbf{m}), \quad (12)$$

where  $C_d(\mathbf{m})$  is the data misfit term based on a norm of the residuals between observed and modeled data in the data space, and  $C_m(\mathbf{m})$  is the model term based on a norm of a model penalty function in the model space.  $\lambda$  is the regularization parameter that balances contributions between the data and the model penalty term.

In standard Tikhonov regularization approach, the above model penalty function is based on the first or second spatial derivative of the current model that should have a minimal norm, and thus gives a smooth model (Fomel 2007). Despite the mathematically tractable advantages, however, the Tikhonov method usually results in over-smoothing results, and is only applicable for estimating smooth models. It is a particularly undesirable limitation in processing real data, where it is a high priority to preserve both sharp and smooth properties of subsurface models. In TV regularization approach, the model penalty restricts the domain of possible solutions to those having sparse gradient (Bertete-Aguirre et al. 2002), i.e. the solution of formula (11) for which  $|\mathbf{m}|_{\text{TV}} = |\mathbf{D}_1 \mathbf{m}|_1$  is minimal for discrete one-dimensional problems. The TV regularization forces the gradient to be sparse, leading to a piecewise constant solution. Therefore, while preserving edge discontinuities, it loses fine scale information in the regularized solution.

As subsurface strata usually contain edge discontinuities that separate two smooth regions, neither Tikhonov nor TV regularization is able to identify both edge discontinuities and smooth structures in the regularized solution. In this study, we propose to develop a model with a combination of piecewise constant part  $\mathbf{m}_1$  and smooth part  $\mathbf{m}_2$ . Our goal is to maximize the sparseness of  $\mathbf{m}_1$  and smoothness of  $\mathbf{m}_2$ , which would

match observed seismic and well log data within a given tolerance level prescribed for the noise. Figure 1a shows a piecewise smooth model  $\mathbf{m}$ , and Fig. 1b presents the gradient of  $\mathbf{m}$ . Decomposing the spikes from the gradient in Fig. 1b produces two sets of properties, as indicated in Fig. 1d and f. The corresponding models  $\mathbf{m}_1$  and  $\mathbf{m}_2$  are shown in Fig. 1c and e which can be superimposed to the original model  $\mathbf{m}$ . It is obvious that  $\mathbf{m}_1$  and  $\mathbf{m}_2$  cannot simultaneously accurately recovered by TV or Tikhonov regularization alone.

We propose to consider the subsurface physical model  $\mathbf{m}$  as a combination of two parts: a piece-wise constant part  $\mathbf{m}_1$  and a smooth part  $\mathbf{m}_2$ :

$$\mathbf{m} = \mathbf{m}_1 + \mathbf{m}_2. \quad (13)$$

Then, the inverse problem (11) can be expressed as follow:

$$J(\mathbf{m}) = \left\| \mathbf{d} - \mathbf{G}(\mathbf{m}_1 + \mathbf{m}_2) \right\|_2^2 + \lambda_1 \left\| \mathbf{D}_1 \mathbf{m}_1 \right\|_1 + \lambda_2 \left\| \mathbf{D}_2 \mathbf{m}_2 \right\|_2^2, \quad (14)$$

where  $\lambda_1$  and  $\lambda_2$  are two regularization parameters used to allow weighting of the regularization terms.  $\mathbf{D}_i$  is the regularization operator which is based on the  $i$ th order spatial derivative of the current model. The first-order derivative operator is shown in formula (2) and the second-order derivative operator can be approximated as:

$$\mathbf{D}_2 = \begin{bmatrix} 1 & -2 & 1 & & & \\ & 1 & -2 & 1 & & \\ & & & \ddots & & \\ & & & & 1 & -2 & 1 \\ & & & & & 1 & -2 & 1 \end{bmatrix}. \quad (15)$$

A priori information is generally introduced through regularization in the inverse formalism. If a priori information on the model can be established, a third penalty term, which estimates residuals between current model and a priori model at a given iteration, should be added to the misfit function in the inversion process, and the cost function can be expressed as:

$$J(\mathbf{m}) = \left\| \mathbf{d} - \mathbf{G}(\mathbf{m}_1 + \mathbf{m}_2) \right\|_2^2 + \lambda_1 \left\| \mathbf{D}_1 \mathbf{m}_1 \right\|_1 + \lambda_2 \left\| \mathbf{D}_2 \mathbf{m}_2 \right\|_2^2 + \lambda_3 \left\| \mathbf{m}_1 + \mathbf{m}_2 - \mathbf{m}_{\text{prior}} \right\|_2^2, \quad (16)$$

where  $\mathbf{m}_{\text{prior}}$  is the a priori information that drives the inversion toward a more representative final model.  $\lambda_3$  is the trade-off parameter that balances contributions between the a priori model and the data terms.

Minimizing the cost function (16) produces a solution that can explain both data and model information. Generally, finding the above inverse solution is complicated. One efficient way is using quasi conjugate gradient method (Zhang et al. 2013). The iterative procedure can be summarized as follows:

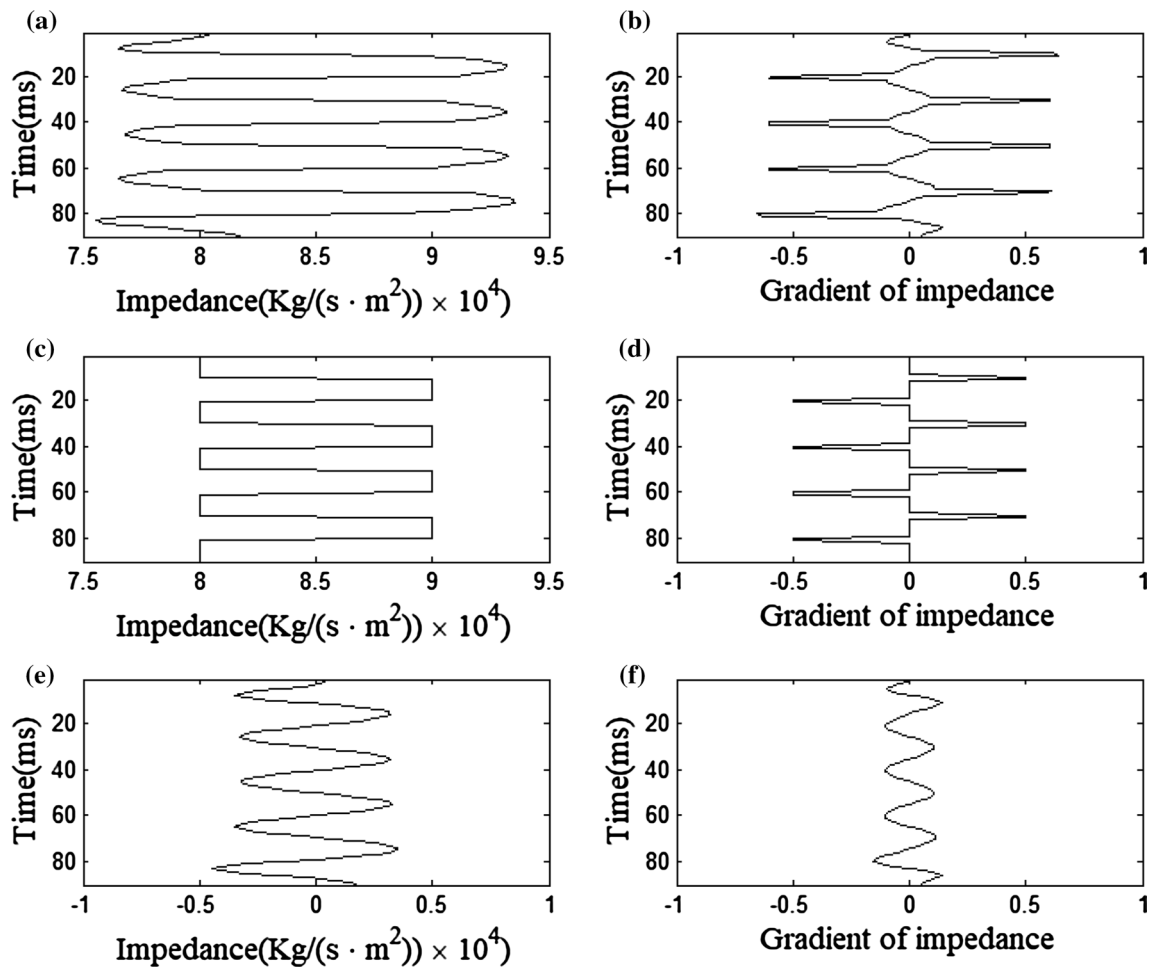


**Fig. 1** Models and their derivatives. **a** The impedance model of the real subsurface stratum  $m$  and **b** its gradient. Separating the spikes in **b** from the gradient produces a sparse gradient **(d)** and a smooth gra-

dent **(f)** It is the same as decomposing the model  $m$  into piece-wise constant part  $m_1$  **(c)** and smooth part  $m_2$  **(e)**

- (1) Calculate the objective function  $J$  for the current model  $k$  (formula 16).
- (2) Calculate the gradient vector  $g$  for the current model  $k$ . The gradient of the cost function is being updated in the optimization algorithm to iteratively approach a joint model that minimizes the cost function, which are expressed respectively as

$$\begin{aligned}
 \mathbf{g}_{m_1} = & -2G^T \{d - G(m_1 + m_2)\} \\
 & + \lambda_1 D_1^T Q(m_1) D_1 m_1 \\
 & + 2\lambda_3 (m_1 + m_2 - m_{\text{prior}}),
 \end{aligned}
 \tag{17}$$

$$\begin{aligned}
 \mathbf{g}_{m_2} = & -2G^T \{d - G(m_1 + m_2)\} \\
 & + 2\lambda_2 D_2^T D_2 m_2 \\
 & + 2\lambda_3 (m_1 + m_2 - m_{\text{prior}}),
 \end{aligned}
 \tag{18}$$

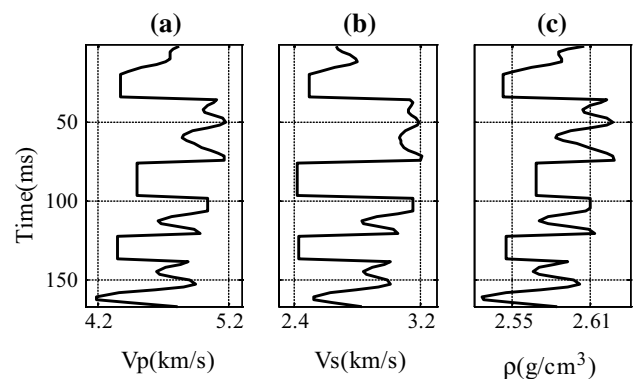


**Fig. 2** True model derived from depth-domain logging by depth-time conversion. **a** P-wave velocity, **b** S-wave velocity, **c** density



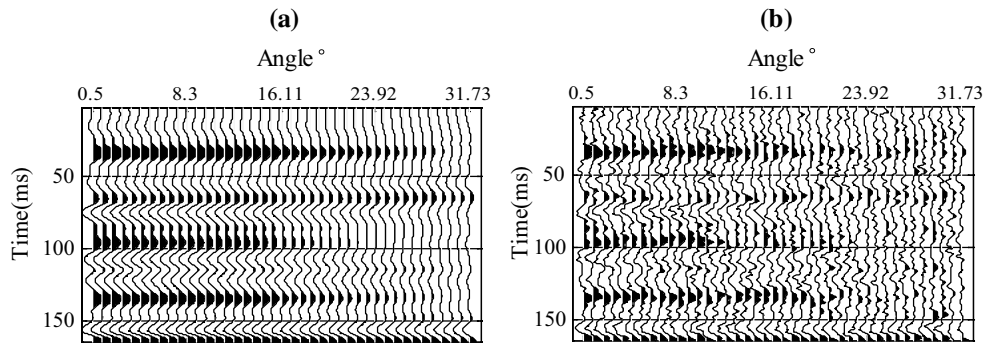


**Fig. 3** **a** Noise-free angle gather data, **b** angle gather data with Gaussian random noise ( $S/N=2$ )

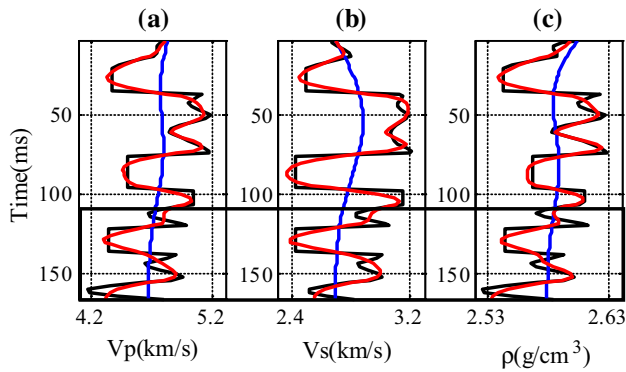


**Fig. 4** AVA inversion result with the Tikhonov regularization method (true value in black, initial value in blue and inverted value in red). **a** P-wave velocity, **b** S-wave velocity, **c** density

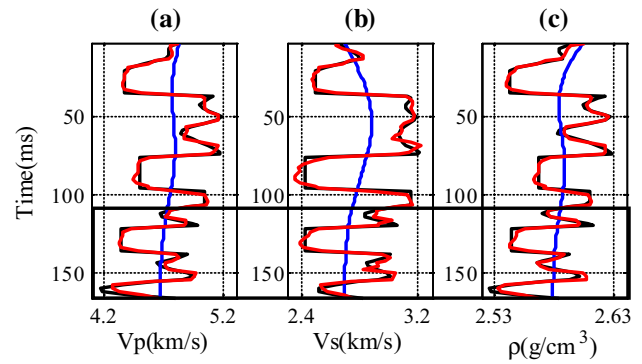


**Fig. 6** AVA inversion result with the proposed regularization method (true value in black, initial value in blue and inverted value in red). **a** P-wave velocity, **b** S-wave velocity, **c** density

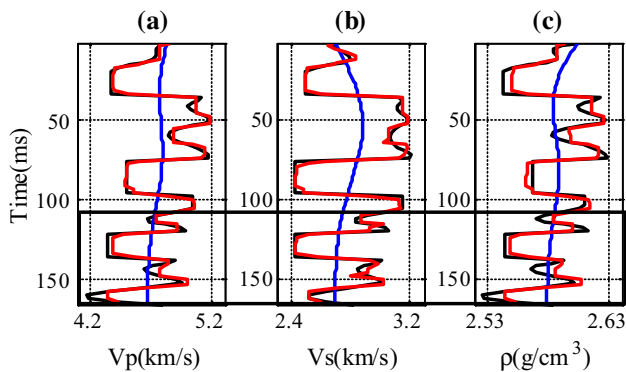


**Fig. 5** AVA inversion result with TV regularization method (true value in black, initial value in blue and inverted value in red). **a** P-wave velocity, **b** S-wave velocity, **c** density

where  $Q(m_1) = \text{diag}_{i=1,\dots,n}([D_1 m_1]_i^2 + \epsilon)^{-1/2}$  for a small positive constant  $\epsilon$ .

- (3) Calculate the search direction  $p$  for the current model  $k$  for the joint model

$$p^k = -g^k + \beta^k p^{k-1} - \theta^k (g^k - g^{k-1}), \tag{19}$$

$$\beta^k = (g^{k+1} - g^k)^T g^{k+1} / (g^{kT} g^k), \tag{20}$$

$$\theta_k = g^{kT} p^{k-1} / (g^{k-1T} g^{k-1}). \tag{21}$$

- (4) Define the step size  $\alpha$  for the current model  $k$  using MINPACK line search algorithm (Moré and Thunent 1994), calculate the constant part  $m_1$  and smooth part  $m_2$  update

$$m_1^{k+1} = m_1^k + a_{m_1}^k p_{m_1}^k, \tag{22}$$

$$m_2^{k+1} = m_2^k + a_{m_2}^k p_{m_2}^k. \tag{23}$$

- (5) Update the joint model and return to step 1

$$m^{k+1} = m_1^{k+1} + m_2^{k+1}. \tag{24}$$

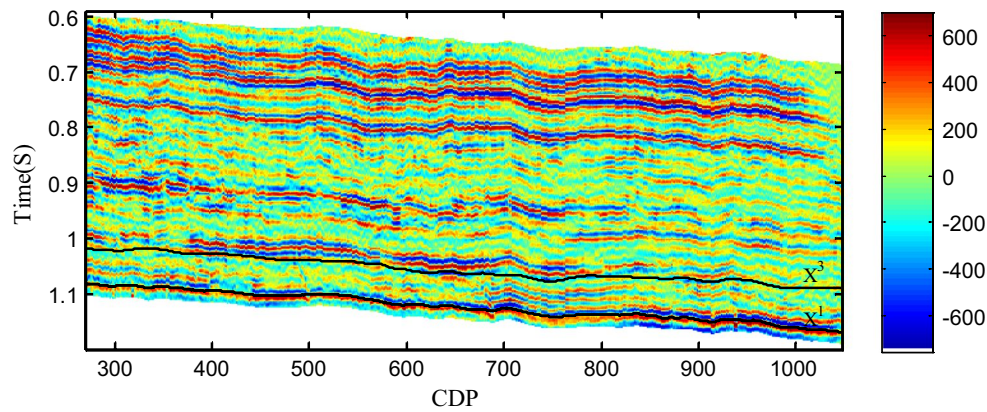


Fig. 7 The stacked seismic profile used in this test

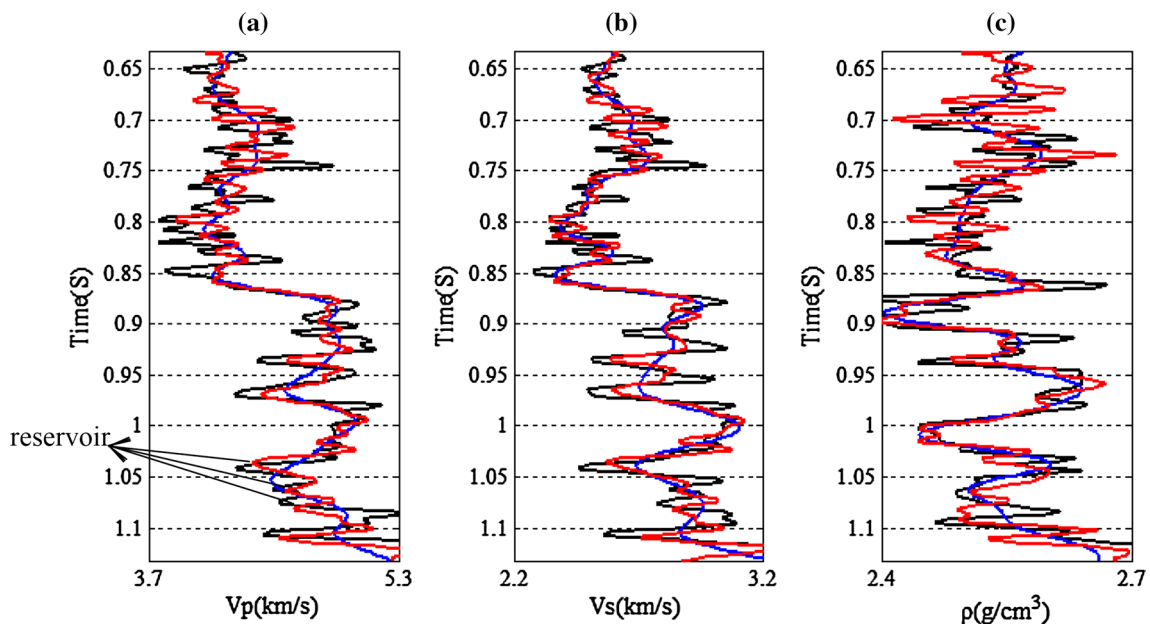


Fig. 8 The  $V_p$ ,  $V_s$  and  $\rho$  of Well A with the Tikhonov regularization method (well log in black, initial value in blue and inverted value in red)

## Synthetic data example

To assess the performance of the proposed method, the time series true model was derived from depth-domain logging by depth-time conversion, as shown in Fig. 2. Then, synthetic angle gather was synthesized by convolving the reflectivity series calculated from impedance model with a seismic wavelet with 35-Hz central frequency. The generated angle gather is presented in Fig. 3a (no noise) and Fig. 3b (with Signal to Noise Ratio  $S/N=2$ ). The gather includes 41 traces with incidence angles ranging from 0.5 to 31.73. Our goal is to find a model  $m$  that best fits the noised angle gather  $d$  using the proposed method.

The selection of the regularization parameters is essential in all regularized optimization schemes. In our study, the

regularization parameter  $\lambda_1$  determines the relative weight of data and TV norm term in recovering the rough parts of the final solution, while  $\lambda_2$  balances data and Tikhonov norm term in recovering the smooth parts of the final solution. As is known, the solution produced from over-regularization cannot fit well for the data due to the large residual error of  $d - G(m_1 + m_2)$ , while if the regularization is inadequate, the error will increase despite good match with data. The regularization parameter  $\lambda_3$  determines the weight between data and a priori model term to enhance convergence towards expected models. If the priori model is correct,  $\lambda_3$  should be a constant to ensure stability of the model. While the priori model is intrinsically incorrect, a fixed  $\lambda_3$  in the priori term cannot recast an accurate model, because the final result can keep a footprint of the priori information. In

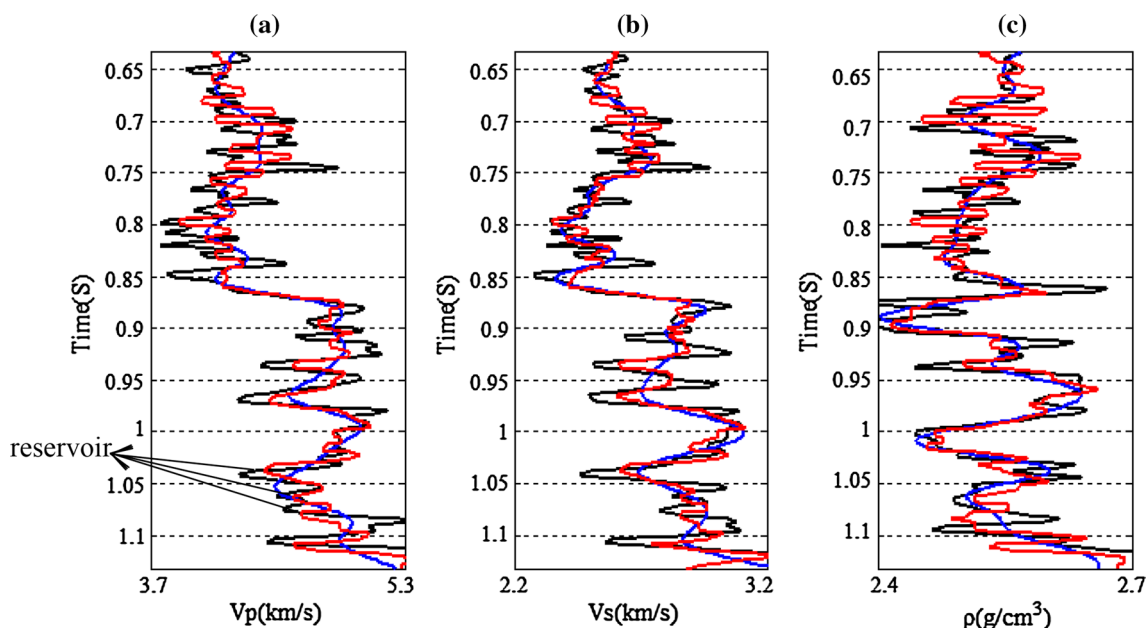


Fig. 9 The  $V_p$ ,  $V_s$  and  $\rho$  of Well A with the TV regularization method (well log in black, initial value in blue and inverted value in red)

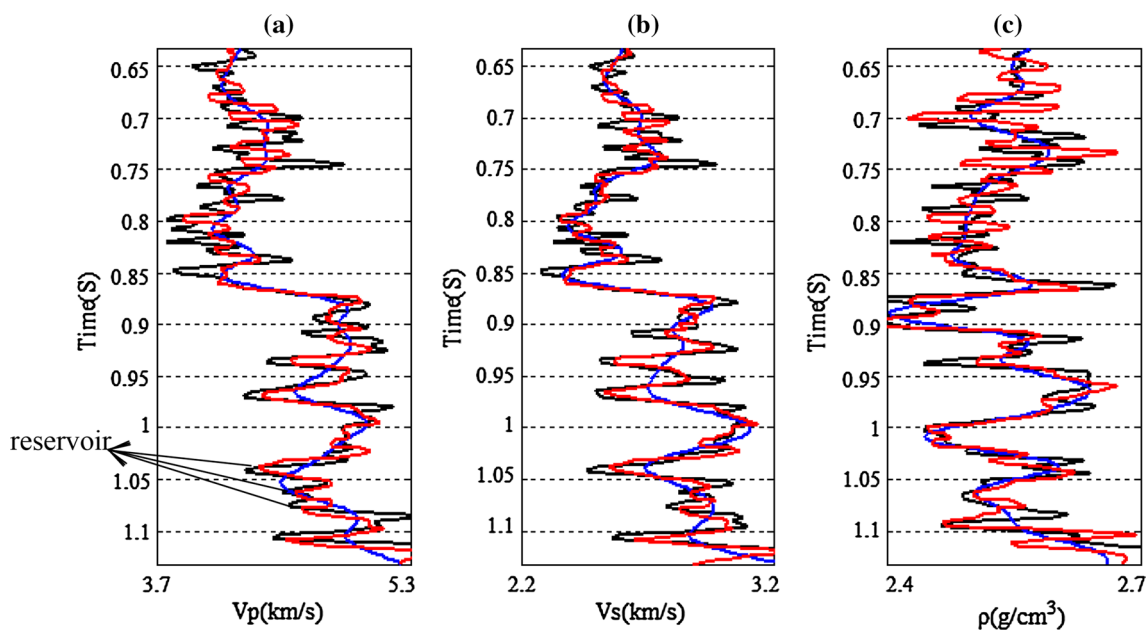


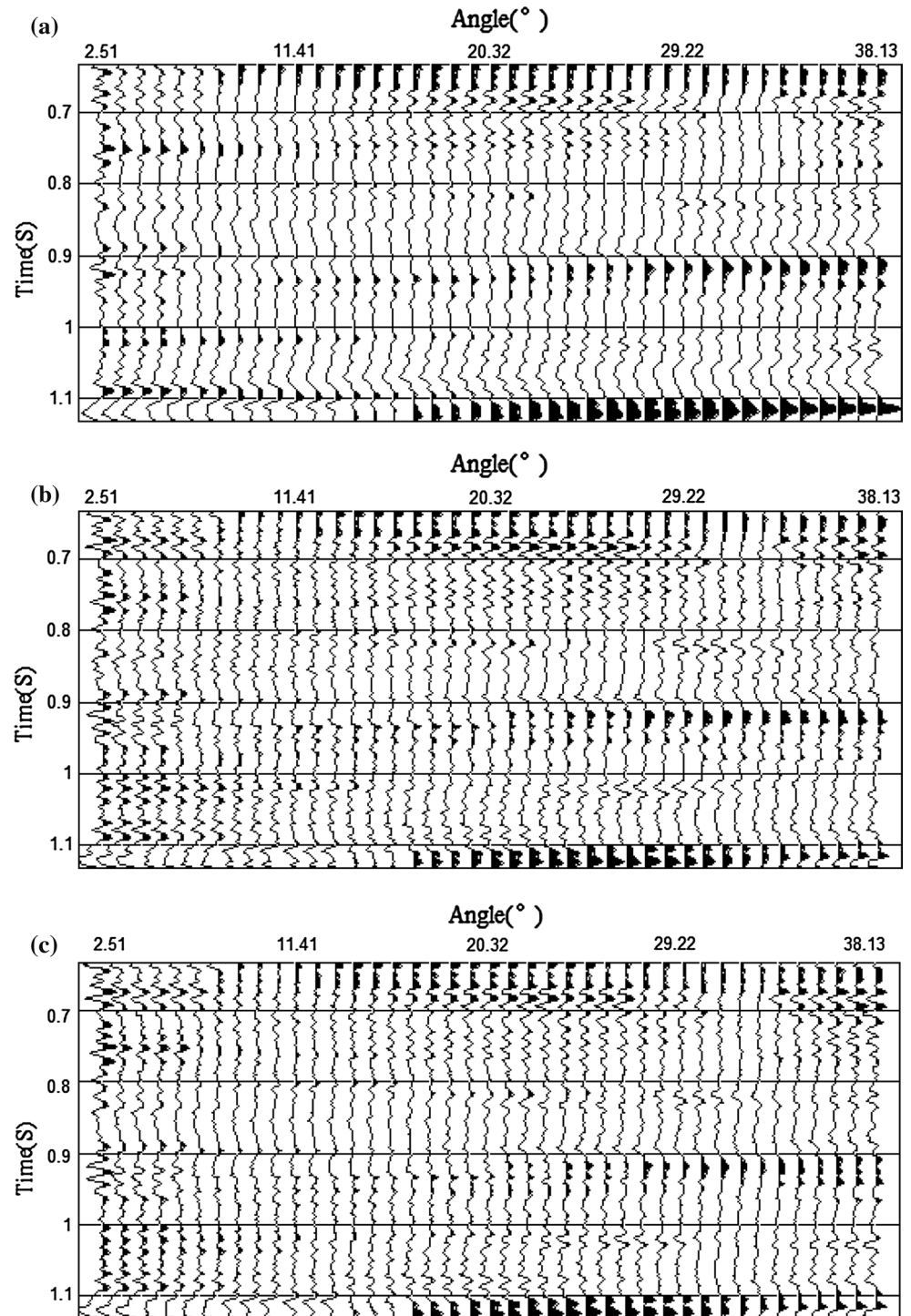
Fig. 10 The  $V_p$ ,  $V_s$  and  $\rho$  of Well A with the proposed method (well log in black, initial value in blue and inverted value in red)

many geophysical inversions, it has been proven successful to choose a dynamic weighting approach to decrease the weight of the priori term in the process of iterations for optimal solution (Asnaashari et al. 2013; Li et al. 2016a, b).

As gradient based optimization methods tend to fall into local extremes, and their solutions depend heavily on initial guess, a very low frequency initial model is usually used. In this part, we choose the initial model equal to the priori

model in the inversion procedure. The Tikhonov and TV regularization methods were applied to the inverse problem that satisfies observed seismic and low frequency priori model within a given tolerance level prescribed for the noise, and results are presented in Figs. 4 and 5, respectively. The TV method effectively preserves the spikes while severely penalizing the small derivative coefficients. It is obvious that smooth regions of final solution were transformed into

**Fig. 11** The seismic residuals of Well A with the **a** Tikhonov regularization method **b** TV regularization method **c** proposed regularization method



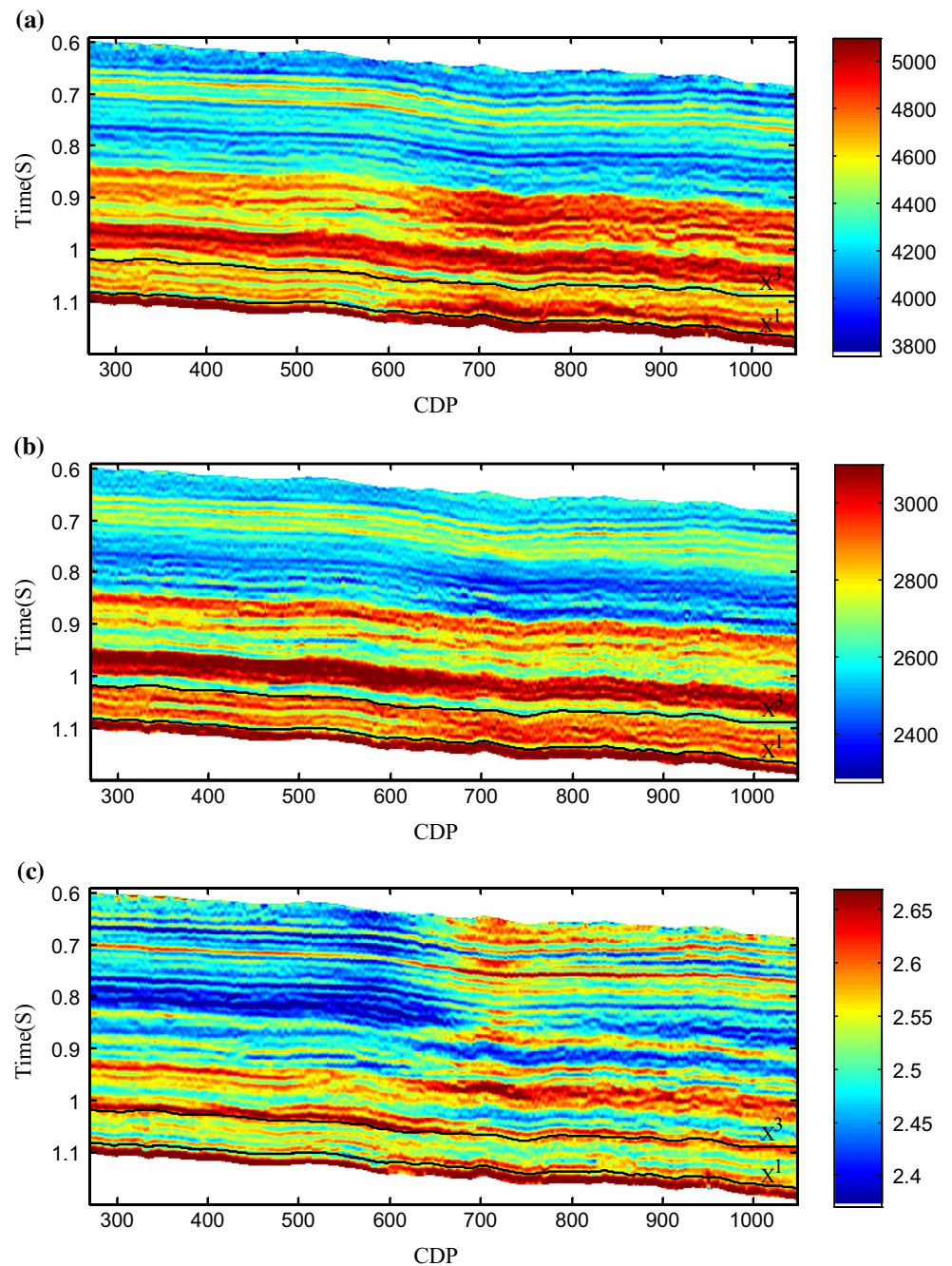
staircases while fine scale and smoothly varying properties were lost. In contrast, the Tikhonov method effectively preserves small derivative coefficients while severely penalizing the spikes. It is obvious that smooth regions were recovered while edge discontinuities were smoothed. Obviously, either Tikhonov or TV regularization only reflects partial information of the model, and is insufficient to converge towards global minimum if used independently. Therefore,

an appropriate combination of Tikhonov and TV regularization is necessary for more accurate representation of the final model.

Figure 6 shows results of the proposed regularized inversion by maximizing the TV-norm of piecewise constant part and minimizing the smoothness of smooth part, while satisfying the observed seismic data and a priori model within a given tolerance level prescribed for the noise. Significant



**Fig. 12** The AVA inversion result of the field data with the Tikhonov regularization method **a** P-wave velocity **b** S-wave velocity **c** density

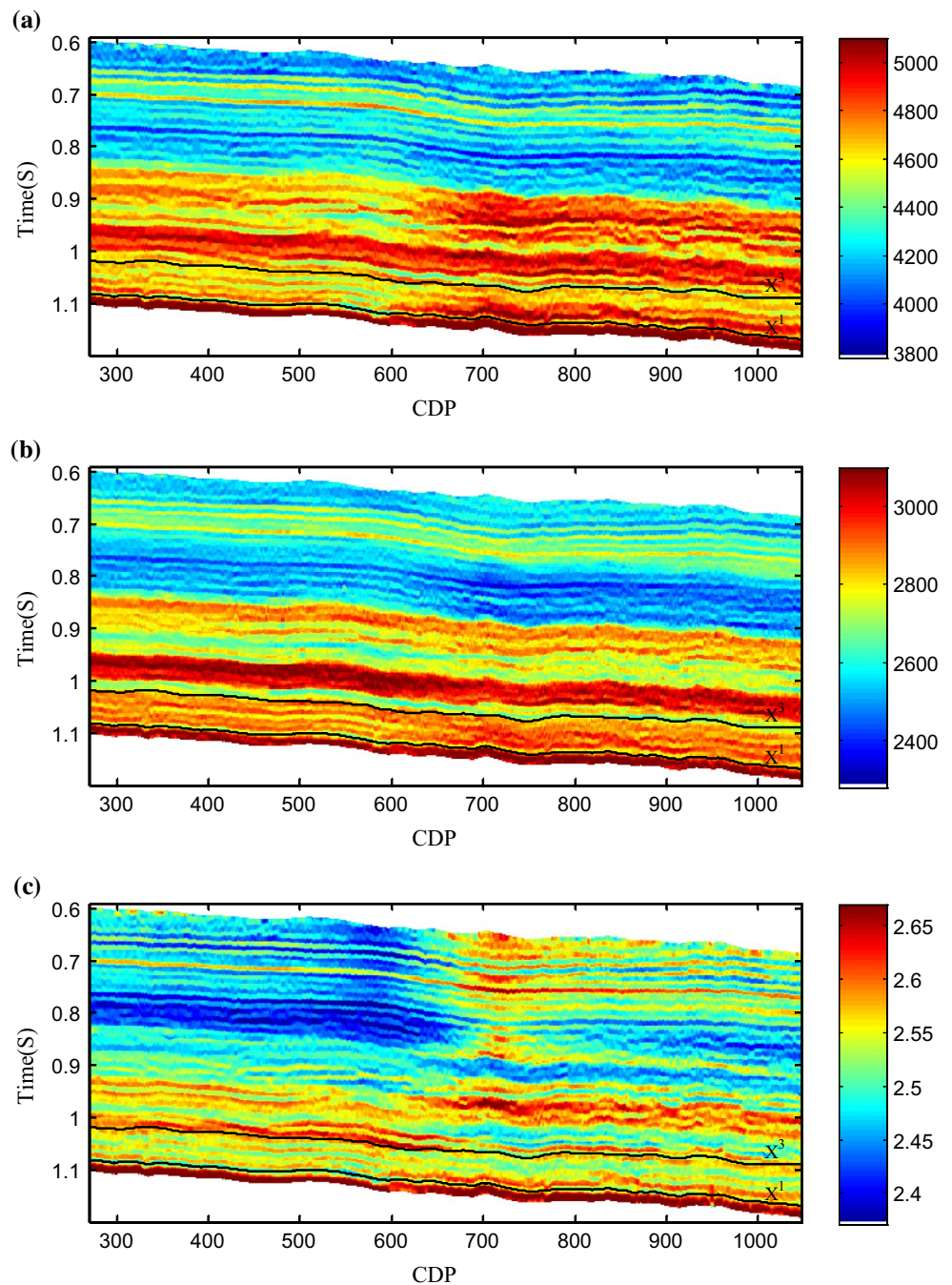


performance of the proposed method over Tikhonov and TV regularization is obvious based on the obtained results. The discrepancies between true and inverted model using the proposed regularized inversion are smaller than that using TV regularization across the jumps and even around the discontinuities, and more detail information in fine scale and smoothly varying features are successfully inverted (As shown in the black box).

### Real data application

Real pre-stack seismic data was used to demonstrate the proposed method for inversion. The field dataset was collected from An'Yue gas field which is the first large-scale integrated gas reserves in the south of Sichuan basins of China. The dataset consists of 778 Normal Moveout Corrected (NMO) angle-gathers, and each gather has incidence angles ranging from 2.51 to 38.13. After optimized processing such as denoising and NMO, the seismic gather data in

**Fig. 13** The AVA inversion result of the field data with the TV regularization method. **a** P-wave velocity, **b** S-wave velocity, **c** density



the study region have high S/N, and are thus suitable for pre-stack seismic inversion.

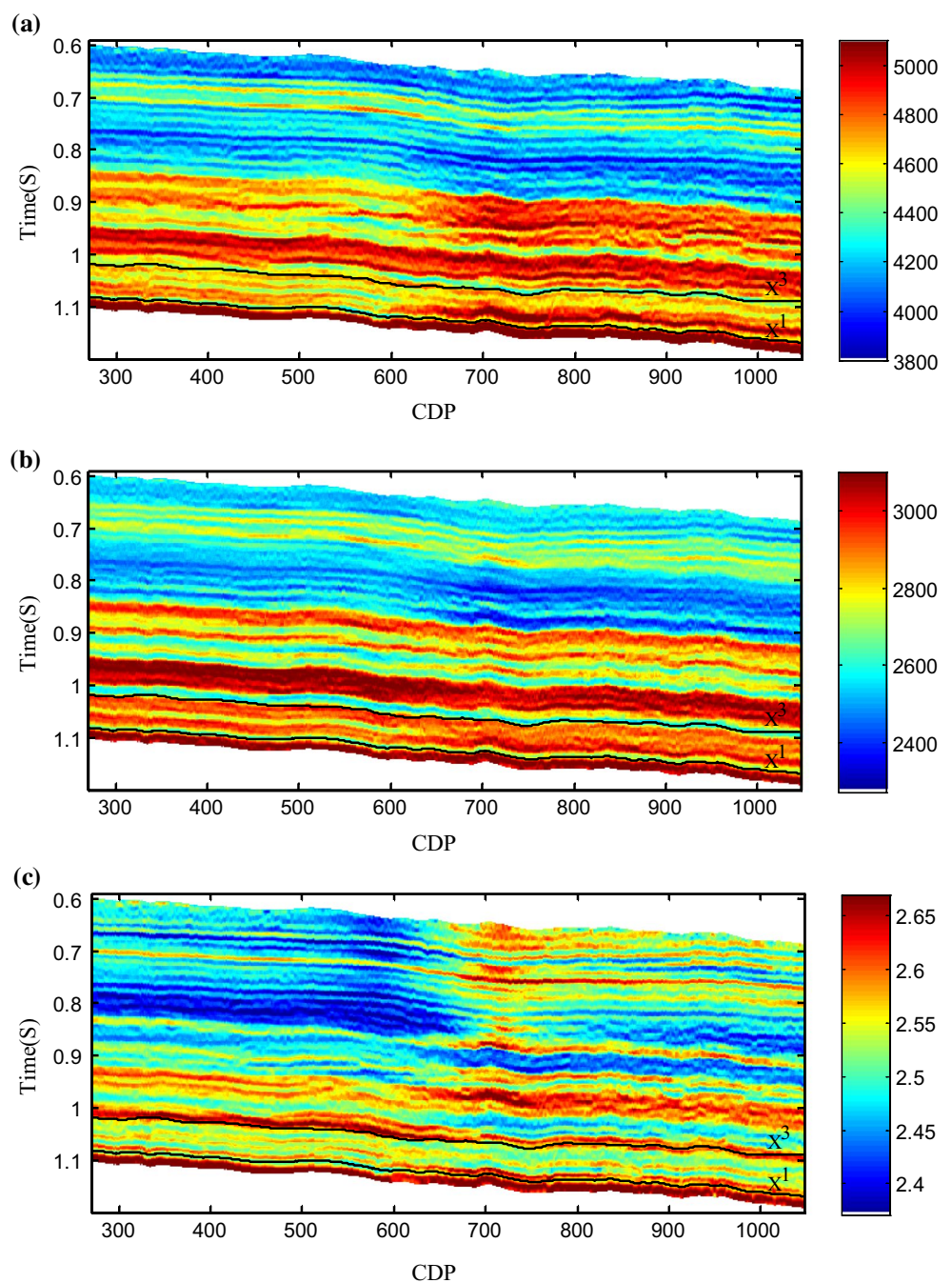
A time window of 0.5 s with a sampling interval of 2 ms was used for the inversion (Fig. 7), and main orientation is from west-south to north-east, going through well A and well B. The Common Middle Point (CDP) numbers of each well are 581 and 718 from south to north, respectively. Only two seismic reflection layers in the time window were considered, and are  $x^3$  and  $x^1$  from shallow to deep (two black curves in Fig. 7 are the horizon curves of  $x^3$  and  $x^1$ ). The characteristics of each reflective layer are:  $x^3$  reflective layer

consists of two weaker phases, with the early phase slightly stronger than the later one, and the time difference between  $x^3$  and underlying  $x^1$  is getting smaller from north to south;  $x^1$  reflective layer is characterized by a single strong phase which displays stable feature and good continuity. The target interval of this study is  $x^2$  which is a relatively low velocity layer in sandstone located between  $x^3$  and  $x^1$  and is the main production section of this gas field.

To test the proposed inversion method, a start point in real data application is source wavelet estimation. We first globally calibrated the seismic data and well log data to



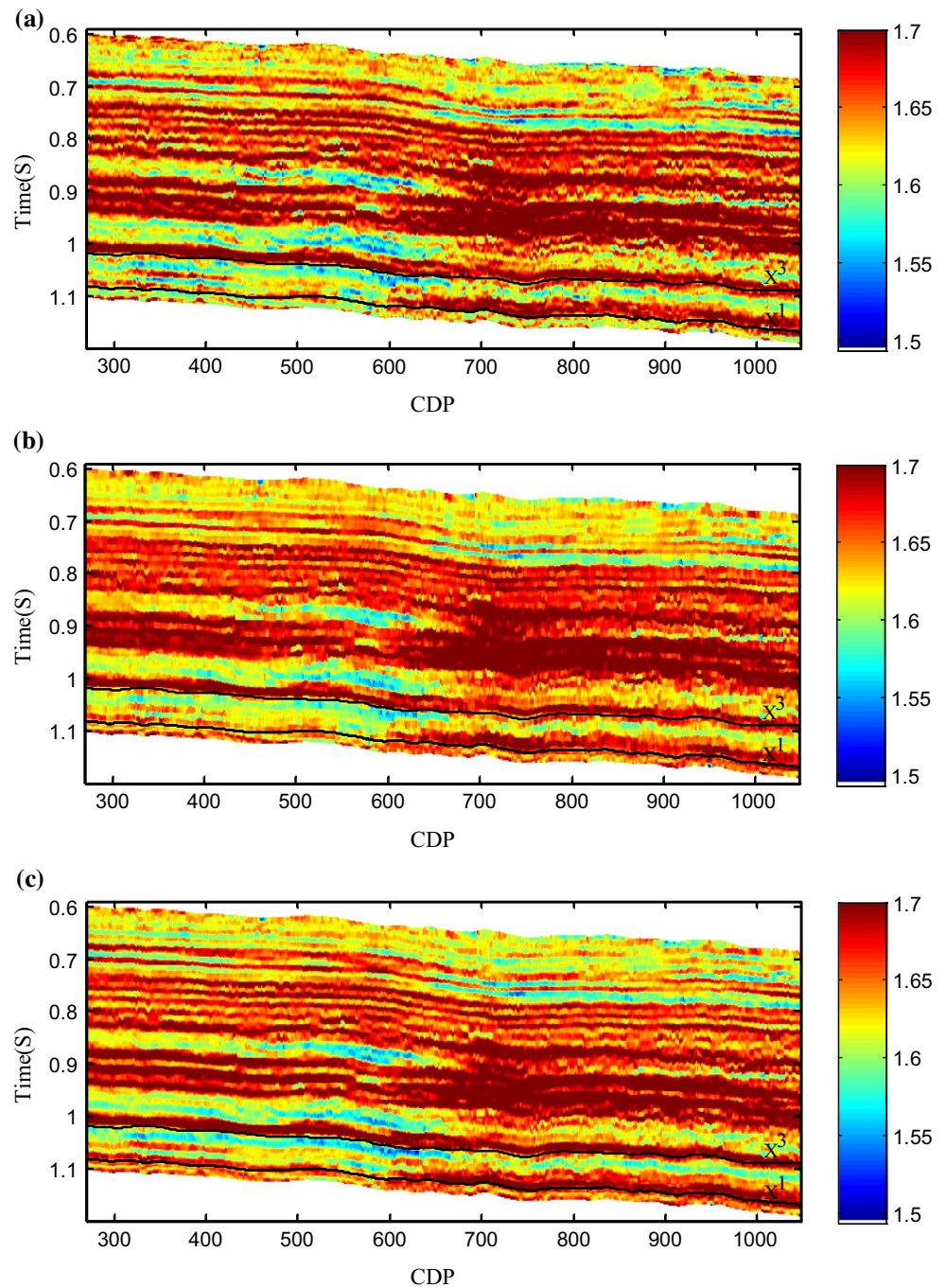
**Fig. 14** The AVA inversion result of the field data with the proposed regularization method. **a** P-wave velocity, **b** S-wave velocity, **c** density



derive one unique wavelet that is valid for the entire field. The wavelet was estimated for each well, and an averaged wavelet was used for each CDP gather. We consider that the measurements acquired in well A and well B provide accurate estimation of the local vertical density and velocity. A priori model has been created from distance weighted inverse interpolation of the well logs, following the picked horizons in the migrated section. After a Ricker wavelet with central frequency of 40-Hz was obtained, AVA inversion was then applied using linear interpolated smoothed well logs as the initial model.

Another key point in our regularized optimization schemes is the selection of the regularization parameters  $\lambda_1$ ,  $\lambda_2$  and  $\lambda_3$ . As already mentioned, the  $\lambda_3$  value chosen is relatively large ( $\lambda_3 = 100$ ) to constrain the magnitude of estimated parameters determined by a priori information. In practice, to select the  $\lambda_1$  and  $\lambda_2$ , we compute the misfit function for the starting model for  $\lambda_1 = 1$  and  $\lambda_2 = 1$ . Based on the ratio between the regularization term and the data term misfit, we adjust  $\lambda_1$  and  $\lambda_2$  values such that  $1 < \lambda_1, \lambda_2 < 100$ . Therefore, by selecting these reasonable  $\lambda_1, \lambda_2$ , the inversion is prevented from minimizing the regularization term heavily

**Fig. 15** The inverted  $V_p/V_s$  ratio of the field data with the **a** Tikhonov regularization method, **b** TV regularization method, **c** proposed regularization method



at early iterations. The estimated properties were presented following two steps to highlight the significance of each type of regularization in the inversion problem: the first one was to maximize the sparseness of the model  $m_1$ ; the second one was to maximize the smoothness of the model  $m_2$ . All the two tests also satisfied the observed seismic and low frequency well logs within a given tolerance level prescribed for the noise.

Smoothed well logs of Well A were tested. Figures 8, 9 and 10 indicate the inversion results using the Tikhonov, TV

and proposed regularization methods, respectively, which reveals that all inverted results match the actual well logs. It indicates that the same seismic data might correspond to different model patterns. However, the proposed inversion algorithm successfully obtained piecewise-smooth results, while TV regularization method is well suited for recovering piecewise constant results and Tikhonov regularization method for recovering smooth results. Figure 11 present the seismic residuals of Well A that were calculated by the Tikhonov, TV and proposed regularization methods,



respectively. It is seen that the value in most cases remains relatively small, suggesting a perfect fit. This indicates that our algorithm converges to a satisfying solution when specifically designed to minimize the proposed objective function.

The property section further validated the proposed inversion method in Figs. 12, 13 and 14 which present estimated property fields obtained from the Tikhonov, TV and proposed regularization methods, respectively. It is seen that there is a slight decrease in the velocity in the gas bearing sandstone between  $x^3$  and  $x^1$ , but the difference between reservoir and mudstone in density inversion profile increased significantly with low density for sandstone and high density for mudstone. It shows that density could effectively distinguish the reservoir in this area, and the lithology recognition is superior to velocity inversion profile. However, there are great errors in reservoir identification by using single elastic parameters such as P-wave velocity, S-wave velocity or density. The  $V_p/V_s$  ratio sections were also calculated in Fig. 15 which presents  $V_p/V_s$  ratio obtained from the Tikhonov, TV and proposed regularization methods, respectively. After using  $V_p/V_s$  ratio to identify reservoir, the accuracy of reservoir identification has been significantly improved, the threshold value for reservoir identification is  $V_p/V_s < 1.64$ . However, the characteristic geological structures, as well as their relative lateral and vertical amplitude variations, are only correctly recovered using the proposed inversion algorithm.

## Conclusion

We proposed a regularized AVA inversion scheme that includes structure information of subsurface stratum itself as optimization penalty terms. The subsurface strata are considered as the combination of a piecewise smooth part and a constant part, and then the model is optimized by maximizing the sparseness of piecewise constant part and the smoothness of piecewise smooth part. Meanwhile, the combination of both parts also satisfies the observed low frequency well log data. The description of the misfit function with three regularization terms should increase potential perspectives of the AVA inversion, because the seismic data constraints of this approach may be relaxed at the expense of a better knowledge of expected model features to be reconstructed. Commonly used iterative approach was employed as an efficient solver which is valuable for large scale inverse problems. Synthetic examples and applications demonstrate high performance of the proposed method for solutions that have varying features ranging from very smooth to very rough.

**Acknowledgements** This research is financially supported by the National Natural Science Foundation of China (U1562218 and youth

project 41604107) and Agricultural Information Engineering Key Laboratory of Sichuan Provincial Universities.

## References

- Acar R, Vogel CR (1994) Analysis of bounded variation penalty methods for ill-posed problems. *Inverse Prob* 10(6):1219
- Anagaw AY, Sacchi MD (2012) Edge-preserving seismic imaging using the total variation method. *J Geophys Eng* 9(2):138
- Asnaashari A, Brossier R, Garambois S et al (2013) Regularized seismic full waveform inversion with prior model information. *Geophysics* 78(2):R25–R36
- Bertete-Aguirre H, Cherkaev E, Oristaglio M (2002) Non-smooth gravity problem with total variation penalization functional. *Geophys J Int* 149(2):499–507
- Bosch M, Mukerji T, Gonzalez EF (2010) Seismic inversion for reservoir properties combining statistical rock physics and geostatistics: a review. *Geophysics* 75(5):75A165–75A176
- Bouchon M, Aki K (1977) Discrete wave-number representation of seismic-source wave fields. *Bull Seismol Soc Am* 67(2):259–277
- Fatti JL, Smith GC, Vail PJ et al (1994) Detection of gas in sandstone reservoirs using AVO analysis: a 3-D seismic case history using the Geostack technique. *Geophysics* 59(9):1362–1376
- Fomel S (2007) Shaping regularization in geophysical-estimation problems. *Geophysics* 72(2):R29–R36
- Gholami A, Hosseini SM (2013) A balanced combination of Tikhonov and total variation regularizations for reconstruction of piecewise-smooth signals. *Sig Process* 93(7):1945–1960
- Guitton A, Symes WW (2003) Robust inversion of seismic data using the Huber norm. *Geophysics* 68(4):1310–1319
- Hampson DP, Russell BH, Bankhead B (2005) Simultaneous inversion of pre-stack seismic data. *SEG Techn Progr Expand Abstr* 2005:1633–1637
- Li G, Zhang H, Wang Y et al (2014) Prestack AVO inversion using edge-preserving regularization with directional constraints. *SEG Techn Progr Expand Abstr* 2014:3080–3085
- Li Z, Hu G, Li Y et al (2016a) Regularized amplitude-versus-angle (AVA) inversion with travelttime information. *SEG Techn Progr Expand Abstr* 2016:548–552
- Li Z, Song B, Zhang J et al (2016b) Joint elastic and petrophysical inversion using prestack seismic and well log data. *Explor Geophys* 47(4):331–340
- Li Z, Hu G, Zhang J (2017a) Adaptive mixed-norm seismic inversion for non-Gaussian errors. *Explor Geophys* 48(4):413–421
- Li Z, Hu G, She B (2017b) A hybrid regularization approach for AVA inversion of the piecewise smooth model. *SEG Techn Progr Expand Abstr* 2017:793–797
- Lin Y, Huang L (2015) Acoustic-and elastic-waveform inversion using a modified total-variation regularization scheme. *Geophys J Int* 200(1):489–502
- Moré JJ, Thuente DJ (1994) Line search algorithms with guaranteed sufficient decrease. *ACM Trans Math Softw (TOMS)* 20(3):286–307
- Theune U, Jensås IØ, Eidsvik J (2010) Analysis of prior models for a blocky inversion of seismic AVA data. *Geophysics* 75(3):C25–C35
- Tikhonov AN, Arsenin VIA (1977) *Solutions of ill-posed problems*. Winston, Washington DC
- Wang H, Fehler MC (2018a) The wavefield of acoustic logging in a cased hole with a single casing—part II: a dipole tool. *Geophys J Int* 212(2):1414–1428
- Wang H, Fehler MC (2018b) The wavefield of acoustic logging in a cased-hole with a single casing—part I: a monopole tool. *Geophys J Int* 212(1):612–626

- Wang H, Tao G (2011) Wavefield simulation and data-acquisition-scheme analysis for LWD acoustic tools in very slow formations. *Geophysics* 76(3):E59–E68
- Wang Y, Cao J, Yang C (2011) Recovery of seismic wavefields based on compressive sensing by an  $l_1$ -norm constrained trust region method and the piecewise random subsampling. *Geophys J Int* 187(1):199–213
- Wang H, Tao G, Zhang K (2013) Wavefield simulation and analysis with the finite-element method for acoustic logging while drilling in horizontal and deviated wells. *Geophysics* 78(6):D525–D543
- Zhang X, Zhang J (2017) Model regularization for seismic travel time tomography with an edge-preserving smoothing operator. *J Appl Geophys* 138:143–153
- Zhang J, Lv S, Liu Y et al (2013) AVO inversion based on generalized extreme value distribution with adaptive parameter estimation. *J Appl Geophys* 98:11–20
- Zhang F, Dai R, Liu H (2014a) Seismic inversion based on  $L_1$ -norm misfit function and total variation regularization. *J Appl Geophys* 109:111–118
- Zhang H, Cao C, Shang Z (2014b) A nonlinear method of simultaneous inversion for pre-stack seismic data based on edge-preserving regularization. *SEG Techn Program Expand Abstr* 2014:3226–3230



# Integrated geophysical survey on the ancient Deák Ferenc Sluice of Hungary

Ali Ismet Kanli<sup>1</sup> · Zsolt Pronay<sup>2</sup> · Peter Tildy<sup>2</sup> · Endre Toros<sup>2</sup> · Borislav Neduca<sup>3</sup> · Peter Nagy<sup>3</sup>

Received: 29 March 2018 / Accepted: 24 September 2018 / Published online: 28 September 2018  
© Institute of Geophysics, Polish Academy of Sciences & Polish Academy of Sciences 2018

## Abstract

The west channel of the ancient Deák Ferenc which was constructed in 1875 in Hungary was used for controlling the water amount and the east channel was used for the shipping. In the study, four geophysical nondestructive methods were used to this old channel which needs the restoration and reinforcement works. The high-frequency seismic and acoustic measurements were carried out, the resistivity measurements were carried out to map the resistivity distribution of the slab, the seismic direct wave method was used to map the seismic velocities for understanding the stability conditions of the walls and the ground penetrating radar measurements were carried out on the slab and on the walls. The results of integrated study showed us that voids, faults and cracks were detected and the inhomogeneous construction materials were used in the slab. The obtained results emerged that the usage of nondestructive geophysical methods is essential in all stages of restoration and reinforcement works, especially for the ancient structures.

**Keywords** Ultrahigh frequency · Acoustic · Seismic · Geoelectric · GPR · Ancient structures

## Introduction

Ground penetrating radar (GPR) as a nondestructive testing method is used in geological surveys (Nyari and Kanli 2007), to investigate ancient structures (Pieraccini et al. 2005; Masini et al. 2010; Garcia et al. 2007; Pérez-Gracia et al. 2008) to monitor the restoration works of the structures and their stabilization (Ranalli et al. 2004; Kanli et al. 2015). Two- or three-dimensional electrical and electromagnetic methods often involve permanent electrode installations which have proved to provide dynamic volumetric information while being either noninvasive (Park 1998; Kanli and Neduca 2015; Tildy et al. 2017) or minimally invasive (Daily and Ramirez 1995; Daily et al. 1992; Nyari et al. 2010). Success of integrated seismic measurements is well known used for various purposes (Grit and Kanli 2016).

Archaeologists require to investigate shallow water (< 5 m) sites nondestructively using terrestrial and/or marine methods. Acoustic methods have become an essential alternative method in archaeological excavations (Pléts et al. 2008). In this study, joint interpretations and parallel geophysical measurements were implemented to investigate the conditions of the ancient channel.

The two main rivers in Hungary, Danube and Tisza, were connected in the eighteenth–nineteenth century by a canal named Ferenc. This canal was used for inland navigation, watering and to remove inundation. After some tens of years after completing the canal, mud accumulation limited the navigation heavily. To overcome this problem, a water transport canal was built in 1870–1875 with a brick-walled lock and sluice between the canal and river Danube. At that time, the sluice was unique in Europe with its masonry structure and separated water inlet and navigation channel (Fig. 1). The total size of the sluice is 97 m, length 61.5 m width and 8.8 m high. The length and width of the navigation and water inlet channels are 47, 15, 82.4 and 13.8 m, respectively. The thickness of the outer walls is 2.9 m, while the one between the two channels is 2.3 m thick. The whole structure was built of brick excluding the base slab which is a concrete slab with the thickness of 2 m. After about 60 years of operation, extensive repair and renovation works were carried out.

✉ Ali Ismet Kanli  
kanli@istanbul.edu.tr

<sup>1</sup> Department of Geophysical Engineering, Faculty of Engineering, Istanbul University-Cerrahpasa, Avcilar Campus, 34320 Istanbul, Turkey

<sup>2</sup> Geological and Geophysical Institute of Hungary, Budapest, P.O. Box 35, 1440, Hungary

<sup>3</sup> MinGeo Ltd., Budapest, Kassai u. 96, 1142, Hungary

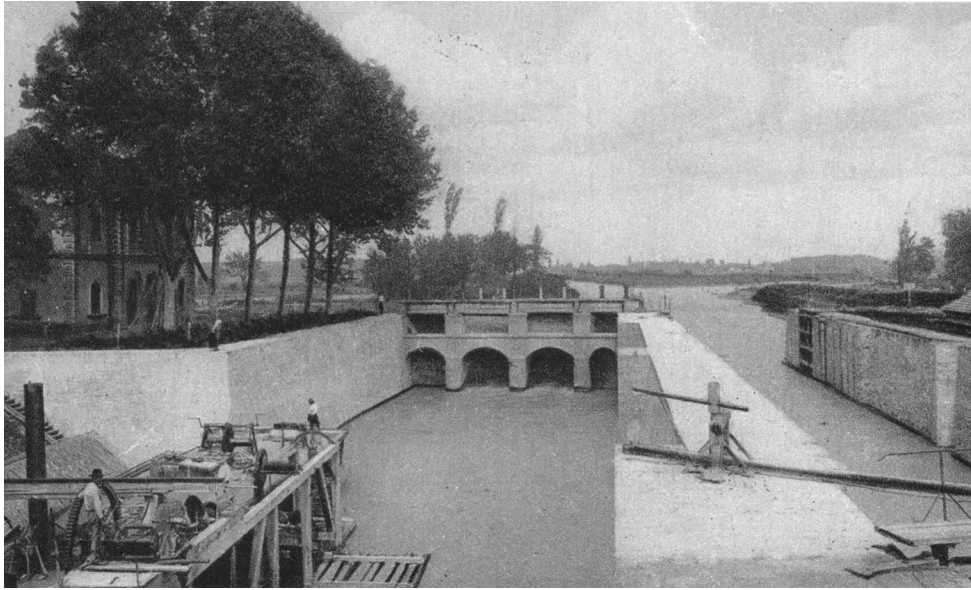


**Fig. 1** Deák Ferenc Sluice in 1930 (Hungaricana)

The frost damages were repaired by replacing the affected bricks, and the inner structure was stabilized by cement injections from boreholes in a regular grid on the top of the wall. The voids below the base slab were injected as well. The water level in 1956 exceeded the height of the sluice by 60 cm and caused considerable damages. It was repaired immediately with improvised solutions, and it was topped by a 1.2-m-high concrete structure to avoid future overtopping. The eastern wall of the water inlet channel near the gate had to be supported by a reinforced concrete box (Fig. 2) of a size of 2.5 m wide, 12 m long and 4 m high, and the thickness of its walls is 1 m.

Nowadays, the support system is faulted again with heavy foliation and the signs of incompetent repairs and fractures are visible on the surface of the brick wall. Some of them are shown in Fig. 3. The main question to be answered is: What is the depth of the brick damages and do the fractures intersect the whole structure? The another problem is the stability and condition of the base slab which holds the weight of the sluice and the support structure. The outwashes below the base slab were injected in 1930, but there is no any detailed information about the recent condition of it. The sluice is not only a part of national heritage, but it is in the first line of

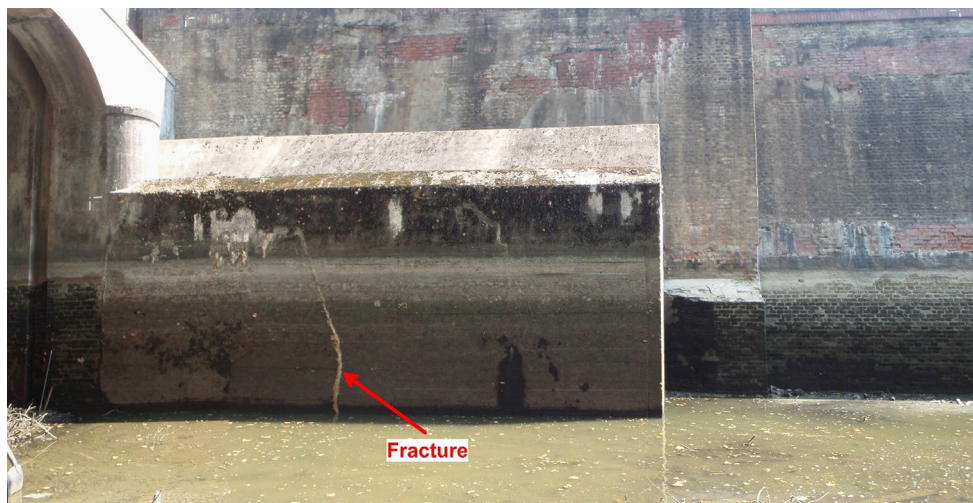


**Fig. 2** The reinforced concrete support system





**Fig. 3** Recent state of the western wall (1. incompetent repair, 2–3. brick and fugue damages, 4. fault and dissolved mortar, 5–6. wet wall with vegetation)



**Fig. 4** Bottom of the navigation channel after removing the water

flood protection as well. There is a need for maintaining its stability and to restore it as close to its original form as possible. As it is known a reality, all types of drillings can harm the structure of the sluice, especially in such ancient constructions. Therefore, nondestructive geophysical measurements were implemented to test the structure, integrity of the walls and the base slabs to help the design of the restoration process with minimizing the drilling activity of ancient structure (Fig. 4).

### The base slab

To understand the real condition of the base slab, the high-resolution GPR measurements were conducted. The measurements were executed while the sluice was still working, and we had a limited time to remove the water from the channels. The conditions of muddy surface with puddles were not suitable for good-quality GPR records and measurements. There was no possibility to remove the mud totally, and the slab was forced to be in dry condition. For that reason, we had to select a method which can map the surface of the slab with high resolution below the water and mud layer. Ultrasound method was selected using Pubi-80 source and receiver with 80 kHz frequency. The wavelength (resolution) of the method is comparable with a 4–5-GHz GPR system. The investigation was carried out from a boat. The water level was approximately 2 m, and the mud thickness was about 30 cm. The water provides very good coupling for the waves, and the loose mud has practically not attenuated the signal. The system is suitable to detect fractures on the top of the slab by finding low amplitudes where discontinuities scatter waves. The measurements were carried out in both channels of the sluice in a quasi-regular grid. The total length of the ultrasound profiles was 5624.9 m which means in average 11.4 channels for one square meter.

Figure 5 shows both the amplitude of ultrasound reflections from the top of slab and the interpretation as well. White colors show small reflection strengths, where only a

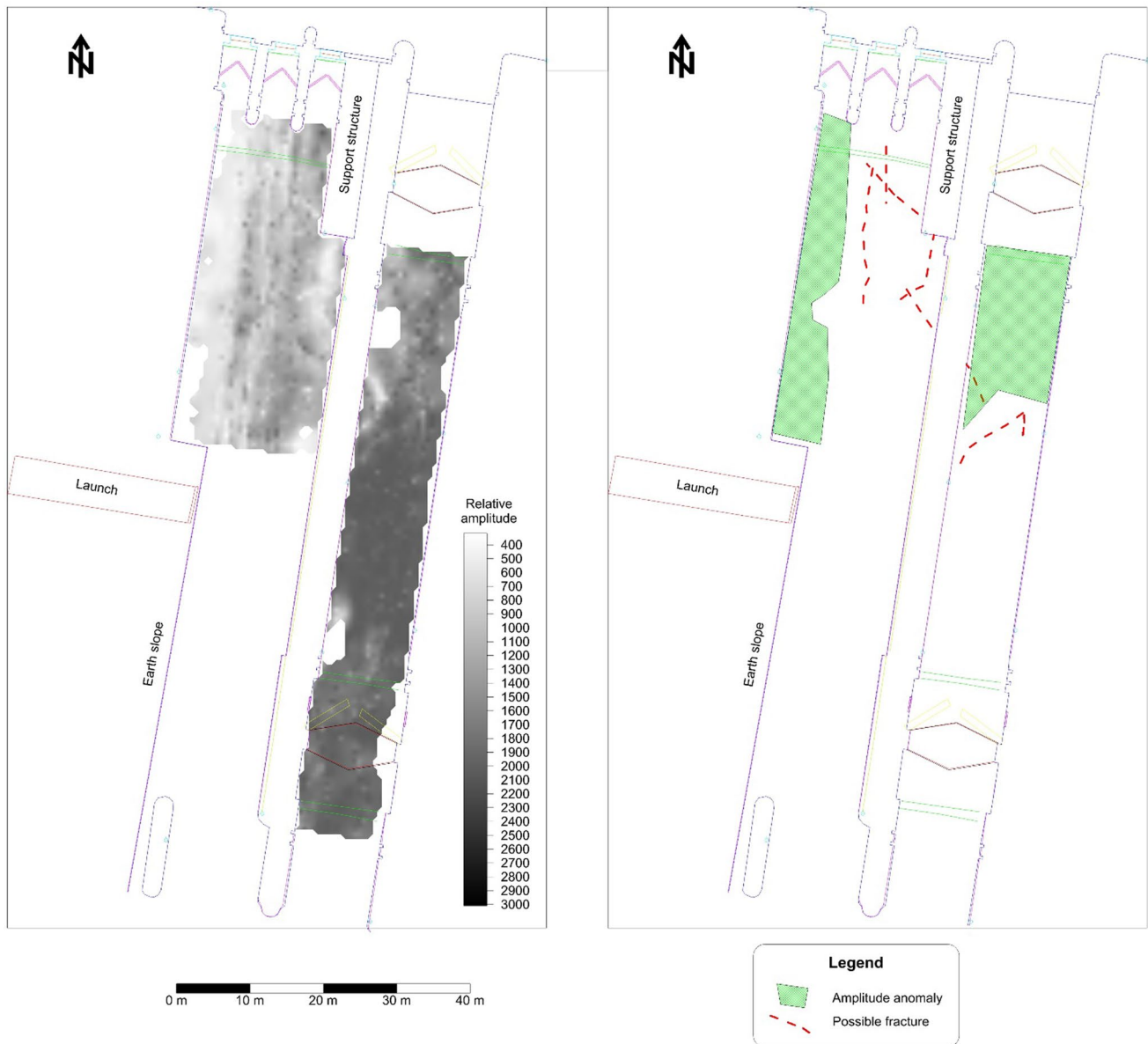


**Fig. 5** Ultrasound reflection amplitudes from the top of the slab and interpretation

small portion of the energy is reflected back to the receiver. The data are unprocessed and represent real reflectivity in A/D counts. The lineaments on the top of the slab are interpreted as fractures and marked with red-dashed lines. The reflection amplitudes, together with the mechanical properties of the slab in the two channels, are quite different. The low amplitude anomalies, compared to the average in the same channel, are marked with cross-hatched areas on the figure. It is possible that this inhomogeneous behavior is caused by differences in building material or undocumented repairs of the slab. 80-kHz signal could not penetrate the concrete slab. For that reason, a 5-kHz high-frequency one-channel seismic (acoustic) system by Taktronic and SyQwest

StrataBox was applied as well on the same grid as in the 80-kHz case. The resolution of this method is equal to a 300-MHz GPR system, and it could penetrate the slab. The reflection amplitude from the bottom of the slab was analyzed on the unprocessed records (Fig. 6). High negative amplitudes (dark colors) show us the lower velocity below the concrete layer and can indicate water filled voids below the slab. It is an interesting result that those anomalies have a quasi-linear structure which can be washouts below the broken slab.

To help to investigate the slab itself and the geological layers which are located in deeper, DC multielectrode geoelectric method was tested in both channels using AGI

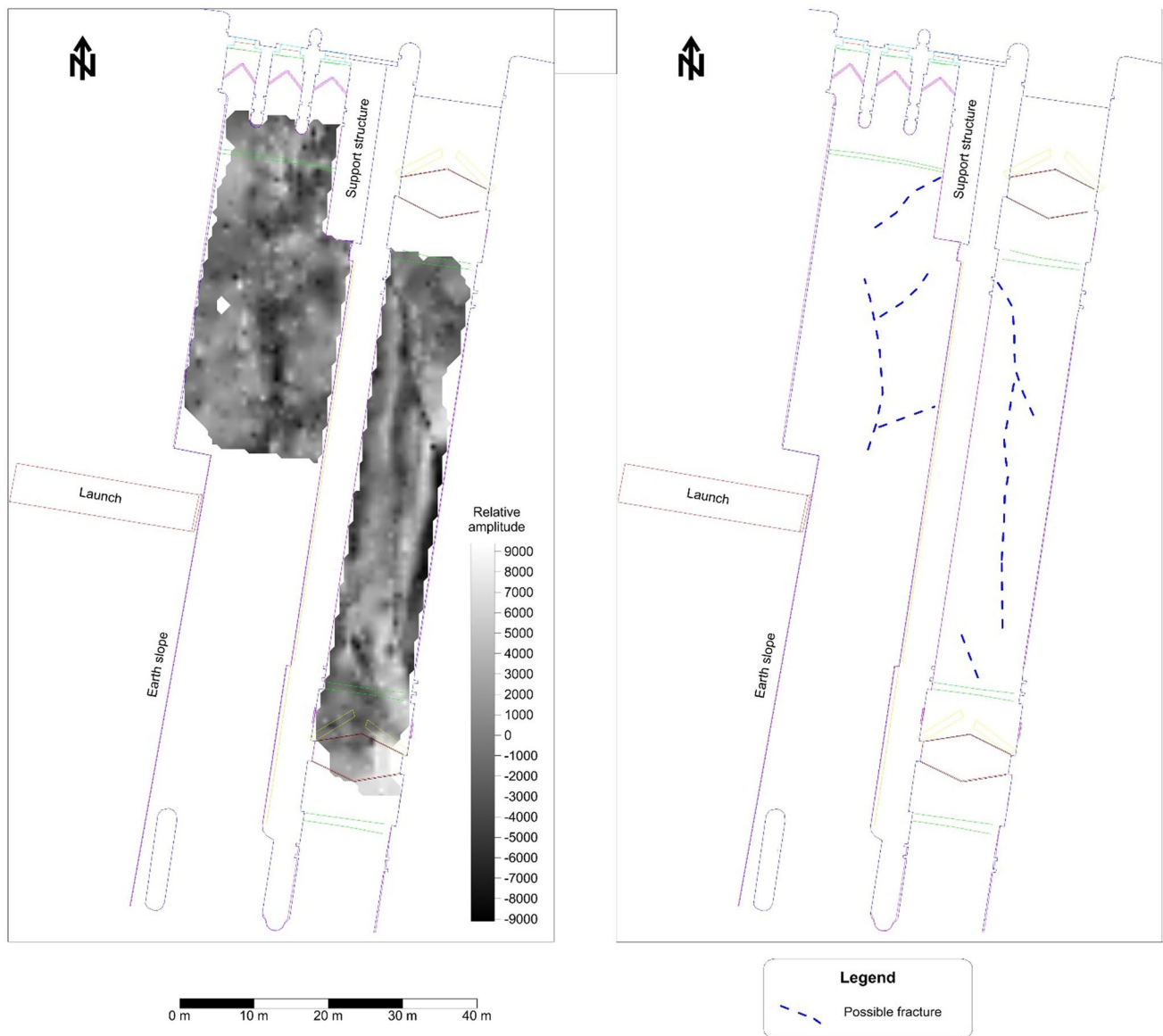


**Fig. 6** Acoustic reflection amplitudes from the bottom of the slab and interpretation

SuperSting instrument and marine electrode cable with floats. Wenner electrode array was selected, because it is successful in resolving horizontal structures (Loke 2004). The number of electrodes was 42 with 1-m spacing. Unfortunately, the method could not separate slab and geological layers below. It is very interesting that the anomaly caused by the slab is visible on the measured data (Fig. 7, the supposed anomaly from the bottom slab is marked by black arrow). The processing with refined grid parameters was repeated several times without having more realistic result. Models including water depth with constant and slightly varying resistivity and the thickness of the concrete slab were also tested. The water depth and/or the thickness of the slab was taken into account in the processing derived

from the ultrasound and/or acoustic reflection data. Data processing with Günther's Dc2dInvRes inversion program (Günther 2004) resulted similar results, but with lower resistivity values. The model parameters and the RMS errors after the fourth iteration step are summarized in Table 1. Except on Res2DInv results with default parameters, there are at least 2–4 grids in the slab, as well as in the water; hence, in theory, its resistivity could have been calculated. The results after processing the data with different parameters are visible in Fig. 8. Despite the fact that the quality of the data was extremely good, because of the perfect coupling and RMS error after the fourth iteration step which were below 3%, the geoelectric sections were excluded from the final interpretation.



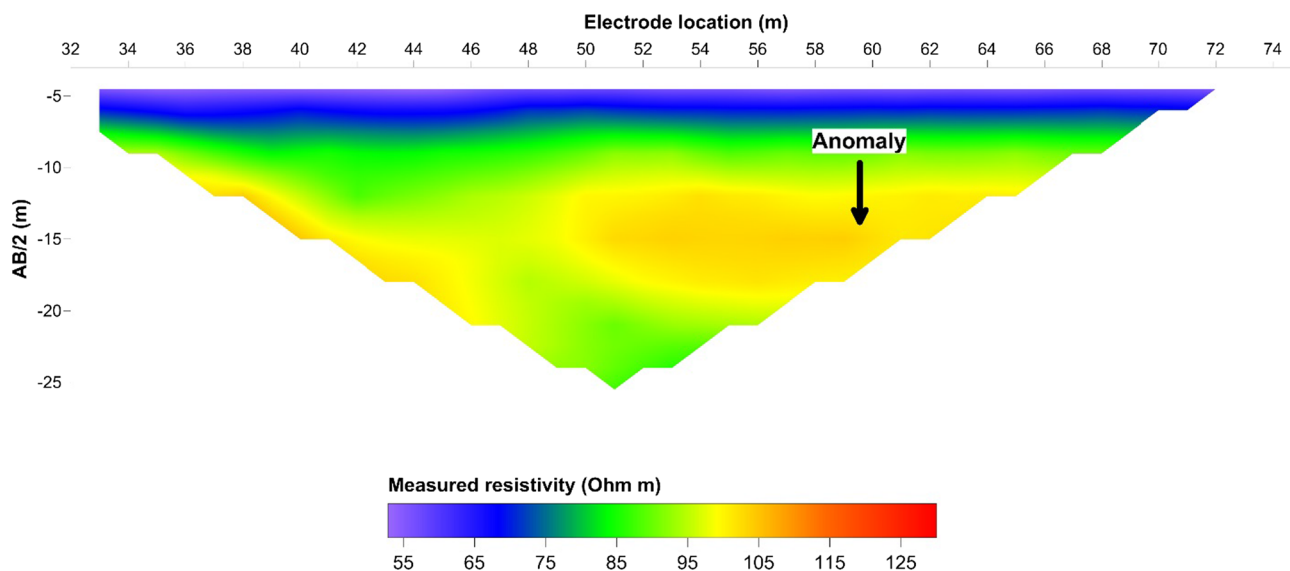


Fig. 7 Measured resistivity data

Table 1 Layer depth at different processing parameters

No.	Processing	Thickness of the first layer	Thickness rate	Remarks	RMS error (%)
1	Dc2dInvRes			Default	
2	Res2DInv	1	1.1	Default	3.39
3	Res2DInv	0.5	1.1		2.11
4	Res2DInv	0.5	1.05		2.09
5	Res2DInv	0.5	1		2.55
6	Res2DInv	0.5	1.05	Water depth added (damp. fact. = 2)	2.47
7	Res2DInv	0.5	1.05	Water depth added (damp. fact. = 10)	2.47
8	Res2DInv	0.5	1.05	Two layers defined	2.37
9	Res2DInv	0.5	1.05	Water depth added (damp. fact. = 5) and a layer with constant depth defined	2.83
10	Res2DInv	0.5	1.05	Water depth added (damp. fact. = 5) and a layer with real depth defined	2.27

### The inner structure of the walls

The second problem to be solved is the depth and location of the brick damages and if the fractures intersect the whole structure or not. To overcome problem and to understand the conditions of the structure, the GPR measurements were taken. Because of the 2.3–2.9 m thickness of the walls, to obtain the good resolution and penetration, it was used different antennas with different frequencies. To image the top brick layers with high resolution, it was used 1.5-GHz antenna, to detect the anomalies with medium resolution below the 1 m depth, it was used 400-MHz antenna, and to observe behind the whole thickness of the wall with lower resolution, it was used 100-MHz

antenna. The wall with a thickness of 2.3 m between the two channels could be accessed from both sides. In this case, usage of 100 MHz was not necessary to penetrate the whole structure. On the side walls, the question of the fractures intersect the entire wall could not be answered directly. In that case, the anomalies on all frequencies were correlated, and if they coincided it was supposed that the full thickness is affected.

GSSI SIR-3000 GPR unit was used for the measurements with the aforementioned antennas. The distances were measured by a calibrated survey wheel. The processing steps were as follows:

- Editing the geometry
- t0 correction



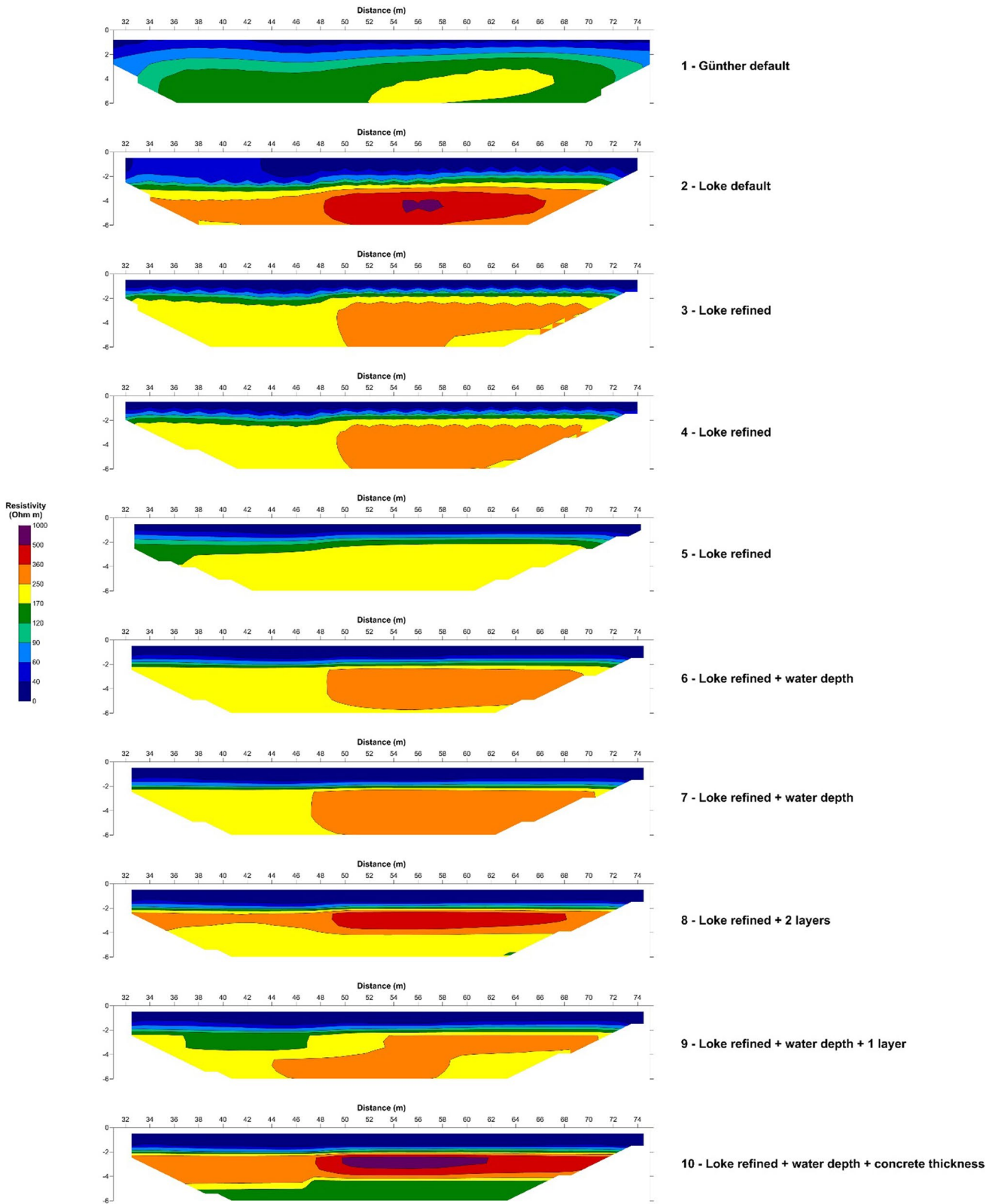


Fig. 8 A selected geoelectric section with different processing parameters in the navigation channel



Fig. 9 GPR measurement using pole or boat

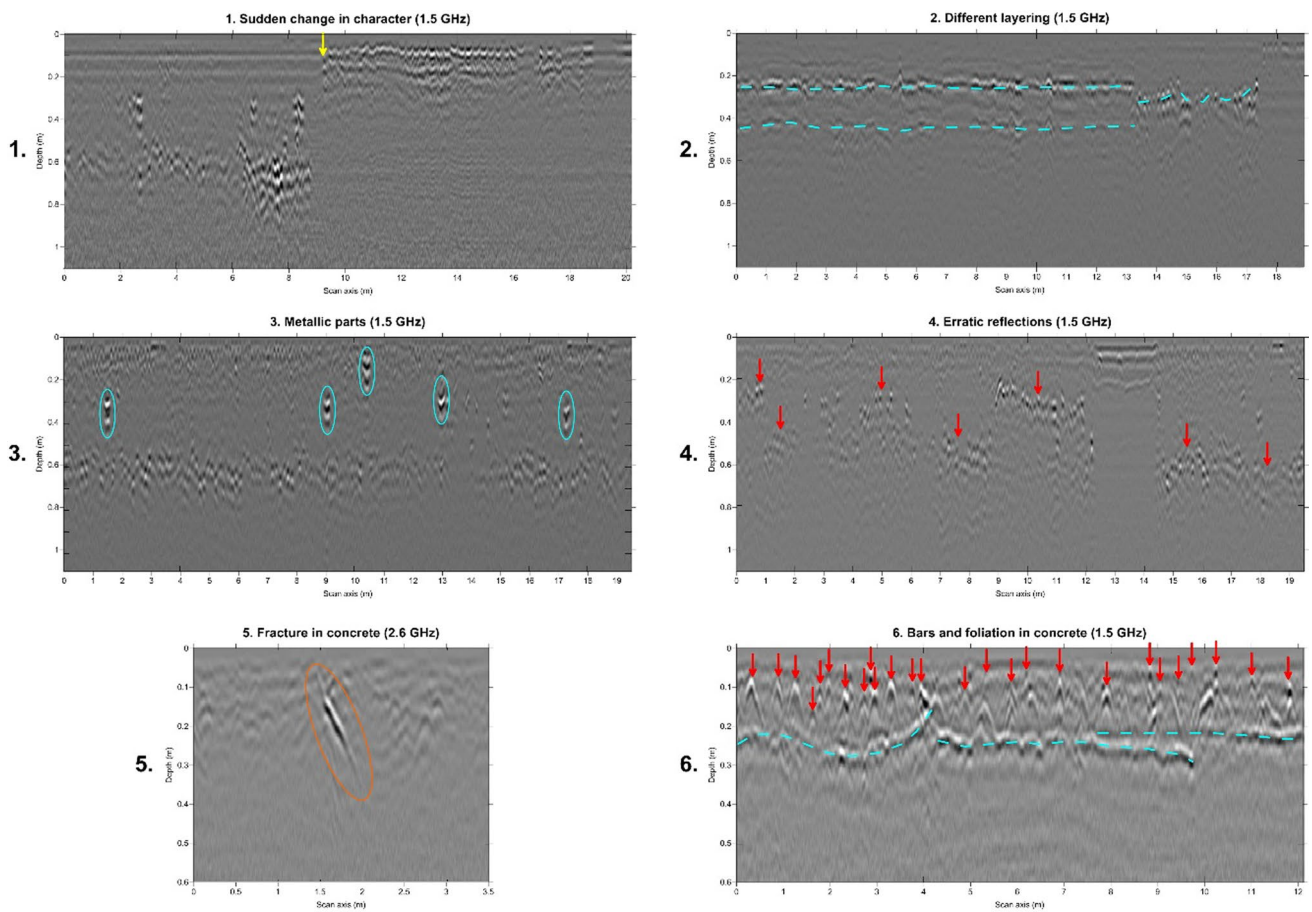
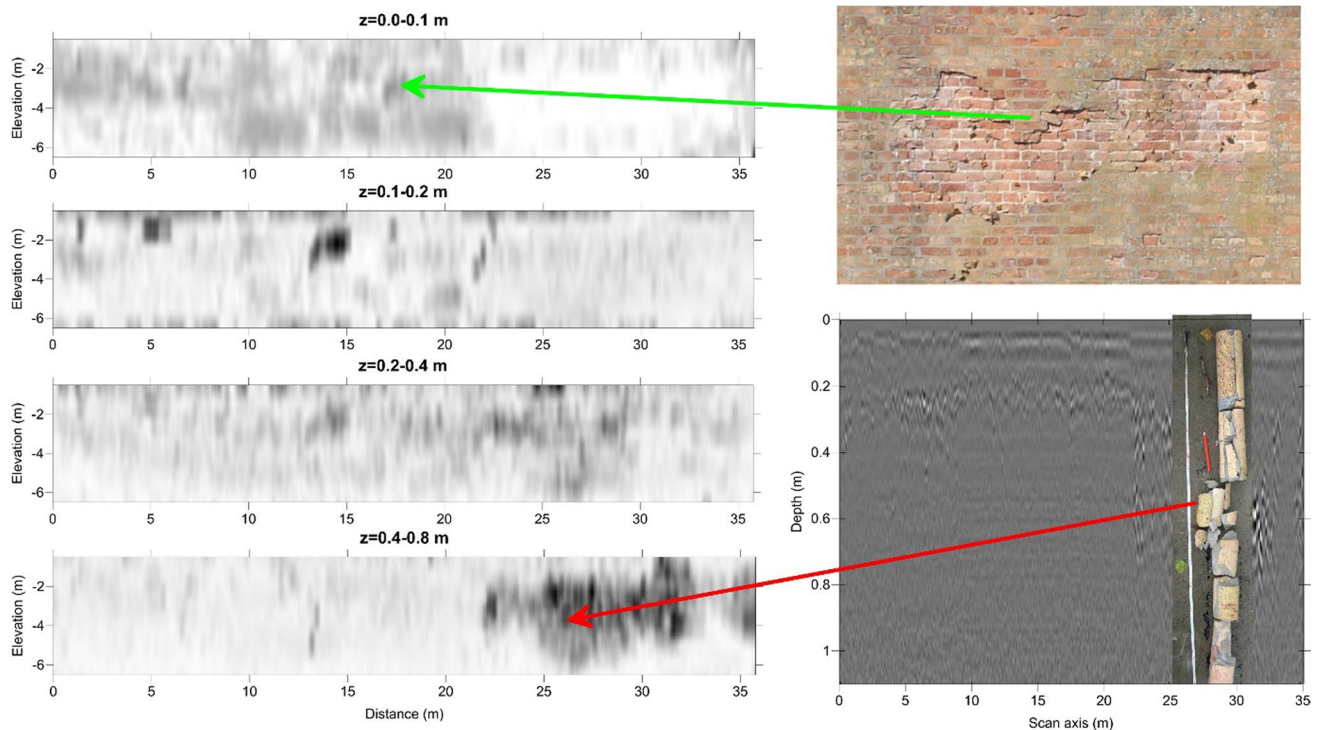


Fig. 10 Characteristic radar sections on the masonry (1–4.) and reinforced concrete retaining wall (5–6.)



**Fig. 11** GPR time slices at different depths (on the left), damaged bricks (top right) and a 2D depth section with an overlaid photograph of the core (bottom right)

- Background removal
- Amplitude correction
- Velocity analysis using hyperbolas
- Migration
- Assemble 2D sections to 3D
- Generating the time/depth slices

Besides depth slices, 2D sections were analyzed to identify the origin of the anomalies. In many cases, unmigrated 2D sections were also analyzed, because the local events were better recognizable by hyperbolas. To measure the long horizontal sections in a grid was preferred, but if the wall was divided by small features, the vertical grid was used. The grid spacing was 0.5 m in case of using 1.5-MHz antennas and 1 m in other cases. The long poles were used to move the antennas in the desired height, or the measurements took place from a boat (Fig. 9).

The final interpretation is based primarily on the 1.5-GHz data, because the most anomalies were within the depth range of 0–1 m. In Fig. 10, characteristic GPR sections are shown. In the top row, changes in the general structure are visible. On the top left, there is a sudden vertical change in the structure marked by yellow arrow. On the right side of the section, hollow bricks were used instead of regular one to repair previous damages. On the top left on the left side of the section, brick layers are visible with a thickness of

25 cm, but on the right side of the section the number of visible interfaces decreases (light blue-dashed lines). It is probably caused by the use of different size bricks at previous repairing stages. On the middle left, migrated section reflections (diffractions, marked with light blue ellipses) from metallic parts are visible. They are probably iron or steel reinforcements. On the middle right, erratic surfaces (red arrows) appear and disappear with sudden changes. The possible cause of them is the existing or missing mortar between brick layers. In the third row, the records were measured on the reinforced concrete retaining wall at the NE part of the water control canal. On the left section, a heavy fracturing is visible. The bottom right section shows the foliation in the concrete (dashed light blue line) and the metal reinforcements (red arrows) in an erratic way in space and depth as well. In Fig. 11 on the left side, the GPR depth slices from different depth ranges are visible (0–0.1 m, 0.1–0.2 m, 0.2–0.4 m and 0.4–0.8 m). To help the interpretation, picture of a frost damage is displayed on the top right of the figure. The exact location of it, a dark gray spot, is marked by a green arrow on the shallowest depth slide. On the second depth slide, this anomaly is not visible that can be supposed to such type of surface disturbances which do not affect the deeper depth slices. On the bottom right, a 2D GPR section is visible with an overlaid picture of a core on it. The core shows signs of heavy fracturing which causes



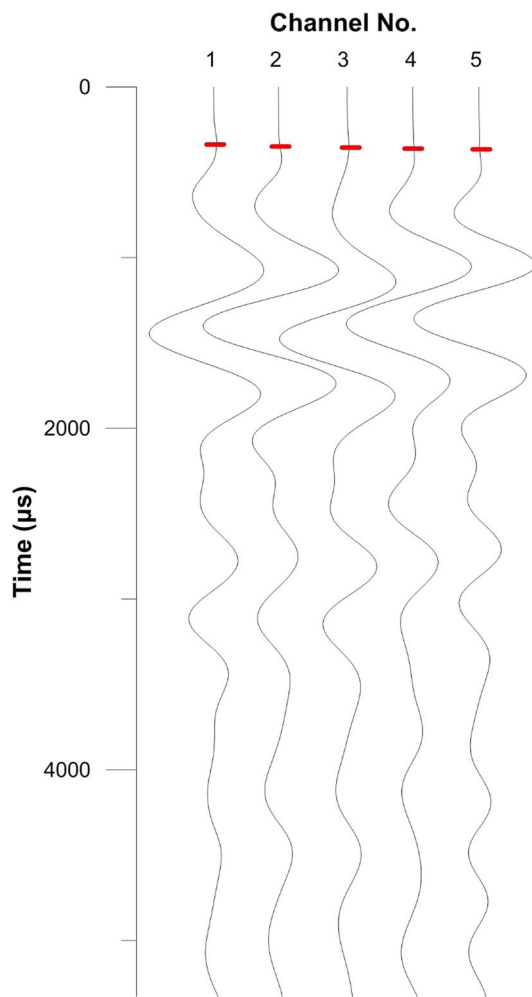


**Fig. 12** Seismograms from the western wall with the picked first breaks

high-amplitude anomaly on the GPR section, visible just to the right of the cracks on picture. The extension of corresponding anomaly is clearly visible on the depth section at the depths between 0.4 and 0.8 m. The exact location of the borehole is marked by a red arrow.

**Table 2** UCS, stiffness categories and seismic velocities (Törös 2007)

Stiffness category	<i>P</i> -wave velocity (m/s)	Unidirectional compressive strength (MPa)
Low	< 2000	< 10
Medium	2000–2500	10–20
High	2500–3500	20–60
Very high	> 3500	> 60

## The stability of the walls

Another question to be answered is the general stability and bearing capacity of the walls. It is well known that seismic velocities are in direct connection with mechanical properties. It was not possible to cover the whole surface of the walls with a seismic grid that is why the most critical part was investigated in our study. The most vulnerable part of the wall is the transitional zone, which is periodically flooded or dry. The investigation was carried out at 2.5 m height above the actual water level. To measure the *P*-wave velocity, a small hammer (0.1 kg) and a piezo receiver were used with a constant offset. The seismograms were recorded by a PC-controlled digital oscilloscope (Fig. 12). The locations were fixed by plummet and measuring tape. Depending on the quality of the records, 4–10 seismograms were recorded at each location and the mean time of the picked first arrivals was used for further calculations. In some cases, the damaged bricks were affecting the source waveform. In that case, hammer blows were repeated until the similar waveforms were recorded. The basic parameters can be given as:

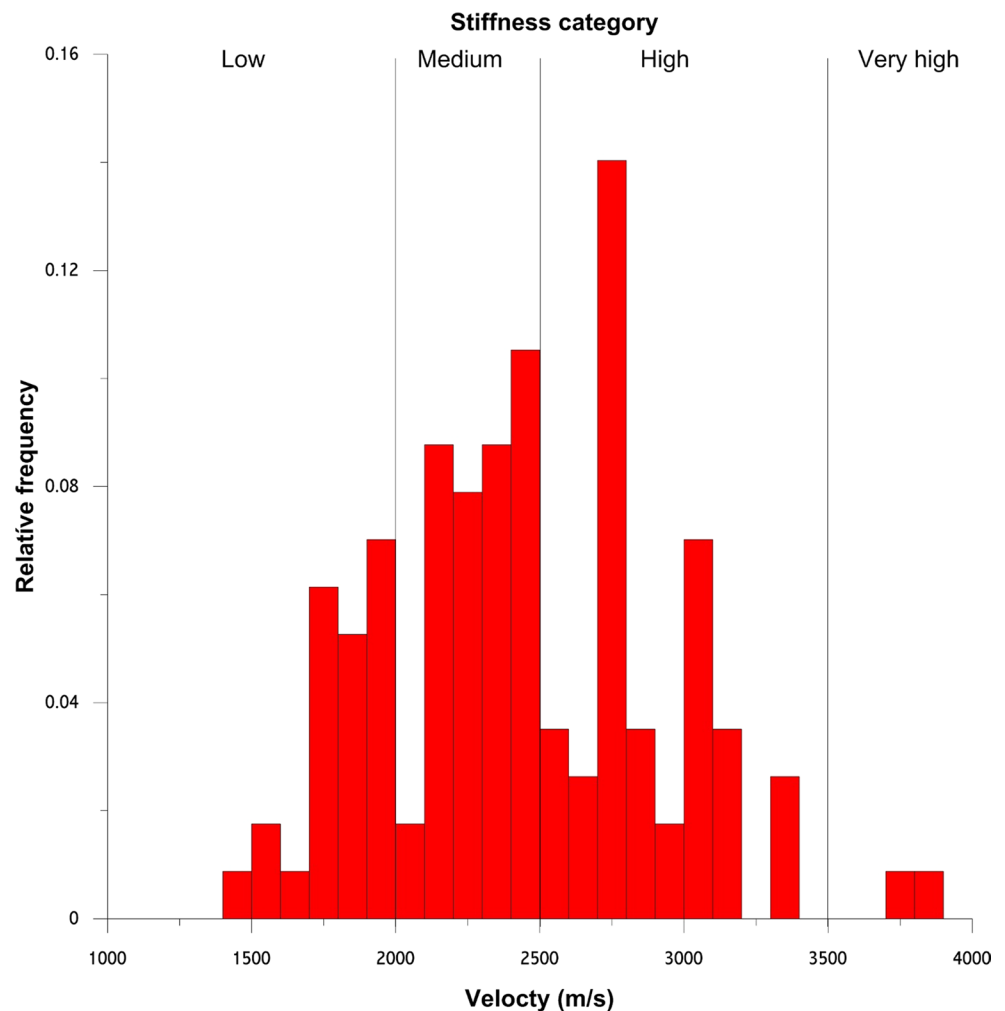
- Step size: 1 m.
- Offset: 1 m
- Sampling rate: 24 μs
- Dominant frequency: 1.5 kHz

The waves represent the mechanic properties in the range of the half wavelength. In our case, the velocity range is 1500–3800 m/s which corresponds to about 0.5–1.3 m penetration depths. To help civil engineers to calculate stability of the structure, the unidirectional compressional strength (UCS) categories were estimated from *P*-wave velocities (Table 2). The distribution of seismic velocities with UCS categories is shown in Fig. 13. Figure 14 shows the distribution of UCS categories on the walls of the sluice. Low stiffness values are mostly located in the water inlet channel and on the southern part of the navigation channel. Singular low and medium categories on the wall between the two channels coincide with visible fractures on the surface or on the GPR sections.

## Conclusions

As it is well known, all geophysical methods reflect to different physical parameters and have its advantages and disadvantages. Joint evaluation and integrated interpretation of results from different methods can enhance reliability of the final interpretation. When there are some limitations of a method due to the local physical conditions, it can be



**Fig. 13** Distribution of seismic velocities with UCS categories

used by another method to overcome the limitations. The final interpretation of GPR measurements on the walls is presented in Fig. 15. On the top, the picture of the western wall is visible containing the GPR profiles marked by red lines. The depth slice at the range of 0.4–0.8 m, at the third–fourth row of bricks, can be seen in the second row with a high-amplitude anomaly on the right. There is an overlaid of the picture, and GPR depth slice can be both visible in the third row. The bottom part shows the interpretation of GPR data which is more useful for the civil engineering. These anomalies can be easily followed from a brick to another brick to make possible to design in reconstruction process with detail. Figure 16 shows the final interpretation of all available data except shallow brick damages which are shown in Fig. 15. It is clearly visible that the fractures in the wall nearby the support structure are in connection with quasi-linear amplitude

anomalies on the top of the base slab. In many cases, interpreted faults or weak zones are closely correlated. By using nondestructive geophysical methods, especially in the most critical features, the number of drillings can be reduced significantly. Furthermore, core samples with the geophysical data can be better help for the future critical reinforcement process and time gaining.

As a result of nondestructive geophysical measurements with the interpretation results of the study, it was suggested to remove one layer of bricks seal of the walls and to build back the surface with authentic bricks. Additionally, there is a need to the injection into the voids of the wall and to reinforce to the bottom slab.

**Fig. 14** Distribution of UCS categories on the walls



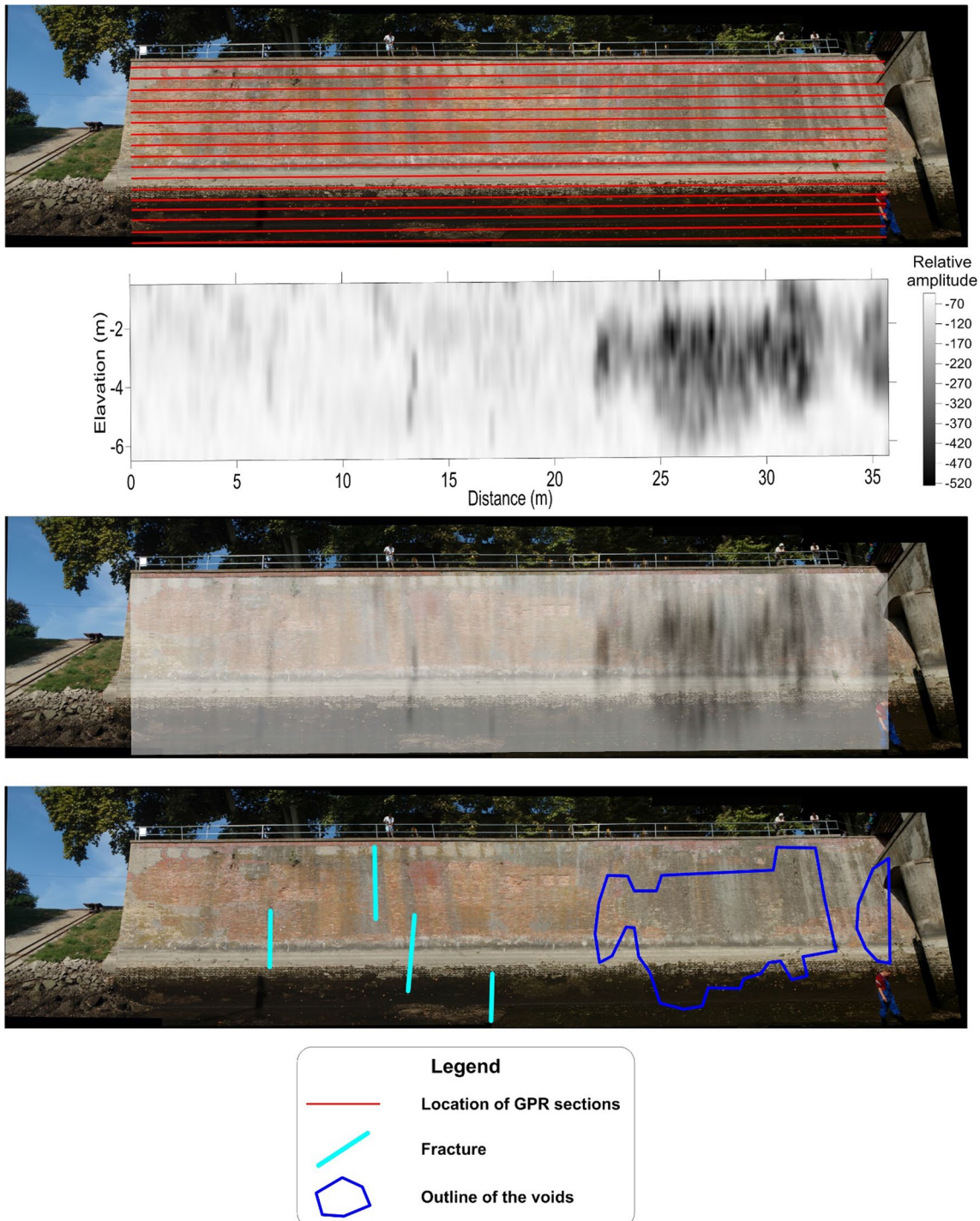
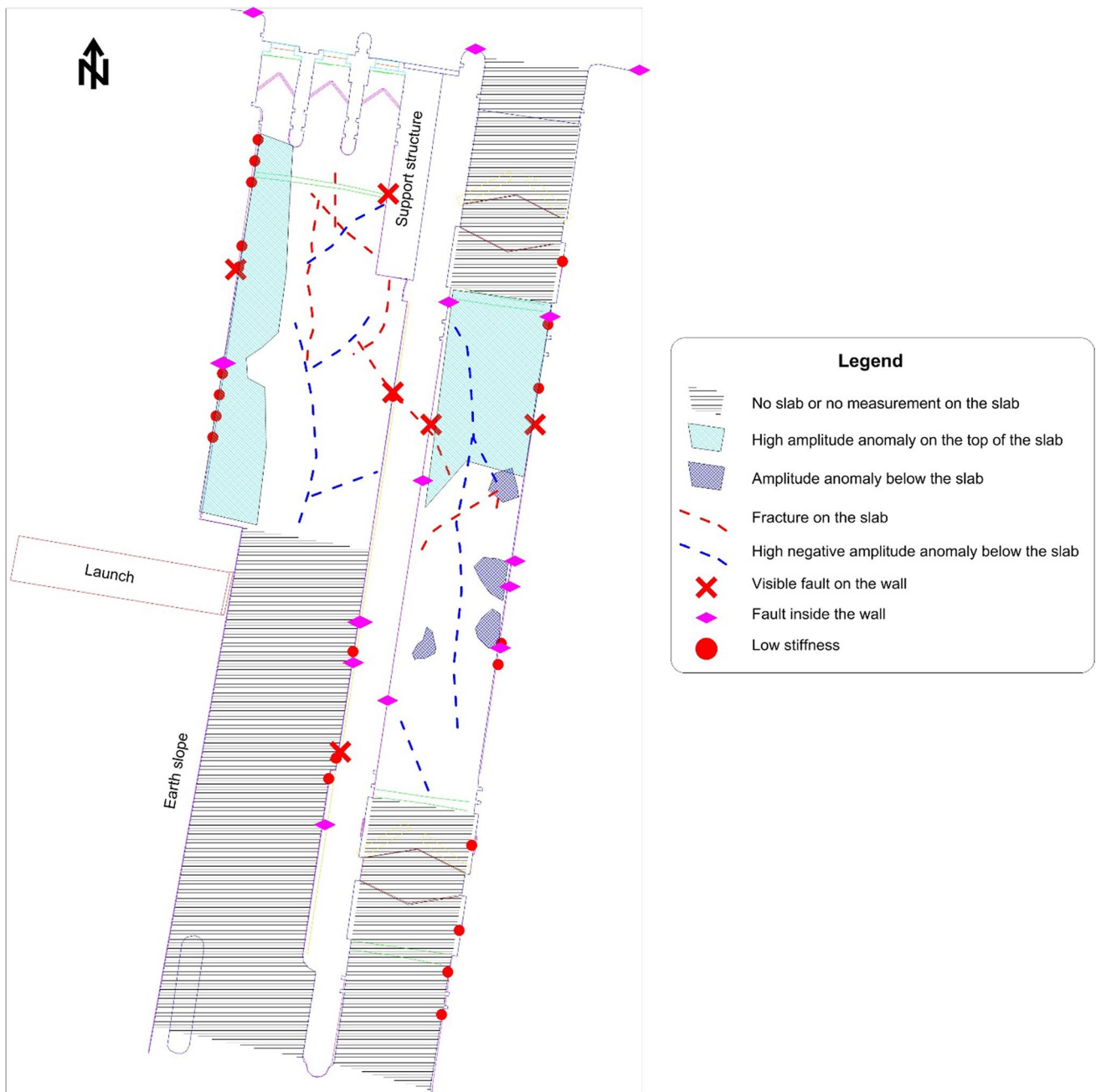


Fig. 15 Interpretation of GPR data on the western wall



**Fig. 16** Joint interpretation of all the data



**Acknowledgements** The authors thank the anonymous reviewers and the associate editor Dr. Ilias Fikos for their constructive remarks in the preparation of the final form of the paper. The author “Ali Ismet Kanli” was supported by The Division of Scientific Research Projects of Istanbul University, Project Number: BEK-2017-27284.

## References

- Daily W, Ramirez A (1995) Electrical resistance tomography during in situ trichloroethylene remediation at the Savannah River site. *J Appl Geophys* 33:239–249
- Daily W, Ramirez A, LaBrecque D, Nitao J (1992) Electrical resistivity tomography of vadose water movement. *Water Resour Res* 28:1429–1442
- Garcia GF, Blanco R, Abad RI, Sala M, Ausina T, Marco B, Conesa MJL (2007) GPR technique as a tool for cultural heritage restoration: San Miguel de los Reyes Hieronymite Monastery, 16th century (Valencia, Spain). *J Cult Herit* 8:87–92
- Grit M, Kanli AI (2016) Integrated seismic survey for detecting landslide effects on high speed rail line at Istanbul-Turkey. *Open Geosci* 8:161–173
- Günther T (2004) Inversion methods and resolution analysis for the 2D/3D reconstruction of resistivity structures from DC measurements. Ph.D. thesis, University of Mining and Technology Freiberg
- Kanli AI, Neduczka B (2015) Electromagnetic measurements for monitoring molybdenum contamination in near-surface survey. *Earth Sci Res J* 19:107–111
- Kanli AI, Taller G, Nagy P, Tildy P, Pronay Z, Toros E (2015) GPR survey for reinforcement of historical heritage construction at fire tower of Sopron. *J Appl Geophys* 112:79–90
- Loke MH (2004) Tutorial: 2-D and 3-D electrical imaging surveys. Geotomo Software, Res2dinv 3.5 Software
- Masini N, Persico R, Rizzo E (2010) Some examples of GPR prospecting for monitoring of the monumental heritage. *J Geophys Eng* 7:190–199
- Nyari Z, Kanli AI (2007) Imaging of buried 3D objects by using electrical profiling methods with GPR and 3D geoelectrical measurements. *J Geophys Eng* 4:83–93
- Nyari Z, Kanli AI, Stickel J, Tillmann A (2010) The use of non-conventional CPTe data in determination of 3-D electrical resistivity distribution. *J Appl Geophys* 70:255–265
- Park S (1998) Fluid migration in the vadose zone from 3-D inversion of resistivity monitoring data. *Geophysics* 63:41–51
- Pérez-Gracia V, García F, Pujades LG, González-Drigo R, DiCapua D (2008) GPR survey to study the restoration of a Roman monument. *J Cult Herit* 9:89–96
- Pieraccini M, Mecatti D, Luzi G, Seracini M, Pinelli G, Atzeni C (2005) Non-contact intrawall penetrating radar for heritage survey: the search of the ‘Battle of Anghiari’ by Leonardo da Vinci. *Nondestruct Test Eval Int* 38:151–157
- Plets RMK, Dix JK, Adams JR, Best AI (2008) 3D reconstruction of a shallow archaeological site from high-resolution acoustic imagery: the Grace Dieu. *Appl Acoust* 69:399–411
- Ranalli D, Scozzafava M, Tallini M (2004) Ground penetrating radar investigations for the restoration of historic buildings: the case study of the Collemaggio Basilica (L’Aquila, Italy). *J Cult Herit* 5:91–99
- Tildy P, Neduczka B, Nagy P, Kanli AI, Hegymegi C (2017) Time lapse 3D geoelectric measurements for monitoring of in-situ remediation. *J Appl Geophys* 136:99–113
- Törös E (2007) Critical review of the application of seismic-based methods in civil engineering. Ph.D. thesis, University of West Hungary, Sopron



# The investigation of soil–structure resonance of historical buildings using seismic refraction and ambient vibrations HVSR measurements: a case study from Trabzon in Turkey

Ali Erden Babacan<sup>1</sup> · Özgenç Akın<sup>1</sup>

Received: 8 January 2018 / Accepted: 24 September 2018 / Published online: 26 September 2018  
© Institute of Geophysics, Polish Academy of Sciences & Polish Academy of Sciences 2018

## Abstract

In this study, two different historical structures built in Trabzon have been processed by ambient vibrations and seismic refraction measurements. One of the investigated historical structures is the Atatürk Pavilion built in the nineteenth century, and the other one is Hagia Sophia which was built in the thirteenth century. These two buildings are among the most important historical buildings in Trabzon and are very important for the tourism of the city. In order to determine peak/s frequency and amplitude from the horizontal-to-vertical spectral ratios (HVSRS), we have performed several measurements of ambient vibrations both inside (at different floors) and outside (on the ground) of structures. We have also conducted seismic prospecting to evaluate the vertical 1D and 2D profile of longitudinal and shear seismic waves,  $V_p$  and  $V_s$ , respectively. To this purpose, we have performed seismic refraction tomography and MASW. Ambient vibrations and seismic measurements were compared with each other. The results show that average predominant frequencies and HVSR amplitudes of inside and outside of Atatürk Pavilion are 4.0 Hz, 7.8 Hz and 2.6, 2.3, respectively. The  $V_p$  values vary from 300 to 2070 m/s, and the  $V_s$  for maximum effective depth is up to 790 m/s in Atatürk Pavilion. On the other hand, average predominant frequencies and HVSR amplitudes of inside and outside of Hagia Sophia and its tower are 4.7, 4.4 and 2.4 Hz and 1.6, 1.8 and 6.9, respectively.  $V_p$  values range from 450 to 2200 m/s, and  $V_s$  for maximum effective depth is also up to 1000 m/s in Hagia Sophia. The frequency values ( $F_0 = V_s/4$  h) calculated from the velocities up to the maximum effective depth for Atatürk Pavilion are in good agreement with the predominant frequency values determined from ambient vibrations. Atatürk Pavilion and Hagia Sophia soils have been classed according to Eurocode 8 by using  $V_{S30}$  values. The class was defined as “B.” Moreover, the bedrock in studied area is basalt. The high  $V_p$  and  $V_s$  values are also compatible with the lithology. The HVSR curves measured at the Hagia Sophia show the presence of clear peaks when compared to the Atatürk Pavilion. At the same time, there are marked velocity changes in the  $V_s$  sections calculated in both areas. As a result, in both areas there are significant impedance contrasts in the subsoil. However, this impedance contrast is more evident in Hagia Sophia. This could be also compatible with a lithological transition. The possible soil–structure interaction was investigated by using all the results and evaluated in terms of resonance risk. It is thought that the probability of resonance risk at Atatürk Pavilion is low according to the ambient vibrations measurements. However, resonance risk should be taken into consideration at Hagia Sophia site since the predominant frequency values are very close to each other. Finally, this site should be investigated in detail and necessary precautions should be taken against the risk of resonance.

**Keywords** Historical structures · Ambient vibrations · Seismic refraction tomography · MASW

## Introduction

Turkey is located on Alpine–Himalayan orogenic belt. There are many important fault systems such as the North Anatolian Fault Zone, East Anatolian Fault and Aegean Graben System in Turkey. Over the years, many destructive earthquakes have occurred due to tectonic structure. Therewithal, there are also many natural disasters such as

✉ Ali Erden Babacan  
a.babacan@ktu.edu.tr  
Özgenç Akın  
ozgencakin@ktu.edu.tr

<sup>1</sup> Department of Geophysics Engineering, Karadeniz Technical University, 61080 Trabzon, Turkey

landslides and floods in different parts of Turkey. Trabzon province, which is the studied area, is located in the Eastern Black Sea of Turkey. Moreover, Trabzon province is situated to the North Anatolian Fault Zone at about 110 km (Fig. 1a). It is thought that the big earthquakes that have occurred on this fault zone have also affected this region. An example of these is earthquakes that occurred in Erzurum Province in 1939 and 1992 with magnitude of 7.9 Ms and 6.8 Ms, respectively (URL-1). In addition, because of geographical, topographical and climatic conditions, a lot of landslides occur every year in Trabzon. For this reason, it is important to investigate historical structures located in such a region in order to determine the current situation and to take necessary precautions against the risks. Historical structures suffer from significant damage from

the high humidity rate, deterioration over time and natural disasters such as earthquakes and landslides.

Since many historical buildings are under legal protection, in Turkey it is allowed to conduct research only through nondestructive geophysical measurement techniques. Ambient vibrations measurements are one of the nondestructive techniques that have been widely used in last decades to investigate site effects and the structure–soil interaction (e.g., Gosar et al. 2010; Kržan et al. 2015; Hailemichael et al. 2017; Hadianfard et al. 2017). The site predominant resonant frequency can be retrieved as well as the building resonant frequency, and the resonance risk can be investigated (e.g., Herak 2011).

Seismic refraction tomography (SRT) and multichannel surface wave analysis (MASW) are also applied in these

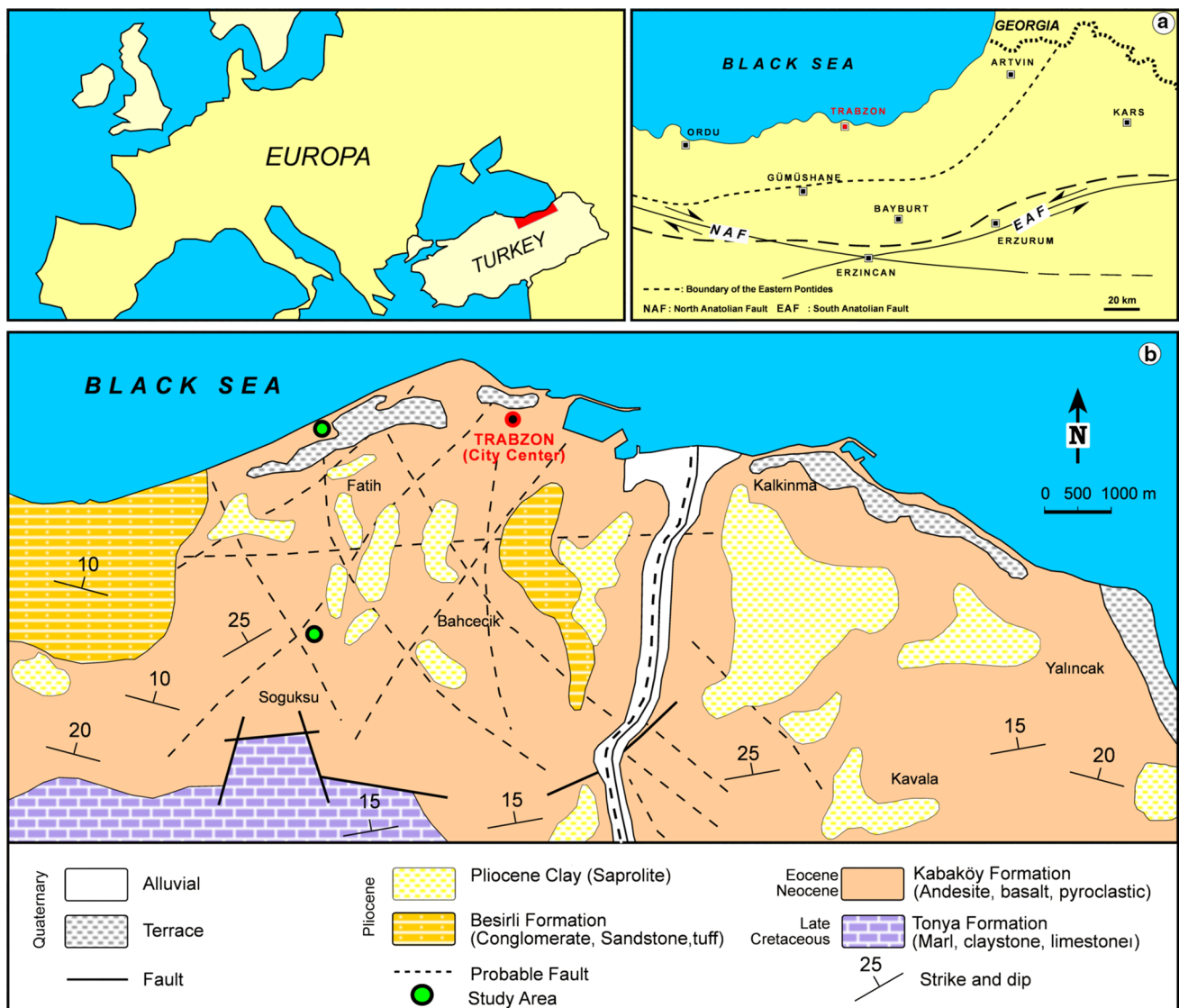


**Fig. 1** a Location of the studied area in the Eastern Pontide Orogenic Belt, Turkey, and b simplified geological map of the studied area (modified from Güven 1993)

areas to reveal the engineering properties of the soil below historical structures. The engineering features such as soil amplification, bearing capacity and dynamic-elastic parameters determined from the analysis of the seismic wave velocities have significance in geology and geotechnical engineering (Junior et al. 2012). The joint interpretation of both seismic and ambient vibrations data will give better reliable results in evaluating the resonance risk at the historical buildings.

Trabzon is one of the most important tourism locations in the Black Sea Region with its history and nature. Historical and touristic sites are visited by thousands of people every year. The first study site is Hagia Sophia historical building (thirteenth century), and the second one is the more recent Atatürk Pavilion (nineteenth century). Both these sites are characterized by the presence of Kabaköy geological formation in the subsoil, consisting of andesite, basalts and pyroclastic rocks (Fig. 1b). This formation has a wide spread in the province of Trabzon. In order to evaluate the fundamental resonance frequency in the subsoil, we totally performed 20 ambient vibration measurements, around and inside the two historical buildings. In addition, 5 seismic profiles (SRT and MASW) were performed, to retrieve  $V_p$  (2D) and  $V_s$  (1D) profiles. Finally, in order to evaluate the soil–structure interaction, we jointly interpreted all the obtained results.

## Description of historical structures

### Atatürk Pavilion

The pavilion was built in pine forests on the back of the Soğuksu, which dominates Trabzon, as a summer house by Constantin Kabayanidis in 1890 (Fig. 3). Large and fancy European symbols have been used in the building which is influenced by European and Western Renaissance architecture. Stone workmanship was used on the outer of the pavilion, and Baghdadi technique was used on the inner side. The pavilion was named as the “Atatürk Pavilion” by the people of Trabzon and started to be used as a museum (URL 2–3).

### Hagia Sophia

Hagia Sophia (Fig. 4) was built in Trebizond between 1238 and 1263 during the reign of Manuel Comnenos I, king of the Empire of Trabzon. Hagia Sophia is a former Chalcedonian church located in the Trabzon Province, Turkey. The church was converted to a mosque after Sultan Mehmet, the Conqueror, took Trabzon in 1461. The Hagia Sophia, partially damaged over time, was restored in 1864. During World War I, it was used as a hospital and depot and then returned to use again as a mosque. It was restored in 1958–1962 with the cooperation of the General Directorate

of Foundations and the University of Edinburgh. Then, it was opened as a museum after 1964. Nowadays, Hagia Sophia began to be used as a mosque again in 2013 (URL 4–5).

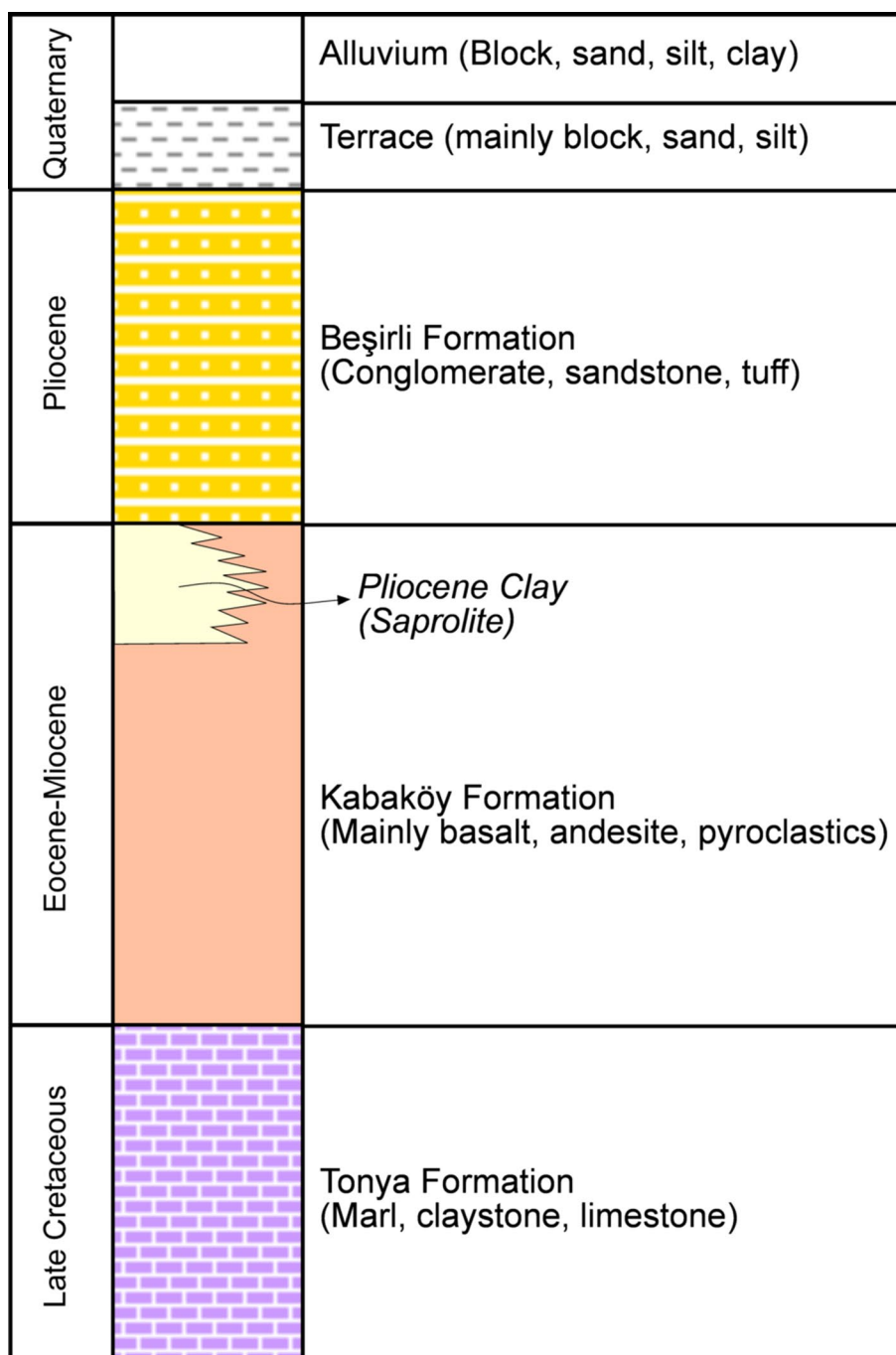
The Hagia Sophia is a good example of late Byzantine architecture, with a high central dome and four marble monolithic columns with arches supporting the weight of the dome and ceiling. The church is a cross in a square plan, but with north and south porches, the outside takes the shape of a cross. The building is covered with different vaults around the central dome, and tiles have been arranged to give different heights to the roof. The structure is 22 m long, 11.6 m wide and 12.7 m tall (URL 4–5). The bell tower which is about located the west garden of Hagia Sophia was also dated to 1427 by G. Finlay. The tower has a rectangular plan. The height of tower is approximately 23.5 m. It consists of a tower, a main structure and a crown. There is an entrance door on the south side.

## Geological setting

Trabzon Province in northeastern Turkey has generally exposed rough irregular land morphology with steep slopes and peaks based on the tectonic features and geology of the Eastern Black Sea region. The Eastern Pontide Orogenic Belt is a major metallogenetic province in the Eastern Black Sea coastal region and forms a mountain chain, which is about 500 km long and 100 km wide, throughout the southeastern coast of the Black Sea. Tectonically as a paleo-island arc, the Northeastern Pontides experienced multiple episodes of volcanic activity since the Liassic to Tertiary (Arslan et al. 1997). The Eastern Pontides is subdivided into Northern and Eastern zones according to structural and lithological differences (Gedikoğlu et al. 1979; Bektaş et al. 1995). The Northern Zone is dominated by late cretaceous and middle Eocene volcanics and volcanoclastic rocks, whereas the pre-Late Cretaceous sedimentary rocks are widely exposed in the Southern Zone. Around Trabzon Province, the studied areas consist of the Tertiary-aged volcano-sedimentary rocks, related to the Plio-Quaternary regolith and Pliocene deposits containing sandstones, claystones, conglomerates and agglomerates. The main lithological features in the Tertiary-aged unit are andesitic, basaltic and pyroclastic volcanic rocks (Fig. 1b). The unit consisting of andesite, basalt and pyroclastic rocks is called Kabaköy formation (Güven 1993) (Fig. 2). Both structures (Atatürk Pavilion and Hagia Sophia) in study area are located within the Kabaköy formation. However, as a result of observations made in the study area, it is understood that the outcropping rocks are only composed of basalts. The saprolite has no internal bedding and grades vertically and laterally into partially or intensely altered basalt and



**Fig. 2** Stratigraphic section for studied area



andesites from Kabaköy Formation (Fig. 2). Saprolite in the study area is a soft, earthy, clay-rich material formed by the extensive in situ chemical weathering of the volcanic rocks (Arslan et al. 2006). The general geology of the area where both historical structures are built is similar characteristic, and it is expected that the seismic velocity values obtained in both areas will show similar changes.

## Data, methods and results

In this study, ambient vibrations, seismic refraction tomography (SRT) and multichannel analysis surface wave (MASW) methods were used to determine the soil–structure interaction.

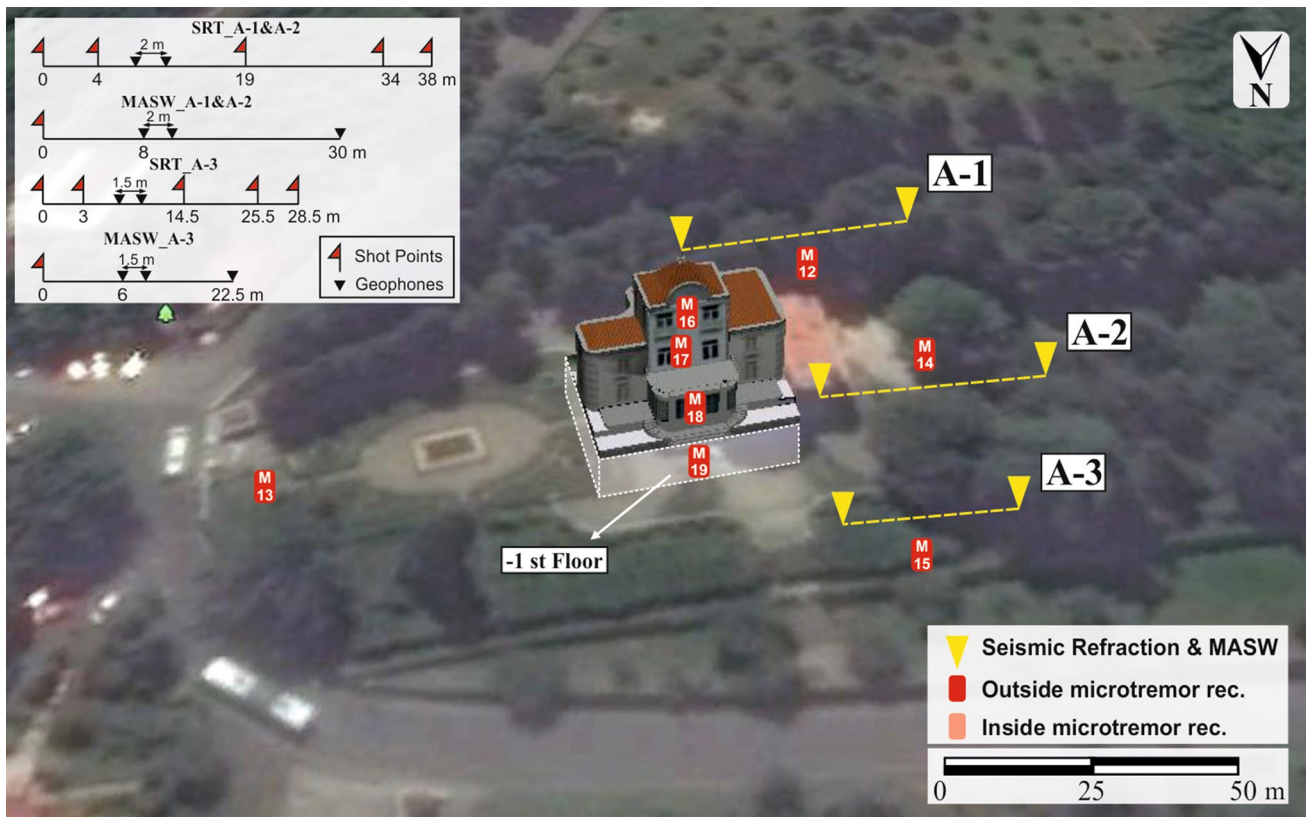


**Fig. 3** The location of ambient vibrations, SRT and MASW measurements at Atatürk Pavilion. The geometric scheme of the measurement profiles is shown at the top left

### H/V spectral ratios on ambient vibrations

We performed ambient vibration measurements at several points, inside and outside the structures. In the Atatürk Pavilion site, we chose 4 points inside the building (a station for each story) and 4 points at the outside, at distance intervals from 25 to 50 m (Fig. 3). In the Hagia Sophia site, we found 5 locations at the outside with the same distance interval, 5 stations in different sectors inside the building and 2 stations in the bells tower (at the first and top story, respectively) (Fig. 4). The ambient vibrations data were collected with a portable, three-component digital broadband seismometer (Guralp System CMG-6TD). Like many researchers, the SESAME criteria (SESAME 2004) have been considered in order to collect quality data (Chatelain et al. 2008; Guillier et al. 2008; Bard 1998; Büyüksaraç et al. 2013; Akin and Sayil 2016; Pamuk et al. 2017). Although the minimum recording time recommended by SESAME is 45 min, it has been extended up to 75 min to minimize the effect of any environmental and cultural disturbance. “Geopsy” program has been used to evaluate the ambient vibrations recordings according to Nakamura HVSR method (Nakamura 1989). Before proceeding with the analysis, we applied the trend and mean

removal to raw data, as well as a bandwidth Butterworth filter ranging 0.5–20 Hz. The recordings have been divided into 25-s-long windows (URL-6) after an automatized selection based on short-term average/long-term average (STA/LTA) ratio ( $0.2 \cdot \text{STA} / \text{STALTA} \cdot \text{LTA} \cdot 2$ ) according to SESAME criteria and have been noted that the number of selected windows should be at least 10 (Fig. 5a) (Wathelet et al. 2004). This time window selection has been applied to keep the most stationary parts of ambient vibrations and to avoid the transients. In this way, effects of specific sources such as footsteps, traffic and cultural disturbances are removed from the recordings. In cases where the number of windows is less than 10, length of window is reduced to 20 s or 5% overlap has been used. Energy leakage had been blocked by applying a cosine window (5%) to the data. Fourier amplitude spectra were calculated for the three components of ground motion, separately on the selected windows. They were smoothed through a Konno–Ohmachi filter (1998) (Fig. 5b–d). The “b” value of Konno Ohmachi window was selected as 40. Then, the ratio between the horizontal and vertical components was calculated by using the geometric mean of the two horizontal EW and NS components, obtaining HVSR (horizontal-to-vertical spectral ratio) curves (Eq. 1). The

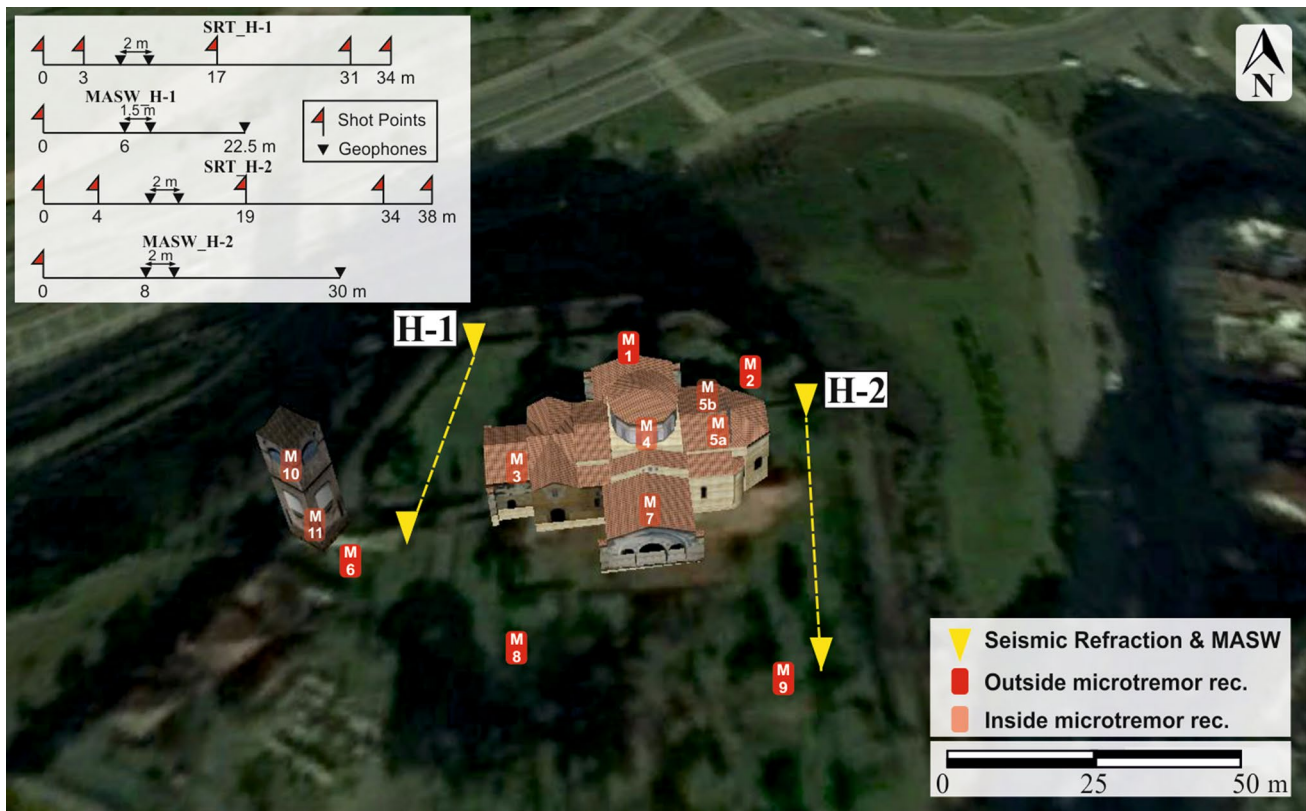


**Fig. 4** The location of ambient vibrations, SRT and MASW measurements at Hagia Sophia and its tower. The geometric scheme of the measurement profiles is shown at the top left

basic assumption of this technique is that, when considering ambient vibrations, the vertical component is assumed to be not affected by any amplification effects, according to Nakamura (1989) (Eq. 2). Conversely, the horizontal components can show amplification effects due to the site response. Thus, the HVSR curves (Fig. 5e) are representative of the ground transfer function. It is seen that in Fig. 5e, there are two peaks on the  $H/V$  curve. In order to decide correct peak, the spectrum of every single components has been examined. It can be understood that the second peak at 6 Hz is a spurious peak because there are no peaks at 6 Hz of the horizontal components. Hence, these minimum values increase the  $H/V$  ratio and cause a spurious peak. As a result, the peak giving the true predominant frequency and  $H/V$  value is in 3.8 Hz.

$$H_S(\omega) = \sqrt{NS(\omega)^2 + EW(\omega)^2} \quad (1)$$

$$S_M(\omega) = \frac{H_S(\omega)}{V_S(\omega)} \quad (2)$$

All the ambient vibrations data were processed with Nakamura method, and the results are given in Table 1.

The results of HVSR were examined according to the SESAME reliability criteria (Table 2). It was seen that all results were found to provide reliable  $H/V$  curve criteria. However, the same situation was not observed in the clear  $H/V$  peak criteria. Both HVSR spectra of the inside and outside data obtained from the historical buildings have been separately graphed to make interpretation easier in Figs. 6, 7 and 8. The average predominant frequency values of inside and outside of Atatürk Pavilion are 4.0 Hz and 7.8 Hz, respectively. On the other hand, the average predominant frequency values of inside, outside and tower of Hagia Sophia are 4.7 Hz, 4.4 Hz and 2.4 Hz, respectively. HVSR amplitudes generally show similar characteristics in both historical structures. However, higher amplitude was only observed at the top of Hagia Sophia's tower (HVSR amplitude is 11.9). As expected, the HVSR amplitude increases with the building height. This result is compatible with predominant frequency of the structure. The ambient vibrations data are separated in three groups as Atatürk Pavilion, Hagia Sophia and the bell tower. It is seen that the dominant frequency range of each group is consistent with itself.



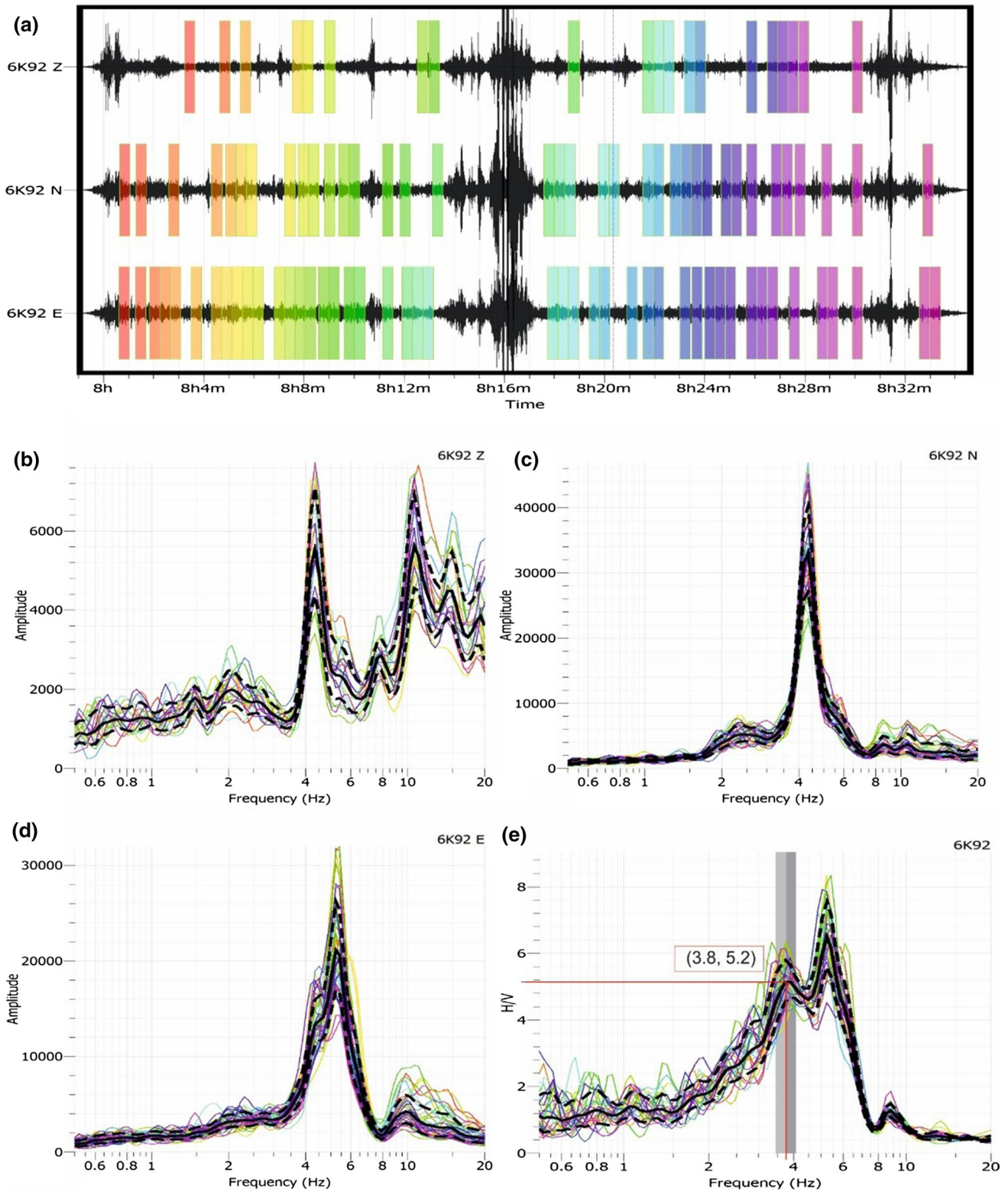


**Fig. 5** Ambient vibrations data taken at the third floor of Atatürk Pavilion (M16). **a** Selected windows (25 s length), each colored window shows the amplitude spectrum of this color, **b** amplitude spec-

trum of vertical component, **c** amplitude spectrum of NE component, **d** amplitude spectrum of EW component and **e** calculated  $H/V$  spectrum



**Table 1** The parameters obtained from HVSR measurements

Location	Points	Predominant frequency (Hz)	Predominant period (s)	H/V	$F_0 = V_s/4 h$
<b>Hagia Sophia</b>					
Bell tower	M11	2.5	0.40	2.03	–
	M10	2.4	0.41	11.90	–
Inside	M3	5.1	0.20	1.50	–
	M5a	4.3	0.23	2.10	–
	M5b	4.25	0.24	2.06	–
	M7	5.1	0.20	1.40	–
	M4	4.5	0.22	1.70	–
Outside	M1	4.1	0.24	2.30	–
	M6	4.1	0.24	2.00	9.0
	M8	4.4	0.23	1.20	–
	M9	5.1	0.20	1.50	8.3
	M2	4.3	0.23	2.40	–
<b>Atatürk Pavilion</b>					
Inside	M19	4.1	0.24	1.30	–
	M18	4.2	0.23	0.80	–
	M17	4.0	0.25	3.20	–
	M16	3.8	0.26	5.20	–
Outside	M13	7.7	0.13	2.80	–
	M12	9.3	0.11	2.00	9.0
	M14	7.0	0.14	1.20	6.1
	M15	7.4	0.14	3.20	7.2

**Seismic prospecting: SRT and MASW**

SRT and MASW data were collected along 5 profiles (Figs. 3, 4) to determine the  $V_p$  and  $V_s$  and depths to foundation bedrock of soil of Atatürk Pavilion and Hagia Sophia. Three of the seismic measurements were taken at Atatürk Pavilion, and two of them were also taken in Hagia Sophia. ES-3000 Geometrics Seismograph was used to acquire seismic data (SRT and MASW). Sledgehammer weighing 8 kg that is used to strike on an impact plate was used as a seismic source. The seismic data were collected with 4.5 Hz 12 geophones. The source–receiver positions for seismic measurements (SRT and MASW) are given in Figs. 3 and 4.

**SRT: seismic refraction tomography**

The seismic refraction is one of the most effective and reliable methods for determining the P and S velocities, elastic properties and geometry of the underground geological units. The method is based on the analysis of the first arrival times of the seismic waves recorded by the geophones on the ground surface. Using first arrival times, wave velocities ( $V_p/V_s$ ) and underground structure can be calculated by using different techniques such as delay time, reciprocal time

**Table 2** Criteria for a reliable H/V curve and a clear H/V peak recommended by European SESAME research project

SESAME criteria	No.	M1	M2	M3	M4	M5a	M5b	M6	M7	M8	M9	M10	M11	M12	M13	M14	M15	M16	M17	M18	M19
Reliable H/V curve	i	OK	OK	OK	OK	OK	OK	OK	OK	OK	OK	OK	OK	OK	OK	OK	OK	OK	OK	OK	OK
	ii	OK	OK	OK	OK	OK	OK	OK	OK	OK	OK	OK	OK	OK	OK	OK	OK	OK	OK	OK	OK
	iii	OK	OK	NO	OK	OK	OK	OK	OK	OK	OK	OK	OK	OK	OK	OK	OK	OK	OK	OK	OK
Clear H/V peak	i	NO	NO	OK	OK	OK	OK	OK	OK	OK	NO	OK	OK	OK	NO	NO	NO	OK	OK	NO	OK
	ii	OK	OK	OK	OK	OK	OK	OK	OK	NO	NO	OK	OK	OK	NO	NO	NO	OK	OK	NO	NO
	iii	OK	OK	NO	NO	NO	NO	NO	NO	NO	NO	NO	NO	NO	NO	NO	NO	NO	NO	NO	NO
	iv	NO	NO	NO	NO	NO	NO	NO	NO	NO	NO	NO	NO	NO	NO	NO	NO	NO	NO	NO	NO
v	NO	NO	NO	NO	NO	NO	NO	NO	NO	NO	NO	NO	NO	NO	NO	NO	NO	NO	NO	NO	NO
vi	OK	OK	OK	OK	OK	OK	OK	OK	OK	OK	OK	OK	OK	OK	OK	OK	OK	OK	OK	OK	OK

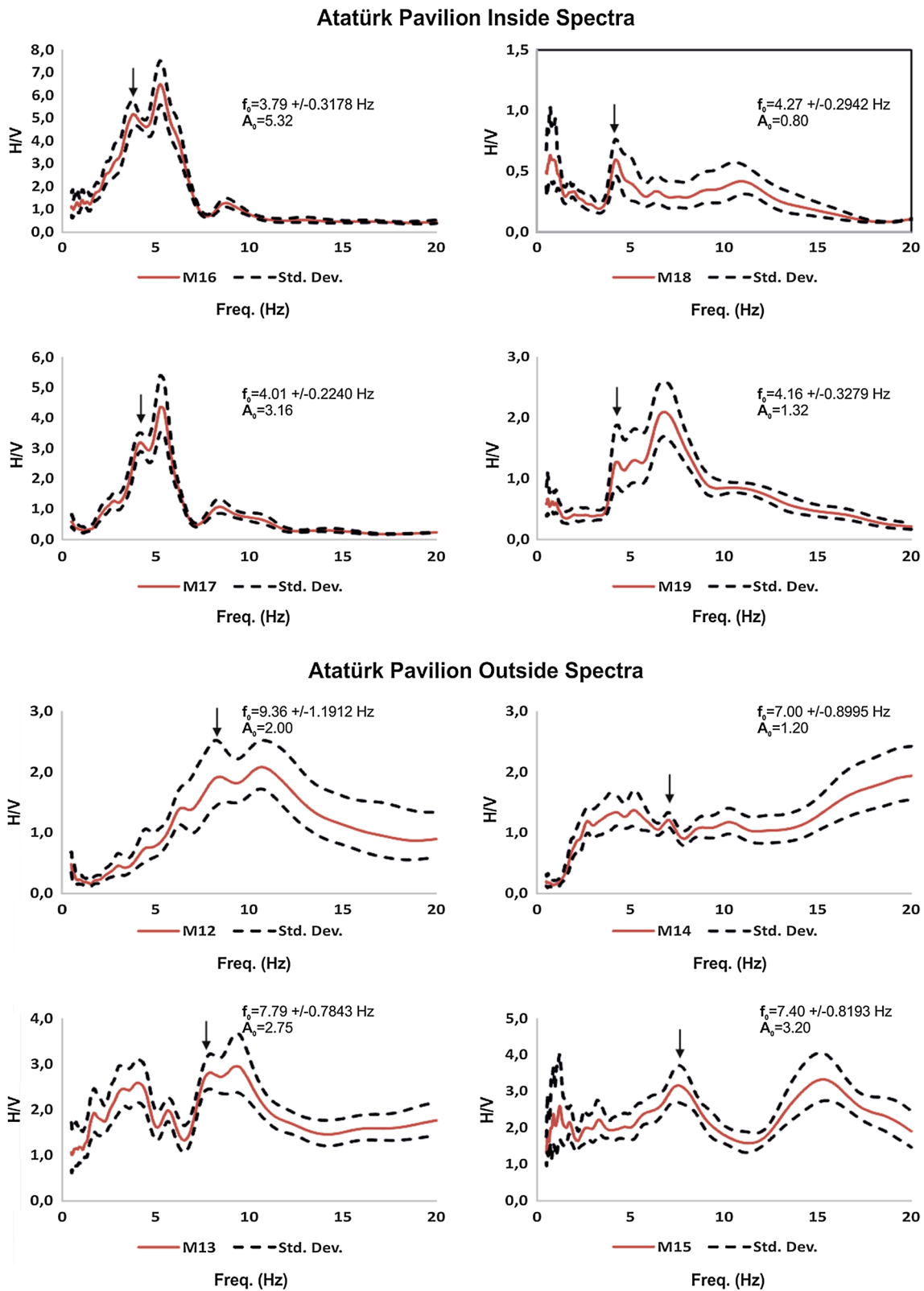


Fig. 6 H/V spectra obtained from ambient vibrations measurements at the inside and outside of Atatürk Pavilion

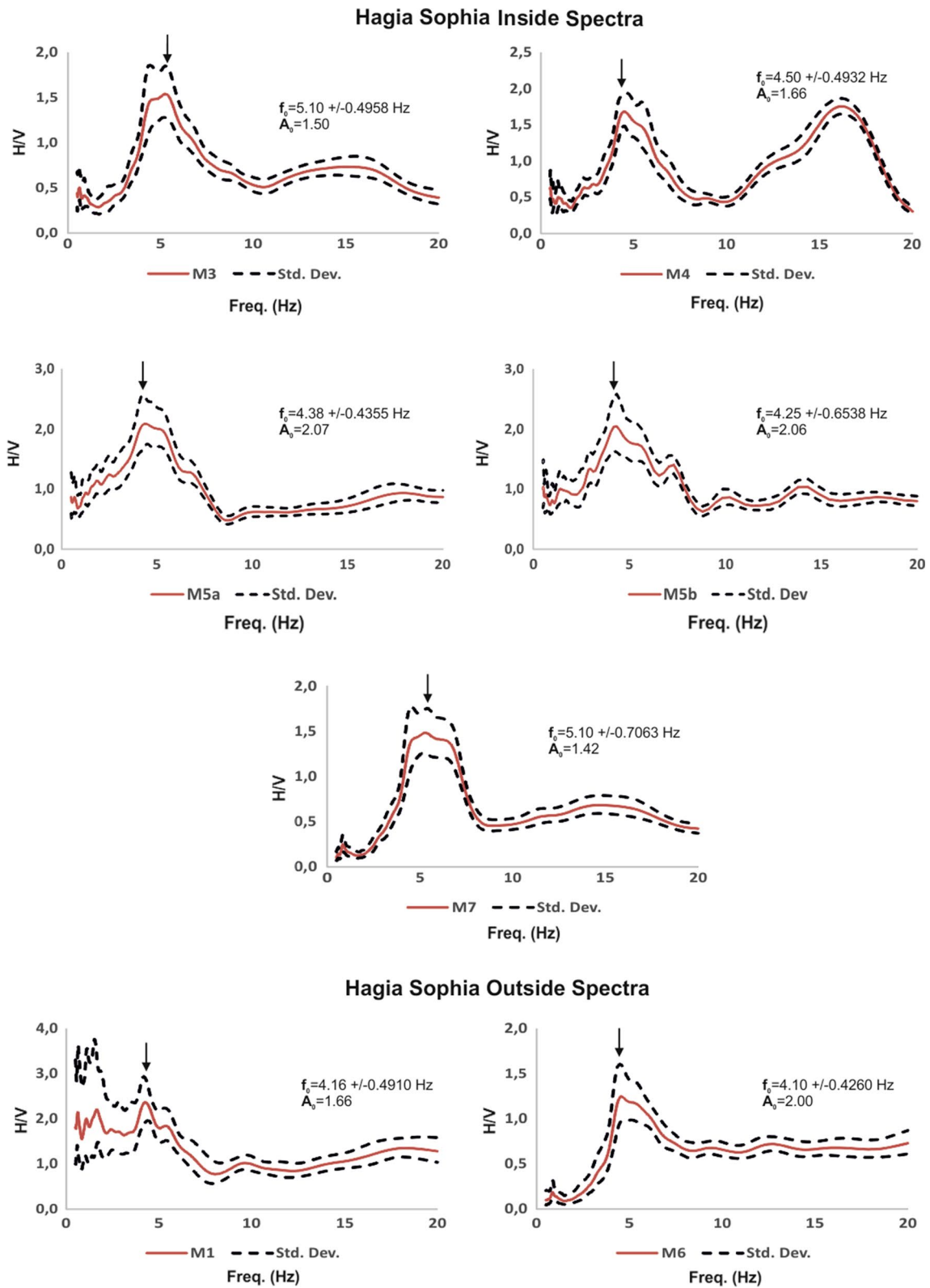


Fig. 7  $H/V$  spectra obtained from ambient vibrations measurements at the inside and outside of Hagia Sophia

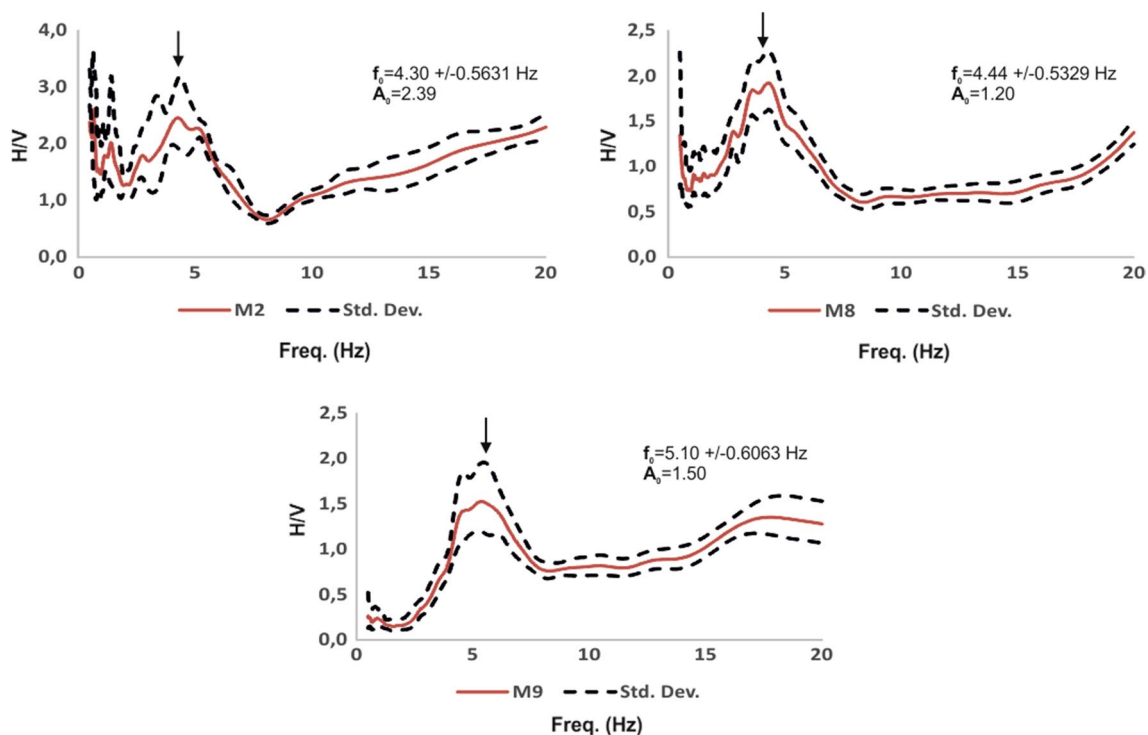
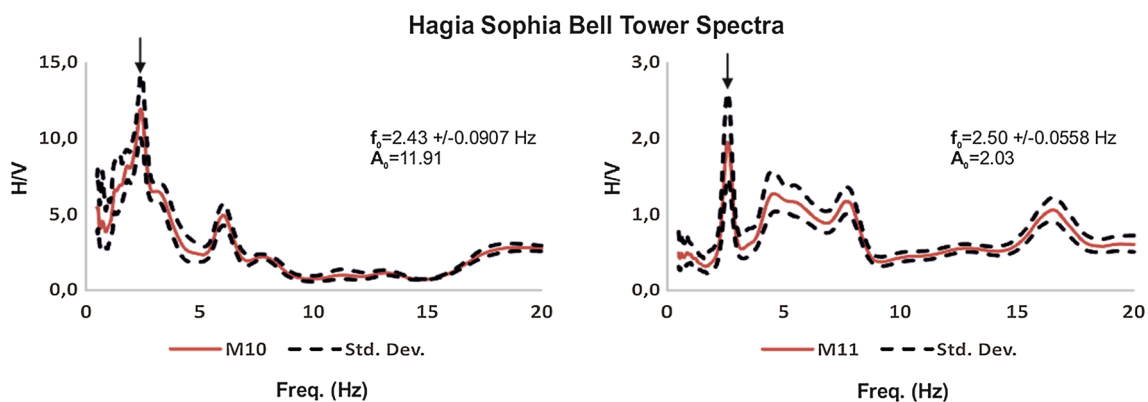


Fig. 7 (continued)

Fig. 8  $H/V$  spectra obtained from ambient vibrations measurements at the inside of Hagia Sophia bell tower

and tomographic inversion. SRT is utilized to image of the underground velocity distribution of a geologic unit rely on the first arrival times of seismic waves (Sharma 1997). SRT can resolve velocity gradients and lateral velocity changes and can be applied in environments where conventional refraction method fails, such as areas of karst, compaction and fault zones (Zhang and Toksoz 1998). SRT inversion is an iterative method. It comprises travel time calculation, initial velocity model construction and minimization of the difference among observed and calculated travel time (Bishop et al. 1985). SRT is useful for both lateral and vertical  $V_p$

variation and topography of the subsurface (Azwin et al. 2013). In this study, the SRT data were analyzed with SeisImager program (Geometrics 2009). The program is based on a nonlinear travel time method (Hayashi and Takahashi 2001). The first arrival times on seismic refraction records were picked, and time–distance graphs were plotted for SRT data. There are two approaches of generating the initial velocity model. The first approach is the use of a time-term inversion algorithm for a simple layered underground model. This layered model is then transformed into a grid model. In the second approach, the initial velocity model is



created by the user. In parallel with, a model is generated by specifying the minimum and maximum velocity range, dimensions and number of layers (Sheehan et al. 2005). An initial velocity model for tomographic inversion was created from the time-term method in the study. Tomographic inversion uses the simultaneous iterative reconstruction technique (SIRT) (Gilbert 1972). SIRT is one of the prominent iterative reconstruction techniques (Lehmann 2007). The most stable results can be obtained with the SIRT technique (Lehmann 2007).

SRT data were taken on profiles length ranging from 28 to 38 m depending on field conditions. Receiver spacing was chosen to be 1.5 and 2 m. Five shots were made at different offsets for the SRT. Several shots were made to increase the

signal-to-noise ratio for each source location. Figures 3 and 4 show the source–receiver geometry in detail. The signals were recorded for 0.25 s with a sampling rate of 0.2 ms. Time–distance graphs were drawn from seismic shot gather.  $V_p$  cross sections were obtained from tomographic inversion of time–distance graphs. We used ten iterations for this process. Obtaining the tomographic velocity model from the seismic data at the first profile of Atatürk Pavilion is detailed in Fig. 9. All 2D  $V_p$  sections for Atatürk Pavilion and Hagia Sophia are shown in Figs. 10 and 11, respectively.

The  $V_p$  velocities obtained from 3 seismic profiles at Atatürk Pavilion vary between 300 and 2000 m/s. The first and second profiles display three-layered structure, while the third profile displays two-layered structure. There is a top

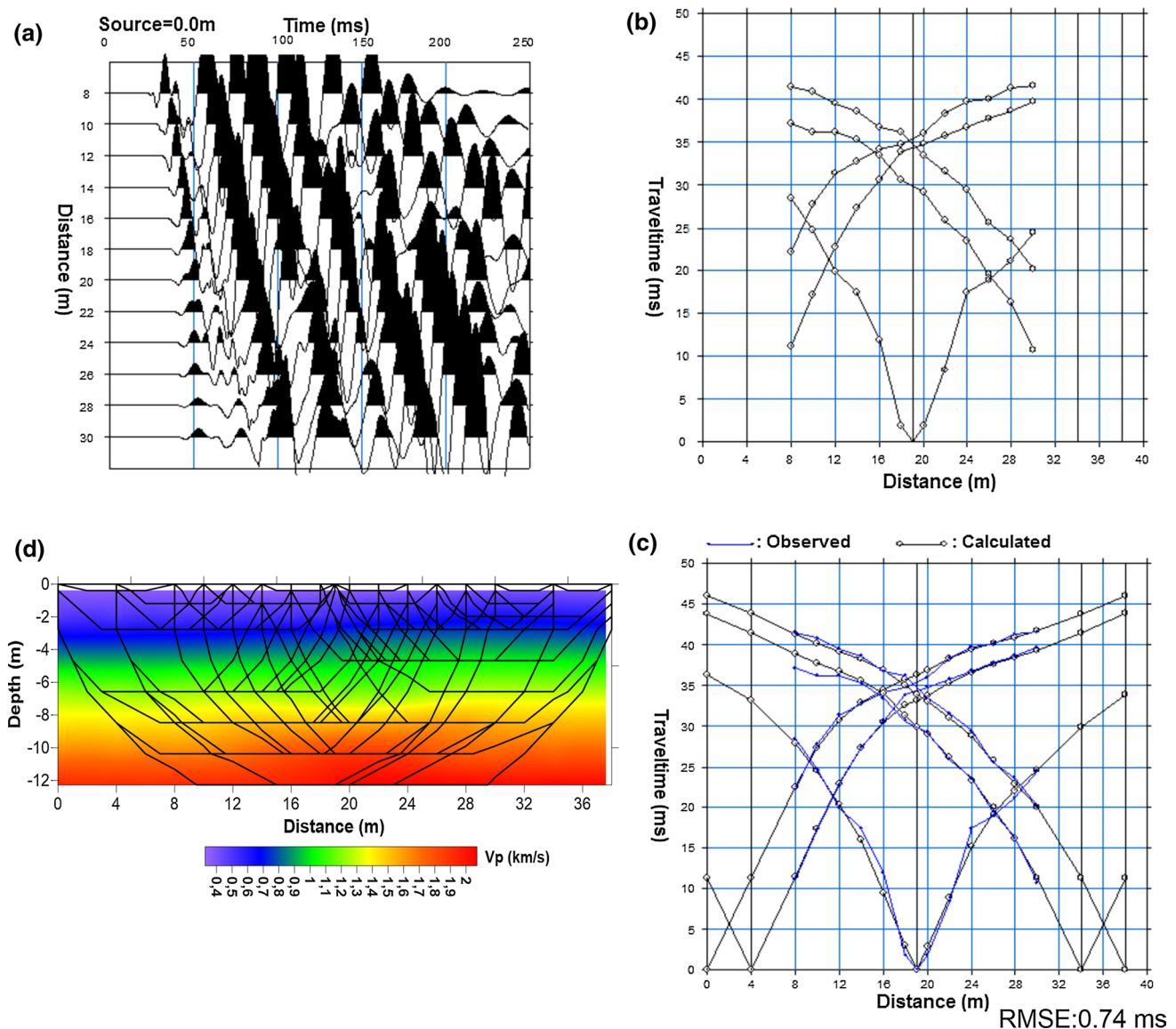


**Fig. 9** The results of SIRT for first profile at the Atatürk Pavilion **a** seismic data, **b** travel time–distance graphs, **c** comparing of observed and calculated travel times, **d**  $V_p$  tomographic section. Solid black lines show the raypath

**Fig. 10** The results of SRT for Atatürk Pavilion **a** first profile (A-1), **b** second profile (A-2) and **c** third profile (A-3)

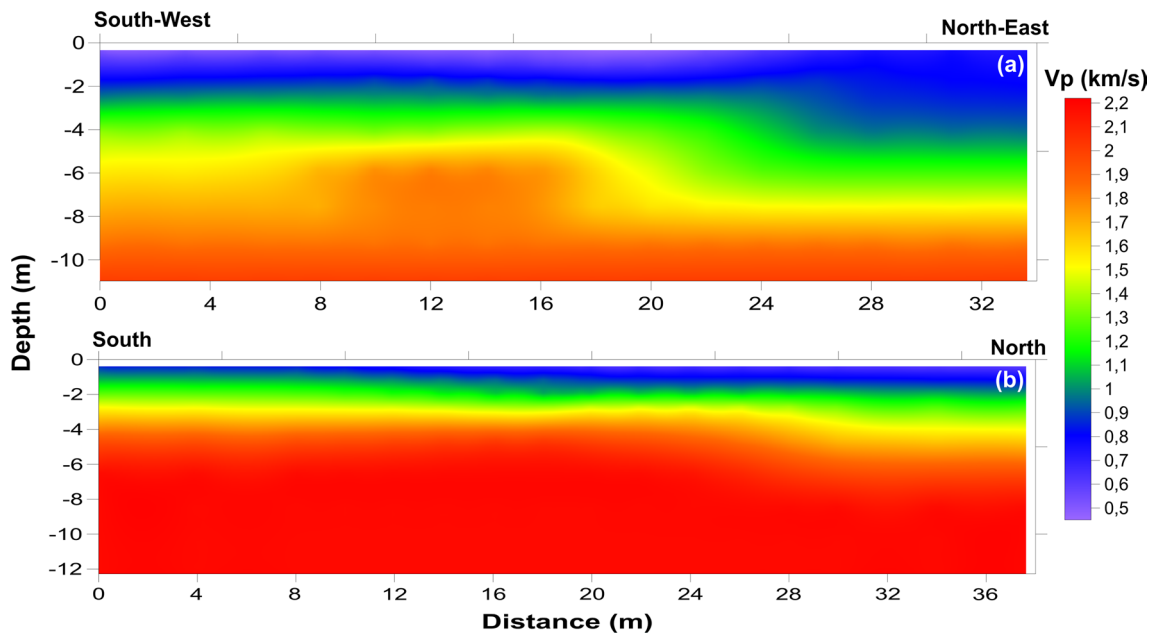
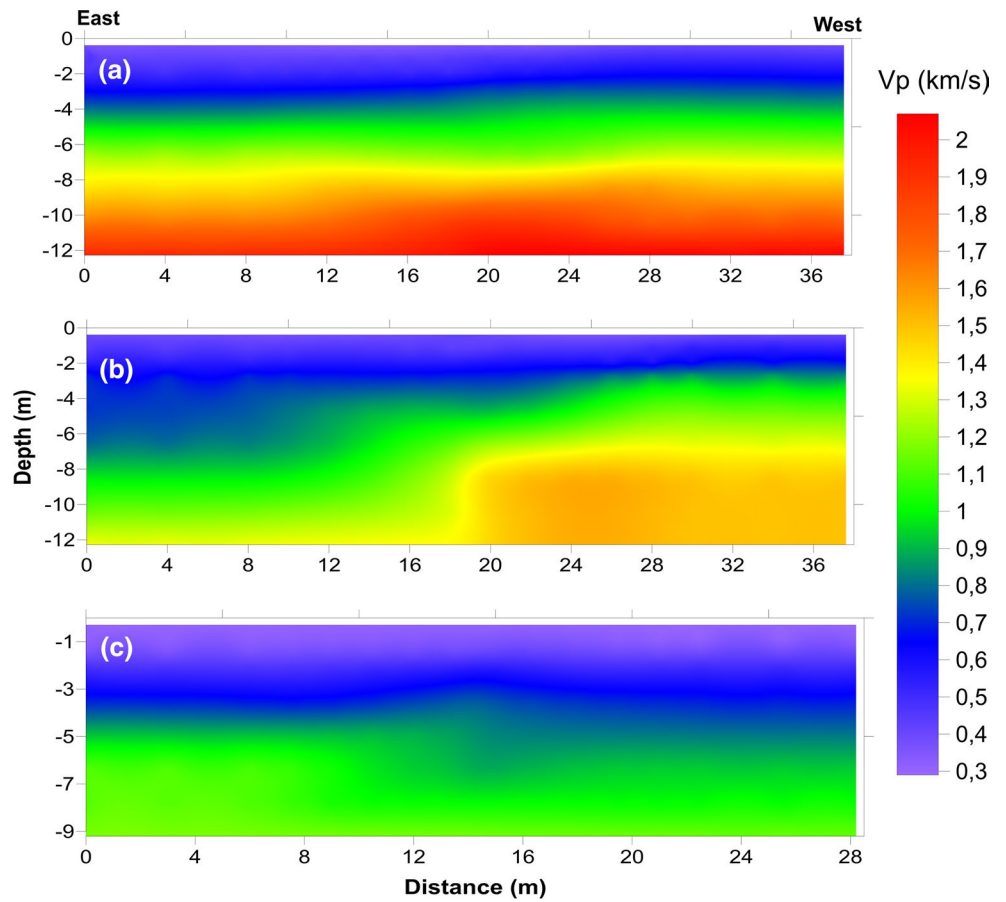


**Fig. 11** The results of SRT for Hagia Sophia, **a** first profile (H-1) and **b** second profile (H-2)

layer of 4–5 m thickness, and the thickness slightly increases in the head parts of the second profile. The first profile contains a massive unit with an average velocity of 2000 m/s at approximately 8 m depth. However, the unit with high velocity cannot be seen in second and third profiles. There is a significant decrease in velocity values toward from south to north direction in the study area. Especially, the maximum velocities on the third profile are on average 1000–1100 m/s. The reason for this is that the measurement area is soil embankment (mainly clay), and as the profile length is short, sufficient depth of penetration is not achieved. In addition, a discontinuity zone of about 8 m in depth was observed between the 18 and 20 m in the second profile.

In the Hagia Sophia area, the  $V_p$  values obtained from two profiles range from 450 to 2200 m/s. There is a 3-layer underground structure on both profiles. However, the thickness of the intermediate layer is very shallow in the second profile. The thickness of the top layer varies from 2 to 2.5 m on the first profile, while this thickness falls to 1 m on the second profile. Both profiles have high-velocity (> 2000) layer, and these layers are observed after about 4 m. The depth of the bedrock is shallower on the east side in the study area. The main rock outcrops in the study area and its around are observed. In addition, a discontinuity zone of about 6 m in depth was observed between the 16 and 22 m in the first profile.

#### MASW: multichannel analysis of surface wave

This method is based on the principle of obtaining the shear wave velocity ( $V_s$ ) by taking advantage of Rayleigh waves which are propagated in layered media (Xia et al. 2004). It is possible to obtain an estimation of the  $V_s$  in three steps with the MASW method. The first step is to record the shot gather of the surface wave in the field. During the second step, the dispersion curve is generated by Rayleigh waves. Most of the methods used for obtaining the dispersion curve are based on the appropriate transformation (Fourier, radon and phase shift) techniques. The wave dispersion is shaped according to the variation of the velocities of the layers. Theoretically, long-wavelength events occur because of the increase in layer velocities with depth and the decrease in wave frequency. Dispersive properties can be seen from the original seismic records. By looking at the grouping of the wave fields, roughly the variation range of the surface wave phase velocity can be determined from the slope–velocity relationship. The following basic assumptions are made in order to obtain the depth of investigation and the dispersive properties of surface waves at high quality (Xia et al. 1999). In most cases, at least distance of half the maximum wavelength is needed to comprise surface wave and to record the dispersive properties. As general acceptance, the maximum penetration depth is half the longest wavelength in a

homogeneous environment. The maximum penetration depth increases as the investigated frequency values decrease and the profile length increases. In this study, phase-shift (Park et al. 1999) method was used to obtain the dispersion curve from each shot gather. A shot gather is decomposed into individual frequency component through fast Fourier transformation (FFT) in this method. Then, the amount of phase shifts is determined to recompense for the time delay corresponding to a specific offset for a given phase velocity, and it is performed to each individual component. All of them are gathered together to make a summed amplitude corresponding to a phase velocity at that frequency (Eker 2009). Dispersion curve is picked as the maximum amplitude in each frequency on the velocity spectrum via phase shift (Hayashi 2008). Finally, iterative solution is applied to the dispersion curve. A model can be identified with forward solution. The model is created according to the velocity of the surface wave on the shot gather and the characteristics of the dispersion curve. Then,  $V_s$  is obtained by performing the nonlinear least square method on this model (Hayashi 2003). MASW (Park et al. 1999; Xia et al. 1999) is one of the most important methods for seismic site characterization (Anbazhagan et al. 2009).  $V_s$  obtained from MASW is reliable and the differences between MASW and borehole results are about 15% or less (Xia 2014). MASW has been progressively utilized in engineering projects. MASW has been successfully carried out seismic site characterization (Trupti et al. 2012; Rahman et al. 2016; Pischiutta et al. 2017).

MASW data were acquired on profiles length ranging from 24.5 to 30 m. Receiver spacing was two (2) m. However, it has been only chosen as 1.5 m on the third profile of Atatürk Pavilion. The source locations were taken at 0 m (zero) and only forward shot was done. The source–receiver distance was generally chosen to be 4 times the receiver spacing. The record length and the sampling time were 1024 ms, and 3 vertical stacks to increase the signal-to-noise ratio were conducted by seismic profiles. Figures 3 and 4 show the source–receiver geometry in detail. MASW measurements were taken on the same seismic refraction lines at Atatürk Pavilion and Hagia Sophia. In the study, 1D  $V_s$  sections were generally obtained after 20 iterations. RMS error rates were given in the figures. All 1D  $V_s$  results for Atatürk Pavilion and Hagia Sophia are given in Figs. 12 and 13, respectively. The dark part on the  $V_s$  sections shows effective depth ( $VR_{max}$ ). The reliability of the velocity information after this dark part is low. While the average  $V_s$  at the Atatürk Pavilion is changed between 472 and 543 m/s, they range from 595 to 596 m/s in Hagia Sophia. The 1D  $V_s$  sections were highly compatible with the  $V_p$  sections. The effective depths in  $V_s$  sections obtained from Atatürk Pavilion and Hagia Sophia are about between 11–17 and 12–17 m, respectively.

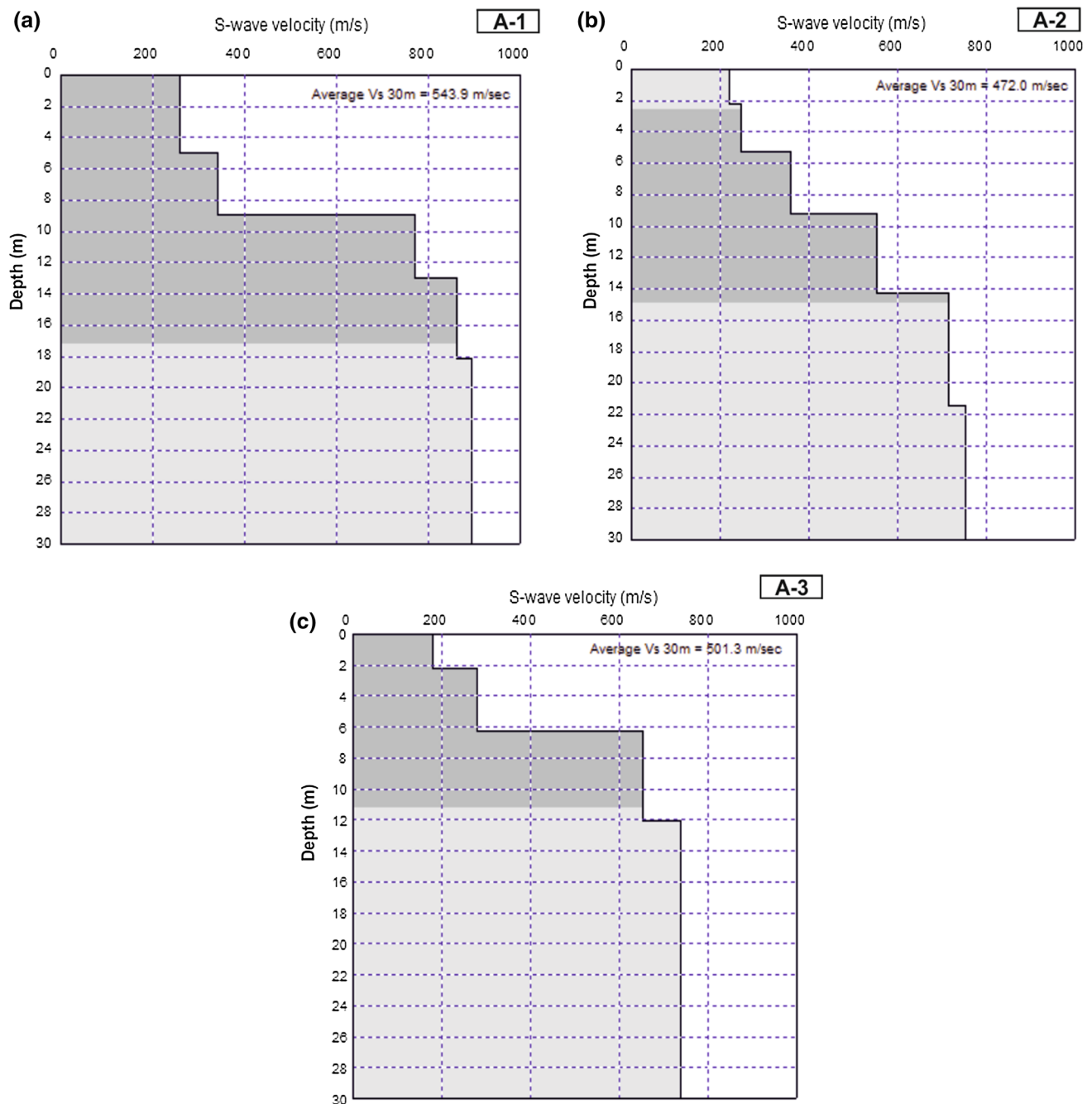


**Fig. 12** 1D  $V_s$  results obtained from MASW (A-1, A-2, A-3) at Atatürk Pavilion

At the same time, we applied the joint inversion to the dispersion curves and the HVSR curves obtained from studied areas using genetic algorithm (GA). The GA is described as a global search method and can avoid local minima to which the inversion of dispersion curve may fall (Hayashi 2012). The results from joint inversion are given in Figs. 14, 15, 16, 17 and 18. Dispersion curve and  $H/V$  data can be utilized in inversion simultaneously to

further constrain the model (Suzuki and Yamanaka 2010). In general, the joint inversion of the  $H/V$  data with the dispersion curve can increase the accuracy and penetration depth (SeisImager/SW-Pro 2016). As a result of the joint inversion, the velocities and depths of layers vary. However, it is thought that these changes are not a very important change.



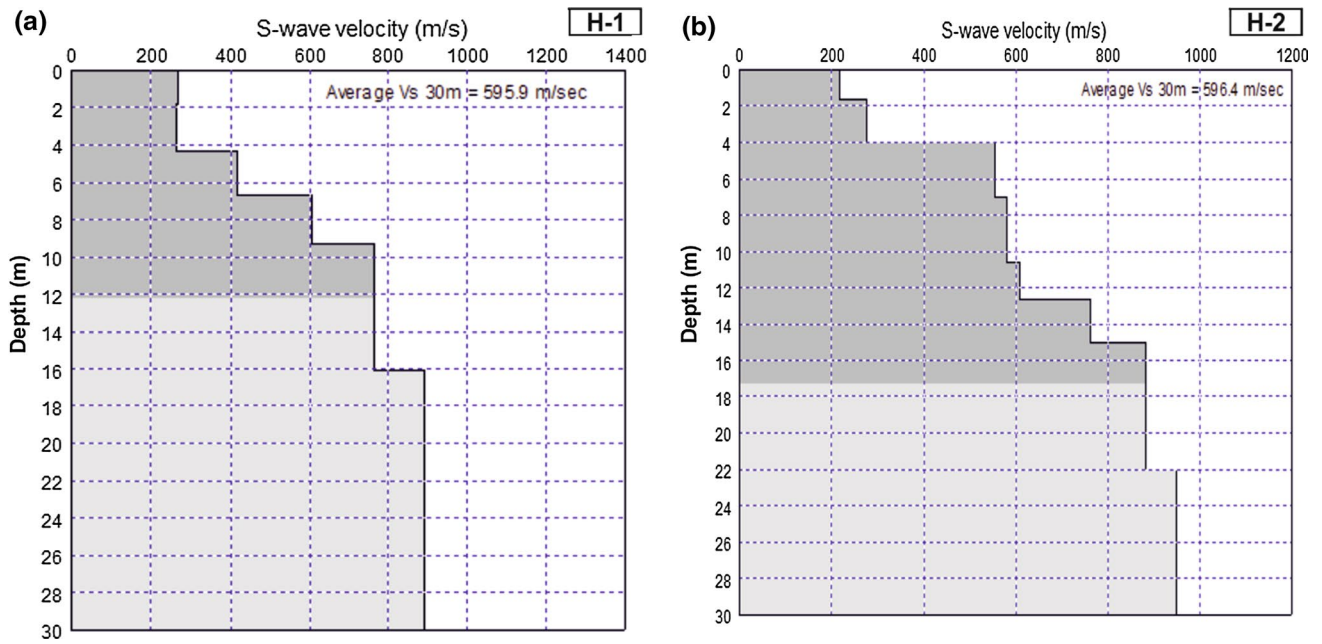


Fig. 13 1D  $V_s$  results obtained from MASW (H-1, H-2) at Hagia Sophia

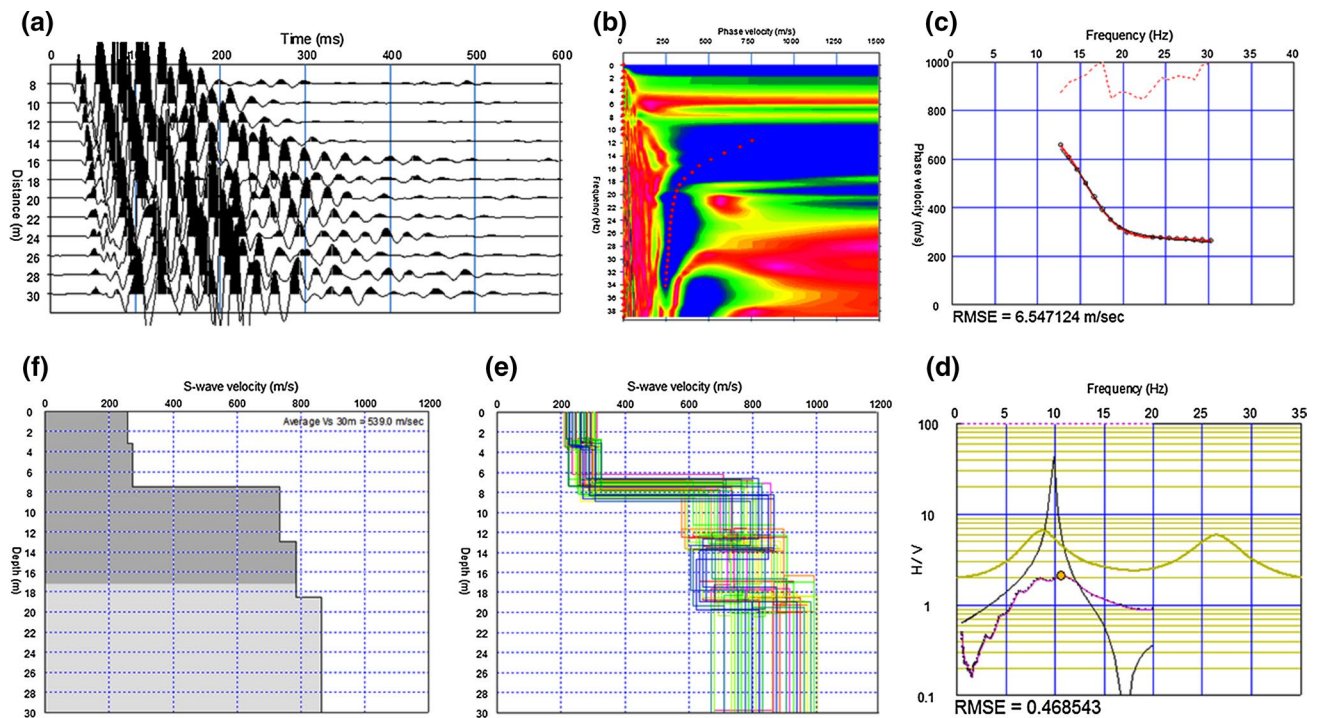
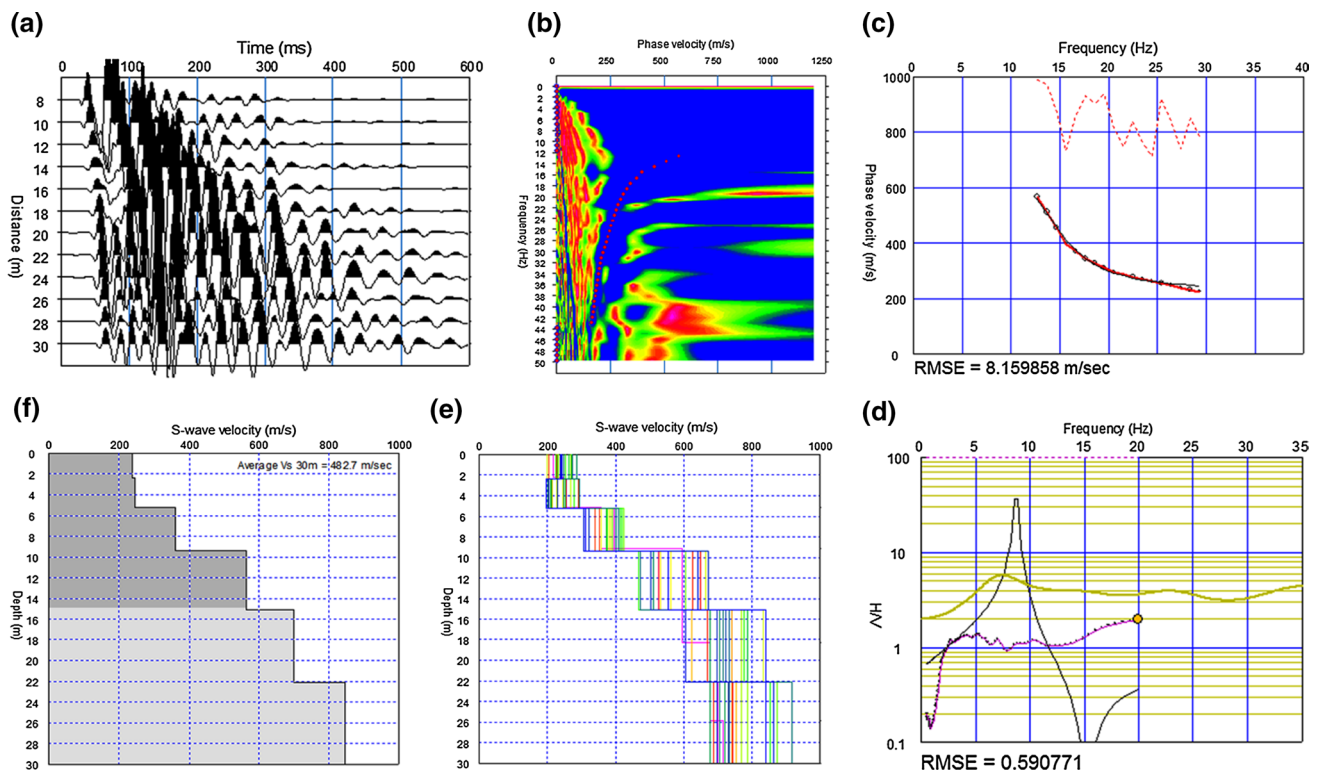


Fig. 14 Joint inversion results for first profile at the Atatürk Pavilion. **a** Seismic data. **b** Phase velocity versus frequency. **c** Comparing observed and calculated dispersion curves. A red line and black line indicate observed and calculated data, respectively. **d** Comparison of

$H/V$  spectra. A pink line and black line indicate observed and calculated data, respectively. Also, a yellow line indicates 1D transfer function. **e** S-wave velocity models. **f** Best-fit S-wave velocity model



**Fig. 15** Joint inversion results for second profile at the Atatürk Pavilion. **a** Seismic data. **b** Phase velocity versus frequency. **c** Comparing observed and calculated dispersion curves. A red line and black line indicate observed and calculated data, respectively. **d** Comparison of

*H/V* spectra. A pink line and black line indicate observed and calculated data, respectively. Also, a yellow line indicates 1D transfer function. **e** S-wave velocity models. **f** Best-fit S-wave velocity model

## Discussion and conclusion

This study attempts to calculate the soil–structure interaction and potential resonance phenomena of two significant historical structures in Eastern Black Sea using ambient vibrations, SRT and MASW methods.

The results of HVSR were evaluated in accordance with the SESAME reliability criteria. All results were found to provide reliable *H/V* curve criteria. However, the same situation was not observed in the clear *H/V* peak criteria. The most important reason for this is the fact that both areas are located in the city center. However, the HVSR results are consistent with seismic velocities and general geology. According to ambient vibrations results, the predominant frequency values obtained from the outside of Atatürk Pavilion are larger than Hagia Sophia. However, the predominant frequency values obtained in the inside parts of both structures are almost close to each other. The predominant frequency values obtained at different points on the inside and outside of both structures show similar characteristics. However, the predominant frequency values obtained from the lower and upper parts of the Hagia Sophia's tower are equal to almost half of the other predominant frequencies (outside and inside in Hagia Sophia). There are almost two times the

difference between the predominant frequencies obtained from the inside (building frequency) and outside (site frequency) in the Atatürk Pavilion. In this case, it is considered that there is no or very low risk of resonance in a possible earthquake. Conversely, in Hagia Sophia, we found very similar predominant frequency values from inside (average building frequency is 4.7 Hz) and outside (average site frequency is 4.4 Hz). On the other hand, it should be considered that the ambient vibrations recorded on the base in Hagia Sophia can also be effect from soil. Because of this reason, frequency values in records taken in Hagia Sophia may be closer to the frequency values of the soil. However, similar frequency value was obtained in ambient vibrations measurement (point of M5b) taken in front of a window above the ground in Hagia Sophia. For that reason, the resonance risk should be considered in this structure. This structure should be studied in detail and strengthened if necessary. The predominant frequencies between Hagia Sophia's tower (average frequency is 2.4 Hz) and its foundation (average frequency is 4.4 Hz) are very different. Therefore, the tower has not a significant resonance risk. Moreover, the frequency ( $F_0$ ) values were also calculated from seismic velocities and layer thicknesses (Table 1).  $F_0$  values calculated from seismic velocities and predominant frequencies determined from

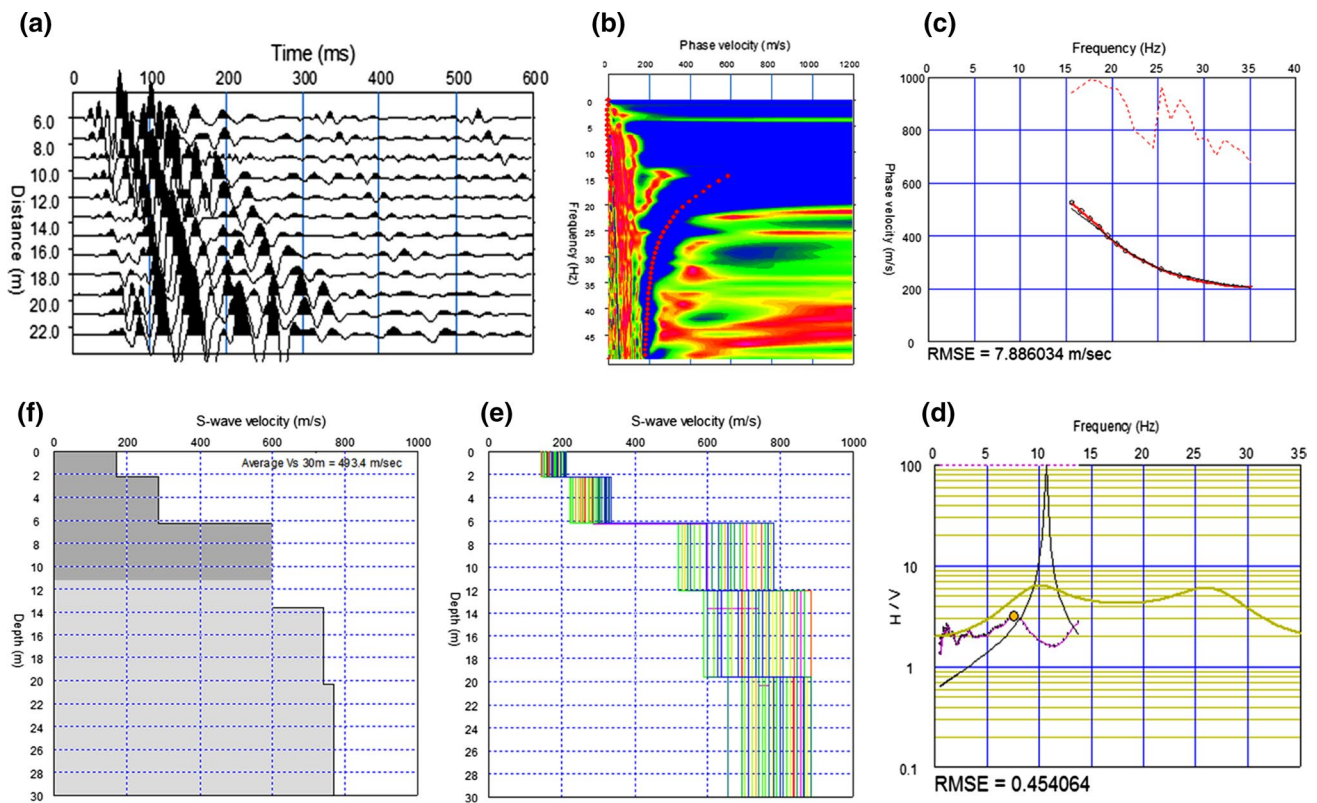


**Fig. 16** Joint inversion results for third profile at the Atatürk Pavilion. **a** Seismic data. **b** Phase velocity versus frequency. **c** Comparing observed and calculated dispersion curves. A red line and black line indicate observed and calculated data, respectively. **d** Comparison of

$H/V$  spectra. A pink line and black line indicate observed and calculated data, respectively. Also, a yellow line indicates 1D transfer function. **e** S-wave velocity models. **f** Best-fit S-wave velocity model

HVSR are quite compatible with in Atatürk Pavilion. This indicates that the studied area is relatively homogeneous. At the same time, these results are in line with the general geology of the region. On the other hand, this harmony was not observed in Hagia Sophia. There is a significant difference between the values ( $F_0$ ) calculated from both methods. The underlying reason for this is the existence of a highly heterogeneous structure in the area. We also see this phenomenon from the scattering of Rayleigh waves on the phase velocity frequency image. Therefore, energy cannot be concentrated on a field on the phase-frequency frequency image.

According to the results of the SIRT and MASW for two different historical buildings, the study area shows a structure with 2 and 3 layers from  $V_p$  sections. Depth information is about 12 m. The southern parts of the Atatürk Pavilion show a stiffer structure, and the depth of bedrock is about 8 m (Fig. 9a). On the other hand, the other two profiles (Fig. 9b, c) have lower velocities. Especially, the average maximum  $V_p$  in third profile (Fig. 9c) is about 1100 m/s. According to  $V_p$  values and field observations, the area where is located the third profile is soil embankment. According to the 1D  $V_s$  sections, reliable velocity information was obtained from the depth of maximum

16 m. However, in some profiles, the depth of penetration decreases depending on the length of seismic line and velocity. In the  $V_s$  sections, higher velocities were found in the southern part as in the  $V_p$  sections. A value of 650 m/s was calculated at approximately 8 m in the  $V_s$  section obtained from the southern part.

According to seismic measurement results in Hagia Sophia, depth information could be taken up to 10 and 19 m, in  $V_p$  and  $V_s$  sections, respectively. A top layer of about a few meters was seen on the first  $V_p$  profile (Fig. 10a). Furthermore, top layer in the second  $V_p$  profile is very thin and covering less than 1 m top to the south of the section (Fig. 10b). In addition, while the  $V_p$  of the second profile exceeds the 2000 m/s at approximately 4 m, these values are reached after 6–7 m at the first profile. The basement outcropping top to the north of the study area can be seen from the field observations (Fig. 19). According to field observations and results of seismic sections, the depth of the bedrock is quite shallow in the north and east parts of studied area. The average  $V_s$  is relatively high, and there is a significant increase in velocity after about 4–5 m in both sections. The study area also shows stiff soil or weathered rock according to the  $V_s$  velocities.



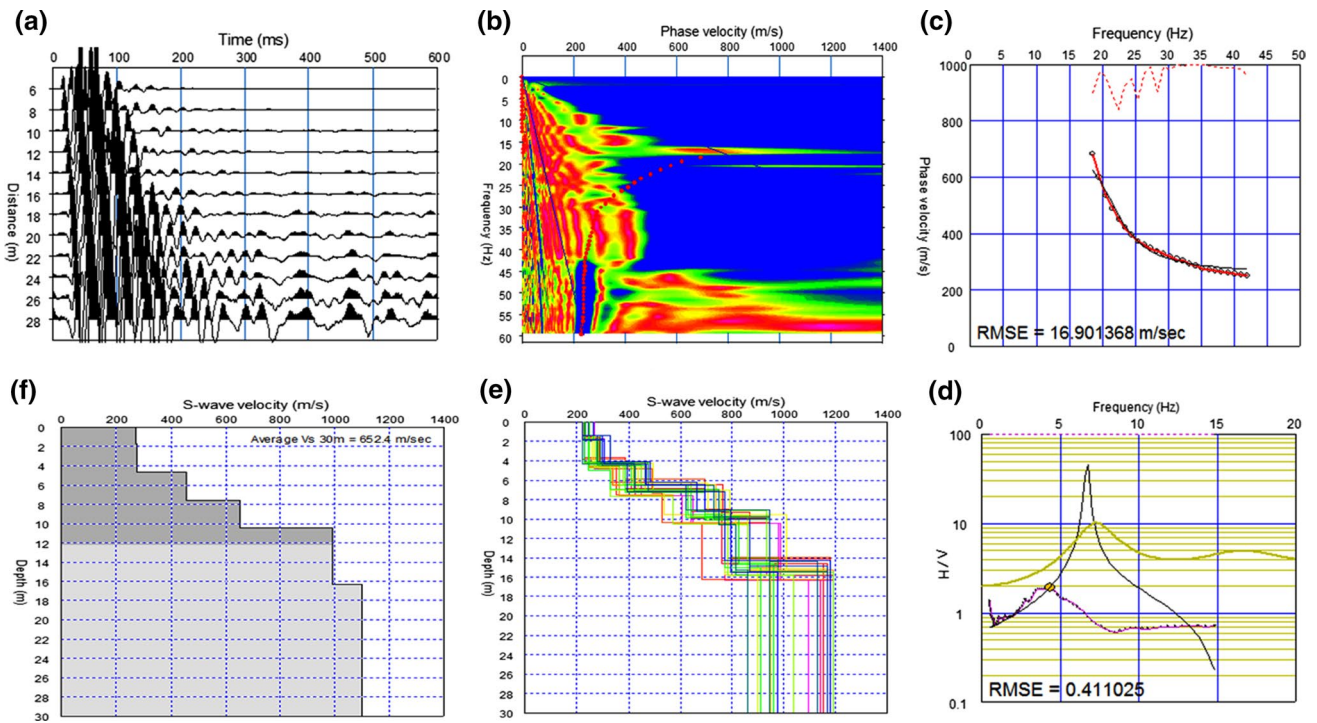


**Fig. 17** Joint inversion results for first profile at the Hagia Sophia. **a** Seismic data. **b** Phase velocity versus frequency. **c** Comparing observed and calculated dispersion curves. A red line and black line indicate observed and calculated data, respectively. **d** Comparison of

*H/V* spectra. A pink line and black line indicate observed and calculated data, respectively. Also, a yellow line indicates 1D transfer function. **e** S-wave velocity models. **f** Best-fit S-wave velocity model

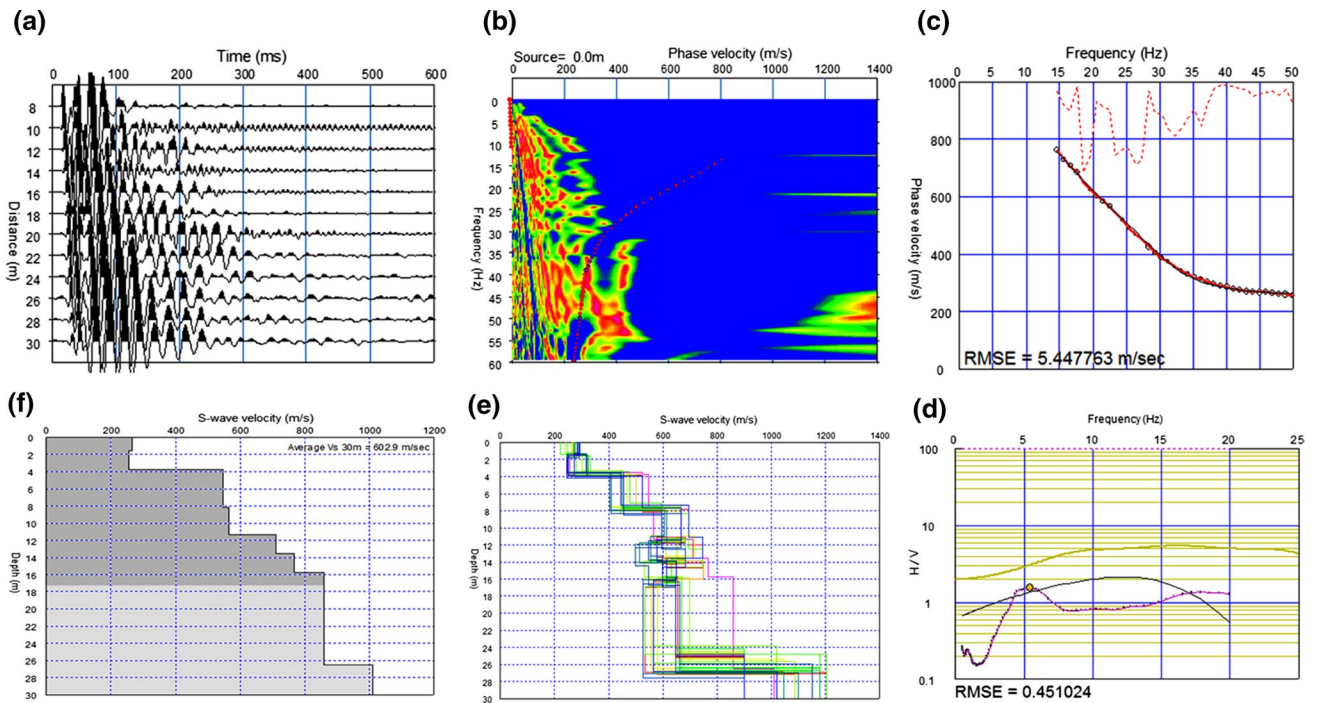


**Fig. 18** Joint inversion results for second profile at the Hagia Sophia. **a** Seismic data. **b** Phase velocity versus frequency. **c** Comparing observed and calculated dispersion curves. A red line and black line indicate observed and calculated data, respectively. **d** Comparison of

*H/V* spectra. A pink line and black line indicate observed and calculated data, respectively. Also, a yellow line indicates 1D transfer function. **e** S-wave velocity models. **f** Best-fit S-wave velocity model



**Fig. 19** A view of a rock outcropping in Hagia Sophia



The general geology of the area where both historical structures are built is similar characteristic, and the formation is composed of andesite, basalt and pyroclastic rocks containing sedimentary levels. Therewithal, field observations (Fig. 19) and other studies have shown that the bedrock of the study fields is basalt. The basaltic rocks in the region show partly weathering. Especially, this weathering is further increased at the near surface. Accordingly, it is considered that the calculated  $V_p$  and  $V_s$  values represent the velocities of basaltic rocks.

We have finally classified the subsoil in terms of  $V_{S30}$  parameter, according to Eurocode 8 (CEN 2003), finding the following values of  $V_{S30}$  for Atatürk Pavilion (EC08-B class) and  $V_{S30}$  for Hagia Sophia (EC08-B class). They both belong to B class as defined by Eurocode 8 (CEN 2003). Also, the predominant periods obtained from HVSr measurements, range 0.11–0.24 s, were used for a classification according to Kanai and Tanaka (1961), and the classes were defined as “Class I.” The all classification results show the same geologic structure as “Very dense sand, gravel or soft rock.” According to  $V_p$  and  $V_s$  sections, the soil thickness is relatively shallow and the velocities are high in the studied areas. Moreover, the low predominant periods obtained from ambient vibrations in these areas are consistent with seismic velocities. The results obtained from both methods show basaltic rocks.

Finally, it is thought that there is no resonance risk in the Atatürk Pavilion and the tower part of Hagia Sophia according to both ambient vibrations data and seismic velocity sections. However, although the Hagia Sophia is shallow to the depth of the bedrock with regard to the seismic sections and the velocities increase above  $V_p = 2000$  m/s, a resonance phenomena in this area (Hagia Sophia) may occur according to the predominant frequency values obtained from the ambient vibrations. To identify the possible soil–structure risk in Hagia Sophia, more detailed studies are required.

Ambient vibrations measurements give very useful results in making a quick preliminary assessment of the possible resonance risk.

**Acknowledgements** The authors are grateful to the Ortahisar District Governorate and Trabzon Metropolitan Municipality for their precious helps. The authors would like to thank students of Geophysical Engineering Department for their help in field measurements. We also thank Dr. Koichi Hayashi for his help joint inversion of the  $H/V$  and dispersion curves. We would like to thanks Dr. Marta Pischiutta, other reviewer and editor for their helpful suggestions and comments.

## References

- Akin O, Sayil N (2016) Site characterization using surface wave methods in the Arsin-Trabzon province, NE Turkey. *Environ Earth Sci* 75:72
- Anbazzhagan P, Sitharam TG, Vipin KS (2009) Site classification and estimation of surface level seismic hazard using geophysical data and probabilistic approach. *J Appl Geophys* 68:219–230
- Arslan M, Tüysüz N, Korkmaz S, Kurt H (1997) Geochemistry and petrogenesis of the Eastern Pontide volcanic rocks, Northeast Turkey. *Chem Erde* 57:157–187
- Arslan M, Kadir S, Abdioglu E, Kolayli H (2006) Origin and formation of kaolin minerals in saprolite of Tertiary alkaline volcanic rocks Eastern Pontides (NE Turkey). *Clay Miner* 41:597–617
- Azwin IN, Saad R, Nordiana M (2013) Applying the seismic refraction tomography for site characterization. In: 4th international conference on environmental science and development, ICESD 2013. *APCBEE Procedia*, vol 5, pp 227–231
- Bard PY (1998) Microtremor measurements: a tool for site effect estimation? In: Second international symposium on the effects of surface geology on seismic motion. ESG98, Japan
- Bektaş O, Yılmaz C, Taslı K, Akdağ K, Özgür S (1995) Cretaceous rifting of the Eastern Pontides carbonate platform (NE Turkey): the formation of the carbonate breccias and turbidites as evidence of a drowned platform. *G Geol* 57(1–2):233–244
- Bishop TN, Bube KP, Cutler RT, Langan RT, Love PL, Resnick JR, Shuey RT, Spindler DA, Wyld HW (1985) Tomographic determination of velocity and depth in laterally varying media. *Geophysics* 50:903–923

- Büyüksaraç A, Bektaş Ö, Yılmaz H, Arısoy MO (2013) Preliminary seismic microzonation of Sivas city (Turkey) using microtremor and refraction microtremor (ReMi) measurements. *J Seismol* 17:425–435
- CEN (2003) prEN 1998-1-Eurocode 8: design of structures for earthquake resistance—part 1: general rules, seismic actions and rules for buildings. Draft no. 6, Doc CEN/TC250/SC8/N335, Jan 2003, Brussels
- Chatelain JL, Guillier B, Cara F, Duval AM, Atakan K, Bard PY (2008) Evaluation of the influence of experimental conditions on HVSR results from ambient noise recordings. *Bull Earthq Eng* 6:33. <https://doi.org/10.1007/s10518-007-9040-7>
- Eker AM (2009) Determination of the dynamic characteristics and local site conditions of the Plio–Quaternary sediments situated towards the North of Ankara through surface wave testing methods. Master thesis, The Graduate School of Natural and Applied Sciences of Middle East Technical University
- Gedikoğlu A, Pelin S, Özsayar T (1979) The main lines of geotectonic development of the East Pontids in Mesozoic age. In: *Proceeding of the 1st Geological Congress of the Middle East*, pp 555–580
- Geometrics Inc. (2009) SeisImager/2D software manual. <http://www.geometrics.com>. Accessed 1 Dec 2017
- Geometrics Inc. (2016) SeisImager/SW-Pro manual
- Gilbert P (1972) Iterative methods for the three-dimensional reconstruction of an object from projections. *J Theor Biol* 36:105–117
- Gosar A, Rošar J, Motnikar BŠ, Zupancic P (2010) Microtremor study of site effects and soil–structure resonance in the city of Ljubljana (Central Slovenia). *Bull Earthq Eng* 8:571–592
- Guillier B, Atakan K, Chatelain JL, Havskov J, Ohrnberger M, Cara F, Duval AM, Zacharopoulos S, Costa PT, Team TS (2008) Influence of instruments on the HVSR spectral ratios of ambient vibrations. *Bull Earthq Eng* 6:3. <https://doi.org/10.1007/s10518-007-9039-0>
- Güven İH (1993) Doğu Pontidlerin jeolojisi ve 1/250.000 ölçekli kompilasyonu. MTA Yayınları, Ankara, Türkiye (in Turkish)
- Hadianfard MA, Rabiee R, Sarshad A (2017) Assessment of vulnerability and dynamic characteristics of a historical building using microtremor measurements. *Int J Civ Eng* 15:175–183
- Hailemichael S, Milana G, Cara F, Vassallo M, Pischiutta M, Amoroso S, Bordoni P, Cantore L, Giulio GD, Naccio DD, Famiani D, Mercuri A (2017) Sub-surface characterization of the Amphitheatrum Flavium area (Rome, Italy) through single-station ambient vibration measurements. *Ann Geophys* 60:4
- Hayashi K (2003) Data acquisition and analysis of active and passive surface wave methods. In: *SAGEEP 2003, short course*
- Hayashi K (2008) Development of surface-wave methods and its application to site investigations. Phd thesis, Kyoto University
- Hayashi K (2012) Analysis of surface-wave data including higher modes using the genetic algorithm. In: *GeoCongress 2012*. American Society of Civil Engineers, pp 2776–2785
- Hayashi K, Takahashi T (2001) High resolution seismic refraction method using surface and borehole data for characterization of rocks. *Int J Rock Mech Min Sci* 38:807–813
- Herak M (2011) Overview of recent ambient noise measurements in Croatia in free-field and in buildings. *Geofizika* 28:21–40
- Junior SBL, Prado RL, Mendes RM (2012) Application of multichannel analysis of surface waves method (MASW) in an area susceptible to landslide at Ubatuba City, Brazil. *Rev Bras Geofis* 30(2):213–224
- Kanai K, Tanaka AT (1961) On microtremors VII. *Bull Earthq Res Inst* 39:97–114
- Konno K, Ohmachi T (1998) Ground-motion characteristics estimated from spectral ratio between horizontal and vertical components. *Bull Seismol Soc Am* 88(1):228–241
- Kržan M, Gostic S, Bosiljkov V (2015) Application of different in situ testing techniques and vulnerability assessment of Kolizej palace in Ljubljana. *Bull Earthq Eng* 13:389–410
- Lehmann B (2007) Seismic traveltime tomography for engineering and exploration applications. EAGE Publications, Amsterdam
- Nakamura Y (1989) A method for dynamic characteristics estimation of sub-surface using microtremor on the ground surface. *Q Rep Railw Tech Res Inst* 30(1):25–33
- Pamuk E, Akgun M, Ozdag OC, Gonenc T (2017) 2D soil and engineering-seismic bedrock modeling of eastern part of Izmir inner bay/Turkey. *J Appl Geophys* 137:104–117
- Park CB, Miller RD, Xia J (1999) Multi-channel analysis of surface waves. *Geophysics* 64(3):800–808
- Pischiutta M, Villani F, D’Amico S, Vassallo M, Cara F, Di Naccio D, Farrugia D, Di Giulio G, Amoroso S, Cantore L, Mercuri A, Famiani D, Galea P, Akinci A, Rovelli A (2017) Results from shallow geophysical investigations in the northwestern sector of the island of Malta. *Phys Chem Earth* 98:41–48
- Rahman MZ, Siddiqua S, Maksud Kamal ASM (2016) Shear wave velocity estimation of the near-surface materials of Chittagong City, Bangladesh for seismic site characterization. *J Appl Geophys* 134:210–225
- SESAME (2004) Guidelines for the implementation of the HVSR spectral ratio technique on ambient vibrations: measurements, processing and interpretation. <http://sesame-p5.obs.ujfgrenoble.fr/Delivrables/Del-D23HVUserGuidelines.pdf>. Accessed 1 Jan 2018
- Sharma PV (1997) Environmental and engineering geophysics. Cambridge University Press, Cambridge
- Sheehan J, Doll W, Mandell W (2005) An evaluation of methods and available software for seismic refraction tomography analysis. *J Environ Eng Geophys* 10:21–34
- Suzuki H, Yamanaka H (2010) Joint inversion using earthquake ground motion records and microtremor survey data to S-wave profile of deep sedimentary layers. *BUTSURI-TANSA* 65:215–227 (in Japanese)
- Trupti S, Srinivas KNSSS, Kishore PP, Seshunarayana T (2012) Site characterization studies along coastal Andhra Pradesh—India using multichannel analysis of surface waves. *J Appl Geophys* 79:82–89
- URL-1 (2017) <http://www.koeri.boun.edu.tr/sismo/2/deprem-bilgileri/buyuk-depremler/> Accessed 24 Oct 2017
- URL-2 (2017) <http://www.kultur.gov.tr/EN,103988/trabzon-ataturk-pavilion.html>. Accessed 17 Oct 2017
- URL-3 (2017) <http://www.kulturvarliklari.gov.tr/TR,44047/trabzon-ataturk-kosku-muzesi.html>. Accessed 17 Oct 2017
- URL-4 (2012) [http://en.wikipedia.org/wiki/Hagia\\_Sophia,\\_Trabzon](http://en.wikipedia.org/wiki/Hagia_Sophia,_Trabzon). Accessed 3 Apr 2012
- URL-5 (2017) [http://www.karadenizgezi.net/Trabzon\\_Ayasofya\\_Muzesi.htm](http://www.karadenizgezi.net/Trabzon_Ayasofya_Muzesi.htm). Accessed 17 Oct 2017
- URL-6 (2018) [http://www.geopsy.org/wiki/index.php/H/V\\_spectral\\_ratio#Window\\_selection](http://www.geopsy.org/wiki/index.php/H/V_spectral_ratio#Window_selection)
- Wathelet M, Jongmans D, Ohrnberger M (2004) Surface wave inversion using a direct search algorithm and its application to ambient vibration measurements. *Near Surf Geophys* 2:211–221
- Xia J (2014) Estimation of near-surface shear-wave velocities and quality factors using multichannel analysis of surface-wave methods. *J Appl Geophys* 103:140–151
- Xia J, Miller RD, Park CB (1999) Estimation of near-surface shear-wave velocity by inversion of Rayleigh wave. *Geophysics* 64(3):691–700
- Xia J, Miller RD, Park CB (2004) Utilization of high-frequency Rayleigh waves in near-surface geophysics. *Lead Edge* 23(8):753–759
- Zhang J, Toksoz M (1998) Nonlinear refraction traveltime tomography. *Geophysics* 63(5):1726–1737



# An analysis and interpretation of the signals in gamma-absorption measurements of liquid–gas intermittent flow

Marcin Zych<sup>1</sup>

Received: 26 May 2018 / Accepted: 15 October 2018 / Published online: 22 October 2018  
© The Author(s) 2018

## Abstract

The intermittent flow (slug and plug type) of liquid–gas mixtures in a horizontal pipeline measured by the specific radiometric apparatus is presented. The measurement system consists of two sources of Am-241 gamma radiation and two scintillation probes. An analysis of the signals measured by the radiometric equipment is performed in the domain of time and of frequency. Recognised signal parameters are directly referred to physical quantities associated with a liquid–gas flow. The employed methodology enables determination of gas-phase flow velocity and estimation of the average depth and length of bubble gas structures. In the paper, the processing and interpretation results of the selected experiment are presented to show the in-depth description of gas structures and the type of flows recognition.

**Keywords** Liquid–gas flow · Slug flow · Plug flow · Flow structures · Gamma absorption · Signals analysis

## Introduction

Multiphase flows, including two-phase liquid–gas and liquid–solid particle flows, are very common in industrial processes, for example in the production of crude oil, which is accompanied by natural gas extraction, in the petrochemical industry in the processing of crude oil.

Two-phase liquid–gas mixtures, depending on the angle of inclination and the diameter of the pipeline, the velocity of the transport or the relationship between the content of both phases may produce various flow structures. Therefore, it is difficult to describe and to measure such a flow. This necessitates the development of measurement technology on the basis of parameters such as flow velocity or the coefficients of the contribution of the particular phases. The recognition of the type of flow (Roshani et al. 2017b; Hanus et al. 2018) and the imaging of a multiphase flow (Mosorov 2008) also becomes crucial. The information which is provided owing to experiments enables progress as far as better mathematical modelling of such flows is concerned (Jaszczur and Portela 2008; Gulhane and Mahulikar 2009).

The advanced measurement technologies of multiphase flows include tomographic methods: electrical ones (capacitance, resistance, impedance), which use the absorption of X-rays and gamma rays, nuclear magnetic resonance (NMR) and optical ones (e.g. PIV—particle image velocimetry) (Mosorov 2006a; Powell 2008; Falcone et al. 2009; Rząsa 2009; Rahim et al. 2012; Xue et al. 2012; Tamburini et al. 2013; Banasiak et al. 2014; de Oliveira et al. 2015; Kaniżawa and Ribatski 2016; Ameran et al. 2017; Vlasak et al. 2017). Tomographic methods are also used to establish crucial petrophysical parameters of rocks, such as porosity and permeability (Krakowska and Puskarczyk 2015; Jarzyna et al. 2016; Kundu et al. 2017). Although the technology of tomographic measurements is a familiar phenomenon, research in the development of such methods continues because the measurement systems usually constitute complex multi-sensor systems. As far as environment protection and hydrogeology is concerned, radiotracer methods are applied (Witczak et al. 2009; García et al. 2017; Biswal et al. 2018). The development of the aforementioned measurement methods is also facilitated by the progress in the analysis of signals which uses advanced mathematical methods. The latter are widely used, for example, in geotechnics, environment protection and geophysics (Buttkus 2000; Pietsch et al. 2007; Gołębiowski et al. 2016; Kozłowska et al. 2016; Szabó and Dobróka 2017).

✉ Marcin Zych  
zych@geol.agh.edu.pl

<sup>1</sup> Faculty of Geology, Geophysics and Environmental Protection, AGH University of Science and Technology, 30 Mickiewicz Av., 30-059 Kraków, Poland



Considering the fact that a significant part of the liquid–gas flows is transported in pipelines whose diameter is less than 100 mm (e.g. during the extraction of oil and natural gas in oil rigs), the problem of hydrotransport frequently may be reduced from a description in three or two dimensions to a description in one dimension. Due to this, complex systems intended for tomography may be replaced with simpler and frequently less expensive systems. That is why this article presents the application of a system which consists of two probes with NaI(Tl) scintillating crystals and two sealed sources of gamma-ray Am-241. The electrical signals which are obtained at the output of the measurement systems were subject to an analysis in the domain of time and of frequency. The properties of signals which were distinguished were related by author to physical quantities in the two-phase liquid–gas flow, such as the length and the depth of gas structures.

## The measurement system

The idea of using the absorption of gamma rays in the measurements of two-phase flows was discussed in a more comprehensive way in the following articles: Chaouki et al.

(1997), Johansen and Jackson (2004), Heindela et al. (2008), Kumara et al. (2010), Vlasak et al. (2014), Roshani et al. (2017a). The measurement systems which were applied are used above all to establish the contribution of the particular phases and to identify a flow structure. Therefore, the gamma-ray detectors which were used were a part of spectrometric tracks (Knoll 2000).

The research station is located in the AGH University of Science and Technology in Kraków.

Using the described measurement system, a number of experiments were carried out aimed at the development of the gamma-ray absorption method to determine the transport time delay and velocity of the dispersed phase, and recognition of flow types. The results of the experiments and the research station were detailed in the following works: Zych et al. (2014, 2015, 2016, 2018), Hanus (2015), Hanus et al. (2018).

The main part of the radiometric measurement system is presented in Fig. 1a, b. It consists of two scintillating detectors (2) with NaI(Tl) 2" × 2" crystals on which lead collimators are superimposed (3) whose purpose is to reduce scattered radiation. Sealed sources of gamma radiation are placed in lead collimators (1) with a slot, whose shape enables the appropriate shape of the radiation beams (5). Due to

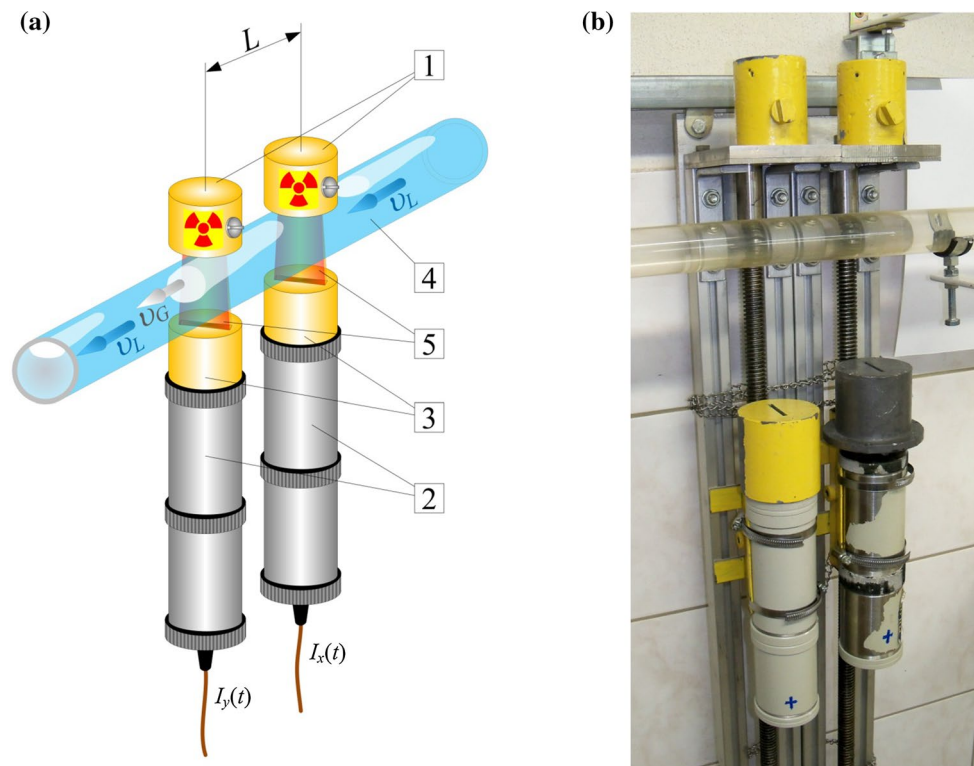


**Fig. 1** System intended for the research of two-phase liquid–gas flows by means of the absorption method: **a** the design of the system: 1—collimators with sources of Am-241, 2—scintillation probes, 3—probe collimators, 4—a pipeline with the flowing mixture, 5—a

beam of gamma rays,  $L$ —the distance between probes,  $v_L$ —the average velocity of the flow of a liquid,  $v_G$ —the average velocity of the flow of a gas,  $I_x(t)$ ,  $I_y(t)$ —signals from probes, **b** a photograph of the absorption apparatus (Zych et al. 2014; Hanus 2015)



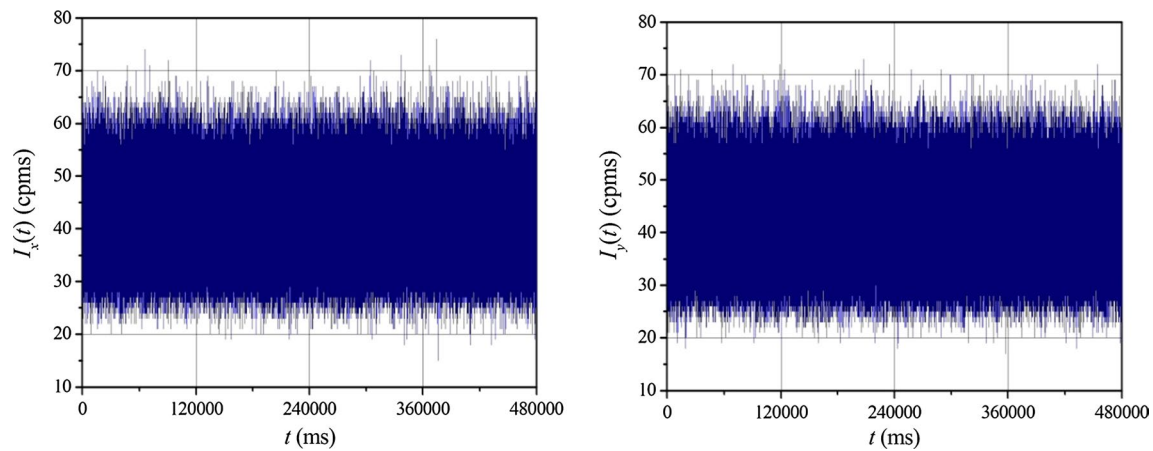


**Fig. 2** Signals registered in the LIW0004 experiment for the intermittent flow

**Table 1** Basic characteristics of analysed flows:  $v_L$ —average velocity of water,  $Re$ —Reynolds number,  $Fr$ —Froude number,  $\alpha$ —average void fraction of gas phase,  $q_G$ —air expense

Run	$v_L$ (m/s)	$\alpha$ (–)	$Re$ (–)	$Fr^2$ (–)	$q_G$ (l/min)	Type of flow
LIW0005	1.66	0.434	$1.9 \times 10^4$	1.01	18	Slug
LIW0003	2.16	0.312	$2.7 \times 10^4$	1.14		
LIW0004	2.92	0.266	$3.7 \times 10^4$	5.89		Plug
LIW0002	3.28	0.240	$4.3 \times 10^4$	7.43		

the low density of the water–air mixture, in order to ensure appropriate sensitivity for the method which is presented, one applied linear sources of Am-241 whose radiation energy is 59.54 keV and whose activity is 100 mCi. The mixture which was studied is transported in a horizontal pipeline (4), made of a Plexiglas pipe whose internal diameter is 30 mm and whose wall has the thickness of 5 mm and whose length is 4.5 m. The flow of the mixture is prompted by a rotary pump whose rotational speed may be regulated. This enables the maintenance of an average flow velocity  $v_L$  for a liquid phase from 0.15 to 3.6 m/s. The two-phase liquid–gas flow is obtained by regulation of the supply of air from the compressor to the installation before the measurement section. The airflow of up to 18 l/min enables the following flow structures to be obtained: the stratified-wavy, the intermittent (for which one also distinguishes the slug and the plug flows) and the bubble flow. Moreover, the measurement station was equipped with an ultrasound flow meter used to measure the velocity of the water and with a camera used to conduct optical measurements.

The detectors operated in the meter mode, registering the intensity (which varied in the course of time) of the radiation which passed through the flowing mixture. The probes were connected by a measuring card, which was a part of the data acquisition system. The measuring card and the dedicated software enable the sampling of the signal with a minimal period, i.e.  $\Delta t = 1$  ms. An example register of the signals which was provided by the measurement system

**Table 2** Average values of the velocity of gas phase  $v_G$  and the values of the measurement uncertainty  $u_c(v_G)$  for the flow of gas in the measurements which were analysed

Run	$v_G$ (m/s)	$u_c(v_G)$ (m/s)
LIW0005	1.325	0.053
LIW0003	1.792	0.055
LIW0004	2.059	0.054
LIW0002	2.304	0.062

that was used for the LIW0004 measurement is presented in Fig. 2. Experiment LIW0004 was made with a pump speed of 1900 r/min and air flow from the compressor 18 l/min. This allowed, in the measuring section, to obtain an average flow velocity  $v_L = 2.92$  m/s, while the average air velocity was  $v_G = 2.059$  m/s (Tables 1, 2). The gas structures that formed during the flow were classified as a plug flow. The distinction between the observed flow structures is described in the following chapters.

## Characteristics of analysed structures of a liquid–gas flow

The present article analyses two types of intermittent flows which are produced at various velocities of water and the contribution of water and air in the mixture (Salgado et al.

2010; Zhao et al. 2013; de Oliveira et al. 2015; Kanizawa and Ribatski 2016; Roshani et al. 2017a).

Figure 3 shows the distribution of flow structures for LIW0004 measurement (plug flow). This distribution is similar for the other analysed experiments. The intermittent flow can be distinguished by a large gas structure consisting of a large bubble with a free surface at the gas–liquid interface and a small gaseous structure (consisting of small bubbles).

Figure 4a, b presents the largest gas structures for the flow of the slug type (runs LIW0005 and LIW0003). Due to the length of such a bubble, which may reach even up to circa 2 m, selected fragments are indicated. The flow of the slug type is characterised by long, large bubbles filling almost the entire cross section of the pipeline. Between these bubbles are smaller gas structures. However, Fig. 4c, d illustrates the structures which are peculiar to the flow of the plug type (LIW0004 and LIW0002 runs).

These bubbles are considerably shorter, which to a lesser extent fill the cross section of the pipeline (see the values of void fraction  $\alpha$ —Table 1). In a plug flow, there are a much larger number of small bubbles in the gas structure between the large bubbles.

The basic quantities which describe the analysed flows are presented in Table 1.

The following relations were assumed in reference to the calculations:

- Reynolds number for water phase:

$$Re = \frac{v_L \cdot D_{ch} \cdot \rho}{\eta} \quad (1)$$

- Square of Froude number (Morgado et al. 2016; García et al. 2017):

$$Fr^2 = \frac{(v_L - v_G)^2}{a_g \cdot D_{ch}} \quad (2)$$

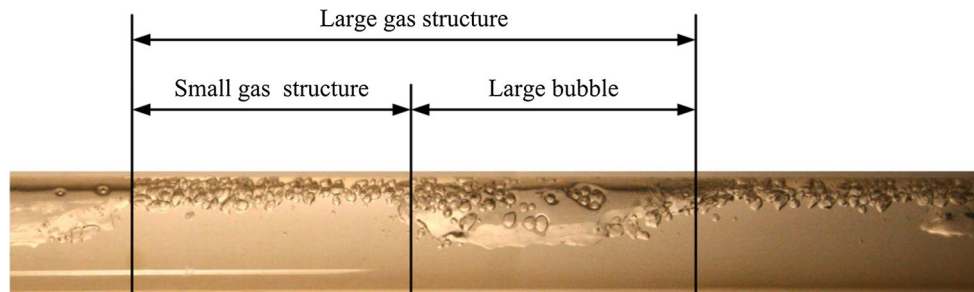


**Fig. 3** Distribution of gas structures in the intermittent flow, on the example of the LIW0004 experiment

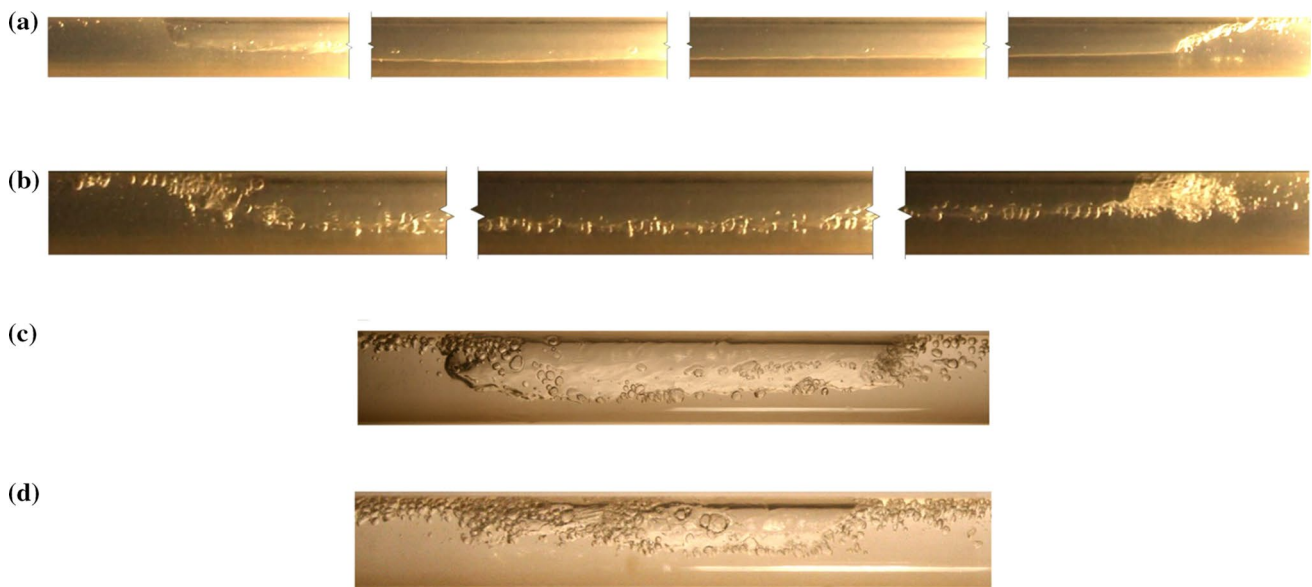


**Fig. 4** Characteristic gas structures in intermittent flows: the slug flow type—**a** LIW0005, **b** LIW0003 and the plug flow type—**c** LIW0004, **d** LIW0002

- Characteristic dimension for liquid phase:

$$D_{ch} = r\sqrt{1-\alpha} \tag{3}$$

where  $\eta$  is the dynamic viscosity (Pa s),  $a_g$  the gravity acceleration ( $m/s^2$ ),  $\alpha$  the average void fraction (-),  $r$  the radius of pipeline (m) and  $\rho$  the density of liquid ( $kg/m^3$ ).

## Methodology of signal analysis

### Determining the average velocity of gas phase

In reference to the measurement system presented in Fig. 1, the establishment of the average velocity of the flow of the gas phase (which in this case is a dispersed phase) is performed by determining the time of the transport delay  $\tau_0$  between two signals from probes placed at a distance  $L$ . Then, the average velocity of the flow of the gas phase may be expressed by the following relationship:

$$v_G = \frac{L}{\tau_0} \tag{4}$$

Various statistical methods are used to determine  $\tau_0$ . The most popular ones include the cross-correlation function (CCF) and methods based on a modification of CCF, such as differential and complex functions, CCF with Hilbert’s transform, conditional averaging, deconvolution and the phase method (Hanus 2003; Mosorov 2006b; Sommerlatt and Andruszkiewicz 2008; Hanus 2009; Kowalczyk et al. 2011; Hanus et al. 2014; Zych et al. 2015; Zeng et al. 2016; Arkani et al. 2017). The cross-correlation function may be applied to signals whose relation of the signal to noise is unfavourable. The present work uses the cross-correlation function which is described by the equation for discrete signals (Beck and Plaskowski 1987):

$$R_{xy}(\tau) = \frac{1}{N} \sum_{n=0}^{N-1} x(n) \cdot y(n + \tau) \tag{5}$$

where  $x(n)$  and  $y(n)$  constitute digital realisation of  $I_x(t)$  and  $I_y(t)$  signals,  $n$  is linked with the time of the measurement and of sampling by the  $n = t/\Delta t$  relationship and  $N$  is the number of the discrete values of signals.

The argument of the maximum course of CCF is assumed to be the most likely duration of the transport delay (estimator)  $\tau_0$ :

$$\hat{\tau}_0 = \arg\{\max R_{xy}(\tau)\} = \arg\{R_{xy}(\tau_0)\} \tag{6}$$

The fragment of CCF, which is subject to the analysis, along with the determined maximum and the standard deviation  $\sigma$ , is presented in Fig. 5 for the run LIW0004 (Zych et al. 2017).

The complex uncertainty of the measurement of the velocity of the gas phase was determined on the basis of the law of the propagation of uncertainty, according to (Guide 1995):

$$u_c(v_G) = \sqrt{\left(\frac{1}{\hat{\tau}_0} u_B(L)\right)^2 + \left(\frac{L}{(\hat{\tau}_0)^2} u_A(\hat{\tau}_0)\right)^2} \tag{7}$$

whereas the uncertainty of the time of the transport delay was determined on the basis of the relationship:

$$u_A(\hat{\tau}_0) = \frac{\sigma}{\sqrt{m}} \tag{8}$$

where  $m$  is the number of points which belong to the CCF graph, which is shaded in Fig. 5, whereas the value  $u_B(L)$  designates the precision of the measurement with the help of a vernier calliper gauge, equal to 0.1 mm.

The determination/evaluation of the velocity of the flow of the gas phase is crucial for a further analysis and interpretation of the measurements which are presented. It is also one of the basic parameters which characterise the two-phase liquid–gas-type flow.

Table 2 presents the average velocities of the flow of gas  $v_G$  along with the uncertainties of the measurement  $u_c(v_G)$  which were calculated for the analysed measurements.

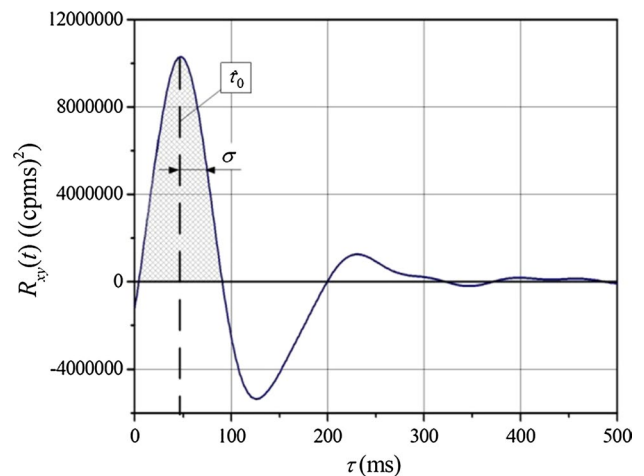


**Fig. 5** Cross-correlation function for the LIW0004 run:  $\hat{\tau}_0$ —estimator of the duration of the transport delay,  $\sigma$ —standard deviation of the distribution

### Determining the depth of gas structures

The radiometric measurement system which is presented in the “The measurement system” section may also be utilised in a classical way to determine the density of the mixture or the void fraction  $\alpha$  for the gas phase (Arvoh et al. 2012; Zhao et al. 2013; Roshani and Nazemi 2017). This requires prior experimental calibration of the apparatus due to which one obtains a relationship which links the number of the combined calculations  $I$  of gamma quanta registered by the scintillation probe with  $\alpha$ . A detailed description of the process of calibration and the utilisation of the relationship which was obtained is presented in the following article: Zych et al. (2016).

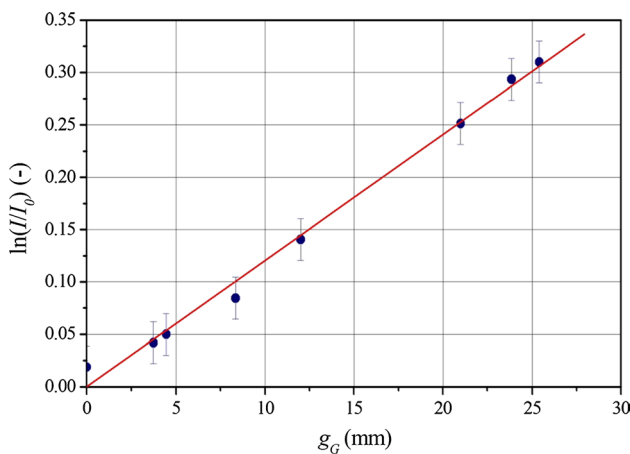


**Fig. 6** Relationship between the intensity of radiation  $I$  and the depth of the gas— $g_G$

As a result of the calibration, relationship was determined by Eq. 9, where  $g_G$  is the depth of the structure of the transported gas. This relationship is presented in Fig. 5. It is described by the Lambert–Beer law:

$$\ln(I/I_0) = \mu \cdot g_G \tag{9}$$

where  $\mu$  is the coefficient of the attenuation of radiation in the mixture,  $I$  the intensity of gamma radiation after the scanning of the mixture and  $I_0$  the intensity of radiation registered by the probe for a pipeline which is filled completely with water.

Based on Eq. 9, one may evaluate the average depth of the bubbles (Zych et al. 2018).

Due to the adjustment of the straight line to the measurement points indicated in Fig. 6, one obtained the value of the attenuation coefficient of radiation— $\mu = (0.01204 \pm 0.00042) \text{ mm}^{-1}$ .

The idea of the measurement of the depth and the length of the gas structures in the time domain is presented in Fig. 7. In order to illustrate the variability of the signal for the run LIW0003 better, the signal was subject to prior filtration. Due to this fact, the intensity of gamma radiation was designated  $I_y^*(t)$  on the vertical axis. However, for the purposes of the calculations one uses data which were not subject to filtration. Figure 7 presents the length of a large bubble— $l_b$ , which corresponds to the temporal duration of the signal  $t_b$ . The parameter  $t_l$  is the duration of a large gas structure, which consists of a large bubble and gas structures located between large bubbles. Due to the fact that one may separate individual gas structures and large bubbles from a duration of a signal for intermittent flows, one may estimate their average depth. Then, one must separate a fragment of a signal with an amplitude  $I_b$ , which enables

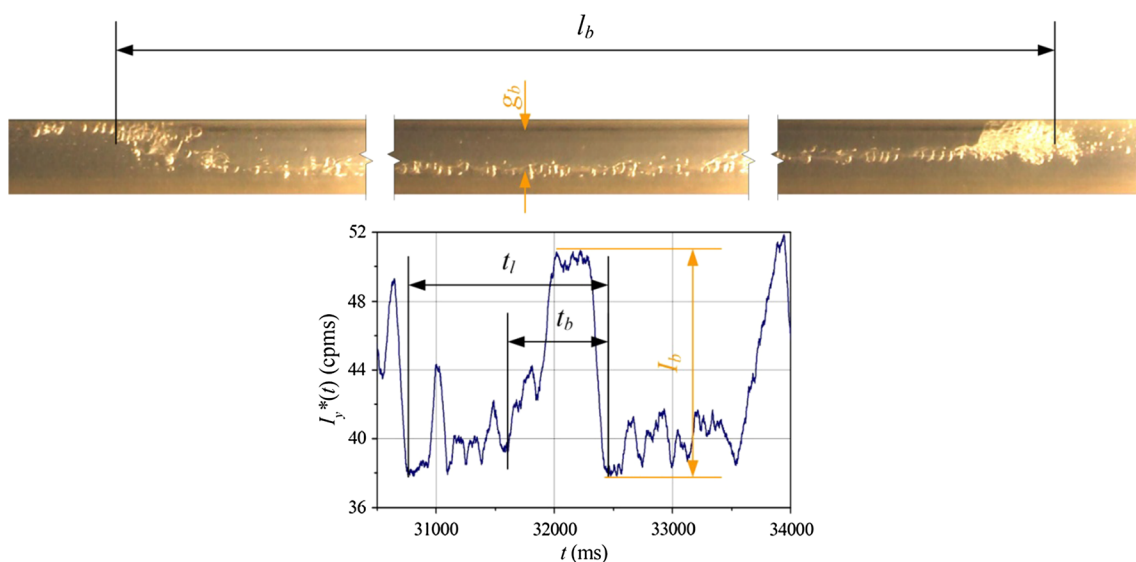


**Fig. 7** Idea of the measurement of the depth  $g_b$  and the length  $l_b$  of large gas bubbles in an intermittent flow (run LIW0003)



the establishment of an average depth of a large bubble  $g_b$  by means of an equation (Eq. 9). This means that in reference to individual structures one assumes an ersatz model of a bubble in a projection on a lateral plane contiguous with the pipeline, as a rectangle whose height is  $g_b$ . However, as far as the establishment of an average depth  $g_G$  of a gas bubble in a pipeline for the entire measurement is concerned, one assumed an equivalent model of the structure, as in the case of a stratified flow.

The precision of the establishment of the average depth of a gas structure was estimated on the basis of the law of the propagation of uncertainty from the following relationship (Eq. 9):

$$u_c(g_G) = \sqrt{\left(\frac{1}{\mu \cdot I} u_A(I)\right)^2 + \left(\frac{1}{\mu \cdot I_0} u_A(I_0)\right)^2 + \left(\frac{\ln(I/I_0)}{\mu^2} u_A(\mu)\right)^2} \tag{10}$$

Due to the fact that the process of radioactive decay is a stochastic process, one assumed the following equation in reference to the uncertainty of the establishment of the intensity of radiation  $I$ :

$$u_A(I) = \frac{\sqrt{I}}{n} \tag{11}$$

where  $n$  is the number of data.

As far as the measurements which are presented are concerned, one performed analyses in the domain of time for further 50 fragments of the signal. The part of the signal which was analysed was selected in such a way as to be representative for the whole measurement. As a result of the calculations which were performed, one obtained average values of the depths of large gas structures  $g_l$ , of large gas bubbles  $g_b$  and of small gas structures  $g_{sb}$ , which arise between large bubbles. The distribution of the values of the depth of the structures is presented in Fig. 8a, b for the flows of the slug type and Fig. 8c, d, for the flows of the plug type. The black circles represent the depths of gas structures, the blue squares represent the depths of large gas bubbles, whereas the triangles represent the depths of small gas structures. Continuous lines designated  $\bar{g}_l, \bar{g}_b, \bar{g}_{sb}$  represent the average values for all 50 fragments of the signals which were analysed, respectively. Table 3 presents the average values of the depths of the structures and indicates the uncertainty of the measurements and the respective standard deviation— $\sigma_l, \sigma_b, \sigma_{sb}$ .

An analysis of the graphs presented in Fig. 8 and the values of standard deviation, presented in Table 3, indicate that the flows of the slug type are characterised by a lesser extent of

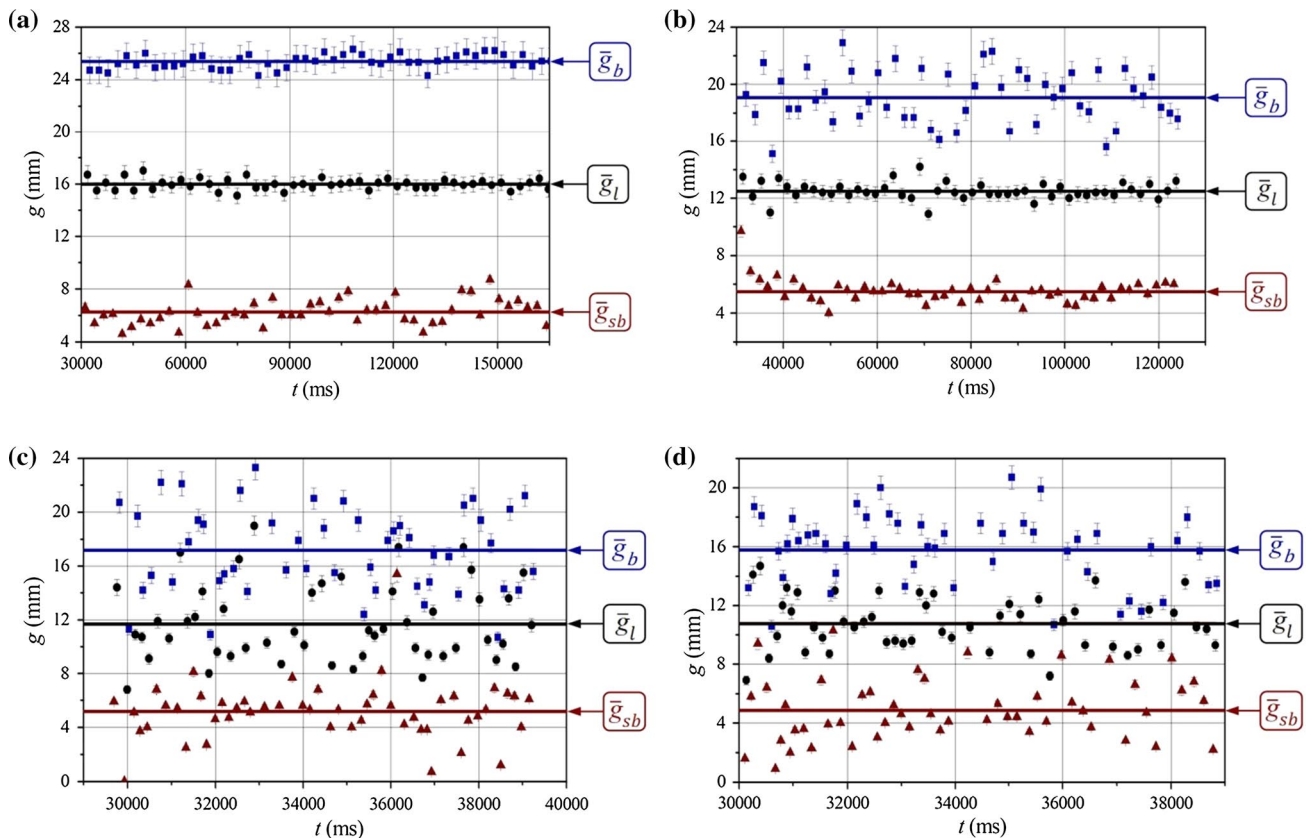


**Fig. 8** Distribution of the average values of the depths of gas structures for the flows of the slug type: **a** LIW0005, **b** LIW0003 and the flows of the plug type: **c** LIW0004, **d** LIW0002

diversity of the average depths of gas structures (Fig. 8a, b) than the flows of the plug type (Fig. 8c, b).

In order to present a supplementary description of the gas structures which arise in the flow, one defined the following non-dimensional quantities:

- (a) the ratio of average depth of the large gas structure  $\bar{g}_1$  to the average depth of a large bubble  $\bar{g}_b$ , which may be represented by the following relationship:

$$\xi_1 = \frac{\bar{g}_1}{\bar{g}_b} \tag{12}$$

- (b) the ratio of the average depth of small gas structures  $\bar{g}_{sb}$  located between large bubbles, to the average depth of large bubbles  $\bar{g}_b$ :

$$\xi_s = \frac{\bar{g}_{sb}}{\bar{g}_b} \tag{13}$$

It follows from the law of the propagation of uncertainty (Guide 1995), respectively:

$$u_c(\xi_1) = \sqrt{\left(\frac{1}{\bar{g}_b} u_c(\bar{g}_1)\right)^2 + \left(\frac{\bar{g}_1}{(\bar{g}_b)^2} u_c(\bar{g}_b)\right)^2} \tag{14}$$

$$u_c(\xi_s) = \sqrt{\left(\frac{1}{\bar{g}_b} u_c(\bar{g}_{sb})\right)^2 + \left(\frac{\bar{g}_{sb}}{(\bar{g}_b)^2} u_c(\bar{g}_b)\right)^2} \tag{15}$$

Considering the fact that the values in Table 3 are values derived from a sample and not for the whole measurement, one provided the values of uncertainty for  $\xi_1$  and  $\xi_s$ , as extended uncertainties:

$$u_c(\xi) = \chi \cdot u_c(\xi) \tag{16}$$

where the extension coefficient  $\chi = 2$ .

Table 4 presents the values  $\xi_1$  and  $\xi_s$ , along with the average value of the depth of the gas phase for the entire duration of the measurement in the particular runs. By analysing this table, one may notice that  $\xi_1$  and  $\xi_s$  are very similar to the measurements which are described regardless of the type of the flow and the velocity of the flow of the particular phases.

### Determining the length of the gas structure

The length of the structures in a two-phase liquid–gas flow may be described in two basic domains: time and frequency (Zych et al. 2014). Even though both types of flow, i.e. slug and plug, are similar to each other, one may also distinguish such features in the domain of time and in the domain of frequency that set them apart.

In order to perform a frequency analysis, one used the module of cross-spectral density function (CSDF). Zych et al. (2014) show that the CSDF function is emphasised more efficiently the characteristic frequencies, including those associated with a useful signal, than the traditional autospectral density function. On the basis of Bendat and Piersol (2010), the cross-spectral density function  $\underline{G}_{xy}(f)$  is determined by the following relationship:

**Table 3** Average values of the depths of gas structures, standard deviations and uncertainties for 50 fragments of the measurements which were analysed

Run	$\bar{g}_1$ (mm)	$\sigma_1$ (mm)	$u_c(\bar{g}_1)$ (mm)	$\bar{g}_b$ (mm)	$\sigma_b$ (mm)	$u_c(\bar{g}_b)$ (mm)	$\bar{g}_{sb}$ (mm)	$\sigma_{sb}$ (mm)	$u_c(\bar{g}_{sb})$ (mm)
LIW0005	16.0	0.4	0.1	25.4	0.5	0.1	5.4	1.0	0.1
LIW0003	12.5	0.6	0.1	19.1	1.8	0.3	4.7	0.8	0.1
LIW0004	11.7	2.9	0.4	17.2	3.2	0.5	4.4	2.3	0.3
LIW0002	10.8	1.8	0.3	15.8	2.4	0.3	4.1	2.1	0.3

**Table 4** Average value of the depth  $g_G$  of the gas phase for the particular measurements which are analysed and the values  $\xi_1$  and  $\xi_s$ , calculated on the basis of the average values in along with the uncertainties of the measurement

Run	$g_G$ (mm)	$u_c(g_G)$ (mm)	$\xi_1$ (–)	$u_c(\xi_1)$ (–)	$\xi_s$ (–)	$u_c(\xi_s)$ (–)
LIW0005	15.8	0.6	0.63	0.01	0.25	0.02
LIW0003	12.3	0.5	0.65	0.02	0.29	0.02
LIW0004	11.1	0.4	0.68	0.06	0.30	0.04
LIW0002	10.4	0.4	0.68	0.04	0.31	0.04

$$\underline{G}_{xy}(f) = 2 \int_{-\infty}^{\infty} R_{xy}(\tau) e^{-j2\pi f \tau} d\tau \quad (17)$$

and the model CSDF is determined by this relationship:

$$|\underline{G}_{xy}(f)| = \left\{ \operatorname{Re}[\underline{G}_{xy}(f)]^2 + \operatorname{Im}[\underline{G}_{xy}(f)]^2 \right\}^{0.5} \quad (18)$$

where  $f$  is the frequency.

### Slug flow

Figure 9a, b presents fragments of the original signals in the domain of time for the measurements LIW0005 and LIW0003 identified as flows of the slug type. Large red frames indicate where the flow of a large bubble of gas was registered, whereas small orange frames indicate the movement of small gas structures, which consist of small bubbles. Due to a substantial level of noise, the gas structures

between large bubbles are indicated considerably more faintly. Therefore, in order to present a clearer picture of the structure, one applied the procedure of smoothing by means of a moving average with a window whose duration is 10 ms. The signals produced after the operation of averaging are presented in Fig. 9c, d, respectively.

Even though the noise, which originates, i.e. in a stochastic process associated with the emission of gamma quanta by a radioactive source, distorts the signal, one may provide an approximate image of it by means of a rectangular run. Thus, the signal which is registered should constitute superposition of numerous signals of this kind which are generated as a result of the flow of large bubbles with a free surface and the much smaller bubbles which are located between them. For such signals in the |CSDF| spectrum, in the range of a useful signal, indicated in Fig. 10a, b with a single-point framed line, there occur dominant frequencies. It follows from the theory of signals that a rectangular signal should generate, apart from the dominant frequency  $f_0$ , also harmonic frequencies of values which are odd multiples of

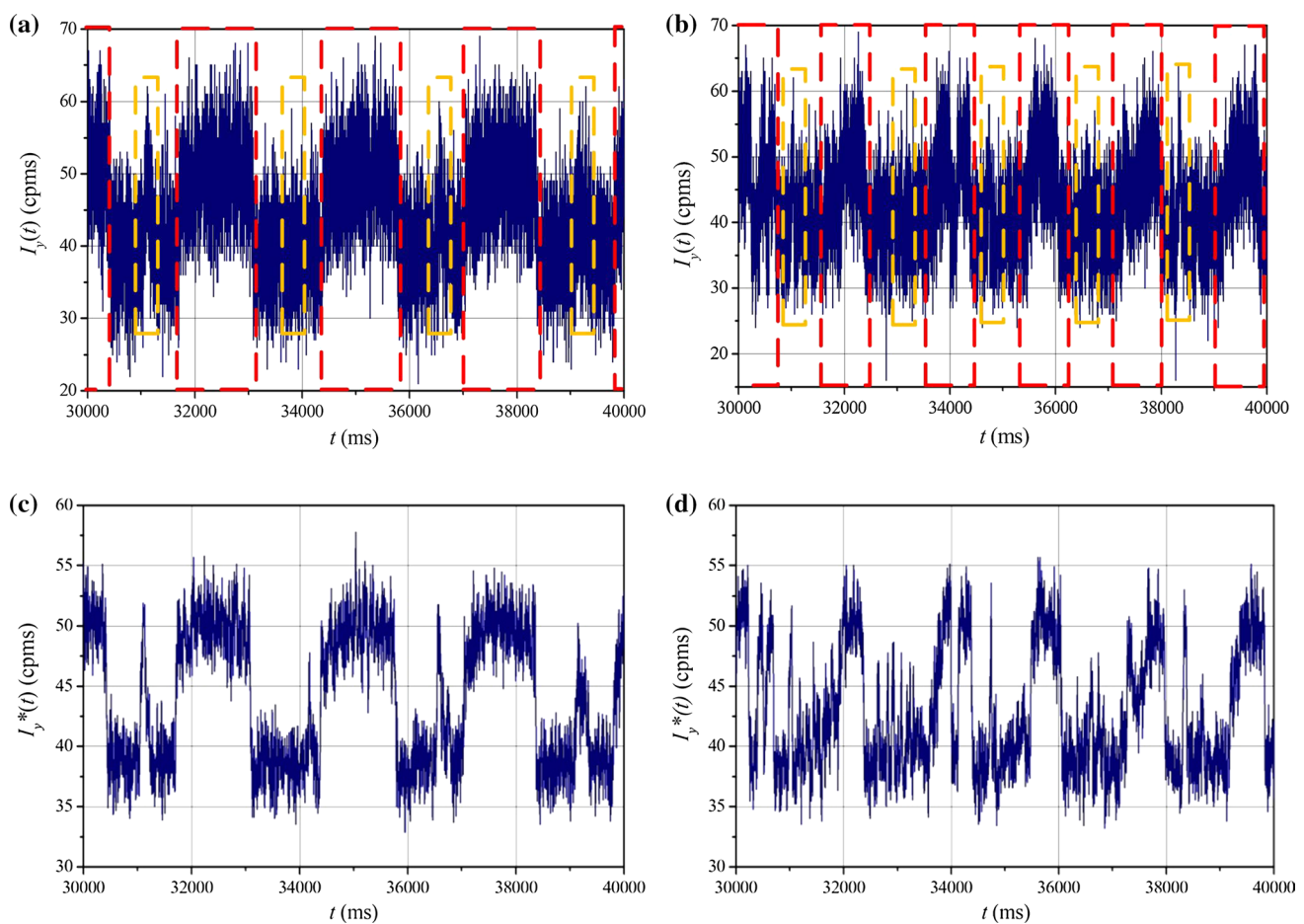


**Fig. 9** Fragments of signals registered between 30 s and 40 s for the experiments: **a** LIW0005—the original signal, **b** LIW0003—the original signal, **c** LIW0005—the signal after the application of smoothing

with a moving average, **d** LIW0003—the signal after the application of smoothing with a moving average

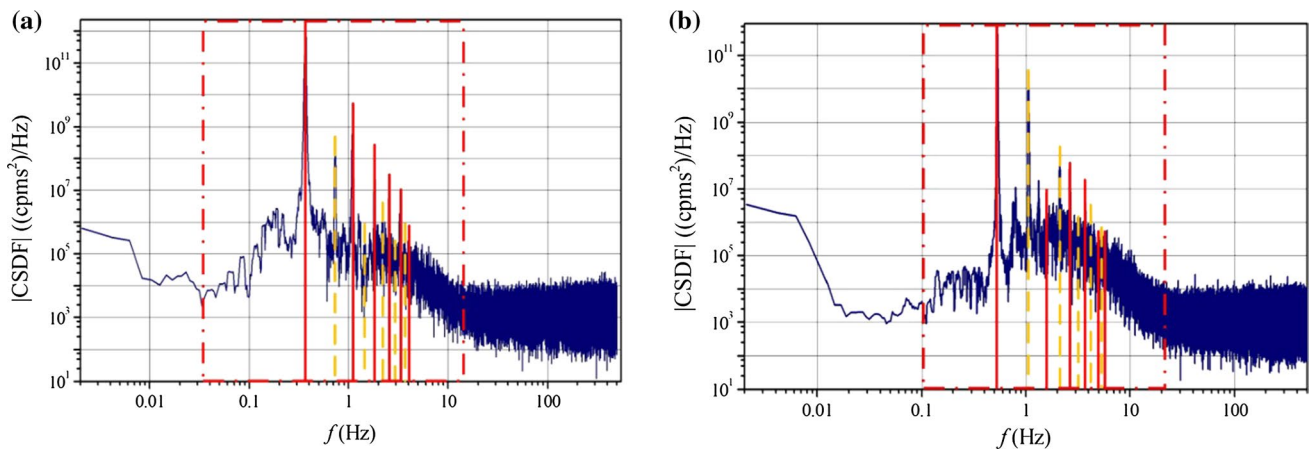


**Fig. 10** |CSDF| spectra of the signals from radiometric probes in a flow of the slug type for the measurements: **a** LIW0005 (Zych et al. 2018), **b** LIW0003

**Table 5** Values of the frequencies which dominate in a |CSDF| spectrum for the slug-type flow and the successive numbers of the harmonic  $r$  of the basic frequency  $f_0$

LIW0005		LIW0003	
$f_r$ (Hz)	$r$ (-)	$f_r$ (Hz)	$r$ (-)
$f_0=0.36$	1	$f_0=0.53$	1
0.73	2	1.06	2
1.09	3	1.57	3
1.47	4	2.12	4
1.83	5	2.65	5
2.20	6	3.16	6
2.57	7	3.71	7
2.91	8	4.20	8
3.27	9	4.75	9
3.65	10	5.29	10
4.01	11	5.79	11

$f_0$ . The graphs in Fig. 10a, b and Table 5 indicate that such harmonic frequencies (indicated by a solid red line in the graphs) are a part of the |CSDF| spectrum. However, apart from these frequencies there are also harmonic frequencies which are even multiples of  $f_0$  (indicated by a dashed orange line in Fig. 10a, b). Eventually, the dominant frequencies in the range of the useful signal may be described by the following formula:

$$f_r = r \cdot f_0 \tag{19}$$

where  $r \in \{1, 2, \dots\}$  is the number of subsequent harmonic frequency.

The linking of dominant frequencies with a flow is possible only by performing a supplementary analysis of the signal in the domain of time, i.e. by establishing the duration of a large gas structure  $t_1$  (Fig. 7). It is also crucial to determine the duration of a large bubble  $t_b$ . By taking into

consideration the average velocity of the movement of the gas phase, one may calculate their lengths.

The instantaneous lengths of large structures are defined by the following relationship (Zych et al. 2018):

$$l_1 = t_1 \cdot v_G \tag{20}$$

similarly in the case of a large bubble:

$$l_b = t_b \cdot v_G \tag{21}$$

On the basis of the law of the propagation of uncertainty, one may establish the complex uncertainty of a measurement of the length of a structure:

$$u_c(l_1) = \sqrt{(v_G \cdot u_B(t_1))^2 + (t_1 \cdot u_c(v_G))^2} \tag{22}$$

Considering the fact that the sampling time is  $\Delta t = 1$  ms, one assumed the estimated uncertainty of the duration of the structure  $u_B(t_1) = 2$  ms.

Figure 11a, b presents the distributions of the lengths of large gas structures (indicated by black circles) and the lengths of the bubbles (small blue squares). Continuous lines indicate average values:  $\bar{l}_1$ —the lengths of large structures (black line),  $\bar{l}_b$ —the lengths of large bubbles (blue line). Table 6 contains average values of the lengths of the structures along with the respective standard deviations and the uncertainties of a measurement.

The values of the lengths of the structures obtained on the basis of an analysis of the signal in the domain of time are congruous with the supplementary photographic documentation. On this basis, one estimated the length of a large structure, which was about 3.6 m for the LIW0005 measurement, whereas the length of the bubble was about 1.8 m. For the LIW0003 measurement, the length of a large structure was about 3.4 m, and the length of a large bubble was about 1.7 m.



Identification of the salient frequencies may be conducted by taking the reverse of the duration values  $t_1$  and  $t_b$ . On this basis, one may calculate the average frequency for a large structure  $\bar{f}_1$ , from the following relationship:

$$\bar{f}_1 = \frac{1}{\bar{t}_1} \tag{23}$$

and the average frequency for a large gas bubble  $\bar{f}_b$ :

$$\bar{f}_b = \frac{1}{\bar{t}_b} \tag{24}$$

Table 7 presents the values of the frequencies  $\bar{f}_1$  and  $\bar{f}_b$ , calculated on the basis of formulae (Eq. 23) and (Eq. 24).

When one analyses Tables 5 and 7, one may notice considerable congruity of the frequencies  $\bar{f}_1=f_0$  and  $\bar{f}_b=f_2$  in both of the measurements which were analysed. One may draw a conclusion that one should interpret these frequencies to be directly associated with an average size and with the movement of large gas structures and large bubbles. On this basis, one may provide a relationship which describes

the average duration of gas structures for a flow of the slug type (Zych et al. 2018):

$$\bar{t}_1 = \frac{v_G}{f_0} \tag{25}$$

and for large gas bubbles:

$$\bar{t}_b = \frac{v_G}{f_2} = \frac{v_G}{2 \cdot f_0} \tag{26}$$

A physical analysis of the successive frequencies which are multiples of  $f_0$  is more difficult due to the fact that their footprint in the radioisotope signal is weaker. By analysing the photographic documentation and by comparing it with the signals which were analysed, one may state that it is necessary to associate even frequencies of higher orders with the movement of smaller gas structures, located in the space between large bubbles.

Eventually, it followed from the ICSDFI analysis that the average length of gas structures for the LIW0005 measurement is  $\bar{l}_1=(3.64 \pm 0.15)$  m, whereas for the LIW0003 it is  $\bar{l}_1=(3.37 \pm 0.11)$  m. The average length of large bubbles for

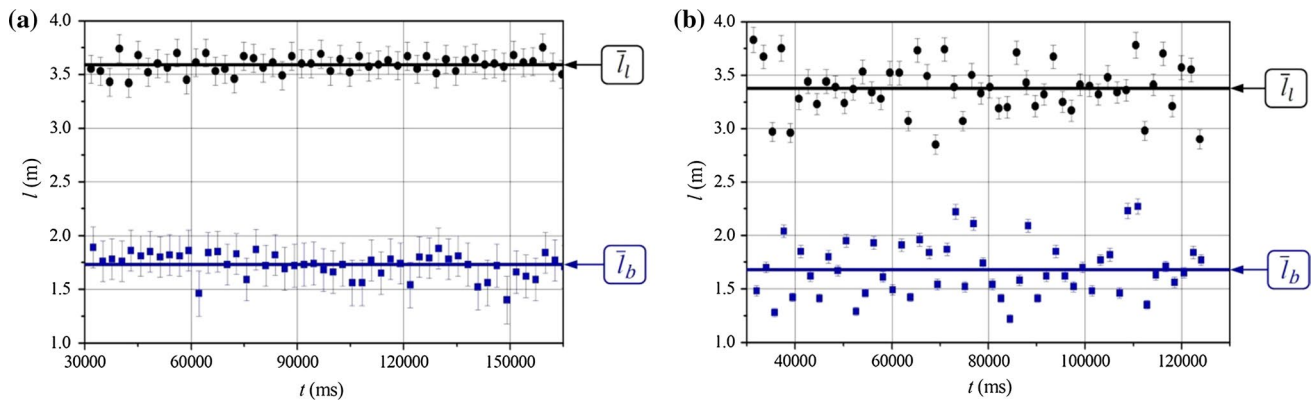


Fig. 11 Distributions of the values of the lengths of gas structures for flows of the slug type: **a** LIW0005, **b** LIW0003

**Table 6** Average values of the lengths of the structures  $\bar{l}_1$  and  $\bar{l}_b$  along with the standard deviations  $\sigma_1$ ,  $\sigma_b$  and the uncertainties  $u_c(\bar{l}_1)$ ,  $u_c(\bar{l}_b)$  for flows of the slug type

Run	$\bar{l}_1$ (m)	$\sigma_1$ (m)	$u_c(\bar{l}_1)$ (m)	$\bar{l}_b$ (m)	$\sigma_b$ (m)	$u_c(\bar{l}_b)$ (m)
LIW0005	3.59	0.08	0.14	1.73	0.11	0.07
LIW0003	3.38	0.24	0.11	1.68	0.26	0.06

**Table 7** Values of the average durations of gas structures  $\bar{t}_1$ ,  $\bar{t}_b$  and the corresponding frequencies  $\bar{f}_1$  and  $\bar{f}_b$

LIW0005				LIW0003			
$\bar{t}_1$ (ms)	$\bar{f}_1$ (Hz)	$\bar{t}_b$ (ms)	$\bar{f}_b$ (Hz)	$\bar{t}_1$ (ms)	$\bar{f}_1$ (Hz)	$\bar{t}_b$ (ms)	$\bar{f}_b$ (Hz)
2712	0.37	1305	0.77	1885	0.53	940	1.06

the LIW0005 measurement is  $\bar{l}_b = (1.81 \pm 0.07)$  m, and for the LIW0003 measurement, it is  $\bar{l}_b = (1.69 \pm 0.05)$  m. By comparing these results with the values indicated in Table 6, one may observe that there is a considerable congruity of the values obtained due to an analysis of the signal in the domain of time and frequency.

As far as the modelling of signals is concerned, the average duty cycle, which may be defined in the following way for the measurements which were performed, is also important:

$$\zeta_t = \frac{\bar{l}_b}{l_1} \quad (27)$$

$$\zeta_f = \frac{f_0}{f_2} \quad (28)$$

After an analysis of a sample of 50 fragments of the signal for the LIW0005 measurement, one established  $\zeta_t = 0.48$  and  $\zeta_f = 0.50$ . As far as the LIW0003 measurement is concerned, the average duty cycle is  $\zeta_t = \zeta_f = 0.50$ , respectively.

### Plug flow

The flow of the plug type, despite many similarities to the flow of the slug type, also manifests features which are peculiar only to itself in reference to the signal which was registered, both in the domain of time and in the domain of frequency.

Figure 12a, b presents signals from radioisotope probes registered in the LIW0004 and LIW0002 measurements.

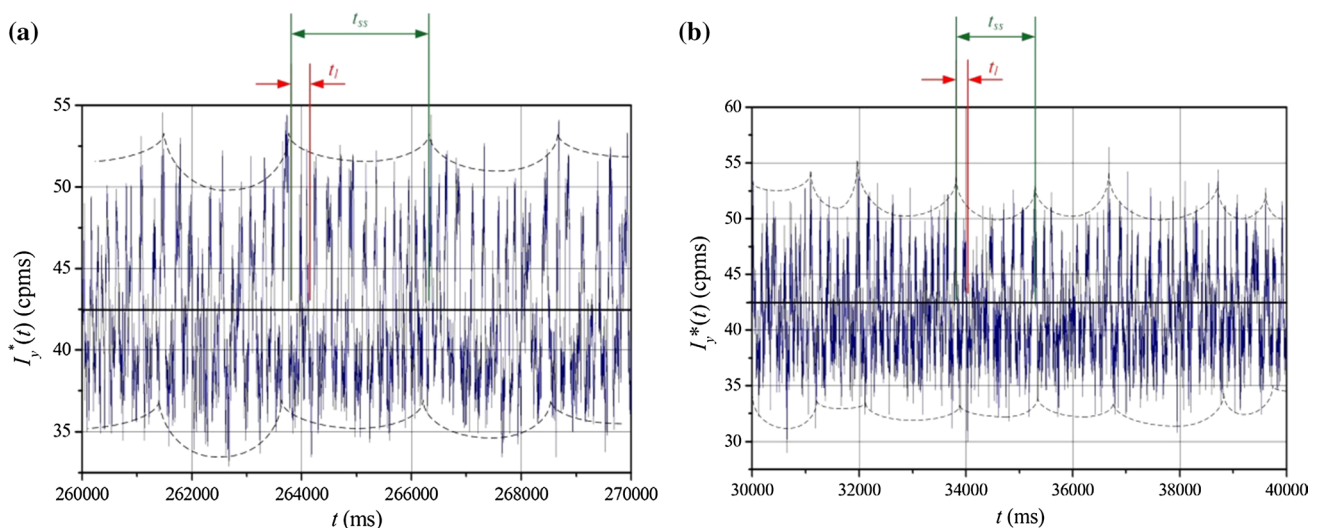


**Fig. 12** Fragments of signals from radiometric probes for the flows of the plug type, obtained in the measurements: **a** LIW0004, **b** LIW0002

The flow of this type features a basic (large) structure which consists of a large gas bubble (whose duration is  $t_l$ ), and whose length is considerably smaller than in the case of the slug flows (images in Fig. 3c, d), as well as the area in which smaller bubbles are located. Moreover, on the basis of an analysis of the signal, one may distinguish one more greater structure—the so-called superstructure (duration  $t_{ss}$ ), which consists of a few or of up to a dozen or so basic structures.

The graphs in Fig. 13a, b present the distributions of the lengths of large structures and bubbles calculated according to the relationships (Eqs. 20, 21) for selected subsequent 50 fragments of signals in the LIW0004 and LIW0002 measurements.

A comparison of the graphs in Fig. 11a, b with the graphs in Fig. 13a, b, as well as Tables 6 and 8, demonstrates that not only gas structures in the flow of the plug type are shorter but also the relative variation of their length is greater than in the case of the flows of the slug type.

Considerable variation of the depths of gas structures (Fig. 7c, d) and their lengths may be caused by the existence of superstructures of a gas phase. The distribution of the lengths of these superstructures for the 50 fragments of the signals is indicated by the graphs in Fig. 14a, b. The lengths of the superstructures of gas were calculated analogously as in the case of gas structures (Eq. 20). In both graphs, the average value of their lengths  $\bar{l}_{ss}$  was indicated by means of a continuous line, whereas Table 9 presents the average values of the lengths of the superstructures, their uncertainties  $u_c(\bar{l}_{ss})$  and standard deviations  $\sigma_{ss}$ . On the basis of an analysis which was performed, one stated that the superstructures consist of two to 21 large gas structures.

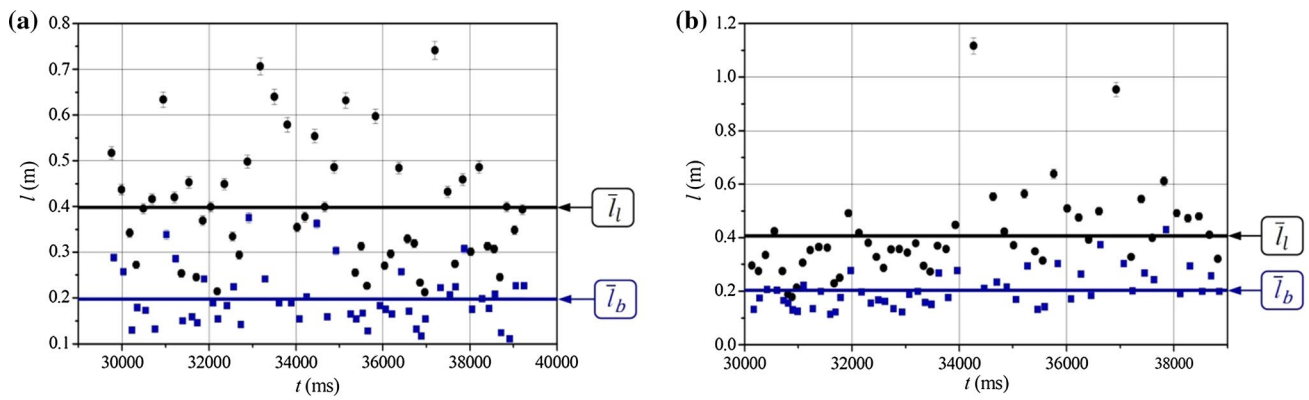


**Fig. 13** Distribution of the values of the lengths of gas structures for the flows of the plug type: **a** LIW0004, **b** LIW0002

**Table 8** Average values of the lengths of structures  $\bar{l}_l$  and  $\bar{l}_b$  along with the standard deviations  $\sigma_l$ ,  $\sigma_b$  and the uncertainties  $u_c(\bar{l}_l)$ ,  $u_c(\bar{l}_b)$  for the flows of the plug type

Run	$\bar{l}_l$ (m)	$\sigma_l$ (m)	$u_c(\bar{l}_l)$ (m)	$\bar{l}_b$ (m)	$\sigma_b$ (m)	$u_c(\bar{l}_b)$ (m)
LIW0004	0.398	0.134	0.021	0.198	0.063	0.010
LIW0002	0.406	0.167	0.026	0.202	0.067	0.011

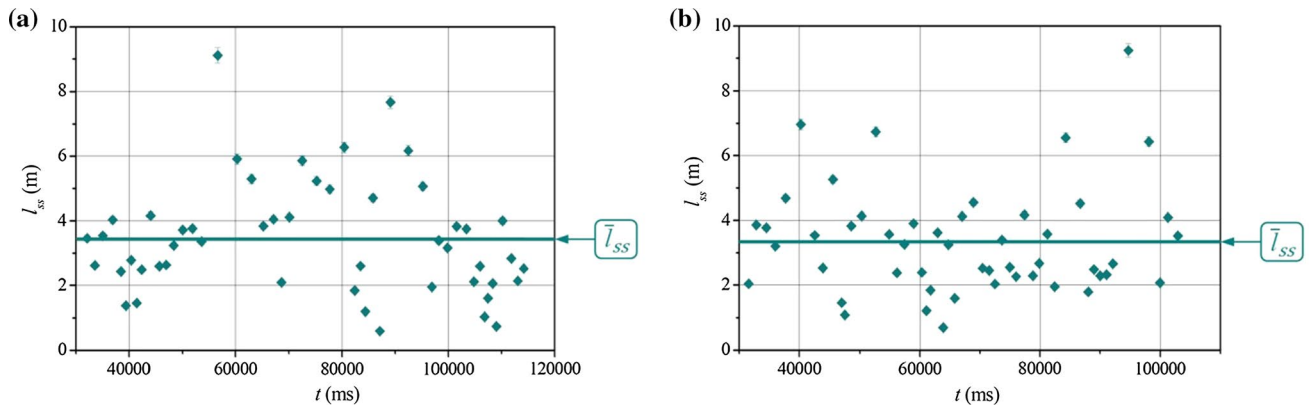


**Fig. 14** Distribution of the values of the gas superstructures for the flows of the plug type: **a** LIW0004, **b** LIW0002

Such a form of durations (Fig. 12a, b) manifests itself in a peculiar way in the domain of frequency. |CSDF| spectra for the measurements which were analysed are illustrated by the graphs in Fig. 15a, b. In these graphs, the frame (1) indicates the range in which the dominant frequency  $f_0$  is located, whereas the frame (2) indicates the range of the useful signal, for which the maximum is indicated by a purple dashed line—the frequency  $f_u$ . Table 10 presents the values  $f_0$  and  $f_u$  for both measurements which were analysed.

Similarly as in the case of the flow of the slug type (Chapter 4.3.1), also in this case the association of the frequency (frequencies) with physical phenomena which occur in a flow

**Table 9** Average lengths of the superstructures  $\bar{l}_{ss}$  with the standard deviation  $\sigma_{ss}$  and the uncertainty of the measurement  $u_c(\bar{l}_{ss})$ , for the measurement of the plug type

Run	$\bar{l}_{ss}$ (m)	$\sigma_{ss}$ (m)	$u_c(\bar{l}_{ss})$ (m)
LIW0004	3.44	1.75	0.09
LIW0002	3.34	1.67	0.09

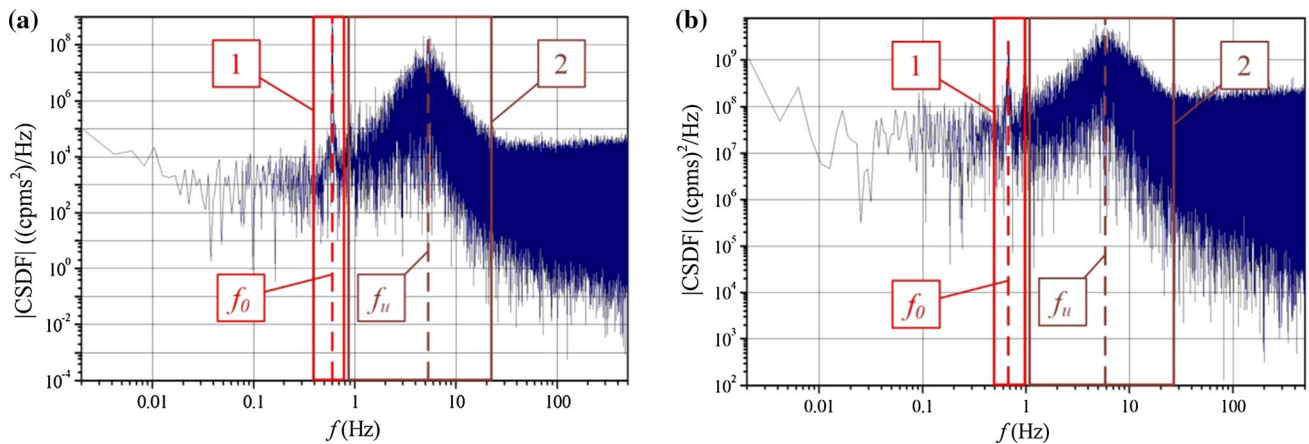


**Fig. 15** |CSDF| spectra for the measurements: **a** LIW0004, **b** LIW0002

**Table 10** Values of the dominant frequencies  $f_0$  and  $f_u$  in the |CSDF| spectrum for the flow of the plug type

Run	$f_0$ (Hz)	$f_u$ (Hz)
LIW0004	0.60	5.18
LIW0002	0.67	5.70

may be conducted by calculating the frequencies for the average durations of the flow of gas structures. Hence, one may calculate the frequency for the average duration of a superstructure  $\bar{t}_{ss}$ :

$$\bar{f}_{ss} = \frac{1}{\bar{t}_{ss}} \tag{29}$$

whereas for the average duration of a large gas structure  $\bar{t}_1$  and the average duration of a large bubble  $\bar{t}_b$ , the respective frequencies are calculated according to the formulae (Eqs. 23, 24). Table 11 presents a average durations  $\bar{t}_{ss}$ ,  $\bar{t}_1$ ,  $\bar{t}_b$  and the corresponding frequencies  $\bar{f}_{ss}$ ,  $\bar{f}_1$  and  $\bar{f}_b$ .

It follows from a comparison of Tables 10 and 11 that there is a considerable congruity of the values of the frequencies  $\bar{f}_{ss}$  and  $f_0$  as well as  $\bar{f}_1$  and  $f_u$ . Hence, it follows that the dominant frequency  $f_0$  should be associated with the flow of superstructures. Therefore, the average length of a superstructure may be calculated on the basis of the following formula:

$$\bar{t}_{ss} = \frac{v_G}{f_0} \tag{30}$$

This implies the establishment of a dependency on the complex uncertainty of  $\bar{t}_{ss}$ :

$$u_c(\bar{t}_{ss}) = \sqrt{\left(\frac{1}{f_0} u_c(v_G)\right)^2 + \left(\frac{v_G}{(f_0)^2} u_B(f_0)\right)^2} \tag{31}$$

The uncertainty  $u_B(f_0)$  was assumed to be equal to 0.0042 Hz, which results from the precision of the interpretation of the value of the frequency  $f_0$  from the |CSDF| spectrum.

On the basis of the analyses which were performed, one may claim that the length of a superstructure calculated on the basis of the formula (Eq. 28) for the measurement LIW0004 is:  $\bar{t}_{ss} = (3.43 \pm 0.09)$  m, whereas for the measurement LIW0002:  $\bar{t}_{ss} = (3.41 \pm 0.09)$  m. The considerations which were conducted also indicate that the frequency  $f_0$  is responsible for the modulations of the amplitude of the signal in the domain of time.

The equality of frequencies  $\bar{f}_1$  and  $f_u$  allows to write an alternative dependence on the length  $l_1$  in relation to the formula (Eq. 20):

$$\bar{t}_1 = \frac{v_G}{f_u} \tag{32}$$

while the complex uncertainty  $u_c(\bar{t}_1)$  may be described by a dependency similar to (Eq. 29).

By analysing the average duty cycle  $\zeta_i$ , calculated on the basis of data presented in Table 8, one may claim that for both measurements—LIW0004 and LIW0002— $\zeta_i \approx 0.50$ . Therefore, one may present the expression which refers to the average length of a large bubble as:

**Table 11** Average values of the durations of superstructures  $\bar{t}_{ss}$  and gas structures  $\bar{t}_1$ ,  $\bar{t}_b$  and the corresponding frequencies  $\bar{f}_{ss}$ ,  $\bar{f}_1$  and  $\bar{f}_b$

LIW0004						LIW0002					
$\bar{t}_{ss}$ (ms)	$\bar{f}_{ss}$ (Hz)	$\bar{t}_1$ (ms)	$\bar{f}_1$ (Hz)	$\bar{t}_b$ (ms)	$\bar{f}_b$ (Hz)	$\bar{t}_{ss}$ (ms)	$\bar{f}_{ss}$ (Hz)	$\bar{t}_1$ (ms)	$\bar{f}_1$ (Hz)	$\bar{t}_b$ (ms)	$\bar{f}_b$ (Hz)
1670	0.60	193	5.17	96	10.38	1452	0.69	176	5.67	88	11.38



$$\bar{l}_b = \frac{v_G}{2 \cdot f_u} \quad (33)$$

The calculations which were made on the basis of the equations (Eqs. 32, 33) enable us to estimate the average length of gas structures for the LIW0004 measurement  $\bar{l}_1 = (0.398 \pm 0.010)$  m and for LIW0002  $\bar{l}_1 = (0.404 \pm 0.011)$  m, whereas the lengths of large bubbles for the LIW0004 measurement are  $\bar{l}_b = (0.199 \pm 0.005)$  m, and for LIW0002 measurement  $\bar{l}_b = (0.202 \pm 0.05)$  m.

## Conclusion

The article presents an analysis of the signals from the radiometric measurement system for the absorption of gamma rays which consists of a set of two scintillation probes and from two sealed sources of Am-241. The analyses were performed in the time and frequency domain for intermittent flows of the slug and plug types. One distinguished the parameters of signals which were associated with physical quantities of the mixture which flowed. The amplitudes of the signals were associated with the depth of gas structures, whereas the dominant frequencies were associated with the lengths of these structures. One additionally introduced non-dimensional quantities for the description of the liquid–gas flow such as the average coefficient of the duty cycle  $\zeta$ , the relationship of the average depth of the large gas structure to the average depth of a large bubble  $\xi_1$ , and the relationship of the average depth of small gas structures located between large bubbles to the average depth of large bubbles  $\xi_s$ . The obtained values of these parameters are similar for the analysed measurements.

Apart from the similarities, one also established the existence of differences of parameters of signals which occur in the time and frequency domain for the types of flows which were described.

In a flow of the slug type, there occur basic structures which consist of a large bubble and of a number of smaller structures which are situated in the space between large bubbles. The values of the amplitudes of signals from probes are at a constant level, which results in a decreased standard deviation of the estimated average depths of gas in the fragments of the gas which were analysed. In a frequency spectrum |CSDF|, there occur harmonic dominants which are even and odd multiples of the frequency  $f_0$ . After the results of the analysis were compared, one stated that the frequency  $f_0$  is associated with the movement of a large gas structure. The knowledge of the average speed of the movement of gas enables the estimation of the average length of such structures. The frequency which is the double multiple of  $f_0$  is associated with the average length of large bubbles in a large gas structure.

However, in the flow of the plug type, one may distinguish in the duration considerably greater superstructures, apart from large gas structures, which are similar to the ones in the flow of the slug type. In a frequency spectrum |CSDF|, this manifests itself by two salient ranges: the range of the dominant frequency  $f_0$ , associated with the flow and the average size of superstructures, and the range of the frequency of the useful signal. The harmonic dominant for this range  $f_u$  is associated with the flow and the average size of large gas structures. Hence, one may draw a conclusion that the frequency  $f_0$  is directly associated with the modulation of the signal, i.e. periodical change of an amplitude. As a result, the standard deviation of the changes of the depths of gas structures is greater for flows of the plug type than in the case of the flows of the slug type.

On the basis of the measurements and analyses which were performed, one may develop models of signals for the liquid–gas flows in question, studied by means of the method of the absorption of gamma rays. The results which are obtained may be used in the more efficient identification of two-phase liquid–gas flows in the installations intended for hydrotransport of gas, in which there is no optical access to the mixture which flows through.

**Acknowledgements** The author would like to specially thank Prof. Robert Hanus, Prof. Marek Jaszczur, Dr Paweł Jodłowski, Prof. Volodymyr Mosorov, Dr Leszek Petryka, Prof. Dariusz Świsulski for their cooperation during the measurements and support in the writing of the manuscript.

**Funding** This publication was financed by the AGH University of Science and Technology, Faculty of Geology Geophysics and Environmental Protection (Grant No 11.11.140.645).

## Compliance with ethical standards

**Conflict of interest** The author declares that there is no conflict of interest regarding the publication of this paper.

**Open Access** This article is distributed under the terms of the Creative Commons Attribution 4.0 International License (<http://creativecommons.org/licenses/by/4.0/>), which permits unrestricted use, distribution, and reproduction in any medium, provided you give appropriate credit to the original author(s) and the source, provide a link to the Creative Commons license, and indicate if changes were made.

## References

- Ameran HLM, Mohamad EJ, Muji SZM et al (2017) Multiphase flow velocity measurement of chemical processes using electrical tomography: a review. In: Proceedings—2016 IEEE international conference on automatic control and intelligent systems, I2CACIS 2016
- Arkani M, Khalafi H, Vosoughi N, Khakshournia S (2017) Development and experimental validation of a correlation monitor tool

- based on the endogenous pulsed neutron source technique. *Metrologia* 24:441–461. <https://doi.org/10.1515/mms-2017-0043>
- Arvoh BK, Hoffmann R, Halstensen M (2012) Estimation of volume fractions and flow regime identification in multiphase flow based on gamma measurements and multivariate calibration. *Flow Meas Instrum* 23:56–65. <https://doi.org/10.1016/j.flowmeasinst.2011.11.002>
- Banasiak R, Wajman R, Jaworski T, Fiderek P, Fidos H, Nowakowski J, Sankowski D (2014) Study on two-phase flow regime visualization and identification using 3D electrical capacitance tomography and fuzzy-logic classification. *Int J Multiphase Flow* 58:1–14. <https://doi.org/10.1016/j.ijmultiphaseflow.2013.07.003>
- Beck MS, Płaskowski A (1987) Cross-correlation flowmeters. Their design and application. Adam Hilger, Bristol
- Bendat JS, Piersol AG (2010) Random data. Analysis and measurement procedures, 4th edn. Wiley, New York
- Biswal J, Pant HJ, Goswami S et al (2018) Measurement of flow rates of water in large diameter pipelines using radiotracer dilution method. *Flow Meas Instrum* 59:194–200. <https://doi.org/10.1016/j.flowmeasinst.2017.12.014>
- Buttkus B (2000) Spectral analysis and filter theory in applied geophysics. Springer, Berlin
- Chaouki J, Larachi F, Dudukovic M (1997) Non-invasive monitoring of multiphase flows. Elsevier, Amsterdam
- de Oliveira WR, de Paula IB, Martins FJWA, Farias PSC, Azevedo LFA (2015) Bubble characterization in horizontal air–water intermittent flow. *Int J Multiphase Flow* 69:18–30. <https://doi.org/10.1016/j.ijmultiphaseflow.2014.10.014>
- Falcone G, Hewitt GF, Alimonti C (2009) Multiphase flow metering: principles and applications. Elsevier, Amsterdam
- García JT, Viguera-Rodríguez A, Castillo LG, Carrillo JM (2017) Evaluation of sulfide control by air-injection in sewer force mains: field and laboratory study. *Sustainability* 9(3):402. <https://doi.org/10.3390/su9030402>
- Gołębiowski T, Porzucek S, Pasierb B (2016) Ambiguities in geophysical interpretation during fracture detection—case study from a limestone quarry (Lower Silesia Region, Poland). *Near Surf Geophys* 14:371–384. <https://doi.org/10.3997/1873-0604.2016017>
- Guide (1995) Guide to the expression of uncertainty in measurement. International Organization for Standardization, Geneva
- Gulhane NP, Mahulikar SP (2009) Variations in gas properties in laminar micro-convection with entrance effect. *Int J Heat Mass Transf* 52:1980–1990. <https://doi.org/10.1016/j.ijheatmasstransfer.2008.08.037>
- Hanus R (2003) Statistical error analysis of time delay measurement by using phase of cross-spectral density function. *Syst Anal Model Simul* 43(8):993–998. <https://doi.org/10.1080/0232929031000080632>
- Hanus R (2009) The application of the Hilbert transform to correlation measurements of time delay. *Prz Elektrotech* 85(7):45–48
- Hanus R (2015) Application of the Hilbert transform to measurements of liquid–gas flow using gamma ray densitometry. *Int J Multiphase Flow* 72:210–217. <https://doi.org/10.1016/j.ijmultiphaseflow.2015.02.002>
- Hanus R, Petryka L, Zych M (2014) Velocity measurement of the liquid–solid flow in a vertical pipeline using gamma-ray absorption and weighted cross-correlation. *Flow Meas Instrum* 40:58–63. <https://doi.org/10.1016/j.flowmeasinst.2014.08.007>
- Hanus R, Zych M, Kusy M, Jaszczur M, Petryka L (2018) Identification of liquid–gas flow regime in a pipeline using gamma-ray absorption technique and computational intelligence methods. *Flow Meas Instrum* 60:17–23. <https://doi.org/10.1016/j.flowmeasinst.2018.02.008>
- Heindela TH, Grayb JN, Jensenb TC (2008) An X-ray system for visualizing fluid flows. *Flow Meas Instrum* 19:67–78. <https://doi.org/10.1016/j.flowmeasinst.2007.09.003>
- Jarzyna JA, Krakowska PI, Puskarczyk E, Wawrzyniak-Guz K, Bielecki J, Tkocz K, Tarasiuk J, Wroński S, Dohnalik M (2016) X-ray computed microtomography—a useful tool for petrophysical properties determination. *Comput Geosci* 20(5):1155–1167. <https://doi.org/10.1007/s10596-016-9582-3>
- Jaszczur M, Portela LM (2008) Numerical data for reliability of LES for non-isothermal multiphase turbulent channel flow. In: Meyers J, Geurts B, Sagaut P (eds) Quality and reliability of large-eddy simulations. Springer, New York, pp 343–354. [https://doi.org/10.1007/978-1-4020-8578-9\\_28](https://doi.org/10.1007/978-1-4020-8578-9_28)
- Johansen G, Jackson P (2004) Radioisotope gauges for industrial process measurements. Wiley, New York
- Kanizawa FT, Ribatski G (2016) Two-phase flow patterns across triangular tube bundles for air–water upward flow. *Int J Multiphase Flow* 80:43–56. <https://doi.org/10.1016/j.ijmultiphaseflow.2015.11.004>
- Knoll GF (2000) Radiation detection and measurement, 3rd edn. Wiley, New York
- Kowalczyk A, Hanus R, Szlachta A (2011) Investigation of the statistical method of time delay estimation based on conditional averaging of delayed signal. *Metrologia* 17(2):335–342. <https://doi.org/10.2478/v10178-011-0015-3>
- Kozłowska M, Orlecka-Sikora B, Rudziński Ł, Cielesta S, Mutke G (2016) A typical evolution of seismicity patterns resulting from the coupled natural, human-induced and coseismic stresses in a longwall coal mining environment. *Int J Rock Mech Mini Sci* 86:5–15. <https://doi.org/10.1016/j.ijrmms.2016.03.024>
- Krakowska P, Puskarczyk E (2015) Tight reservoir properties derived by nuclear magnetic resonance, mercury porosimetry and computed microtomography laboratory techniques Case study of Palaeozoic clastic rocks. *Acta Geophys* 63(3):789–814. <https://doi.org/10.1515/acgeo-2015-0013>
- Kumara WAS, Halvorsen BM, Melaaen MC (2010) Single-beam gamma densitometry of oil–water flow in horizontal and slightly inclined pipes. *Int J Multiphase Flow* 36:467–480. <https://doi.org/10.1016/j.ijmultiphaseflow.2010.02.003>
- Kundu S, Kumbhakar M, Ghoshal K (2017) Reinvestigation on mixing length in an open channel turbulent flow. *Acta Geophys*. <https://doi.org/10.1007/s11600-017-0109-7>
- Morgado AO, Miranda JM, Araújo JDP, Campos JBLM (2016) Review on vertical gas–liquid slug flow. *Int J Multiphase Flow* 85:348–368. <https://doi.org/10.1016/j.ijmultiphaseflow.2016.07.002>
- Mosorov V (2006a) A method of transit time measurement using twin plane electrical tomography. *Meas Sci Technol* 17:753–760. <https://doi.org/10.1088/0957-0233/17/4/022/meta>
- Mosorov V (2006b) Phase spectrum method for time delay estimation using twin-plane electrical capacitance tomography. *Electron Lett* 42(11):630–632. <https://doi.org/10.1049/iel:20060338>
- Mosorov V (2008) Flow pattern tracing for mass flow rate measurement in pneumatic conveying using twin plane electrical capacitance tomography. *Part Part Syst Charact* 25(3):259–265. <https://doi.org/10.1002/ppsc.200700034>
- Pietsch K, Marzec P, Kobylarski M, Danek T, Leśniak A, Tatarata A, Gruszczyk E (2007) Identification of seismic anomalies caused by gas saturation on the basis of theoretical P and PS wavefield in the Carpathian Foredeep, SE Poland. *Acta Geophys* 55(2):191–208. <https://doi.org/10.2478/s11600-007-0002-x>
- Powell RL (2008) Experimental techniques for multiphase flows. *Phys Fluids* 20:040605. <https://doi.org/10.1063/1.2911023>
- Rahim AR, Yunus MY, Rahiman MHF, Muji SZM, Thiam ChK, Rahim HA (2012) Optical tomography: velocity profile measurement using orthogonal and rectilinear arrangements. *Flow Meas Instrum* 23:49–55. <https://doi.org/10.1016/j.flowmeasinst.2011.10.006>
- Roshani GH, Nazemi E (2017) Intelligent densitometry of petroleum products in stratified regime of two phase flows using gamma

- ray and neural network. *Flow Meas Instrum* 58:6–11. <https://doi.org/10.1016/j.flowmeasinst.2017.09.007>
- Roshani GH, Nazemi E, Roshani MM (2017a) Application of radial basis function in densitometry of stratified regime of liquid–gas two phase flows. *Radiat Meas* 100:9–17. <https://doi.org/10.1016/j.radmeas.2017.03.001>
- Roshani GH, Nazemi E, Roshani MM (2017b) Identification of flow regime and estimation of volume fraction independent of liquid phase density in gas–liquid two-phase flow. *Prog Nucl Energy* 98:29–37. <https://doi.org/10.1016/j.pnucene.2017.02.004>
- Rzasa MR (2009) The measuring method for tests of horizontal two-phase gas–liquid flows, using optical and capacitance tomography. *Nucl Eng Des* 239:699–707. <https://doi.org/10.1016/j.nucengdes.2008.12.020>
- Salgado CM, Pereira C, Schirru R, Brandão LEB (2010) Flow regime identification and volume fraction prediction in multiphase flows by means of gamma-ray attenuation and artificial neural networks. *Prog Nucl Energy* 52:555–562. <https://doi.org/10.1016/j.pnucene.2010.02.001>
- Sommerlatt H-D, Andruszkiewicz A (2008) Dynamic measurement of particle diameter and drag coefficient using the ultrasonic method. *Arch Acoust* 33:351–362
- Szabó NP, Dobróka M (2017) Robust estimation of reservoir shaliness by iteratively reweighted factor analysis. *Geophysics* 82(2):D69–D83. <https://doi.org/10.1190/geo2016-0393.1>
- Tamburini A, Cipollina A, Micale G, Brucato A (2013) Particle distribution in dilute solid liquid unbaffled tanks via a novel laser sheet and image analysis based technique. *Chem Eng Sci* 87:341–358. <https://doi.org/10.1016/j.ces.2012.11.005>
- Vlasak P, Chara Z, Krupicka J, Konfrst J (2014) Experimental investigation of coarse particles–water mixture flow in horizontal and inclined pipes. *J Hydrol Hydromech* 62(3):241–247. <https://doi.org/10.2478/johh-2014-00>
- Vlasak P, Chara Z, Konfrst J (2017) Flow behaviour and local concentration of coarse particles–water mixture in inclined pipes. *J Hydrol Hydromech* 65(2):183–191. <https://doi.org/10.1515/johh-2017-0001>
- Witeczak S, Zuber A, Kmiecik E, Kania J, Szczepańska J, Róžański K (2009) Tracer based study of the Badenian Bogucice Sands Aquifer, Poland. *Nat Groundw Qual*. <https://doi.org/10.1002/9781444300345.ch15>
- Xue T, Qu L, Cao Z, Zhang T (2012) Three-dimensional feature parameters measurement of bubbles in gas–liquid two-phase flow based on virtual stereo vision. *Flow Meas Instrum* 27:29–36. <https://doi.org/10.1016/j.flowmeasinst.2012.07.007>
- Zeng X, Zhu Z, Chen Y (2016) Remote evaluation of rotational velocity using a quadrant photo-detector and a DSC algorithm. *Sensors (Switzerland)*. <https://doi.org/10.3390/s16050587>
- Zhao Y, Qincheng B, Richa H (2013) Recognition and measurement in the flow pattern and void fraction of gaseliquid two-phase flow in vertical upward pipes using the gamma densitometer. *Appl Therm Eng* 60:398–410. <https://doi.org/10.1016/j.applthermaleng.2013.07.006>
- Zych M, Hanus R, Petryka L (2014) Application of spectral analysis in radiometric measurements of two-phase liquid–gas flow. *MATEC Web Conf* 18:02004. <https://doi.org/10.1051/mateconf/20141802004>
- Zych M, Hanus R, Petryka L, Świsulski D, Strzępowicz A, Zych P (2015) Application of gamma densitometry and statistical signal analysis to gas phase velocity measurements in pipeline hydrotransport. *EPJ Web Conf* 92:02122. <https://doi.org/10.1051/epjconf/20159202122>
- Zych M, Hanus R, Jaszczur M, Strzępowicz A, Petryka L, Mastej W (2016) Determination of void fraction in two phase liquid–gas flow using gamma absorption. *JPCS* 745:032124. <https://doi.org/10.1088/1742-6596/745/3/032124>
- Zych M, Hanus R, Vlasák P, Jaszczur M, Petryka L (2017) Radiometric methods in the measurement of particle-laden flows. *Powder Technol* 318:491–500. <https://doi.org/10.1016/j.powtec.2017.06.019>
- Zych M, Hanus R, Jaszczur M, Świsulski D, Petryka L, Jodłowski P, Zych P (2018) Evaluation of the structures size in the liquid–gas flow by gamma-ray absorption. *EPJ Web Conf* 180:02123. <https://doi.org/10.1051/epjconf/201818002123>



# A novel approach to the quantitative interpretation of petrophysical parameters using nano-CT: example of Paleozoic carbonates

Edyta Puskarczyk<sup>1</sup> · Paulina Krakowska<sup>1</sup> · Mariusz Jędrychowski<sup>2</sup> · Magdalena Habrat<sup>1</sup> · Paweł Madejski<sup>3</sup>

Received: 6 March 2018 / Accepted: 25 October 2018 / Published online: 31 October 2018  
© The Author(s) 2018

## Abstract

The main goal was the analysis of parameters describing the structure of the pore space of carbonate rocks, based on tomographic images. The results of CT images interpretation, made for 17 samples of Paleozoic carbonate rocks were shown. The qualitative and quantitative analysis of a pore system was performed. Objects were clustered according to the pore size. Within the clusters, the geometry parameters were analysed. The following dependences were obtained for carbonate rocks, also for individual clusters (due to the volume): (1) a linear relationship (on a bilogarithmic scale) between the specific surface and the Feret diameter and (2) a strong linear relationship between specific surface area and Feret diameter and average diameter of the objects calculated for the sphere. The results were then combined with available results from standard laboratory tests, including NMR and MICP.

**Keywords** Computed X-ray tomography · Carbonates · Paleozoic rocks · Petrophysics · Rock properties

## Introduction

Hydrocarbons trapped in carbonate rocks (limestone and dolomite) account for approximately 50% of oil and gas production around the world. Carbonate Paleozoic deposits are found in the interest of geologists and geophysicists due to possible hydrocarbon accumulation (Jaworowski and Mikołajewski 2007). Petrophysical properties of Paleozoic rocks are the target of investigation especially in the face of new research techniques and measuring capabilities (Akbar et al. 1995). Reservoirs in carbonate rocks are multiporosity and present significant petrophysical heterogeneity in the reservoir scale. That is the main reason of huge petrophysical heterogeneity to the reservoirs (Mazzullo and Chilingarian 1992). The distribution and volume of pores

exert strong control on the production and stimulation characteristics of carbonate reservoirs (Wardlaw 1996).

New technologies in laboratory researches together with well-known conventional laboratory techniques on rocks were the basis of detailed rock analysis. Nano-CT (nano-computed X-ray tomography) with high image resolution is one of the novel techniques, which can be used for evaluation of key reservoir parameters in tight formations (Arns et al. 2005; Wennberg et al. 2009; Dohnalik 2013; Exner et al. 2015; Teles et al. 2016). Standard quantitative interpretation algorithms of CT (computed X-ray tomography) image analysis linked to petrophysical information were used in the paper. On this basis, a unique information on the low porosity and low permeability carbonates was obtained (Krakowska and Puskarczyk 2015; Krakowska et al. 2017).

We focused on non-classical carbonate reservoir rocks. As a research material, carbonate formations with low porosity and low permeability were chosen. This type of carbonates is much more difficult to interpret using standard techniques (Wei et al. 2017).

In this paper, we describe research material based on the standard laboratory results, e.g. density, formation factor, porosity, permeability. Also a brief description of main laboratory technique is shown. In a following section, we describe more detailed nano-CT technique. Results section contains plots, tables and description of analysed parameters.

✉ Edyta Puskarczyk  
puskar@agh.edu.pl

<sup>1</sup> Faculty of Geology, Geophysics and Environmental Protection, AGH University of Science and Technology, Kraków, Poland

<sup>2</sup> Faculty of Physics and Applied Computer Science, AGH University of Science and Technology, Kraków, Poland

<sup>3</sup> Faculty of Mechanical Engineering and Robotics, AGH University of Science and Technology, Kraków, Poland



In the discussion, we compared nano-CT analysis results with the other conventional parameters and discuss usefulness of the CT method in carbonates. New approach is presented: pore size analysis in carbonates based on nano-CT with division into clusters, quantitative interpretation and evaluation of low porosity and low permeability carbonates based only on the results of quantitative analysis of CT images.

New software poROSE was presented as porous materials examination software for images qualitative and quantitative interpretation (Habrát et al. 2017).

## Materials and Methods

The research material consisted of carbonate samples—limestones (8 samples) and dolomites (9 samples). All samples were collected from several wells located at the northern part of Poland. Six limestone samples belongs to Devonian (D), one to Permian (P) and one to Ordovician (O) age deposits. Among dolomites, four belong to Devonian (D) and five to Permian (P) age deposits.

### Conventional petrophysical measurements

Standard laboratory measurements of petrophysical properties (e.g. skeletal density, bulk density, formation factor, P—wave velocity, S—wave velocity, permeability, total porosity, effective porosity) were made for all samples.

The use of different porosity measurement techniques showed the variation of this parameter depending on the measurement method. In this paper, several porosity measurement techniques were used:

- 1) Helium pycnometer (He pyc) for total porosity measurements (Webb 2001a)
- 2) Nuclear magnetic resonance (NMR) for total and effective porosity measurements (Coates et al. 1999)
- 3) Mercury injection capillary pressure (MICP) for effective porosity measurements (Webb 2001b)

### Computed X-ray tomography measurements

Computed tomography (CT) is one of the modern techniques for 3D imaging using X-rays. High-resolution X-ray computed tomography, also referred as micro-CT or nano-CT, emerges as the most appropriate technique applied in order to analyse spatial distribution of pores. This non-invasive method provides the information about porosity and internal structure of the pore space including number of pores, channels, connections and directions.

CT measurements were conducted with Nanotom S General Electric nanotomograph working with high power X-ray tube

with maximum operating voltage equal 180 kV. In CT technique, X-ray radiation passing through the sample is absorbed. Depending on the object properties, the radiation is weakened in varying degree—usually the highest density of the object, the weakness. Initial 3D data consisting in this case (for most of analysed samples) of  $1500 \times 1500 \times 2500$  voxels, where each voxel represents  $0.5 \times 0.5 \times 0.5 \mu\text{m}^3$  in 3D space, were reconstructed using Feldkamp back-projection method. The back-projection algorithm is a process mathematical relying on obtaining a processed image. Segmentation algorithm, as a next step, consists of following parts: (a) initial processing with median filter, (b) first histogram thresholding, (c) application of Fourier bandpass filter, (d) second histogram thresholding with triangle method, (e) morphological operations combined with median filter.

The results of computerized X-ray nano-CT are presented in the form visualization of 3D pore space. Visualization of the 3D pore space allows on the qualitative interpretation of its distribution, with division objects (pores) into subgroups according to the size of the pores.

The quantitative interpretation of CT images includes determination of petrophysical parameters from the geometrical parameters. The following geometrical parameters were calculated: volume of pores,  $x$ ,  $y$  and  $z$ -coordinate of pore centroid, surface area, volume enclosed by surface mesh, moment of inertia around shortest principal axis, middle principal axis and longest principal axis, mean local thickness of pore, standard deviation of the mean local thickness, maximum local thickness, length of best-fit ellipsoid's long radius, intermediate radius and short radius, Feret diameter, sphericity and pore throat diameters. All these parameters are related to the geometry of the imaged pores. Unfortunately, due to the simplifications used in their calculation (e.g. approximation of the pore shape with the sphere or ellipsoid), not all of them can be correlated with the petrophysical parameters of rocks. In this paper, we focused on parameters which show the relation with the petrophysical properties of rocks: Total Porosity from CT ( $\Phi_{\text{CT}}$ , volume of pores), %—calculated as a sum of voxels (converted into  $\mu\text{m}$ ) defined as the pores (low density at the CT images); Surface Area,  $\mu\text{m}^2$ —calculated as a sum of voxels at the edge of the objects; Thickness (mean local thickness of pores approximate as sphere),  $\mu\text{m}$ —defined as a mean local thickness of particle; Pore/Throat—calculated as a mean particle thickness/throat thickness ratio; Feret Diameter,  $\mu\text{m}$ —is a measure of an object size along a specified direction. In 3D objects, the Feret diameter is usually defined as the distance between two parallel tangential lines.

## Results and discussion

### Basic statistics

The basic statistics of conventional petrophysical parameters for analysed lithological types are presented in Table 1 (abbreviations: Ls means limestone, Do means dolomites, He pyc means helium pycnometer, NMR means nuclear magnetic resonance, MICP means mercury injection capillary pressure).

The main goal of the CT measurements is the total porosity calculation. It was done by summarizing the object with the lowest density on the CT images. Results of calculation were added (black points) to the plot in Fig. 1. It can be shown that there is no ambiguous dependency between total porosity from CT and other methods. For some samples, e.g. Ls\_D6 or Do\_D7 results obtained from CT are almost equal to porosity from NMR. However, in the most cases, e.g. Ls\_D3 or Do\_P5, porosity from CT is much higher than from the other methods.

Figure 1 shows the values of porosity from various measurement methods, registered for individual samples. In most cases, the total porosity values from He pyc are close to one from NMR (except samples number Do\_P4 and Do\_P5, where porosity from NMR are much higher than from He pyc). Similar situation can be observed for effective porosity from NMR and MICP (except sample Do\_P5). The largest spread of the values of total porosity from three methods CT, NMR and He pyc was observed for Ls\_O1, Ls\_D3, Ls\_D5 and Do\_P5 samples.

There are several reasons for such large differences:

- various physical phenomena on which measurement methods are based,
- various measurement resolution limits,

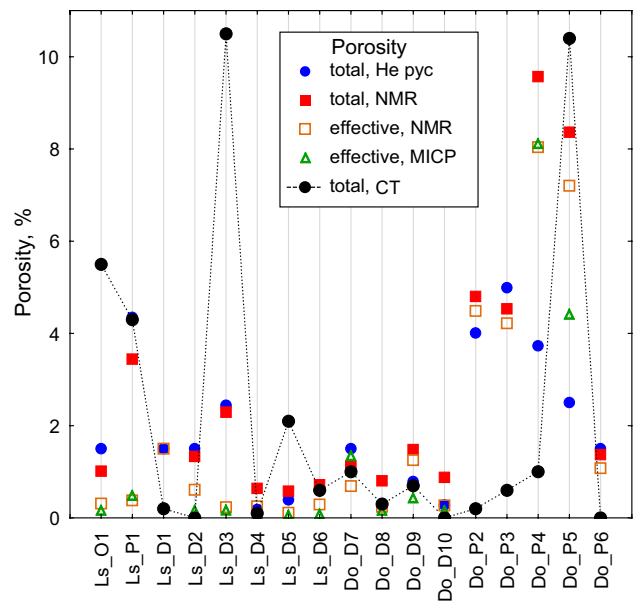


**Fig. 1** Porosity of analysed samples obtained from different measuring technique: *He pyc* helium pycnometer, *NMR* nuclear magnetic resonance, *MICP* mercury injection capillary pressure, *CT* computed X-ray tomography. Symbols in sample numbers mean: *Ls* limestone, *Do* dolomites, *O* Ordovician age, *P* Permian age, *D* Devonian age

- measurements were made on the three different fragments of rock, taken from the same depth. If the rock shows high heterogeneity, it may turn out that the porosity values will be different.

The discrepancy in the results is confirmed only by the fact that the measurements of carbonate rock samples are largely dependent on the test method, the heterogeneity of the material and the representativeness of the material collected for testing. Total porosity from NMR is a function of the amount of hydrogen in the sample. The total helium

**Table 1** Basic statistics of petrophysical parameters, calculated for 8 limestone and 9 dolomite samples

Parameter	Arithmetic mean		Median		Standard deviation		Distribution type		Asymmetry	
	Ls	Do	Ls	Do	Ls	Do	Ls	Do	Ls	Do
Skeletal density [g/cm <sup>3</sup> ]	2.7	2.83	2.7	2.83	0.05	0.05	Leptokurtic	Platokurtic	Right-sided	Left-sided
Bulk density g/cm <sup>3</sup> ]	2.7	2.77	2.7	2.77	0.06	0.07	Normal	Platokurtic	Symmetrical	Symmetrical
Formation Factor [-]	12,555	1302	2731	599	2792	606	Leptokurtic	Leptokurtic	Right-sided	Right-sided
P-wave velocity [m/s]	5878	5090	5934	6091	629	1594	Platokurtic	Platokurtic	Left-sided	Left-sided
S-wave velocity [m/s]	3099	2651	3029	3248	278	744	Platokurtic	Platokurtic	Right-sided	Left-sided
Permeability [nD]	40	100	43	120	3	20	Normal	Leptokurtic	Right-sided	Right-sided
Total Porosity from He pyc [%]	1.56	2.2	1.5	1.5	1.4	1.7	Platokurtic	Platokurtic	Right-sided	Right-sided
Total Porosity from NMR [%]	1.39	3.4	1.01	1.5	1	3.5	Platokurtic	Platokurtic	Right-sided	Right-sided
Effective Porosity from NMR [%]	0.4	3.3	0.3	1.2	0.2	3	Platokurtic	Platokurtic	Right-sided	Right-sided
Effective Porosity from MICP [%]	0.3	2.7	0.2	0.9	0.4	3.5	Leptokurtic	Platokurtic	Right-sided	Right-sided

(He) porosity depicts the volume of pores to which gas has penetrated. Total porosity from CT is calculated on the basis of tomographic images, so it is the number of voxels with an appropriate shades of grey (pores are indicated as black objects) in the grey scale. Each of these methods has its limitations. In most of the samples, similar values for NMR and He porosity were obtained. Effective porosity obtained from NMR and from MICP is also similar in most cases. The highest differences are observed for samples Do\_P5 (differences in total and effective porosities) and Do\_P4 (differences only in total porosity).

In the context of the above-mentioned possible causes of discrepancies in the values of porosity, it is difficult to indicate which value is closest to the real one. According to the authors, it is more desirable to consider the obtained results in the context of differences in measurement methods, e.g. higher NMR porosity than porosity from other methods, may suggest the presence of bound water or the presence of isolated pores. Higher porosity from CT than porosity from other methods may suggest the presence of isolated, unconnected pores. Lower values of CT porosity than those obtained from NMR or He pyc may indicate the presence of pores smaller than the resolution of the computed tomography.

### Interpretation of CT images

Qualitative interpretation of CT images was performed in poROSE software developed for image analysis and dedicated for rocks.

For each sample, the results of the total porosity determination were the basis of the pore space division into classes. Objects were divided into classes regarding their volume. Volume class units are represented as voxel. In the presented results, 1 voxel ( $v$ ) is equal to  $0.5 \times 0.5 \times 0.5 = 0.125 \mu\text{m}^3$  and is the smallest volume, which can be detected using nano-CT.

For analysed samples, total pore space was divided into 6 groups:

- A**—volume from  $0.125$  to  $1.125 \mu\text{m}^3$  (1–9 voxels);
- B**—volume from  $1.25$  to  $12.375 \mu\text{m}^3$  (10–99 voxels);
- C**—volume from  $12.5$  to  $124.875 \mu\text{m}^3$  (100–999 voxels);
- D**—volume from  $125$  to  $1249.875 \mu\text{m}^3$  (1000–9999 voxels);
- E**—volume from  $1250$  to  $12,499.875 \mu\text{m}^3$  (10,000–99,999 voxels);
- F**—volume up to  $12,500 \mu\text{m}^3$  (up to 100,000 voxels).

Figure 2 gives an example of the pore space division. Orange selections depict the pores from group C, yellow—from group D, green—from group E and blue—from group F.

Objects belonging to groups A and B (Table 2) are almost invisible on the photo scale (Fig. 2). Sample Ls\_D6 (Fig. 2a) provides an example of a pore system that is dominated by isolated, medium size pores. Large pores (blue objects) presented on the top of visualization, create a main part of samples porosity. Total number of objects/pores in this sample (2516) is relatively small (Table 2), what resulting in low calculated pore volume from nano-CT. Twice as much pores/objects were calculated for sample Ls\_P1. For this sample, CT porosity is equal to 4.3%.

When we compare samples Ls\_P1 with the sample Do\_P4, we can observe visible differences. Total number of objects in both samples is similar (about 4000); significant differences exist in the number of objects belonging to the different classes (especially F). This difference also results in different porosities (Table 2).

Quantitative analysis was made for whole pore space in the samples and for the classes obtained from qualitative image interpretation. Number of objects assigned for each class in each sample was shown in Table 2. It can be observed that the highest number of identified objects is not always related to the highest porosity, for example: for sample Ls\_O1 39,235, objects were counted, but they were mostly small (mostly groups B and C). For limestones, the number of objects with high pore volume classes is limited. The exception is sample Ls\_D3 with the highest total CT porosity (10.5%), which have 450 objects in classes F (highest volume). In dolomites samples, the highest CT porosity (10.4%) was observed for sample Do\_P5. In this sample also, the highest number of objects was registered (202 in class F). Similar to the limestones groups, the highest number of objects was registered in classes B and C.

Figures 3 and 4 depict the relations between some of them, where colours mean different classes of object size. In the CT images, there was found porosity equal 0% for 3 samples: Ls\_D2, Do\_D10 and Do\_P6. It means that in this samples pore sizes are smaller than the CT resolution or that the samples were no representative. Measured NMR, MICP and He pyc porosity for that samples are also very low. Figure 3 shows the dependence of the Feret diameter on the specific surface area. Two linear trends can be observed for limestones. For a given surface area, it was noted that the three Devonian samples Ls\_D3, Ls\_D4 and Ls\_D5 show smaller values of Feret diameters from the remaining samples. Among the dolomites, a linear relationship was observed for all samples. Figure 4 shows the dependence of the Surface Area/Feret Diameter ratio and Thickness (calculated as a mean local thickness of the particle). For both, limestones and dolomites were observed a division into two groups. Among the limestones, different relations from the rest of the samples were observed for the Ls\_D6 sample (for the same thickness the value of the quotient is higher). Among the dolomites, for the Do\_P3

**Fig. 2** Results of object size classification for selected samples in poROSE software: **a** sample no. Ls\_D6, **b** sample no. Ls\_P1, **c** samples no. Do\_P4. Colours reflect to the volume of the pores: red (group A and B)—volume from 1 to 99 voxels; orange (group C)—volume from 100 to 999 voxels; yellow (group D)—volume from 1000 to 9999 voxels; green (group E)—volume from 10,000 to 99,999 voxels; blue (group F)—volume up to 100,000 voxels

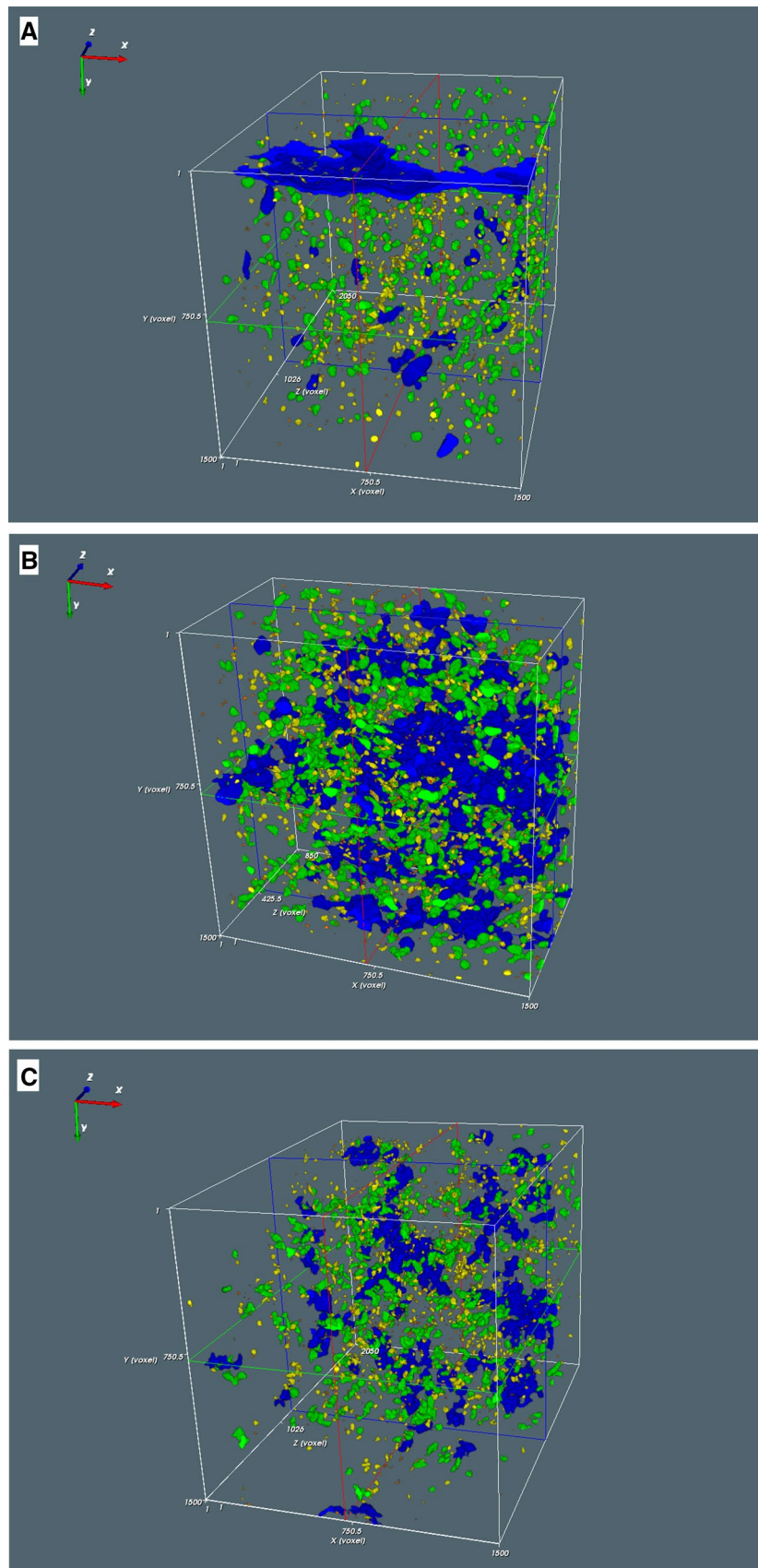




**Table 2** Group table: Numbers of objects assigned for each class in each sample and percentage of the total CT porosity in classes

Sample	No. of objects in classes						Sum of objects in samples	Percentage of the total CT porosity in classes						CT Porosity [%]
	F	E	D	C	B	A		F	E	D	C	B	A	
<b>Limestones</b>														
Ls_O1	437	2979	6940	12,210	12,259	4410	39,235	0.061	0.418	0.973	1.712	1.718	0.618	5.5
Ls_D1	3	217	588	976	671	145	2600	0.000	0.017	0.045	0.075	0.052	0.011	0.2
Ls_D3	450	513	762	954	769	189	3637	1.299	1.481	2.200	2.754	2.220	0.546	10.5
Ls_D4	2	5	50	183	121	43	404	0.000	0.001	0.012	0.045	0.030	0.011	0.1
Ls_D5	158	591	942	903	497	185	3276	0.101	0.379	0.604	0.579	0.319	0.119	2.1
Ls_D6	29	428	835	697	427	100	2516	0.007	0.102	0.199	0.166	0.102	0.024	0.6
Ls_P1	164	636	1081	1307	865	229	4282	0.165	0.639	1.086	1.312	0.869	0.230	4.3
Sum	1243	5369	11,198	17,230	15,609	5301	55,950	1.634	3.036	5.119	6.644	5.309	1.558	
<b>Dolomites</b>														
Do_D7	71	223	794	1496	1140	267	3991	0.018	0.056	0.199	0.375	0.286	0.067	1
Do_D8	3	276	1752	3815	2793	811	9450	0.000	0.009	0.056	0.121	0.089	0.026	0.3
Do_D9	8	98	157	257	223	97	840	0.007	0.082	0.131	0.214	0.186	0.081	0.7
Do_P2	2	173	1185	2797	2786	894	7837	0.000	0.004	0.030	0.071	0.071	0.023	0.2
Do_P3	0	91	588	890	659	439	2667	0.000	0.020	0.132	0.200	0.148	0.099	0.6
Do_P4	89	493	1037	1383	886	269	4157	0.021	0.119	0.249	0.333	0.213	0.065	1
Do_P5	202	640	1540	3705	4479	1948	12,514	0.168	0.532	1.280	3.079	3.722	1.619	10.4
Sum	375	1994	7053	14,343	12,966	4725	41,456	0.214	0.822	2.077	4.394	4.715	1.979	

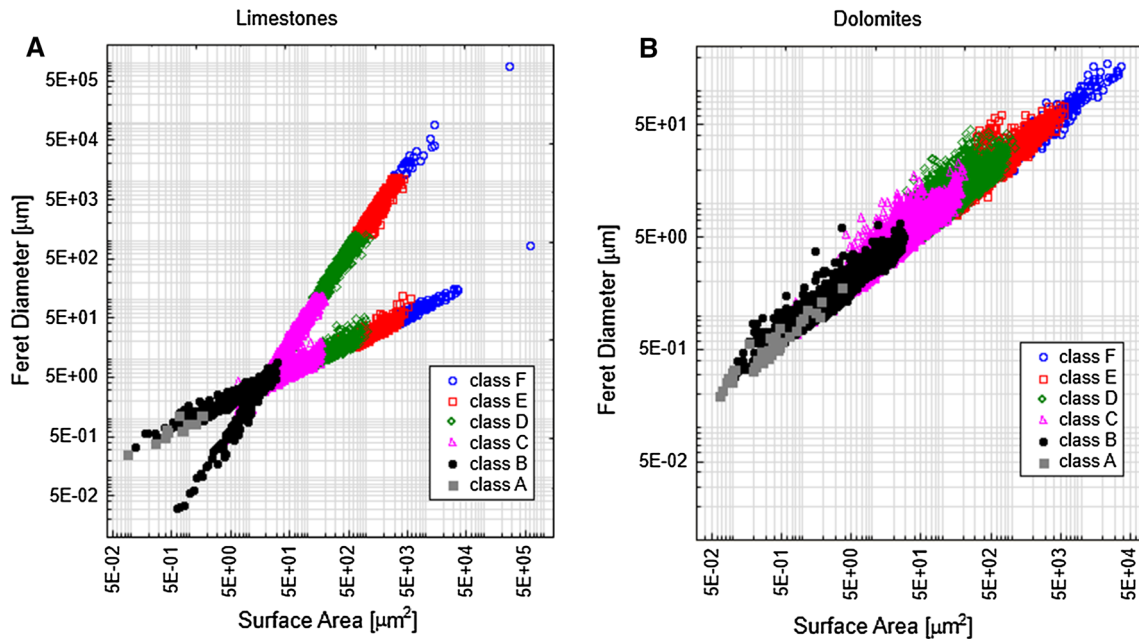


**Fig. 3** Relation between Feret Diameter and Surface Area for limestones (a) and dolomites (b) in classes of volumes

and Do\_P4 samples it was found that the Surface Area/Feret Diameter ratio is smaller than for the other samples in the same thickness ranges. Presented relations indicate differences in the development of the pore space of the analysed samples.

Average values of CT image parameters were calculated for each sample. Figure 5 depicts exemplary relations between these parameters and results of standard petrophysical laboratory measurements. To the laboratory results was added FZI (Flow Zone Index), as a parameter connecting

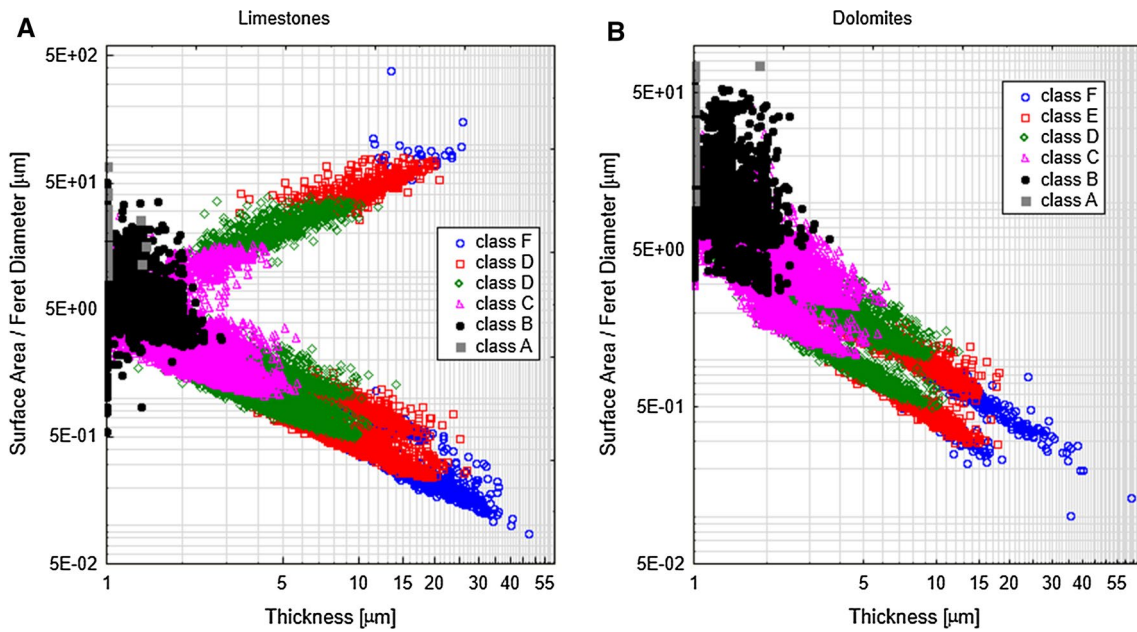


Fig. 4 Relation between Surface Area/Feret Diameter and Thickness for limestones (a) and dolomites (b) in classes of volumes

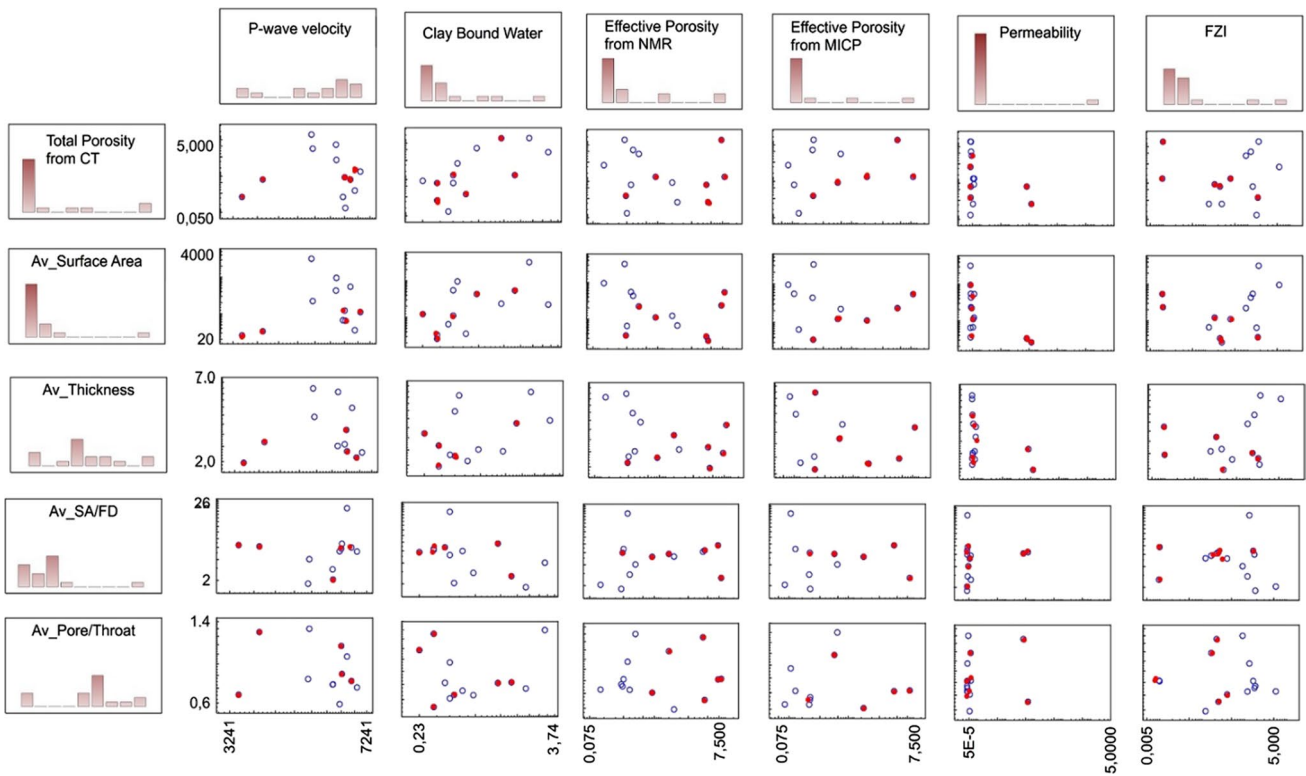


Fig. 5 Matrix plots between standard laboratory measurements (X-axis, logarithmic scale) and results of quantitative interpretation of CT images (Y-axis, logarithmic scale); red—dolomites, blue—limestones. Symbols: SA/FD Surface Area/Feret Diameter, FZI Flow Zone Index

porosity and permeability (Amaefule et al. 1993, Prasad 2000, Tiab and Donaldson 2000; Jarzyna et al. 2009). The FZI contains information on rock ability to transport fluid through its pore space. Reservoir parameters in units with constant FZI undergo only small changes.

There were calculated Pearson correlation coefficients ( $R$ ) for all samples and for limestones and dolomites separately.

For limestones, the best linear relationship was observed between:

- CT Porosity and P-wave velocity ( $R = -0.6$ ) and Clay Bound Water ( $R = 0.6$ );
- Average Surface Area and P-wave velocity ( $R = -0.5$ ), FZI ( $R = 0.65$ ) and Permeability ( $R = -0.5$ );
- Average Thickness and FZI—Flow Zone Index ( $R = 0.6$ ) and Effective Porosity from NMR ( $R = -0.45$ );
- Average SA/FD (Surface Area/Feret Diameter) and P-wave velocity ( $R = 0.7$ );
- Average Pore/Throat ratio and P-wave velocity ( $R = -0.5$ ).

For dolomites, the best linear relationship was observed between:

- CT Porosity and P-wave velocity ( $R = 0.5$ ), Clay Bound Water ( $R = 0.6$ ) and Effective Porosity from NMR ( $R = 0.6$ );
- Average Surface Area and Clay Bound Water ( $R = 0.9$ ), Effective Porosity from NMR ( $R = 0.75$ ), Effective Porosity from MICP ( $R = 0.97$ ) and P-wave velocity ( $R = 0.6$ );
- Average Thickness and FZI—Flow Zone Index ( $R = -0.7$ ), Effective Porosity (from NMR and MICP) ( $R = 0.6$ ) and Permeability ( $R = -0.6$ );
- Average Pore/Throat ratio and FZI ( $R = -0.7$ ).

Summing up the obtained relationships, it should be noted that the geometrical parameters obtained from CT images can be combined with the standard results of laboratory measurements. Much better linear relationship was obtained for the dolomites than for limestones. This may be related to the diversities of the limestone group (Figs. 3a, 4a). The combination of parameters, e.g. Surface Area and Feret Diameter, or porosity and permeability (as FZI) improved the relationship between the parameters. FZI shows a high correlation with average thickness, but also with SA/FD ratio. It shows that the hydraulic flow ability described by FZI can also be specified using parameters obtained from CT.

The obtained parameters from CT images and relations with standard petrophysical parameters allow to conclude that the applied algorithms are useful in assessing the structure of pore space. On the basis of the tested samples, due to the high heterogeneity of carbonates, the authors did

not attempt to generalize the results in relation to whole reservoirs.

## Conclusions

The article presents the use of geometric parameters for image analysis to assess the properties of rocks.

- Nanotomography allowed analyzing the pore space structure. Nano-CT images informed about the pore space parameters graphically and numerically (qualitative and quantitative). Advantages of using CT are: (a) pore visualization, (b) pore class division, (c) calculation of parameters for pore classes, e.g. porosity, tortuosity, surface area.
- Qualitative analysis allows to find pores orientation in pore space formation, microfractures presence and their directions, porosity values and distribution. The division of the pore space into groups depending on the pore size was obtained. This division shows the internal pore structure of rocks, allows full characterization of reservoir abilities (simulations of fluid and gas flows based on CT images).
- Quantitative analysis allows determining such parameters as average pore diameter or specific surface area. There was a strong linear relationship between the Feret Diameter and the Surface Area. Dividing these two parameters allowed refining the relationship and linking it to the local thickness of particle.
- The combination of geometrical parameters obtained from CT images gives new, unique information about the analysed samples.
- The combination of CT parameters and standard laboratory measurements results gives the possibility to describe fluid flow ability based on CT images—without complicated calculations.
- 3D investigations in nano-CT explained the complexity of pore space in tight carbonates.
- poROSE (poROUs materials examination SoftwarE) is a new tool which is dedicated to rock analysis. The software is useful and gives many advantages in rock analysis.

It can be concluded that computed tomography is a powerful tool in rock analysis and can be used for low porosity and low permeability carbonates. The use of CT images helps in the assessment of reservoir parameters of even very heterogeneous and complicated pore structures that are observed in carbonates.

**Acknowledgments** poROSE software is created thanks to the funding of the project LIDER/319/L-6/14/NCBR/2015: *Innovative method of*

*unconventional oil and gas reservoirs interpretation using computed X-ray tomography*. The project is funded by the National Centre for Research and Development in Poland, program LIDER VI, project no. LIDER/319/L-6/14/NCBR/2015: *Innovative method of unconventional oil and gas reservoirs interpretation using computed X-ray tomography*. The authors wish to thank the Polish Oil & Gas Company for the data and core samples.

## Compliance with ethical standards

**Conflict of interest** All authors declare that they have no conflict of interest.

**Open Access** This article is distributed under the terms of the Creative Commons Attribution 4.0 International License (<http://creativecommons.org/licenses/by/4.0/>), which permits unrestricted use, distribution, and reproduction in any medium, provided you give appropriate credit to the original author(s) and the source, provide a link to the Creative Commons license, and indicate if changes were made.

## References

- Abkar M, Petricola M, Watfa M, Badri M, Charara M, Boyd A, Grace M, Kenyon B, Roestenburg J (1995) Classic interpretation problems: evaluating carbonates. *Oilfield Rev* 7:38–57
- Amaefule JO, Altunbay M, Tiab D, Kersey DG, Keelan DK (1993) Enhanced reservoir description: using core and log data to identify hydraulic (Flow) units and predict permeability in uncored intervals/wells. In: SPE annual technical conference and exhibition, Houston (3–6 October), paper SPE-26436-MS. <https://doi.org/10.2118/26436-ms>
- Arns CH, Bauget F, Ghous A, Sakellariou A, Senden TJ, Sheppard AP, Sok RM, Pinczewski WV, Kelly JC, Knackstedt MA (2005) Digital core laboratory: petrophysical analysis from 3D imaging of reservoir core fragments. *Petrophysics* 46(4):260–277
- Coates GR, Xiao L, Prammer MG (1999) NMR logging principles & applications. Halliburton Energy Services, Houston
- Dohnalik M (2013) Improving the ability of determining reservoir rocks parameters using X-ray computed microtomography. Ph.D. Thesis, AGH University of Science and Technology, Kraków, Poland
- Exner U, Barnhoorn A, Baud P, Reuschlé T (2015) Porosity, permeability and 3D fracture network characterisation of dolomite reservoir rock samples. *J Pet Sci Eng* 127:270–285. <https://doi.org/10.1016/j.petrol.2014.12.019>
- Habrat M, Krakowska P, Puskarczyk E, Jędrychowski M, Madejski P (2017) The concept of a computer system for interpretation of tight rocks using X-ray computed tomography results: technical note. *Stud Geotech Mech* 39(1):101–107
- Jarzyna J, Puskarczyk E, Bała M, Papiernik B (2009) Variability of the Rotliegend sandstones in the Polish part of the Southern Permian Basin—per meability and porosity relationships. *Ann Soc Geologorum Poloniae* 79:13–26
- Jaworowski K, Mikołajewski Z (2007) Oil-and gas-bearing sediments of the Main Dolomite (Ca2) in the Międzzychód region: a depositional model and the problem of the boundary between the second and third depositional sequences in the Polish Zechstein Basin. *Geol Rev* 55(12/1):1017–1024
- Krakowska P, Puskarczyk E (2015) Tight reservoir properties derived by nuclear magnetic resonance, mercury porosimetry and computed microtomography laboratory techniques: case study of palaeozoic clastic rocks. *Acta Geophys* 63(3):789–814
- Krakowska P, Puskarczyk E, Jędrychowski M, Habrat M, Madejski P, Jarzyna J (2017) Analiza petrofizyczna łupków sylurskich z synklinorium lubelskiego—petrofizyczna analiza of Silurian shales from the Lublin. *Zeszyty Naukowe Instytutu Gospodarki Surowcami Mineralnymi i Energią PAN* 101:293–301
- Mazzullo SJ, Chilingarian GV (1992) Diagenesis and origin of porosity. In: Chilingarian GV, Mazzullo SJ, Rieke HH (eds) Carbonate reservoir characterization: a geologic-engineering analysis Part I: Elsevier Publ. Co., Amsterdam, vol 30. *Developments in Petroleum Science*, pp 199–270
- Prasad M (2000) Velocity-permeability relations with hydraulic units. *Geophysics* 68:108–117
- Teles AP, Lima I, Lopes RT (2016) Rock porosity quantification by dual-energy X-ray computed microtomography. *Micron* 83:72–78
- Tiab D, Donaldson EC (2000) *Petrophysics, theory and practice of measuring reservoir rock and fluid transport properties*, 2nd edn. Elsevier, N.Y., p 899
- Wardlaw NC (1996) Factors affecting oil recovery from carbonate reservoirs and prediction of recovery. In: Chilingarian GV, Mazzullo SJ, Rieke HH (eds) Carbonate reservoir characterization: a geologic-engineering analysis, Part II, vol 44. *Developments in petroleum science*, pp 867–903
- Webb PA (2001a) Volume and density determinations for particle technologists. Micromeritics Instrument Corp., World Wide Web [www.micromeritics.com](http://www.micromeritics.com). Accessed 22 May 2018
- Webb PA (2001b) An introduction to the physical characterization of materials by mercury intrusion porosimetry with emphasis on reduction and presentation of experimental data. Micromeritics Instrument Corp., World Wide Web [www.micromeritics.com](http://www.micromeritics.com). Accessed 22 May 2018
- Wei X, Chen H, Zhang D, Dai R, Guo Y, Chen J, Ren J, Liu N, Luo S, Zhao J (2017) Gas exploration potential of tight carbonate reservoirs: a case study of Ordovician Majiagou formation in the eastern Yi-Shan slope, Ordos Basin, NW China. *Pet Explor Dev* 44(3):347–357
- Wennberg OP, Rennan L, Basquet R (2009) Computed tomography scan imaging of natural open fractures in a porous rock; geometry and fluid flow. *Geophys Prospect* 57(2):239–249





# Indicative features of local magnetic anomalies from hydrocarbon deposits: examples from Azerbaijan and Ukraine

V. G. Gadirov<sup>1</sup> · L. V. Eppelbaum<sup>2</sup> · R. S. Kuderavets<sup>3</sup> · O. I. Menshov<sup>4</sup> · K. V. Gadirov<sup>5</sup>

Received: 20 July 2018 / Accepted: 7 November 2018 / Published online: 12 November 2018  
© Institute of Geophysics, Polish Academy of Sciences & Polish Academy of Sciences 2018

## Abstract

Magnetic surveys are one of the most mobile and low-cost geophysical methods. However, direct searching of hydrocarbon deposits by the magnetic method was questioned for a long time because of the virtual absence of the magnetic properties of oil and gas. Last investigations indicate that physical–chemical reactions of hydrocarbon deposits with the host media often create precursors for detecting directly magnetic signals from the oil and gas deposits even in the cases of large depths. Extraction of low-signal magnetic anomalies generated by hydrocarbon deposits is demonstrated on examples of several deposits from the Middle Kur Depression (Azerbaijan) and Dnieper-Donets Depression (Ukraine). Application of the proposed magnetic data analysis will allow not only to optimize hydrocarbon deposit searching in complex geological environments but also to decrease the number of prospecting boreholes.

**Keywords** Precise magnetic investigations · Epigenetic changes · Local anomalies · Hydrocarbon deposits · Middle Kur Depression · Dnieper-Donets Depression

## Introduction

Magnetic prospecting began to be widely used in the middle of the last century, mainly to study the structure of the basement and for mapping of deep faults. Due to the appearance of highly sensitive magnetometers, valuable results of using magnetometry were obtained in the discovery of anticlinal structures, traps as peculiar structural terraces, flexures, zones of wedging out, thrust zones, reef genetic structures, ore deposits, archaeological targets, etc. (e.g., Lapshov 1975; Nettleton 1976; Berezkin et al. 1982, 1998; Khesin et al.

1996; Mavrichev 1997; Bezukladnov and Mavrichev 1997; Eppelbaum and Khesin 2012; Hinze et al. 2013; Eppelbaum 2015a, b).

However, high-resolution magnetic data acquisition requires careful removal (eliminating) of different noise effects (Fig. 1). General explanations of the various kinds of noise (disturbances) appearing in detailed magnetic investigations and methods for their removal are described in Eppelbaum et al. (2001) and Eppelbaum (2015a, b).

At the present stage, employment of magnetometry in hydrocarbon searching is based on certain assumptions, for example: belonging of oil and gas accumulation zones to certain structural–tectonic elements of the crystalline basement or sedimentary cover, differentiation of rocks according to the lithological composition, magnetic properties and morphology of geological structures or traps in the sedimentary cover and influence of hydrocarbon fluids on the magnetic properties of rocks occurring over oil and gas deposits (e.g., Berezkin et al. 1982; Foote 1992; Eventov 1997; Gadirov and Eppelbaum 2012). This leads to three main directions for the magnetic prospecting application: (1) mapping the crystalline basement, (2) identifying local structures possibly containing hydrocarbons and (3) “direct” searches of hydrocarbon deposits. The successful use of magnetometry for the first two directions is proved by the wide practice

✉ L. V. Eppelbaum  
levap@post.tau.ac.il

<sup>1</sup> “OilGasScientificResearchProject” Institute of the State Oil Company of Azerbaijan Republic (SOCAR), Baku, Azerbaijan

<sup>2</sup> Department of Geosciences, Faculty of Exact Sciences, Tel Aviv University, Tel Aviv, Israel

<sup>3</sup> Carpathian Branch of Subbotin Institute of Geophysics of the National Academy of Sciences of Ukraine, Lviv, Ukraine

<sup>4</sup> Taras Shevchenko National University of Kiev, Kiev, Ukraine

<sup>5</sup> Geophysics and Geology Department of SOCAR, Baku, Azerbaijan

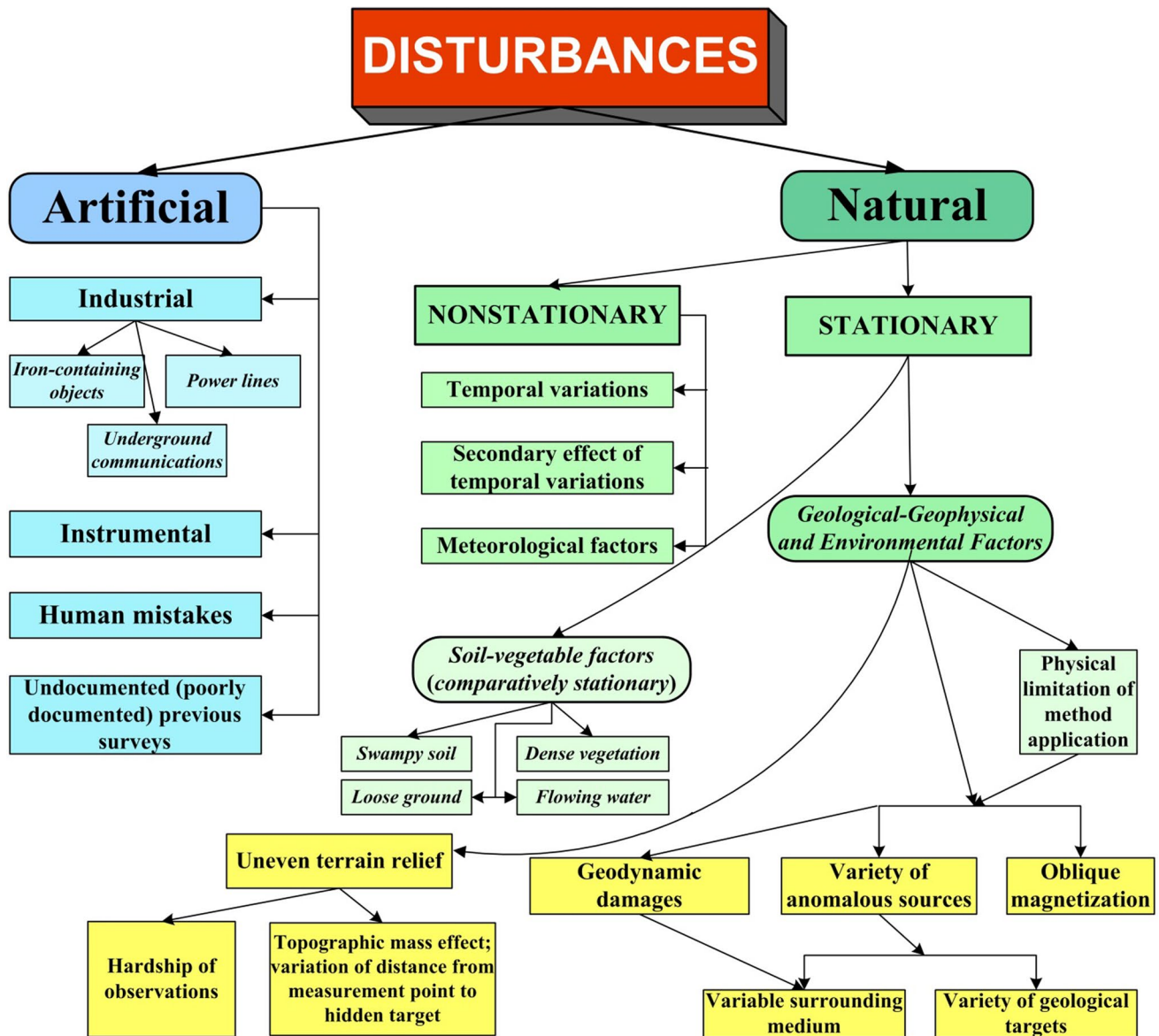


Fig. 1 General scheme of noise appearing in high-resolution magnetic investigations

of geophysical studies (e.g., Nettleton 1976; Khesin et al. 1996; Mavrichev 1997; Saunders et al. 1991; Mavrichev et al. 2002; Eppelbaum and Khesin 2012; Hinze et al. 2013).

For the “direct” magnetic searching of oil and gas accumulations, it is necessary to study a “thin” structure of the anomalous magnetic field with identification of the local effects not only from desired targets, but also from created by them epigenetic changes. For “direct” detection of magnetic signatures of oil and gas accumulations, it is necessary to study a “thin” structure of the anomalous magnetic field with identification of the local effects, not only from desired targets, but also that resulted from epigenetic changes. The detailed study of the geological structure and the magnetic properties of the rocks composing the geological section

(including the soil cover), as well as results from geomagnetic modeling, can light the genetic connection between the hydrocarbons and observed magnetic anomalies (e.g., Seifulin 1980; Berezkin et al. 1982; Donovan et al. 1984; Gadirov and Eppelbaum 2012). Notably, Donovan et al.’s (1984) studies first reliably showed that oil and gas fields often are accompanied by low-amplitude (up to 10 nT) negative and positive local magnetic anomalies of very complex morphology.

The purpose of this work is to study the morphological aspects of the anomalous magnetic field over local oil and gas deposits and to develop the corresponding physical–geological models (PGMs) of the desired targets. To examine this issue, several hydrocarbon fields were selected in the

Middle Kur Depression (Azerbaijan) and Dnieper-Donets Depression (Ukraine) where detailed magnetic surveys were carried out.

It should be noted that integration of magnetic data with other geophysical methods strongly increases the reliability and effectivity of the developed PGM (Eppelbaum et al. 2004; Eppelbaum and Mishne 2011).

## The state of the problem

Formation of magnetic anomalies associated with oil and gas deposits is caused by various factors. Many works are devoted to the relationship between magnetic anomalies and some geological factors, for example influence of the terrain and lateral inhomogeneity of hydrocarbon deposits (Suvorov 1989), influence of the abnormally high formation reservoir pressure (Abdulabekov and Golovkov 1974), presence of vertical electric currents forming zones with magnetic and thermal contrast properties at the boundaries of the reservoir-containing rocks (Seifulin 1980; Pirson 1971a, b; Elmore et al. 1987), influence of temperature and pressure to rock magnetization to the oil and gas zones (Cisowski and Fuller 1987; Orlyuk et al. 1998), presence of annular anomalies around the reservoir in the form of “jet” metals that complicate magnetic field pattern at the edges of the structure (Putikov et al. 2000), effect of epigenetic altered minerals around the deposit under influence of hydrocarbon fluids to the magnetic field intensity and its ruggedness (Bagin and Malumyan 1976; Schumacher and Abrams 1996; Bezukladov and Marichev 1997; Berezkin et al. 1998; LeSchack and Van Alstin 2002). One of the most important discovered factors is that prolonged interaction between the hydrocarbons and host rocks resulted in subvertical inhomogeneities over oil and gas deposits. These inhomogeneous zones contain some secondary minerals which actually affect various geophysical (including magnetic) fields (Gadirov 1994; Ustinova 2002; Perez–Perez et al. 2011; Gadirov and Eppelbaum 2012).

In the geophysical literature, such zones are called “columns of epigenetically altered rocks,” “geochemical halo,” “geochemical chimney” and “microseepage.” These subvertical zones appearing above the deposit cause a number of anomalous effects that may be considered as searching criteria for oil and gas deposit recognition (Machel and Burton 1991a; Gadirov 1994; Berezkin et al. 1998; LeSchack and Van Alstin 2002; Schumacher 2010; Gadirov and Eppelbaum 2012). The main search criterion in the magnetic field analysis is an essential dispersion of magnetic properties of the strata at zones where hydrocarbon deposits occur. It was proposed that epigenetic magnetic and nonmagnetic minerals can be formed over and below oil- and gas-bearing structure, and generation of these minerals is responsible for the

appearance of weak magnetic anomalous effects observed over the hydrocarbon fields (Machel and Burton 1991a, b; Saunders et al. 1999; Aldana et al. 2003; Liu et al. 2004).

Migration of hydrocarbon fluids upward to the near-surface geological layers and soil cover changes their magnetic properties (e.g., Donovan et al. 1984). This prompted the necessity to study the magnetic properties of soils and the effect that the hydrocarbons had on soil magnetic properties (Foote 1992, 1996; Kuderavets et al. 2013; Menshov et al. 2014). Influence of organic matter of the possible hydrocarbon origin, resulting in the formation of new authigenic magnetic minerals, triggers the oxidation–reduction reactions. The physical basis for the application of the magnetic method is the presence of magnetic (e.g., magnetite, maghemite, pyrrhotite) and paramagnetic (hematite and pyrite) minerals in various combinations (Gay and Hawley 1991; Foote 1996; Emmerton et al. 2012). The presence of these minerals under the prolonged contacts of hydrocarbon fluids with host rocks can both increase and decrease their magnetic properties. This feature allows making an assumption about the effect of hydrocarbons to change the magnetic properties of the upper part of the geological section and the soil cover in the immediate vicinity of the hydrocarbon deposits. However, until the present, the relationship between the anomalous magnetic field (and other geophysical fields) and the oil and gas accumulations is still debatable (Gay and Hawley 1991; Maher and Thompson 1991; Gay 1992; Schumacher 2010; Gadirov and Eppelbaum 2012; Lukin 2017).

## Middle Kur Depression, Azerbaijan

### Brief geological description and the MKD oil and gas potential

The Middle Kur Depression (MKD) covers a large part of the Kur intermountain trough (between the Greater and Lesser Caucasus) with a complex heterogeneous geological structure. In the depression, thickness of the sedimentary complex is estimated within 12–14 km. The surface of the Mesozoic complex to which the identified structures are confined lies in the axial zone of the Yevlakh-Agjabedi trough at depths of 7–8 km, in the onboard deflection zones of 3–4 km and in the pre-Caucasian zone of 500–700 m (Alizadeh et al. 2017). Deep wells have discovered rocks from the Middle Jurassic (in the area of the Saatly superdeep SD-1 well) to the anthropogenic.

Azerbaijan became famous since the thirteenth century of the healing effect of Naftalan heavy oil, the natural exits of which are located within the MKD. At the beginning of the late 40s of the twentieth century, the oil field Gazanbulak and the commercial oil and gas potential of separate areas

(Dalimammadli, Ajidere, Terter, Sovietlar, Borsunlu, etc.) were identified in exploration wells in various areas of the region (Amirarh, Bozgobu, Gedakboz and Shikhbagi). A discovery of a new type of oil field in the volcanogenic and volcanic–sedimentary formations in 1971 (Muradkhanly deposit) triggered a careful study of these formations distribution and hydrocarbons (HC) occurring. Later, during 20 years, Zardab, Tarsdallar, Jafarly HC deposits were discovered, and the commercial HC potential of the Amirarh, Gedakboz, Shikhbagi and Bozgobu areas was established. In these areas, beneath the thick layer of the sedimentary complex, prospecting wells revealed effusive and partially intrusive formations of Cretaceous and Eocene age. The oil deposits here were confined mainly to effusive rocks of the Upper Cretaceous, volcanogenic–sedimentary and mergegum of the Eocene strata. To study the patterns of magmatic formation distribution, as well as to search HC deposits in the region, magnetic and gravity data were examined in detail (Gadirov 2009; Gadirov and Eppelbaum 2012).

### Field surveys and magnetic equipment

Over many identified structures, ground-based magnetic surveys (combined with the precise gravity studies) have been carried out. Both the vertical ( $Z$ ) magnetic field component and the total magnetic field ( $T$ ) were measured. These investigations were performed along rectilinear, parallel profiles by the use of optical–mechanical (M27-M), quantum (M-33) and proton (MMP-203) magnetometers, with application of a magneto-variational station at the control point. Observation step was 100 m, and distance between profiles was 500–700 m. The accuracy of the M27-M survey was estimated as 2–2.5 nT, while for the M-33 and MMP-203 magnetometers an accuracy of 1–1.5 nT was obtained.

### Morphology of the magnetic field observed over hydrocarbon deposits

Local magnetic anomalies retrieved from the observed field over the MKD deposits are usually characterized by a complex structural form indicating a complex distribution of magnetic properties of the rocks in the geological section. Both on  $Z$  and  $\Delta T$  fields, rugged so called sawtooth shapes were detected. Size and contours of the magnetic minima selected against the maxima background usually correspond to the contours of the buried HC deposits (Table 1). Simultaneously, gradient zones in the magnetic field pattern are allocated corresponding to the contour of the deposit. Analyzing these zones enables to restore the local maxima and separate the local minima on their background. It was established that in the MKD the magnetic maxima are morphologically associated with the volcanogenic structures characterized by a high magnetic susceptibility (for instance, Muradkhanly,

Jafarly, Alvend and Tarsdallar deposits (Eppelbaum and Khesin 2012; Gadirov and Eppelbaum 2012). Besides this, the extracted low-amplitude negative magnetic anomalies are morphologically associated with the HC reservoirs and the subvertical zones formed above and below the deposits; these zones have a relatively lower magnetic susceptibility compared with the host rocks (Gadirov 1994; Gadirov and Eppelbaum 2012).

Magnetic susceptibility of Muradkhanly (and partially Jafarly) areas is presented in Table 2.

## Dnieper-Donets Depression, Ukraine

### Brief geological review

The Dnieper-Donets Depression (DDD) (Ukraine) is one of the largest oil- and gas-bearing provinces in the Eastern Europe. More than 200 oil, gas, and oil and gas condensate fields have been discovered in the DDD over the years of geological exploration from the middle of the twentieth century. At present, this region is still one of the priorities for oil and gas exploration (Ulmishek 2001). The main prospects for the DDD are associated with hydrocarbon (HC)-bearing complexes of the Lower Carboniferous where 68.5% of the undiscovered resources are concentrated. The Lower Carboniferous deposits consist of a set of genetically and structurally connected marine, rhythmic and regionally mature horizons of limestones, clays, coal, sandstones and salt. Geological studies have shown the absence of volcanism, high rate of immersion and sedimentation and development of numerous folds (salt pumping). Carbonate deposits of the Upper Visean form a chain of reefogenic barrier-type arrays where organogenic structures, containing oil and gas reserves, are concentrated. To such structures, our research targets are confined—Seluchy oil and Pryrichna oil and gas condensate deposits. They are located in the central part of the DDD on the SW slope of the Sribne depression (Maevski and Babko 2006) (Fig. 2). The depression is complicated by low-amplitude uplifts, system of faults and salt structures. The HC-bearing of the Seluchy and Pryrichna deposits is associated with the carbonate and sandy reservoirs of the Lower Visean-Tournaisian oil- and gas-bearing complex (horizons V-20, V-24, V-25) at the depths of 3–5 km. Seismic reflection data display the horizons of the Lower Carboniferous as small anticlinal uplifts broken by faults of different orientations.

The DDD territory mainly is characterized by low-intensity magnetic anomalies (with amplitudes of a few nT) over the HC deposits. The anomalous magnetic effects are formed by a wide set of sources. The sedimentary rocks of DDD are less magnetized compared with soils that is an important factor for magnetic data interpretation.



**Table 1** Specific features of  $Z$  and  $T$  fields at the oil fields in the Middle Kur Depression (Azerbaijan)

Oil fields (profiles)	Magnetic field behavior: ( $Z$ is the vertical magnetic field component, ( $T$ is the total magnetic field)	Intensity (nT)		Depth of deposit (m)	Thickness of deposit (m)	Conformity contours of magnetic anomalies and deposits
		Local maxima	Local minima			
Muradkhanly (profile 01)	$\Delta Z$ : Local maximum separated from the regional background and sharp gradients. Against the backdrop of the maximum, a local complex minimum is detected	Up to 90	15–40	3000	30 (by well 44)	Corresponded
Muradkhanly (profile 59)	The same	40–60	15–25	4000	100 (by well 23)	Corresponded
Alvend (profile 02)	$\Delta Z$ : The local maximum allocated by the regional background is completed by two minima	40–70	25–35	4200–4400	$\approx$ 30 (by well 203, 208)	Corresponded
Bozqobu (profile 25)	$\Delta Z$ : Local maximum, against which local minima are distinguished with different intensities and sizes	60	20–40	4700	80 (by well 1)	Corresponded
Jafarli (profile 60)	$\Delta Z$ : Local maximum, highlighted by a regional background. Against the background of the maximum, there a local minimum is distinguished	up to 50	30	4000	> 100 (by well 2, 5, 22)	Corresponded
Jafarli (profile 2)	$\Delta Z$ : Local maximum, a clear minimum at the left wing $\Delta T$ : Local maximum, against a background of local minima with variable intensity	80 50	> 40 15–30	3950	> 100	Corresponded
Jafarli (profile 3)	$\Delta Z$ : Local maximum, against a background of several local minima $\Delta T$ : Local maximum, against which there local minima exist	60 90	20–40 15–30	4000	> 100	Corresponded Magnetic max. is shifted to the north for 2 km
Tarsdallar (profile 09)	$\Delta Z$ : Local maximum, complex, divided into three parts. At the background of the maximum, the local minimum is separated $\Delta T$ : Local maximum, against the background of a local minimum	70 65	20–40 35	3500	–	Corresponded Magnetic max. is shifted to the south for 2 km
Tarsdallar (profile 07)	$\Delta Z$ : Local maximum, complex, indented. Against the background of the maximum, a local minimum is highlighted $\Delta T$ : Local maximum, against which exists a local minimum	50 60	up to 35 30	3000	60 (by well 4)	Corresponded

**Table 2** Magnetic susceptibility values of rocks of the Muradkhanly and Jafarly areas (southeastern part of the Middle Kur depression)

Age sediments and indices	Lithology	Depth and average thickness (m)	Magnetic susceptibility, $\kappa \times 10^{-5}$ SI		Relative changes magnetic susceptibility, $\Delta\kappa \times 10^{-5}$ SI
			Behind the contour of the deposit	Within the contour of deposits	
Quaternary	Sandstones, sands	0	–	–	–
Q		400			
Absheron	Sandstones, clays,	400	63	–	–
Q ab	sands	1200			
Akcakyl	“_”	1600	88	–	–
$N_2^2$ ak		500			
Product. stratum (Balakhani stage)	Clay with interbedding of sandstones	2100	75	50	25
$N_2^1$		200			
Upper Miocene	Sandstones, clays	2300	123	19	104
$N_1^3$		500			
Chokrak	Sandstones, interlayers of marls and dolomites	2800	82	20	62
$N_1^2$ č		50			
Maikop	Clays, siltstones, sand and sandstone interlayers	2850	138	16	122
$P_3 + N_1^1$		650			
Eocene	Clay limestone, layers of limestone and dolomite	3500	377	Over the deposit	360 (287)*
$P_2$		700		16 (94)*	263 (226)*
				Under the deposit	
				113 (150)*	
Paleocene	“_”	4200	816	268	548
$P_1$		50			
Upper Cretaceous, $K_2$	Sedimentary & volcanic rocks	Limestones, mudstones, marls, andesites, basalts, porphyrites	> 4250	> 1130	–
			1000	1380–5700	414
					> 1256

\*The values refer to the Jafarly area

The profile magnetic survey (scale 1:50,000) at the Seluchy field was carried out by use of proton magnetometer MMP-203 (with a sensitivity of 1.0 nT). The studies were performed at 14 profiles, and the observation step was 50 m. To introduce corrections for temporal variations, a proton station MV-01 (sensitivity of 0.1 nT) was employed. The standard deviation of the survey was estimated as  $\pm 1.5$  nT (Orlyuk et al. 1998; Maksymchuk et al. 1999; Maevski and Babko 2006). The intricate structure of the local anomalous magnetic field indicates the presence of dozens of separate positive magnetic anomalies with amplitudes of 4–6 nT caused by magnetic inhomogeneities in the upper part of the sedimentary cover.

A PGM of the Seluchy structure is constructed in the framework of the epigenetic model of Berezkin et al. (1998). It provides the presence of an oxidation zone with magnetic minerals (magnetite and/or pyrrhotine) in the upper part of

the deposit (Orlyuk et al. 1998). A magnetic survey was also performed at the Pryrichna gas condensate field along seven profiles. They also documented a complex structure of the magnetic field with the separation of local magnetic anomalies perhaps of the epigenetic nature (Maksymchuk et al. 2001). Two objects of research are located almost close to each other, but there were no attempts to generalize the results of the studies including data from 21 profiles. For this purpose, in this article the results of the magnetic surveys at the Seluchy and Pryrichna fields (DDD) both in the regional and local aspects are analyzed.

### Observation methodology

A study of the distribution of the magnetic susceptibility ( $MS$ ) of rocks has been carried out using a KT-5 device with a sensitivity of  $1 \times 10^{-5}$  SI.  $MS$  examination has been

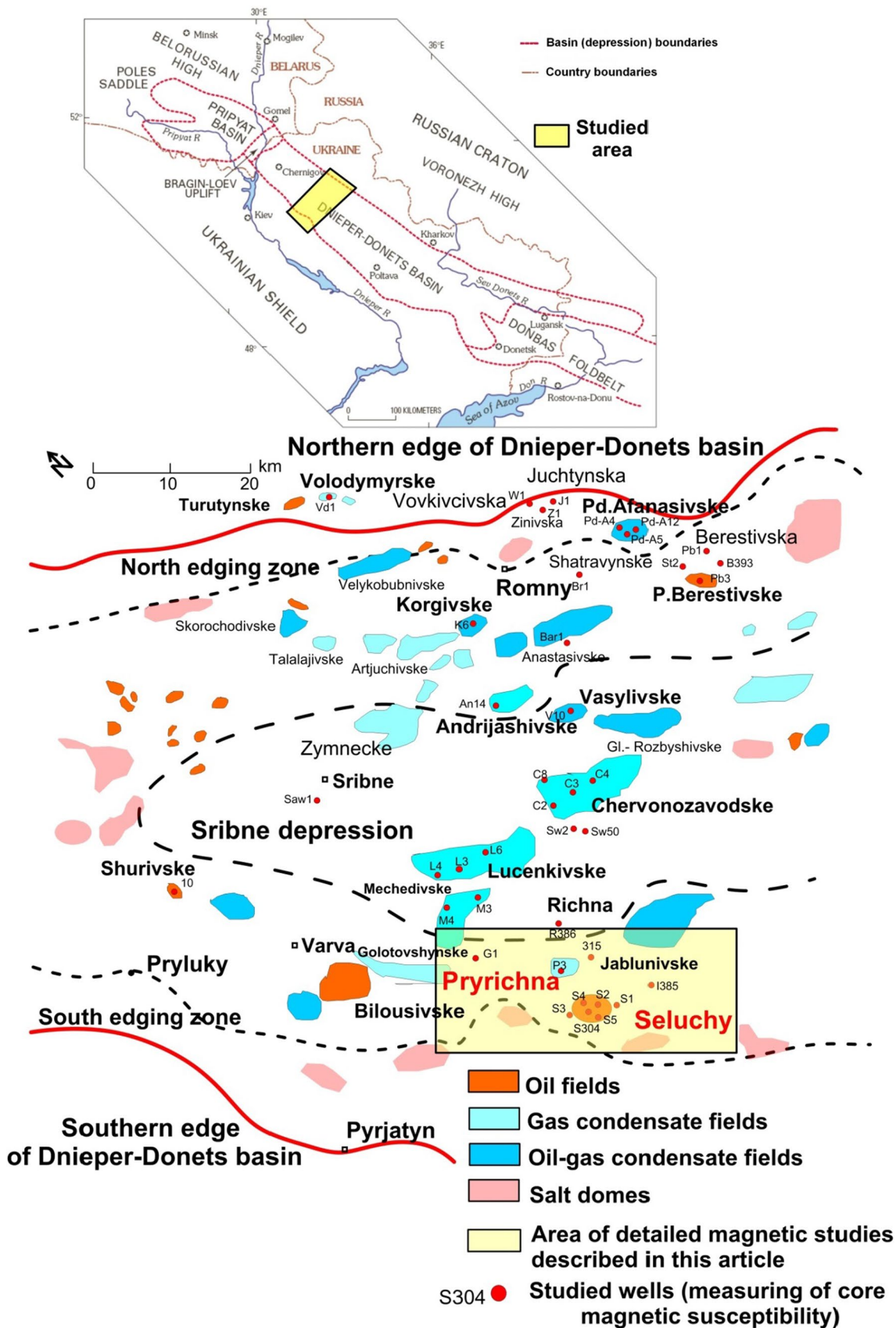


Fig. 2 Studied area on south edges of Sribne depression in the Dnieper-Donets Depression (Ukraine), after Ulmichek (2001), with modifications

carried out on core material from exploration and parametric wells within and outside the research facilities. The cores are selected only from the prospective HC-bearing horizons; therefore, only a very small part, 4–5% of the depth of the well, is available for studies of the material composition of the structure section. Stratigraphically, almost all the cores relate to the HC deposits of the Lower Carboniferous. *MS* measurements were done for examination of vertical and lateral changes within the Seluchy deposit of the DDD.

Magnetic studies of soils were conducted both in situ and in laboratory. Field magnetic susceptibility measurements of soils were conducted using the PIMV-M portable *MS* meter (Geologorazvedka, Russia). The PIMV-M is roughly analogous to the conventional Czech KT-5 (Menshov et al. 2015). In the laboratory, we used the KLY (Agico, Czech Republic) and MS2 (Bartington) to measure and then calculate a mass-specific magnetic susceptibility. The magnetization analyses were conducted using the JR-4. The samples were analyzed under natural conditions (without drying immediately after sampling). Each sample was prepared as a homogeneous mass and placed into a standard volume measurement glass that was followed by calculating the mass-specific magnetic susceptibility.

## Results of anomalous magnetic field studies

The Seluchy and Pryrichna fields are located in the zone of high horizontal gradients of  $\Delta T$ , in the peripheral parts of the Lochvytsia regional magnetic anomaly. At the Seluchy site, the magnetic field  $\Delta T$  sharply increases from south to north with intensity from  $-30$  to  $+130$  nT (Figs. 3, 4). In the central part of the area and to the north, at the Pryrichna and Richna structures,  $\Delta T$  anomalies change their direction from the sublatitudinal to submeridional. Thus, the intensity of the regional magnetic anomalies is not of great importance. Figure 3 shows an anomalous magnetic field along several separated profiles. In spite of certain natural and man-caused disturbances (production wells, gas pipelines, power lines, settlements, etc.), against the regional background  $\Delta T_a$ , residual local anomalies  $\Delta T$  of different amplitudes and widths with high magnetic field dispersion can be traced. All anomalies are characterized by a positive sign from 4 to 6 nT and a width from 3 to 4.5 km. In their morphology, they are close to the dome-shaped and undulating form with a very strong dispersion of the field (Fig. 3).

The combination of application of the graphical method for removing the regional magnetic field  $\Delta T$  and using the orthogonal polynomials allowed us to obtain a residual magnetic field  $\Delta T_{a, \text{resid}}$  (summarizing the magnetic data analysis along 21 profiles).

The most interesting is the spatial pattern of the local magnetic field over two hydrocarbon deposits confined to the organogenic carbonate sediments of the Lower and Upper

Visean. It can be seen from Fig. 3 that the field  $\Delta T_{a, \text{resid}}$  has a very complex morphology with separation of some specific maxima. There are five local magnetic maxima exceeding 4 nT and six maxima with the intensity of 3–4 nT. At the eastern part of the Seluchy structure and at the southern end of the Pryrichna deposit (profile V–V), the maxima of the local magnetic field are the most clearly expressed, stretched along the profiles and extended for 3–4 km (Fig. 3). Anomalies  $\Delta T_{a, \text{resid}}$  are characterized by a submeridional direction (Fig. 4), and they were correlated with a structural map of the Lower Visean and with the map of the carbonate thicknesses. The maxima of the magnetic field do not completely correlate with the arched parts of the low-amplitude uplifts along the seismic reflecting horizon of the Lower Visean. The same situation is observed in the zones of maximum thickness of bioherms. Only in the viable part of the Selyukhovskaya structure, a maximum of  $\Delta T_{a, \text{resid}}$  is observed (it is located over the bioherm thicknesses zone of 25–75 m). In contrast, almost all the peaks of the local magnetic field are concentrated in the areas of tectonic disturbances or closely located to them. It should be noted that productive wells Seluchy-2, 4, 5 and 304 are located in the magnetic zones of maxima of  $+(2-4)$  nT. The well Pryrichna-3 is located at the marginal part of the magnetic anomaly (Fig. 4). It can be concluded that the magnetic anomalies are associated with tectonic faults through which microseepage of the hydrocarbon fluids is generated.

## Studies of magnetic properties of rocks and soil cover

Lithologically, the Lower Carboniferous oil and gas complex is composed of terrigenous carbonate formations of the polyfacial type, which is represented by interbedding of argillites, siltstone, sandstone, limestone and dolomites. Commonly, the value of the *MS* of the Lower Carboniferous strata  $\kappa = (0-30) \times 10^{-5}$  SI. Separate fragments of the section of the Famennian stage of the Devonian system were also studied, where among the terrigenous carbonate rocks, the most magnetic formations are recrystallized (e.g., fissured basalt-like rocks have  $\kappa = 100-5000 \times 10^{-5}$  SI). In the vertical distribution of the *MS* of the investigated sequences from the Famennian to the Serpukhovian stage, in the value of  $\kappa$  and its dispersion, separate lithomagnetic horizons (LMH) are recognized: the Famennian-Tournaisian with the mean values of  $\kappa = (5-15) \times 10^{-5}$  SI and with the large values of  $\kappa$  for clays; the Lower Visean with the low values of  $\kappa = (0-5) \times 10^{-5}$  SI and low dispersion, and the Upper Visean-Serpukhovian which is characterized by high values of  $\kappa = (20-30) \times 10^{-5}$  SI and medium dispersion.

In addition, in each of the LMH, it is possible to distinguish individual subhorizons of different thicknesses that may coincide with the productive and microfaunistic



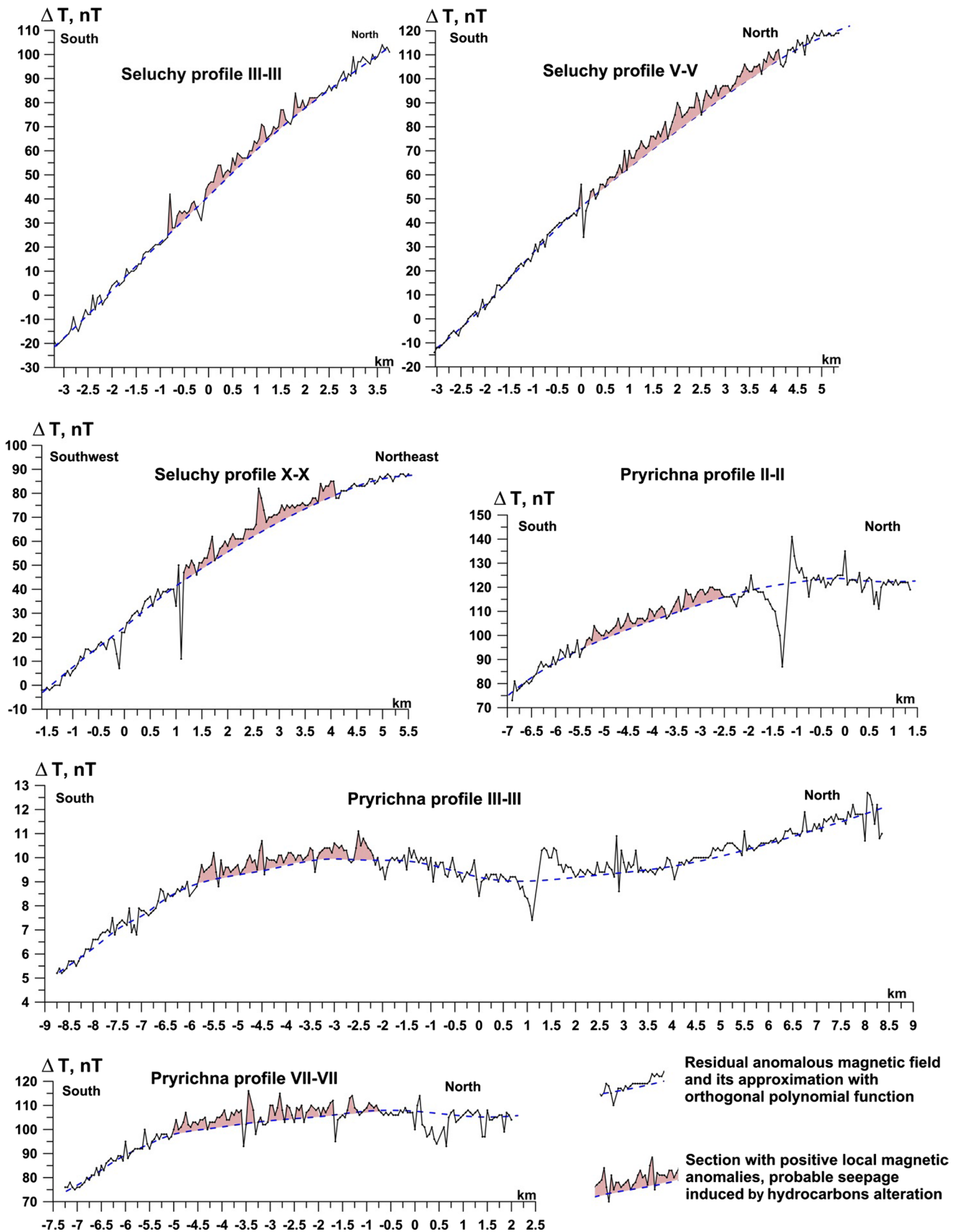
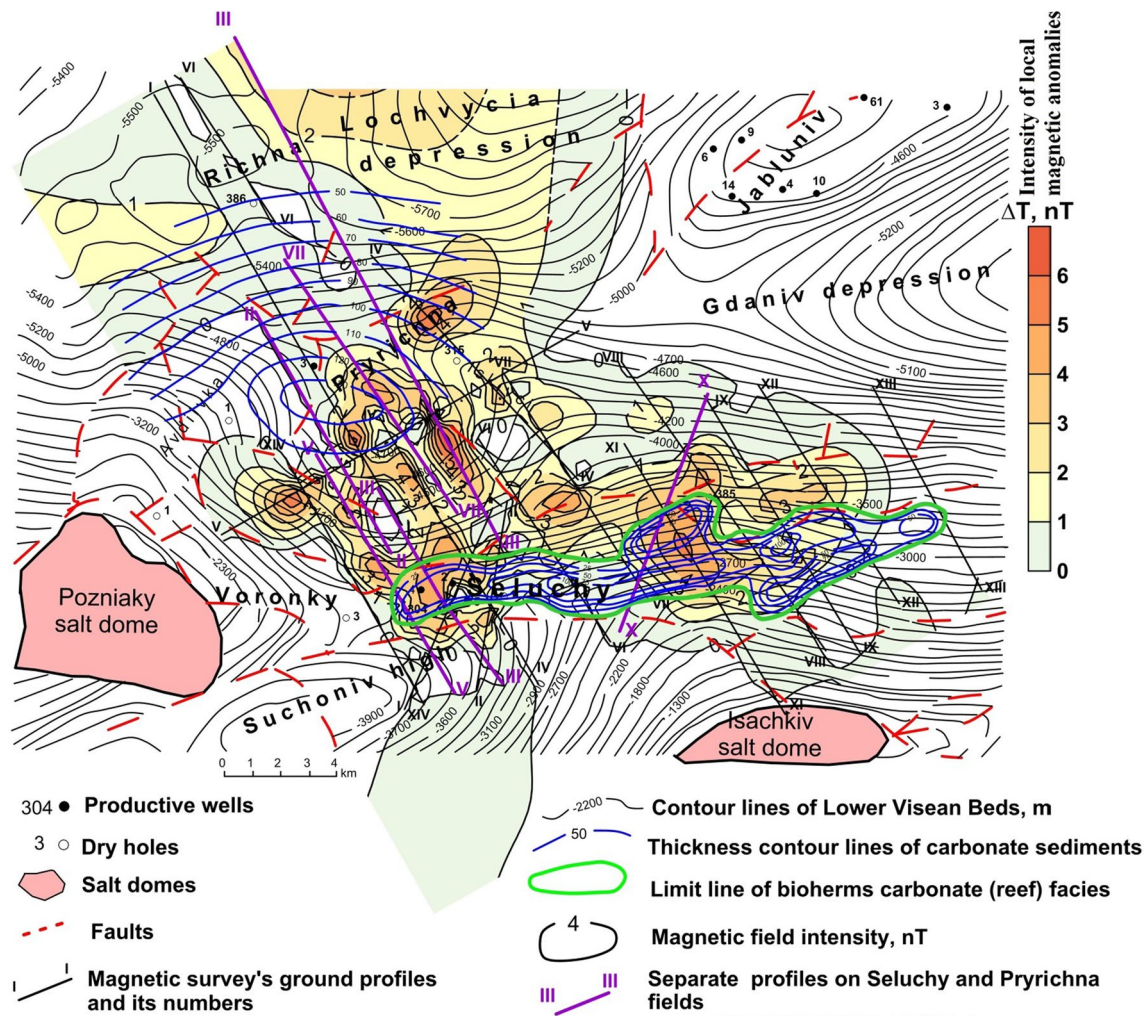


Fig. 3 Residual anomalous magnetic field at the separate profiles on Seluchy and Pryrichna fields in the Dnieper-Donets Depression



**Fig. 4** Spatial character of local residual anomalous magnetic field on Seluchy and Pryrichna hydrocarbon fields in the Dnieper-Donets Depression (modeling of magnetic field along profile III–III is shown in Fig. 11)

horizons recognized in the section, suites, bundles of rocks, etc. The separated LMH are well correlated among themselves in the lateral direction between the wells in the investigated areas. The main reason for the *MS* differentiation in the LMH strata and subhorizons is first of all, changes in the lithological formation composition and paleotectonic and paleofacial conditions of their formation. However, the presence of hydrocarbon deposits also affects the differentiation of the *MS* in sediments. Results of statistical data processing indicate significant decrease of the *MS* values and dispersions inside in the hydrocarbon field contour. Table 3 presents the calculated average values of  $\kappa$  and the mean-square deviation  $\delta_\kappa$  for the main rock types of the Tournaisian and Visean stages from the productive and unproductive wells of the Seluchy and Pryrichna hydrocarbon fields.

In most cases, the values of  $\kappa$  and  $\delta_\kappa$  in the productive wells practically do not correlate with the rocks' age. The fact of joint existence of several different  $\kappa$  samples over

hydrocarbon deposits may indicate the presence of rocks with significantly different magnetic properties. According to the results of the X-ray diffraction and X-ray fluorescence spectrometry, samples for the *MS* processing contain nodules and spherulites of iron carbonates: siderite–siderite-pletitic and siderite-ankerite mineralization. By comparing the material composition of the same type of rocks of Upper Visean LMH in productive and nonproductive wells, a significantly higher content of total iron (+2Fe, +3Fe)  $\text{Fe}_2\text{O}_3$  was found, as well as  $\text{TiO}_2$ , S, V, Zn, Sr, Zr in the covering clays of deposits comparing these contents outside the hydrocarbon fields (Maksymchuk et al. 2007). The presence of such minerals as siderite, kaolinite and chlorite over oil and gas deposits may be a signature of certain epigenetic changes of the rocks mineral composition under influence of the hydrocarbon fluids occurring in the zones of hydrocarbon fields (Bagin and Malumyan 1976).

**Table 3** Average values of MS and standard deviation ( $\delta_\kappa$ ) (both in  $10^{-5}$  SI unit) of the main types of Lower Carboniferous rocks at the Seluchy and Pryrichna hydrocarbon fields (Dnieper-Donets Depression, Ukraine)

Areas		Seluchy						Pryrichna					
Well		304		5		1		385		3		386	
Stage	Rock type	$\kappa_{av}$	$\delta_\kappa$	$\chi_{av}$	$\delta_\chi$	$\kappa_{av}$	$\delta_\kappa$	$\kappa_{av}$	$\delta_\kappa$	$\kappa_{av}$	$\delta_\kappa$	$\kappa_{av}$	$\delta_\kappa$
C <sub>1v2</sub>	Argillite (mudstone)	15.71	7.39			18.71	6.14	20.56	6.62	6.80	2.32	18.20	6.01
								29.07	5.34	17.10	5.39	17.96	17.82
	Siltstone									11.96	3.26	17.30	5.01
	Sandstone	3.31	1.81					18.17	4.22	14.90	4.12	12.09	8.77
	Limestone	3.50	1.60			15.50	12.59	27.11	5.92			7.1	1.45
C <sub>1v1</sub>	Argillite	4.57	2.58	10	0.49	6.21	1.95	6.50	5.38	3.50	1.12	2.73	1.42
				1.26	0.64					3.70	1.26	4.20	2.28
	Siltstone									3.80	2.10		
	Limestone	3.03	1.93	1.40	1.00			2.00	1.09	3.40	1.00		
C <sub>1tr</sub>	Argillite	2.83	1.14			30.66	14.46						
	Sandstone	1.45	0.89			3.77	1.81	12.60	8.31				

Productive wells are indicated and the results of the mean values of  $\chi$  and  $\delta_\chi$

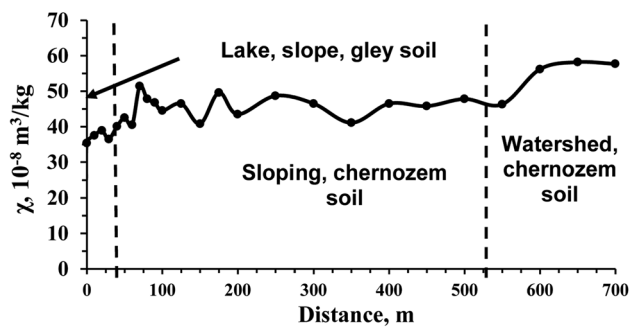


**Fig. 5** Top soil mass-specific magnetic susceptibility along the profile near the Seluchy-304 well, Dnieper-Donets Basin (see Fig. 4)

We performed the studies at the Seluchy oil field in the DDD (Chernuchy district, Poltava region of Ukraine) for more clear understanding of spatial distribution of soil magnetic susceptibility at the HC-bearing area and for finding relations between the MS and microseepage processes. The soil is predominantly ‘chernozem’ (Laktionova et al. 2015) occurring at the watershed and slops. The ‘chernozem’ soil in Ukraine is characterized by comparatively high magnetic properties. Slightly magnetic gley soils (gleysols) occur at the lowland of the investigated region.

The soil magnetic susceptibility was measured along the profile located near the productive oil well 304 (Fig. 5). The mass-specific MS of the gleysols near the lake was  $\kappa_p = 10\text{--}20 \times 10^{-8} \text{ m}^3/\text{kg}$ . At the slope (about  $40^\circ$ ), the mass-specific MS increases up to  $40 \times 10^{-8} \text{ m}^3/\text{kg}$ . At the distance from 150 to 600 m, there is a gradual increase in terrain altitudes (a few degrees). Here, the values of mass-specific MS

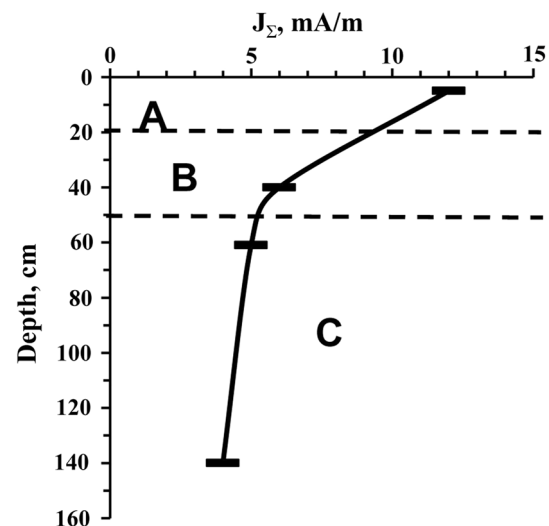


**Fig. 6** Total magnetization of soil distribution along the vertical profile in the genetic horizons of the Seluchy hydrocarbon field (Dnieper-Donets Basin)

were measured as  $\kappa_p = 40\text{--}50 \times 10^{-8} \text{ m}^3/\text{kg}$ . We identified the watershed with chernozems near the points of 600–700 m of this profile ( $\kappa_p = 50\text{--}60 \times 10^{-8} \text{ m}^3/\text{kg}$ ).

We studied the magnetization of soils near the Seluchy-304 well along the vertical profile to find relations with the direct hydrocarbon impact on the soil and magnetic mineralogical content (Fig. 6). We registered the significant increase of soil magnetization near the well (up to 2–10 times). The parameter  $Q$  (Koenigsberger factor), showing the ratio of remnant to induced magnetization, is here about

4–16. This fact could be interpreted as the microseepage impact and presence of authigenic magnetic minerals formation in soil.

The obtained results demonstrate a significant differentiation of magnetic parameters of soils both laterally and vertically that stipulates observed fluctuations of the anomalous magnetic field.

## Discussion

### Middle Kur Depression (Azerbaijan)

To justify the expediency of using magnetic prospecting for searching HC deposits in Azerbaijan, the features of changing of rock physical properties (laterally and vertically) in the sections of Muradkhanly, Jafarly and Zardab fields (MKD) were considered in detail. Data of the rock magnetic susceptibility for these areas were obtained from the selected cores in laboratory conditions (e.g., Salekhli 1979). Analysis of the magnetic properties of rocks selected from “empty” and oil-bearing wells and related to different stratigraphic complexes showed that the magnetic susceptibility of the rocks above and below the hydrocarbon deposits sharply differs by the magnetic susceptibility from the side host rocks. For example, in the Absheron and Akchagyl deposits, the average value of the magnetic susceptibilities ( $MS$ ) of the rocks outside and within the contour of the deposits was  $75 \times 10^{-5}$  and  $50 \times 10^{-5}$  SI, respectively. In some sedimentary rocks,  $MS$  decreases by a factor of 2–8. Such a distribution of the  $MS$  undoubtedly creates favorable prerequisites for effective application of magnetic prospecting for searching HC accumulations within the MKD.

Thus, magnetic modeling was carried out at the well-studied Muradkhanly and Jafarly deposits (Gadirov 1997; Gadirov and Eppelbaum 2012; Gadirov 2013) with the aim of clarifying the peculiarities of the magnetic field anomalies over HC deposits. These areas were chosen as they have been studied in detail and petrophysical rock properties are available from numerous deep wells.

On the basis of magnetic field modeling, it was found that local positive anomalies retrieved from the magnetic field are associated with the volcanic formations occurring in the sedimentary complex. Beside this, it has also been established that local magnetic (as well as gravity) minima of different intensities appear over the productive parts of the buried structures (Gadirov 1996, 2002, 2013). Volcanogenic rocks in the region are characterized by a high  $MS$  ( $1380\text{--}5700 \times 10^{-5}$  SI) in contrast to the surrounding sediments of very low  $MS$ . The magnetic field significantly decreases over the HC reservoirs that creates favorable conditions for mapping the oil deposits.

The geological section of the Muradkhanly and Jafarly fields, composed of volcanic formations of the Upper Cretaceous, is characterized by a high  $MS$  with the averaged value  $\kappa_{av} = 3140 \times 10^{-5}$  SI. To compile the initial PGM of the deposits, the numerous data for different kinds of sediments (e.g., Gadirov 2012; Gadirov and Eppelbaum 2012) were used.

We modeled that in the Muradkhanly area, an effect of the subvertical zone above the hydrocarbon reservoir can reach  $-15$  to  $-20$  nT. Reducing the  $MS$  below the reservoir in effusive formations creates an additional negative magnetic effect exceeding  $-20$  nT. Thus, the entire zone associated with the oil deposit can produce a magnetic anomaly of about  $-40$  nT. In contrast to the Muradkhanly deposit, the Jafarly deposit is associated with the Middle Eocene sedimentary deposits. Volcanogenic rocks in this area are exposed in the well No. 7 at a depth of 4408 m. Depth of the volcanogenic rock occurrence in the PGM was calculated on the basis of gravity and magnetic data forward modeling and cores selected from wells No. 7 (Jafarly) and No. 1 (Karaly). The calculated magnetic effect above and below the oil deposit is 15 and 17 nT, respectively. In both models, the theoretical reservoir effect with a thickness of 100–150 m and depth of 3000 m does not exceed 2 nT while the effect of the entire vertical zone reaches 30–40 nT (Gadirov 1997; Gadirov and Eppelbaum 2012).

The Tarsdallar area is located on the northwestern part of the MKD (Fig. 7). This structure was discovered in 1978 in Upper Cretaceous and Eocene sediments on the basis of seismic data analysis. In 1982, well No. 1 from the Middle Eocene complex gave commercial (initial production rate of 200 tons/day) oil and opened a new hydrocarbon deposit. Later wells 4, 8 and 9 also gave a commercial inflow of oil. Until the beginning of the 1990s of the twentieth century, seismic and drilling works were continued in this and adjacent areas. As a result, the Western Tarsdallar fold consisting of the hemianticline and the Northern Tarsdallar structure was identified. At further stages, gravity and magnetic studies were carried out to examine the Upper Cretaceous sediments and estimate the possible commercial oil and gas content.

The results of magnetic prospecting indicate that the anomalous magnetic field  $\Delta T$  in the Tarsdallar region varies within 300–400 nT. Magnetic field behavior clearly divides this area into southern, northern and central parts. The Tarsdallar magnetic field anomaly acquires a sublatitudinal direction, and the field intensity decreases up to 50 nT to the north.

Along the profiles crossing the Tarsdallar area, the field  $\Delta T$  is manifested by ruggedness; nevertheless, local magnetic maxima can be distinguished from the regional field (Fig. 8). Local maxima with intensities of up to 60 nT have been singled out at all parallel profiles, and a scheme of



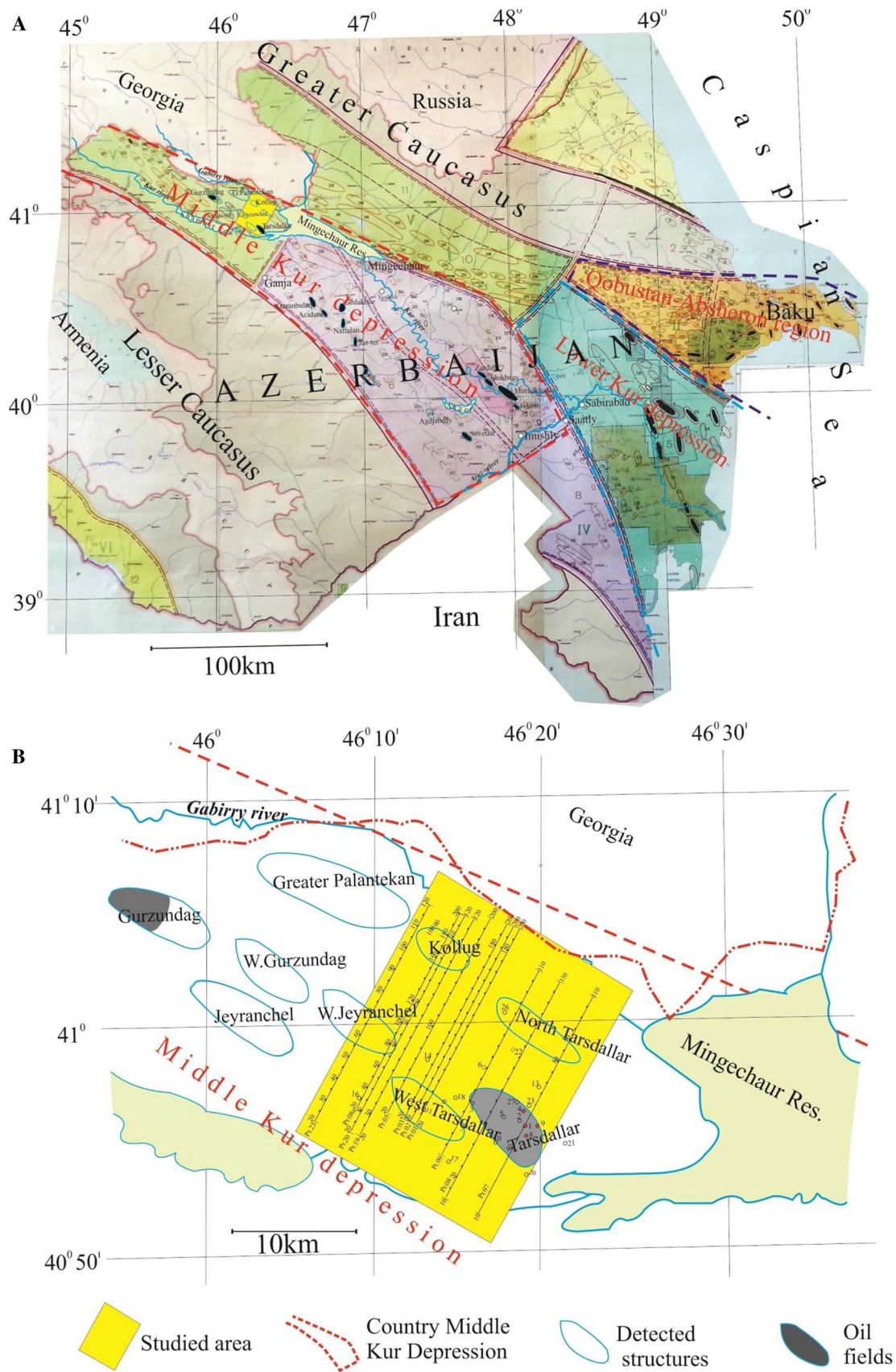
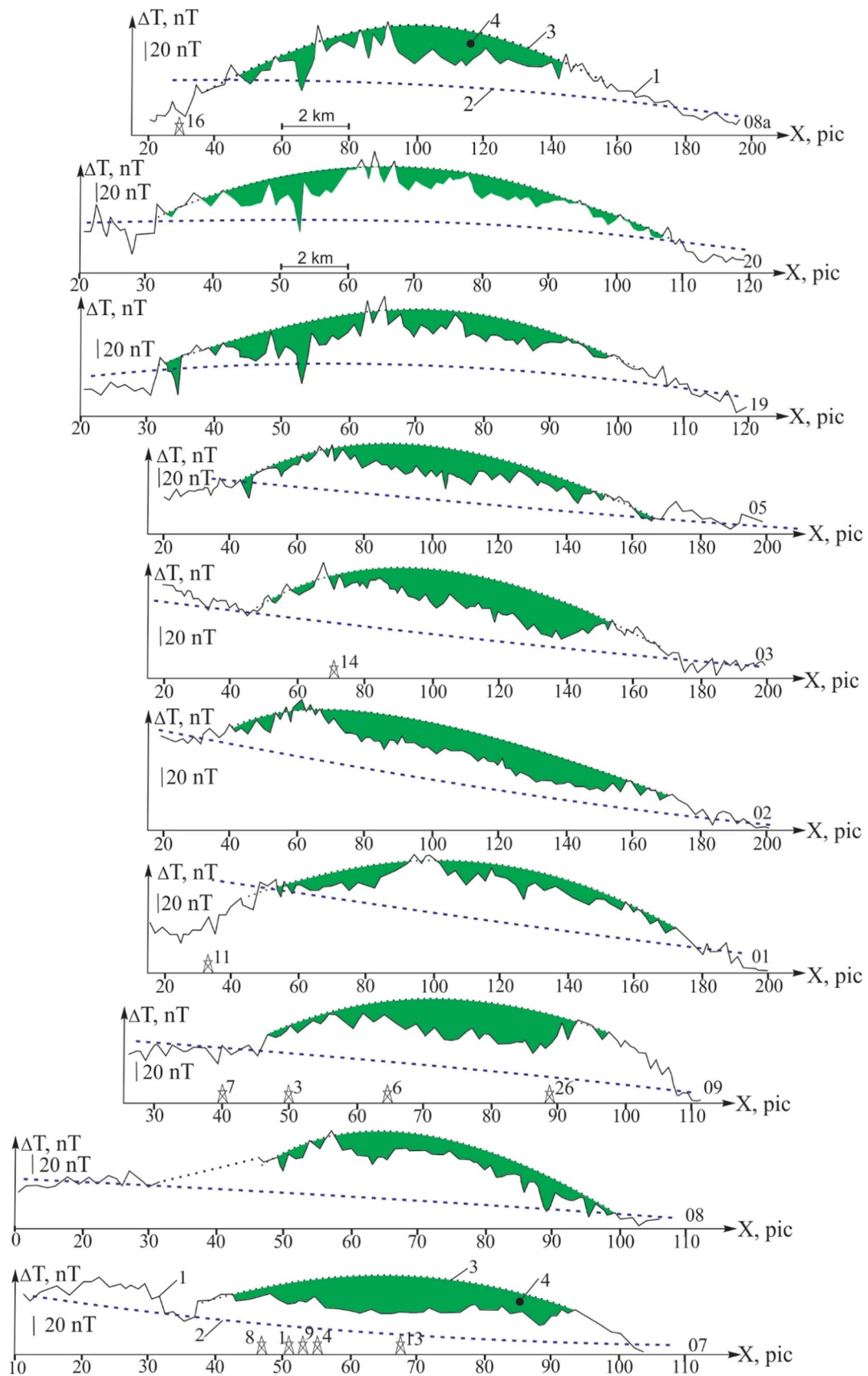


Fig. 7 Map of the region under study. **a** Map of Azerbaijan and surrounding regions and **b** scheme of some oil deposits location within the Middle Kur Depression



**Fig. 8** Magnetic profiles observed in the Tarsdallar area (Middle Kur Depression, Azerbaijan) (see scheme of studied area in Fig. 7). (1) Observed field  $\Delta T$ , (2) regional background, (3) retrieved local maximum and (4) local minimum (numbers are explained in the lower profile)

local maxima reflecting the zones of development of volcanic rocks (Fig. 9) has been constructed. Note that almost in all wells drilled in this area, tuffaceous rocks of Eocene and Upper Cretaceous with high magnetic susceptibility  $(2500\text{--}3700) \times 10^{-5}$  SI were discovered, and in well No. 9 basalts with a magnetic susceptibility of  $6000 \times 10^{-5}$  SI were revealed. The zone of the most intense maxima covers Tarsdallar area, passes between the western and northern Tarsdallar, and stretches to the west (Fig. 9).

Against the backdrop of local maxima, local magnetic minima with an intensity of 20–30 nT are detected. These anomalies are associated with the presence of HC accumulation. Using these data, a scheme for the magnetic minima distribution (Fig. 10) was constructed. In fact, wells 1, 4, 8 and 9 which gave a commercial inflow of oil from the Middle Eocene are located in the zone of magnetic minimum. A similar pattern is observed in other areas of the MKD (e.g., Muradkhanly, Zardab, Jafarly, Alvend, etc.) (Gadirov and Eppelbaum 2012; Gadirov 2013). In the area limited by wells 16, 11, 18, 3, 7, 10 and 17, no magnetic minima are observed. All other wells in these areas were closed without testing because of some technical and geological reasons. Possibly, in the zone of intense local minima, one could expect an HC accumulation in the intervals of the Middle Eocene and Upper Cretaceous, for example, in wells 6, 22, 13, etc. (Fig. 10).

Thus, results of magnetic studies performed in the MKD indicate a decrease in the intensity of the magnetic field ( $\Delta Z$ ,  $\Delta T$ ) from numerous to a few dozens of nT over a number of hydrocarbon deposits (e.g., Muradkhanly, Jafarly, Alvend, Tarsdallar, etc.). Analysis of magnetic data along profiles indicates that practically all negative anomalies are associated with buried hydrocarbon deposits (Mamedov and Gadirov 1982; Gadirov 1994).

### Dnieper-Donets Depression (Ukraine)

Interpretation of detected local anomalies  $\Delta T_a$  is associated here with certain difficulties. The amplitudes of local anomalies of  $\Delta T_a$ , as a rule, do not exceed 6–7 nT at a width of 3–4 km. There are no data of rock magnetic properties in the upper part of the structure (up to 2.5–3 km). An interpretation model should explain the mechanism of magnetic anomalies and the facts of their affinity to oil and gas fields. Therefore, interpretation of local anomalies of  $\Delta T_a$  has been carried out within the framework of theoretical models assuming the zones with different magnetic properties

inside and above the oil and gas reservoirs (Gadirov 1994; Schumacher and Abrams 1996; Berezkin et al. 1998; Machel and Burton 1991a, b; Saunders et al. 1999).

The proposed interpretation model assumes the existence in the sedimentary stratum of three sources as A, B and C layers which contribute to the observed magnetic field (Fig. 11).

Layer A is represented by the Famennian-Tournaisian LMH, lenticular bodies of which are composed of tuffs, insignificant interbedding of basalts and small-amplitude protrusions of the crystalline basement. We assumed that the magnetization of the basement rocks (granitoids) has a magnetization  $J=150$  mA/m (by analogy with surrounding regions).

Layer B presents an anticlinal structure along the seismic reflecting horizon of the Viséan stage. It was assumed that the Viséan-Serpukhovian LMH include thin layers of rock with siderite and ankerite mineralization ( $J=7$  mA/m). We assume that in some cases, a *MS* of sideritized layers can be significantly higher with the formation of a paragenetic association of siderite–magnetite (Bagin and Malumyan 1976).

Layer C reflects a lithological heterogeneity in the upper part of the sedimentary cover with magnetite–pyrrhotite mineralization ( $J=4$  mA/m and 17 mA/m) at a depth of up to 1 km above the hydrocarbon deposits. It is proposed that formation of magnetic minerals exists according to the model of mineralogical changes of rocks under the influence of hydrocarbons in the oxidation zone by bacterial or chemical means during formation of magnetite or pyrrhotite. The thickness of layer B is chosen to be about 1.0 km, since according to theoretical data, chemical processes causing formation of magnetite are possible only in the depth interval of 0–1000 m (Schumacher and Abrams 1996; Machel and Burton 1991a, b). Findings of rounded nodules of the mineral slurry in the drilling wells at depths of 500–600 are also known (Aldana et al. 2003; Liu et al. 2004). All other parts of the sedimentary stratum between the layers A and B located in the reduction zone are assumed to be very weakly magnetized:  $J \approx 1$  mA/m.

We present here 2D magnetic field modeling results along profile III–III of the Seluchy field where  $\Delta T_a$  anomaly has the most contrast and reaches values of about 6 nT at the width of up to 4 km (Kuderavets et al. 2009). In the performed modeling, all three aforementioned sources (A, B and C) were utilized in the form of separate layers. Geological bodies were approximated by rectangular parallelepipeds of unlimited strike in the submeridional direction. The corresponding algorithm applied in the modeling is described in detail in (Kuderyavets et al. 2009).

Figure 11 shows the results of the comparison of the anomalous effects calculated from the layers A, B and C. The obtained data indicate that more adequate model was received from three layers where layer C does the main



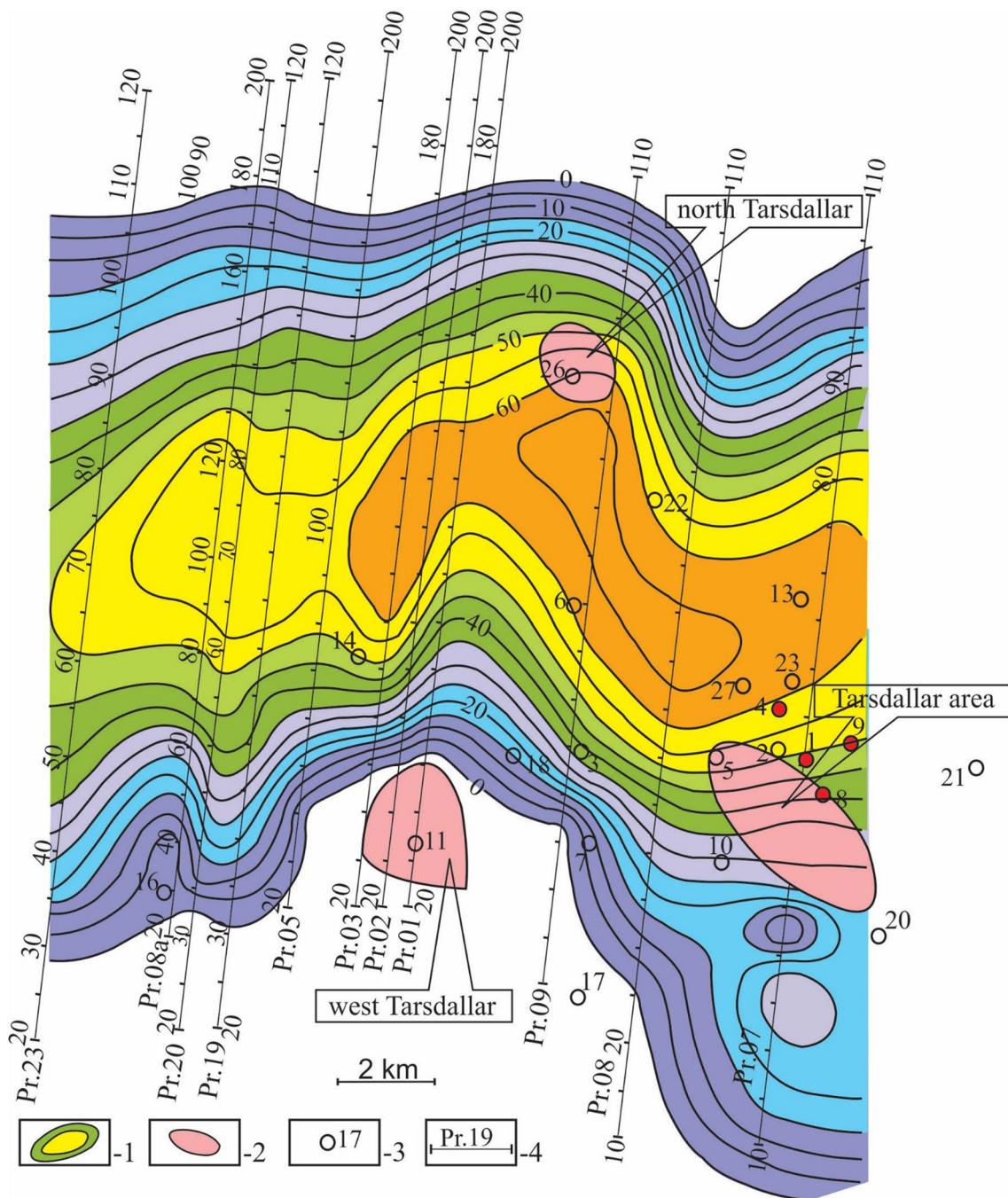


**Fig. 9** Scheme of distribution of local magnetic maxima (values are given in nT) in the Tarsdallar area (Middle Kur Depression) (see scheme of studied area in Fig. 7). (1) Positive local magnetic anomalies, (2) arch of the structure, (3) exploration wells and (4) observation profiles

contribution to formation of the local magnetic anomaly. This layer represents the lithological heterogeneity in the upper part of the section. With magnetization  $J = 4 \text{ mA/m}$ , a thickness of 1 km and a length of about 3 km, the magnetic anomaly  $\Delta T_a$  at a width of 3.7 km reaches an amplitude of more than 5 nT that agrees with the observed curve  $\Delta T_a$ . The possible presence of diabbases and siderite layers at depths of 3.6 and 3.1 km, respectively, will provide at the earth's

surface a magnetic anomaly with an amplitude of 0.6–0.8 nT and a width of 7–8 km that contradicts the observed magnetic anomaly.

The dotted line in Fig. 11 shows the curves  $\Delta T_a$  computed from the layers A–C with the latitudinal orientation of the magnetic profile. The obtained modeling results are consistent with the preliminary PGM constructed earlier for the Selucky field (Orlyuk et al. 1998).



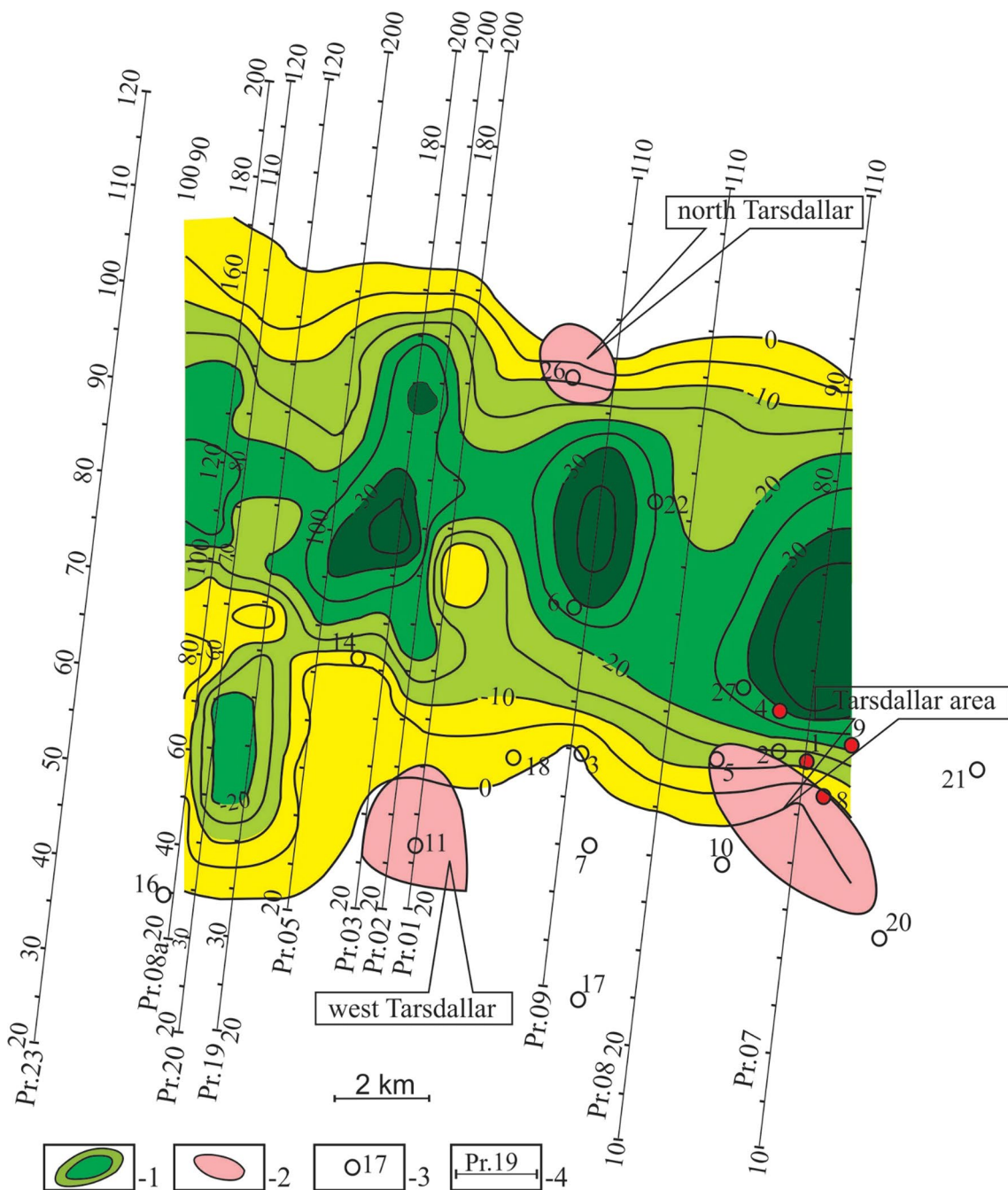


**Fig. 10** Scheme of distribution of local magnetic maxima (values are given in nT) in the Tarsdallar area (Middle Kur Depression). (1) Local positive magnetic anomalies, (2) uplifted part of the structure, (3) exploration wells and (4) observation profiles

The results of magnetic field modeling indicate that magnetic field heterogeneities of epigenetic origin in the near-surface layers up to 1 km contribute to appreciable effect in the observed field  $\Delta T$ . The conducted studies have shown the existence of genetic links between the fine structure of the anomalous magnetic field and the hydrocarbon deposits in the carbonate and sandy reservoirs of the DDD Lower Carboniferous oil and gas complex.

The considered results of magnetic studies of soil confirm the theory of migration of hydrocarbons and their influence on the formation of authigenic minerals in rocks and soils (Liu et al. 2006). To increase the level of understanding of formation of authigenic magnetic minerals under the hydrocarbons influence, the transformation of magnetic minerals (Porsch et al. 2014) should be investigated in more detail. Contribution of the microbiological

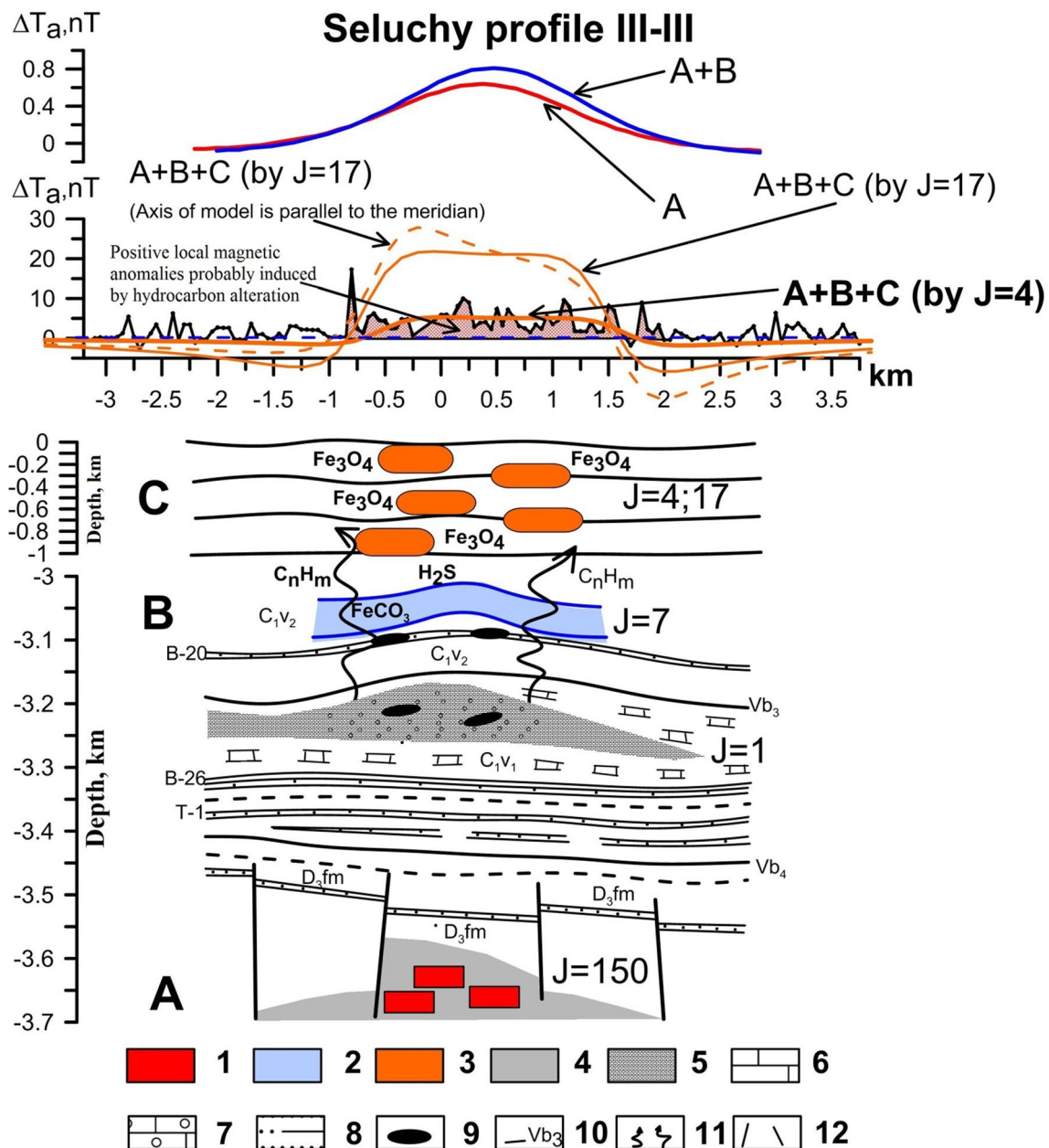


**Fig. 11** Local anomalous magnetic field along profile III–III of the Seluchy field (Dnieper-Donets Basin) and schematic PGM (see location of Profile III–III in Fig. 4). (1) Basalt layers of the Famen strata, (2) siderite layers in Upper Visean sediments, (3) magnetic minerals in oxidation zone, (4) salt, (5) limestone, (6) limestone in flanking facies, (7) bioherm facies, nuclear part, (8) sandstone, (9) oil reser-

voir, (10) seismic horizons, (11) flank of the field, subvertical zones of increased permeability of heterogeneous medium and (12) faults. A, B, C are the floors of the physical–geological model (C is the upper, B is the intermediate and A is the lower floor). The values of magnetization ( $J$ ) of layers A–C are given in mA/m

metabolism demands comprehensive examination of the dynamics of aerobic and anaerobic processes (e.g., Klueglein et al. 2013). The oxidation processes predominate in the near-surface horizons and soils; here, such authigenic minerals as hematite and magnetite are widely distributed. According to Machel (2001), epigenetic magnetite can be

retrieved as a result of the hematite transformation under the common influence of hydrogen sulfide, microorganisms and atmospheric water. The mechanism of the hydrocarbon migration from deep reservoirs to the surface may be significantly accelerated to be conducted along faults and cracks.

## Conclusions

Analyses of the observed data indicate that the dimensions and contours of the selected magnetic minima against the magnetic maxima background usually correspond to the contours of the buried hydrocarbon deposits.

Performed studies have shown an existence of genetic links between the thin structure of the anomalous magnetic minima over the hydrocarbon deposits and the anomalous subvertical zone (associated with the oil and gas deposits) above and below the reservoirs.

It is recognized that in the Middle Kur Depression (Azerbaijan), the magnetic maxima are morphologically connected with the buried volcanogenic structures. In the Dnieper-Donets Depression (Ukraine), they are maxima associated with tectonic faults through which microseepages of hydrocarbon fluids are developed.

Based on the results of magnetic field modeling of the investigated structures of MKD and DDD, it was established that magnetic field heterogeneity of epigenetic origin under the influence of hydrocarbon fluids significantly contributes to the observed magnetic field structure.

Magnetic field examination and constructed physical–geological models for the well-studied hydrocarbon deposits in Azerbaijan and Ukraine indicate that the detailed magnetic prospecting could be successfully applied to localization of oil and gas deposits occurring at different depths.

All aforementioned data indicate that optimal application and utilization of high-resolution magnetic measurements in the hydrocarbon regions may help to decrease the number of prospecting wells that finally will reduce the burden on the environment and the exploration cost.

**Acknowledgements** The authors would like to thank Assoc. Editor Dr. Ralf Schaa and two anonymous reviewers who thoroughly reviewed the manuscript, and their critical comments and valuable suggestions were very helpful in preparing this paper.

## References

- Abdulabekov KP, Golovkov VP (1974) Geomagnetic field changing and processes in the Earth's crust. *Izvestiya Acad Sci USSR Ser Phys Earth* (3):93–100
- Aldana M, Costanzo-Alvarez V, Bolivar S, Diaz M (2003) Magnetic and mineralogical studies to characterize oil reservoirs in Venezuela. *Lead Edge* (6):526–529
- Alizadeh AM, Guliyev IS, Kadirov FA, Eppelbaum LV (2017) Geosciences of Azerbaijan. Volume II: economic minerals and applied geophysics. Springer, Heidelberg
- Bagin VI, Malumyan LM (1976) Iron-containing minerals in oil-impregnated sedimentary rocks of the productive series of Azerbaijan. *Izvestiya Acad Sci USSR Phys Earth* (4):73–79
- Berezkin VM, Loshakov AI, Nikolaev MI (1982) Application of magnetic prospecting for searching oil and gas deposits. *Appl Geophys (Prikladnaya Geofizika)*, Moscow (103):128–136 (**in Russian**)
- Berezkin VM, Filatov VG, Ovsepyan ML (1998) Geomagnetic model of hydrocarbons field and identify of local magnetic anomalies of epigenetic mineralization on the background of geological and industrial noise. *Appl Geophys (Prikladnaya Geofizika)*, Moscow 132:156–164 (**in Russian**)
- Bezukladnov VA, Mavrichev VG (1997) Identification of anomalies such a “deposit” by use magnetic field analysis. *Geol Oil Gas* (7): 21–24 (**in Russian**)
- Cisowski SM, Fuller M (1987) The generation of magnetic anomalies by combustion metamorphism of sedimentary rock and its significance to hydrocarbon exploration. *Geol Soc Am Bull* 99:21–29
- Donovan TJ, Hendricks JD, Roberts AA, Eliason PT (1984) Low altitude aeromagnetic reconnaissance for petroleum in the Arctic National Wildlife Refuge. *Geophysics* 49(8):1338–1353
- Elmore RD, Engel MH, Crawford KN, Imbus S, Sofer Z (1987) Evidence for a relationship between hydrocarbon and authigenic magnetite. *Nature* 325:6103–6106
- Emmertson S, Muxworthy AR, Sephton MA (2012) Magnetic characterization of oil sands at Osmington mills and Mupe bay, Wessex Basin. *Geol Soc Spec Publ*, London 371(1):189–198
- Eppelbaum LV (2015a) Quantitative interpretation of magnetic anomalies from bodies approximated by thick bed models in complex environments. *Environ Earth Sci* 74:5971–5988
- Eppelbaum LV (2015b) Quantitative interpretation of magnetic anomalies from thick bed, horizontal plate and intermediate models under complex physical-geological environments in archaeological prospecting. *Archaeol Prospect* 23(2):255–268
- Eppelbaum LV, Khesin BE (2012) *Geophysical studies in the caucasus*. Springer, Heidelberg
- Eppelbaum LV, Mishne AR (2011) Unmanned airborne magnetic and VLF investigations: effective geophysical methodology of the near future. *Positioning* 2(3):112–133
- Eppelbaum LV, Khesin BE, Itkis SE (2001) Prompt magnetic investigations of archaeological remains in areas of infrastructure development: Israeli experience. *Archaeol Prospect* 8(3):163–185
- Eppelbaum L, Ben-Avraham Z, Katz Y (2004) Integrated analysis of magnetic, paleomagnetic and K-Ar data in a tectonic complex region: an example from the Sea of Galilee. *Geophys Res Lett*. <https://doi.org/10.1029/2004GL021298>
- Eventov L (1997) Applications of magnetic methods in oil and gas exploration. *Lead Edge* (3):489–497
- Foote RS (1992) Use of magnetic field aids oil search. *Oil&Gas J* (4):137–142
- Foote RS (1996) Relationship of near-surface magnetic anomalies to oil and gas producing areas. In: AAPG Memoir 66 “hydrocarbon migration and its near surface expression”, pp 111–126
- Gadirov VG (1994) The physical-geological principles of application of gravity and magnetic prospecting in the search of oil and gas deposits. In: Proceedings of the 10th petroleum congress and exhibition of Turkey. Ankara, pp 197–203
- Gadirov VG (1996) Some foundations of magnetic prospecting employment for searching hydrocarbon deposits in the Middle Kur Depression. *Azerbaijan Oil Ind* (6):7–10 (**in Russian**)
- Gadirov VG (1997) The problem of interpreting local gravity and magnetic anomalies in oil and gas fields. *Geophys News Azerbaijan* 4:23–24
- Gadirov VG (2002) Gravity-magnetic studies of buried volcanogenic rocks in the in the Middle Kur Depression in connection with their oil&gas bearing. *Azerbaijan's Geol* (7):130–141 (2002)
- Gadirov VG (2009) Results of application of gravity and magnetic prospecting for prognosis of oil and gas deposits in the Kur

- Depression of Azerbaijan. *Geophysics (Geofizika)*, Moscow (2):51–56 (**in Russian**)
- Gadirov VG (2012) Integration of gravity and magnetic prospecting for searching oil and gas deposits in Azerbaijan. *Geophysics (Geofizika)*, Moscow (6):73–77 (**in Russian**)
- Gadirov VG (2013) Application of magnetic prospecting for searching oil and gas on the perspective areas of Azerbaijan. *Geophys J*, Kiev 35(6):182–189
- Gadirov VG, Eppelbaum LV (2012) Detailed gravity, magnetic successful in exploring Azerbaijan onshore areas. *Oil&Gas J* (5):60–73
- Gay SP (1992) Epigenetic versus syngenetic magnetite as a cause of magnetic anomalies. *Geophysics* 57:60–68
- Gay SP, Hawley BW (1991) Syngenetic magnetic anomaly sources: three examples. *Geophysics* 56(7):902–913
- Hinze WJ, Von Vrese RRB, Saad AH (2013) Gravity and magnetic exploration: principles, practices and application. Cambridge University Press, Cambridge
- Khesin BE, Alexeyev VV, Eppelbaum LV (1996) Interpretation of geophysical fields in complicated environments. *Modern approaches in geophysics*. Springer, Boston
- Klueglein N, Sekann-Behrens T, Obst M, Behrens S, Appel E, Kappler A (2013) Magnetite formation by the novel Fe(III)-reducing *Geothrix fermentans* Strain HradG1 isolated from a hydrocarbon-contaminated sediment with increased magnetic susceptibility. *Geomicrobiol J* (30):863–873
- Kuderavets RS, Maksymchuk VYu, Horodys'kyy YuM (2009) Geomagnetic models of hydrocarbon deposits and perspective structures of the central part of the Dnipro-Donets Depression. *Sci Bull Ivan-Frankivsk Natl Tech Univ Oil Gas* 1(19):73–81 (**in Ukrainian**)
- Kuderavets RS, Maksymchuk VYu, Chobotok IO, Klymkovych TA, Tymoschuk VR, Pyrizhok NB (2013) Practice of magnetic surveys over hydrocarbon fields in the Carpathian foredeep, Ukraine. *Geodynamics*, Kiev 2(15):186–188 (**in Russian**)
- Laktionova TN, Medvedev VV, Savchenko KV, Bigun ON, Nakis'ko SG, Sheyko SN (2015) Ukrainian soil properties Database and its application. *Agric Sci Pract* 2(3):3–8
- Lapshov VA (1975) Additional criteria in employment of magnetometric data by searching hydrocarbon deposits. *Oil Coal Geol* (3):24–28 (**in Russian**)
- LeSchack LA, Van Alstin DR (2002) High-resolution ground-magnetic (HRGM) and radiometric surveys for hydrocarbon exploration: six case histories in Western Canada. In: Schumacher D, LeSchack LA (eds) *Surface exploration case histories: applications of geochemistry, magnetics and remote sensing*. AAPG Studies in Geology, 48(11):67–156
- Liu QS, Chan L, Liu Q, Li H et al (2004) Relationship between magnetic anomalies and hydrocarbon microseepage above the Jingbian gas field, Ordos basin, China. *AAPG Bull.* 88(2):241–251
- Liu Q, Cui Z, Etsell TH (2006) Characterization of Athabasca oil sands froth treatment tailings for heavy mineral recovery. *Fuel* 85(5–6):807–814
- Lukin AE (2017) The Earth outgasing, naphtidogenesis and petroleum potential. *Collection of scientific works of UkrDGRI* 3:9–33 (**in Russian**)
- Machel HG (2001) Bacterial and thermochemical sulfate reduction in diagenetic settings—old and new insights. *Sed Geol* 14:143–175
- Machel HG, Burton EA (1991a) Causes and spatial distribution of anomalous magnetization in hydrocarbon seepage environments. *AAPG Bull* 75:1864–1876
- Machel HG, Burton EA (1991b) Chemical and microbial processes causing anomalous magnetization in environments affected by hydrocarbon seepage. *Geophysics* 56:598–605
- Maevski BY, Babko IM (2006) On the issue of the prospects of oil and gas content in the central part of the Dnieper-Donets basin (taking into account the experience of work in various basins of the world. *Prospect Exploit Oil Gas Depos* 18(1):78–81 (**in Ukrainian**)
- Maher BA, Thompson R (1991) Mineral magnetic record of the Chinese loess and paleosols. *Geology* 19:3–6
- Maksymchuk VYu, Kuznetsova VG, Chobotok IO (1999) Experience of using precise magnetometry for searching hydrocarbon deposits. *Collection of Papers, Ukraine Academy of Science, Geophysics* 3(6):154–158 (**in Ukrainian**)
- Maksymchuk V, Gorodyskiy Yu, Kuznetsova V (2001) Dynamics of the earth's anomalous magnetic field. *Eurosvit, L'vov* (**in Ukrainian**)
- Maksymchuk VYu, Kuderavets RS, Gorodyskiy JM, Gaupp R (2007) Anomalous magnetic field and rocks magnetic features in the Pryrichna gas-condensate deposit. *Prospect Dev Oil Gas Fields* 1(22):19–30 (**in Ukrainian**)
- Mamedov SG, Gadirov VG (1982) Application of precise gravity and magnetic prospecting for searching local structures and prognosis uia zones of development of oil&gas collectors in the south-west part of the Evlakh-Agdzhabedy Depression. *Report* 313-81, Baku, pp 1–136
- Mavrichev VG (1997) Airborne magnetic prospecting on the regional stage of studying perspective hydrocarbon areas. *Homeland Geol* (12):34–39 (**in Ukrainian**)
- Mavrichev VG, Kozeyev SI, Petrova AA, Antonov KV, Shadrin VF (2002) Airborne geophysics for prognosis of oil&gas bearing of ancient rocks. *Interval* (3):64–69 (**in Russian**)
- Menshov AI, Kuderavets RS, Chobotok IA (2014) Examination of magnetic field and magnetic susceptibility in areas of hydrocarbons exploration in the Carpathian Foredeep. In: *Transmission of the 13th international conference on geoinformatics: theoretical and applied aspects*, 12–15 May, Kiev, Ukraine (**in Russian**)
- Menshov O, Kuderavets R, Vyzhva S, Chobotok I, Pastushenko T (2015) Magnetic mapping and soil magnetometry of hydrocarbon prospective areas in western Ukraine. *Stud Geophys Geod* 59(4):614–627
- Nettleton LL (1976) *Gravity and magnetics in oil prospecting*. McGraw-Hill, New York
- Orlyuk MI, Maksymchuk VE, Vakarchuk GI, Chepil' PM (1998) Magnetometric studies with regional and local prognosis of oil and gas potential of the Earth's Crust in the Dniepr-Donets basin. *Geophys J* (3):92–102 (**in Russian**)
- Perez-Perez A, D'Onofrio L, Bosch M, Zapata E (2011) Association between magnetic susceptibilities and hydrocarbon deposits in the Barinas-Apure Basin, Venezuela. *Geophysics* 76(6):35–41
- Pirson SJ (1971a) New electric technique can locate gas and oil. *World Oil* 172(5, Part 1):69–72
- Pirson SJ (1971b) New electric technique can locate gas and oil. *World Oil* 172(6, Part 2):72–74
- Porsch K, Rijal M, Borch T, Troyer L, Behrens S, Wehland F, Appel E, Kappler A (2014) Impact of organic carbon and iron bioavailability on the magnetic susceptibility of soils. *Geoch Cosmoch Acta* 128:44–57
- Putikov OA, Veshev SA, Voroshilov NA, Alekseyev SG, Tzyun Ch, Kasyankova NA (2000) “Jet” scattering halos over oil and gas deposits in heterogeneous rocks. *Geophysics (Geofizika)*, Moscow (1):52–56 (**in Russian**)
- Salekhli TM (1979) Regularities of physical parameters changing in sections of Kura Depression and their relationships with epigenetic processes. Deposited in the VINITI USSR Academy of Science, No. 2828-79 Dep.: 1–32 (**in Russian**)
- Saunders DF, Burson KR, Thompson CK (1991) Observed relation of soil magnetic susceptibility and soil gas hydrocarbon analysis to subsurface petroleum accumulations. *AAPG Bull* 75:389–408
- Saunders DF, Burson KR, Thompson CK (1999) Model for hydrocarbon microseepage and related near-surface alterations. *AAPG Bull* 83(1):170–185



- Schumacher D (2010) Non-seismic detection of hydrocarbons. In: Transmission of the AAPG European region annual conference, Kiev, Ukraine, October 17–19, 2010. [http://www.searchanddiscovery.com/documents/2011/40722schumacher/ndx\\_schumacher.pdf](http://www.searchanddiscovery.com/documents/2011/40722schumacher/ndx_schumacher.pdf). Last visited on 15 July 2018
- Schumacher D, Abrams M (1996) Hydrocarbon migration and its near-surface expression. AAPG Memoir 66
- Seifulin RS (1980) Relationship of thermal and magnetic anomalies over hydrocarbon deposits with natural electric fields. Oil Gas Geol Geophys (8):42–43 (in Russian)
- Suvorov VV (1989) On the nature of magnetic anomalies over hydrocarbon structures. In: Geophysical methods of searching and prospecting of oil and gas deposits. Perm', Russia, pp 58–63
- Ulmishek GF (2001) Petroleum geology and resources of the Dnieper-Donets Basin, Ukraine and Russia. US Geol Surv Bull 2201-E:1–17
- Ustinova VN (2002) Hydrocarbon deposits and peculiarities of their appearing in geophysical fields. Geofizika (Geophysics) (5):25–31 (in Russian)



# Developing nonlinear models for sediment load estimation in an irrigation canal

Fahad Ahmed<sup>1</sup> · Muhammad Hassan<sup>2</sup> · Hashim Nisar Hashmi<sup>3</sup>

Received: 9 June 2018 / Accepted: 29 October 2018 / Published online: 3 November 2018  
© Institute of Geophysics, Polish Academy of Sciences & Polish Academy of Sciences 2018

## Abstract

The study was performed to estimate the weekly sediment load in Thal canal located in Mianwali district Punjab, Pakistan. Past records of sediments and discharge have been considered as the input parameters. The best input combinations have been identified with the help of advanced algorithms including full, sequential and increasing embedding, genetic algorithm and hill climbing in combination with the gamma test. Model training has been carried out using two artificial neural network-based algorithms, namely Broyden–Fletcher–Goldfarb–Shanno (BFGS), back-propagation and a local linear regression technique. A variety of statistical parameters including  $R$  square, root mean squared error, mean square error and mean bias error (MBE) has been calculated in order to evaluate the best models. The results strongly suggested that BFGS-based model performed better than all other models with remarkably low values of MBE. Significantly high values of correlation coefficient ( $R$  square) in both training and testing evidenced a close similarity between actual and predicted sediment load values for the same model.

**Keywords** Artificial neural networks · Gamma test · Sediment load · Training · Testing

## Introduction

The phenomenon of sedimentation has utmost importance in open-channel hydraulics as it can alter hydraulic properties of open channels by either creating “scour” or producing “deposition,” thus reducing channel capacity in the former case and facilitating island formation in the latter case (Shirin et al. 2010; Ashkarian et al. 2010). Sedimentation can cause aggradation which can increase flood risk, and also it can cause erosion of hydraulic structures like bridge piers

which can lead to their failure during floods (Ballio and Tait 2012). The deposition of sediments can cause a decrease in channel cross-sectional area by changing its hydraulic resistance or friction (Ackers et al. 1996; Ota and Nalluri 2003; De Sutter et al. 2003), causing an extra cost required for sediment cleaning (Safari et al. 2016). The deposition of sediments occurs when the sediment transport or sediment carrying capacity of a system is less than the sediment load present in the system. With the increased channel flow, the transport capacity of system is increased and results in flushing of sediments from the bed of channel. Further increase in flow may result in erosion of channel which is not required, so to establish a dynamic equilibrium there should be non-erosive or non-scouring velocity of flow by which these sediments can be discharged at the end of the channel (Ochiere et al. 2015). Not only this, sedimentation can seriously affect the operation and performance efficiency of the cross-river structures which get water from natural sources (Sajedi 2010).

In recent past, sediment transport in non-erodible channels has also received interest because of the environmental effects of sediments like contamination of sediments due to toxic substances and materials, especially in urban drainage channels (Ashley et al. 1992). The particles are moved and

✉ Fahad Ahmed  
fahad.ahmed@uos.edu.pk

Muhammad Hassan  
hassan.ce@must.edu.pk

Hashim Nisar Hashmi  
hashim.nisar@uettaxila.edu.pk

<sup>1</sup> Department of Civil Engineering, College of Engineering and Technology, University of Sargodha, Sargodha 40100, Pakistan

<sup>2</sup> Department of Civil Engineering, Mirpur University of Science and Technology, Azad Kashmir, Pakistan

<sup>3</sup> Department of Civil Engineering, University of Engineering and Technology Taxila, Taxila, Pakistan

transported due to conditions called incipient motion and incipient deposition, respectively (Safari et al. 2015). These conditions of defining sediment motion and transportation in rigid boundary channels were studied and investigated by Novak and Nalluri (1984), El-Zaemey (1991), Ab Ghani et al. (1999), Mohammadi (2005), Bong et al. (2013) and Safari et al. (2013a). Loveless (1992) performed experiments in University of London, UK, in circular-, rectangular- and U-shaped cross-sectional channels at incipient deposition condition. Safari et al. (2014, 2015) extended the experimental work of Loveless (1992) by developing regression models to compute critical velocity and incipient deposition condition and found that critical velocity is higher for incipient deposition as compared to incipient motion with same flow condition but with non-cohesive sediments. The effect of discharge and temperature upon suspended sediment load and its transportation was investigated by Rajesh Kumar et al. (2018). Sedimentation process and sediment transport were investigated analytically by the use of sediment and hydraulic analysis for rehabilitation of canals (SHARC) software in lined channels by Sajedipoor et al. (2010). Suspended load and bed load sediment concentrations were estimated by the use of SHARC software for the concrete canals of the western water intake in the Dez irrigation and drainage scheme and in main Sabilli canal in Iran (Sajedipoor et al. 2010). Ochiere et al. (2015) did simulation of sediment transport for an underground lined channel in Kenya by the use of Hydrologic Engineering Center—River Analysis System (HEC-RAS) model.

Computing sediment load is the first step toward designing and maintaining the capacity of a canal system. A continuous record of discharge and sediment load not only is essential for operation but should also be utilized to estimate the incoming sediment load in order to manage the system pro-actively. The importance of this estimation increases exponentially, when change in regimes of channel happens due to construction of new structure or damage in the part of a canal system. This damage is basically a failure of system that may result in reduced channel capacity or breaching of channel due to increased erosion. If there is no external agent like earthquake or a flood that has caused this damage, then certainly it is the result of altered design parameters including full supply levels, channel discharge and sediment rate. So, the regimes of hydraulic parameters should be analyzed and checked properly. As each parameter is dependent upon one another, e.g., sediment transport capacity depends upon the amount of sediments present in the system. Similarly, the amount of incoming sediment is a deciding factor for the discharge on which the system will be regulated safely without causing any further damage, thus emphasizing the importance of accurate estimate for sediment load of a canal system. On the other hand, this “accurate estimation”

of sediment transport is one of the most laborious problems in water resources engineering. Daily records of flows and sediment load determined at the head of channel provide us an opportunity to analyze and develop relationships between different hydrologic parameters. Without considering the underlying process, the utilization of “data only” leads us to the use of statistical approaches that are not only economical but also time saving. Recently, the use of artificial intelligence specifically ANN has been successfully proved beneficial to the designers and managers and provides them an accurate estimation tool for a variety of hydraulic, hydrologic and environmental details (Tsai et al. 2015; Chang and Tsai 2016; Chang et al. 2016). Examples of hydrologic parameter estimation using ANN includes prediction of total monthly rainfall (Freiwan and Cigizoglu 2005), precipitation forecasting (Hall 1999), stream flow (Hassan et al. 2015a, b), runoff for the watersheds (Cannon and Whitfield 2002), (Reddy 2003), (Zhang and Govindaraju 2003) and reservoir levels (Shamim et al. 2015a, b); suspended sediment at the mouth of reservoir (Hassan et al. 2015a, b), sediment concentration in rivers (Nagy et al. 2002), sediment yield for Banha watershed in India (Sarangi and Bhattacharya 2005), mean grain size (Rezaei et al. 2009), daily and weekly sediment load (Melesse et al. 2011), (Cigizoglu 2004), (Lafdani et al. 2013), river flow forecasting (Cigizoglu 2003a, b), sediment discharge (Mustafa et al. 2011), suspended sediment (Bhattacharya et al. 2007; Azamathulla et al. 2010), (Partal and Cigizoglu 2008), (Alp and Cigizoglu 2007), and other applications of ANN for sediment prediction are Abrahart and White (2001), Yitian and Gu (2003), Zhu et al. (2007), Wang et al. (2008), Atieh et al. (2015), Thompson et al. (2016) and Yang et al. (2009), river suspended sediment modelling was done by using the CART model (Choubin et al. (2018)). The most recent studies on sediment modeling include: suspended sediment load estimation using artificial bee colony (ABC), multivariate adaptive regression splines (MARS) and teaching–learning-based optimization algorithm (TLBO) models (Banu Yilmaz et al. 2018); modeling of suspended sediment of river using support vector machine (SVM) (Nourani et al. 2016); estimation of suspended sediment load (SSL) using artificial neural networks (ANNs), support vector machine (SVM) and adaptive network-based fuzzy inference system (ANFIS) models (Buyukyildiz and Kumcu 2017) and (Adib and Mahmoodi 2017). Suspended sediment load was estimated in a watershed by using regression trees (RTs) and model trees (MTs) (Talebi et al. 2017). Modeling of runoff, sediment and water balance in a river was done by using Soil and Water Assessment Tool (SWAT) (Himanshu et al. 2017) and (Duru et al. 2018). While training ANN models, it is very crucial to determine best input combination prior to modeling phase to carry out the modeling

phase very smoothly. The gamma test (GT) is a novel tool that can be used for best possible input combination selection of parameters. Previously, gamma test was used to determine best input combination for the forecasting of groundwater level (Choubin and Malekian 2017), rainfall–runoff (Remesan et al. 20018a, b), flood flow (Jaafar et al. 2011), evaporation (Han and Yan 2009), global solar radiation (Shamim et al. 2015a, b) and soil moisture deficit (GT) (Zhuo et al. 2016).

Pakistan is a rich agriculture country and has one of the best irrigation systems in the world that covers almost 75% of its cultivable land. Agriculture of Bhakkar, Khushab, Layyah, Mianwali and Muzaffargarh Districts of Punjab province depends upon Thal canal. Thal canal main line was very badly damaged in the head-reach portion and resulted in improper operation of canal system. The damage in canal resulted in change in sediment regime and caused erosion where sediment suspension is less than the capacity of system and induced sediment deposition at the part of system where the reverse case happened. It is highly desirable to provide an economical solution by establishing a balance between sediment transport capacity of system and amount of sediments present in the system. Furthermore, for proper regulation of suspended particles the outlets should have their fair share of silt as the presence of fine silt means enhanced productivity of crops. Accurate and reliable estimates of sediment amount will not only be required to establish a dynamic equilibrium between the sediment load and carrying capacity of the

channel but also help to identify the need of increased water demand in the system. The use of ANN in conjunction with advanced algorithms as model identification techniques acted as helping tools to achieve this goal.

## Methodology

### Study area and dataset

The Thal canal with a designed capacity of 9000 cusecs is located in Mianwali district Punjab, Pakistan, and off takes from left bank of Jinnah barrage which is located at three miles downstream of “Kalabagh” as shown in Fig. 1. It was completed in 1946 and opened on January 1947. The purpose of the project was to irrigate the Sindh Sagar Doab between Indus and Jhelum rivers. The canal irrigated a total of cultivable commanded area (CCA) 21.23 lac acres out of 24.90 lac acres in Bhakkar, Khushab, Layyah, Mianwali and Muzaffargarh districts. Its water allowance is 3.18 cusecs/1000 acres of CCA. With the passage of time, more lands have come under irrigation and small patches of land adjoining the existing irrigation area have also been leveled and are partially benefiting from the irrigation system getting the water from the neighboring farms. For sediment estimation models, antecedent data condition of discharge and temperature has been considered and advanced algorithms have been used in conjunction with ANN to train models for Thal canal system information is given in Table 1.



**Fig. 1** Thal canal location (Source: Google Map)



**Table 1** Thal canal system information (1 canal mile = 5000 ft)

S no.	Description	Unit	Mianwali division	Khushab division	Bhakkar division	Layyah division	Total
1	Main canal and branches	Canal miles	51.55	44.45	76.00	43.46	215.46
2	Distys/minors and subminors	Canal miles	486.41	400.12	536.56	628.11	2051.20
3	Drains	Canal miles	0	223.25	0	0	223.25
4	G.C.A	Acres	504,364	517,779	609,651	734,576	2,366,370
5	C.C.A	Acres	432,156	446,620	528,412	628,164	2,035,352
6	Outlets	No.	1101	1029	1129	1401	4660

**Table 2** Dataset (parameters and data length)

S no.	Station	Parameters	Inputs	Outputs	Data length
1	Thal canal head regulator	Sediment load ( $S_t$ ), discharge ( $Q_t$ )	$Q_t, Q_{t-1*}, Q_{t-2*}, S_{t-1*}, S_{t-2*}$	$S_t$	2010–2015

$t-1$  and  $t-2$  are discharge and sediment load values lagged by 1 week and 2 weeks, respectively

## Datasets

Weekly observations of suspended sediment load and discharge of Thal canal were obtained from irrigation department. The datasets included sediment load and discharge. The detail of datasets is given in Table 2.

Length for training and testing of data was decided through hit-and-trial method. From the total available data length of 284 vectors, 70% of data (200 vectors) were used for training and 30% of data (84 vectors) were used for testing purpose. Initial trials were based upon a thorough literature review, e.g., Litta et al. (2013) used 67% and 33% data, respectively, for training and testing of ANN-based models, whereas Kisi and Cimen (2012) used 80% and 20% data for model training and testing, respectively.

## Data normalization

The data have been made unitless and uniformly distributed through logarithmic transformation. The formula used for the normalization is given as follows:

$$P_n = \frac{P_i - P_{\min}}{P_{\max} - P_{\min}} \quad (1)$$

where  $P_n$  = normalized value,  $P_{\min}$  = the minimum value of  $P$  and  $P_{\max}$  = the maximum value of  $P$ .

## Input combination selection using gamma test and advanced model identification techniques

Gamma test is a mathematical tool that enables us to estimate the value of best mean square error (MSE). This is achieved through creating a number of input combinations and calculating MSE for each and every set of inputs. The

combination of inputs that gives the least value of MSE is considered as the “best combination” for a particular “targeted output” and models developed using this combination are noise-free and smooth. Basically, the MSE or gamma statistic is the variance of noise on our required output. If  $x$  and  $y$  are two variables and  $y$  is a function of  $x$ , then the relationship between these variables can be expressed through an algorithm based upon initial dataset  $\{(x_i, y_i), 1 \leq i \leq M\}$ . Now by disintegrating this function into smooth and noisy parts, expressing  $f$  as a smooth model between  $x$  and  $y$  and  $r$  as a noise that cannot be a part of any smooth model then mathematically (Agalbjorn et al. 1997)

$$Y = f(x) + r. \quad (2)$$

By considering the mean of noise “ $r$ ” is zero, a constant bias can be engaged into the unknown function  $f$  which will be our desired gamma statistics.

Gamma test could be performed on a total of  $2^n - 1$  possible combination, but this may result in many unrealistic input combinations so the best input combination has been determined using many model identification techniques in the WinGamma environment, and only 84 realistic combinations were made. The model identification techniques used in this study are applied without altering their coding or structure. Full embedding utilizes the concept of “a selection of outputs selected from all the possible inputs.” In sequential embedding, the algorithm is executed sequentially once through, from start to finish. The increasing embedding, algorithm starts by taking only one input that is situated furthest to the right and running from right to left, the number of bits is increased in the mask and the value of gamma statistics is computed for each set of mask, separately. Genetic algorithm (GA) mimics biological evolution of the species by survival of the fittest, as described by Charles Darwin. The algorithm repeatedly modifies a population of

individual solutions. In hill climbing, a mask is selected and then flipped every bit of it to calculate the gamma value till we reach end of the mask. This is reiterated till no single flips produce betterment over the gamma statistics.

## Model development

### Local linear regression (LLR)

Local linear regression is a reliable technique which is normally used in low-dimensional forecasting and may result in high degree of precision. The criterion of influence statistics is used to select the number of nearest neighbors which are required to solve a linear matrix Eq. 3.

$$\begin{bmatrix} x_{11} & x_{12} & x_{13} & \dots & x_{1d} \\ x_{21} & x_{22} & x_{23} & \dots & x_{2d} \\ x_{31} & x_{32} & x_{33} & \dots & x_{3d} \\ \vdots & \vdots & \vdots & \ddots & \vdots \\ x_{xpmax1} & x_{xpmax2} & x_{xpmax3} & \dots & x_{xpmaxd} \end{bmatrix} \begin{bmatrix} m_1 \\ m_2 \\ m_3 \\ \vdots \\ m_d \end{bmatrix} = \begin{bmatrix} y_1 \\ y_2 \\ y_3 \\ \vdots \\ y_{max} \end{bmatrix}, \quad (3)$$

whereas  $X$  is a  $d$  matrix having input points  $p_{max}$  in  $d$  dimension,  $x_i (1 \leq i \leq p_{max})$  defines the nearest neighbor points,  $y$  is a column vector of length  $p_{max}$  of the corresponding outputs and  $m$  is a column vector of parameters.

### Artificial neural networks (ANNs)

The idea of ANN was inspired by the biological neuron system. An ANN is an interconnected group of nodes that are similar to the neurons in brain. Each node acts like an artificial neuron, and an arrow denotes a connection from the output of one neuron to the input of another. The model of an artificial neuron is composed of connecting links which receive the input signals and then multiply these signals with the corresponding weights. Signals are then added up through a linear combiner in the summing junction.

An input layer is comprised of three or more layers, and intermediate layer which is also called hidden layer is comprised of one or more layers and also an output layer (Remesan et al. 20018a, b). There are two types of learning

methodologies, which are supervised learning and unsupervised learning. The most commonly used learning methodology is supervised learning in which we add the inputs and the desired outputs into the network and then we adjust the weights to decrease the error in output.

The study utilizes two artificial neural network-based training algorithms including two-layer back-propagation (TLBP) and Broyden–Fletcher–Goldfarb–Shanno (BFGS) (Fletcher 1987). The optimum number of nodes in each layer was determined using simple hit-and-trail method on the criterion of maximum model efficiency ( $R$  square) and Nash–Sutcliffe coefficient (NSE). The efficiency of these ANN-based models was also compared with LLR-based model. Each model development process is explained separately in Table 3.

## Statistical indexes

### Coefficient of determination ( $R$ square)

$$R^2 = 1 - \frac{SS_{res}}{SS_{tot}}, \quad (4)$$

where  $SS_{res} = \text{Sum}(x_i - f_i)^2$ ,  $SS_{tot} = \text{Sum}(x_i - x^{mean})^2$ ,  $x$  = observed values,  $f$  = predicted values and  $x^{mean}$  = mean of observed data.

### Nash–Sutcliffe coefficient (NSE)

$$NSE = 1 - \frac{\sum_{i=1}^n (x_i^{obs} - x_i^{sim})^2}{\sum_{i=1}^n (x_i^{obs} - x^{mean})^2}, \quad (5)$$

where  $x_i^{obs}$  =  $i$ th observation,  $x_i^{sim}$  =  $i$ th simulated value,  $x^{mean}$  = mean of observed data and  $n$  = total number of observations.

### Root mean square error (RMSE)

$$RMSE = \sqrt{\frac{x_1^2 + x_2^2 + x_3^2 + \dots + x_n^2}{n}}, \quad (6)$$

where  $x_1, x_2, x_3 \dots x_n$  = data points up to the  $n$ th value and  $n$  = total number of data points.

**Table 3** Model development of LLR, TLBP and BFGS models

Test no.	Mask	LLR	TLBP				BFGS		
			Nearest neighbors (NN)	No. of hidden layers	Nodes (layer 1)	Nodes (layer 2)	Learning rate	No. of hidden layers	Nodes (layer 1)
1	10010	10	2	5	5	0.25	2	7	7
2	10011	10	2	5	5	0.25	2	6	6
3	10011	10	2	7	7	0.25	2	5	4

**Variance**

$$\sigma^2 = \frac{\sum (x - \bar{x})^2}{n}, \tag{7}$$

where  $\sigma^2$  = variance,  $x$  = data point given in the data,  $\bar{x}$  = mean of the data and  $n$  = total number of data points.

**Bias**

$$\text{Bias} = f^{\text{mean}} - x^{\text{mean}}, \tag{8}$$

where  $f^{\text{mean}}$  = mean of predicted values and  $x^{\text{mean}}$  = mean of measured values.

**Results**

**Gamma test results**

For each input combination or mask, the gamma values were calculated. The graph between gamma values and number of observations for different model identification techniques is shown in Fig. 2.

On the foundation of least gamma value, three out of 84 input combinations were selected for model development process. The selected input combinations with their respective gamma values, gradient, standard error and V ratios are given in Table 4. It is well clear that all selected

combinations not only have very low gamma values but also have low standard error, gradient and V ratio.

**LLR results**

The LLR-based models were trained using value of nearest neighbors as 10. The number of nearest neighbors depends upon the length of data, so in this case, 10–20 number of nearest neighbors is a good option because of the relatively shorter data length, but for larger data length the value of number of nearest neighbors should be amplified for accurate solution (Jones et al. 2002).

**ANN results**

For ANN-type models, the structure, i.e., number of nodes and layers were selected that gave the MSE close to the targeted MSE. The structure of ANN models developed is explained in Table 5.

**Discussion**

The scatter plots for all models developed were drawn and are shown in Figs. 3, 4 and 5. The detailed comparison of these models was made on the basis of different statistical parameters such as model efficiency (*R* square), Nash–Sutcliffe coefficient efficiency (NSE), root mean square error

**Fig. 2** Change in gamma values for different model identification techniques

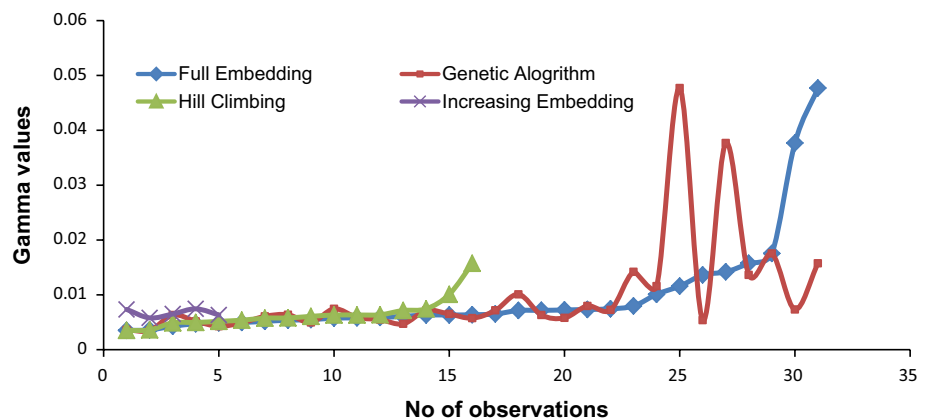


**Table 4** Combination masks with gamma values and other characteristics

S no.	Trial no.	Modeling technique	Mask	Gamma value	Gradient	Standard error	V ratio
1	1	Full embedding	10010	0.00351379	0.345821	0.000421757	0.217562
2	2	Genetic algorithm	10010	0.00351379	0.345821	0.000421757	0.217562
3	3	Hill climbing	10010	0.00351379	0.345821	0.000421757	0.217562
4	4	Sequential embedding	10011	0.00361263	0.18491	0.000739884	0.223681
5	5	Increasing embedding	10011	0.00579581	-0.101334	0.00101375	0.358856

**Table 5** Structure of TLBP and BFGS models

Test no.	Mask	TLBP				BFGS			
		Nodes (layer 1)	Nodes (layer 2)	Target MSE	Achieved MSE	Nodes (layer 1)	Nodes (layer 2)	Target MSE	Achieved MSE
1	10010	5	5	0.0028	0.0027	7	7	0.0032	0.0031
2	10011	5	5	0.0024	0.0023	6	6	0.0025	0.0024
3	10011	7	7	0.0032	0.0031	5	4	0.0032	0.0031

**Fig. 3** LLR-based best models (training and testing)

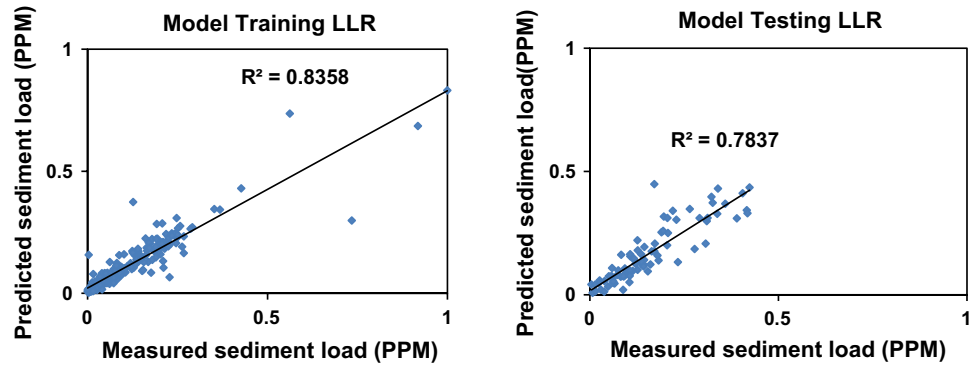


**Fig. 4** TLBP-based models (training and testing)

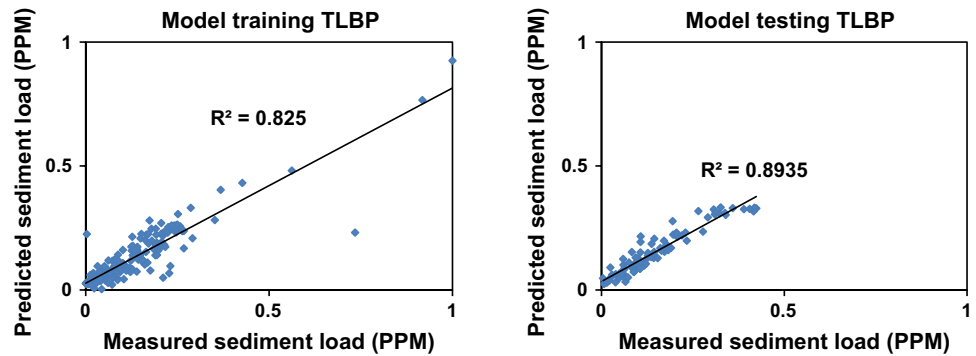
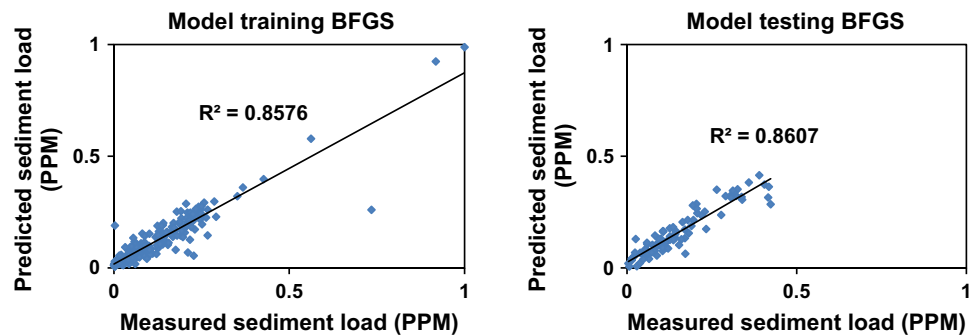


**Fig. 5** BFGS-based models (training and testing)



(RMSE) and mean bias error (MBE) as given in Tables 6 and 7.

Gamma test revealed that the input combination (10011) performed best as compared to the rest input combinations for the estimation of sediment load at Thal canal because of

the less value of gamma statistic. Full embedding, genetic algorithm, hill climbing, sequential embedding and increasing embedding determined 10010, 10010, 10010, 10011 and 10011 input combinations, respectively, but 10011 input combination performed best and gave noticeable high



**Table 6** Comparison of selected input combinations for training

Model	Training				
	Mask	<i>R</i> sq.	NSE	Bias	RMSE
LLR-based model	10011	0.8358	0.835	−8.6228	340.362
TLBP-based ANN model	10010	0.825	0.823	12.415	352.21
BFGS-based ANN model	<b>10011</b>	<b>0.8576</b>	<b>0.858</b>	<b>0.4972</b>	<b>315.95</b>

Bold values show the mask and statistical parameters of the best model

**Table 7** Comparison of selected input combinations for testing

Model	Testing				
	Mask	<i>R</i> sq.	NSE	Bias	RMSE
LLR-based model	10011	0.7837	0.733	65.7486	354.488
TLBP-based ANN model	10010	0.8935	0.883	30.083	234.39
BFGS-based ANN model	<b>10011</b>	<b>0.8607</b>	<b>0.856</b>	<b>44.421</b>	<b>260.66</b>

Bold values show the mask and statistical parameters of the best model

values of model efficiency (*R* square) 0.8576 and 0.8607, Nash–Sutcliffe coefficient (NSE) 0.858 and 0.856 and also low mean bias error (MBE) 0.4972 and 44.421 for training and testing phases, respectively (Tables 6, 7). The LLR-based model performed well in training phase and showed high value of *R* square and Nash–Sutcliffe coefficient but did not perform well in testing phase because of large values of bias and root mean square (RMSE) with low value of *R* square and Nash–Sutcliffe coefficient (Tables 6, 7). The back-propagation (BP) ANN-based model performed well in testing phase because of high value of *R* square = 0.8935 and Nash–Sutcliffe coefficient = 0.883 but fails to perform in training phase and gave relatively higher value of root mean square error (RMSE) = 352.21 as compared to other models.

### Limitations of research

1. The data points/observations were considered as independent and normally distributed; therefore, only parametric techniques were applied.
2. The input selection/mask identification was carried out in WinGamma environment, and for this purpose, model identification techniques were considered as reliable.
3. To increase the number of input parameters, time lag of only 1 and 2 units (1 and 2 weeks) was considered.

### Conclusions

It is concluded that the best input combination for local linear regression model has a mask (**10011**); for two-layer back-propagation model, the best input combination was (**10010**). And finally, the best input combination selected for BFGS model was (**10011**). The above comparison clearly depicts that BFGS-based model outdid as compared to other models with significantly high values of *R* square and low values of RMSE and MBE in both testing and training phases. This is due to the fact that this quasi-Newton-based method, BFGS, utilizes an iterative approach which is quite efficient in solving nonlinear problems.

The study showed that for the estimation and prediction of sediment load at Thal canal the ANN-based models can be used with high degree of accuracy and precision. It also revealed that for the development of smooth ANN models gamma test can be used for the selection of best input combination. The study also evidenced the importance of model identification techniques in combination selection process as it is clearly shown in the results that many techniques determined the same combination out of large possible combinations, i.e., full embedding, genetic embedding and hill climbing determined 10010 as a best combination while sequential embedding and increasing embedding found 10011 as the most suitable combination for model development.

### References

- Abrahart RJ, White SM (2001) Modelling sediment transfer in Malawi: comparing back-propagation neural network solutions against a multiple linear regression benchmark using small data sets. *Phys Chem Earth (B)* 26(1):19–24
- Ackers JC, Butler D, May RWP (1996) Design of sewers to control sediment problems. *Constr Ind Res Inf Assoc (CIRIA)* 141:181
- Adib A, Mahmoodi A (2017) Prediction of suspended sediment load using ANN GA conjunction model with Markov chain approach at flood conditions. *KSCE J Civ Eng* 21(1):447–457
- Agalbjorn S, Koncar N, Jones AJ (1997) A note on the gamm test. *Neural Comput Appl* 5:131
- Alp M, Cigizoglu HK (2007) Suspended sediment load simulation by two artificial neural network methods using hydrometeorological data. *Environ Model Softw* 22:2–13
- Ashkarian S, Kiamanesh H, Hedayat N (2010) Simulation of flow pattern using FLOW 3D in Dez Diversion Dam in Dezful. In: Proceedings of national conference on water, soil, plant sciences and agricultural mechanization, Islamic Azad University- Dezful Branch, Dezful, Iran
- Ashley RM, Wotherspoon DJJ, Coghlan BP et al (1992) The erosion and movement of sediments and associated pollutants in combined sewers. *Water Sci Technol* 25(8):101–114
- Atieh M, Mehlretter SL, Gharabaghi B et al (2015) Integrative neural networks model for prediction of sediment rating curve parameters for ungauged basins. *J Hydrol* 531:1095–1107

- Azamathulla HMD, Ab Ghani A, Chang CK et al (2010) Machine learning approach to predict sediment load: a case study. *Clean-Soil Air Water* 38(10):969–976
- Ballio F, Tait S (2012) Sediment transport mechanics. *Acta Geophys* 60(6):1493–1499
- Bhattacharya B, Price RK, Solomatine DP (2007) Machine learning approach to modelling sediment transport. *J Hydraulic Eng* 133(4):440–450
- Bong CHJ, Lau TL, Ab Ghani A (2013) Verification of equations for incipient motion studies for a rigid rectangular channel. *Water Sci Technol* 67(2):395–403
- Buyukyildiz M, Kumcu SY (2017) An estimation of the suspended sediment load using adaptive network based fuzzy inference system, support vector machine and artificial neural network models. *Water Resour Manag* 31(4):1343–1359
- Cannon AJ, Whitfield PH (2002) Downscaling recent stream-flow conditions in British Columbia, Canada using ensemble neural networks. *J Hydrol* 259:136–151
- Chang FJ, Tsai MJ (2016) A nonlinear spatio-temporal lumping of radar rainfall for modeling multi-step-ahead inflow forecasts by data-driven techniques. *J Hydrol* 535:256–269
- Chang FJ, Wang YC, Tsai WP (2016) Modelling intelligent water resources allocation for multi-users. *Water Resour Manag* 30:1395–1413
- Choubin B, Malekian A (2017) Combined gamma and M-test-based ANN and ARIMA models for groundwater fluctuation forecasting in semiarid regions. *Environ Earth Sci* 76:538
- Choubin B, Darabi H, Rahmati O et al (2018) River suspended sediment modelling using the CART model: a comparative study of machine learning techniques. *Sci Total Environ* 615:272–281
- Cigizoglu HK (2003a) Estimation, forecasting and extrapolation of flow data by artificial neural networks. *Hydrol Sci J* 48(3):349–361
- Cigizoglu HK (2003b) Incorporation of ARMA models into flow forecasting by artificial neural networks. *Environmetrics* 14(4):417–427
- Cigizoglu HK (2004) Estimation and forecasting of daily suspended sediment data by multi layer perceptrons. *Adv Water Resour* 27:185–195
- De Sutter R, Rushforth P, Tait S et al (2003) Validation of existing bed load transport formulas using in-sewer sediment. *J Hydraul Eng* 129(4):325–333
- Duru U, Arabi M, Whol EE (2018) Modeling stream flow and sediment yield using the SWAT model: a case study of Ankara River basin, Turkey. *Phys Geogr* 39(3):264–289
- El-Zaemey AKS (1991) Sediment transport over Deposited beds in sewers. Ph.D. Thesis, Department of Civil Engineering, University of Newcastle upon Tyne
- Fletcher R (1987) *Practical methods of optimization*. Wiley, New York
- Freiwan M, Cigizoglu HK (2005) Prediction of total monthly rainfall in Jordan using feed forward backpropagation method. *Fresenius Environ Bull* 14(2):142–151
- Ghani Ab, Salem A, Abdullah AM et al (1999) Incipient motion of sediment particles over loose deposited beds in a rigid rectangular channel. In: Eighth international conference on urban storm drainage. Sydney, p 157–163
- Hall T (1999) Precipitation forecasting using a neural network. *Weather Forecast* 14:338–345
- Han D, Yan W (2009) Validation of the Gamma test for model input data selection: with a case study in evaporation estimation, In: Fifth international conference on natural computation, Tianjin, China, p 469–473
- Hassan M, Shamim MA, Hashmi HN et al (2015a) Predicting stream flows to a multipurpose reservoir using artificial neural networks and regression techniques. *Earth Sci Inf* 8(2):337–352
- Hassan M, Shamim MA, Sikandar A et al (2015b) Development of sediment load estimation models by using artificial neural networking techniques. *Environ Monit Assess* 187:686
- Himanshu SK, Pandey A, Shrestha P (2017) Application of SWAT in an Indian river basin for modeling runoff, sediment and water balance. *Environ Earth Sci* 76(1):3
- Jaafar WZW, Liu J, Han D (2011) Input variable selection for median flood regionalization. *Water Resour Res* 47(7):W07503
- Jones AJ, Tsui A, De Oliveira AG (2002) Neural models of arbitrary chaotic systems: construction and the role of time delayed feedback in control and synchronization. *Complex Int* 9:1–9
- Kisi O, Cimen M (2012) Precipitation forecasting by using wavelet support vector machine conjunction model. *Eng Appl Artif Intell* 25:783–792
- Kumar R, Singh S, Singh A et al (2018) Dynamics of suspended sediment load with respect to summer discharge and temperatures in Shaune Garang glacierized catchment, Western Himalaya. *Acta Geophys* 66(5):1109–1120
- Lafdani EK, Nia AM, Ahmadi A (2013) Daily suspended sediment load prediction using artificial neural networks and support vector machines. *J Hydrol* 478:50–62
- Litta AJ, Idicula SM, Mohanty UC (2013) Artificial neural network model in prediction of meteorological parameters during monsoon thunderstorms. *Int J Atmos Sci* 2013(525383):14
- Loveless JH (1992) Sediment transport in rigid boundary channels with particular reference to the condition of incipient deposition, Ph.D. Thesis. University of London
- Melesse AM, Ahmad S, McClain ME (2011) Suspended sediment load prediction of river systems: an artificial neural network approach. *Agric Water Manag* 98(5):855–866
- Mohammadi M (2005) The initiation of sediment motion in fixed bed channels. *Iran J Sci Technol* 29(B3):365–372
- Mustafa M, Isa M, Rezaur R (2011) A comparison of artificial neural networks for prediction of suspended sediment discharge in river—a case study in Malaysia. *Int J Civil Environ Struct Constr Archit Eng* 5(9):368–372
- Nagy HM, Watanabe K, Hirano M (2002) Prediction of sediment load concentration in rivers using artificial neural network model. *J Hydraulic Eng (ASCE)* 128(6):588–595
- Nourani V, Alizadeh F, Roushangar K (2016) Evaluation of a two-stage SVM and spatial statistics methods for modeling monthly river suspended sediment load. *Water Resour Manag* 30(1):393–407
- Novak P, Nalluri C (1984) Incipient motion of sediment particles over fixed beds. *J Hydraul* 22(3):181–197
- Ochiero HO, Onyando JO, Kamau DN (2015) Simulation of sediment transport in the canal using the Hec-Ras (Hydrologic Engineering Centre: river analysis system) In an Underground Canal in Southwest Kano Irrigation Scheme-Kenya. *Int J Eng Sci Invent* 4(9):15–31
- Ota JJ, Nalluri C (2003) Urban storm sewer design: approach in consideration of sediments. *J Hydraul Eng* 129(4):291–297
- Partal T, Cigizoglu HK (2008) Estimation and forecasting of daily suspended sediment data using wavelet–neural networks. *J Hydrol* 358:317–331
- Reddy SB (2003) Estimation of watershed runoff using artificial neural networks. Ph.D Thesis in Agric. Engineering (unpubl.). Post Graduate School, IARI, New Delhi
- Remesan R, Shamim MA, Han D (2008) ANFIS and NNARX based rainfall-runoff modeling. In: IEEE International conference on systems, man and cybernetics. Singapore, p 1453–1458
- Remesan R, Shamim MA, Han D (2008b) Model input data selection using gamma test for daily solar radiation estimation. *Hydrol Process* 22:4301–4309
- Rezaei K, Guest B, Friedrich A et al (2009) Feed forward neural network and interpolation function models to predict the soil and

- subsurface sediments distribution in Bam, Iran. *Acta Geophys* 57(2):271–293
- Safari MJS, Mohammadi M, Gilanizadehdizaj G (2013) Investigation on incipient deposition and incipient motion of sediment particles in rigid boundary channels. *Water Soil Sci* 23(3):13–24
- Safari MJS, Mohammadi M, Gilanizadehdizaj G (2014) On the effect of cross-sectional shape on incipient motion and deposition of sediments in fixed bed channels. *J Hydrol Hydromech* 62(1):75–81
- Safari MJS, Aksoy H, Mohammadi M (2015) Incipient deposition of sediment in rigid boundary open channels. *Environ Fluid Mech* 15(5):1053–1068
- Safari MJS, Aksoy H, Mohammadi M (2016) Artificial neural network and regression models for flow velocity at sediment incipient deposition. *J Hydrol* 541:1420–1429
- Sajedi AH (2010) Analytical study of the sediment formation using the SHARC computer model: a case study of the western water Intake in the Dez diversion weir in Dezfū Iran. M.Sc dissertation, I.Azad University, Dezfū, Iran
- Sajedipoor AH, Hedayat N, Rohani A et al (2010) Analytical study of sedimentation formation in lined canals using the SHARC Software: a case study of the Sabilli Canal in Dezfū, Iran. *Int J Environ Chem Ecol Geol Geophys Eng* 4:11
- Sarangi A, Bhattacharya AK (2005) Comparison of artificial neural network and regression models for sediment loss prediction from Banha watershed in India. *Agric Water Manag* 78:195–208
- Shamim MA, Bray M, Remesan R et al (2015a) A hybrid modelling approach for assessing solar radiation. *Theoret Appl Climatol* 122(3–4):403–420
- Shamim MA, Hassan M, Ahmad S et al (2015b) A comparison of artificial neural networks (ANN) and local linear regression (LLR) techniques for predicting monthly reservoir levels. *J Korean Soc Civil Eng* 20:971
- Shirin H, N Hedayat, H Kiamanesh (2010) Investigating the sedimentation process using the SHARC software: a case study of the in the Eastern water intake of the Dez Diversion Weir in Dezfū. In: Proceedings of the national conference in water, soil, plant and agricultural mechanization, Islamic, Azad University, Dezfū, Iran
- Talebi A, Mahjoobi J, Dastorani MT et al (2017) Estimation of suspended sediment load using regression trees and model trees approaches (Case study: Hyderabad drainage basin in Iran). *ISH J Hydraul Eng* 23(2):212–219
- Thompson J, Sattar AM, Gharabaghi B et al (2016) Event-based total suspended sediment particle size distribution model. *J Hydrol* 536:236–246
- Tsai WP, Chang FJ, Chang LC et al (2015) AI techniques for optimizing multi-objective reservoir operation upon human and riverine ecosystem demands. *J Hydrol* 530:634–644
- Wang YM, Traore S, Kerh T (2008) Monitoring event-based suspended sediment concentration by artificial neural network models. *WSEAS Trans Comput* 7(5):559–568
- Yang CT, Marsooli R, Aalami MT (2009) Evaluation of total load sediment transport formulas using ANN. *Int J Sedim Res* 24(3):274–286
- Yilmaz B, Aras E, Nacar S et al (2018) Estimating suspended sediment load with multivariate adaptive regression spline, teaching-learning based optimization, and artificial bee colony models. *Sci Total Environ* 639:826–840
- Yitian L, Gu RR (2003) Modeling flow and sediment transport in a river system using an artificial neural network. *Environ Manag* 31(1):122–134
- Zhang B, Govindaraju R (2003) Geomorphology based artificial neural networks (GANNs) for estimation of direct runoff over watersheds. *J Hydrol* 273:18–34
- Zhu YM, Lu XX, Zhou Y (2007) Suspended sediment flux modeling with artificial neural network: an example of the Longchuanjiang River in the Upper Yangtze Catchment, China. *Geomorphology* 84:111–125
- Zhuo L, Han D, Dai Q (2016) Soil moisture deficit estimation using satellite multi-angle brightness temperature. *J Hydrol* 539:392–405



# A statistical analysis of seismo-ionospheric TEC anomalies before 63 $M_w \geq 5.0$ earthquakes in Turkey during 2003–2016

Erman Şentürk<sup>1</sup> · Murat Selim Çepni<sup>1</sup>

Received: 12 July 2017 / Accepted: 17 October 2018 / Published online: 24 October 2018  
© Institute of Geophysics, Polish Academy of Sciences & Polish Academy of Sciences 2018

## Abstract

In this study, pre-seismic and post-seismic total electron content (TEC) anomalies of 63  $M_w \geq 5.0$  earthquakes in Turkey ( $36^\circ$ – $42^\circ$ N,  $26^\circ$ – $45^\circ$ E) were statistically investigated. The largest earthquake that occurred in Turkey during 2003–2016 is the  $M_w$  7.1 Van earthquake on October 23, 2011. The TEC data of epicenters is obtained from CODE-GIM using a simple 4-point bivariate interpolation. The anomalies of TEC variations were determined by using a quartile-based running median process. In order to validate GIM results, we used the GPS-TEC data of available four IGS stations within the size of the Van earthquake preparation area. The anomalies that are detected by GIM and GPS-TEC show a similar pattern. Accordingly, the results obtained with CODE-GIM are reliable. The statistical results show that there are not prominent earthquake precursors for  $M_w \leq 6.0$  earthquakes in Turkey.

**Keywords** Total electron content · Earthquake precursor · Statistical analysis · CODE-GIM · GPS/GNSS

## Introduction

Forecasting earthquakes are a critical study field for human life and seismo-ionospheric studies have become a hot topic for earthquake prediction. Many studies have clearly stated that earthquake-related anomalies appear before earthquakes in the ionosphere (Dogan et al. 2011; Ouzounov et al. 2011; Yao et al. 2012; Aggarwal 2015; Guo et al. 2014; Pundhir et al. 2015). Many researchers have introduced different theories about the physical mechanism of anomalies in the ionosphere before the earthquakes, such as electric field (Sorokin et al. 2006; Pulinets 2009), acoustic-gravity waves (Rozhnoi et al. 2007; Kaladze et al. 2008; Klimenko et al. 2011) and electromagnetic (Hayakawa and Fujinawa 1994; Hayakawa and Molchanov 2002), but any physical explanation of lithosphere-ionosphere coupling is still not entirely approved. For this reason, statistical studies are becoming more important and many studies have previously been published using ionosonde (Liu et al. 2004, 2006), GPS-TEC (Liu et al. 2004, 2010), GIMs (Kon et al. 2011; Le et al. 2011; Fuying et al. 2011; Liu et al. 2013a), radio techniques (Maekawa et al. 2006; Hayakawa et al. 2010;

Wen et al. 2012) and DEMETER (Akhoondzadeh et al. 2010; Parrot 2012). Liu et al. (2006) investigated 184  $M \geq 5.0$  earthquakes during 1994–1999 in Taiwan using 15-min time resolution data of Chung-Li ionosonde station. Results show that ionospheric  $f_0F_2$  values are decreased more than about %25 during 12:00–18:00 LT, generally appears within 5 days before earthquakes. Le et al. (2011) statistically analyzed TEC variations obtained from CODE-GIM at 736  $M \geq 6$  earthquakes in the global area between 2002 and 2010. The rate of anomalies before and after earthquakes reveals that anomalies of several days before earthquakes should be a more significant indicator for earthquake precursors. Furthermore, pre-earthquake anomalies were detected more clearly in  $M \geq 7$  and 20 km deep earthquakes. Fuying et al. (2011) examined GIM-TEC variations of 50  $M \geq 7$  earthquakes during 2007–2009 worldwide. In the study, positive and negative anomalies were observed in 47 of 50 earthquakes, after eliminating the interference caused by geomagnetic activity, within 10 days before earthquakes. In addition, the frequency of positive anomalies is appeared approximately 12:00–18:00 LT, while the frequency of negative anomalies was irregular. Kon et al. (2011) and Hattori et al. (2014) analyzed TEC anomalies before earthquakes in Japan and found that positive TEC anomalies were usually observed during 1–5 days before  $M_w > 6.0$  earthquakes with the focal depth of fewer than 40 km. In the present study, temporal variations of the GIM-TEC values over epicenters related

✉ Erman Şentürk  
erman.senturk@kocaeli.edu.tr

<sup>1</sup> Department of Surveying Engineering, Kocaeli University, Kocaeli, Turkey



to 63  $M_w \geq 5.0$  earthquakes in Turkey during 2003–2016 obtained from United States Geological Survey (USGS) are statistically investigated. In order to determine ionospheric anomalies before and after the earthquakes, a quartile-based running median process was applied to TEC variations.

### Data and analysis

Turkey is generally affected by  $24 \pm 1$  mm/yr northward movement of Arabian Plate,  $9 \pm 1$  mm/year westward movement of Anatolian Plate (McClusky et al. 2003; Reilinger et al. 2006). West Anatolian Extension Zone and two main strike-slip fault systems called North Anatolian and East Anatolian Fault Zones (NAFZ and EAFZ, respectively) were caused by these tectonic features. The seismo-tectonic process is mainly controlled by the complex fundamental settings, and Turkey has been directly faced with high seismic activity within the geometry and mechanism of the continental deformation that can generate lots of large earthquakes, sequences and swarms. Investigation of the seismicity of Turkey is important for different kind of scientific studies. This country has a great source of the various geotectonic setting of the fault systems that normal, trust and strike-slip.

In order to investigate seismo-ionospheric anomalies over Turkey, 63  $M_w \geq 5.0$  (magnitude 5–7.1) earthquakes from 2003 to 2016 were selected. Details of the earthquakes obtained from USGS. Firstly, we found 108 earthquakes in the region, but less severe earthquakes that occurred 10 days before and after earthquakes were eliminated to ensure that anomalies were not due to another seismic activity. As a result, 63 earthquakes were selected. Detailed information and distribution of the earthquakes are shown in Table 1 and Fig. 1.

Global Ionosphere Maps (GIM) data produced by the Center for Orbit Determination in Europe (CODE) are used to obtain TEC values of epicenters. The CODE-GIM data covers  $\pm 87.5^\circ$  latitude and  $\pm 180^\circ$  longitude ranges with  $2.5^\circ \times 5^\circ$  spatial resolutions (5184 cells) and 2-h temporal resolutions. TEC values of the epicenters are calculated from nearest four GIM grid point using a simple 4-point bivariate interpolation (Schaer et al. 1998). A simple 4-point formula is shown in Eq. 1,

$$TEC(\lambda_e, \beta_e) = \left| 1 - m \right| \left| \begin{matrix} TEC_{00} & TEC_{01} \\ TEC_{10} & TEC_{11} \end{matrix} \right| \left| \begin{matrix} 1 - n \\ n \end{matrix} \right| \quad (1)$$

where  $m = |\lambda_e - \lambda_0| / \Delta\lambda_{GIM}$  latitudinal scale factor,  $n = |\beta_e - \beta_0| / \Delta\beta_{GIM}$  longitudinal scale factor,  $\beta_e$  and  $\lambda_e$  is geocentric latitude and longitude of the epicenter,  $\beta_0$  and  $\lambda_0$  is geocentric latitude and longitude of the nearest grid point,  $\Delta\beta_{GIM}$  and  $\Delta\lambda_{GIM}$  is spatial resolutions of the latitude and longitude of the GIM,  $vTEC_{00}$ ,  $vTEC_{01}$ ,  $vTEC_{10}$ ,  $vTEC_{11}$  is TEC value of the nearest four grid points. The IONEX files

are downloaded from the NASA Web site (<ftp://cddis.gsfc.nasa.gov/gps/products/ionex/>).

The Geometry-Free Linear Combination ( $L_4 = L_1 - L_2$ ) is used to calculate GPS-based slant TEC (STEC) values. We used “leveling carrier to code” algorithm based on differences of carrier and code ionospheric observable at a continuous arc (Ciraolo et al. 2007). The final form of the STEC formula as below,

$$L_4 = a \left( \frac{1}{f_1^2} - \frac{1}{f_2^2} \right) STEC + b_4^k + b_{4,i} + B_4 \quad (2)$$

where  $b^k$  satellite and  $b_i$  receiver hardware delays (differential code biases DCB),  $B_4$  continuous arc difference between ionospheric observables,  $a \left( \frac{1}{f_1^2} - \frac{1}{f_2^2} \right)$  is a constant. The detailed information of the GPS-TEC calculation process can be seen in Şentürk and Çepni (2018).

Because the ionosphere consists of several layers, the Single-Layer Model (SLM) is an assumption that all free electrons are gathered in a layer with an infinite thickness (Alizadeh et al. 2011). STEC values are converted to vertical TEC (VTEC) values using the SLM assumption and a mapping function. In Eq. 3, a well-known mapping function is shown.

$$\frac{VTEC}{STEC} \cong \cos \epsilon' = \sqrt{1 - \left( \frac{R_E}{R_E + h_m} \right)^2 \cos^2 \epsilon} \quad (3)$$

The station-based TEC value is calculated by the weighted average of the VTECs or a surface interpolation technique (Şentürk and Çepni 2018).

$$TEC = \frac{\sum_{i=1}^N W_i VTEC_i}{\sum_{i=1}^N W_i} \Bigg|_{T_1}^{T_2}; \quad T_1 - T_2 \text{ is time lapse interval} \quad (4)$$

In Eq. 4,  $W_i$  indicates the weight of a satellite VTEC where  $n$  is equal to all visible satellite at any epoch.  $W_i$  is generally described as a component of the satellite elevation and/or azimuth angle.

In order to detect anomalous TEC variations, a quartile-based running median process was performed. At each time point, the median ( $\tilde{M}$ ) and standard deviation ( $\sigma$ ) for the TEC of 1–10 days before the day were computed. The TEC variation was accepted as a normal distribution with mean  $\tilde{m}$  and standard deviation  $\sigma$ . To determine the level of the divergence, the lower quartile (LQ) and the upper quartile (UQ) are computed. To detect an anomaly in the TEC values, the lower bound and upper bound were defined.

$$LB = \tilde{M} - 1.5(\tilde{M} - LQ) \quad (5)$$

**Table 1** Information on the earthquakes as ordered the earthquakes date

Date time (UTC)	Epicenter coordinates	Depth (km)	Mag (Mw)	The abnormal days*
2003-01-27 05:26:23	39.500°N 39.878°E	10.0	6.1	6pr-, 4pr-, eq-, 2po-
2003-04-10 00:40:15	38.221°N 26.958°E	10.0	5.8	1po-, 2po-, 3po-, 4po-, 5po-
2003-05-01 00:27:04	39.007°N 40.464°E	10.0	6.4	4pr+, 4po-, 5po+, 7po-, 8po-
2003-05-03 11:22:40	36.884°N 31.536°E	135.3	5.5	6pr+, 2po-, 10po-
2003-07-06 19:10:28	40.445°N 26.024°E	17.1	5.7	8pr-, 5pr+, 4pr+, 3pr+, eq-, 4po+
2003-07-13 01:48:21	38.288°N 38.963°E	10.0	5.6	10pr+, 9pr+, 3pr+, 10po+
2003-07-26 08:36:49	38.019°N 28.927°E	10.0	5.4	3pr+, 2po-
2003-09-13 13:46:14	36.629°N 26.918°E	155.0	5.3	7pr-, 6pr-, 5pr-, 3pr-, 2 pr-, 1pr-, eq-, 1po-, 3po-, 10po+
2004-02-07 21:17:24	36.040°N 26.910°E	25.0	5.1	9pr-, 8pr-, 6pr+, 5pr+, 4pr+, 2po+, 3po+, 10po-
2004-03-28 03:51:10	39.847°N 40.874°E	5.0	5.6	9pr+, 8pr+, 7pr+, 6pr+, 5pr+, 2pr+, 1pr+, 1po+, 4po-, 7po-
2004-07-01 22:30:09	39.766°N 43.979°E	5.0	5.1	9pr+, 4pr-, 2pr+, 1pr-, eq-, 1po-, 2po-, 3po-, 4po-, 5po-, 6po-, 7po-
2004-08-04 03:01:07	36.833°N 27.815°E	10.0	5.6	1pr+, 3po+, 9po+, 10po+
2004-08-11 15:48:26	38.377°N 39.261°E	7.4	5.7	4pr+, 1po+, 2po+, 3po+, 4po+, 5po+, 6po+, 9po+
2004-10-07 01:05:12	36.429°N 26.796°E	128.9	5.5	9pr+, 7pr+, 5pr+, 4pr+, 2pr+, 1pr+, eq+, 2po+, 3po+, 8po-, 9po-
2004-12-20 23:02:12	37.042°N 28.206°E	5.0	5.4	7pr-, 4pr-, 2pr+, 2po+, 3po+, 5po+
2005-01-10 23:48:50	37.017°N 27.804°E	15.9	5.5	10pr-, 3pr-, 1pr-, 1po+, 6po+
2005-01-25 16:44:16	37.622°N 43.703°E	41.2	5.9	1po-, 2po-, 4po+, 5po+, 6po+, 8po+
2005-03-14 01:55:55	39.354°N 40.890°E	5.0	5.8	9pr+, 8pr+, 1pr+, eq+, 1po+, 2po+, 3po+, 8po-, 9po-
2005-06-06 07:41:28	39.220°N 41.080°E	10.0	5.6	9pr+, 8pr+, 2pr+, eq-, 2po-, 5po+, 6po+, 8po-
2005-07-30 21:45:00	39.437°N 33.089°E	5.0	5.2	6pr-, 4pr+, 3pr+, 1pr+, 1po+, 2po+, 3po+, 4po+, 9po-, 10po-
2005-10-20 21:40:04	38.152°N 26.751°E	10.0	5.9	10pr-, 9pr+, 8pr-, 6pr-, 4pr+, 2pr+, eq+, 4po-, 8po-, 9po-
2005-11-26 15:56:55	38.260°N 38.814°E	8.5	5.1	9pr-, eq-, 1po-, 3po+, 4po+, 6po+
2005-12-10 00:09:50	39.394°N 40.946°E	10.0	5.4	10pr+, 8pr+, 7pr+, 3pr-, 2pr+, eq+, 3po-, 4po-, 5po-, 6po-
2006-07-02 19:39:39	39.274°N 40.960°E	3.0	5.0	7pr+, 3pr+, 2pr+, 5po-, 6po-, 7po-, 9po-, 10po-
2006-10-24 14:00:21	40.424°N 29.107°E	9.3	5.0	7pr-, 6pr-, 1pr-, 4po+, 7po-, 8po-, 10po-
2007-01-21 07:38:57	39.592°N 42.863°E	3.1	5.2	10pr+, 6pr-, eq-, 1po-, 4po-, 5po-, 8po+
2007-02-21 11:05:28	38.318°N 39.275°E	6.0	5.7	9pr+, 1pr+, 1po-, 3po+, 4po+, 5po+, 10po+
2007-04-10 22:00:34	38.005°N 30.923°E	5.8	5.1	5pr-, 2pr-, 1pr+, 1po+, 2po+, 5po+, 8po-, 9po-, 10po-
2007-08-25 22:05:49	39.282°N 41.124°E	10.0	5.3	9pr-, 4pr+, 2pr+, 1po+, 2po+, 5po-, 8po+, 10po-
2007-08-31 20:52:43	36.655°N 26.272°E	25.1	5.2	8pr-, 7pr+, 6pr+, 5pr+, 4pr+, 3pr+, eq+, 1po+, 2po+, 4po+, 5po+, 8po-
2007-10-29 09:23:14	37.033°N 29.233°E	5.0	5.3	10pr+, 9pr+, 8pr-, 1pr-, 2po+, 5po+, 6po-, 7po-, 8po-, 9po-, 10po-
2007-12-20 09:48:29	39.417°N 33.212°E	10.0	5.7	10pr+, 6pr-, 4pr-, 1pr-, eq-, 1po-, 2po-, 4po-, 8po+, 9po+, 10po+
2008-04-25 04:48:54	37.819°N 29.256°E	5.0	5.0	10pr+, 3pr+, 2po-, 10po+
2008-09-03 02:22:47	37.507°N 38.503°E	5.7	5.0	8pr-, 6pr+, 1pr-, eq+, 3po-, 7po+, 8po+, 10po-
2008-11-12 14:03:18	38.841°N 35.524°E	10.0	5.1	7pr+, 5pr-, 3pr+, 2po-, 3po-, 4po+, 7po-, 9po-, 10po-
2009-02-17 05:28:19	39.107°N 29.039°E	7.3	5.2	10pr-, 8pr+, 7pr+, 1po+, 4po+, 8po+, 10po-
2009-06-20 08:28:19	37.680°N 26.860°E	12.0	5.1	10pr-, 9pr+, 7pr+, 1po-, 6po+, 7po+, 8po+, 9po+
2009-07-30 07:37:51	39.588°N 39.726°E	10.0	5.0	6pr-, 3pr-, eq+, 2po+, 4po+, 7po+, 9po-, 10po-
2010-03-08 02:32:34	38.864°N 39.986°E	12.0	6.1	10pr-, 7pr+, 5pr+, 2pr-, 4po+, 5po-, 6po+, 7po-, 8po+, 9po+, 10po+
2010-07-16 08:11:01	36.810°N 26.910°E	165.0	5.1	10pr-, 7pr-, 4pr+, 2pr+, 1pr+, eq+, 4po+, 7po+, 10po+
2010-11-03 02:51:27	40.423°N 26.333°E	15.3	5.3	9pr-, 8pr-, 7pr-, 6pr-, 5pr-, 4pr-, eq-, 3po-, 5po-, 6po-, 7po-, 8po+
2010-11-11 20:08:00	37.899°N 27.343°E	11.8	5.0	8pr-, 5pr-, 3pr-, 2pr-, 1pr-, eq+, 8po+, 9po+, 10po+
2011-05-08 06:50:24	36.704°N 27.238°E	11.0	5.1	9pr+, 3pr-, 1pr-, eq-, 1po-, 3po-, 4po-, 5po-, 6po-, 7po-, 9po-, 10po-
2011-05-19 20:15:22	39.149°N 29.103°E	7.0	5.8	9pr+, 8pr+, 6pr-, 4pr+, 1pr-, eq-, 1po-, 3po-, 4po-, 5po-
2011-06-23 07:34:42	38.578°N 39.640°E	6.1	5.2	5pr+, eq-, 1po-, 3po+, 6po-, 7po-, 8po-, 9po-

**Table 1** (continued)

Date time (UTC)	Epicenter coordinates	Depth (km)	Mag (Mw)	The abnormal days*
2011-07-25 17:57:20	40.802°N 27.752°E	16.4	5.1	9pr+, 8pr+, 7pr+, eq+, 1po-, 2po-, 7po-, 8po+
2011-09-22 03:22:36	39.785°N 38.842°E	5.0	5.5	7pr+, 6pr+, 5pr+, 3pr+, 2pr+, 1pr+, 8po-
2011-10-23 10:41:23	38.721°N 43.508°E	18.0	7.1	8pr+, 7pr+, 4pr-, 2pr+, 1pr+, eq+, 1po+, 6po-, 7po-
2011-10-27 08:04:22	37.256°N 43.860°E	10.0	5.1	6pr+, 5pr+, 4pr+, 2po-, 3po-
2011-11-14 22:08:15	38.658°N 43.170°E	10.0	5.2	6pr+, 5pr+, 2po-, 3po-, 4po-, 5po-, 6po-, 7po+, 10po-
2011-11-30 00:47:21	38.474°N 43.454°E	4.3	5.4	10pr-, 9pr+, 6pr-, 2pr-, 1pr+, 2po-, 6po-, 7po-, 8po-, 9po-
2012-03-26 10:35:32	39.171°N 42.330°E	5.0	5.0	6pr+, 5pr-, 3pr+, 2pr+, eq+, 1po+, 6po+, 9po-
2012-05-03 15:20:25	39.175°N 29.092°E	3.1	5.2	10pr+, 5pr+, 4pr+, eq-, 2po+, 3po+, 4po+, 7po-, 9po-
2012-06-10 12:44:16	36.420°N 28.880°E	35.0	6.0	7pr+, 6pr+, 3po-, 4po-, 5po-, 9po-
2013-12-28 15:21:04	36.028°N 31.310°E	40.7	5.9	10pr-, 8pr-, 7pr-, 6pr-, 5pr-, 4pr-, 3pr+, 1pr-, eq-, 1po-, 3po+, 4po+, 10po+
2014-08-24 19:43:30	37.683°N 30.629°E	7.4	5.1	10pr-, 9pr-, 5pr+, 4pr+, 2pr+, 1pr+, 1po+, 2po+
2014-09-04 21:00:04	36.210°N 30.820°E	46.0	5.3	9pr+, 2pr-, 2po+, 3po+, 4po+, 5po+, 7po+, 8po+, 9po-
2014-12-06 01:45:06	38.894°N 26.272°E	12.4	5.1	10pr+, 9pr+, 8pr+, 7pr+, 3pr-, 1pr-, 5po-, 7po-, 8po-
2015-10-06 21:27:33	36.168°N 29.895°E	22.4	5.2	9pr-, 8pr+, 7pr+, 6pr+, 5pr+, eq-, 10po+
2015-10-09 14:39:15	40.685°N 36.690°E	5.0	5.1	10pr+, 9pr+, 8pr+, 3pr-, 7po+, 8po+, 10po+
2015-12-02 23:27:09	39.283°N 40.255°E	10.0	5.4	10pr-, 9pr-, 8pr-, 7pr-, 6pr-, 5pr+, 4pr+, 1po-, 2po-, 6po-, 8po+
2016-01-10 17:40:49	39.565°N 34.337°E	10.0	5.0	10pr+, 7pr-, 6pr-, 4pr+, 3pr+, 2pr+, 1po+, 3po-, 4po+, 6po-, 9po+
2016-09-27 20:57:08	36.389°N 27.614°E	85.2	5.1	9pr-, 5pr-, 3pr+, 2pr+, 10po+

\**pr* pre-seismic, *po* post-seismic, *eq* earthquake day, + positive – anomaly, – negative anomaly

$$UB = \tilde{M} + 1.5(UQ - \tilde{M}) \quad (6)$$

$$dTEC = \begin{cases} TEC > UB; & TEC - UB \\ TEC < UB, TEC > LB; & 0 \\ TEC < LB; & TEC - UB \end{cases} \quad (7)$$

When an observed TEC is exceeding UB or LB, the positive or negative abnormal TEC signal is approved, respectively. The observed TEC value between the UB and LB defines no abnormal condition in the ionosphere.

Compared to the perturbations caused by geomagnetic storms, the duration of the seismic-related ionospheric anomalies lasts about 4–6 h. (Pulinets et al. 2003; Pulinets and Boyarchuk 2004). Therefore, the days with continuous anomalies for at least 6-h (3/12) were considered as abnormal day. In addition, if there were both positive and negative anomalies on an abnormal day, the higher-level anomaly defines sign of the abnormal day (positive or negative).

The ionospheric TEC has secular and regular changes (Jin et al. 2015), e.g., diurnal and seasonal scales, and abnormal variations caused by irregular events, such as space weather (solar and geomagnetic activities), natural event (e.g., earthquake, tsunami and volcanic eruption) and anthropogenic activities (e.g., rocket launching, nuclear explosions). In order to reinforce the claim that an abnormal day is caused

by seismic activity, it is necessary to eliminate the space-weather effect on the TEC variation. For this purpose, threshold values have been determined for possible geomagnetic and solar activity that could affect the TEC variation. For quiet geomagnetic activity, absolute Dst < 20 nanoTesla (nT) values are selected and it is assumed that there is no geomagnetic activity that would affect the TEC variation by this assumption. If any epoch the Dst value exceeds the threshold value, the anomaly was removed from the TEC variation. F10.7 and SSN values were taken into account to determine possible changes due to solar activity. First, the daily median value of the TECs at the 2-h temporal resolution and 5 longitudes (25°–45°) × 4 latitudes (35°–42.5°) spatial resolution was calculated to compare with solar indexes. Accordingly, daily TEC values were obtained from 240 grid point (20 × 12) in the region for each day between 2003 and 2016. F10.7, SSN and TEC time series from 2003 to 2016 is shown in Fig. 2. Correlations between TEC values and F10.7 and SSN indices were calculated and found to 0.8227 and 0.7616, respectively.

It is seen that F10.7 index shows a higher correlation with TEC values than SSN index. It has also been shown in previous studies that the F10.7 index has a high correlation with TEC values (Chakrabarty et al. 2012; Hajra et al. 2016). Accordingly, the F10.7 index was considered to determine the solar effect in the study. While it is known that solar activity is the main parameter effect the ionosphere (Hocke 2008), it has been proven that this

**Fig. 1** The study area and  $M_w \geq 5.0$  earthquakes during 2003–2016. The red circles show earthquake epicenters. In addition, earthquake focal mechanisms are represented. The red circles and focal mechanisms were scaled according to earthquakes magnitude

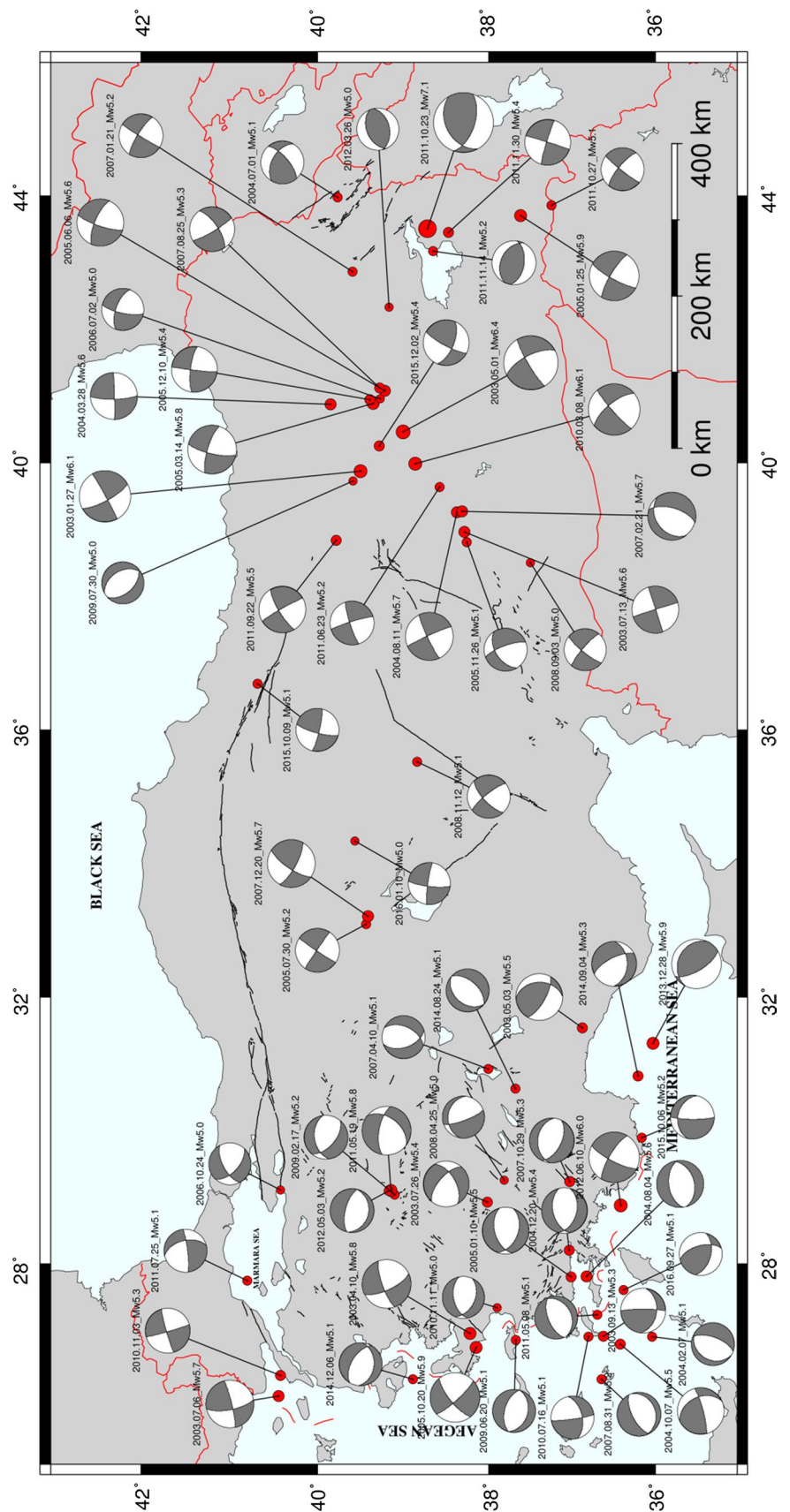
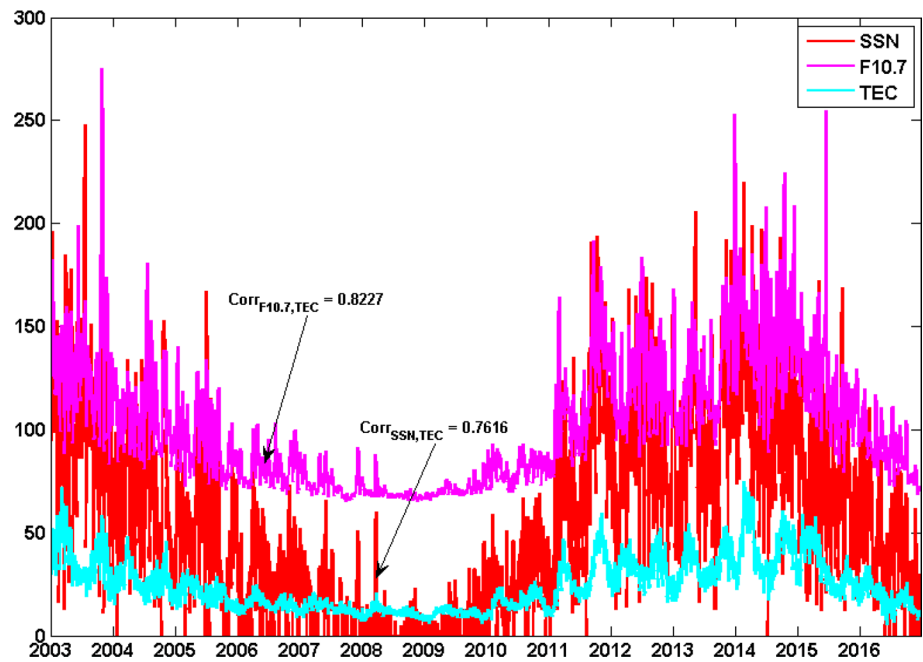




**Fig. 2** The F10.7, SSN and TEC time series from 2003 to 2016. The red, magenta and cyan solid lines are shown SSN, F10.7 and TEC, respectively



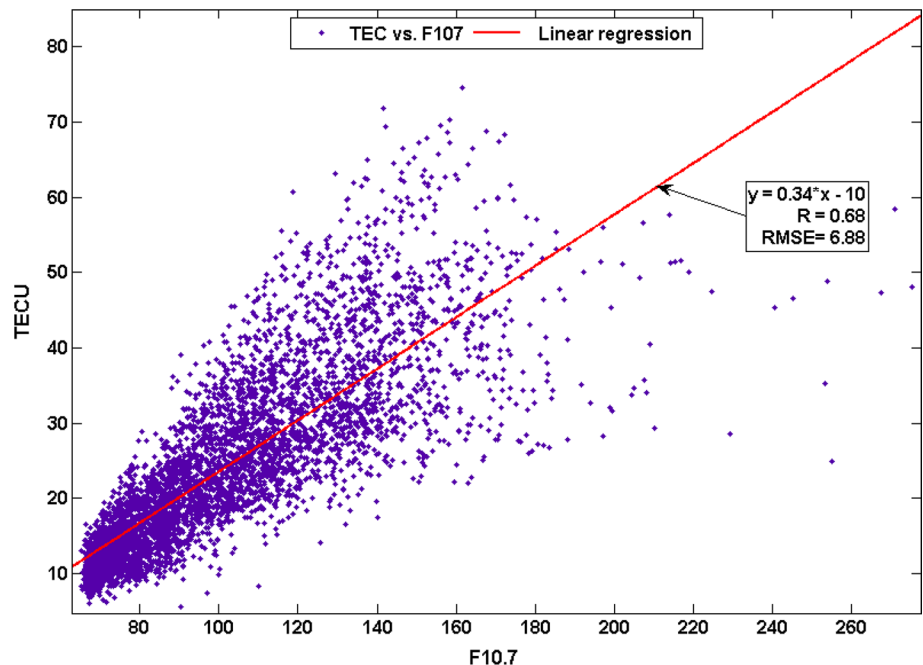
effect is highly positive correlated to TEC variation. To understand the effect of the change in F10.7 on TEC values, the linear regression was applied to two values for each day for 14 years period. The results are shown in Fig. 3 and the figure depicts that a change of about 20 solar flux units (sfu) in F10.7 causes ~5–7 TECU difference in the TEC value with  $R=0.68$  and  $RMSE=6.88$ . Accordingly, 20 sfu difference in F10.7 between consecutive days was considered, and anomalies of the relevant days were removed from the TEC variation. Dst and F10.7 data are

obtained from OMNI Web site (<https://omniweb.gsfc.nasa.gov/form/dx1.html>).

## Results

An example of the process applied for 63 earthquakes in Fig. 4 is shown only for the Mw7.1 Van earthquake on October 23, 2011, which is the biggest magnitude earthquake in the study. Figure 4a shows observed TECs, median TECs,

**Fig. 3** Linear regression between TEC and F10.7 values



upper bounds, lower bounds and defined anomalies according to upper and lower bounds. Figure 4b shows 6-h continuous anomalies after removing geomagnetic and solar effects by defined criteria. In reference to, positive abnormal days were defined as 1, 2, 7 and 8 days before the earthquake, earthquake day, 1 day after earthquake. In addition, negative abnormal days were defined as 4 days before earthquake, 6 and 7 days after the earthquake. Figure 4c, d show Dst and F10.7 indices, respectively.

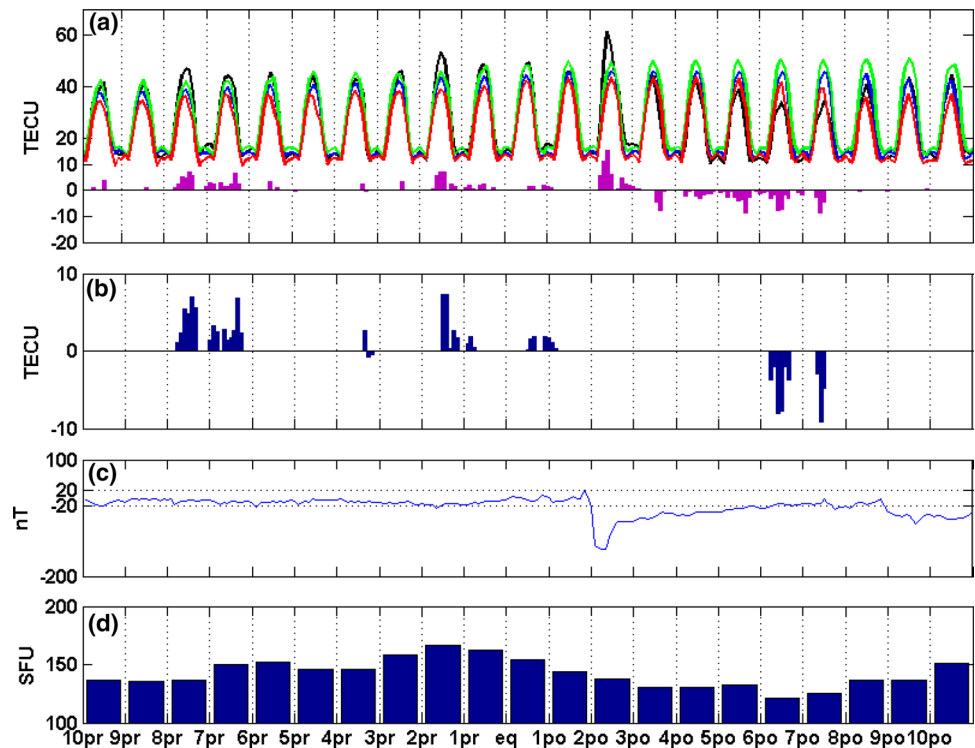
In order to validate our GIM results, we used the GPS-TEC data of available four IGS stations within the size of the Van earthquake preparation area. The GPS-TEC provides the high-resolution data for ionospheric studies. The earthquake preparation area was calculated according to Dobrovolsky equation,  $r = 10^{0.43M}$  km, where M is the magnitude (Dobrovolsky et al. 1979). Figure 5 shows the TEC variation of available IGS stations which is named ANKR, BSHM, CRAO and ZECK, 1–10 days before and after the Van earthquake. Maps on the right side of figure show location of the corresponding stations and the earthquake epicenter. Anomalies in the GPS-TEC variation were determined using the same process steps as in the GIM-TEC data. Only the GPS-TEC data here has a 30 s time interval, not 2 h like GIM-TEC. GPS-TEC time series and abnormal days in Fig. 5 show great similarities with GIM results shown in Fig. 4a. This similarity is more evident in ANKR and BSHM stations, which are located in the west and southwest direction of the epicenter, especially on the 2nd day after the earthquake when an intense magnetic storm occurred. It is

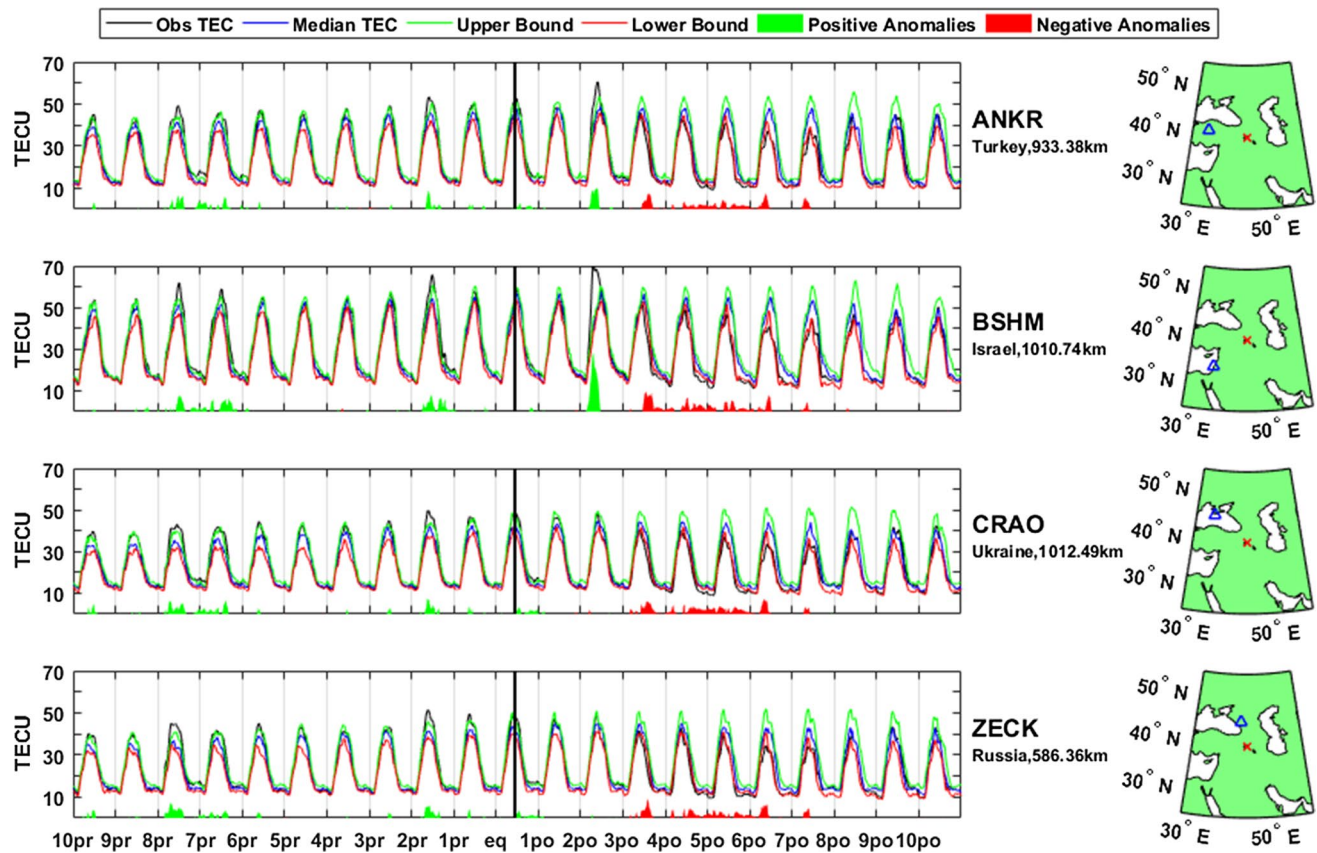
necessary to state that we have not removed any anomalies by applying some criteria in Fig. 5.

Figure 6 shows abnormal days related to earthquakes magnitude. 38.4% (508/1323) of total days were detected as abnormal day. 51.8% (263) of abnormal days are positive, and 48.2% (245) of abnormal days are negative. A total of 226 abnormal days (135 positives and 91 negatives) 10 days before the earthquakes, 27 abnormal days (12 positives and 15 negatives) on the earthquake days and 255 abnormal days (116 positives and 139 negatives) 10 days after the earthquakes were defined. Figure 7 shows abnormal days related to earthquakes focal mechanism. 132 positive and 115 negative abnormal days were defined as vertical (normal or reserve fault) displacement, and 131 positive and 130 negative abnormal days were defined to horizontal (strike-slip) displacement. As a meaningful result here, positive anomalies are seen more frequently than negative anomalies 5 days before earthquakes only in strike-slip fault. However, the frequency of negative anomalies is increased in comparison with the positive ones on the day of the earthquake and afterward, and there is no clear distinction between the numbers of anomalies before and after the earthquakes.

The magnitude of the anomalies relative to the TEC values may be more significant to define the amplitude of the perturbation in some cases. As the ionosphere reveals the difference between day and night due to its strong relationship with the sun, the relative dTEC is more successful to show a daily trend of the anomalies than the normal dTEC. The relative TEC

**Fig. 4** TEC variation, abnormal days, Dst index and F10.7 index for 1–10 days before and after the Van earthquake. **a** The black, blue, green and red curves show the observed TEC, median TEC, upper bound and lower bound, respectively. The magenta bars show anomalies. **b** 6-h continuous anomalies after removing geomagnetic and solar effects by defined criteria **c** Dst values and **d** F10.7 values





**Fig. 5** TEC variations of ANKR, BSHM, CRAO and ZECK stations 1–10 days before and after the Van earthquake. The vertical black line shows the earthquake time. The black, blue, green and red curves

show the observed TEC, median TEC, upper bound and lower bound, respectively. The green and red areas show positive and negative anomalies, respectively

contribution (dTEC, %) is calculated from dTEC divided by the observed TEC value.

$$\text{relative dTEC(\%)} = \frac{\text{dTEC}}{\text{TEC}} \times 100 \quad (8)$$

In Fig. 8, the mean of relative dTEC values of 63 earthquakes is presented. Figure 8 depicts that the positive anomalies are higher than the negative ones before the earthquakes except for 1 day before. The positive anomalies show a similar pattern during the 21 days. The positive mean of relative dTEC values ranges between ~0.15 and 2.5%. The negative anomalies increase after the earthquakes. The negative mean of relative dTEC values ranges between ~0.01 and 4.7%. It can be said that the positive anomalies more dominant than the negative anomalies before the earthquakes, and there is an opposite case after the earthquakes.

## Discussion

In the study, we have tried to find a statistical relationship between anomalies obtained from TEC variations and earthquakes according to some assumptions. However, it

does not seem a particular case for anomalies, except for seismic activities. The assumptions envisaged in the study may be incomplete. These assumptions are summarized below with some references.

A quartile-based running median process was used in the study. Here, the method was applied for a period of 21 days including 10 days before the earthquake, 1 earthquake day and 10 days after the earthquake. Liu et al. (2004) investigated 20  $M \geq 6.0$  earthquakes in the Taiwan area from September 1999 to December 2002. Researchers have used a 15-day running median method, and they have looked for anomalies before and after the earthquake a 15-day period and in earthquake day. The results show that seismic-related ionospheric anomalies were detected 5 days before the earthquakes with an 80% success rate. Pulnits (1998) state that seismo-ionospheric anomalies appear every day during a period up to 5 days prior to the earthquake. Ke et al. (2016) analyzed 24  $M_s > 5.0$  earthquakes in China from 2003 to 2013. They considered 20 days before and 10 days after earthquakes. Shah and Jin (2015) researched 1492  $M_w \geq 5.0$  earthquakes from 1998 to 2014 in the global area. The study covers 10 days before

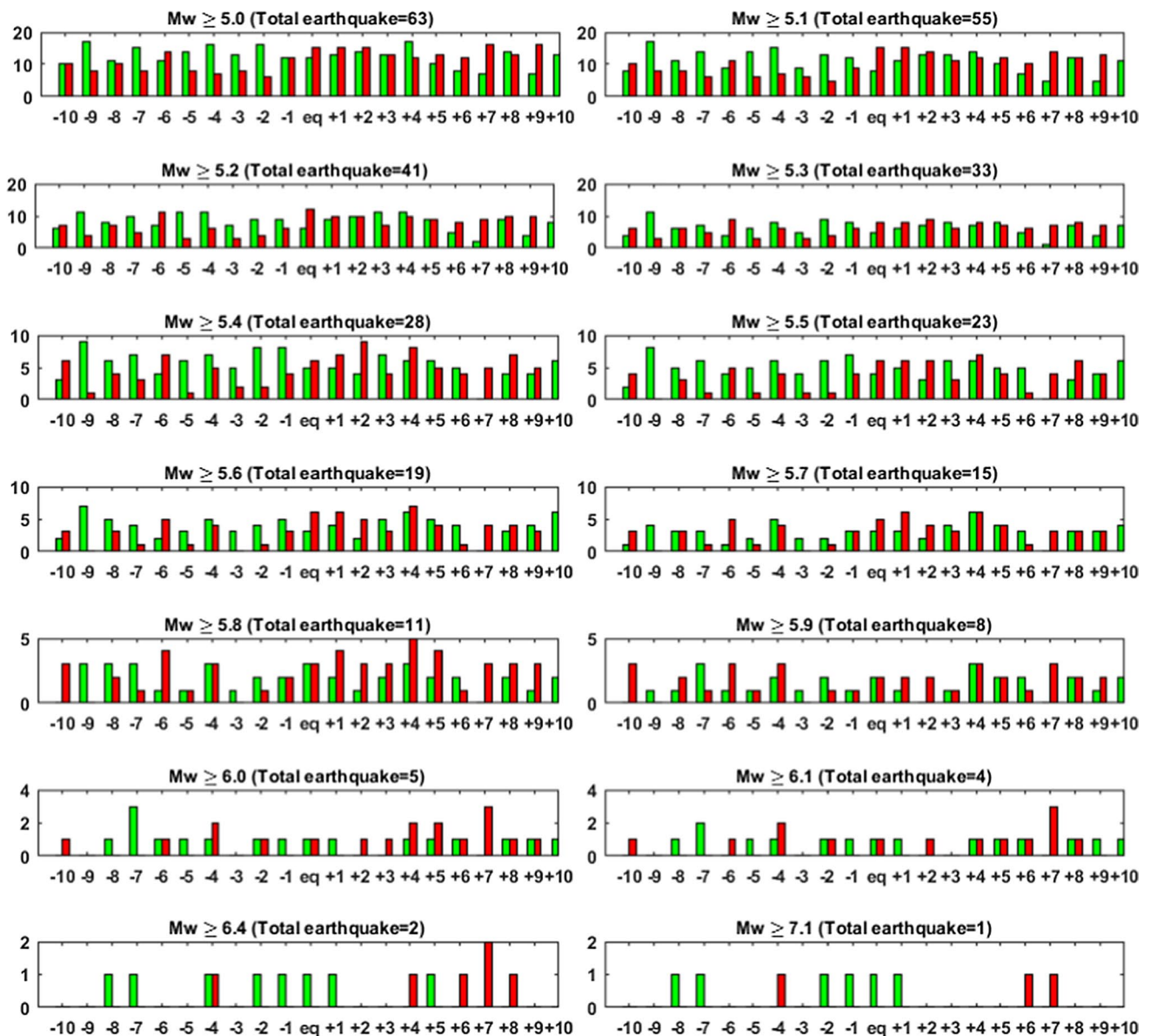


**Fig. 6** Abnormal days grouped by earthquakes magnitude. The x-axis defines 1–10 days before and after the earthquakes and the y-axis defines count of abnormal days. The green bars show positive abnormal days, and the red bars show negative abnormal days, respectively

and after earthquakes. Liu et al. (2013a) looked for anomalies in the 15-day period before and after earthquakes. Le et al. (2011) analyzed TEC variations only 1–21 days prior to earthquakes. Kon et al. (2011) investigated TEC variations of the  $M \geq 6.0$  earthquakes in Japan on a widely time interval (1–30 days before and after earthquakes). #Question 1: How many days before and/or after the earthquake should it be expected for an anomaly that can actually be caused by seismic activity?

In order to eliminate the effect of geomagnetic and solar activity, some threshold values and assumptions have been determined. The absolute  $Dst < 20$  nT was selected for geomagnetic activity, and when the absolute  $Dst$  value

exceeds 20 nT, the related anomaly is removed from TEC variation. In addition, to eliminate the effect of the solar activity on anomalies, the F10.7 index was selected, and if there were 20 sfu difference between consecutive days, all anomalies of the relevant day were removed. Liu et al. (2013b) statistically investigate ionospheric storm effects response to GPS-TEC variations over Taiwan. The results show that positive anomalies are effective on the storm day and one day after, and negative anomalies can be seen even four days after the storm onset. Ke et al. (2016) selected absolute  $Dst < 50$  nT and sum of daily  $Kp > 30$  as thresholds to exclude geomagnetic effects on TEC variations. Kon et al. (2011) removed the 2 days TEC data after the



**Fig. 7** Abnormal days grouped by earthquakes focal mechanism. The green bars show positive abnormal days, and the red bars show negative abnormal days, respectively

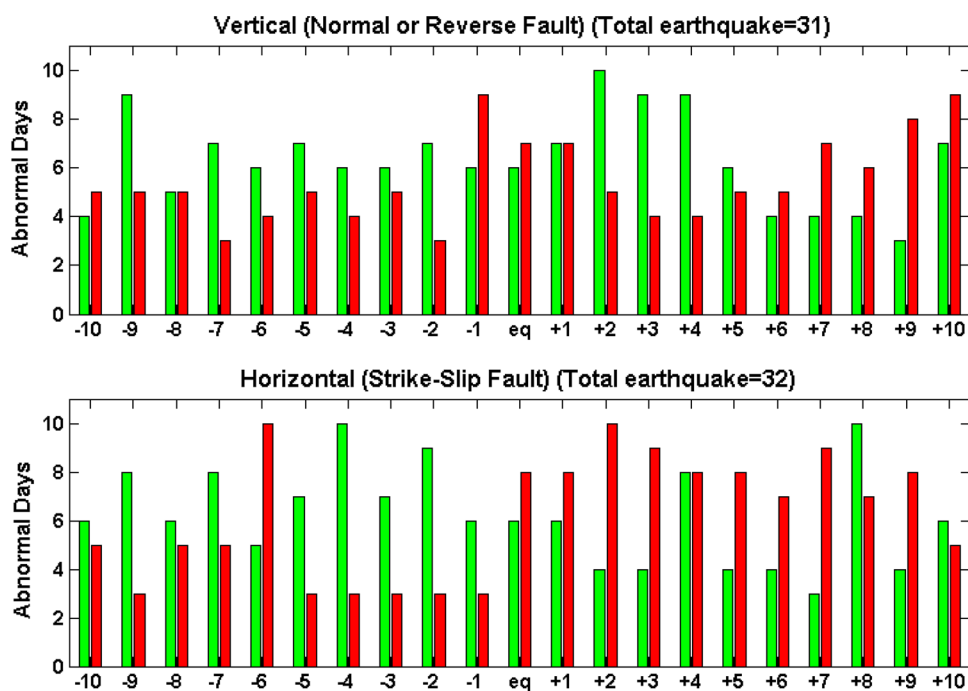
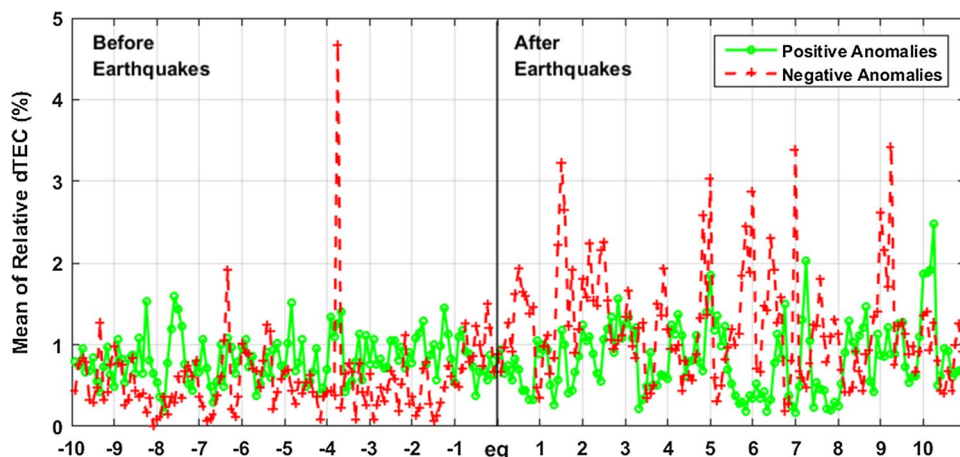


**Fig. 8** The mean of relative dTEC before and after the earthquakes



storm (Dst index exceed  $-60$  nT) onset. Gulyaeva and Arikan (2016) accepted  $AE_{\max} \geq 500$ ,  $aa_{\max} > 45$ ,  $ap_{\max} > 30$ ,  $ap(\tau) > 18$  and  $Dst_{\min} \leq 30$  values as non-storm geomagnetic conditions. Le et al. (2011) selected  $Dst < -40$  nT or the decreasing amplitude of the Dst index within a day larger than  $40$  nT to decide magnetic storm, and they have removed earthquakes occurring within 4 days after the magnetic storm. Liu et al. (2006) defined a major storm day together with geomagnetic indices  $Kp \geq 6$  and  $Dst \geq 60$  nT and a few hours to 2 days after geomagnetic storms were accepted disturbed time interval for TEC variation. Fuying et al. (2011) utilized only the Kp index to describe geomagnetic storm, and Kp values larger than 4 were selected as a geomagnetic activity. #Question 2: What should be the right strategy for space-weather conditions?

Besides, how can we distinguish precisely other phenomena that bring about change in the ionosphere other than geomagnetic and solar activity?

In the study, more than 6-h continuous anomalies were considered to define abnormal days. Liu et al. (2004) selected only 2-h continuous anomalies to avoid detecting other short lifetime perturbations caused by some other phenomena. Pulnits (1998) describe seismo-ionospheric anomaly time only 3-4 h. Shah and Jin (2015) approved six or more hours for a single day as an abnormal. Le et al. (2011) selected only more than six successive abnormal points (corresponding to 6-h) in a day. Kon et al. (2011) considered more than 10-h of positive or negative anomalies appear in one day. #Question 3: How long are the seismic-related anomalies expect to be continuous?

Alternatively, should seismic-related anomalies be continuous?

Interestingly, in many statistical studies either the solar effect is not considered or solar indices are defined but not used to remove the solar effect on TEC variations. Solar effect indices are highly correlated to TEC values, and this correlation is positive linear. In particular, power fluctuations in solar indices are adversely affected TEC variations in the generally applied moving median and sliding window methods at statistical studies. In addition, some important questions need to give a meaning, such as should the seismic effect of the TEC variation is expected only at the epicenter? How is the correlation between seismic parameters (time, location, magnitude, depth, focal mechanism, etc.) and seismic-related anomalies? Statistical studies are needed to answer these questions, but it is necessary to answer these questions to obtain meaningful results from the statistic. Answers to these questions, however, can only be made by demonstrating the theory of the relationship between the earthquake and the ionosphere.

It is assumed that there is a significant relationship between the earthquake and the ionosphere, but some statistical and case studies have found no relationship between ionospheric anomalies and earthquakes (Afraimovich and Astafyeva 2008; Dautermann et al. 2007; Thomas et al. 2017). Thomas et al. (2017) statistically investigate 1279  $M \geq 6.0$  earthquakes for 2000–2014 worldwide using GIM-TEC values  $\pm 15$  days of earthquakes. Results show that there are no significant changes prior to earthquakes in the ionosphere. Afraimovich and Astafyeva (2008) utilized “check-region” approach to the calculation of global and local electron content with low seismic activity. The result shows that some anomalies believed to be of seismic related might be an effect of global changes of the TEC related to the 27-day variation and/or other variations due to solar and geomagnetic activity. Dautermann et al. (2007) investigated Southern California earthquakes during 2003–2004 using 265 continuous GPS stations, and they applied three different statistical tests. They find abnormalities on TEC variations but no statistically significant correlation between these abnormalities and earthquakes. More information on this topic can be found in various reviews (Masci 2012; Masci et al. 2015; Thomas et al. 2012).

## Conclusion

In this study, 63  $M_w \geq 5.0$  earthquakes in Turkey located in mid-latitude during 2003–2016 are statistically investigated. A quartile-based running median process is used to define anomalies, and Dst and F10.7 indices are

considered to eliminate solar and geomagnetic effects on TEC variations. The results can be summarized as follows.

1. F10.7 is highly correlated to TEC values than SSN in Turkey during 2003–2016. The correlation coefficient for F10.7, SNN and TEC is 0.8227 and 0.7616, respectively.
2. Abnormal days determined by GIM are similar to those determined with high-resolution GPS-TEC. It means that GIM-TEC data has a good agreement with GPS-TEC data and GIMs be accepted as successful in determining local changes.
3. It is not possible to determine a meaningful precursor for  $M_w \leq 6.0$  earthquakes since the counts of the abnormal days before and after earthquakes are nearly equal to each other. Moreover, abnormal days after earthquakes are more than before earthquakes.
4. Positive abnormal days during days before earthquakes and negative abnormal days during days after earthquakes are more frequent. However, since numbers are almost equal to each other, it is not possible to conclude a meaningful conclusion.
5. According to the focal mechanisms of earthquakes, when abnormal days are investigated, significant results have not been achieved. However, for earthquakes with horizontal displacements (strike-slip fault), positive abnormal days observed 5 days before earthquakes are noteworthy.
6. The relative dTEC values showed that the positive anomalies more dominant than the negative anomalies before the earthquakes, and there is an opposite case after the earthquakes.

In particular, the lack of larger magnitude ( $M_w \geq 5.0$ ) earthquake in Turkey makes difficult to achieve the promising results for seismo-ionospheric coupling. It is more probable that larger magnitude earthquakes cause distinctive increase/decrease on TEC variations than lower magnitude earthquakes. That’s why results of this study do not completely disprove the possibility of precursory phenomena related with seismic activities.

## References

- Afraimovich EL, Astafyeva EI (2008) TEC anomalies: local TEC changes prior to earthquakes or TEC response to solar and geomagnetic activity changes? *Earth Planets Space* 60(9):961–966
- Aggarwal M (2015) Anomalous changes in ionospheric TEC during an earthquake event of 13–14 April 2010 in the Chinese sector. *Adv Space Res* 56(7):1400–1412
- Akhoondzadeh M, Parrot M, Saradjian MR (2010) Electron and ion density variations before strong earthquakes ( $M > 6.0$ ) using DEMETER and GPS data. *Nat Hazards Earth Syst* 10(1):7–18


- Alizadeh M, Schuh H, Todorova S, Schmidt M (2011) Global ionospheric maps of VTEC from GNSS, satellite altimetry and FORMOSAT-3/COSMIC data. *J Geod* 85(12):975–987
- Chakrabarty D, Bagiya MS, Thampi SV, Iyer KN (2012) Solar EUV flux (0.1–50 nm), F10.7 cm flux, sunspot number and the total electron content in the crest region of equatorial ionization anomaly during the deep minimum between solar cycle 23 and 24. *Indian J Radio Space Phys* 41(2):110–120
- Ciraolo L, Azpilicueta F, Brunini C, Meza A, Radicella SM (2007) Calibration errors on experimental slant total electron content (TEC) determined with GPS. *J Geod* 81(2):111–120
- Dautermann T, Calais E, Haase J, Garrison J (2007) Investigation of ionospheric electron content variations before earthquakes in southern California, 2003–2004. *J Geophys Res B Solid Earth* 112:1–20
- Dobrovolsky IP, Zubkov SI, Miachkin VI (1979) Estimation of the size of earthquake preparation zones. *Pure appl Geophys* 117:1025–1044
- Dogan U, Ergintav S, Skone S, Arslan N, Oz D (2011) Monitoring of the ionosphere TEC variations during the 17th August 1999 Izmit earthquake using GPS data. *Earth Planets Space* 63(12):1183–1192
- Fuying Z, Yun W, Yiyan Z, Jian L (2011) A statistical investigation of pre-earthquake ionospheric TEC anomalies. *Geod Geodyn* 2(1):61–65
- Gulyaeva T, Arikani F (2016) Statistical effects under geomagnetic quiet and storm conditions. *Geomat Nat Hazards Risk*. <https://doi.org/10.1080/19475705.2016.1246483>
- Guo J, Li W, Yu H, Liu Z, Zhao C, Kong Q (2014) Impending ionospheric anomaly preceding the Iquique Mw8.2 earthquake in Chile on 2014 April 1. *Geophys J Int* 203(3):1461–1470
- Hajra R, Chakraborty SK, Tsurutani BT, DasGupta A, Echer E, Brum CGM, Gonzalez WD, Sobral JHA (2016) An empirical model of ionospheric total electron content (TEC) near the crest of the equatorial ionization anomaly (EIA). *J. Space Weather Space Clim*. <https://doi.org/10.1051/swsc/2016023>
- Hattori K, Hirooka S, Kunimitsu M, Ichikawa T, Han P (2014) Ionospheric anomaly as an earthquake precursor: case and statistical studies during 1998–2012 around Japan. In: General assembly and scientific symposium (URSI GASS), 2014 XXXIth URSI
- Hayakawa M, Fujinawa Y (eds) (1994) c. Terra Science Publishing Company, Tokyo, p 667
- Hayakawa M, Molchanov OA (eds) (2002) Seismo electromagnetics: lithosphere–atmosphere–ionosphere coupling. TERRAPUB, Tokyo, p 477
- Hayakawa M, Kasahara Y, Nakamura T, Muto F, Horie T, Maekawa S, Hobara Y, Rozhnoi AA, Solovieva M, Molchanov OA (2010) A statistical study on the correlation between lower ionospheric perturbations as seen by subionospheric VLF/LF propagation and earthquakes. *J Geophys Res* 115:1–9
- Hocke K (2008) Oscillations of global mean TEC. *J Geophys Res Space Phys* 113:1–13
- Jin S, Occhipinti G, Jin R (2015) GNSS ionospheric seismology: recent observation evidences and characteristics. *Earth Sci Rev* 147:54–64
- Kaladze TD, Pokhotelov OA, Shah HA, Khan MI, Stenflo L (2008) Acoustic-gravity waves in the Earth's ionosphere. *J Atmos Solar-Terr Phys* 70(13):1607–1616
- Ke F, Wang Y, Wang X, Qian H, Shi C (2016) Statistical analysis of seismo-ionospheric anomalies related to Ms > 5.0 earthquakes in China by GPS TEC. *J Seismolog* 20(1):137–149
- Klimenko MV, Klimenko VV, Karpov IV, Zakharenkova IE (2011) Modeling of seismoionospheric effects initiated by internal gravity waves. *Russ J Phys Chem* 30(5):41–49
- Kon S, Nishihashi M, Hattori K (2011) Ionospheric anomalies possibly associated with M ≥ 6.0 earthquakes in the Japan area during 1998–2010: case studies and statistical study. *J Asian Earth Sci* 41(4):410–420
- Le H, Liu JY, Liu L (2011) A statistical analysis of ionospheric anomalies before 736 M6.0 + earthquakes during 2002–2010. *J Geophys Res* 116:1–5
- Liu JY, Chuo YJ, Shan SJ, Tsai YB, Chen YI, Pulinets SA, Yu SB (2004) Pre-earthquake ionospheric anomalies registered by continuous GPS TEC measurements. *Ann Geophys* 22(5):1585–1593
- Liu JY, Chen YI, Chuo YJ, Chen CS (2006) A statistical investigation of preearthquake ionospheric anomaly. *J Geophys Res* 111:1–5
- Liu JY, Chen CH, Chen YI, Yang WH, Oyama KI, Kuo KW (2010) A statistical study of ionospheric earthquake precursors monitored by using equatorial ionization anomaly of GPS TEC in Taiwan during 2001–2007. *J Asian Earth Sci* 39(1–2):76–80
- Liu JY, Chen CH, Tsai HF (2013a) A statistical study on seismo-ionospheric precursors of the total electron content associated with 146 M ≥ 6.0 earthquakes in Japan during 1998–2011. *Earthquake prediction studies: Seismo Electromagnetics*, edited by M. Hayakawa, 1–13
- Liu JY, Yang WH, Lin CH, Chen YI (2013b) A statistical study on the characteristics of ionospheric storms in the equatorial ionization anomaly region: GPS total electron content observed over Taiwan. *J Geophys Res Space Phys* 118(6):3856–3865
- Maekawa S, Horie T, Yamauchi T, Sawaya T, Ishikawa M, Hayakawa M, Sasaki H (2006) A statistical study on the effect of earthquakes on the ionosphere, based on the subionospheric LF propagation data in Japan. *Ann Geophys* 24:2219–2225
- Masci F (2012) The study of ionospheric anomalies in Japan area during 1998–2010 by Kon et al.: an inaccurate claim of earthquake-related signatures? *J Asian Earth Sci* 57:1–5
- Masci F, Thomas JN, Villani F, Secan JA, Rivera N (2015) On the onset of ionospheric precursors 40 min before strong earthquakes. *J Geophys Res A: Space Phys* 120(2):1383–1393
- McClusky S, Reilinger R, Mahmoud S, Sari DB, Tealeb A (2003) GPS constraints on Africa (Nubia) and Arabia plate motions. *Geophys J Int* 155:126–138
- Ouzounov D, Pulinets SA, Romanov A, Romanov A, Tsybulya K, Davidenko D, Kafatos M, Taylor P (2011) Atmosphere-ionosphere response to the M9 Tohoku earthquake revealed by multi instrument space-borne and ground observations: preliminary results. *Earthq Sci* 24(6):557–564
- Parrot M (2012) Statistical analysis of automatically detected ion density variations recorded by DEMETER and their relation to seismic activity. *Ann Geophys* 55(1):149–155
- Pulinets SA (1998) Seismic activity as a source of the ionospheric variability. *Adv Space Res* 22(6):903–906
- Pulinets SA (2009) Physical mechanism of the vertical electric field generation over active tectonic fault. *Adv Space Res* 44(6):767–773
- Pulinets SA, Boyarchuk KA (2004) Ionospheric precursors of earthquakes. Springer, Germany, p 315
- Pulinets SA, Legen'ka AD, Gaivoronskaya TV, Depuev VK (2003) Main phenomenological features of ionospheric precursors of strong earthquakes. *J Atmos Sol Terr Phys* 65(16–18):1337–1347
- Pundhir D, Singh B, Lakshmi DR, Reddy BM (2015) A study of ionospheric precursors associated with the major earthquakes occurred in Pakistan region. *J Ind Geophys Union* 19(1):71–76
- Reilinger R et al (2006) GPS constraints on continental deformation in the Africa-Arabia-Eurasia continental collision zone and implications for the dynamics of plate interactions. *J Geophys Res* 111:B05411. <https://doi.org/10.1029/2005JB004051>
- Rozhnoi A, Solovieva M, Molchanov O, Biagi P-F, Hayakawa M (2007) Observation evidences of atmospheric Gravity Waves induced by seismic activity from analysis of subionospheric LF signal spectra. *Nat Hazards Earth Syst Sci* 7(5):625–628

- Schaer S, Gurtner W, Feltens J (1998) IONEX: the ionosphere map exchange format version 1. In: Proceedings of the IGS AC workshop, Darmstadt, Germany
- Şentürk E, Çepni MS (2018) Performance of different weighting and surface fitting techniques on station-wise TEC calculation and modified sine weighting supported by the sun effect. *J Spatial Sci* 5:2–10.1080/14498596.2017.1417169
- Shah M, Jin S (2015) Statistical characteristics of seismo-ionospheric GPS TEC disturbances prior to global  $M_w \geq 5.0$  earthquakes (1998–2014). *J Geodyn* 92:42–49
- Sorokin VM, Chmyrev VM, Yaschenko AK (2006) Possible DC electric field in the ionosphere related to seismicity. *Adv Space Res* 37(4):666–670
- Thomas JN, Love JJ, Komjathy A, Verkhoglyadova OP, Butala M, Rivera N (2012) On the reported ionospheric precursor of the 1999 Hector Mine, California earthquake. *Geophys. Res. Lett.* <https://doi.org/10.1029/2012GL051022>
- Thomas JN, Huard J, Masci F (2017) A statistical study of global ionospheric map total electron content changes prior to occurrences of  $M \geq 6.0$  earthquakes during 2000–2014. *J Geophys Res Space Phys.* <https://doi.org/10.1002/2016JA023652>
- Wen S, Chen CH, Yen HY, Yeh TK, Liu JY, Hattori K, Peng H, Wang CH, Shin TC (2012) Magnetic storm free ULF analysis in relation with earthquakes in Taiwan. *Nat Hazards Earth Syst Sci* 12:1747–1754
- Yao YB, Chen P, Zhang S, Chen JJ, Yan F, Peng WF (2012) Analysis of pre-earthquake ionospheric anomalies before the global  $M = 7.0 +$  earthquakes in 2010. *Nat Hazards Earth Syst Sci* 12:575–585





# Assessment of climate change and associated impact on selected sectors in Poland

Zbigniew W. Kundzewicz<sup>1,4</sup> · Mikołaj Piniewski<sup>3,4</sup> · Abdelkader Mezghani<sup>2</sup> · Tomasz Okruszko<sup>3</sup> · Iwona Pińskwar<sup>1</sup>  · Ignacy Kardel<sup>3</sup> · Øystein Hov<sup>2</sup> · Mateusz Szcześniak<sup>3</sup> · Małgorzata Szwed<sup>1</sup> · Rasmus E. Benestad<sup>2</sup> · Paweł Marcinkowski<sup>3</sup> · Dariusz Graczyk<sup>1</sup> · Andreas Dobler<sup>2</sup> · Eirik J. Førland<sup>2</sup> · Joanna O’Keefe<sup>3</sup> · Adam Choryński<sup>1</sup> · Kajsia M. Parding<sup>2</sup> · Jan Erik Haugen<sup>2</sup>

Received: 3 April 2018 / Accepted: 29 October 2018 / Published online: 3 November 2018  
© The Author(s) 2018

## Abstract

The present paper offers a brief assessment of climate change and associated impact in Poland, based on selected results of the Polish–Norwegian CHASE-PL project. Impacts are examined in selected sectors, such as water resources, natural hazard risk reduction, environment, agriculture and health. Results of change detection in long time series of observed climate and climate impact variables in Poland are presented. Also, projections of climate variability and change are provided for time horizons of 2021–2050 and 2071–2100 for two emission scenarios, RCP4.5 and RCP8.5 in comparison with control period, 1971–2000. Based on climate projections, examination of future impacts on sectors is also carried out. Selected uncertainty issues relevant to observations, understanding and projections are tackled as well.

**Keywords** Climate change · Climate change impact · Projections · Poland

## Introduction

The topical area of climate change and associated impacts, recognized as very important in many European countries, does not generally get a high status in the public discourse in Poland. Generally, Poles are aware of climate change, but this topical area is not broadly considered as a high priority (Kundzewicz and Matczak 2012; Kundzewicz et al. 2017f). Observed climate change impacts are not dramatic, and the attribution of these impacts is rather complex, due to the existence of multiple driving factors. Public discourse is influenced by combination of strong natural variability of hydro-meteorological phenomena and significant

uncertainty of projections for the future. Consequently, adaptation to climate change is not taken as such a serious issue as it deserves. Mitigation policy is even more challenged, because the public perception is driven by the deeply rooted wisdom that Poland “sits on coal” and coal guarantees the national energy security. The carbon footprint per inhabitant and per unit GDP in Poland has been high (Ceglarz et al. 2018).

The present paper offers a review of selected results generated within the CHASE-PL (Climate change impact assessment for selected sectors in Poland) project, carried out in 2014–2017, within the framework of the Polish–Norwegian Research Programme under the Norwegian Financial Mechanism. The CHASE-PL project aimed to provide substantial intellectual support for counteracting climate change and its adverse impacts in Poland, hence potentially contributing to sustainable economic development and environmental protection. The CHASE-PL project was jointly implemented by three institutional partners of the project consortium (Institute for Agricultural and Forest Environment of the Polish Academy of Sciences, Poznań, Poland; Norwegian Meteorological Institute, Oslo, Norway; and Warsaw University of Life Sciences, Warsaw, Poland). The research topics tackled in the project were the following:

✉ Iwona Pińskwar  
iwona.pinskwar@isrl.poznan.pl

<sup>1</sup> Institute for Agricultural and Forest Environment of the Polish Academy of Sciences, Poznan, Poland

<sup>2</sup> Norwegian Meteorological Institute (Met Norway), Oslo, Norway

<sup>3</sup> Warsaw University of Life Sciences (SGGW), Warsaw, Poland

<sup>4</sup> Potsdam Institute for Climate Impact Research (PIK), Potsdam, Germany

- Detection of change in observation records of climate and climate impact variables;
- Projections of climate variability and change for the future;
- Model-based assessment of climate change impact;
- Index-based assessment of climate change impacts on agriculture and ecosystems;
- Uncertainty in understanding, observations and projections—a system framework.

The present paper is organized as follows. After discussion of observations and projections of climate change, climate change impacts in selected areas are tackled, and finally—uncertainty and perception issues are discussed.

## Change detection in observed climate data

Change detection in observation records of climatic variables in Poland was carried out for a range of variables of particular relevance and interest, such as temperature (Graczyk et al. 2017), mean precipitation (Pińskwar et al. 2018b; Szwed 2018), as well as intense precipitation (Pińskwar et al. 2018a) and snow cover (Szwed et al. 2017).

Figure 1 summarizes changes in mean annual temperature and precipitation in Poland for the time interval 1961–2017. The positive trend in temperature is well visible, even if deviations from the trend in particular years are quite large. For precipitation, the trend is weak and inter-annual and inter-decadal variability is dominating.

## Temperature

Graczyk et al. (2017) examined observed changes in several “hot” indices, based on temperature observation records

collected at 60 meteorological stations in Poland. Values of multiple indices associated with heat waves were determined. Among the indices were: the duration of the longest hot spell, the number of hot days ( $T_{\max} \geq 30 \text{ }^\circ\text{C}$ ), the number of extremely hot days ( $T_{\max} \geq 35 \text{ }^\circ\text{C}$ ), as well as the number of tropical nights ( $T_{\min} \geq 20 \text{ }^\circ\text{C}$ ) in the year. The same authors analyzed also the spatial distribution of change in indices, with the help of the Mann–Kendall test, as well as the significance level of the resultant trends. Values of indices for the 1991–2013 interval were examined and compared to the reference period, 1961–1990. The increase was detected for most indices at the 5% significance level, for many examined stations. Graczyk et al. (2017) found statistically significant increasing trends in three variables: the number of hot days and the duration of the longest hot spell in summer, as well as the number of tropical nights in a year, for most of the data. In 1961–1990, the longest duration of hot spell reached 10 days, while in 1991–2013, several longer hot spells, up to the duration of 17 days, were recorded.

## Precipitation

Pińskwar et al. (2018b) examined changes in values of indices of observed mean precipitation, based on a set of daily precipitation records for 45 stations in Poland, most of which spanned over the interval 1951–2017. They examined changes in annual, semi-annual, seasonal and monthly precipitation totals, as well as in the number of days with daily precipitation equal to or greater than 1 mm, and in the SDII (Simple Daily Intensity Index) and in the ratio of precipitation in the summer half-year (April–September) to precipitation in the winter half-year (October–March). Many changes were detected, most of which were statistically insignificant, at the 10% level. Yet, regionally consistent seasonal changes

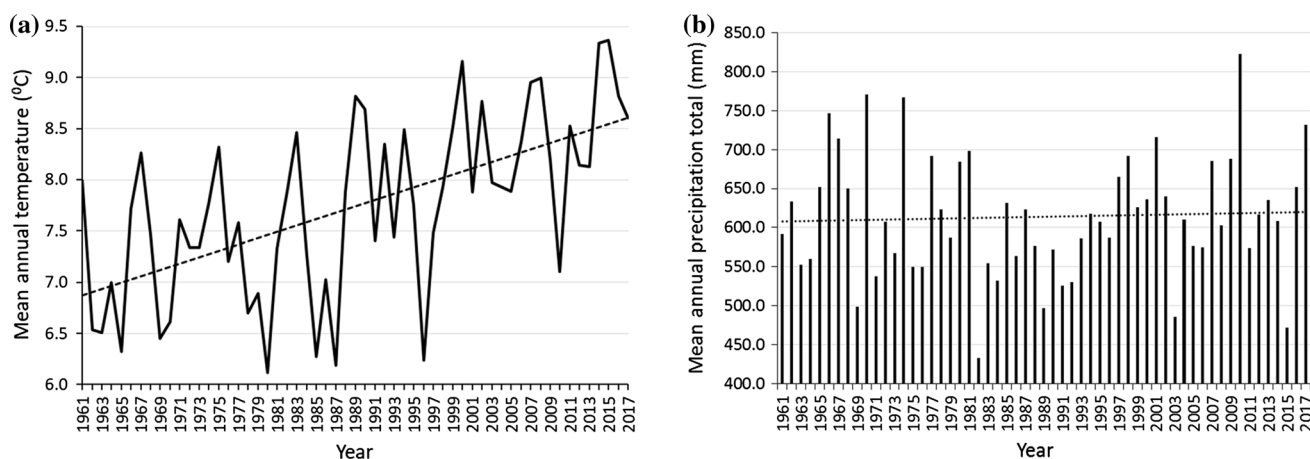


**Fig. 1** Observed mean annual **a** temperature and **b** precipitation in Poland. Temperature diagram illustrates a mean of 60 stations. Precipitation diagram illustrates the annual mean at 42 stations situated at the altitude below 400 m a.s.l. Dotted lines indicate trends

were also found, with dominating precipitation increase in spring and winter.

Szwed (2018) examined observed precipitation changes, tackling their spatial and temporal (seasonal) distribution and spotted a slight increase in annual precipitation. A stronger increase was noted in the northern part of Poland. Based on the precipitation unevenness index, an intra-year variability precipitation on the country territory can be defined as moderate and rather unevenly distributed. However, no statistically significant (at 5% level) changes in the mean were found for 1951–2013. The most variable monthly precipitation was recorded in July and June, while the most stable—from January to March. The share of June–July precipitation can reach more than 40% of the annual precipitation total, while the share of winter months—no more than a dozen or so percent each. The most visible increases in the monthly precipitation totals as well as in the share of monthly precipitation within the annual total were found during the colder half-year, especially in March, with statistically significant trend detected for several stations in the northern and central parts of Poland.

### Extreme precipitation

Pińskwar et al. (2018a) noted the occurrence of many episodes of extreme precipitation excess and deficit in Europe and in Poland in recent decades that had caused considerable, and adverse, economic and social impacts. In Poland, the changes in values of climate indices were found to exhibit complex, spatial and temporal, variability. Pińskwar et al. (2018a) analyzed changes in such indices of observation records as: maximum seasonal 24 h precipitation for winter and summer half-years; maximum 5-day precipitation; maximum monthly precipitation; as well as the number of days with intense or very intense precipitation (with daily rate in excess of, respectively, 10 mm or 20 mm). Also, the maximum number of consecutive dry days (defined as those with daily precipitation below 1 mm) in the summer half-year was analyzed. Examination of precipitation extremes showed that maximum 24-h precipitation for the summer half-year as well as 5-day and monthly precipitation sums increased for many stations. The number of days with intense precipitation was also found to increase especially in the northwestern part of Poland, while the increase in the number of consecutive dry days was noted for many stations in the summer half-year. Comparison of the 1961–1990 interval and the later, warmer, 1991–2015 interval revealed that during the last 25 years most statistical precipitation indices (25th and 75th percentiles, median, mean and maximum) were higher than in 30 years before. However, most changes detected by Pińskwar et al. (2018a) were statistically insignificant. Yet, it is interesting to note that some of these results contradict the findings of other authors (see

discussion in Pińskwar et al. (2018a) and Łupikasza (2010)) that had been based on earlier observation records that do not include the recent interval, 2007–2015. However, a study by Łupikasza (2017) with data records extending to February 2008 and for several stations to 2015, showed increasing trends especially for spring and during winter in the northern part of Poland. The predominant decreasing trends during summer and autumn were also detected in the study.

### Snow

Szwed et al. (2017) examined the variability of such snow cover characteristics in Poland as: snow depth, number of days with snow cover and dates of the beginning and the end of snow cover. A set of 43 long time series of station observation records in the country in 1952–2013 were used for change detection. Trends in analyzed data were sought, with the help of the Mann–Kendall test. In order to interpret temporal changes in snow cover characteristics, the intervals of 1952–1990 and of 1991–2013 were compared. However, the observed behavior of snow-related variables was found to be complex and difficult to interpret. Among the potential reasons was the location of Poland in the zone of transitional moderate climate, which is known for strong climate variability. It was possible to find statistical links between the North Atlantic Oscillation (NAO) index and such snow characteristics in Poland, as the snow depth and the number of snow cover days.

### Climate projections

Projections of climate variability and change in Poland were obtained with the help of downscaling of General Circulation Models (GCMs) simulations for future conditions. All analyses of model-based projections in the CHASE-PL project were carried out with the ensemble of climate projections comprising nine regional climate model outputs (bias-corrected and downscaled to a 5 km × 5 km grid) stemming from the EURO-CORDEX ensemble for two future time horizons: near future, 2021–2050 and far future, 2071–2100. The two so-called representative concentration pathways (associated greenhouse gas emission scenarios) RCP4.5 (intermediate emissions) and RCP8.5 (high emissions) were assumed. Simulations for the historical control period, 1971–2000, were used for comparison. Quantile-mapping method was applied to correct for systematic seasonal biases in simulations before assessing the changes in annual and seasonal means of precipitation and temperature over Poland.

Mezghani et al. (2016) compiled and published the CHASE-PL climate projections—gridded daily precipitation and temperature—5 km (CPLCP-GDPT5) dataset,

comprising projected daily minimum and maximum values of air temperature as well as of precipitation totals. Projected changes for Poland, estimated from the multi-model ensemble, showed that annual temperature mean is expected to increase by approximately 1 °C until 2021–2050 and by about 2 °C until 2071–2100, under the RCP4.5 scenario. Under assumption of the RCP8.5 scenario, the warming was projected to increase to almost 4 °C by the 2071–2100 horizon. Also, likely increase in regional annual precipitation is projected, being of the order of 6–10% and 8–16%, respectively, for the near and remote future horizon. Individual model simulations reflected warmer and wetter conditions on the annual scale. The magnitude of change was found to be higher in the far future than in the near future. The same statement can be made for projected changes in seasonal temperature means, showing a higher winter warming rate by up to 0.5 °C, as compared to other seasons. However, projected changes in seasonal precipitation means, obtained with the help of individual models, do largely differ and are sometimes inconsistent. They exhibit spatial variations, depending on the future horizon, the emission scenario, as well as the season and the location of interest. The overall range of the 90% confidence interval predicted by the ensemble of multi-model simulations was found to vary in the range between 7% (in summer, under RCP4.5) and 40% (in winter, under RCP8.5), for far future projection horizon (Mezghani et al. 2017).

Although seasonal precipitation was projected to increase considerably in all four combinations of RCPs and projection horizons for winter and spring, the model spread was quite high, especially for the remote future. In contrast, the ensemble members agreed that summer and autumn precipitation is not likely to undergo statistically significant changes. It is important to note that regional climate models were used to downscale a small number (four for RCP4.5) of GCMs, and that even one single GCM can produce very different local and regional projections due to the presence of pronounced nondeterministic natural variability on decadal timescales (Deser et al. 2012). Hence, estimates based on a small set of climate model simulations are subject to the “law of small numbers” (Benestad et al. 2017), for which the estimates may be misleading, the true range underestimated and the real uncertainties appear to be smaller than they really are.

Mezghani et al. (2018) tested the influence of selecting a subset of global climate models to drive two downscaling strategies (Empirical–Statistical and Dynamical Downscaling, i.e., ESD and DD, respectively) on the resultant regional and local climate information. As the method of dynamical downscaling is highly demanding and expensive, climate modelers typically run a small set of simulations instead of downscaling a large ensemble (like CMIP5 simulations). Mezghani et al. (2018) found that selecting a subset of GCMs in downscaling (EURO-CORDEX simulations) has

an impact on the magnitude of the estimated signal. Results over Poland show that taking a small subset of GCMs to drive regional climate models leads to a significant reduction in the spread of future climatic changes, especially for precipitation, while the ensemble mean remains less affected. Both approaches, ESD and DD, showed similar tendencies of change signal for the near future but disagreed in projecting changes for the far future.

Piniewski et al. (2017b) examined projections of future changes in temperature and precipitation in the drainage basins of two large rivers, the Vistula and Odra/Oder (VOB), covering 88% of the Polish territory and also smaller areas in five Poland’s neighbor countries (Czech Republic, Slovakia, Ukraine, Belarus, and Germany). Results were similar to those obtained by Mezghani et al. (2016) that spanned over the whole territory of Poland. Piniewski et al. (2017b) found that changes in annual mean of daily minimum and maximum temperature were fairly robust among models. These values were projected to increase by 1–1.5 °C in the near future and by 1.8–3.7 °C in the remote future (areal-means of the ensemble median values), depending on the emission scenario. Higher increases were consistently associated with minimum temperature. The lowest and highest increases were projected in SW and NE Poland, respectively. Seasonal projections of both minimum and maximum temperature were found to be less robust. Future warming in winter was projected to be higher than in other seasons, in particular for the remote future under the RCP8.5 scenario. However, projected changes in annual precipitation totals were highly uncertain, even though the climate models agreed on the increase. The mean multi-model increase ranged from 5.5% in the near future under RCP4.5 to 16.2% in the remote future under RCP8.5.

Pińskwar and Dobler (2018) examined projected changes in heavy precipitation in Poland, carrying out analysis for annual and seasonal data. The examined indices were: number of days with intense precipitation (in excess of 10 mm per day), as well as 95th and 99th percentiles of daily precipitation. The number of days with heavy precipitation was shown to increase for both annual and seasonal data, in particular during spring and summer. Trends detected for all stations showed increases for winter and spring. Also, the 95th and 99th percentiles of precipitation increased for annual data, while the highest seasonal increase for the 99th percentile was found during winter and spring. Generally, increases in extreme precipitation were projected in all seasons, time horizons and scenarios. The increases grew from the near to the far future and from RCP4.5 to RCP8.5.

Szwed et al. (2018) examined the projections of maximum snow cover depth in Poland for near and remote future, under two emission scenarios (RCP4.5 and RCP8.5). The bias-adjusted daily temperature and precipitation projections (Mezghani et al. 2017) were used as the input data



to the seNorge ([www.seNorge.no](http://www.seNorge.no)) snow model to generate future daily snow conditions. Projections suggest that the maximum snow depth may decrease by both future horizons of relevance and under both RCPs. This rate of decrease is expected to be about 15% and 20%, assuming the RCP4.5 and RCP8.5 emission scenarios, respectively, for near time horizon, as compared to the reference dataset. Overall, the rate of decrease could even double by the far future, regardless of the emission scenario and may go down to more than 40% when assuming the high emission scenario RCP8.5. Nevertheless, even if most areas in Poland are expected to get affected, changes in central regions are less pronounced.

## Climate change impacts

### Trend detection in river discharge

Piniewski (2017) analyzed classification of natural regimes of river discharge in Poland. Piniewski et al. (2018a) examined long-term trends in values of selected observed discharge indices in small- and medium-sized, near-natural catchments (with relatively unmodified flow regime) in Poland, over two time intervals (1956–2016 and 1981–2016). Geographical coverage of this study can be rated as adequate, while some regions with less human impact (such as NE Poland) have a relatively stronger representation. Piniewski et al. (2018a) examined changes in indices describing annual and seasonal average conditions as well as annual extremes—low and high discharges. The special focus was on the spatial analysis of trends, on the basis of a comprehensive, representative, river flow record in Poland. Piniewski et al. (2018a) filled a substantial gap existing in the scientific literature, because there have been no earlier studies on trend detection in observed discharge records covering the entire country or its large parts, carried out for recent data. The results of Piniewski et al. (2018a) suggest that a strong random (or natural variability) component exists in the river discharge process. The detected changes are rather weak and their spatial pattern is complex. For both studied periods of observation records and for two subsets of stations (providing a longer time series of records at fewer stations and a shorter series at more stations), negative trends in mean annual river discharge were found to prevail. Yet, the results of trend detection in values of various indices of river discharge in Poland demonstrated the existence of a spatial divide that seems to hold quite generally for different analyses—for annual, seasonal, as well as low and high discharge records. Decreases in river discharge dominate in the north of Poland and increases usually dominate in the south, while stations in the central belt of the country mostly do not show any trend. However, the spatial gradient is apparent only for the data for the shorter, more recent,

interval (1981–2016) and not for the entire, longer, interval, 1956–2016, for which records are available. It seems that the magnitude of increases in river flow is generally lower than that of decreases. In contrast, for the longer time interval 1956–2016, no trends were identified for about half of the stations throughout Poland. It can be interesting to note that decreases in low flow were observed in areas where the mean river discharge is low already; hence, the streamflow-drought problems have likely been exacerbated there. It was found that some catchment properties correlate well with river discharge indices and the strongest predictor was the distance from the geographical center of the examined catchment to the Baltic Sea coast.

### Projections of river runoff

Model-supported studies of projections of river runoff have been undertaken in many countries and regions of Europe in the framework of climate change impact assessment for the water sector (cf. Hattermann et al. 2011), yet such large-scale studies have been very scarce in Poland. Piniewski et al. (2017a) assessed climate change impacts on spatiotemporal distribution of annual and seasonal runoff in the entire Vistula and Odra basins (VOB). They used the SWAT model, set up at high resolution and driven by a multi-model ensemble of nine bias-corrected EURO-CORDEX simulations under two representative concentration pathways (RCPs), 4.5 and 8.5. Piniewski et al. (2017d) illustrated the annual and seasonal runoff in the reference period as well as projections for the future, including the multi-model spread based on the agreement between models and statistical significance of change according to each model. Annual runoff increases were found to dominate, regardless of RCP and future horizon. The magnitude of the mean, spatially averaged, runoff was found to increase, meaningfully, by 15.8% (RCP4.5, near future) up to 41.6% (RCP8.5, remote future). The seasonal patterns indicate the highest increase in winter and the lowest in spring, whereas the spatial patterns show the highest increase in the inner, lowland part of VOB, and the lowest in the southern, mountainous, part. Accompanying projections of potential evapotranspiration estimated using the Hargreaves method implemented in SWAT suggested modest ensemble mean increase, ranging from 2.9% for RCP 4.5 in the near future to 8.8% for RCP 8.5 in the far future (Piniewski et al. 2017d).

Piniewski et al. (2017a) compared the projections of mean annual and mean seasonal river runoff obtained with the help of the SWAT model with projections derived with the help of the lumped, conceptual, HBV model, for eight catchments in Poland, of small and medium size. Although increases in mean discharge indices were projected in both studies, the magnitudes of changes were largely different, in particular for the lowland catchments and especially in

the remote future. In the latter case, the SWAT-projected increases were significantly lower than the HBV-projected increases in all seasons, except for winter. Thus, uncertainty in river flow projections was found to be high and this creates a serious challenge for practitioners. Work on hydrological model inter-comparison should be continued, so that the mechanisms responsible for differences in hydrological projections in Poland derived using different models are better understood and interpreted.

### Water quality

Two mesoscale models were calibrated and used, for two medium-sized lowland catchments in Poland, the Barycz and the Upper Narew (which are subcatchments of the VOB), for nitrogen, phosphorus and sediment load assessments and projections (Marcinkowski et al. 2016, 2017). These catchments represent two important categories of conditions characteristic for the Polish Plain: a higher human pressure on water resources in the West (Barycz) and a lower pressure in the East (Upper Narew). Projections of the amount of total nitrogen (TN) and total phosphorus (TP) losses and of sediment that is transported from land areas to the stream network were derived, using the same climate model dataset as in Piniewski et al. (2017a), but only for the RCP4.5 scenario. Ensemble median in TN losses for the Barycz catchment in the remote future was projected to increase by 35%, whereas an even stronger increase, by 45%, was projected for the Upper Narew basin. Projections of TP losses indicate moderate increases for the Upper Narew catchment, whereas there is high uncertainty for the Barycz catchment. A strong correlation was found (Marcinkowski et al. 2016, 2017) between the river runoff and TN load (in particular nitrates), related to high mobility of nitrates that are not assimilated by plants during the dormancy season, but rather transported to streams via subsurface flow. These processes are favored especially in winter and spring, when evapotranspiration is typically low and infiltration can be fairly high due to snowmelt.

### Floods and droughts

Climate extremes tend to have considerable impact on sectors (cf. Hanson et al. 2007). In Poland, several destructive floods and extensive droughts have occurred in the last three decades (for example: floods in 1997, 2001 and 2010 and droughts in 1992, 1994, 2006, 2008, 2015 and 2018). As phrased by Milly et al. (2008, 2015), “stationarity is dead,” hence projections of high and low discharges are of considerable interest. They can play an important role in assessment and reduction in flood and drought risk (e.g., determination of a 100-year flood or a 100-year drought). Piniewski et al. (2017e) developed projections of high and low river discharges in the VOB. Despite a substantial spread of the

resultant projections, the principal finding was that increases in both high and low discharges are likely to dominate in the future (Fig. 2). The magnitude of increase in low discharge was found to be considerably higher than that of high discharge, that is, future streamflow droughts were projected to be less severe, whereas, in contrast, river floods were projected to increase. This latter change is likely to exacerbate a challenge for river flood risk reduction, water management, and climate change adaptation. Piniewski et al. (2017e) also took a broader perspective, presenting a review of projections of high and low discharges in Central and Eastern European river basins reported in the literature, and unveiling uncertainty. However, they noted an overall qualitative agreement of their findings for the VOB region with projections of hydrological extremes from large-scale models forced by EURO-CORDEX results in the European-scale studies.

Kundzewicz et al. (2017g) examined observed and projected changes in flood hazard in Europe. They analyzed spatial and temporal variability of large floods, using a time series of flood-related information for 1985–2016, collected by the Dartmouth Flood Observatory (USA). They noted that it is difficult to disentangle the climatic change component from strong natural variability and direct human impacts. The climate change impact on river flood hazard in Europe is complex and depends on the flood generation mechanism. No ubiquitous, spatially consistent, changes in flood hazard characteristics in observation records have been detected, so far. However, Kundzewicz et al. (2017g) found an increasing tendency in the number of observed floods with large magnitude and severity in Europe, even if the year-to-year variability was strong.

Kundzewicz et al. (2017e, g) found considerable differences in a set of studies of flood hazard projections in Europe and tried to interpret them. They noted a considerable spread of projections among studies reported in the academic literature, carried out under different assumptions. Therefore, caution must be exerted by practitioners when trying to interpret conflicting pieces of information on flood hazard projections, stemming from different sources.

Wyźga et al. (2018) examined various approaches to river flood risk reduction in the region of the Upper Vistula Basin, demonstrating that nature-based methods can lend themselves well to extend the traditional, structural, flood defense strategy. The work by Wyźga et al. (2018) extends the scope of the FLORIST project (Kundzewicz et al. 2014, 2017h), carried out for the northern foothills of the Tatra Mountains.

### Environment

In accordance with the projections that showed a prevailing increase in annual and seasonal runoff, as well as in low and high flows in the majority of rivers in the VOB,

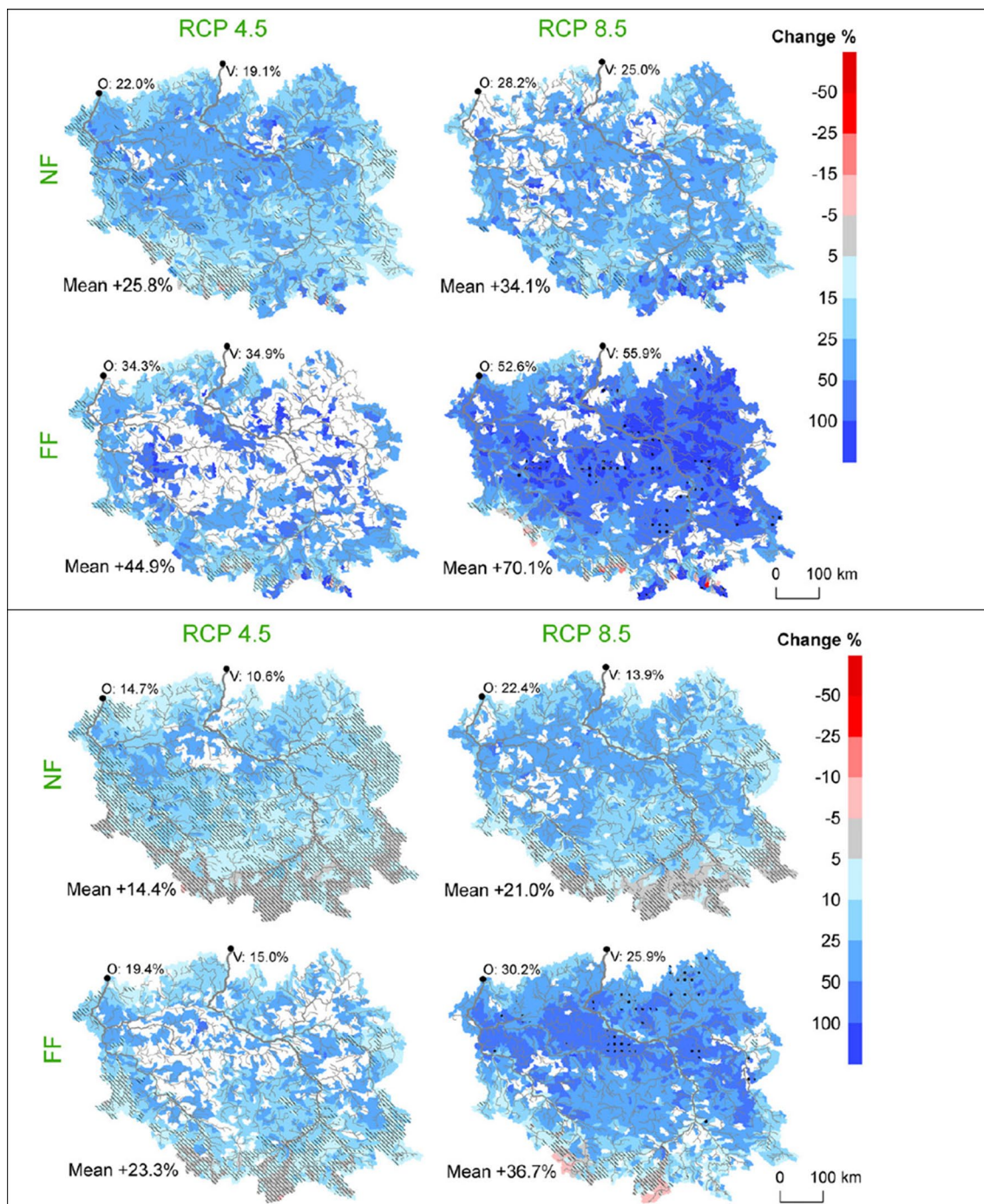


**Fig. 2** Changes in low flow indicator—daily Q90 (top) and in high flow indicator—daily Q10 (bottom) *Source:* Piniewski et al. (2017e, by permission), modified

other hydrological variables such as inundation frequency and soil moisture content in selected groundwater-fed wetlands were also projected to be on the rise in the future climate (Kundzewicz et al. 2017a, b). The rate of increase was found to be typically higher for the far future than for the near future, and higher for RCP8.5 than for RCP4.5. An overall conclusion was that in-stream and riparian biota

would face a new norm in their habitats. Projected changes in soil moisture for groundwater-fed wetlands suggest that their abiotic conditions are not likely to change significantly. The changes in high flows as well as in soil moisture content obtained with the help of models forced by rainfall and temperature projections for changing climate suggest that wetlands which are well adapted to wet conditions should



be the least affected ecosystems. However, potential increase in soil moisture or in frequency of flooding may initiate the biological and ecological processes of changes in the wetland. Research on this topic is especially important in Natura 2000 special areas of conservation, where the current status of habitats is protected.

Derived projections suggest that the future climate will cause significant alterations in streamflow conditions important for migration and spawning of northern pike (*Esox lucius*), chub (*Squalius cephalus*) and Atlantic salmon (*Salmo salar*) in the VOB (O’Keeffe et al. 2018). Atlantic salmon, which is a species migrating long distances to spawn, is under the highest impact. Increased streamflow during spawning migration (September–October), along with the increased number and duration of low pulses, may cause deceptive spawning cues and impact the breeding success by suspending or reducing the number of spawning individuals. The projected increase in streamflow during spawning (November–December) and rising duration of high pulses could contribute to washing out eggs and alevins mortality. Chub prefers high flows for spawning and is slightly affected by flooding thus increase in the median duration of low pulses could be harmful to this fish but the increased flow in the spring might be beneficial. Furthermore, increased spring flows might impact the spawning success of northern pike. As this species deposits eggs in flooded areas, this can impact northern pike in a dual way. Either it can increase days with floodplain inundation and connectivity which would be advantageous for the species or cause an abnormal high streamflow or flash floods that could wash away the fish. Northern pike favors little variability in flow and, in the conditions of climate change, a fluctuation between low and high flows could become more rare.

Whether those fish will be able to adapt, considering the speed of changes projected to occur, is uncertain. Projecting impact of climate change on fish is a pressing matter, and the study of O’Keeffe et al. (2018) allowed to get a glimpse into what might happen when streamflow conditions important for migration and spawning are altered.

## Agriculture

Agricultural sector in Poland is of high social and economic importance and the number of professionally active population in agriculture in Poland is higher (both in absolute and relative terms) than in any other country of the European Union. Since agriculture strongly depends on climatic conditions, the observed and projected climate change raises considerable interest and concern in the sector. Kundzewicz and Kozyra (2017) tackled climate change impacts on agriculture in Poland, both in the context of past observations (where strong inter-year variability is evident) and model-based projections for the future. Climate changes, and in

particular increases in temperature and changes in rainfall, have strong impacts on agriculture notably via weather extremes—droughts and heat waves as well as heavy precipitation and do indeed significantly affect crop growth.

Marcinkowski and Piniewski (2018) examined the impact of climate change on sowing and harvesting dates of selected crops in Poland. They found that projected warmer climate considerably affects scheduling of agricultural practices, accelerating sowing and harvesting dates across the entire country. The acceleration rate is strongly dependent on the future time horizon of concern and the RCP scenario, and the highest advancement is projected for far future under RCP8.5, reaching 23 and 30 days, for spring barley and maize, respectively. Evidence shows that soil moisture anomalies (deficits or excesses) are the key factor affecting crop growth in rain-fed agriculture, dominating in the country. In recent decades, major soil moisture anomalies have been recorded, leading to severe crop failures. Piniewski et al. (2018b) simulated multi-annual variability of soil moisture anomalies in Poland and assessed the effect of climate change on extreme soil moisture conditions in the future, that can adversely affect crop yields. A crop-specific (winter cereals, spring cereals, potato and maize) indicator based on simulated daily soil moisture content during the crop development stages with critical soil moisture requirements) was designed, evaluated for the past conditions against empirical crop-weather indices and applied for studying future climate conditions. For spring cereals, potato and maize, despite a large model spread, projections generally showed increasing severity of soil moisture deficits, as well as an increase in the total area affected by them. The signals of change in soil moisture excesses for potato and maize largely depended on selection of RCP and future horizon.

## Heat waves and mortality

Graczyk et al. (2018) examined mortality triggered by heat waves in Poland. They estimated a likely number of additional fatalities in 10 largest cities of Poland, recorded during, and immediately after, heat waves in particularly hot summer seasons. Since 1989, four summer seasons with intense, long-lasting, heat waves occurred in 1992, 1994, 2006 and 2010, with a considerable increase in the number of deaths in the largest towns in the country. The numbers of fatalities in heat wave days and some interval afterward were compared to the numbers of fatalities in the same calendar days in reference years without heat waves. An increase in mortality risk for people over 65 years of age and for those with cardiovascular deficiencies was noted. The total number of additional fatalities related to heat waves could have exceeded a thousand in 1994. During the hottest days in the analyzed period, in some cities, the number of fatalities was



more than three times higher than the mean value for the reference period.

In the scientific literature related to mortality increase due to heat waves, it is often underlined that densely populated areas are at the highest risk. Nevertheless, since increase in mortality during heat waves can occur in smaller towns and in rural areas, the number of additional fatalities in the entire Poland is likely to be considerably higher.

The results of Graczyk et al. (2018) indicate that the increase in mortality related to heat waves is a serious threat in Poland already in the present climate and is likely to be even more severe in a future “warmer” climate. If climate model projections come true, then the most tragic heat wave in Poland, that took place in 1994, will be more commonplace in the coming decades. The “load” is increasing, because heat waves get more intense and last longer, while the “resistance” is decreasing because the number of aged people in the Polish society is growing fast.

## Uncertainty and perception

The scientific evidence related to climate change and its attribution, impacts and possibilities of mitigation has been dynamically increasing. Yet, “climate change contrarianism” persists in many countries, rhyming with the observed general crisis of confidence to scientists and the triumphal advent of alternative post-truth realities, wherein discourse is framed largely by appeals to emotion disconnected from facts. This general tendency can be noted in many countries, including Poland and Norway, that is countries collaborating in the CHASE-PL project—that are fossil fuel giants with vocal contrarians, cf. Kundzewicz et al. (2017c) and Ceglaz et al. (2018). The public discourse in Poland, related to energy issues, concentrates to a large extent on the energy independency and security that are grounded on the rich domestic coal deposits, whereas the environmental dimension of the energy policy is conveniently downplayed. The access to the domestic fossil fuels is believed to ensure a regular economic development and low electricity price. It is also an argument for less interest in developing renewable energy sources in Poland. Most politicians, backed by the media and the coal and energy industry, explicitly undermine the scientific evidence of climate change.

Climate change and climate change impact studies would be incomplete without consideration of uncertainties that are plentiful in understanding, observations and projections, as well as the issues of perception. Three related uncertainty aspects of particular relevance can be distinguished: identification of uncertainty sources, quantification of uncertainty components, and devising a framework for uncertainty reduction. The concepts of uncertainty play a prominent role in the research on global environmental change. We

are uncertain about the future, but also—to some extent—about the recorded history and even the present. Kundzewicz et al. (2018) reviewed the use of the uncertainty notion to process understanding and modeling of systems, detection of change in observation records, and—foremost—projections of climate change impact on water resources for future time horizons. They presented a framework of proposing and assessing measures that could improve uncertainty communication, by relying on model ensembles and multi-model probabilistic approaches. Kundzewicz et al. (2018) distinguished two management strategies for the case of irreducible uncertainty—the precautionary principle and the adaptive management.

Kundzewicz et al. (2017d) discussed the challenges for developing national climate services in two countries—Poland and Norway, whose fossil fuel production is high. Poland is a major producer of coal while Norway—of oil and gas. In both countries, weather services are advanced, but the stages of development of climate services are largely different. In Norway, where downscaling of climate models commenced more than 20 years ago, tailored climate change projections have been made available to the broad society. Now, climate services are well developed—the Norwegian Centre for Climate Services (NCCS) has been operating since 2011. In contrast, climate services in Poland actually do not exist and this is not an exception among countries of Central and Eastern Europe. Many countries in the region neither have their national climate services nor are interested in European climate services enhanced via EU initiatives. The information generated within the CHASE-PL project, that has been broadly disseminated in Poland, could be regarded as a temporary (extending over the project duration) substitute for the kind of information that in other countries is delivered to the society by national climate services.

## Generated datasets

In order to prepare the basis for water-related impact studies, Piniewski et al. (2017d) applied the SWAT (Soil Water Assessment Tool) model in the entire Vistula and Odra basins (VOB), in order to assess the water balance and simulate natural streamflow. Since these basins include parts of five Poland’s neighbor countries, the study has an international relevance. This was quite a large task, because model-based high-resolution analysis for the whole river basins of the Vistula and the Odra has never been conducted in Poland before. The CHASE-PL forcing data—gridded daily precipitation and temperature dataset-5 km (CPLFD-GDPT5) that consisted of daily minimum and maximum air temperatures and precipitation totals, for the control interval, 1951–2013, interpolated onto a 5-km grid based on daily meteorological

observations (Berezowski et al. 2016) was used as driving climate dataset. A multi-site calibration approach allowed to achieve satisfactory goodness-of-fit across a range of catchment sizes and types. Model calibration and evaluation, driven by high-resolution climate data, showed satisfactory overall behavior for 80 benchmark catchments divided into eight clusters. The spatial evaluation performed for 30 gauges led to the conclusion that the designed parameter regionalization scheme performed quite well, with the median value of Kling–Gupta efficiency (KGE) of 0.76. The study by Piniewski et al. (2017d) can serve as a basis for work on projections of climate change impacts on water resources and their management, assessing flow alterations, agriculture and environment. The model output dataset (CHASE-PL natural hydrology, CPL-NH) is publicly available as an online research data archive (<https://data.4tu.nl/repository/uuid:b8ab4f5f-f692-4c93-a910-2947aea28f42>).

Mezghani et al. (2016) compiled and published the CHASE-PL climate projections—gridded daily precipitation and temperature dataset-5 km (CPLCP-GDPT5), consisting of projected daily minimum and maximum air temperatures and precipitation totals. This high-resolution bias-corrected product can serve as a basis for climate change impact and adaptation studies for selected sectors in Poland.

The CHASE-PL project provided open access datasets for researchers. This included forcing data for

environmental models (historical, observation-based, for the interval 1951–2013) and model-based projections for two future time horizons: 2021–2050 and 2071–2100, as well as SWAT simulations: water balance and streamflow in the historical control interval and future horizons. The data are available in open access at online data repository—4TU Centre for Research Data <https://data.4tu.nl/repository/> (or Google search: CHASE-PL data). Selected data were published in high-impact, open access, data journals (Berezowski et al. 2016; Mezghani et al. 2017). The dataset of model outputs based on all simulations, driven by the results of bias-corrected models in the EURO-CORDEX initiative (Mezghani et al. 2016), called CHASE-PL—future hydrology (CPL-FH), is also publicly available (Piniewski et al. 2017f).

The datasets produced within the project are freely available for research purposes. When reusing the data, one should clearly refer to the name(s) of the original author(s). Yet, for commercial purposes, no free use of data is guaranteed.

Within the CHASE-PL project, a geoportal was developed at the Warsaw University of Life Sciences (SGGW) under the leadership of Ignacy Kardel (Fig. 3). This interactive web-mapping system (<http://climateimpact.sggw.pl>) provides spatial, interactive, visualization of observed and projected climate change and its impact on selected sectors in Poland. The geoportal was awarded a prize in the Internet

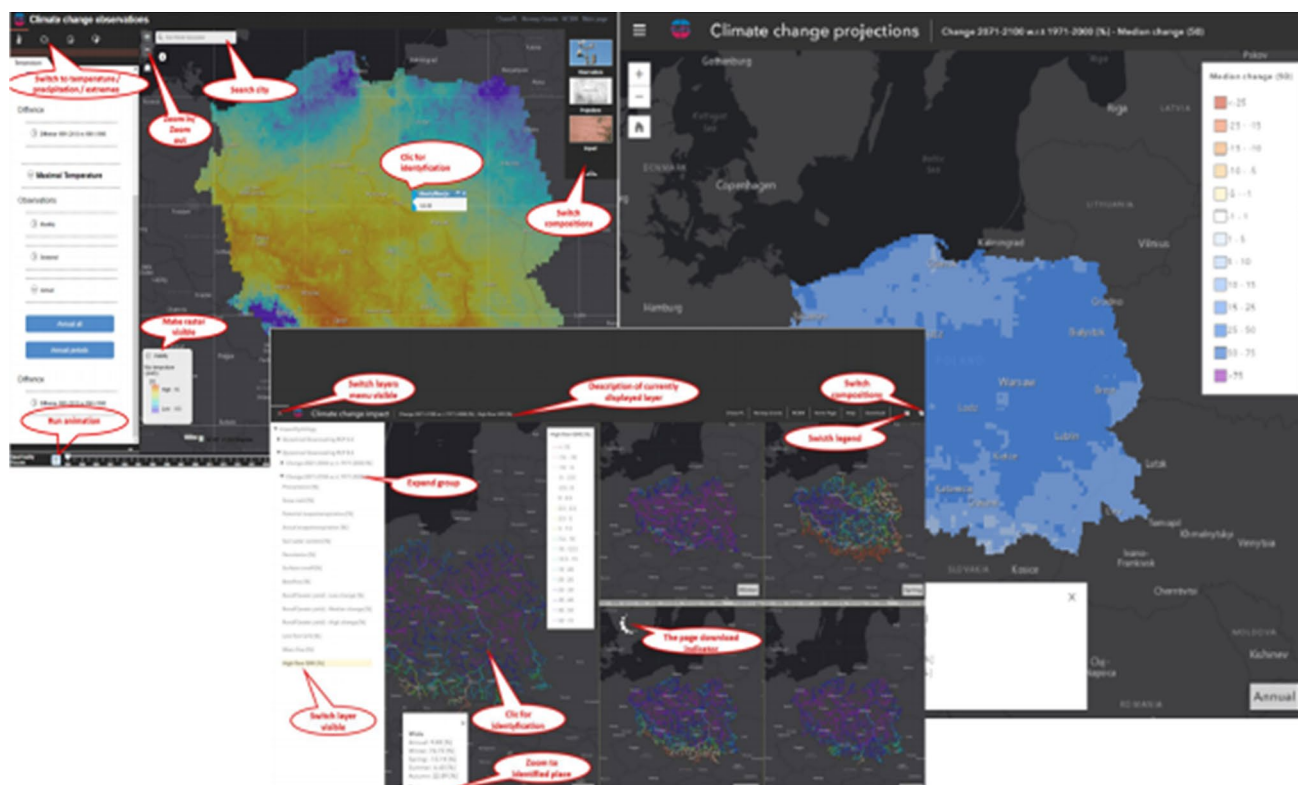


**Fig. 3** A sample of screenshots from the climate change geoportal, created within the CHASE-PL project (<http://climateimpact.sggw.pl>)

**Table 1** The summary of findings on observed changes in climate variables in Poland

Variable	Observed change	Projected change	References
Temperature	Well visible positive trend. Yet, large deviations from the trend in particular years	Projected changes, estimated from the multi-model ensemble (nine climate simulations), showed that annual temperature mean is expected to increase by about 1 °C until 2021–2050 and by about 2 °C until 2071–2100 under RCP4.5 emission scenario. Under RCP8.5, the warming is likely to be stronger, reaching almost 4 °C by 2071–2100. The warming is projected to be stronger in winter than in other seasons	Graczyk et al. (2017), Mezghani et al. (2016), Piniewski et al. (2017b)
Precipitation	Many changes detected, but mostly statistically insignificant at the 10% level. In general, the trend is weak and inter-annual and inter-decadal variabilities are dominating. Increases in the monthly sums and in the share of monthly precipitation within the annual sum were observed during the colder half-year, especially in March (with statistically significant trend for several stations)	Increase in regional annual precipitation is expected, of the order of 6–10% and 8–16% for 2021–2050 and 2071–2100, respectively	Pińskwar et al. (2018a, b), Szwed et al. (2017), Mezghani et al. (2016), Piniewski et al. (2017b)
Thermal extremes	Statistically significant increases in the number of hot days in summer, the number of tropical nights in a year, and duration of the longest hot spell in summer for most of the data	Not assessed in the CHASE-PL project. Yet, thermal extremes are projected to be on the rise	Graczyk et al. (2017), Szwed et al. (2010)
Precipitation extremes	Daily maximum precipitation in summer half-year as well as 5-day and monthly precipitation totals increased for many stations. The number of days with intense precipitation was found to increase, especially in NW Poland. The number of consecutive dry days has increased for many stations in the summer half-year. During 1991–2015, most statistical indices (25th and 75th percentiles, median, mean and maximum) of precipitation were higher than during 1961–1990. However, most detected changes were statistically insignificant	The number of days with heavy precipitation was shown to increase in both annual and seasonal analysis, in particular during spring and summer. In analysis of annual data, the 95th and 99th percentiles of precipitation were projected to increase. The highest seasonal increase for the 99th percentile was projected during winter and spring. Generally, increases in extreme precipitation were projected in all seasons, time horizons and scenarios, growing from the near to the far future and from RCP4.5 to RCP8.5	Pińskwar et al. (2018a), Pińskwar and Dobler (2018)
Snow	In general, less abundant snow cover in Poland. Yet, complex change, with strong temporal and spatial variability. Statistical links between the North Atlantic Oscillation (NAO) index and the snow characteristics (snow depth, and the number of snow cover days) were detected	The maximum snow depth is projected to decrease by two future horizons and under both RCPs. This decreasing rate is expected to be about 15% and 20%, under RCP4.5 and RCP8.5, respectively, for the near time horizon. The rate of decrease could even double by the far future under RCP8.5	Szwed et al. (2017, 2018)

**Table 2** The summary of findings on observed and projected changes in climate impact variables in Poland

Variable	Observed change	Projected change	Reference
River discharge	Negative trends in mean annual river flow were prevailing. Results of trend detection in various indices of river flow in Poland demonstrated existence of a spatial divide, holding quite generally for annual and seasonal values. Decreases in river discharge dominate in the north of Poland and increases usually dominate in the south, while stations in the central belt mostly do not show any trend. Trends were apparent only for the shorter, more recent, interval (1981–2016), while for the longer interval 1956–2016, no trends were identified in about half of gauging stations analyzed	Annual runoff increases were found to dominate, regardless of RCP and future horizon. The magnitude of the multi-model ensemble mean of spatially averaged runoff increase varied between 15.8% (RCP4.5, near future) and 41.6% (RCP8.5, far future). The seasonal patterns show the highest increase in winter and the lowest in spring, whereas the spatial patterns show the highest increase in the inner, lowland part, and the lowest in the southern, mountainous, part of VOB	Piniewski et al. (2017c, 2018a)
Low and high flows	There exists a spatial divide, holding for both low and high discharges as for mean values (see cell above). Decreases dominate in the north of Poland and increases usually dominate in the south. Decreases in low flow were observed in areas where the mean river flow is low already, hence, the streamflow-drought problems have been exacerbated	Increases in both low and high flows are likely to dominate. The magnitude of increase in low flow is considerably higher than that of high flow, that is, future streamflow droughts were projected to be less severe, whereas, in contrast, river floods are projected to increase, exacerbating a challenge for flood risk reduction, water management, and climate change adaptation	Piniewski et al. (2018a, 2017e)
Water quality	Not assessed in the CHASE-PL project	Increase in TN losses projected for two analyzed catchments (of the Barycz and the Upper Narew). Projections of TP losses show moderate increases for the Upper Narew basin	Marcinkowski et al. (2016, 2017)
Environment	Not assessed in the CHASE-PL project	In-stream and riparian biota may face a new norm in their habitats. A significant increase in soil moisture and in frequency of flooding may initiate biological and ecological processes of changes in the wetlands. Alterations in streamflow conditions are important for migration and spawning of fish	O'Keeffe et al. (2018)
Agriculture	Changes in several agriculture-related indices observed, with large inter-annual variability	Projected warming considerably affects scheduling of agricultural practices, accelerating sowing and harvesting dates. The highest advancement is projected for the far future under RCP8.5, reaching 23 and 30 days, for spring barley and maize, respectively. For spring cereals, potato and maize, increasing severity of soil moisture deficits, as well as increase in the total area affected by them were projected	Kundzewicz and Kozyra (2017), Marcinkowski and Piniewski (2018), Piniewski et al. (2018a, b)
Health	An increase in mortality risk for people over 65 years of age and for those affected with cardiovascular diseases was noted. The total number of additional heat-related fatalities could have exceeded 1070 in the summer of 1994	The increase in mortality during heat waves is a serious threat in Poland already in the present climate and is likely to be even more severe in a future “warmer” climate, since the heat waves are projected to be more commonplace in the future. The “load” will likely increase (heat waves get more intense and last longer), while the “resistance” will likely decrease, because the number of aged people in Poland is virtually certain to continue to grow faster	Graczyk et al. (2018), Szwed et al. (2010)



**Fig. 4** Cover of the monograph, in English and in Polish, summarizing the results of the CHASE-PL project (Kundzewicz et al. 2017a, b)



Map of the Year contest, 2016/2017, organized by the Society of Polish Cartographers.

The information contained in the geoportal enables other researchers to use project results in their own studies on climate change and climate change impact. The co-authors of this paper believe that free and easy access to processed historical data as well as projections enhances further work, hence contributing to better understanding and interpretation of climate change and associated impacts in Poland.

## Discussion and conclusions

Tables 1 and 2 illustrate the summary of CHASE-PL project's findings on observed and projected changes in climate variables, as well as in climate impact variables, respectively.

The co-authors of this paper, who participated in the Polish–Norwegian CHASE-PL project trust that the project results contributed, in a considerable way, to improvement of understanding and interpretation of climate change impacts in such sectors, as: water resources, natural hazard risk reduction, health, agriculture and environment of Poland. It extended the state-of-the-art of the detection of change, projection of climate change and its impacts, as well as interpretation of uncertainty, and could contribute to improving general awareness. Planned project's objectives have been fully achieved and, actually, largely exceeded. Scientific outputs comprise: a book in Polish and English (Kundzewicz

et al. 2017a, b), cf. Fig. 4, and many journal papers, some of which are listed in references overleaf, generation of scientific data, and development of a climate change geoportal.

The CHASE-PL project linked strengths of scientists from both participating countries: Norway's traditions and achievements in climate research and Poland's expertise in climate impact research. Norwegian partners provided common climatic foundations by producing downscaled projections, while Polish partners took the lead in impact research. The CHASE-PL project scientists made an attempt to bring the activities of the climate impact and the climatology communities closer together. This helped reduce the traditional, disciplinary, “disconnect” between communities developing assessment and modeling frameworks for impact studies (e.g., related to water resources) and the communities developing climate modeling frameworks.

Valuable inputs were also obtained from co-authors from beyond the project, as documented in several references listed overleaf.

The lessons learned from climate change impact studies, applying the CHASE-PL information, can help in shaping adaptation strategies and rising awareness of importance of this area in Poland.

The project contributed to reduction in the knowledge gap on climate change and associated impacts among the policy-makers, stakeholders and the broad Polish society. It can be viewed as the substitute for national climate services that do not exist in Poland, even if the process updating the information was discontinued after the project end in April 2017.

**Acknowledgements** The CHASE-PL (climate change impact assessment for selected sectors in Poland) project was funded in the framework of the Polish–Norwegian Research Programme under the Norwegian Financial Mechanism 2009–2014 (Project Contract No. Pol Nor/200799/90/2014) is gratefully acknowledged. The Alexander von Humboldt Foundation and the Polish Ministry of Science and Higher Education supported Mikołaj Piniewski. Finally, the Institute of Meteorology and Water Management–National Research Institute (IMGW-PIB) provided the meteorological and hydrological data used in this study.

**Open Access** This article is distributed under the terms of the Creative Commons Attribution 4.0 International License (<http://creativecommons.org/licenses/by/4.0/>), which permits unrestricted use, distribution, and reproduction in any medium, provided you give appropriate credit to the original author(s) and the source, provide a link to the Creative Commons license, and indicate if changes were made.

## References

- Benestad R, Parding K, Dobler A, Mezghani A (2017) A strategy to effectively make use of large volumes of climate data for climate change adaptation. *Clim Serv* 6:48–54. <https://doi.org/10.1016/j.cliser.2017.06.013>
- Berezowski T, Szcześniak M, Kardel I et al (2016) CPLFD-GDPT5: high-resolution gridded daily precipitation and temperature dataset for two largest Polish river basins. *Earth Syst Sci Data*. <http://www.earth-syst-sci-data.net/8/127/2016/>. Accessed 2 Nov 2018
- Ceglarz A, Benestad R, Kundzewicz ZW (2018) Inconvenience vs. rationality. Reflections on different faces of climate contrarianism in Poland and Norway. *Weather Clim Soc (American Geophysical Union)*. <https://doi.org/10.1175/WCAS-D-17-0120.1>
- Deser C, Knutti R, Solomon S, Phillips AS (2012) Communication of the role of natural variability in future North American climate. *Nat Clim Change* 2:775–779. <https://doi.org/10.1038/nclimate1562>
- Graczyk D, Pińskwar I, Kundzewicz ZW et al (2017) The heat goes on—changes in indices of hot extremes in Poland. *Theor Appl Climatol* 129(1–2):459–471
- Graczyk D, Kundzewicz ZW, Choryński A et al (2018) Heat related mortality during hot summers in Polish cities. *Theor Appl Climatol*. <https://doi.org/10.1007/s00704-018-2554-x>
- Hanson CE et al (2007) Modelling the impact of climate extremes: an overview of the MICE project. *Clim Change* 81:163–177. <https://doi.org/10.1007/s10584-006-9230-3>
- Hattermann FF et al (2011) Model-supported impact assessment for the water sector in Central Germany under climate change—a case study. *Water Resour Manag* 25(13):3113–3134. <https://doi.org/10.1007/s11269-011-9848-4>
- Kundzewicz ZW, Matczak P (2012) Climate change regional review: Poland. *Wiley Interdiscip Rev Clim Change* 3(4):297–311
- Kundzewicz ZW, Kozyra J (2017) Climate change impact on Polish agriculture. In: Kundzewicz ZW, Hov Ø, Okruszko T (eds) *Climate change and its impact on selected sectors in Poland*. Ridero IT Publishing, Poznań, pp 158–171. ISBN 978-83-8104-735-7
- Kundzewicz ZW et al (2014) Floods at the northern foothills of the Tatra Mountains: a Polish–Swiss research project. *Acta Geophys* 62(3):620–641
- Kundzewicz ZW, Hov Ø, Okruszko T (eds) (2017a) *Climate change and its impact on selected sectors in Poland*. Ridero IT Publishing, Poznań
- Kundzewicz ZW, Hov Ø, Okruszko T (eds) (2017b) *Zmiany klimatu i ich skutki w wybranych sektorach w Polsce*. Poznań
- Kundzewicz ZW, Benestad RE, Ceglarz A (2017c) Perception of climate change and mitigation policy in Poland and Norway. In: Kundzewicz ZW, Hov Ø, Okruszko T (eds) *Climate change and its impact on selected sectors in Poland*. Ridero IT Publishing, Poznań, pp 216–244. ISBN 978-83-8104-735-7
- Kundzewicz ZW, Førland EJ, Piniewski M (2017d) Challenges for developing national climate services: Poland and Norway. *Clim Serv* 8:17–25
- Kundzewicz ZW, Krysanova V, Dankers R et al (2017e) Differences in flood hazard projections in Europe: their causes and consequences for decision making. *Hydrol Sci J* 62(1):1–14
- Kundzewicz ZW, Painter J, Kundzewicz WJ (2017f) Climate change in the media: Poland’s exceptionalism. *Environ Commun*. <https://doi.org/10.1080/17524032.2017.1394890>
- Kundzewicz ZW, Pińskwar I, Brakenridge GR (2017g) Changes in river flood hazard in Europe: a review. *Hydrol Res*. <https://doi.org/10.2166/nh.2017.016>
- Kundzewicz ZW et al (2017h) Changes of flood risk on the northern foothills of the Tatra Mountains. *Acta Geophys* 65(4):799–807
- Kundzewicz ZW, Krysanova V, Benestad RE et al (2018) Uncertainty in climate change impacts on water resources. *Environ Sci Policy* 79:1–8
- Łupikasza E (2010) Spatial and temporal variability of extreme precipitation in Poland in the period 1951–2006. *Int J Climatol* 30:991–1007. <https://doi.org/10.1002/joc.1950>
- Łupikasza E (2017) Seasonal patterns and consistency of extreme precipitation trends in Europe, December 1950 to February 2008. *Clim Res* 72:217–237
- Marcinkowski P, Piniewski M (2018) Climate change effect on sowing and harvest dates of spring barley and maize in Poland. *Int Agrophys* 32:265–271
- Marcinkowski P, Piniewski M, Kardel I et al (2016) Challenges in modelling of water quantity and quality in two contrasting meso-scale catchments in Poland. *J Water Land Dev* 31(X–XII):97–111. <https://www.degruyter.com/view/j/jwld.2016.31.issue-1/jwld-2016-0040/jwld-2016-0040.xml>. Accessed 2 Nov 2018
- Marcinkowski P, Piniewski M, Kardel I et al (2017) Effect of climate change on hydrology, sediment and nutrient losses in two lowland catchments in Poland. *Water* 9(3):156. <http://www.mdpi.com/2073-4441/9/3/156>. Accessed 2 Nov 2018
- Mezghani A, Dobler A, Haugen JE (2016) CHASE-PL climate projections: 5-km gridded daily precipitation and temperature dataset (CPLCP-GDPT5). Norwegian Meteorological Institute, Oslo. <https://doi.org/10.4121/uuid:e940ec1a-71a0-449e-bbe3-29217f2ba31d> (Dataset)
- Mezghani A, Dobler A, Haugen JE et al (2017) CHASE-PL climate projection dataset over Poland: bias adjustment of EURO-CORDEX simulations. *Earth Syst Sci Data* 9(2):905–925
- Mezghani A, Dobler A, Benestad R (2018) Subsample effect on the climate change signal based on simulations from statistical and dynamical downscaling. *J Clim* (submitted)
- Milly PCD et al (2008) Stationarity is dead: whither water management? *Science* 319:573–574
- Milly PCD et al (2015) On critiques of “stationarity is dead: whither water management?”. *Water Resour Res* 51(9):7785–7789. <https://doi.org/10.1002/2015WR017408>
- O’Keefe J, Piniewski M, Szcześniak M, Oglęcka P, Parasiewicz P, Okruszko T (2018) Index-based analysis of climate change impact on streamflow conditions important for northern pike, chub and Atlantic salmon. *Fish Manag Ecol*. <https://doi.org/10.1111/fme.12316>
- Piniewski M (2017) Classification of natural flow regimes in Poland. *River Res Appl* 33(7):1205–1218
- Piniewski M, Meresa HK, Romanowicz R et al (2017a) What can we learn from the projections of changes of flow patterns? results from Polish case studies. *Acta Geophys* 65(4):809–827

- Piniewski M, Mezghani A, Szcześniak M et al (2017b) Regional projections of temperature and precipitation changes: robustness and uncertainty aspects. *Meteorol Z* 26(2):223–234
- Piniewski M, Szcześniak M, Huang S, Kundzewicz ZW (2017c) Projections of runoff in the Vistula and the Odra river basins with the help of the SWAT model. *Hydrol Res*. <https://doi.org/10.2166/nh.2017.280>
- Piniewski M, Szcześniak M, Kardel I et al (2017d) Hydrological modelling of the Vistula and Odra river basins using SWAT. *Hydrol Sci J* 62(8):1266–1289
- Piniewski M, Szcześniak M, Kundzewicz ZW et al (2017e) Changes in low and high flows in the Vistula and the Odra basins: model projections in the European-scale context. *Hydrol Process* 31(12):2210–2225
- Piniewski M, Szcześniak M, Kardel I (2017f) CHASE-PL: future hydrology data set: projections of water balance and streamflow for the Vistula and Odra basins, Poland. Data <http://www.mdpi.com/2306-5729/2/2/14>. Accessed 2 Nov 2018
- Piniewski M, Marcinkowski P, Kundzewicz ZW (2018a) Trend detection in river flow indices in Poland. *Acta Geophys* <https://link.springer.com/article/10.1007%2Fs11600-018-0116-3>. Accessed 2 Nov 2018
- Piniewski M, Marcinkowski P, O’Keeffe J et al (2018b) Model-based reconstruction and projections of soil moisture anomalies and crop losses in Poland. *Agric For Meteorol* (submitted)
- Pińskwar I, Dobler A (2018) Observed and projected changes in heavy precipitation in Poland. *Met Hydrol Water Manag* (submitted)
- Pińskwar I, Choryński A, Graczyk D, Kundzewicz ZW (2018a) Observed changes in extreme precipitation in Poland: 1991–2015 versus 1961–1990. *Theor Appl Climatol*. <https://doi.org/10.1007/s00704-018-2372-1>
- Pińskwar I, Choryński A, Graczyk D, Kundzewicz ZW (2018b) Observed changes in precipitation in Poland. *Geografie* (submitted)
- Szwed M (2018) Variability of precipitation in Poland under climate change. *Theor Appl Climatol*. <https://doi.org/10.1007/s00704-018-2408-6>
- Szwed M, Karg G, Pińskwar I, Radziejewski M, Graczyk D, Kędziora A, Kundzewicz ZW (2010) Climate change and its effect on agriculture, water resources and human health sectors in Poland. *Nat Hazards Earth Syst Sci* 10:1725–1737. <https://doi.org/10.5194/nhess-10-1725-2010>
- Szwed M, Pińskwar I, Kundzewicz ZW et al (2017) Changes of snow cover in Poland. *Acta Geophys* 65(1):65–76
- Szwed M, Dobler A, Mezghani A, Saloranta TM (2018) Change of maximum snow cover depth in Poland. *Idojaras* (submitted)
- Wyźga B, Kundzewicz ZW, Konieczny R et al (2018) Comprehensive approach to the reduction of river flood risk: case study of the Upper Vistula Basin. *Science Total Environ* 631–632:1251–1267. <https://doi.org/10.1016/j.scitotenv.2018.03.015>



# Correction to: Application of Multichannel Analysis of Surface Waves to S-Phase Wave Anisotropy Estimation

Iwona Stan-Kłeczek<sup>1</sup> · Maciej J. Mendecki<sup>1</sup>

Published online: 29 November 2018  
© Institute of Geophysics, Polish Academy of Sciences & Polish Academy of Sciences 2018

## Correction to:

**Acta Geophysica vol. 64, no. 5, Oct. 2016, pp. 1593–1604**  
<https://doi.org/10.1515/acgeo-2016-0058>

In the original version of this article, the authors did not add on page 1602 the acknowledgement section between Conclusion and References.

The new section should be as follows:

## Acknowledgements

The project was partially funded by the National Science Centre granted under Decision No. UMO-2012/05/N/ST10/03943.

---

The original article can be found online at <https://doi.org/10.1515/acgeo-2016-0058>.

---

✉ Iwona Stan-Kłeczek  
[iwona.stan-kleczek@us.edu.pl](mailto:iwona.stan-kleczek@us.edu.pl)

Maciej J. Mendecki  
[mmendecki@us.edu.pl](mailto:mmendecki@us.edu.pl)

<sup>1</sup> University of Silesia, Faculty of Earth Sciences, Sosnowiec, Poland